Studi
Tissue Enginee

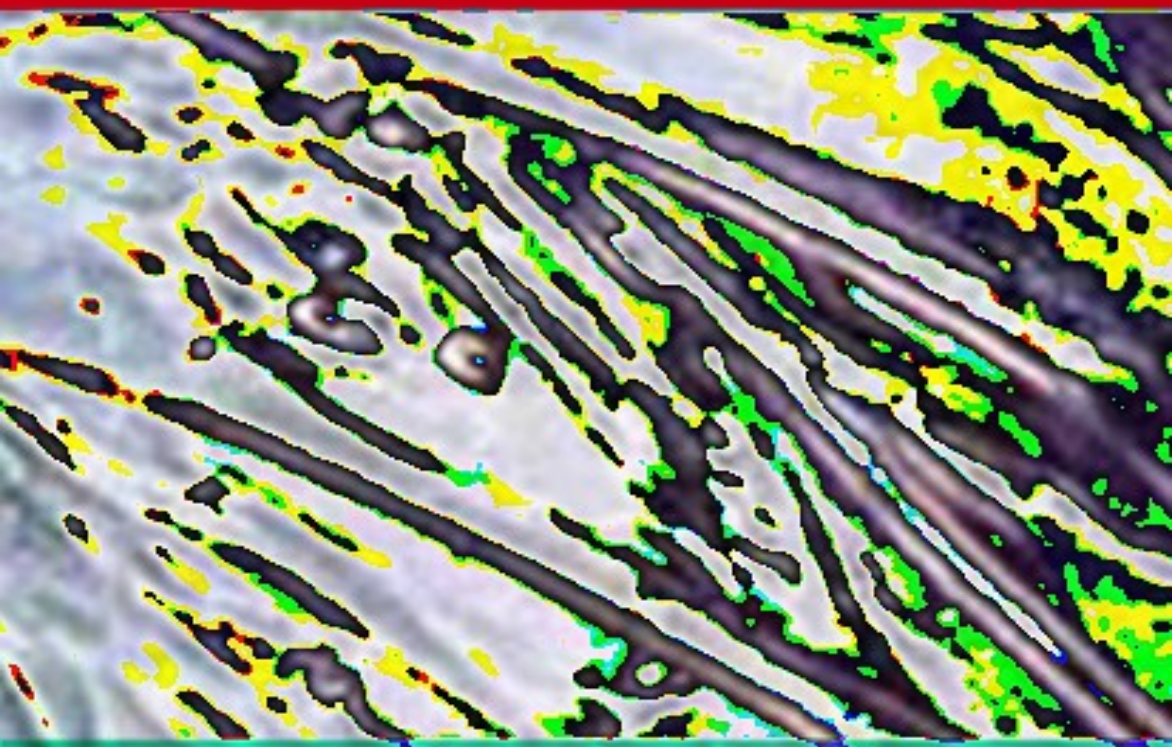

Cellular and
Biomolecula
and Mechan

Studies in Mechanobiology, Tissue Engineering and Biomaterials

Further volumes of this series can be found on our homepage:
http://www.springer.com/series/8415

Amit Gefen
Editor

Cellular and Biomolecular Mechanics and Mechanobiology

Springer

Prof. Dr. Amit Gefen
Department of Biomedical Engineering
Faculty of Engineering
Tel Aviv University
69978 Ramat Aviv
Israel
e-mail: gefen@eng.tau.ac.il

ISSN 1868-2006 e-ISSN 1868-2014

ISBN 978-3-642-14217-8 e-ISBN 978-3-642-14218-5

DOI 10.1007/978-3-642-14218-5

Springer Heidelberg Dordrecht London New York

Cover design: WMXDesign GmbH, Heidelberg

Printed on acid-free paper

Springer is part of Springer Science+Business Media (www.springer.com)

Preface

This volume focuses on one of the most innovative and exciting topics in biomedical engineering, and in biomechanics in particular: the new research domain of cellular and biomolecular mechanics, which practically only exists as a defined sub-field of biomechanics for the last 10 years or so.

Several factors contributed to our ability as biomechanists to now look at mechanical processes at the cellular and subcellular scales. First, there are the vast advances made in the field of microscopy, including fluorescence microscopy with specific staining of cellular and subcellular structures (some of which can be stained while cells are kept alive), as well as confocal microscopy which allows looking at cells in three-dimensions (3D). Second, there has been huge progress with mechanical testing methods at the cellular and subcellular levels, which today, other than classical cytoindentation and pipette aspiration, now include atomic force microscopy as well as magnetic and optical tweezers. Third, the progress in computational modeling, supported by the ever-increasing computer power, presently allows complex simulations that consider chemo- and mechano-communication between hundreds and thousands of cells, or calculation of mechanical loads within and around individual cells, where these cannot be measured directly. The abilities to observe living cells at high spatial and temporal resolutions and in 3D, to measure their mechanical properties or even mechanical properties of their components, and to model their behavior in computer simulations altogether allowed the major breakthroughs described in this book, in regard to basic cell science as well as applications in understanding disease processes or enabling design of better tissue engineering constructs. Accordingly, chapters in the book fall under the following categories: fundamental concepts and basic research, experimental methods in cell mechanics, computational modeling methods and applications, and the mechanobiology of cancer. Cancer in particular has been chosen as a paradigm for a disease that demonstrates the kind of progress allowed by cell mechanics research in understanding pathophysiological processes that not long ago were thought to have nothing in common with mechanics, whereas now, mechanics emerges as a key factor in the cell scale processes during the cascade of the disease

The research groups who contributed to this book, from 7 different countries - mostly in the USA and Europe - are all very well known internationally for their fundamental contributions to the field of cellular mechanics, and the book as a whole therefore represents the state-of-the-art of research in cell mechanics. The book also nicely demonstrates how cell mechanics research interacts with other recent scientific breakthroughs, including nanotechnology, tissue engineering and multiscale computation. Faculty and students with interest in these fields should find this book an excellent source of information indicating where cellular and biomolecular mechanics research brought us so far, and what are some of the open questions that wait to be answered.

Prof. Dr. Amit Gefen

Contents

Part IV Mechanobiology in Cancer

Part I
Fundamental Concepts

Cytoskeletal Mechanics and Cellular Mechanotransduction: A Molecular Perspective

Hamed Hatami-Marbini and Mohammad R. K. Mofrad

Abstract Cells are highly complex structures with unique physiology and biomechanical properties. A multiscale multiphysics methodology is required to properly understand the intrinsically coupled mechanobiology of the cell and describe its macroscopic response to externally applied stresses. This indeed is both a challenge and an excellent research opportunity. This chapter reviews the latest advancements in this field by bringing together the recent experimental and theoretical studies on the cytoskeletal rheology and mechanics as well as the dynamic response of the cell to environmental stimuli. The experimental observations along with computational approaches used to study the mechanical properties of the individual constituents of the cytoskeleton are first presented. Various computational models are then discussed ranging from discrete filamentous models to continuum level models developed to capture the highly dynamic and constantly changing properties of the cells to external and internal stimuli. Finally, the concept of cellular mechanotransduction is discussed as an essential function of the cell wherein the cytoskeleton plays a key role.

1 Introduction

Cells, the basic building blocks of all living things, are dynamic and ever changing systems composed of numerous components with distinct mechanical, chemical

H. Hatami-Marbini (✉)
Mechanical Engineering Department, Stanford University, Stanford, CA 94305, USA
e-mail: hhatami@stanford.edu

M. R. K. Mofrad
Department of Bioengineering, University of California, Berkeley, CA 94720, USA
e-mail: mofrad@berkeley.edu

Stud Mechanobiol Tissue Eng Biomater (2011) 4: 3–27
DOI: 10.1007/8415_2010_35

Published Online: 2 November 2010

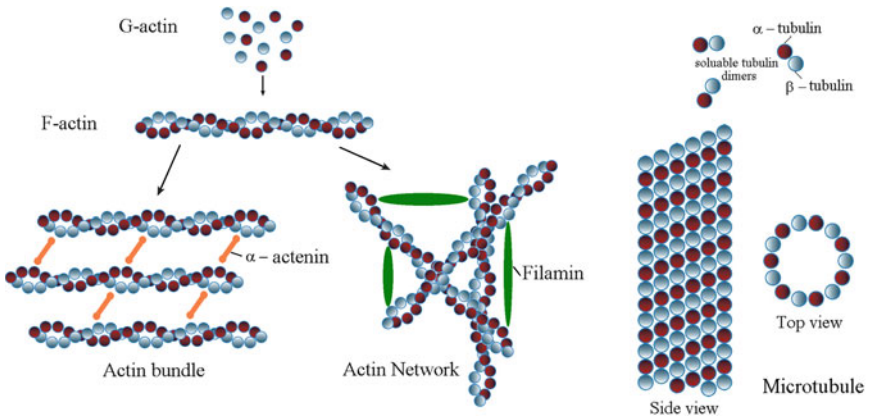

Fig. 1 Schematic representation of an actin filament and a microtubule

and biological properties. They perform a variety of biological functions many of which directly depend on their shape and structural stiffness. Cells respond to external mechanical stimuli and interact with their surroundings by changing their morphology and biological signaling which ultimately lead to functional adaptation and/or pathological conditions. The integrity and particular shape of a cell are maintained by the interplay of cell membrane with cytoskeleton, which forms the majority of cell's mass.

Cytoskeleton is a three-dimensional dynamic network through which water, solutes and small organelles diffuse while resisting weak osmotic fluid flows and serving as scaffolds for weak contractions. Cell can exhibit a range of material properties from a viscous fluid to an elastic gel depending on the length of its filamentous constituents and the degree of their cross-linkings in the solution. It behaves elastically in response to quick deformations while showing a viscous fluid-like behavior in slow deformations. A wide range of computational and experimental investigations have been conducted to understand the rheology and mechanics of the cytoskeleton and its main constituents. Current models show remarkable disparity largely due to the varied length scales and/or biomechanical issues of interest. Therefore, there is no unified and general model describing cytoskeleton rheology yet.

The three main building blocks of the cytoskeleton are actin microfilaments (MFs), microtubules (MTs), and intermediate filaments (IFs), each of which is a polymer comprised of protein subunits. Microfilaments and microtubules are both made of a chain of globular proteins but intermediate filaments are composed of long fibrous subunits. G-actin, the globular protein subunit forming the microfilaments, consists of two domains separated by a nucleotide binding cleft. G-actins bind together through their nucleotide clefts to form the filamentous actin (F-actin) that is basically two chains loosely wrapped around other, see Fig. 1.

The polymerization of actin occurs though the hydrolysis of the Adenosine-5′-triphosphate (ATP) of the actin subunit to adenosine diphosphate (ADP) plus an inorganic phosphate. This process yields a microfilament with distinguishable polar ends; the negative end is the exposed nucleotide cleft and the positive end is the one with the buried cleft. The polymerization prominently happens at the plus end. ATP is an unstable molecule, consisting of adenosine (formed by adenine ring and a ribose sugar) and three phosphate groups, which hydrolyses to ADP and phosphate. The conversion of ATP to ADP releases energy of about 30 kJ/mol. The subunits of a microtubule are called tubulin heterodimers; α-tubilin and β-tubilin, which bind guanine nucleotides. Fibrous proteins such as Keratin assemble to build different types of intermediate filaments. Unlike MFs and MTs, IFs do not bind to nucleotides.

The components of the cytoskeleton are constantly changing in order to accommodate cell dynamic processes such as cellular movement and division. The assembly and disassembly of microfilaments allow a cell to change its shape and to accommodate cellular movement. White blood cells are prefect examples where cells remodel microfilaments to move through capillary walls and enter damaged tissues. In order to change its shape, a cell uses various proteins such as capping, branching, and severing ones to regulate microfilament dynamics. For example, treadmilling is a dynamic process within the cell where the net rate of addition and removal of actin subunits from two ends of a microfilament are equal. The formation and morphology of actin cytoskeleton network is regulated by a variety of actin binding proteins (ABPs). ABPs are essential part of eukaryotic cells and play very important functions ranging from regulating assembly and disassembly of F-actins to controlling actin network dynamics and structure. A plethora of actin monomers along with a large number of actin-monomer-binding proteins are required for the rapid growth of actins in motile cells and also for sudden reorganization of actins in response to intra- and extra-cellular stimuli. These proteins are also essential for maintenance of cell structure integrity as they interconnect different cytoskeletal elements together. They connect actin to microtubules, actin to intermediate filaments or even actin to both of them (e.g., plectin). Another group of ABPs are molecular motor protein myosins which are necessary for the cytoskeleton dynamic behavior. They bind to actin filaments and move along them to do work within the cell by generating tensile forces. Myosin converts the chemical energy of the ATP into mechanical energy to move along the cytoskeletal substrate. For example, two-headed myosin II generates tension and contraction inside the cytoskeleton, Fig. 2.

The structure of the myosin consists of two identical heavy chains and two pairs of light chains. There are three distinguishable domains in each heavy chain, the head, neck and tail. The globular head domain contains binding sites for actin and is formed due to the folding one half of a single heavy chain. The other halves of the heavy chains twist around each other and form a helical fibrous structure. A pair of light chains exists in the neck domain (the connection between the head and the tail) in order to stiffen and stabilize this domain.

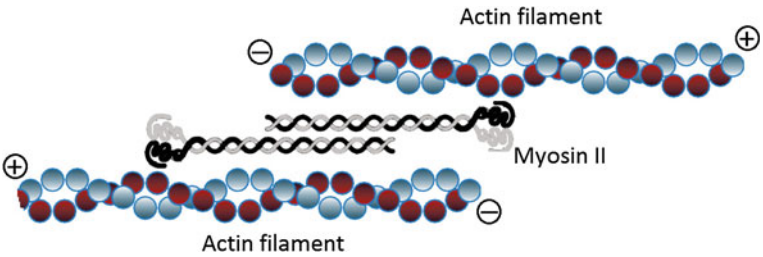

Fig. 2 Schematic of a bipolar myosin filament interacting with two actin filaments. The ± signs indicates the polarity of actin (myosin moves toward the plus end)

The energy required for myosin movement along the actin filaments is directly linked to ATP hydrolysis. The nucleotide binding sites are at a distance of about 3.5 nm from actin binding sites. Therefore, the presence of the gamma phosphate sensor and the relay helix is essential within the myosin. Myosin distinguishes between ATP- and ADP-bound states using the gamma phosphate protein sensor. In muscle cells, the myosin head moves 5–10 nm with respect to the sarcomere due to the lever arm rotation of about 70° in each power stroke, the large sweeping movement of the myosin head. This process starts by myosin head being released from the actin because of the ATP binding to myosin. The ATP is hydrolyzed quickly to ADP plus inorganic phosphate. The myosin head rotates from the sarcomere midline and attach to the actin filament through ADP at a further location. Upon attachment, the ADP and inorganic phosphate are released. This causes the myosin lever arm to rotate and slide the myosin head toward the sarcomere midline.

Cytoskeleton is a random fibrous material undergoing constant arrangement and re-arrangement by actin cross-linking filaments such as α-actinin as well as myosin motor molecules. Therefore, the overall mechanics of the cytoskeleton is derived from both physical and mechanical properties of its microstructure. Physical properties include relative position of bio-polymer constituents, network fiber density, cross-linker types among many others. The strength, elasticity, plasticity, and creep behavior of individual filaments are examples of mechanical properties. Here, various theoretic and experimental attempts in order to analyze and understand the mechanics and micro- and macro-rheology of the cytoskeleton and its main ingredients are discussed. The structure of this chapter is as follows. First, recent experimental and computational studies to characterize the response of individual cytoskeletal filaments are reviewed. The chapter proceeds by presenting the main advances in modeling the macroscopic behavior of cells under external loads using experimental techniques as well as computational continuum- and micro-level models. The mechanics of stress fibers where motor molecules play a very important role is then discussed. Finally, the cellular mechanotransduction (a mechanism by which cells convert mechanical stimuli into chemical activities) along with its importance in physiological processes is reviewed. In subjects where

recent specialized reviews are available, the reader is referred to those references to avoid repetition.

2 Biophysical Properties of Actin Filaments

The linear aggregation of globular G-actin subunits with diameter of about 2–3 nm forms filamentous actin chains with diameter of about 7–9 nm and length of up to ~ 100 μm. The actin fibers, discovered first in 1942 [1], are polar structures and undergo constant polymerization and depolymerization which are regulated by ionic strength and the presence of capping, branching and severing proteins. The function of actin filaments derives from their mechanical properties; therefore, a proper understanding of actin properties is essential. Due to the large persistence length, the length over which the thermal bending becomes appreciable, F-actin is considered as a semiflexible polymer and is among very few of such polymers that can be visualized by video microscopy. Theoretically, it can be shown [2].

$$\langle \mathbf{t}(s) \cdot \mathbf{t}(s+r) \rangle_s = \exp(-r/2L_p)$$

where L_p denotes the persistence length, $\mathbf{t}(s)$ is the tangent vector, r is the distance from initial position s along a filament and $\langle\rangle_s$ denote averaging over s. The persistence length of actin filaments are reported to be from 5 to 25 μm depending on the experimental techniques that are used to take the measurements [3–9]. For example, using fluorescence microscopy and by measuring the correlation function (defined as the dot product of tangent vectors of isolated filaments), L_p is measured to be about ~ 17 μm [9]. The persistence length of a filament is defined as the ratio of its bending stiffness to thermal energy, i.e. $L_p = \kappa/K_B T$ where K_B is Boltzmann constant, T is the temperature in Kevin, $\kappa = EI$ denotes the bending rigidity, E is the Young's modulus and I is the second moment of inertia. Therefore, actin's EI and subsequently its Young's modulus can be determined from persistence length measurements. Actin filament Young's modulus is about 1 GPa; however, they are soft and have small bending stiffness mainly because of very small cross-sectional dimensions of about few nanometers. It is noted that thermal fluctuations caused by the thermal energy introduce an entropic elasticity to the F-actin mechanics. This is a mechanism which maximizes the system entropy through increasing the number of available configurations for the filaments [10]. Several experimental and computational techniques have been used to examine the mechanical properties of actin filaments directly. For example, in order to directly measure the stiffness of ~ 1 μm long single actin filaments, a nano-manipulation technique is developed based on attaching filaments to microneedle and observing their deformation under a microscope [11]. In this method, the time resolution is at submillisecond and the resolution of forces and displacements are at subpiconewton and subnanometer, respectively. The elastic modulus of ~ 1.8 GPa was reported by modeling actin filaments as homogenous rods with cross sectional area

of $A \sim 25$ nm^2 based on the results of computer simulations. Moreover, the silicon-nitrade microfabricated levers have been used to stretch single actin filaments to characterize their longitudinal elasticity [12]. Single actin filaments are initially non-linear and highly compliant; however, as the tensile forces increase, they become linear and very stiff. In these experiments, no viscoelastic behavior has been observed for actin filaments and the stiffness of $\sim 34.5 \pm 3.5$ pN/nm has been found. Fitting the worm-like chain model to the results gives a persistence length of ~ 8.75 μm. Besides methods mentioned so far, laser traps have also been used to estimate the flexural rigidity (EI) of actin filaments [13]. In this approach, the ends of fluorescently labeled filament are attached to two microsphere handles which are manipulated using laser traps.

Another important factor in elasticity of actin filaments is the presence of various actin binding proteins and ionic conditions [14–16]. The F-actin elasticity, which is highly correlated with its helical microstructure, is changed due to any factor affecting its microstructure and stability. The metal ions and actin binding proteins strongly influence the functional and structural properties of G-actin monomers and subsequently F-actins. It is actually observed that actin filaments can transition from rigid to flexible due to variations in the bound divalent cations and/or the nucleotides [17, 18]. Pure actin filaments are stiffer than those decorated with myosins since myosin induces more flexible states in actins [5, 17, 19]. The above actin dynamic rigidity has been suggested for the stereocilia of the inner ear and as a possible cause of the noise induced hearing loss [20, 21].

Bound divalent cations do not have the same influence on torsional and flexural rigidities of actin filaments. The torsional motion of a single F-Ca^{2+}-actin and a single F-Mg^{2+}-actin under optical microscope shows that torsional rigidities of filaments are of the same order of magnitude as their flexural stiffnesses. While the flexural rigidity does not depend on the species of the bound divalent cation, quantitatively the F-Ca^{2+}-actin torsional rigidity is three times larger than that of F-Mg^{2+}-actin [16].

Mechanical and structural properties of actin filaments have also been studied using atomistic and molecular dynamics (MD) simulations [22–26]. From MD simulations the persistence lengths of F-ATP and F-ADP (F-actins that are composed of ATP-bound and ADP-bound G-actins) are, respectively, estimated to about 16 and 8.5 μm which agree with experimental measurements [23]. The main drawbacks of all atom MD simulations are the limited accessible time scales (on order of hundreds of nanoseconds) and length scales (of about tens of nanometer) which inhibit studying long filaments and the F-actin interactions with motor protein myosin. Coarse graining is one way to get around this problem and to increase the scales of the problem. In coarse grained models, certain features of a system are included in the model based on the properties and details obtained from its atomistic description. The crystal structure of filamentous actin is essential for these simulations; however, no high-resolution crystal structure of filamentous actin is currently available. The available molecular structures are obtained from X-ray diffraction of whole muscle and electron microscopy [27–31]. The interested reader is referred to the review done by Egelman [32] to learn more about the

low-resolution actin structural studies. The F-actin helical structure is composed of 13 actin molecule per 6 turns and a repeat of about 36 nm [33]. Holmes and colleagues solved the first crystal structure of G-actin in 1990 and proposed the F-actin atomic model, which has been widely accepted and commonly known as Holmes model [33, 34]. This is however a low resolution structure from which the detailed interaction between F-actin and actin biding proteins is described. Recently, Oda et al. obtained a high resolution fiber diffraction data by using an intense magnetic field and placing the crystal structure of G-actin molecule in the best possible orientation in the F-actin helix [35, 36]. They achieved a very good fit to the fiber diffraction pattern.

3 Structural Properties of Microtubules

Cytoskeleton consists of a network of microtubule filaments with important biological functions but different than those of actin filaments. They provide structural supports for extended cells like axons and cilia, control the directional migration of polarized interphase cells and transmit and generate forces, for example the mitotic spindle. Microtubules while stabilizing the structure, they serve as tracks for intracellular vesicle transport in neuronal axons. In cell division, they along with motor molecules form complex networks, the mitotic spindle, around chromosomes and separate chromosomes through their constant polymerization and depolymerization combined with the activity of a variety of microtubule-based motor proteins [37]. Microtubules are hollow cylinders with outer diameters of about 25 nm and inner diameters of about 17 nm, see Fig. 1. They are tens of nanometer to tenths of millimeter long filaments often spanning the whole cell. Microtubule Young's modulus is the same as in the F-actin; however, they are much stiffer due to their tubular structures. This large flexural rigidity is essential to enable microtubules to play their functional role, i.e., to resist the compressive and tensile forces of the motor proteins while maintaining the cell shape. They are created from the polymerization of α- and β-subunits of tubulin which are bound to a guanosine triphosphate (GTP) molecule. Shortly after assembly the GTP is hydrolyzed to guanosine diphosphate (GDP), which remains bound at the same site and very prone to depolymerization. Therefore, microtubules are very dynamic polar structures undergoing constant depolymerization and polymerization [38]. The fast dynamics of microtubules causes considerable dispersions (beyond the usual systematic measurement errors) in their properties reported in literature. This inconsistency is usually associated to the polymerization conditions and growth velocity which is believed to yield a defective crystalline microtubule lattice [39, 40]. There has been a great research effort to elucidate the unique properties of microtubules. Here only some of main structural and physical features of microtubules are reiterated; the interested reader is referred to recent reviews illustrating the mechanics of microtubules [41–44].

The mechanical properties of individual microtubules can be determined either using an active method or a passive approach. In active approach, the mechanics is derived from probing the structure via applying a direct force using optical tweezers, atomic force microscopy, osmotic pressure, and hydrodynamics flow among others [45–53]. For example, in hydrodynamic flow method, the flexural rigidity can be obtained from the quantitative analysis of equilibrium bending shapes of microtubules which are adhered to a glass coverslip and are subjected to hydrodynamic flow. Using motor proteins is another way to apply active forces on microtubules and measure their properties while they are interacting with the molecular motors [54–56]. Here, a portion of a microtubule filament is chemically clamped to a substrate and the conformational changes caused due to the interaction with motor molecules are measured.

Passive methodologies are those approaches in which the flexural rigidity of these filaments is derived from observation of their structural features, which are directly related to their mechanics. For example, observing conformational changes induced by thermal energy is proved to be a powerful tool to study the mechanics of biopolymers [57]. The method rests on the following two principles; (1) the amount of bending of filaments due to thermal fluctuations is directly related to their bending rigidity and (2) the result of equi-partition theorem, i.e. for a system in thermal equilibrium, each independent mode has on average an energy given by K_BT. Therefore, the dynamics and mechanics of microtubules can be studied from direct measurements of their shape fluctuations in three dimension using light microscope images [58, 59]. The analysis of images using automated image analysis algorithm yields the variation in curvature from which the filament bending rigidity is obtained. The accuracy of this method strongly relies on the filament tracking method, which is limited by uncertainties resulting from noise in images. This passive method has also been used to derive the properties of other biopolymers including actin filaments [9].

It is noted that passive and active experiments probe the linear response regime and nonlinear regime, respectively. The images of rapid thermally agitated bending modes only allow consideration of longest modes due to rapid decrease of signal-to-noise [57]. However, one is able to apply locally high forces along the filament length to study both the filament nonlinear response and its possible local defective structure. In the above the properties of the individual filaments were discussed; nevertheless, microtubules in vivo are surrounded by cytoskeletal network which affect their effective properties [60]. Figure 3 shows how the presence of the cytoskeletal network around the microtubule reinforces its behavior under compressive loading by prohibiting long wavelength buckling.

4 Intermediate Filaments

Intermediate filaments (IFs), a large family of about 60 proteins, are also present in cytoskeleton and play distinct functions in the mechanics and structure of

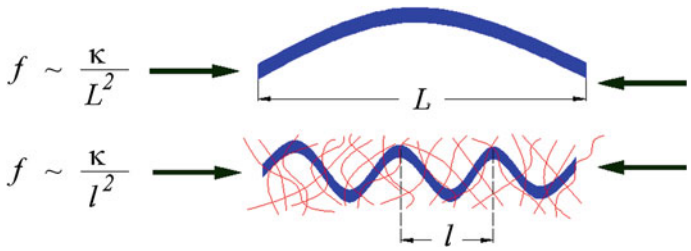

Fig. 3 Schematic plot representing the effect of the surrounding elastic cytoskeleton on the bucking behavior of microtubules in living cells [61]

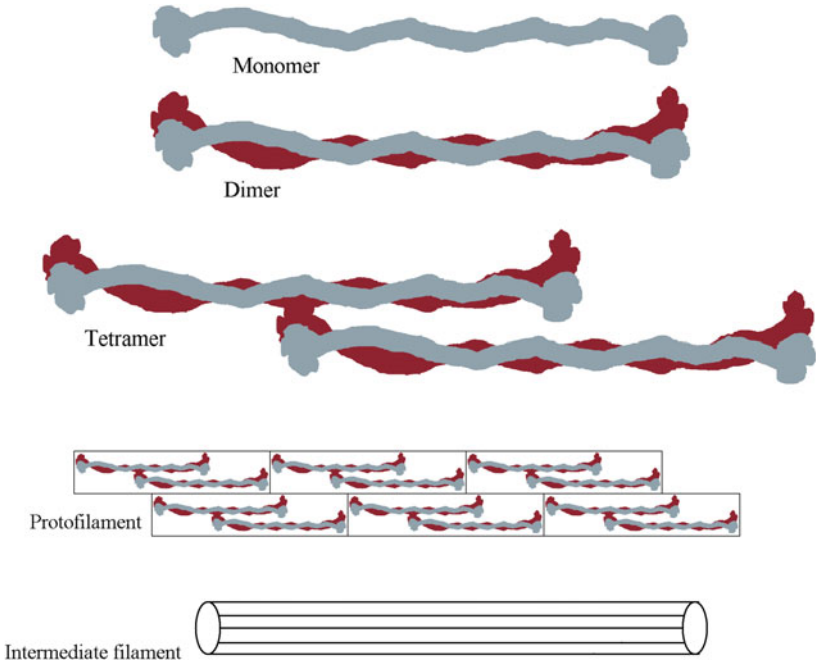

Fig. 4 Schematic plot for the structure of an intermediate filament

cytoskeleton. The proteins found in these filaments are divided into five groups based on their gene structure, primary structure, assembly properties, and their development regulated tissue-specific expression patterns [62]. Unlike actins and microtubules, IFs are made of filamentous proteins with no enzymatic activity. Intermediate filaments are actually coiled coil bundles of protofilaments which are obtained from staggered in arrays α-helical domains, see Fig. 4. They have no vectorial transport role because of their non-polarity and show different properties

from those observed for F-actins and microtubules. For example, they have long-term stability and little solubility in salts. It is believed that intermediate filaments provide structural stability to the cell and have a supplementary function to other components of the cytoskeleton when the cell is under mechanical stress. The IF's mechanics and structure have been the subject of different research efforts [62–66]. The atomic force microscopy was used to estimate the IF persistence length to be few micrometers and also their bending modulus of about 300 MPa by elastically deforming single filaments [63, 67]. With few exceptions, IFs are very flexible in bending with remarkable extensibility up to three-folds [66, 68].

5 Rheology and Mechanics of Cytoskeleton Network

In the previous sections, some of main structural and biochemical features of cytoskeleton network constituents were reviewed. The three main ingredients of the cytoskeleton, i.e., filamentous actins, microtubules and intermediate filaments, bundle together and form a dynamic network with unique properties and prominent role in a variety of essential cell functions including but not limited to adhesion, migration and mechanotransduction. The complete understanding of the behavior of this complicated structure requires investigating the properties of its individual ingredients and more importantly determining and indentifying their interactions with each other in the resulting network. This section discusses both computational and experimental models that have been proposed over the past years regarding the cytoskeletal rheology and mechanics.

Many of artificial polymers can be categorized as being flexible, i.e., the polymer persistence length is much smaller than its contour length and therefore it turns many times in the solution and looks like a relatively compact disordered coil. The theory for the behavior of network formed by these flexible polymers, where the persistence length is small compared with both the length of the polymer and the entanglement distance in the solution, has been very well developed [2]. As the persistence length becomes larger and comparable to (or larger than) the contour length, the dynamic of the filament changes. These filaments are called semiflexible and the properties of the networks formed by these fibers are less developed.

Cytoskeleton is a highly heterogeneous and consists of semiflexible filaments with interconnection lengths of the same order as fiber persistence length. It is also an active and dynamic structure undergoing constant remodeling in response to external and internal stimulants. The biophysical properties of cytoskeleton have been studied and measured in living cells; however, we are far from understanding their physical origins due to the complexity and heterogeneity of the cytoskeleton microstructure. For example, F-actin networks subjected to oscillatory shear deformation show negative normal stresses as large as shear stresses [69]. This phenomenon does not appear in the behavior of flexible polymer networks; their

response is like most materials where the tendency to expand in the direction normal to the applied shear forces yields positive normal stresses. Another unique property of actin networks is the observation of both stiffening and softening. Unlike simple polymer gels, networks of semiflexible filaments nonlinearly stiffen in order to resist large deformations and maintain the network integrity [70, 71]. A reversible stress-softening behavior in compression, essential in preventing catastrophic fracture of actin networks, has also been reported [72]. Flexible and rigid polymers exhibit only monotonic stiffening in compression. The origins of these unique macroscopic behaviors are under study and there is no comprehensive theory yet.

5.1 Experimental Studies

The cytoskeletal network has viscoelastic properties and shows characteristics of both elastic solids and viscous fluids. Oscillatory external stresses are used to determine its effective elastic modulus as well as the amount of stored mechanical energy. The mechanical response of actin networks is non-linear and strongly depends on the stress and experimental conditions. Depending on the length scales at which the measurements are taken, the network can show very different properties [73, 74]. The inclusion of length scale of observation is essential for analyzing and developing models for the mechanics of cytoskeleton and any other semiflexible networks [75].

Experimentally, the behavior of the cytoskeleton is determined either by monitoring the Browning movements of inherent or introduced particles (passive method) or by direct application of external forces (active measurements). Passive microrheology, fluorescence correlation spectroscopy and dynamic light scattering are among passive experimental measurements developed to measure the probe and measure the mechanics of actin solutions [76]. Active rheology measurements methods, where the system properties are probed by applying localized forces, include atomic force microscope, optical traps, microplates, micropipette aspiration, magnetic traps among many others [76]. These methods can be used to identify the properties of the network at various length scales. For example, while the bulk rheology of the network is estimated from two-particle microrheology method, the short-length fluctuations are isolated in one-particle microrheology [73, 77, 78].

5.2 Computational Studies

The biomechanical models developed for the mechanics of a cell are either based on the continuum level and macroscopic observations (phenomenological models) or derived from its nano-structure (micromechanics models). In the former, it is

assumed that cell behaves as a continuum material for which a constitutive model based on the experimental observations can be chosen to describe its behavior. The cytoskeleton has been modeled as a simple viscoelastic continuum, porous gel and soft glassy material [77]. These continuum-level models may only be used to describe cell behavior if the length scale of interest is much larger than the dimensions of the cell microstructure. In micromechanics methods, the main microstructural features of the system, which are usually studied and characterized separately, are included in the model.

There are instances where a cell behaves at macroscopic length scales which are two to three orders of magnitudes larger than its microstructural characteristic lengths. The behavior of erythrocytes/neutrophils in micropipette aspiration and magnetocytometry induced deformations are among cases where continuum models successfully describe the overall mechanical properties [79–84]. In micropipette aspiration, the cellular elasticity and viscosity are measured by pulling on cells, such as monocytes, erythrocytes (red blood cells) and leukocytes (white blood cells). In magnetocytometry, magnetic microbeads tightly bound to the cell are used to apply controlled forces to a single cell. In these situations, the scales of observed deformation are such that a continuum model can be developed to capture cell response. The cell environment consists of ionic water solution and charged macromolecules that are influencing its biomechanical and biochemical properties. For example, it is observed that the cell volume changes under osmotic loadings due to changes in ion concentrations. While many of continuum level models neglect the interactions of these different phases and consider the cell as a single-phase material, multi-phasic models have been developed to take into account the interactions among solid, fluid and free ions in the cytoskeleton [85]. Most of the work in this area as well as the first multi-phasic model have been developed in order to study the articular cartilage and chodrocyte cells. Few notes are in-place about the range of applicability and accuracy of continuum-level modeling of the cell behavior. In these models, the small but important Brownian motions of cytoskeleton due to thermal fluctuations are neglected. Moreover, the infinite number of time scales, a characteristic feature of power-law rheology of the cell response, is replaced with a limited number of time constants [86]. Finally, although we have the freedom to incorporate inhomogeneous as well as isotropic properties for the representative continuum domain through selecting proper constitutive laws (i.e., force displacement relation), these models often cannot be related to and derived from the cell microstructure. Therefore, the continuum-level methods are highly specific to experimental observations and usually cannot be generalized [87].

It is clear that one of the main missing features in continuum-level models is the consideration of the fibrous and discrete structure of cytoskeleton. In discrete models, the cytoskeleton microstructure is represented by a network of randomly cross-linked fibers. A complete review of these models has been presented in [90]. Since actin filaments are heavily cross-linked on the scale of their thermal persistence length, their common modes of deformation are bending, twisting and stretching. Therefore, cytoskeleton is classified as being a semiflexible network

whose behavior is strongly non-affine. The behavior of a semiflexible network and its relationship to the mechanical properties of its constituents are much more complicated than what it is for a flexible network. The accepted models for flexible networks [2] are not appropriate to study the mechanics of semiflexible networks. There have been various research efforts to develop a unified and general model to describe the elasticity and unique features of semiflexible gels such as large shear moduli, nonlinear response and power-law scaling of the cytoskeletal rheology, [75, 91–96]. The cytoskeletal filaments resist bending and exhibit thermally induced fluctuations due to Brownian forces. A filamentous protein is therefore considered as an elastic rod with bending and stretching rigidities resulting from both elastic and entropic effects. The langevin equation can be employed to describe the hydrodynamics drag force of the filaments through the solvent. The presence of cross-linker in semiflexible gels causes significant change in network properties resulting from two distinct single-filament responses, i.e., bending and stretching modes. If individual filaments only rotate and uniaxially deform under uniform loadings and the macroscopic strain distribute uniformly throughout the domain (affine deformation), the behavior of the network can be modeled by affine network models [10]. These models are not valid where the behavior is non-affine and bending motions of the filaments become important. The reader is referred to recent papers for a detailed discussion on affine versus non-affine behavior [91, 92, 95]. A new methodology has recently been proposed by Hatami-Marbini and Picu to solve boundary value problem on dense random fiber networks by determining the statistics of their behavior and accounting for all possible configurations at the desired length scale using Stochastic Finite Element Method [75]. In this methodology, the nodal displacements of the network subjected to far-field loadings are obtained by minimizing the potential energy of the entire network. Then a regular

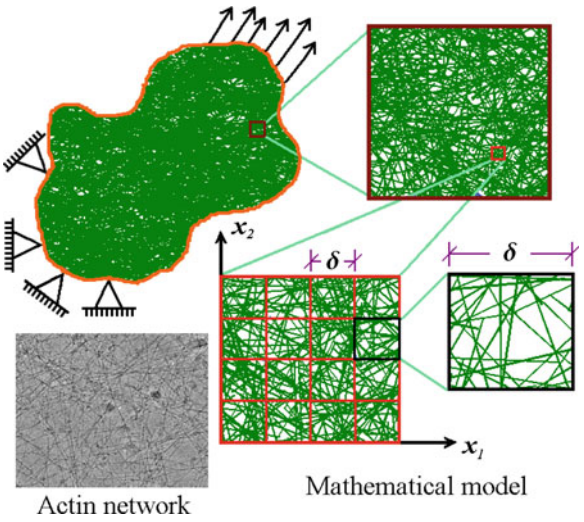

Fig. 5 Schematic plot showing F-actin network divided into a regular mesh of characteristic dimension δ. The size of *square* elements, δ, denotes the length scale of observation. The plot also shows the in vitro visualization of the actin cytoskeleton [88, 89]

mesh of square elements of size δ (see Fig. 5) is overlaid on the network. Calculating the average stress and strain distribution over each square element, these elements are replaced with homogeneous continuum domains with correlated elastic moduli. Therefore, the respective equivalent continuum domain has the main features and correlations of the network microstructure. A note is in place about the fiber cross-links in cytoskeleton. In mechanical models for F-actin network, the fibers are often assumed to be permanently hinged or rigidly cross-linked. Nevertheless, these cross-links undergo constant disassociation in cytoskeleton and have variable strength depending on the ABPs' structures and properties. For instance, filamin, an approximately 150 nm long V-shape ABP, preferentially cross-link actin fibers. It is composed of β-sheets which are unfolding under load and induce a sawtooth force displacement curve for this ABP cross-link [97–101]. Therefore, the cross-links between filaments are not simple rigid structural element and are rather very important to the overall network stiffness and elasticity. This is an important detail which is conveniently ignored in many network models.

As it is stated earlier, cytoskeleton is an active biological system responding to external stimuli through actin–myosin interactions which lead to formation of stress fibers. The interplay of multiple phenomena including myosin contraction, actin network elasticity, the internal and external constraints imposed on the cytoskeleton creates the stress distribution inside the cell. The plethora of actin binding proteins controls the organization, i.e., local microstructure and connectivity, of actin filaments which are assembled and disassembled in response to various kinds of signals resulting from cell locomotion, cell division and extension [102–104]. The mechanical stability of the cell is due to dynamic arranging and rearranging of cytoskeletal filaments via crosslinking molecules. For instance, Arp2/3 complex forms 70° branching networks, fimbrin and α-actinin put F-actins in parallel bundles, and filamin and spectrin form three-dimensional actin networks. Filamin and spectrin are protein complexes consisting of multiple actin-binding domains which arrange actin filaments into dense meshworks. Other types of ABPs are those which are used as a physical support or scaffold and are less "directly" involved in regulating actin structure. Myosins are a member of this category of ABPs.

There are over 15 different types of myosins using actin filaments to move their specific cargo inside the cell. Myosins are molecular motors which produce movement through ATP hydrolysis and can generate forces on order of pico-Newtons inside the actin network or bundles. The mechanical properties and structure of cytoskeleton is greatly influenced through the contribution of forces generated by myosin so their effect in cell mechanics cannot be overlooked. The effect of motor molecules may be included in the filamentous network models for the cytoskeleton. In these models, internal forces exerted by myosin motor molecules induce a state of pre-stress condition inside the system, see Fig. 6. These networks, whose elasticity is controlled by myosin, are often called active networks and their behavior is different than that of passive networks. It has been shown experimentally that these active myosin stresses stiffen the network by two

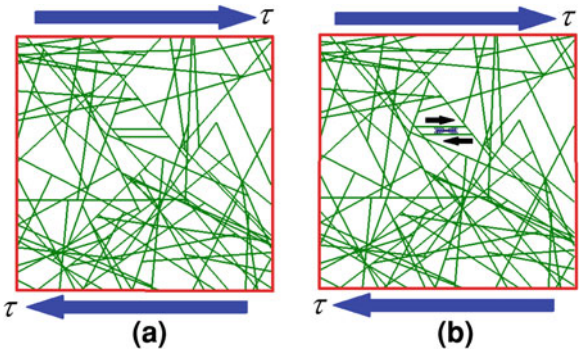

Fig. 6 Schematic network models for **a** passive networks and **b** active networks subjected to external loadings. In active networks, myosin molecular motors control network elasticity and induce a state of pre-stress inside the network

orders of magnitude [105]; however, a mathematical and theoretic model of active network has not yet been developed.

The stress field in the cytoskeletal network depends on the contractile machinery called stress fibers. They are formed by the actin–myosin interactions and are characterized by the repeating units of myosin proteins. The movement of myosin motors in the stress fibers causes actin filaments to contract and slide past one another. The dynamics of stress fibers has not yet been well understood and is currently under study. However, it is known that their elasticity is a function of myosin spacings and changes over time. Cellular functions such as wound healing, proliferation, shape stability, and apoptosis depend strongly on how the force is acted upon the cell. Forces transmit into and out of the cell cytoskeleton through these bundles at the basal surface, where it interacts with the surrounding extracellular matrix, and where cytoskeletal contractility is resisted. At these interaction sites (called the focal adhesion), stress fibers often form [106, 107]. They also from along the direction of external forces, e.g., it is seen that stress fibers form and orient with the direction of fluid flow in the endothelial cells under shear stress [108, 109]. The mechanical properties of stress fibers can be non-uniform because of the variations in myosin spacings along the length of stress fibers. Moreover, the direction and strength of stress fibers depend on stress field within the cell. Forces are transferred and propagated directly and in a band-like structure from cytoskeleton stress fibers to discrete sites on the nuclear envelop [110, 111]. Stress fibers enable cells to focus myosin contractility along a specific direction of resistance; therefore, cells can stiffen directionally to protect themselves against excess stress and strains in this particular direction. Moreover, cells explore the matrix rigidity and migrate in the direction of increasing rigidity through stress fibers [112]. Cell locomotion is believed to depend on and even be controlled by changes in substrate rigidity. In particular, cell response on culture surfaces is dictated by substrate rigidity: actin stress fibers are oriented along the stiffest direction of the microfabricated substrates [113].

In literature, stress fibers have often been simulated by continuum models. These models predict the diffusion of stress away from the points of matrix attachment, as opposed to the directed and focused stress propagation observed in experiments.

A recent study, however, showed that in translating the discrete microscale actin–myosin interaction to the continuum scale, these models are missing the perpendicular component of the myosin force acting on the actin filaments [111, 114, 115]. Inclusion of this correction in the model recovers the directed and focused nature of the stress fibers. Moreover, the stress fiber arrangements for simple cell–matrix attachments predicted by this model match those observed in experimental studies. It is noted that key aspects of the interactions are missing in coarse graining and in approximating discrete macromolecular interactions by a continuum model. Therefore, a multi-scale approach retaining the discrete nature of the macromolecular interactions and keeping material properties in the discrete macromolecular scale is required. Such a model requires taking into account the discrete nature of the cytoskeleton as well as the effects of hydrodynamic interactions on the behavior of individual filaments [114, 115].

It has been shown that the elastic modulus of stress fibers in living endothelial cells is approximately 10–15 kPa which remains constant over large strains up to 12% [116]. This stiffness is a function of myosin II since disturbing its activity by adding myosin inhibitor blebbistatin causes a 30% loss of the modulus [117]. The elastic modulus of fibroblast cells also decreases due to the application of this myosin inhibitor [118]. This further confirms the importance of the tension generated by myosin to the overall cellular stiffness. Despite considerable experimental and computational efforts to study basic physical principles of cell contractility due to myosin II motors, our understanding is still limited. It is not yet clear how contractility and pattern formation changes with microscopic parameters such as the number of myosin motors, the number of cross-linkers and the density of actin filaments. It is known that the motor activity inside the cell is a controlled process which results in formation of stress fibers in cells on flat substrates and the contractile rings during cytokinesis [119–121]. The contractile rings, which are composed of actin, myosin II, septins and GTP-binding hetero-oligomers, generate a furrow which partitions one cell into two. There have been some efforts to describe these rings using continuum-level hydrodynamics models whose accuracy have been confirmed by in vitro studies [122, 123]. In these models, the actin network is modeled as an active viscoelastic polar gel which is forced out of its equilibrium state because of the ATP hydrolysis. These studies suggested that the assembly and disassembly of cytoskeletal structures can be tuned via varying the concentration of local myosin II. Furthermore, F-actin cross-linkers such as filamin A and α-actinin must be present for the contraction of F-actin networks induced by myosin II at physiological ATP concentrations [124]. In other words, the myosin cannot generate large forces if actin filaments are not cross-linked. The dependence of contractility on the number of cross-linkers and myosin motors per actin filament has been studied by constructing well-controlled model system of purified actin, myosin, and α-actinin [125]. The results of recent theoretical studies show that the force generated by myosin is not sufficiently large for ring contraction during cytokinesis unless the actin filaments are heavily cross-linked [126].

The study of reconstituted biopolymer networks is an excellent way to model and understand the important mechanical features of the living cell cytoskeleton

[105, 123, 125]. These reconstituted networks of filamentous actin combined with myosin motors are a new class of active materials whose mechanical properties can be adjusted and tailored by enzymatic activity [127]. It has been observed that molecular motor proteins can either stiffen or weaken the F-actin solution depending on the density of F-actin cross-linkers. While the presence of actin cross-linker provides sites for mechanical anchorage and accommodates internal tension, active filament sliding occurs in their absence because of myosin activity. The protein myosin permits active control over the mechanical behavior of F-actin network solutions. For instance, the stress relaxation time of actin solutions will shorten upon addition of molecular motor myosins due to their interaction with actin filaments. The interaction of single polymer chains with surrounding polymer yields an effective viscoelastic behavior. The viscoelasticity of actin–myosin networks can be modulated using the ability of the myosin to supersede reputation with sliding motion. Myosin II replaces the thermally driven transport of individual polymers (snake-like movement described by reputation model) with active filament sliding motion. In the reputation model, a tube represents the topological constraints of neighboring polymers on the movement of a single chain [2]. A modified tube model has been proposed to model the dynamics of polar actin filaments with active, motile centers generating a longitudinal motion [128]. Molecular dynamics simulations have also been used to investigate the rheology and the structure of F-actin solutions interacting with molecular motors [129].

6 Cellular Mechanotransduction

In the previous sections, we focused on the mechanical properties of the cytoskeleton. It was mentioned that the highly dynamic mechanics of the cell is derived from its constantly changing cytoskeletal structure in response to external stimuli. A cell actively responds to the mechanical signals it receives from the environment. This implies that cells are capable of sensing the mechanical force and transducing these signals to the biological response. The mechanism by which a cell converts mechanical signals to biochemical signal is called cellular mechanotransduction [131]. This process has been the subject of intensive studies with the aim of understanding both its mechanism and its implications. Here, for completeness, we present a brief introduction to this phenomenon and refer the reader to the related references for a thorough discussion [130–133].

The changes in biochemical activities (e.g., changes in intracellular calcium concentration or activation of diverse signaling pathways) within the cell in response to the mechanical stress modify cell internal structure and adjust its mechanical properties. Therefore, the biological functions of a cell is highly influenced and even controlled by the mechanical forces and the way they are transduced into biochemical signals. In this process, many structures and components such as myosin motor molecules, cytoskeletal filaments, ion channels, integrin and nuclei are involved. Several cellular phenomena are found to be

influenced by mechanical stress: (1) the membrane strain controls the opening and closing rate of a stretch- or flow-sensitive ion channel, which allows influx of calcium and other ions [134–137]; (2) Hemodynamic forces caused by blood flow deform and align endothelial cells along the arterial walls to maintain a nearly constant shear stress [138–140]; (3) Chemical and mechanical cues closely regulate the assembly of focal adhesions through which cells probe the stiffness of its environment and adjust its response, e.g., cells migrate in the direction of increasing substrate stiffness [112]; (4) The external forces induce conformational changes in cytoskeletal elements which in turn alter and activate signaling pathways, e.g., applying tensile forces to cultured neurons or vascular muscle cells increases the microtubule polymerization [141, 142]. It is also seen that mechanotransduction has a central role in the functions of some of our senses such as hearing and balance, which are resulting from electrochemical responses to sound waves, pressure, and gravity [143].

Abnormality in the cellular mechanotransduction can have serious pathological consequences [130, 131, 144]. The development and maintenance of the muscle tissues and even physiological processes, e.g., the blood flow and the blood pressure, all depends on the ability of cells to sense and respond to changes in their physical environment. For example, the morphology and physiology of the heart and vasculature are affected by the pressure and shear stresses generated from the flowing blood. Since mechanotransduction regulates and influences many cellular functions including protein synthesis, secretion, adhesion, migration, and apoptosis, diseases could arise because of any inherited or acquired defects in the cellular mechanotransduction. The loss of bone mass in a microgravity environment and atherosclerosis, a condition where arterial walls thicken as the result of the build-up of fatty materials and calcification, are two examples of such diseases [145, 146]. In atherosclerosis, the fluid shear stress is disturbed at bifurcations, which in turn causes the remodeling of the vascular system. Many other diseases such as the hearing loss, the muscular dystrophy, the glaucoma, the premature aging, and even the cancer can be related to the malfunctioning of the cellular mechanotransduction.

7 Summary

There have been much learnt about the molecular bases of cytoskeletal mechanics during the past few decades. The mechanics of the cytoskeleton depends highly on its ever varying and dynamic microstructure. Cell maintains its stability and optimizes its response to various external and internal excitements by constant arrangement and re-arrangement of its actin filamentous reinforcements. This dynamic process requires actin cross-linking filaments such as α-actinin as well as myosin motor molecules. In this chapter, the most important and recent experimental and theoretical studies are brought together and are concisely reviewed to shed light on the cytoskeletal rheology and, in turn, on the dynamic response of the cell. The experimental observations along with computational approaches used to

study the mechanical properties of the individual constituents of the cytoskeleton were first presented. The chapter then reviewed various computational models ranging from discrete filamentous models to continuum level models developed to capture the highly dynamic and constantly changing properties of the cells to external stimuli. It is seen that depending on the cellular phenomena under study, either type of the modeling methodology may prove to be the correct and better-suited one. Intuitively, it is expected that while continuum models better describe whole-cell deformations, the details of the filament organization and their interaction with myosin motor molecules are critical and important in cases where the scales of interest become very small, e.g., the scale of an AFM tip. Finally, in the last section, the mechanotransduction was introduced as being an essential function of the cell which controls its growth and proliferation among others. A wide spectrum of pathologies, e.g., atherosclerosis, is caused because of any disturbance in this process.

References

1. Straub, F.B. In: Szent-Györgi (ed.) Studies Inst. Med. Chem. Univ. Szeged **2**, 3–15 (1942)
2. Doi, M., Edwards, S.F.: The theory of polymer dynamics, Clarendon Press, Oxford (1988)
3. Oosawa, F.: Actin–actin bond strength and the conformational change of f-actin. Biorheology **14**, 11–19 (1977)
4. Yanagida, T., Nakase, N., Nishiyama, K., Oosawa, F.: Direct observation of motion of single F-actin filaments in the presence of myosin. Nature **307**, 58–60 (1984)
5. Takebayashi, T., Morita, Y., Oosawa, F.: Electron microscopic investigation of the flexibility of F-actin, Biochim. Biophys. Acta **492**, 357–363 (1977)
6. Ishijima, A., Doi, T., Sakurada, K., Yanagida, T.: Sub-piconewton force fluctuations of actomyosin in vitro. Nature **352**, 301–206 (1991)
7. Gittes, F., Mickney, B., Nettleton, J., Howard, J.: Flexural rigidity of microtubules and actin filaments measured from thermal fluctuations in shape. J. Cell Biol. **120**(4), 923–924 (1993)
8. Kas, J., Strey, H., Barmann, M., Sackmann, E.: Direct measurement of the wave-vector-dependent bending stiffness of freely flickering actin filaments. Europhys. Lett. **21**(8), 865–870 (1993)
9. Ott, A., Magnasco, M., Simon, A., Libchaber, A.: Measurement of the persistence length of polymerized actin using fluorescence microscopy, Phys. Rev. E **48**(3), R1642–R1645 (1993)
10. MacKintosh, F.C., Kas, J., Janmey, P.A.: Elasticity of semiflexible biopolymer networks, Phys. Rev. Lett. **75**(24), 4425–4429 (1995)
11. Kojima, H., Ishijima, A., Yanagida, T.: Direct measurement of stiffness of single actin filaments with and without tropomyosin by in vitro nanomanipulation, Proc. Natl. Acad. Sci., 12962–12966 (1994)
12. Liu X., Pollack, G.H.: Mechanics of F-actin characterized with microfabricated cantilevers, Biophys. J. **83**, 2705–2715 (2002)
13. Dupuis, D.E., Guilford, W.H., Wu, J., Warshaw, D.M.: Actin filament mechanics in the laser trap, J. Muscle Res. Cell Motil. **18**, 17–30 (1997)
14. Isambert, H., Venier, P., Maggs, A.C., Fattoum, A., Kassab, R., Pantaloni, D., Carlier, M.F.: Flexibility of actin filaments derived from thermal fluctuations. Effect of bound nucleotide, phalloidin, and muscle regulatory proteins, J. Biol. Chem. **270**, 11437–11444 (1995)

15. Steinmetz, M.O., Goldie, K.N., Aebi, U.: A correlative analysis of actin filament assembly, structure, and dynamics, J. Cell Biol. **138**, 559–574 (1997)
16. Yasuda, R., Miyata, H., Kinosita, K.: Direct measurement of the torsional rigidity of single actin filaments. J. Mol. Biol. **263**, 227–236 (1996)
17. Orlova, A., Egelman, E.H.: A conformational change in the actin subunit can change the flexibility of the actin filament. J. Mol. Biol. **232**, 334–341 (1993)
18. Egelman, E., Orlova, A.: New insights into actin filament dynamics. Curr. Opin. Cell Biol. **5**, 172–180 (1995)
19. Yanagida, T., Oosawa, F.: Polarized fluorescence from e-ADP incorporated into F-actin in a myosin-free single fiber: conformation of F-actin and change induced in it by heavy meromyosin, J. Mol. Biol. **126**, 507–524 (1978)
20. Howard, J., Hudspeth, A.J.: Mechanical relaxation of the hair bundle mediates adaptation in mechanoelectrical transduction by the bullfrog's saccular hair cell, Proc. Natl. Acad. Sci. USA **84**, 3064–3068 (1987)
21. Tilney, L.G., Saunders, J.C., Egelman, E.H., DeRosier, D.J.: Changes in the organization of actin filaments in the stereocilia of noise damages lizard cochlea, Hear. Res. **7**, 181–198 (1982)
22. Ming, D., Kong, Y., Wu, Y., Ma, J.: Simulation of F-actin filaments of several microns, Biochem. J. **85**, 27–35 (2003)
23. Chu, J.W., Voth, G.A.: Allostery of actin filaments molecular dynamics simulations and coarse-grained analysis. Proc. Natl. Acad. Sci. USA. **102**, 13111–13116 (2005)
24. Chu, J.W., Voth, G.A.: Coarse-grained modeling of the actin filament derived from atomistic-scale simulations. Biophys. J. **90**, 1572–1582 (2006)
25. Paula, D.M., Squireb, J.M., Morris, E.P.: A novel approach to the structural analysis of partially decorated actin based filaments. J. Struct. Biol. **170**, 278–285 (2010)
26. Pfaendtner, J., Lyman, E., Pollard, T.D., Voth, G.A.: Structure and dynamics of the actin filament. J. Mol. Biol. **396**(2), 252–263 (2010)
27. Huxley, H.E.: X-ray analysis and the problem of muscle. Proc. R. Soc. Lond. Ser. B **141**, 59–62 (1953)
28. Huxley, H.E.: Electron microscope studies of the organisation of the filaments in striated muscle. Biochim. Biophys. Acta **12**, 387–394 (1953)
29. Hanson, J., Lowy, J.: The structure of F-actin and of actin filaments isolated from muscle. J. Mol. Biol. **6**, 46–60 (1963)
30. Moore, P.B., Huxley H.E., DeRosier, D.J.: Three-dimensional reconstruction of F-actin, thin filaments and decorated thin filaments. J. Mol. Biol. **50**, 279–295 (1970)
31. DeRosier, D.J., Moore, P.B.: Reconstruction of three-dimensional images from electron micrographs of structures with helical symmetry. J. Mol. Biol. **52**, 355–369 (1970)
32. Egelman, E.H.: The structure of F-actin, J. Muscle Res. Cell Motil. **6**, 129–151 (1985)
33. Holmes, K.C., Popp, D., Gebhard, W., Kabsch, W.: Atomic model of the actin filament. Nature **347**, 44–49 (1990)
34. Kabsch, W., Mannherz, H.G., Suck, D., Pai, E.F., Holmes, K. C.: Atomic structure of the actin: DNase I complex. Nature **347**, 37–44 (1990)
35. Oda, T., Iwasa, M., Aihara, T., Maeda, Y., Narita, A.: The nature of the globular- to fibrous-actin transition. Nature **457**, 441–445 (2009)
36. Holmes, K.C.: Structural biology: actin in a twist. Nature **457**, 389–390 (2009)
37. Wittmann, T., Hyman, A., Desai, A.: The spindle: a dynamic assembly of microtubules and motors. Nat. Cell Biol. **3**, E28–E34 (2001)
38. Mitchison, T., Kirschner, M.: Dynamic instability of microtubule growth. Nature **312**, 237–242 (1984)
39. Janson, M.E., Dogterom, M.: A bending mode analysis for growing microtubules: evidence for a velocity-dependent rigidity. Biophys. J. **87**, 2723–2736 (2004)
40. Diaz, J.F., Valpuesta, J.M., Chacon, P., Diakun, G., Andreu, J.M.: Changes in microtubule protofilament number induced by Taxol binding to an easily accessible site. J. Biol. Chem. **273**, 33803–33810 (1998)

41. Hawkins, T., Mirigian, M., Yasar, M.S., Ross, J.L.: Mechanics of microtubules. J. Biomech. **43**, 23–30 (2010)
42. Bicek, A.D., Tuzel, E., Kroll, D.M., Odde, D.J.: Analysis of microtubule curvature. Methods Cell Biol. **83**, 237–268 (2007)
43. Kasas, S., Dietler, G.: Techniques for measuring microtubule stiffness. Curr. Nanosci. **3**, 79–96 (2007)
44. Gardel, M.L., Kasza, K.E., Brangwynne, C.V.P., Liu, J., Weitz, D.A.: Mechanical response of cytoskeletal networks. Methods Cell Biol. **89**, 487–518 (2008)
45. Kurachi, M., Hoshi, M., Tashiro, H.: Buckling of a single microtubule by optical trapping forces: direct measurement of microtubule rigidity. Cell Motil. Cytoskeleton **30**, 221–228 (1995)
46. Felgner, H., Frank, R., Schliwa, M.: Flexural rigidity of microtubules measured with the use of optical tweezers. J. Cell Sci. **109**, 509–516 (1996)
47. Felgner, H., Frank, R., Biernat, J., Mandelkow, E.M., Mandelkow, E., Ludin, B., Matus, A., Schliwa, M.: Domains of neuronal microtubule-associated proteins and flexural rigidity of microtubules. J. Cell Biol. **138**, 1067–1075 (1997)
48. Kikumoto, M., Kurachi, M., Tosa, V., Tashiro, H.: Flexural rigidity of individual microtubules measured by a buckling force with optical traps. Biophys. J. **90**, 1687–1696 (2006)
49. van Mameren, J., Vermeulen, K.C., Gittes, F., Schmidt, C.F.: Leveraging single protein polymers to measure flexural rigidity. J. Phys. Chem. B **113**, 3837–3844 (2009)
50. de Pablo, P., Schaap, I.A.T., MacKintosh, F.C., Schmidt, C.F.: Deformation and collapse of microtubules on the nanometer scale. Phys. Rev. Lett. **91**(9), 098101 (2003)
51. Schaap, I.A., Carrasco, C., dePablo, P.J., MacKintosh, F.C., Schmidt, C.F.: Elastic response buckling, and instability of microtubules under radial indentation, Biophys. J. **91**, 1521–1531 (2006)
52. Needleman, D.J., Ojeda-Lopez, M.A., Raviv, U., Ewert, K., Jones, J.B., Miller, H.P., Wilson, L., Safinya, C.R.: Synchrotron X-ray diffraction study of microtubules buckling and bundling under osmotic stress: a probe of interprotofilament interactions. Phys. Rev. Lett. **93**(19), 198104 (2004)
53. Venier, P., Maggs, A.C., Carlier, M.F., Pantaloni, D.: Analysis of microtubule rigidity using hydrodynamic flow and thermal fluctuations. J. Biol. Chem. **269**(18), 13353–13360 (1994)
54. Gittes, F., Meyhofer, E., Baek, S., Howard, J.: Directional loading of the kinesin motor molecule as it buckles a microtubule. Biophys. J. **70**, 418–429 (1996)
55. Roos, W., Ulmer, J., Gräter, S., Surrey, T., Spatz, J.P.: Microtubule gliding and cross-linked microtubule networks on micropillar interfaces. Nano Lett. **5**(12), 2630–2634 (2005)
56. Kawaguchi, K., Ishiwata, S., Yamashita, T.: Temperature dependence of the flexural rigidity of single microtubules. Biochem. Biophys. Res. Commun. **366**, 637–642 (2008)
57. Gittes, F., Mickey, B., Nettleton, J., Howard, J.: Flexural rigidity of microtubules and actin filaments measured from thermal fluctuations in shape. J. Cell Biol. **120**(4), 923–934 (1993)
58. Brangwynne, C.P., Koenderink, G.H., Barry, E., Dogic, Z., MacKintosh, F.C., Weitz, D.A.: Bending dynamics of fluctuating biopolymers probed by automated high-resolution filament tracking. Biophys. J. **93**(1), 346–359 (2007)
59. Pampaloni, F., Lattanzi, G., Jonas, A., Surrey, T., Frey, E., Florin, E.L.: Thermal fluctuations of grafted microtubules provide evidence of a length-dependent persistence length. Proc. Natl. Acad. Sci. USA **103**(27), 10248–10253 (2006)
60. Brangwynne, C.P., Koenderink, G.H., MacKintosh, F.C., Weitz, D.A.: Non-equilibrium microtubule fluctuations in a model cytoskeleton. Phys. Rev. Lett. **100**, 118104 (2008)
61. Brangwynne, C.P., MacKintosh, F.C., Kumar, S., Geisse, N.A., Talbot, J., Mahadevan, L., Parker, K.K., Ingber, D.E., Weitz, D.A.: Microtubules can bear enhanced compressive loads in living cells because of lateral reinforcement. J. Cell Biol. **173**(5), 733–741 (2006)
62. Chang, L., Goldman, R.D.: Intermediate filaments mediate cytoskeletal crosstalk. Nat. Rev. Mol. Cell Biol. **5**, 601–613 (2004)

63. Guzman, C., Jeney, S., Kreplak, L., Kasas, S., Kulik, A.J., Aebi, U., Forro, L.: Exploring the mechanical properties of single vimentin intermediate filaments by atomic force microscopy. J. Mol. Biol. **360**(3), 623–630 (2006)
64. Wang, N., Stamenovic, D.: Mechanics of vimentin intermediate filaments. J. Muscle Res. Cell. Motil. **23**, 535–540 (2002)
65. Kreplak, L., Bar, H., Leterrier, J.F., Herrmann, H., Aebi, U.: Exploring the mechanical behavior of single intermediate filaments. J. Mol. Biol. **354**(3), 569–577 (2005)
66. Kreplak, L., Fudge, D.: Biomechanical properties of intermediate filaments: From tissues to single filaments and back. Bioessays **29**(1), 26–35 (2007)
67. Mücke, N., Kreplak, L., Kirmse, R., Wedig, T., Herrmann, H., Aebi, U., Langowski, J.: Assessing the flexibility of intermediate filaments by atomic force microscopy. J. Mol. Biol. **335**, 1241–1250 (2004)
68. Fudge, D.S., Gardner, K.H., Forsyth, V.T., Riekel, C., Gosline, J.M.: The mechanical properties of hydrated intermediate filaments: insights from hagfish slime threads. Biophys. J. **85**, 2015–2027 (2003)
69. Janmey, P.A., McCormick1, M.E., Rammensee, S., Leight1, J.L., Georges, P.C., MacKintosh, F.C.: Negative normal stress in semiflexible biopolymer gels. Nat. Mater. **6**, 48–51 (2007)
70. Gardel, M.L., Shin, J.H., MacKintosh, F.C., Mahadevan, L., Matsudaira, P., Weitz, D.A.: Elastic behavior of cross-linked and bundled actin networks. Science **304**, 1301–1305 (2004)
71. Storm, C., Pastore, J.J., MacKintosh, F.C., Lubensky, T.C., Janmey, P.A.: Nonlinear elasticity in biological gels. Nature **435**, 191–194 (2005)
72. Chaudhuri, O., Parekh, S.H., Fletcher, D.A.: Reversible stress softening of actin networks. Nature **445**, 295–298 (2007)
73. Gardel, M.L., Valentine, M.T., Crocker, J.C., Bausch, A.R., Weitz, D.A.: Microrheology of entangled F-actin solutions. Phys. Rev. Lett. **91**(15), 158302 (2003)
74. Liu, J., Gardel, M.L., Kroy, K., Frey, E., HoVman, B.D., Crocker, J.C., Bausch, A.R., Weitz, D.A.: Microrheology probes length scale dependent rheology. Phys. Rev. Lett. **96**(11), 118104 (2006)
75. Hatami-Marbini, H., Picu, R.C.: Heterogeneous long-range correlated deformation of semiflexible random fiber networks. Phys. Rev. E **80**, 046703 (2009)
76. Mofrad, M.R.K.: Rheology of the cytoskeleton. Annu. Rev. Fluid Mech. **41**, 433–453 (2009)
77. Crocker, J.C., Valentine, M.T., Weeks, E.R., Gisler, T., Kaplan, P.D., Yodh, A.G., Weitz, D.A.: Two-point microrheology of inhomogeneous soft materials. Phys. Rev. Lett. **85**, 888–891 (2000)
78. Lau, A.W.C., Hoffman, B.D., Davies, A., Crocker, J.C., Lubensky, T.C.: Microrheology, stress fluctuations, and active behavior of living cells. Phys. Rev. Lett. **91**(19), 198101 (2003)
79. Band, R.P., Burton, A.C.: Mechanical properties of the red cell membrane. I. Membrane stiffness and intracellular pressure. Biophys. J. **4**, 115–135 (1964)
80. Discher, D.E., Boal, D.H., Boey, S.K.: Simulations of the erythrocyte cytoskeleton at large deformation, II. Micropipette aspiration. Biophys. J. **75**, 1584–1597 (1998)
81. Hochmuth, R.M.: Micropipette aspiration of living cells. J. Biomech. **33**, 15–22 (2000)
82. Mijailovich, S.M., Kojic, M., Zivkovic, M., Fabry, B., Fredberg, J.J.: A finite element model of cell deformation during magnetic bead twisting. J. Appl. Physiol. **93**, 1429–1436 (2002)
83. Karcher, H., Lammerding, J., Huang, H., Lee, R.T., Kamm, R.D., Kaazempur-Mofrad, M.R.: A three-dimensional viscoelastic model for cell deformation with experimental verification. Biophys. J. **85**, 3336–3349 (2003)
84. Mack, P.J., Kaazempur-Mofrad, M.R., Karcher, H., Lee, R. T., Kamm, R.D.: Force induced focal adhesion translocation: effects of force amplitude and frequency. Am. J. Physiol. Cell Physiol. **287**, C954–C962 (2004)

85. Guilak, F., Haider, M.A., Setton, L.A., Laursen, T.A., Baaijens, F.P.T.: Mutiphasic models for cell mechanics, In: Mofrad, M.R.K., Kamm, R. (eds.), Cytoskeletal mechanics: models and measurements. Cambridge University Press, Cambridge (2006)
86. Desprat, N., Richert, A., Simeon, J., Asnacios, A.: Creep function of a single living cell. Biophys. J. **88**, 2224–2233 (2005)
87. Mofrad, M.R.K., Kamm, R.: Cytoskeletal mechanics: models and measurements, Cambridge University Press, Cambridge (2006)
88. Picu, R.C., Hatami-Marbini, H.: Long-range correlations of elastic fields in semi-flexible fiber networks. Comput. Mech. **46**(4), 635–640 (2010)
89. Resch, G.P., Goldie, K.N., Krebs, A., Hoenger, A., Small, J.V.: Visualisation of the actin cytoskeleton by cryo-electron microscopy. J. Cell Sci. **115**, 1877–1882 (2002)
90. Hatami-Marbini, H., Picu, R.C.: Modeling the mechanics of semiflexible biopolymer networks: non-affine deformation and presence of long-range correlations, In: Advances in soft matter mechanics (review0029)
91. Head, D.A., Levine, A.J., MacKintosh, F.C.: Distinct regimes of elastic response and deformation modes of cross-linked cytoskeletal and semiflexible polymer networks. Phys. Rev. E **68**(6), 061907 (2003)
92. Wilhelm, J., Frey, E.: Elasticity of stiff polymer networks. Phys. Rev. Lett. **91**(10), 108103 (2003)
93. Onck, P.R., Koeman, T., van Dillen, T., van der Giessen, E.: Alternative explanation of stiffening in cross-linked semiflexible networks. Phys. Rev. Lett. **95**(17), 178102 (2005)
94. Heussinger, C., Frey, E.: Stiff polymers, foams, and fiber networks. Phys. Rev. Lett. **96**(1), 017802 (2006)
95. Hatami-Marbini, H., Picu, R.C.: Scaling of nonaffine deformation in random semiflexible fiber networks. Phys. Rev. E **77**, 062103 (2008)
96. Hatami-Marbini, H., Picu, R.C.: Effect of fiber orientation on the non-affine deformation of random fiber networks. Acta Mech. **205**, 77–84 (2009)
97. Stossel, T. P., Condeelis, J., Cooley, L., Hartwig, J. H., Noegel, A., Schleicher, M., Shapiro, S. S.: Filamins as integrators of cell mechanics and signaling, Nat. Rev. Mol. Cell Biol. **2**, 138–145 (2001)
98. Furuikea, S., Ito, T., Yamazaki, M.: Mechanical unfolding of single filamin A (ABP-280) molecules detected by atomic force microscopy, FEBS Lett., **498**, 72–75 (2001)
99. Yamazaki, M., Furuikea, S., Ito, T.: Mechanical response of single filamin A (ABP-280) molecules and its role in the actin cytoskeleton. J. Muscle Res. Cell Motil. **23**, 525–534 (2002)
100. Golji, J., Collins, R., Mofrad, M.R.K.: Molecular mechanics of the alpha-actinin rod domain: bending, torsional, and extensional behavior. PLoS Comput. Biol. **5**(5), e1000389, 1–18 (2009)
101. Kolahi, K.S., Mofrad, M.R.K.: Molecular mechanics of filamin rod domain. Biophys. J. **94**, 1075–1083 (2008)
102. Kreis, T., Vale, R.: Guidebook to the extracellular matrix, anchor, and adhesion proteins, Oxford University Press, Oxford, 1999
103. Winder, S.J., Ayscough, K.R.: Actin-binding Proteins. J. Cell Sci. **118**, 651–654 (2005)
104. Mullins, R.D., Heuser, J.A., Pollard, T.D.: The interaction of Arp2/3 complex with actin: nucleation, high affinity pointed end capping, and formation of branching networks of filaments. Proc. Natl. Acad. Sci. **95**(11), 6181–6186 (1998)
105. Koenderink, G.H., Dogic, Z., Nakamura, F., Bendix, P.M., MacKintosh, F.C., Hartwig, J.H., Stossel, T.P., Weitz, D.A.: An active biopolymer network controlled by molecular motors. Proc. Natl. Acad. Sci. **106**(36), 15192–15197 (2009)
106. Burridge, K., Fath, K., Kelly, T., Nuckolls, G., Turner, C.: Focal adhesions: transmembrane junctions between the extracellular matrix and the cytoskeleton. Annu. Rev. Cell Biol. **4**, 487–525 (1988)
107. Burridge, K., Chrzanowska-Wodnicka, M.: Focal adhesions, contractility and signaling. Annu. Rev. Cell Dev. Biol. **12**, 463–519 (1996)

108. Wechezak, A., Viggers, R., Sauvage, L.: Fibronectin and f-actin redistribution in cultured endothelial cells exposed to shear stress. Lab. Invest. **53**, 639–647 (1985)
109. Galbraith, C.G., Skalak, R., Chien, S.: Shear stress induces spatial reorganization of the endothelial cell cytoskeleton. Cell Motil. Cytoskeleton **40**(4), 317–330 (1998)
110. Maniotis, A.J., Chen, C.S., Ingber, D.E.: Demonstration of mechanical connections between integrins, cytoskeletal filaments and nucleoplasm that stabilize nuclear structure. Proc. Natl. Acad. Sci. USA **94**, 849–854 (1997)
111. Chandran, P.L., Wolf, C.B., Mofrad, M.R.K.: Band-like stress fiber propagation in a continuum and implications for myosin contractile stresses. Cell. Mol. Bioeng. **2**(1), 13–27 (2009)
112. Lo, C.-M., Wang, H.-B., Dembo, M., Wang, Y.-L.: Cell movement is guided by the rigidity of the substrate. Biophys. J. **79**, 144–152 (2000)
113. Saez, A., Ghibaudo, M., Buguin, A., Silberzan, P., Ladoux, B.: Rigidity-driven growth and migration of epithelial cells on microstructured anisotropic substrates. Proc. Natl. Acad. Sci. USA **104**, 8281–8286 (2007)
114. Chandran, P.L., Mofrad, M.R.K.: Rods-on-string idealization captures semiflexible filament dynamics. Phys. Rev. E **79**, 011906 (2009)
115. Chandran, P.L., Mofrad, M.R.K.: Averaged implicit hydrodynamic model of semiflexible filaments. Phys. Rev. E **81**, 81(3), 031920 (2010)
116. Lu, L., Oswald, S.J., Ngu, H., Yin, F.C.-P.: Mechanical properties of actin stress fibers in living cells, Biophys. J. **95**, 6060–6071 (2008)
117. Sbrana, F., Sassoli, C., Meacci, E., Nosi, D., Squecco, R., Paternostro, F., Tiribilli, B., Zecchi-Orlandini, S., Francini, F., Formigli, L.: Role for stress fiber contraction in surface tension development and stretch-activated channel regulation in C2C12 myoblasts. Am. J. Physiol. Cell Physiol. **295**, C160–C172 (2008)
118. Martens, J. C., Radmacher, M.: Softening of the actin cytoskeleton by inhibition of myosin II, Pflugers Arch Eur. J. Physiol. **456**, 95–100 (2008)
119. Sanger, J.M., Mittal, B., Pochapin, M.B., Sanger, J.W.: Stress fiber and cleavage furrow formation in living cells microinjected with fluorescently labeled α-actinin. Cell Motil. Cytoskeleton **7**, 209–220 (1987)
120. Edulund, M., Lotano, M.A., Otey, C.A.: Dynamics of α-actinin in focal adhesions and stress fibers visualized with α-actinin-green fluorescent protein. Cell Motil. Cytoskeleton **48**, 190–200 (2001)
121. Maddox, A.S., Lewellyn, L., Desai, A., Oegema, K.: Anillin and the septins promote symmetric ingression of the cytokinetic furrow. Dev. Cell **12**, 827–835 (2007)
122. Kruse, K., Joanny, J.F., Ju licher, F., Prost, J., Sekimoto, K.: Asters, vortices, and rotating spirals in active gels of polar filaments. Phys. Rev. Lett. **92**(7), 078101
123. Backouche, F., Haviv, L., Groswasser, D., Bernheim-Groswasser, A.: Active gels: dynamics of patterning and self-organization. Phys. Biol. **3**, 264–273 (2006)
124. Janson, L.W., Taylor, D.L.: In vitro models of tail contraction and cytoplasmic streaming in amoeboid cells. J. Cell Biol. **123**, 345–356 (1993)
125. Bendix, P.M., Koenderink, G.H., Cuvelier, D., Dogic, Z., Koeleman, B.N., Brieher, W.M., Field, C.M., Mahadevan, L., Weitz, D.A.: A quantitative analysis of contractility in active cytoskeletal protein networks. Biophys. J. **94**, 3126–3136 (2008)
126. Carlsson, A.E.: Contractile stress generation by actomyosin gels. Phys. Rev. E **74**, 051912 (2006)
127. Humphrey, D., Duggan, C., Saha, D., Smith, D., Kas, J.: Active fluidization of polymer networks through molecular motors. Nature **416**, 413–416 (2002)
128. Liverpool, T., Maggs, A., Ajdari, A.: Viscoelasticity of solutions of motile polymers. Phys. Rev. Lett. **86**, 4171–4174 (2001)
129. Ziebert, F., Aranson, I.: Rheological and structural properties of dilute active filament solutions. Phys. Rev. E **77**, 011918 (2008)
130. Mofrad, M.R.K., Kamm, R.D.: Cellular mechanotransduction: diverse perspectives from molecules to tissues, Cambridge University Press, Cambridge (2010)

131. Jaalouk, D.E., Lammerding, J.: Mechanotransduction gone awry. Nat. Rev. Mol. Cell Biol. **10**(1), 63–73 (2009)
132. Ingber, D.E.: Cellular mechanotransduction: putting all the pieces together again. FASEB J. **20**(7), 811–827 (2006)
133. Vogel, V.: Mechanotransduction involving multimodular proteins: Converting force into biochemical signals. Annu. Rev. Biophys. Biomol. Struct. **25**, 459–488 (2006)
134. Barakat, A.I., Gojova, A.: Role of ion channels in cellular mechanotransduction—lessons from the vascular endothelium, In: Mofrad, M.R.K., Kamm, R.D (eds.) Cellular mechanotransduction: diverse perspectives from molecules to tissues, Cambridge University Press, Cambridge (2010)
135. Martinac, B.: Mechanosensitive ion channels: molecules of mechanotransduction. J. Cell Sci. **117**, 2449–2460 (2004)
136. Perozo, E.: Gating prokaryotic mechanosensitive channels. Nat. Rev. Mol. Cell Biol. **7**, 109–119 (2006)
137. Schwartz, G., Droogmans, G., Nilius, B.: Shear stress induced membrane currents and calcium transients in human vascular endothelial cells. Pflugers Arch. **421**, 394–396 (1992)
138. Nerem, R.M., Levesque, M.J., Cornhill, J.F.: Vascular endothelial morphology as an indicator of the pattern of blood flow. J. Biomech. Eng. **103**(3), 172–176 (1981)
139. Pohl, U., Holtz, J., Busse, R., Bessenge, E.: Crucial role of endothelium in the vasodilator response to increased flow in vivo, Hypertension **8**, 37–44 (1986)
140. Koller, A., Sun, D., Kaley, G.: Role of shear stress and endothelial prostaglandins in flow- and viscosity-induced dilation of arterioles in vitro. Circ. Res. **72**, 1276–1284 (1993)
141. Dennerll, T.J., Joshi, H.C., Steel, V.L., Buxbaum, R.E., Heidemann, S.R.: Tension and compression in the cytoskeleton of PC-12 neurites. II: quantitative measurements. J. Cell Biol. **107**, 665–674 (1988)
142. Putnam, A.J., Schultz, K., Mooney, D.J.: Control of microtubule assembly by extracellular matrix and externally applied strain. Am. J. Physiol. **280**, C556–C564 (2001)
143. Hudspeth, A.: How the ear's works work: mechanoelectrical transduction and amplification by hair cells. C R Biol. **328**(2), 155–162 (2005)
144. Ingber, D.E.: Mechanobiology and diseases of mechanotransduction. Ann. Med. **35**(8), 564–577 (2003)
145. Cheng, C., Tempel, D., van Haperen, R., van der Baan, A., Grosveld, F., Daemen, M.J., Krams, R., de Crom, R.: Atherosclerotic lesion size and vulnerability are determined by patterns of fluid shear stress. Circulation **113**, 2744–2753 (2006)
146. Klein-Nulend, J., Bacabac, R.G., Veldhuijzen, J.P., Van Loon, J.J.: Microgravity and bone cell mechanosensitivity. Adv. Space Res. **32**, 1551–1559 (2003)

Forces During Cell Adhesion and Spreading: Implications for Cellular Homeostasis

Shawn P. Carey, Jonathan M. Charest and Cynthia A. Reinhart-King

Abstract Cells adhere and spread by exerting forces against the cell membrane and against the extracellular matrix. Intracellular forces drive the membrane outward during spreading and stabilize cell shape in adherent and migrating cells. A balance of intracellular force with exogenous forces is required for maintenance of basic cell functions and cellular homeostasis. Here, we provide a multi-scale overview of the cellular machinery and intracellular forces at play during cell spreading and adhesion, including description at the molecular, cellular and tissue levels. We describe the cellular machinery required for force generation, explain aspects of its regulation, and show how the machinery operates to direct a cell to a homeostatic target. The biochemical and biophysical events that dominate the process of isotropic cell spreading are examined and the process of spreading is explained as a series of distinct phases, each with their own force signature. In addition, we consider how intracellular force affects mechanical cellular homeostasis and maintenance of tissue structure and function. The disruption of cellular mechanical homeostasis is described in the context of two prominent disease states: cancer and atherosclerosis.

1 Introduction

Current research has brought much attention and interest to the role of cell mechanics in cellular homeostasis and physiological function. Cell adhesion and

S. P. Carey, J. M. Charest and C. A. Reinhart-King (✉)
Department of Biomedical Engineering, Cornell University,
302 Weill Hall, Ithaca, NY 14853, USA
e-mail: cak57@cornell.edu

Stud Mechanobiol Tissue Eng Biomater (2011) 4: 29–69
DOI: 10.1007/8415_2010_22

Published Online: 15 September 2010

spreading is a primary mechanism through which mechanical (and sometimes chemical) homeostasis is achieved. These processes are crucial in both development and the maintenance of normal tissue structure and function. As such, improper cell adhesion and spreading has been implicated in a multitude of disease states, including cancer and atherosclerosis. Here we will take an in-depth look at the processes of cell adhesion and spreading, with a specific emphasis on the role of cell mediated-force: first describing the subcellular machinery employed during adhesion and spreading, then describing the cellular level changes of a single cell through the process, and finally examining how disruption of cell adhesion and spreading can lead to disease.

2 Biological Machinery Required for Force Generation

2.1 Internal Cellular Machinery

Cellular forces are primarily generated in the cytoskeleton. The cytoskeleton is essential for maintaining cell shape and organization, imparting specific mechanical properties to cells. There are three primary cytoskeletal components: microfilaments, microtubules, and intermediate filaments. While each component serves separate functions in the cell, there are several commonalities:

- Each component is composed of repeating subunits that polymerize to form polarized filamentous structures.
- Polymerization of most components requires the binding of either ATP or GTP to its subunits.
- Each polymerized component has characteristic mechanical properties that are directly determined by the structure of its subunits.
- Polymerized structures associate with various other structural and signaling proteins for purposes such as stabilization, regulation, or linkage to other parts of the cell.
- Each component has associated motor proteins that facilitate relative axial movement in a stepwise fashion dependent upon ATPase activity, contributing to the generation of cellular forces.

Here we focus primarily on microfilaments and microtubules, as they are the primary cytoskeletal filaments associated with cellular force generation.

2.1.1 Actin and Myosin

Actin is the primary component of the cytoskeleton required for the generation of cellular forces imposed externally and is by far the most studied in the context of the regulation of cell spreading and adhesion. In a cell, actin can generate forces

through two primary mechanisms: (1) simply through polymerization or (2) through coupling to its associated motor protein, myosin.

Actin Structure and Dynamics

Actin can exist in two distinct forms within the cell: globular actin (G-actin) or filamentous actin (F-actin). G-actin is a ~43 kDa protein that can bind ATP and polymerize to form microfilaments known as F-actin. The nucleation of F-actin filaments is controlled and accelerated by certain chaperone proteins such as Arp2/3 among others. An F-actin filament is polarized and has a positive (+) end and a negative (−) end. Both ends are highly dynamic but have different on/off rates; growth of filaments occurs primarily at the positive end, as it has a much higher on rate. Actin filaments are highly cross-linked and bundled by proteins such as α-actinin to increase their structural integrity. Actin dynamics and the two mechanisms through which it can generate force are summarized in Fig. 1. Figure 1a, b depicts the polymerization of actin which can drive membrane extension. Figure 1c depicts actin's interaction with myosin which can drive filament sliding and the generation of contractile force.

Actin-Interacting Proteins

The cellular actin network owes its highly dynamic nature to the actin-interacting proteins that facilitate its assembly, stabilization, and disassembly. The protein

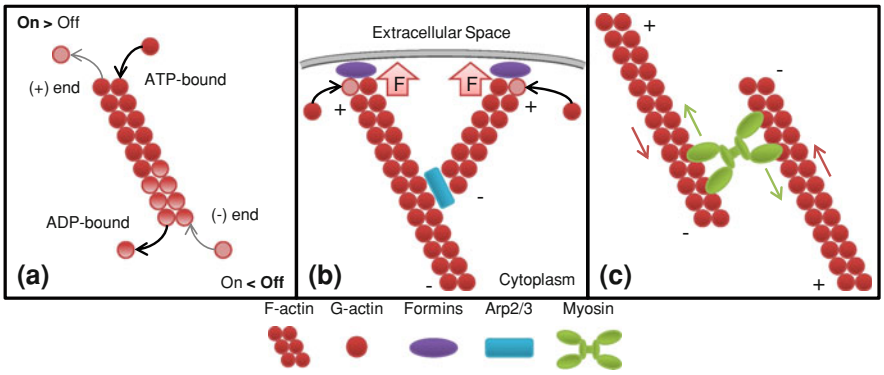

Fig. 1 Actin filament-based force generation. **a** Filament dynamics: filament polymerization and depolymerization occur at opposite ends resulting in filament "treadmilling". **b** Force generation through cortical branching at the cell membrane: Arp2/3 mediates microfilament branching and formins mediate actin polymerization at the cell membrane producing protrusive forces. **c** Myosin-mediated contraction of microfilaments: myosin mediates the contraction of anti-parallel overlapping microfilaments, the mechanism at the core of cell contractile force generation. *Outer arrows* indicate direction of filament displacement, *inner arrows* indicate direction of myosin motor displacement

complex Arp2/3 facilitates actin filament nucleation, enables branching by attaching to a filament and nucleating a new filament and aids in network stabilization. Filament polymerization can be enhanced by the family of proteins known as formins and the protein VASP [1]. Formins act as "processive caps" by attaching the (+) end of the filament to the plasma membrane while simultaneously enabling further polymerization and protecting the filaments from other capping proteins [2]. Complementary to these proteins are ADF/cofilin, which disassembles actin from its (−) end [1]. Another group of important actin-interacting proteins are those that link actin to transmembrane adhesion molecules (discussed in later sections of this chapter). The linkages between actin and the membrane involve a large, multi-component complex of proteins that facilitate transmission of chemical and mechanical signals between the intracellular and extracellular space. Talin is largely implicated as one of the critical structural proteins linking f-actin filaments to transmembrane integrins [3, 4]. These transmembrane complexes are particularly important as they allow actin-generated forces to be transmitted to the cell's environment.

Measurement of Actin-Generated Forces and Mechanical Properties

During cell adhesion and spreading, forces generated by actin polymerization can be exerted directly against the cell membrane. McGrath and colleagues showed that actin polymerization is capable of exerting forces on either curved or flat surfaces, based on their data which shows that the force of actin polymerization can propel micron-sized synthetic disks through solution [5]. These findings implicated that actin polymerization can exert force on a substrate regardless of its curvature. This is particularly important in the context of cell generated forces, as actin polymerization forces are primarily exerted on the highly fluid cell membrane.

Only relatively recently has the force of actin polymerization been quantitatively measured [1, 6]. The force generated by a branching actin network was first investigated by Fletcher and colleagues in 2005 [6] using atomic force microscopy (AFM). An AFM cantilever tip was coated with ActA (an actin-interacting protein from *Listeria monocytogenes* that facilitates polymerization), placed into cell extract, and an actin network was allowed to form (Fig. 2a). The AFM cantilever tip was then used to measure the displacement of, and force exerted on, the growing actin network. The data is depicted using a force–velocity (F_v) curve as shown in Fig. 2d.

F_v curves are used to depict the force profile in biological systems because experimentally, force in biological systems is often measured using optical methods to track displacement against an opposing force. These opposing forces can be provided by objects such as a micron-sized bead in a viscous suspension [5], or an AFM cantilever tip as was the case in these experiments [6, 18]. These measurements of actin polymerization from Fletcher and colleagues [6] revealed two distinct phases of force generation: a load-independent phase and a stalling

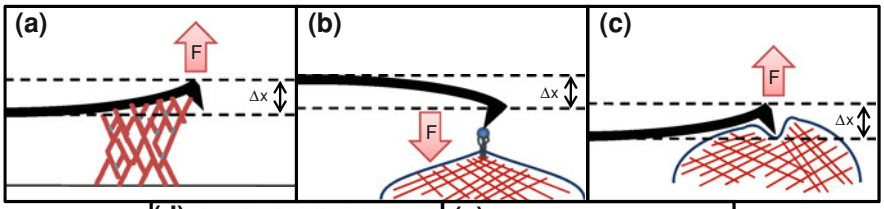

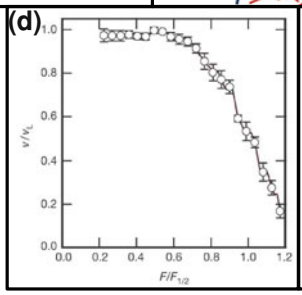

(e)

Adhesion Molecule	Rupture Force (pN)
Integrin α2β1	65
Integrin α4β1	20
Integrin α5β1	35-80
Integrin αLβ2	35-80
Integrin αVβ3	42

Fig. 2 Methods of measuring cellular level forces. **a** Actin polymerization force against an AFM cantilever tip causes tip displacement. **b** Integrin ligands are attached to an AFM cantilever tip, then brought into contact with the cell surface. The tip is then displaced away from the cell until the ligated integrins are torn from the membrane. **c** Lamellipod protrusion force against an AFM cantilever tip causes tip displacement. **d** *Reprinted* by permission from *Macmillan Publishers Ltd*: Nature Cell Biology [6], copyright 2005. Normalized F_v curve of actin polymerization obtained through method depicted in **a** [6]. **e** Single-cell rupture forces for various integrins using the experimental setup depicted in **c**. Ranges are given when more than one value has been reported [7–17]

phase. The load-independent phase indicated that the network was capable of growing at a relatively constant rate over a fairly large range of forces, about 0–300 nN. The stall force (the force at which velocity reaches zero) measured for the network of actin filaments is on the order of hundreds of nano-newtons. Additional studies have used AFM to measure the force exerted by actin polymerization in a protruding lamellipod [18] (Fig. 2b). Data from these experiments illustrates that actin polymerization is the driving mechanism of protrusive force generation in cells, and is critical to cell spreading.

Microfilament rigidity is also critical to the ability of actin fibers to provide stable cellular structure and effectively transmit force. One measure of the stiffness of a given cytoskeletal filament is its persistence length, which represents the rough distance over which a filament may be considered completely rigid. Persistence lengths of actin filaments have been measured by observing their deformation under thermal fluctuations or various loading conditions [19–22]. Early studies concluded that the persistence length of an actin filament is around 17 μm [19]. Later studies examined filaments under different conditions (nucleotide binding, phalloidin binding, etc.) and found the persistence length could vary from 7 to 20 μm [22]. Additionally, actin-interacting proteins such as cofilin have also been shown to influence filament persistence length [21]. The cell's ability to modulate microfilament persistence length is important in fine-tuning force generation.

Myosin Structure and Dynamics

The myosins are a family of motor proteins associated with actin. Actin–myosin complexes generate the cellular forces used in cell contractility and migration. The majority of myosins are (+) end motors, meaning that they move along actin filaments towards the (+) end. There are several different types of myosins and each participates in specific cellular functions. In this chapter, we will be primarily concerned with non-muscle myosin II (NMII), as it is most often implicated in the generation of cellular-level forces [23]. Myosin "heavy chains" consist of one or more head, neck, and tail domains. Head domains bind actin and require ATP to detach. As such, if ATP is depleted within a cell, its myosin molecules remain attached to actin and cannot move. The neck domain contains binding sites for myosin "light chains" (calmodulins) that regulate the head domain. Activation of myosins such as NMII requires phosphorylation of its light chain domain. The tail domain facilitates the interaction of myosin proteins with each other, forming myosins with more than one head and allowing the formation of myosin filaments (a common example of this type of filament can be found in the A-band in the sarcomere of skeletal muscle). Functionally, myosins also strengthen the actin network by cross-linking actin fibers. Studies of myosin molecule interactions with actin fibers using optical trapping techniques indicated that a single myosin molecule is capable of exerting forces on the order of $\sim$3.5 pN while producing a displacement of about 11 nm [24].

2.1.2 Microtubules

In comparison to actin, microtubules are much larger, more rigid [19], and slightly less dynamic. Although their role in cell adhesion and spreading is less understood, it is known that they contribute to the mechanical properties of cells and are involved in the establishment of cellular homeostasis. Like actin, microtubules have specific associated motors that contribute to force generation. However, we will not specifically discuss the microtubule-associated motor proteins (kinesins and dyneins) as they function primarily for transport within the cell and are not directly involved in the generation of cellular-level, adhesion-related forces.

Microtubule Structure and Dynamics

Microtubule subunits are heterodimers made up of the globular proteins α-tubulin and β-tubulin. Their structure is complex: α/β-tubulin dimers first polymerize longitudinally to form protofilaments. The protofilaments then line up side by side to form curved sheets that eventually wrap into a tube consisting of 13 protofilaments in circumference. Both α- and β-tubulin require GTP in order to form a dimer and polymerize into full microtubules. Nucleation and stabilization of long microtubules is mediated by γ-tubulin and its associated proteins (known as the γ-tubulin ring

complex, or γ-TuRC). In the cell, microtubules generally originate from the microtubule organizing center (MTOC), which is found near the centrioles.

Like actin, microtubules are polarized and have both a positive end (which is highly dynamic) and a negative end. Assembly and disassembly occurs primarily at the microtubule (+) end. The assembly rate is lower than the disassembly rate, primarily because disassembly can occur in a "catastrophic" fashion. Conformational changes of the subunits occur when the β-tubulin in the α/β-tubulin heterodimer hydrolyzes its bound GTP to GDP, creating a "kink" between the α- and β-tubulin. This kink can cause unstable microtubule ends to disassemble by peeling apart.

Measurement of Microtubule-Generated Forces and Mechanical Properties

Similar to actin dynamics, both microtubule polymerization and depolymerization are known to generate force. Early studies of microtubule polymerization forces analyzed the buckling of microtubules against an immobile barrier to calculate an F_v curve [25]. These studies found an exponential decay relationship in the F_v curve, closely resembling modeling predictions. Subsequent attempts to observe microtubule assembly dynamics used more advanced techniques such as optical traps, enabling molecular-level resolution [26]. Methods to measure microtubule persistence length are similar to those used to examine actin filaments. As mentioned earlier in this chapter, microtubules have a much higher rigidity than actin filaments. This is evidenced in the relatively high persistence length of microtubules, which is on the order of about 5 mm (as compared to actin filaments, at around 10–20 μm) [19]. This also fits well with observations that microtubules generally support compressive loads within the cell [27, 28].

2.1.3 Intermediate Filaments

Intermediate filaments are the third major class of cytoskeletal elements. As a part of the cytoskeletal network, they contribute to cellular shape and structural integrity, and are largely considered cellular "shock-absorbers" to mediate and mitigate external mechanical stresses [29]. The class of cytoskeleton proteins known as intermediate filaments is really a collection of various proteins, each with different tissue specificities, but a conserved filamentous structure. Depending on the specific filament type, intermediate filaments can have persistence lengths ranging from 200 nm (keratin) to 1,300 nm (vimentin) [30]. Therefore intermediate filament proteins are far softer and more flexible than microtubules and actin filaments. While it is not known if intermediate filaments plan an active role in adhesion and spreading, it is clear they play a mechanical role in the cell by acting as a stress-buffering system. A more extensive review of the structure and mechanical properties of intermediate filaments can be found in the following extensive reviews [29, 30].

2.2 Cell–Environment Connection Machinery

The ability of cells to generate forces through the intracellular machinery described above is critical for a variety of essential cellular functions. Intimately tied to the generation of forces is the ability of a cell to attach to its matrix in order to transmit and stabilize these intracellular forces.

Early studies showed that cell–matrix adhesions are crucial for cell survival [31, 32] and established the concept of "anchorage dependence," referring to the need for a cell to attach to a substrate to survive. Landmark studies using the then newly-purified ECM protein fibronectin revealed the presence of a physical transmembrane link between the specific constituents of the ECM and the cytoskeleton. For example, treatment of transformed cells with fibronectin caused "increased cell-to-substratum adhesion of treated cells, cell spreading and flattening, and elongation of cell processes" [33] as well as reorganization of cytoskeletal F-actin [34]. It was observed that extracellular matrix macromolecules such as fibronectin aggregate into filaments and serve as ligands for specific transmembrane receptors, which cluster and serve as docking stations for intracellular cytoskeleton proteins such as actin [35–37]. Shortly thereafter, the phenomenon of cellular "shape sensing" was identified as the basis for density dependent cell growth inhibition and anchorage dependence [38]. This concept has since grown significantly and implications of this work are important for our understanding of cell adhesion, spreading, and homeostasis.

2.2.1 Integrins

The transmembrane receptors that mediate the dynamic physical interactions between cytoskeleton-extracellular matrix were first purified in 1986 and were termed *integrins* [39, 40]. Integrins are heterodimeric (α- and β-subunits), transmembrane proteins with highly conserved extracellular and cytosolic domains. These transmembrane macromolecules are being studied in a wide number of human health-related fields, including development, cancer, hematology, and immunology. In the past three decades, the integrin family has expanded to include a number of homologous adhesion receptors whose most basic function is to bind to insoluble extracellular matrix protein ligands. However, their role is more complex, as they mediate both physical *and* chemical interactions through their involvement in focal adhesions. Additionally, their signaling functions are bidirectional, capable of both "inside-out" and "outside-in" signaling.

Integrin Specificity

Integrins bind to specific extracellular matrix glycoproteins to allow a cell to adhere, spread, and migrate. The combination of integrin subunits imparts specificity.

Certain cells and their integrins adhere only to specific matrix proteins. Inherent in this is ligand-specific "outside-in" signaling. While integrins bind specific sequences in matrix proteins, integrins do not demonstrate singularity. That is, a given integrin (an α/β combination) can potentially bind with *several* different extracellular matrix ligands. For example, the $\alpha5\beta1$ integrin can act as the adhesion receptor for both fibronectin and collagen. Therefore, adhesion and spreading of a given cell-type are mediated through cell-type specific integrins ligating their corresponding matrix proteins.

Integrin Avidity, Affinity, and Activation

Also important in cell adhesion and spreading is a cell's ability to control and modulate integrin function. This ultimately determines how tightly a cell can adhere to a substrate in its microenvironment. Studies with leukocytes and platelets provided evidence that some cells can change their adhesiveness in response to microenvironmental factors [41]. Changes in cellular adhesiveness or "avidity" do not occur through recruitment of receptors to the membrane, but rather through increased integrin affinity (through integrin activation) and valency (governed by density of receptor and ligand on surfaces). Regulation of integrin *affinity* through intermolecular interactions and intramolecular allostery is an elegant demonstration of the bi-directionality of integrin signaling.

- "Inside-out" signaling:
  - Short cytoplasmic integrin tails (primarily of the β-subunit) interact with membrane-associated intracellular proteins.
  - The ligand-binding site is restructured through long-range allosteric conformational changes that result in increased integrin affinity (or "activation").
- "Outside-in" signaling:
  - Subsequent ligand binding causes conformational changes that are transmitted back to the cell to regulate diverse responses [42].

This "activation" process can also run in reverse, beginning with integrins binding to extracellular ligands and resulting in the presentation of cytoskeletal adapter protein binding sites. Integrin avidity can also be impacted by *valency*: increased integrin clustering, increased membrane diffusivity of β subunits [43]. As is often the case with integrins, movement of integrin receptors laterally within a membrane can be initiated both *extracellularly* (as a result of extracellular ligand availability) and/or *intracellularly* (through F-actin-mediated relocation of integrins) [44]. Integrin organization within the plasma membrane has several implications in terms of both signaling and internal cytoskeletal organization, which will become more apparent in later sections.

Mechanical Characterization of Integrin Interactions

Even though integrins themselves are incapable of generating force, they are essential components in transmitting cell-generated forces to the environment. To achieve this, integrins must be capable of withstanding relatively high levels of mechanical stress. Studies to determine the amount of force integrins can withstand before failing are vast [45], although they generally fall into two categories: whole cell studies and single integrin studies. AFM has been a useful tool in characterizing integrin binding affinities. Using AFM in this setting allows a substrate to be brought into contact with the cell surface and then removed with known displacement and force (Fig. 2c). Using this technique on the single cell level has revealed a rupture force (force at which the ligand unbinds from the receptor) on the order of 30–80 pN, given a loading rate of 1 nN s^{-1} [45]. A more comprehensive review of using AFM to measure cellular binding interactions appears in a recent paper by Helenius et al. [45].

Optical traps (or "optical tweezers") have also been used extensively to measure adhesion molecule load bearing [45]. This method involves using micron-sized beads coated with integrin ligands. These beads can be controlled using optical techniques and used to exert force on a cell once in contact with its adhesion receptors. Galbraith and colleagues used this method to investigate how forces exerted on integrins mediate focal complex formation, a concept we will discuss in more detail in Sect. 4 [44, 46].

2.3 Cell–Cell Connection Machinery

Just as cells have transmembrane integrins to connect their internal machinery to their environment, they also have transmembrane machinery specifically for establishing connections with other cells. These molecules follow the same theme of exhibiting a high degree of specificity in their function, enabling cells to sense their environment. Cell–cell contact also regulates the extent of spreading and cell force generation [47].

The primary mediators of cell–cell adhesion are the cadherin family of proteins. Cadherins are glycoproteins with a single transmembrane domain. There are several types of cadherins, E-, N-, and P-cadherin, and their distribution is tissue-specific. Their extracellular domains (N-terminal) bind other cadherins in a homotypic manner (i.e. a E-cadherin molecule will bind only other E-cadherins) that is Ca^{2+}-dependent. The cytoplasmic domains (C-terminal) link to the actin and microtubules of the cytoskeleton with the help of α- and β-catenin. Dimerization of cadherin molecules is also required for cell–cell adhesion. E-cadherin is the prototypic cadherin and has been implicated in several signaling pathways relating to the establishment of cell polarity, actin polymerization, and Rho activation.

Another family of cell–cell connection molecules is the immunoglobulin (Ig) superfamily. This family includes molecules such as N-CAM, ICAM, VCAM,

PECAM and several others. Like the cadherins, they are transmembrane glycoproteins, however they bind in a heterotypic manner and are not dependent on Ca^{2+} for their ligation. Expression of these molecules is tissue-specific and can be induced by certain cytokines.

Yet another group of transmembrane glycoproteins involved in cell–cell connections are the selectins. This family has several members (E-Selectin, P-Selectin, L-Selectin). Expression is cell type specific and in some cases can be induced by exposure to growth factors such as TNFα. These heterotypically bind sugar moieties on the surface of other cells in a Ca^{2+}-dependent manner.

The cell–cell adhesion molecules, once engaged, are most commonly found clustered in the membrane, similar to the way integrins cluster. Cell–cell junctions mediated by cadherins linked to actin and myosin filaments are collectively known as adherens junctions (AJs). Like matrix adhesions, these sites include proteins such as vinculin, tropomyosin, and α-actinin (many of the same components as focal adhesions). A second type of cell–cell junction is the desmosome. This type of cell junction consists of a cytoplasmic plaque (made up of plakoglobin and desmoplakins) that links keratin fibers (intermediate filaments) to desmoglein and desmocollin, which are both cadherins. These adhesions are thought to contribute to a cell's shape and rigidity. They may also be able to transmit shear forces from one cell to its neighbors.

Cell–cell connection machinery provides yet another pathway through which cells can sense their environment to reach their homeostatic target. In the context of cell spreading, this target takes the form of contact inhibition, a phenomena in which cells will stop spreading if they come into contact with neighboring cells. Such interactions are crucial to normal tissue function, but are disrupted in certain disease states as will be described in Sect. 5.

3 Subcellular Connections and Dynamics

3.1 Matrix Adhesions

As described in the previous section, a cell possesses machinery for internal force generation through cytoskeletal polymerization and machinery for exerting force against its extracellular matrix. Coupling of these two separate but related mechanisms to generate force enables cell–matrix adhesion and cell spreading. Here we discuss the regulation of this coupling and how it translates into a means for cells to sense their environment.

3.1.1 Initiation and Formation

Cell–matrix adhesion formation begins with the ligation of an adhesion receptor. This initiates an "outside-in" signal—usually through conformational change of

the adhesion receptor—that alerts the cell to its new connection. Adhesion-associated scaffolding and signaling proteins are then recruited to the new adhesion site. These recruited proteins often serve multiple purposes ranging from physical reinforcement to propagation of chemical signals and regulation of the adhesion lifetime. Important to their function, the activities of these proteins are transient; the regulatory events governing matrix adhesions and cytoskeletal reorganization require the molecules involved to be intrinsically dynamic. The development and maturation of matrix adhesions is often dependent upon the exertion of forces at the adhesion site.

Focal adhesions are commonly found in cells spread out on a 2D substrate and their formation is based around the ligation of integrins to their specific substrate in the ECM. Focal adhesions are molecular assemblies containing clusters of multiple scaffolding and signaling proteins [48, 49] which are typically elongated adhesions that are greater than 1 μm^2 in area. Focal adhesions mature from focal contacts, which are small dot-like adhesions, typically after the application of force [50]. One of the first proteins to be recruited by a ligated integrin is talin. Talin binds directly to the β-subunits of integrins and serves as a platform for both linking to the cytoskeleton via actin filaments and binding to other recruited proteins such as paxillin (also an integrin-binding protein) and vinculin [51]. Together, talin and paxillin recruit focal adhesion kinase (FAK). FAK has multiple functions within the cell, including contributing to focal adhesion turnover, transduction of signals to regulatory proteins, and phosphorylation of other focal adhesion proteins [3]. Src, a membrane-associated tyrosine kinase, forms a complex with FAK that aids in further signal propagation [3]. The transient formation of this complex and its subsequent intracellular signaling play a role in determining the lifetime of the focal adhesion. Contractile force imposed at adhesion sites and changes in cell shape cause the clustering of additional ligated integrins and their respective linkages to the cytoskeleton [44]. This force contributes to the maintenance and stability of adhesion sites required for cell adhesion and spreading.

3.2 Mechanosensing at the Cell–Matrix Interface

The inside → outside → inside mechanosensory ability of cells is a critical controller of not only cell adhesion and spreading, but also of endogenous cellular force generation, tissue homeostasis, and quiescence [52]. Moreover, the ability of a cell to respond to external mechanical stimuli depends on highly-interconnected and coordinated networks of regulatory signaling that are integrated in the same pathways that regulate cell adhesion. In their role as signaling and structural transmembrane complexes, integrin-mediated complexes have mechanosensing

function and are capable of translating externally applied forces into cellular phenotypic changes.

Although no single sensory molecule has been identified specifically for the purpose of mechanotransduction (as has been identified for chemical stimuli, for example), mechanical stimuli in the cellular microenvironment including exogenous forces, physical properties of the ECM, and forces exerted through cell–cell adhesions have a significant effect on cell behavior. It has been shown that cells can sense external forces through a number of mechanisms, including primary cilia, stretch-modulated ion channels, nuclear lamina, the cytoskeleton, and matrix adhesions [53–55]. Cellular adhesion, spreading, and force generation rely primarily on cytoskeletal dynamics and matrix adhesions as a mechanism to sense and respond to externally applied mechanical forces.

The ability of cells to sense the stiffness of their environment, while an emerging field, is becoming a classic biological example of cellular mechanotransduction resulting in differential cell spreading. Stiffness sensing relies upon "active tactile exploration" of the cellular microenvironment. That is, cells use cytoskeletal contractility to exert contractile forces through matrix adhesions, assessing the resulting substrate strains to determine the appropriate cellular response. While this phenomenon was originally observed and identified in the context of cell morphology, motility, and adhesion strengthening [56, 57], ongoing work has shown that mechanosensing of matrix stiffness is intimately involved in directional cell migration [58], cell differentiation [59], tissue development and maintenance [60–65], disease progression [66, 67], and tensional homeostasis [66, 68].

The maturation and development of matrix adhesions into focal adhesions during cell spreading and adhesion is directly affected by substrate stiffness. Initial cell adhesions to the ECM through integrins initiate integrated feedback and feedforward signaling cascades that actively regulate cell adhesion and cell force generation [69]. Mechanosensing is a driving force for this response, and it has been shown that stable focal adhesions, as evidenced molecularly by an adhesion-localized increase in tyrosine phosphorylation and behaviorally by decreased membrane ruffling and rate of spreading, only develop on sufficiently stiff substrates [56]. Cells perceive stiffness by interpreting the reactive tensile force that results from contracting the ECM through adhesions; less stiff (more compliant) substrates resist less tension, and thus, do not promote the cytoskeletal tension and protein kinase phosphorylation that are required for focal adhesion maturation and stability [44, 48].

Cells use adaptive matrix adhesions to integrate mechanical cues from their microenvironment. Through recruitment of adapter proteins and signaling molecules to sites of initial matrix adhesions, cells can perceive and respond to exogenous forces as well as physical properties of the extracellular matrix. In the following sections we will demonstrate how cells utilize integrated biochemical and biophysical pathways to adhere, spread, change shape, and migrate by providing analysis of the phases of cell spreading.

4 A Spreading Cell

Thus far, we have laid the groundwork for understanding the dynamics of cell adhesion and spreading by describing the cellular structures (cytoskeleton and integrin-mediated adhesions) involved. Given this information, the specific process of cell spreading can be dissected. Cell adhesion and cell spreading are fundamental biological processes essential for establishing connections between a cell's internal machinery and its environment. The establishment of these connections, or lack thereof, will dictate cell behavior by enabling a cell to sense and respond to its environment. These connections are therefore critical for achieving cellular homeostasis.

Cells have been shown to spread either isotropically, where they flatten against a surface like pancake batter on a pan, or anisotropically, where the cells send out membrane extensions unevenly in multiple directions [64]. In earlier work, we showed that when ligand density is decreased, anisotropic spreading is favored; however, when ligand density on a substrate is saturated, isotropic spreading is favored [64]. While there remains much to be understood regarding the mechanisms driving isotropic versus anistropic spreading, our data seem to indicate that the need for a cell to "search" for ligand to bind to, when ligand is sparsely coated on a surface, triggers a cell to send out increased extensions, which favors anisotropic spreading. The rate and directionality of filopodia extension depending on the microenvironment may be one determinant of the mode of spreading.

Although most cell types display both modes of spreading, current literature has primarily focused on isotropic spreading [70–76]. Spreading studies, in general, are useful model systems for simplifying the more complex process of cytoskeletal organization, and isotropic spreading is the simplest form of that model. Spreading can be thought of as a series of cytoskeletal movements that drive membrane protrusion. Given this simplification, spreading becomes a relatively pure system for understanding the forces and factors regulating cytoskeletal reorganization. Once these aspects of spreading are understood, this knowledge can be applied to our understanding of a more complicated cell processes like migration or cell division, where multiple cytoskeletal processes, like adhesion, de-adhesion, ruffling, blebbing, and retraction, occur.

Here, we will dissect the process of cell adhesion and spreading, by describing the changes undergone by a single cell from initial contact to a fully spread state and the establishment of homeostasis. To do this however, we must first make some assumptions:

- The cell is healthy, anchorage-dependent, and spreads isotropically (equally in all directions).
- The substrate exhibits sufficient adhesion molecule ligands on its surface. These ligands can take the form of ECM proteins such as fibronectin, laminin, collagen, etc.

Thus, the specific phases of spreading described here may not apply to all cell types, but because all eukaryotic organisms, including yeast, utilize similar cytoskeletal proteins and dynamics, one might anticipate that cell spreading generally occurs in unique phases. Isotropic spreading is focused on here because it much simpler mechanistically. Anisotropic spreading involves the same mechanisms, except they are spatially biased.

4.1 Defining the Phases of Spreading

Much of what is known about the individual phases of cell spreading is largely based on the work of only a few labs in recent year. Sheetz and colleagues were the first group to define the distinct phases involved in cell spreading [72, 73]. These phases were identified by comparing the spread area (A) of isotropically-spreading mouse embryonic fibroblasts on fibronectin-coated substrates with time (t). Examining a plot of ln(A) vs. ln(t) revealed three distinct rates of area increase, each following a different power law (and thus a different "rate" of spreading, dA/dt). Generally, cells exhibit an initially slow rate of spreading, followed by a period of rapid spreading, before finally reaching a fully spread state with minimal change in area. Upon examining cellular traction forces over the same duration, a biphasic trend emerges: traction forces remain low for a period of time before abruptly rising to higher levels later on, once a constant area is achieved. An example of this behavior can be seen in Fig. 3. The time course over which spreading occurs can vary depending on cell type. However, the phases of spreading as identified [72, 73] occur over the course of roughly an hour, as seen in Fig. 3.

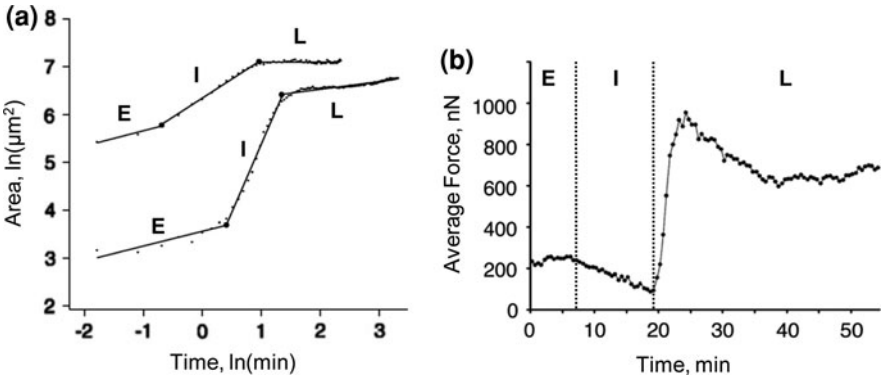

Fig. 3 Identifying the phases of spreading (**a**, *reprinted* with permission from the Journal of Applied Physiology) double logarithmic plot of cell area over time for two different mouse embryonic fibroblasts [73]. **b** Average contractile force of a single spreading mouse embryonic fibroblast over time [76] (Reproduced under Creative Commons Attribution License). *Dotted lines* indicate boundaries between phases. *E*, *I*, and *L* indicate early, intermediate, and late phases of spreading respectively

Integrating these observations with knowledge of cytoskeletal structure and function provides some information regarding the intracellular dynamics involved in spreading. As described earlier in this chapter, a major function of the cytoskeleton is to establish and support cell shape, structure and integrity. Multiple groups of proteins (such as small GTPases) actively regulate cytoskeletal dynamics (actin/microtubule (de)polymerization, myosin activation/inhibition, etc.). These regulatory proteins directly control cell shape, structure, and integrity by regulating the cytoskeleton. A cell's degree of spreading—and more broadly, its morphology—at any given time is thus the collective combination of all active cytoskeletal "states" or activity [72, 73]. Precise spatial and temporal activation of cytoskeletal states gives rise to cellular processes (membrane blebbing, ruffling, lamellipodia or filopodia extension, contraction, etc.) that are then coordinated or biased to achieve global movements such as adhesion, spreading, migration, etc. [76]. Investigation of the molecular players involved in each phase of cell spreading should provide valuable insight into the relative roles that each of these molecules play in regulating more complex processes like migration.

4.2 Phases of Spreading

4.2.1 Early Phase Spreading

Key Events

The early phase of spreading can be thought of as containing two key events: first is the *initial physical contact* between the cell and substrate, followed by the *initial sensing of the substrate surface* ligands. In most cases, cells initially exhibit a spherical or "balled-up" morphology while in suspension.

Initial Physical Contact with Substrate

The dynamics of the initial physical contact between the cell and substrate is governed primarily by the material properties of both entities [74, 75]. Very early spreading and the initial forces experienced by a cell can be analogously compared to a viscous liquid droplet (the cell) contacting a surface (the substrate). This very early spreading is primarily a passive process, dependent upon the mesh-like structure of the cortical actin network of the cell and the stiffness of the cell membrane [74, 75]. The cortical actin network can increase cell rigidity and decrease initial passive spreading. As such, disruption of the cortical actin network (through disrupting either actin polymerization [74], or non-muscle myosin-IIA (NMIIA) contractility [77]) significantly increases the rate at which early spreading occurs by decreasing the amount of force required to deform the cytoskeleton-supported cell membrane. Another material aspect important in

early contact with the substrate is surface charge. The surface of a cell is normally negatively charged due to carbohydrate modifications of surface proteins. As such, the early adhesion dynamics between cell and substrate depend on the thermodynamic balance of charges on each. Predictive models of these cell–substrate interactions in terms of such thermodynamics have been developed [78, 79].

Initial Sensing of Substrate Surface

Coincident with the initial physical contact of the cell and its substrate are the formation of the initial connections between cellular adhesion receptors (predominantly integrins) and substrate-bound extracellular matrix proteins. Membrane-bound adhesion receptors are brought into further contact with the substrate via active cytoskeletal protrusion events in early spreading. These events include either membrane blebbing or filopodia extension [76]. These first connections are significant events because they serve as both anchoring points for the cell facilitating adhesion, and as nexuses to transmit information regarding the composition of the cell substrate. This ability arises from the specificity of its adhesion receptors (e.g. specific integrin subunit pairs bind only specific ligands).

Implications of Early Phase Events

The establishment of initial cell–substrate adhesions characterizes the early phase of spreading, and will ultimately induce a transition to the next phase of spreading. Activation of integrins, via binding to their extracellular ligands, initiates multiple signaling events that can influence cytoskeletal dynamics and the maturation of the initial adhesions.

Transduction of integrin-mediated signals typically requires the intracellular binding of paxillin and talin, which recruit focal adhesion kinase (FAK) and Src. FAK and Src form a complex together to initiate a cascade of signaling that results in stimulation of the Rho GTPases Rac1 and Cdc42. Activity of this FAK-Src complex also mediates suppression of active RhoA (RhoA bound to GTP) levels, which in turn decreases the activity of Rho-associated kinase (ROCK), thereby decreasing cell contractility [3, 80]. Paxillin and talin also serve to link the ligated integrin to the cytoskeleton. Together, increased activity of Rac1 and Cdc42 serve to stabilize the F-actin network of the cell and promote its growth through increased polymerization [80], which is the driving mechanism of the next phase of spreading described below [72, 73, 76].

The density of ligand available on the substrate has been shown to affect the duration of this early phase of spreading [44, 76, 81]; cells initiate spreading more quickly on a surface containing higher ligand density. Likely, a cell exposed to an increased density of initial ligand will exhibit increased early

integrin activation that results in activation of Rac1 and Cdc42. At the end of early phase spreading, the cell has transformed from being a spheroid in suspension, to being a flattened cylinder with roughly the same radius on the 2D substrate.

Cell-Generated Forces During Early Phase Spreading

Studies have shown that a cell at this early stage is capable of exerting contractile forces on the substrate [76, 81]. Contractile forces at this stage, however, are of significantly lower magnitude as compared to later stages of spreading. The generation of early phase contractile forces, shown to be caused by NMIIA [77], is enabled by the linkage of ligated integrins to the cytoskeleton via talin [4]. These weaker contractile forces are to be expected, as RhoA activity is suppressed by the formation of initial adhesions and that the cell's small adherent spread area can only minimally activate ROCK to induce myosin contractility [82]. Our own work has shown that cells are capable of exerting force in these early stages of spreading, even without the detectable presence of actin stress fibers or the clustering of vinculin, one of the earliest recruited focal adhesion-associated proteins [64]. Collectively, these data indicate that to exert force against its substrate, a cell does not need formal focal adhesions to have formed.

Summary: Early Phase spreading is characterized by:

- Passive deformation and disruption of the cortical cytoskeleton occurs, dependent on the stiffness and tension of the cell membrane.
- The formation of initial adhesions between integrins and extracellular matrix proteins, which initiates signaling events through Rac1, Cdc42, and RhoA. Integrin ligation alters the balance of active cytoskeletal processes.
- Weak contractile forces exerted against the substrate, likely due to minimal integrin binding and the lack of focal contacts.

4.2.2 Intermediate Phase

Key Events in Intermediate Phase

The cell enters the intermediate phase of spreading once Rac1 and Cdc42 have been activated beyond a threshold, essentially reached through ligation of adhesion receptors to the substrate [72, 73, 76, 80]. This increased activation of Rac1 and Cdc42 shift the dominant active cytoskeletal state from a primarily stagnant cortical network to polymerization of the cortical actin. Therefore cell area rapidly increases during the intermediate phase of spreading.

Implications of Intermediate Phase Events

Increased peripheral actin polymerization results in an increase in protrusive forces, causing a rapid increase in cell area. Rac1- and Cdc42-induced actin polymerization drives an increase in cell area by exerting protrusive forces directly on the membrane [1]. During intermediate phase spreading, VASP localizes near the tips of cortical protrusive processes [76]. This helps drive expansion of cell area because VASP binds both F-actin and adhesion molecules in the cell membrane [83, 84]. A number of additional actin-interacting proteins including the Arp2/3 complex, formins, and cofilin also play a role in actin polymerization and the protrusion of the cell membrane during spreading. Formins act as "processive caps" by attaching the (+) end of the filament to the plasma membrane while simultaneously enabling further polymerization and protecting the filaments from other capping proteins. The Arp2/3 complex enables branching of the actin network, providing increased stabilization between filaments. To support the expanding cortical actin network, depolymerization of older actin filaments must occur. Depolymerization is mediated by the cofilins, which aid in the dissociation of ADP from G-actin. In the next phase of spreading, actin-interacting proteins (formins, Arp2/3, VASP, and talin) also play a large role in shaping the ability of microfilaments to exert and transmit force. The retrograde flow of actin has been shown to be inversely related to the speed of edge protrusion and driven by a combination of NMIIA activity and membrane resistance to actin polymerization [70, 85, 86].

The increase in cell area, which is a hallmark of this intermediate phase of spreading, also causes several other notable changes to occur in the cell. One of the more obvious changes is the increase in the number of integrin-mediated adhesions. As spread area increases, more of the cell surface comes in contact with the substrate, and more integrin receptors become ligated. Integrin ligation initiates the formation of a positive feedback loop via Rac1 and Cdc42 [80]. Just as occurs during early phase spreading, initial integrin ligation activates these regulatory small GTPases. The intermediate phase of spreading also includes an increase in cytoskeletal tension. Studies of cells on isolated adhesive islands of ECM revealed that cells with a greater spread area exhibit higher levels of cytoskeletal tension [87]. Increased cytoskeletal tension translates to increased intracellular force transmitted to the cell–matrix adhesions, which balances the internally-generated forces across the cell. Increased tension at adhesion sites activates additional signaling pathways inducing activation of RhoA, a key molecular regulator of contractility [82].

Increased protrusion forces also induce the recycling of adhesion sites. As spreading occurs and new adhesion sites are formed, mature adhesion sites (now located towards the center of the cell body) begin to disassemble due to prolonged FAK activation and decreased RhoA activity [70, 88]. Recall that the initial ligation of integrins causes deactivation of RhoA and a number of other events through FAK activation [3]. Integrins from disassembled adhesion sites are now recycled to new sites at the cell periphery [86]. The recycling of integrins has been

linked to ROCK signaling [89] which can become decoupled from RhoA activity [82] (such that RhoA activation does not activate ROCK). Through this pathway, adhesion site disassembly leads to the majority of adhesion sites being located at the expanding cell periphery.

Cell-Generated Forces During Intermediate Phase Spreading

As described earlier, cell-generated forces in intermediate phase spreading are predominantly protrusive. These protrusive forces are driven by actin polymerization directly against the membrane and are facilitated by specific actin-interacting proteins [1]. Protrusive forces have been measured using a variety of tools. The first direct measurement of these forces was in 2006 by Prass et al. [18]. They measured the deflection of an AFM cantilever tip against the advancement of a trout keratocyte lamellipod and used that measurement to calculate the force exerted by the lamellipod. Using this technique, the mean force produced by lamellipodial protrusive forces was determined to be just over 1 nN [18]. The normalized F_v curves obtained in their experiments exhibited the same qualities as the F_v curve for simple actin polymerization as measured by Parekh et al. [6] in Figure 2d, illustrating that such lamellipodial protrusive forces are generated through actin polymerization.

As in early phase spreading, there appears to be weak contractile force generation during this phase due to minimally active ROCK [82]. Together, the increase in cell area, recycling of adhesion molecules, and increased tension induce onset of the third, "late" phase of spreading. The shift is driven primarily by the increased activation of RhoA and its downstream effector ROCK, induced by the cell reaching a critical spread area [71, 82].

Summary: Intermediate Phase cell spreading is characterized by:

- "Steady state" phase of actin polymerization [76], resulting in the generation of protrusive forces at the cell periphery and generation of new adhesion sites.
- Increased cytoskeletal tension.
- Recycling of adhesion receptors from initial locations to the cell periphery.

4.2.3 Late Phase

Key Events in Late Phase Spreading

Similar to the Intermediate Phase of spreading, the onset of Late Phase spreading is induced by an increase in the levels of activated small GTPases involved in contractility. Once the cell's spread area reaches a critical spread area (as determined by substrate properties such as ligand density, stiffness, etc.) [71, 81], RhoA activates its effector ROCK, resulting in NMIIA phosphorylation. This increase in

phosphorylated NMIIA produces the hallmark event of late phase spreading: cytoskeletal contractility.

Implications of Late Phase Events

The resultant increase in RhoA activation and its coupling to ROCK [82] leads to the activation of myosin light chain kinase (MLCK) which in turn activates NMIIA via phosphorylation. Increased NMIIA activation mediates contraction of the cytoskeleton and transmission of the subsequent generated force to the substrate. As in intermediate spreading, the key characteristic event, cell contraction, promotes several changes in the cell. Most notably, contractile forces imposed at sites of cell–matrix adhesion induce reorganization of adhesion molecules and reinforcement of adhesion sites.

First, the increased force on ligated integrins promotes integrin clustering in the membrane and the maturation of focal adhesions [90]. Clustering of integrins and activated RhoA leads to bundling and cross-linking of the associated actin and myosin network into stress fibers. RhoA also serves to inhibit actin fiber disassembly by cofilins and promote its assembly via formins (the "processive caps" described earlier in this chapter) [91].

Contractile "pulses" of the cytoskeleton are also observed in Late Phase spreading. These contractile pulses have been proposed as a way for cells to "sense" substrate stiffness [70, 76].

Cell-Generated Forces in Late Spreading

Late phase spreading is characterized by a rapid increase in cell-generated contractile forces [71, 76]. The degree of cell contractility (and the magnitude of generated forces) is affected by substrate stiffness, ligand concentration, cell area, focal adhesion size, and a variety of other factors [71, 76, 81]. The contractility observed in late phase spreading is transmitted through integrin adhesion to the cell substrate as tractional stresses exerted tangential to the substrate. Multiple techniques have been developed to measure cellular traction stresses, including traction force microscopy (TFM). TFM measures the cell-mediated displacement of fluorescent beads in a deformable substrate of known stiffness to determine forces exerted by a cell that creates these displacements. Studies using TFM have revealed that endothelial cells can exert traction forces almost as high as 2,500 nN [81, 92]. Cells can therefore exert much greater force through contractile mechanisms in late spreading compared to polymerization-driven mechanisms in early spreading.

Summary: Late Phase spreading is characterized by:

- NMIIA-dependent contractility.
- Formation of actin–myosin based stress fibers linked to mature focal adhesions (Fig. 4).

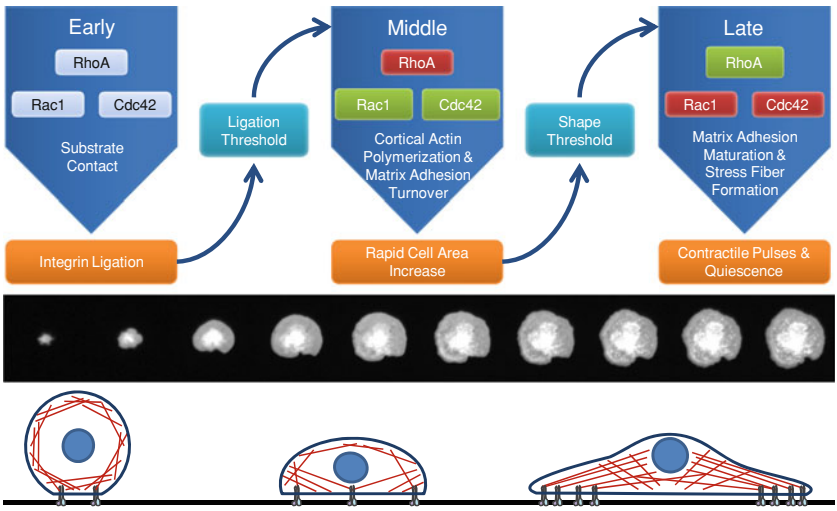

Fig. 4 A summary of the phases of isotropic cell spreading. *Top panel* Flowchart of spreading events; activated and inactivated Rho GTPases are indicated by *green* and *red boxes*, respectively; *orange boxes* indicate the events that directly lead to initiation of the next phase of spreading by crossing the threshold indicated in the *teal boxes*. *Middle panel* Total internal reflection fluorescence (TIRF) microscopy images of the spread area of a mouse embryonic fibroblast over time [76] (Reproduced under Creative Commons Attribution License). *Bottom panel* Cartoon rendition of cell spreading events, viewed from the side

5 Physiologic Environmental Factors Sculpt Cellular Spreading and Homeostasis

5.1 Regulation of Cell Shape by the Extracellular Microenvironment

During active and quiescent cell states, the multi-molecular intracellular machinery that is required for force responsiveness and generation is not static. Rather, the cytoskeleton and cell–matrix adhesion complexes are continually being assembled and disassembled, enabling the cell to generate protrusive and contractile forces. These forces contribute to the maintenance of cellular homeostasis in a potentially dynamic microenvironment, and during cell migration and the formation of tissues [49, 93–95]. In the previous section, this coordination was demonstrated through the phenomenon of isotropic cell spreading, which is generally considered a relatively homogeneous process. Physiologically, however, there are many environmental factors that influence cell spreading and determine the homeostatic shape of a cell. For example, the cellular microenvironment can affect cell contractility, kinetics of spreading, spread area, cell polarization (intracellular components), and isotropy of shape and cell elongation. Notably, while these parameters generally define cell morphology, cell shape is much more

significant than a mere description of the size and appearance of a cell. Over the past 30 years, several landmark studies in which the geometry of cells was precisely controlled have proven that cell shape, as determined by cell–matrix adhesions and the cytoskeleton, has a critical role in cell survival and differentiation as well as in tissue development, architecture, and function in vivo [38, 96–99]. Identifying the environmental factors that contribute to defining cell shape in vivo will enable better understanding of cell and tissue homeostasis as well as the causes and effects of deregulated cell shape in disease.

5.2 Cell Migration: "Shape Change with a Bias"

Cell migration is a dynamic process that occurs through the biochemical and biophysical orchestration of cell–matrix adhesions and cell shape polarization, which itself is a coordination between intracellular contractile and protrusive forces [100–103]. Thus, in the context of cell adhesion and spreading, cell migration can be considered "shape change with a bias". Indeed, the extracellular stimuli that drive cell shape regulation often direct cell migration in tissue development, maintenance, and disease [95, 104, 105]. Such microenvironmental factors can influence migratory characteristics including rate of migration (speed) and directional persistence in a coordinated manner. Highly-polarized stimuli, such as chemical or mechanical gradients, will typically increase the directional persistence of a migrating cell while generally isotropic stimuli, such as uniform chemokinetic factors or ECM stiffness, will alter the migratory behavior (speed) of a cell with no apparent directional bias. While a complete discussion of the mechanisms of cell migration is beyond the scope of this chapter, we will discuss how integration of exogenous stimuli drives endogenous cellular force generation, thus enabling cells to adaptively control their shape and, as necessary, migrate to achieve cellular homeostasis.

5.3 Tissue Specificity

Mesenchymal, connective, muscle, epithelial, and endothelial cells are each exposed to unique microenvironmental factors in vivo that define distinctive cell and tissue morphologies and functions [106–111]. It would be impossible to provide a comprehensive survey of instances where a cell's microenvironment defines its cellular homeostasis within one chapter, as research in this field is vast and entirely tissue-specific. However, to capture the importance of the microenvironment in regulating cellular shape and force generation, two specific tissue types will be discussed: epithelial and endothelial tissues. The environmental factors that contribute to the unique homeostasis of the cells in each tissue will be explored. We will provide evidence that, through mechanosensing, the microenvironment

mediates endothelial and epithelial cellular force generation, which, when orchestrated with matrix adhesions, manifest in cell shape regulation. Finally, this shape regulation, when spatiotemporally coordinated, can lead to cell migration, which has implications in tissue development and disease progression.

5.4 *Overview of Cellular Homeostatic Perturbations and Disease*

Cell shape changes and migration, which are required for embryogenesis, tissue maintenance, and wound healing, are also involved in pathogenesis upon disruption of cellular homeostasis. Perturbations in cell spreading can cause cells to undergo changes in gene expression and phenotype that drive it from its quiescent state. Normal disruption of homeostasis is transient and can be beneficial as it guides cell differentiation and migration during development or wound healing. However, sustained disruption of homeostasis or aberrant cell response to homeostatic microenvironmental conditions can drive disease. If the homeostatic perturbation is sustained and/or excessive, it can initiate and preserve overactive intracellular signaling loops that cause tissue-specific phenotypic changes and promote pathogenesis. For example, changes in ECM stiffness, which are typically a sustained perturbation, can cause deregulation of cell-generated forces, which, as we will discuss, can significantly impact the normal structure and function of cells and tissues. Additionally, if the ability of a cell to respond to environmental cues is abnormal, its behavior in its native environment may be disrupted. For example, transformed cells can have defective mechanosensing machinery, which prevents them from sensing and responding to their mechanical environment appropriately.

5.4.1 Epithelium and Cancer: An Example of Cell Forces Correlating with Disease

Epithelial tissues exist in several unique shapes, including spherical cysts (i.e. thyroid, other glands) and elongated tubular structures (i.e. ducts in mammary epithelial tissue) [112]. Regardless, the most striking characteristics of epithelial tissues in vivo are their apical–basal polarity and tight cell–cell adhesions [113, 114]. Notably, the tissue stroma has been strongly implicated in establishing these traits. Further, the properties and composition of both the cellular and ECM components of the stroma evolve through development and significantly affect tissue organization and function at all epithelial generations [108, 115]. It has been shown that cytoskeletal tension, controlled through Rho and ROCK-mediated contractility, drives basement membrane remodeling required for normal tubulogenesis in mammary epithelium [116, 117]. Additionally, several studies have demonstrated that proper epithelial development and maintenance depends on a

dynamic balance between cell–cell and cell–matrix adhesions [95, 118]. Guo et al. [63] found that cell–cell adhesions compete directly with cell–matrix adhesions to provide cells with mechanical input and thus, maintain tensional homeostasis. If physical signals from the ECM are stronger than those from cell–cell interactions, cells migrate away from each other, while if cell–cell adhesions dominate, cells associate and assemble into tissue structures. This balance of epithelial cell adhesions—to the basal lamina through integrins or to other cells through E-cadherins—plays a critical role in establishing epithelial tissue polarity. The nature of cell adhesions promotes polarization of the membrane and cytoskeletal molecules across the apical and basal cell surfaces [113].

Basal Lamina Stiffness Drives the Malignant Phenotype Through a Cellular Force Pathway

The stroma of epithelial tissues stiffens naturally during both tissue morphogenesis and aging [119]. Naturally occurring tissue stiffening is due to the accumulation of advanced glycation end products which crosslink the matrix as well as increased matrix deposition. It is also well-known that tumors are stiffer than the surrounding stromal tissue. This stiffening is likely a result of increased interstitial tissue pressure and solid stress due to tumor expansion [120], an increase in the intracellular stiffness of malignant cells [121], excessive RhoA-based cell contractility [122, 123], and fibrosis [105]. Furthermore, patients presenting clinically with fibrotic tumors typically have a poor prognosis [124]. Because of the highly interconnected feedforward/feedback nature of mechanosensing, matrix stiffness can initiate and maintain chronically-elevated mechanoresponsive signaling cascades that can lead to malignant transformation of epithelial cells.

Stiffness sensing is an important component of a cell's mechanosensing arsenal, and it has been identified as a major determiner of epithelial cell shape and epithelial tissue homeostasis. Epithelial cells probe the stiffness of the surrounding ECM and respond through the adhesion and cytoskeletal dynamics discussed throughout this chapter [112]. As discussed in earlier sections, matrix stiffness induces focal adhesion formation and stability through an increase in tension at these adhesion sites. This phenomenon is especially important in epithelial tissues, where the balance between cell–cell and cell–matrix adhesions is controlled primarily by properties of the underlying basal lamina [112, 115]. Thus, epithelial tissue architecture is governed in part by the stiffness of ECM and cellular force generation, and increases in stiffness can induce dissociation of cell–cell adhesions [63]. Such deregulation of cell–cell adhesions supports an increased preference for cell–matrix adhesions through integrins, which is critical for cancer progression. In fact, inhibition of $\beta 1$ integrins in breast cancer cells arrested cell growth and promoted cellular apoptosis in 3D cultures and in vivo [125], underscoring the necessity of cell–matrix adhesions and cell spreading in cell survival.

During malignancy and invasion, cells exhibit a more aggressive phenotype, and it is thought that cell force generation is an important element of this

phenotype [126]. Notably, epithelial cell traction forces increase with matrix stiffness [127], which can manifest in basement membrane reorganization, cell shape changes, and migration commonly associated with cancer [115, 117, 128]. Indeed, the expression and activity of the small GTPases Rac and Rho, which are classically linked with cellular contractility, are enhanced in tumors, and elevated Rho expression is clinically associated with cancer progression [122, 129, 130]. Further, Wozniak et al. [116] have implicated Rho-based cell contractility in response to matrix stiffness as the determining factor that drives mammary epithelial cells toward either tubulogenesis on soft substrates or cell proliferation on stiff substrates. Rac and Rho have complementary roles in maintaining cell shape and cell force generation. Cancer cells, which typically exhibit loss of spatiotemporal control over Rac and Rho activation, show disrupted cell polarity, cell shape, and cell force generation [131, 132].

Taken together, the deregulation of cell adhesions, increase in cell force generation, and cell shape changes that occur in response to basement membrane stiffness provide substantial evidence that normal levels of ECM stiffness preserve epithelial tissue architecture (Fig. 5). Several groups have shown that a sustained increase in stromal stiffness disrupts normal cellular and tissue structure and function both in vitro and in vivo, in a manner that is characteristic of cancer. Paszek et al. [66] demonstrated that increased stiffness causes integrin clustering, focal adhesion assembly, disruption of E-cadherin junctions, Rho-mediated contractility, and FAK/ERK activation in non-transformed mammary epithelial cells. These subcellular effects resulted in disruption of acini structure and promoted a highly invasive phenotype. Moreover, Provenzano et al. [67] showed that sustained ERK activation due to matrix stiffness promoted initiation of, and progression through, the cell cycle as well as expression of clinically-relevant proliferation-signature genes, which is consistent with the characteristic over-proliferative behavior of malignant cells. Most recently, it was reported that stiffening of the mammary stroma with lysyl oxidase (a natural collagen crosslinker) facilitates tissue morphology breakdown and invasiveness both in vitro and in vivo [133].

The matrix stiffness-induced intracellular changes shown by Paszek et al. and Provenzano et al. may enable epithelial to mesenchymal transition (EMT), which is generally characterized by fundamental changes in cell adhesion and motility [95, 134]. Specifically, cells having undergone EMT exhibit a loss of E-cadherin expression in favor of N-cadherin expression. These cell–cell adhesions are much weaker, and an increase in cell–matrix adhesions is needed to satisfy the cells' need for mechanical input and tensional homeostasis.

In addition to triggering malignant transformation, stiffness-induced Rho-mediated cell contractility and changes in cell adhesion, when coupled with proteolysis, may also contribute to metastatic migration [135]. This "shape change with a bias" is likely enabled by defective mechanosensing components (discussed in the next section), and allows tumor cells to navigate aggressively away from the primary tumor. While a more thorough discussion of the mechanisms of cell migration is outside the focus of this chapter, Friedl and Wolf [103] provide an excellent review.

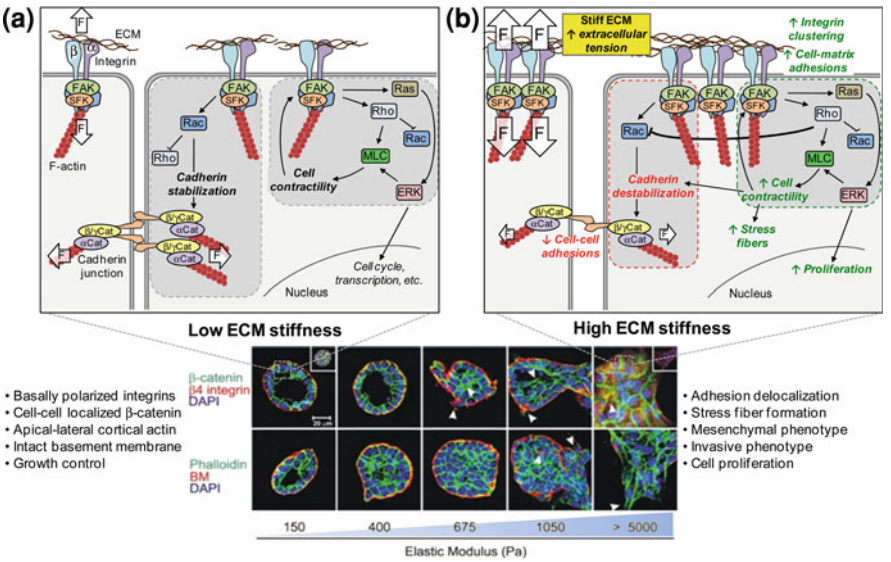

Fig. 5 Normal ECM stiffness promotes epithelial cell quiescence and epithelial tissue structure. **a** Spatiotemporally-localized activation of Ras, Rac, and Rho downstream of FAK phosphorylation contributes to epithelial cell polarity and maintenance of tensional homeostasis under normal ECM conditions (*left side* of figure). Specifically, Rac acts to stabilize cell–cell junctions through recruitment of cortical actin (*dashed gray region on left*), while activated Rho and ERK phosphorylate MLC and drive cell contractility (*dashed gray region on right*). Both cell-generated and perceived extracellular forces are represented by *white arrows*. **b** In response to a stiff extracellular matrix (*right side* of figure), the cell re-establishes its tensional homeostasis by contracting more aggressively (positive feedback pathway within *green dashed region*), which enables stress fiber formation and promotes cell–matrix adhesion through integrin clustering. The impact of stiffness-induced Rho activation on intercellular cadherin junctions is twofold (destructive signaling pathway within red dashed region). Rho directly suppresses (*thick black inhibition arrow*) the laterally-localized Rac activation that stabilized cadherin junctions and, through cell contractility, destabilizes already existing intercellular junctions. ECM stiffness promotes a general loss of cellular polarity, which drives the epithelial cells toward an invasive mesenchymal phenotype. Together, the subcellular and cellular-level responses in *green* and *red* are indicative of a malignant phenotype and the resulting disruption of normal tissue architecture is represented in the confocal immunofluorescence images, with notable events highlighted by *white arrowheads*. Confocal immunofluorescence images *reprinted* with permission from Elsevier [66]

Defective Mechanosensing Components Prevent Epithelial Cells from Responding Appropriately to Mechanical Stimuli

The ability of cells to respond to their environment is critical for maintenance of cellular health and homeostasis. However, the intracellular signaling pathways that are involved in sensing and responding to external stimuli are complex and involve a vast number of molecular players. Gain-of-function mutations in Ras that result in its constitutive activation were among the first discovered oncogenic mutations and represent one of the most prevalent molecular mechanisms for transformation [136]. Overactivation of this molecular intermediate has many downstream effects,

one of which is decreased sensitivity to the mechanical properties of the surrounding ECM. Transformed cells typically exhibit increased cell contractility [66, 134], which is driven by altered RhoGTPase signaling in breast cancer [123]. This defective mechanosensing capability was modeled in vitro by transfecting mammary epithelial cells with a constitutively active isoform of Rho. This modification eliminated the stiffness-sensing ability of these cells, causing elevated cell contractility, increased cell spreading, and enhanced cell–matrix adhesion regardless of matrix stiffness [66].

Mechanical Properties of the ECM Influence Angiogenesis in Cancer

Normal development and maintenance of endothelial tissues also depends on mechanosensing, balance of cell–cell and cell–matrix adhesions, and coordination of contractile and protrusive cytoskeletal dynamics. Interestingly, there is significant evidence that blood vessels associated with tumors, and specifically those that develop within tumors through angiogenesis, are leaky, dilated, and disorganized, and that the cells that reside in these blood vessels are highly proliferative, drug-resistant, and exhibit increased sensitivity to growth factors [137, 138].

The process of neovessel formation through angiogenesis is an essential part of development, wound healing, and pathogenesis [139]. There is evidence that proteolytic activity accompanies angiogenic network formation in vivo, suggesting that matrix composition affects both the initiation and progression of neovessel formation [140]. Furthermore, because sprouting involves directional migration, it requires polarization, which is thought to arise from both biochemical and biophysical means. The ECM plays a significant role in establishing the cell polarization that accompanies endothelial network formation. Through force generation and mechanosensing, cells detect and respond to intrinsic properties of the ECM as well as changes in these properties.

During angiogenic network formation, cell–cell adhesions can directly compete with cell–matrix adhesions [63] to enable the self-assembly of cells into networks structures. This balance supports the formation of networks in more compliant ECM, where to satisfy their tensional homeostasis, endothelial cells increase cell–cell interactions and connectivity [62, 64]. Our own laboratory has showed that when EC-matrix adhesivity is low, either through insufficient matrix stiffness or reduced ligand availability, capillary-like network formation results (Fig. 6) [47]. Alternatively, when EC-matrix adhesions are strong and stable on stiffer substrates, the cells are less likely to organize into networks. While this phenomenon was identified in vitro, it has significant implications in tissue development and maintenance in vivo, particularly in driving endothelial sprouting and network formation during tumor angiogenesis. Specifically, these results suggest that increased intratumoral stiffness may cause the destabilization of endothelial cell–cell adhesions, resulting in excessive vascular permeability [138].

Additionally, we have acquired separate data to show that ECs are capable of mechanosensing adjacent cells over a distance during network formation. That is,

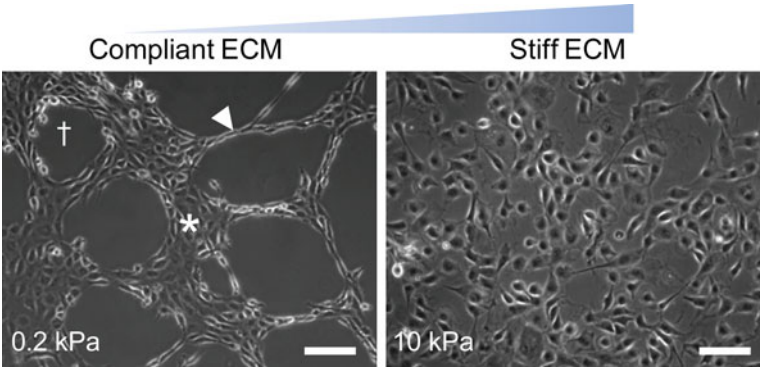

Fig. 6 Matrix stiffness influences endothelial network formation. Compliant (low stiffness) gels ($E \leq 1$ kPa) promote cell–cell interactions and network assembly as evidenced by EC clusters, cords, and lacunae. Stiff gels ($E \geq 2.5$ kPa) prevent proper endothelial network formation by restricting endothelial cells from deforming their ECM to communicate with other cells as well as by encouraging cell–matrix adhesions. This phenomenon is important in cancer because the ability of tumor-associated ECs to satisfy their tensional homeostasis through balance of mechanical inputs is critical for normal vascular function. Increased intratumoral stiffness may cause destabilization of cell–cell adhesions, resulting in vascular permeability. Notably, it was recently reported that ECs extracted from a primary tumor may exhibit some degree of stiffness-insensitivity, shown by a stiffness-independent increase in basal Rho activity, traction force generation, and tubule formation. It is thought that this mechanism enables tumor-associated ECs to form networks, although leaky, in vivo

ECs can communicate through compliant substrates using a form of stiffness sensing in which cells sense directionally-biased increases in matrix stiffness due to the contractility of nearby cells [64]. From these results, a novel model emerged wherein cell-generated contraction forces induce a tension gradient in the surrounding ECM that activates the adhesion and migratory machinery of a second cell in a highly localized and polarized manner, resulting in durotaxis. Thus, durotaxis, first demonstrated by experimentally perturbing the substrate in the vicinity of a cell [58], is presumed to contribute to the cell spreading and migration that is characteristic of angiogenesis [47]. This result supports the finding that a balance between ECM stiffness and cellular traction forces determines the morphological features of endothelial networks [141].

Recently, it was shown that tumor-derived capillary endothelial cells exhibit some degree of stiffness-*in*sensitivity similar to that which was described in epithelial cells [137]. These cells express high basal levels of Rho activity, thus preventing them from dynamically responding to the mechanical properties of their surrounding ECM. As expected, these cells exert higher traction forces, take on distinct cell morphologies, and assemble into tubular networks regardless of the mechanics of the underlying substrate or presence of other cells. However, normal mechanosensing endothelial cell behavior was restored upon ROCK inhibition. These results provide further evidence of the importance of both ECM stiffness and mechanosensitivity in maintaining normal tissue architecture and function.

5.4.2 Endothelium and Atherosclerosis: An Example of Cell Shape Correlating with Disease

Forces in the Endothelium Determine Normal Tissue Structure and Function

In addition to matrix stiffness, there are a multitude of other forces that are present in the normal endothelial environment in vivo that influence cell adhesion and spreading, and thus, endothelial cell homeostasis and angiogenesis. Endothelial cells in vivo display a bi-axial hallmark of polarity (apical–basal and upstream–downstream) in forming a monolayer that lines the interior of blood vessels. Here we will describe two significant mechanical cues inherent in the endothelial environment. The first is cyclic strain, which results from both the elasticity of blood vessels and the pulsatile nature of blood flow. The second is shear stress, which is exerted upon the endothelium as viscous blood flows over the adherent endothelial monolayer. Both of these mechanical cues influences the balance and localization of cell–cell and cell–matrix adhesions and alters cell shape to promote quiescence and thus aid in the maintenance of normal tissue function. In vivo, vessel circumference dynamically changes as a result of blood flow. This change in vessel circumference translates to cyclic strain along the axis perpendicular to the direction of fluid flow. This stretching induces a change in cell shape, accompanied by a re-distribution of matrix adhesions and stress fibers perpendicular to the axis of stretch. Critical to stress fiber maintenance and re-organization is the activity of the small GTPase Rho, without which cells are unable to properly orient stress fibers [80, 142]. Rho activity mediates actin dynamics required for cytoskeletal adaptation to maintain endothelial cell homeostasis. It is hypothesized that stress fibers form perpendicular to the direction of cyclic strain to reduce the net intracellular tension induced by stretch. The maintenance of stress fibers in this orientation through cytoskeletal adaptation has also been implicated in feedback to cellular signaling pathways that contribute to homeostasis [143]. Disruption of the physiological norm due to alterations in cyclic strain therefore has the potential to contribute to disease progression, particularly in increasing susceptibility to atherosclerosis development.

Fluid shear stress imposed by blood flow acts directly on the apical surface of endothelial cells, and similar to cyclic strain, contributes significantly to the geometrical anisotropy and cellular alignment observed in EC monolayers throughout the vasculature [143–145] (Fig. 7a). Because fluid shear stress (FSS)-induced endothelial cell shape change is associated with cytoskeleton rearrangement [146, 147] and is tyrosine kinase-dependent [109], the Rho family of small GTPases and cell-generated forces have been heavily implicated in this cellular response [148]. Furthermore, the establishment and maintenance of the characteristic polarized morphology of ECs is adhesion-dependent and requires spatio-temporally-localized activation of intracellular signaling machinery [148, 149]. One of the earliest observable cellular responses to FSS acting on the apical surface is integrin activation on the basal surface due to an allosteric change that increases integrin affinity [150]. This activation and subsequent adhesion of

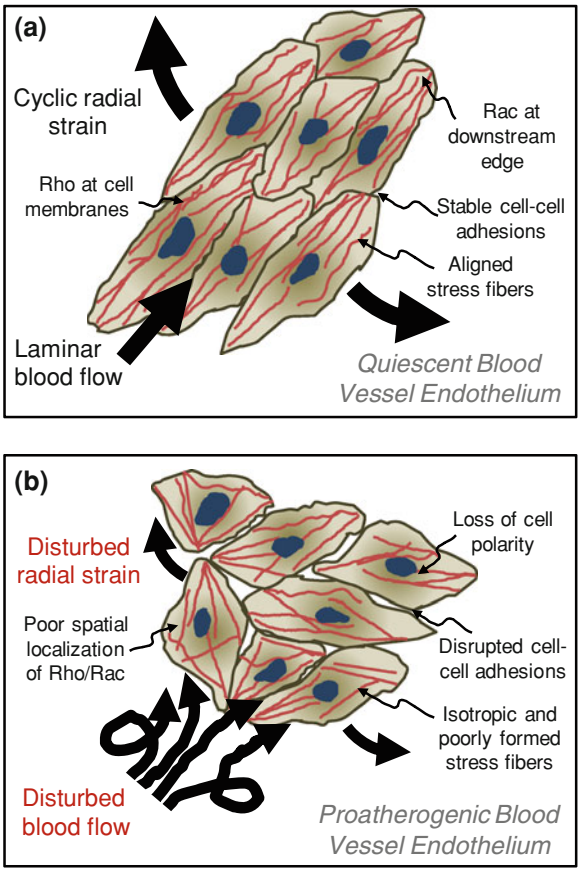

Fig. 7 Physiological forces in the endothelium influence structure and function of the endothelium. **a** In healthy blood vessels, mechanical stimuli such as laminar blood flow and consistent radial cyclic strain determine cell polarity, satisfy EC homeostasis, and promote tissue quiescence. **b** Physiological factors such as disturbed blood flow and reduced radial strain disrupt EC mechanical homeostasis and are proatherogenic

integrins results in rapid focal adhesion remodeling in the direction of the FSS [149], with increased FAK activation at the site of new focal adhesions [151]. Several groups have shown that regulation of intracellular signaling activity by shear stress occurs downstream of new integrin-ligand binding [150, 152–154], further emphasizing the importance of FSS-enhanced cell–matrix adhesion and focal adhesion turnover. Together, these localized biomolecular events contribute to the maintenance of the polarized cell shape shown in Fig. 7a.

In an elegant study by Wojciak-Stothard and Ridley [155], it was shown that cellular response to physiological shear stress occurs through regulation of Rho-based cellular contraction and Rac1-driven protrusion. The authors demonstrated that within 5 min of exposure to shear, endothelial cells exhibit rapid depolarization and contraction, produced by elevated RhoA-GTPase activity and actin stress fiber formation. Shortly thereafter, RhoA activity returns to basal levels as Rac1 activity increases, driving lamellipodial protrusion from the downstream side of cells in the direction of fluid flow. As cells achieve a spread and aligned morphology, Rac1-driven protrusion subsides while RhoA-based contractility and

stress fiber formation increases, reestablishing tensional homeostasis with the underlying substrate. Several studies have confirmed that appropriate alignment and spreading in response to FSS depends upon dynamic regulation of RhoA activity [150, 155, 156] as well as local Rac1 activation within protruding lamellipodia [157, 158]. These FSS-induced effects are observed in the previously discussed middle and late stages of cell spreading, where Rac1 and RhoA have been implicated, respectively. Moreover, EC traction forces—which represent the biophysical manifestation of biomolecular events such as cell–matrix adhesions, intracellular signaling, and cytoskeletal dynamics—were increased and localized along the upstream and downstream edges of the cell in response to FSS, enabling cell shape change and realignment in flow [159].

One of the atheroprotective roles of FSS in vivo is to enable appropriate and efficient tissue maintenance and repair through control of cell shape and polarity. Investigating the time course of shear stress-regulated cell shape, Remuzzi et al. [146] showed that bovine aortic endothelial cells lose their polarized morphology 20 h after removal of flow. After 72 h in this static condition, FSS-conditioned cells reverted back to control (unstressed) levels of spreading, but still contained some aligned cytoskeletal components [146]. These results indicate that shear stress imposed by hemodynamic blood flow is essential for *maintaining* physiological endothelial cell morphology and illustrate how the loss or disruption of flow could have significant implications in pathology. Tissue vessel architecture relies not only upon moderation of cell–matrix adhesions, but also FSS-dependent maintenance of intercellular junctions, which preserve the barrier function of endothelial tissues [160, 161]. EC junctions, like cell–matrix adhesions, are intimately involved with the cytoskeleton, and are in fact regulated by localized Rac and Rho activity, which act antagonistically to stabilize and perturb EC junctions, respectively [155, 162].

Endothelial cell migration is not observed in quiescent blood vessels, but has been observed in disease states. As previously discussed, cell migration can be seen as cell shape change with a bias, and indeed, the forces that determine endothelial cell spreading and shape also contribute to EC migration. Cell migration during in vivo wound healing, in particular, is fluid shear stress-directed [163, 164]. In vitro, both EC orientation and migration increase in response to physiological fluid shear stress in a scrape wound assay [165]. Likewise, Vyalov et al. [164] demonstrated that the healing response of wounded endothelial monolayers exposed to reduced shear stress in vivo is abnormal and insufficient. Thus, fluid shear stress likely plays a dual role in improving the efficiency of wound healing. First, FSS continually maintains ECs in a highly polarized state, thus equipping them to migrate immediately upon disruption of an adjacent cell–cell contact or other injury. This polarized morphology enhances the directional persistence of EC migration through Rac-induced alignment of the cytoskeleton and FSS-oriented cell spreading [166]. Second, as previously discussed, FSS causes increased Rho activation and thus, traction force generation, at the leading edge and rear of a cell, suggesting that FSS promotes a migratory phenotype [159]. Moreover, there is evidence that the biochemical composition of the basement

membrane provides additional cues that influence stress fiber formation, cell spreading, and migration that follow injury in vitro [167].

Mechanical Properties of the Basement Membrane and ECM

It is becoming increasingly apparent that, in addition to fluid shear stress, the mechanical properties of endothelial ECM contribute to its adhesion and spreading, and thus, the establishment and maintenance of cellular homeostasis. Matrix mechanical properties affect all generations of the vascular system, from quiescent ECs lining large arteries to branching ECs during angiogenesis. The fibrillar nature of the ECM allows it to impart mechanical forces on cells through its intrinsic mechanical properties and transmitted forces, like those due to cyclic strain, in established blood vessels [143, 168, 169].

Perturbation of Normal Endothelial Mechanical Homeostasis and Cell Spreading

Atherosclerosis is a vascular disease characterized by the development of plaques or lesions within blood vessels involving proliferation of the vascular smooth muscle layer, thrombus formation, and accumulation of inflammatory mediators [170]. Atherosclerosis progression depends on multiple factors including genetic predisposition, dietary factors and lipid metabolism [170]. In the past two decades it has become apparent that the loss of endothelial mechanical homeostasis (due to factors including aberrant cyclic strain or fluid shear stress) also plays a significant role in the progression of cardiovascular disease. The cellular and molecular processes involved are highly complex and are strongly influenced by mechanical forces and cell shape.

Physiological FSS is atheroprotective, as it contributes to the maintenance of endothelial cell polarity, orientation, cell–cell adhesions, and thus, homeostasis [143, 171]. Regions of the vasculature that are most prone to early atherogenesis are often exposed to disrupted flow. Disruptions primarily occur at points of vascular branching or bifurcations, where flow may become oscillatory (change direction) [172]. Additionally, the architecture of these bifurcations can result in altered magnitude and direction of the cyclic strain exerted on the endothelial layer, which can also be proatherogenic [143] (Fig. 7b). Interestingly, cell shape is one of the most obvious phenotypic differences between endothelial cells in atheroprone versus atheroprotective regions: endothelial cells in these atheroprone areas tend to be square in comparison to the elongated morphology seen in straight portions of the vessel. The ramifications of changes in cell shape in response to flow, including cytoskeletal and adhesion dynamics that permit minimization of flow resistance, have been under active investigation for a number of years [173–175].

Notably, there also is direct evidence that endothelial cell contractility and shape mediated through Rho signaling also contributes to endothelial permeability.

This suggests a mechanism of cross-talk between fluid shear stress and EC contractility through the Rho pathway to affect cell structure and function.

6 Summary

Cells modulate their cytoskeleton to generate forces, which, when coordinated with cell–matrix and cell–cell adhesion regulation, enable cell shape change. This force is born in the molecular-level forces generated by actin polymerization and actin–myosin interactions that drive the membrane outward during spreading and stabilize cell shape of spread cells. Attention has been paid to the early process of spreading because it is a tractable, simplified model of the multistep integrated process of migration. Moreover, cell adhesion, the extent of spreading and cell shape have been shown to determine cell fate and function and drive several other adaptive cellular processes such as migration, growth and proliferation. Therefore knowledge of the biochemical and biophysical mechanism involved in inducing or controlling spreading will lead to greater insight into the factors controlling cellular homeostasis. While multiple examples exist where cell shape and spreading become disrupted during disease, as in cancer and atherosclerosis, there remains much to be learned about the inside-out and outside-in signals present during cell spreading and adhesion that help establish cellular homeostasis.

References

1. Pollard, T.D., Borisy, G.G.: Cellular motility driven by assembly and disassembly of actin filaments. Cell **112**(4), 453–465 (2003)
2. Bindschadler, M., McGrath, J.L.: Formin' new ideas about actin filament generation. Proc. Natl Acad. Sci. USA **101**(41):14685–14686 (2004)
3. Mitra, S.K., Hanson, D.A., Schlaepfer D.D.: Focal adhesion kinase: in command and control of cell motility. Nat. Rev. Mol. Cell. Biol. **6**(1), 56–68 (2005)
4. Zhang, X., et al.: Talin depletion reveals independence of initial cell spreading from integrin activation and traction. Nat. Cell Biol. **10**(9), 1062–1068 (2008)
5. Schwartz, I.M., et al.: The role of substrate curvature in actin-based pushing forces. Curr. Biol. **14**(12):1094–1098 (2004)
6. Parekh, S.H., et al.: Loading history determines the velocity of actin-network growth. Nat. Cell Biol. **7**(12):1219–1223 (2005)
7. Taubenberger, A., et al.: Revealing early steps of alpha2beta1 integrin-mediated adhesion to collagen type I by using single-cell force spectroscopy. Mol. Biol. Cell **18**(5), 1634–1644 (2007)
8. Alon, R., et al.: Alpha4beta1-dependent adhesion strengthening under mechanical strain is regulated by paxillin association with the alpha4-cytoplasmic domain. J. Cell Biol. **171**(6), 1073–1084 (2005)
9. Zhang, X., et al.: Molecular basis for the dynamic strength of the integrin alpha4beta1/VCAM-1 interaction. Biophys. J. **87**(5), 3470–3478 (2004)
10. Li, F., et al.: Force measurements of the alpha5beta1 integrin-fibronectin interaction. Biophys. J. **84**(2 Pt 1), 1252–1262 (2003)

11. Sun, Z., et al.: Mechanical properties of the interaction between fibronectin and alpha5beta1-integrin on vascular smooth muscle cells studied using atomic force microscopy. Am. J. Physiol. Heart Circ. Physiol. **289**(6), H2526–H2535 (2005)
12. Trache, A., Meininger, G.A.: Atomic force-multi-optical imaging integrated microscope for monitoring molecular dynamics in live cells. J. Biomed. Opt. **10**(6), 064023 (2005)
13. Thie, M., et al.: Interactions between trophoblast and uterine epithelium: monitoring of adhesive forces. Hum. Reprod. **13**(11):3211–3219 (1998)
14. Zhang, X., Wojcikiewicz, E., Moy, V.T.: Force spectroscopy of the leukocyte function-associated antigen-1/intercellular adhesion molecule-1 interaction. Biophys. J. **83**(4), 2270–2279 (2002)
15. Zhang, X., Wojcikiewicz, E.P., Moy V.T.: Dynamic adhesion of T lymphocytes to endothelial cells revealed by atomic force microscopy. Exp. Biol. Med. (Maywood) **231**(8), 1306–1312 (2006)
16. Wojcikiewicz, E.P., et al.: Force spectroscopy of LFA-1 and its ligands, ICAM-1 and ICAM-2. Biomacromolecules **7**(11), 3188–3195 (2006)
17. Lehenkari, P.P., Horton, M.A.: Single integrin molecule adhesion forces in intact cells measured by atomic force microscopy. Biochem. Biophys. Res. Commun. **259**(3), 645–650 (1999)
18. Prass, M., et al.: Direct measurement of the lamellipodial protrusive force in a migrating cell. J. Cell Biol. **174**(6), 767–772 (2006)
19. Gittes, F., et al.: Flexural rigidity of microtubules and actin filaments measured from thermal fluctuations in shape. J. Cell Biol. **120**(4), 923–934 (1993)
20. Isambert, H., et al.: Flexibility of actin filaments derived from thermal fluctuations. Effect of bound nucleotide, phalloidin, and muscle regulatory proteins. J. Biol. Chem. **270**(19), 11437–11444 (1995)
21. McCullough, B.R., et al.: Cofilin increases the bending flexibility of actin filaments: implications for severing and cell mechanics. J. Mol. Biol. **381**(3), 550–558 (2008)
22. Pfaendtner, J., et al.: Structure and dynamics of the actin filament. J. Mol. Biol. **396**(2), 252–263
23. Cai, Y., et al.: Cytoskeletal coherence requires myosin-IIA contractility. J. Cell Sci. **123** (Pt 3), 413–423
24. Finer, J.T., Simmons, R.M., Spudich, J.A.: Single myosin molecule mechanics: piconewton forces and nanometre steps. Nature **368**(6467), 113–119 (1994)
25. Dogterom, M., Yurke, B.: Measurement of the force-velocity relation for growing microtubules. Science **278**(5339), 856–860 (1997)
26. Kerssemakers, J.W., et al.: Assembly dynamics of microtubules at molecular resolution. Nature **442**(7103), 709–712 (2006)
27. Wang, N., et al.: Mechanical behavior in living cells consistent with the tensegrity model. Proc. Natl Acad. Sci. USA **98**(14), 7765–7770 (2001)
28. Brangwynne, C.P., et al.: Microtubules can bear enhanced compressive loads in living cells because of lateral reinforcement. J. Cell Biol. **173**(5), 733–741 (2006)
29. Herrmann, H., et al.: Intermediate filaments: from cell architecture to nanomechanics. Nat. Rev. Mol. Cell. Biol. **8**(7), 562–573 (2007)
30. Wagner, O.I., et al.: Softness, strength and self-repair in intermediate filament networks. Exp. Cell Res. **313**(10), 2228–2235 (2007)
31. Macpherson, I., Montagnier, L.: Agar Suspension Culture for the Selective Assay of Cells Transformed by Polyoma Virus. Virology **23**, 291–294 (1964)
32. Stoker, M., et al.: Anchorage and growth regulation in normal and virus-transformed cells. Int. J. Cancer **3**(5), 683–693 (1968)
33. Yamada, K.M., Yamada, S.S., Pastan, I.: Cell surface protein partially restores morphology, adhesiveness, and contact inhibition of movement to transformed fibroblasts. Proc. Natl Acad. Sci. USA **73**(4), 1217–1221 (1976)
34. Ali, I.U., et al.: Restoration of normal morphology, adhesion and cytoskeleton in transformed cells by addition of a transformation-sensitive surface protein. Cell **11**(1), 115–126 (1977)

35. Heggeness, M.H., Ash, J.F., Singer, S.J.: Transmembrane linkage of fibronectin to intracellular actin-containing filaments in cultured human fibroblasts. Ann. N. Y. Acad. Sci. **312**: 414–417 (1978)
36. Ali, I.U., Hynes, R.O.: Effects of LETS glycoprotein on cell motility. Cell **14**(2), 439–446 (1978)
37. Hynes, R.O., Destree, A.T.: Relationships between fibronectin (LETS protein) and actin. Cell **15**(3), 875–886 (1978)
38. Folkman, J., Moscona, A.: Role of cell shape in growth control. Nature **273**(5661), 345–349 (1978)
39. Tamkun, J.W., et al.: Structure of integrin, a glycoprotein involved in the transmembrane linkage between fibronectin and actin. Cell **46**(2), 271–282 (1986)
40. Argraves, W.S., et al.: cDNA sequences from the alpha subunit of the fibronectin receptor predict a transmembrane domain and a short cytoplasmic peptide. J. Biol. Chem. **261**(28), 12922–12924 (1986)
41. Miranti, C.K., Brugge, J.S.: Sensing the environment: a historical perspective on integrin signal transduction. Nat. Cell Biol. **4**(4), E83–E90 (2002)
42. Arnaout, M.A., Mahalingam, B., Xiong, J.P.: Integrin structure, allostery, and bidirectional signaling. Annu. Rev. Cell Dev. Biol. **21**:381–410 (2005)
43. van Kooyk, Y., Figdor, C.G.: Avidity regulation of integrins: the driving force in leukocyte adhesion. Curr. Opin. Cell Biol. **12**(5), 542–547 (2000)
44. Galbraith, C.G., Yamada, K.M., Sheetz, M.P.: The relationship between force and focal complex development. J. Cell Biol. **159**(4), 695–705 (2002)
45. Helenius, J., et al.: Single-cell force spectroscopy. J. Cell Sci. **121**(Pt 11), 1785–1791 (2008)
46. Galbraith, C.G., Sheetz, M.P.: Forces on adhesive contacts affect cell function. Curr. Opin. Cell Biol. **10**(5), 566–571 (1998)
47. Califano, J.P., Reinhart-King, C.A.: A Balance of Substrate Mechanics and Matrix Chemistry Regulates Endothelial Cell Network Assembly. Cell. Mol. Bioeng. **1**, 122–132 (2008)
48. Balaban, N.Q., et al.: Force and focal adhesion assembly: a close relationship studied using elastic micropatterned substrates. Nat. Cell Biol. **3**(5), 466–472 (2001)
49. Zamir, E., Geiger, B.: Molecular complexity and dynamics of cell-matrix adhesions. J. Cell Sci. **114**(Pt 20), 3583–3590 (2001)
50. Riveline, D., et al.: Focal contacts as mechanosensors: externally applied local mechanical force induces growth of focal contacts by an mDia1-dependent and ROCK-independent mechanism. J. Cell Biol. **153**(6), 1175–1186 (2001)
51. Puklin-Faucher, E., Sheetz, M.P.: The mechanical integrin cycle. J. Cell Sci. **122**(Pt 2), 179–186 (2009)
52. Discher, D.E., Janmey, P., Wang, Y.L.: Tissue cells feel and respond to the stiffness of their substrate. Science **310**(5751), 1139–1143 (2005)
53. Shyy, J.Y., Chien, S.: Role of integrins in cellular responses to mechanical stress and adhesion. Curr. Opin. Cell Biol. **9**(5), 707–713 (1997)
54. Hamill, O.P., Martinac, B.: Molecular basis of mechanotransduction in living cells. Physiol. Rev. **81**(2), 685–740 (2001)
55. Ingber, D.E.: Cellular mechanotransduction: putting all the pieces together again. FASEB J. **20**(7), 811–827 (2006)
56. Pelham, R.J., Jr, Wang, Y.: Cell locomotion and focal adhesions are regulated by substrate flexibility. Proc. Natl Acad. Sci. USA **94**(25), 13661–13665 (1997)
57. Choquet, D., Felsenfeld, D.P., Sheetz, M.P.: Extracellular matrix rigidity causes strengthening of integrin-cytoskeleton linkages. Cell **88**(1), 39–48 (1997)
58. Lo, C.M., et al.: Cell movement is guided by the rigidity of the substrate. Biophys. J. **79**(1), 144–152 (2000)
59. Engler, A.J., et al.: Matrix elasticity directs stem cell lineage specification. Cell **126**(4), 677–689 (2006)

60. Tomasek, J.J., et al.: Myofibroblasts and mechano-regulation of connective tissue remodelling. Nat. Rev. Mol. Cell. Biol. **3**(5), 349–363 (2002)
61. Engler, A.J., et al.: Myotubes differentiate optimally on substrates with tissue-like stiffness: pathological implications for soft or stiff microenvironments. J. Cell Biol. **166**(6), 877–887 (2004)
62. Yeung, T., et al.: Effects of substrate stiffness on cell morphology, cytoskeletal structure, and adhesion. Cell Motil. Cytoskeleton **60**(1), 24–34 (2005)
63. Guo, W.H., et al.: Substrate rigidity regulates the formation and maintenance of tissues. Biophys. J. **90**(6), 2213–2220 (2006)
64. Reinhart-King, C.A., Dembo, M., Hammer, D.A.: Cell-cell mechanical communication through compliant substrates. Biophys. J. **95**(12), 6044–6051 (2008)
65. Califano, J.P., Reinhart-King, C.A.: The effects of substrate elasticity on endothelial cell network formation and traction force generation. Conf. Proc. IEEE Eng. Med. Biol. Soc. **2009**, 3343–3345 (2009)
66. Paszek, M.J., et al.: Tensional homeostasis and the malignant phenotype. Cancer Cell **8**(3), 241–254 (2005)
67. Provenzano, P.P., et al.: Matrix density-induced mechanoregulation of breast cell phenotype, signaling and gene expression through a FAK-ERK linkage. Oncogene **28**(49), 4326–4343 (2009)
68. Brown, R.A., et al.: Tensional homeostasis in dermal fibroblasts: mechanical responses to mechanical loading in three-dimensional substrates. J. Cell Physiol. **175**(3), 323–332 (1998)
69. Chen, C.S.: Mechanotransduction - a field pulling together? J. Cell Sci. **121**(Pt 20), 3285–3292 (2008)
70. Giannone, G., et al.: Periodic lamellipodial contractions correlate with rearward actin waves. Cell **116**(3), 431–443 (2004)
71. Dubin-Thaler, B.J., et al.: Nanometer analysis of cell spreading on matrix-coated surfaces reveals two distinct cell states and STEPs. Biophys. J. **86**(3), 1794–1806 (2004)
72. Dobereiner, H.G., et al.: Dynamic phase transitions in cell spreading. Phys. Rev. Lett. **93**(10), 108105 (2004)
73. Dobereiner, H.G., et al.: Force sensing and generation in cell phases: analyses of complex functions. J. Appl. Physiol. **98**(4), 1542–1546 (2005)
74. Cuvelier, D., et al.: The universal dynamics of cell spreading. Curr. Biol. **17**(8), 694–699 (2007)
75. McGrath, J.L.: Cell spreading: the power to simplify. Curr. Biol. **17**(10), R357–R358 (2007)
76. Dubin-Thaler, B.J., et al.: Quantification of cell edge velocities and traction forces reveals distinct motility modules during cell spreading. PLoS One **3**(11), e3735 (2008)
77. Cai, Y., et al.: Nonmuscle myosin IIA-dependent force inhibits cell spreading and drives F-actin flow. Biophys. J. **91**(10), 3907–3920 (2006)
78. Bell, G.I., Dembo, M., Bongrand, P.: Cell adhesion. Competition between nonspecific repulsion and specific bonding. Biophys. J. **45**(6), 1051–1064 (1984)
79. Torney, D.C., Dembo, M., Bell, G.I.: Thermodynamics of cell adhesion. II. Freely mobile repellers. Biophys. J. **49**(2), 501–507 (1986)
80. Huveneers, S., Danen, E.H.: Adhesion signaling - crosstalk between integrins, Src and Rho. J. Cell Sci. **122**(Pt 8), 1059–1069 (2009)
81. Reinhart-King, C.A., Dembo, M., Hammer, D.A.: The dynamics and mechanics of endothelial cell spreading. Biophys. J. **89**(1), 676–689 (2005)
82. Bhadriraju, K., et al.: Activation of ROCK by RhoA is regulated by cell adhesion, shape, and cytoskeletal tension. Exp. Cell Res. **313**(16), 3616–3623 (2007)
83. Stamenovic, D., et al.: Cell prestress. II. Contribution of microtubules. Am. J. Physiol. Cell Physiol. **282**(3), C617–C624 (2002)
84. Mejillano, M.R., et al.: Lamellipodial versus filopodial mode of the actin nanomachinery: pivotal role of the filament barbed end. Cell **118**(3), 363–373 (2004)
85. Sheetz, M.P., Wayne, D.B., Pearlman, A.L.: Extension of filopodia by motor-dependent actin assembly. Cell Motil. Cytoskeleton **22**(3), 160–169 (1992)

86. Giannone, G., et al.: Lamellipodial actin mechanically links myosin activity with adhesion-site formation. Cell **128**(3), 561–575 (2007)
87. Wang, N., et al.: Micropatterning tractional forces in living cells. Cell Motil. Cytoskeleton **52**(2), 97–106 (2002)
88. Ren, X.D., et al.: Focal adhesion kinase suppresses Rho activity to promote focal adhesion turnover. J. Cell Sci. **113**(Pt 20), 3673–3678 (2000)
89. White, D.P., Caswell, P.T., Norman, J.C.: alpha v beta3 and alpha5beta1 integrin recycling pathways dictate downstream Rho kinase signaling to regulate persistent cell migration. J. Cell Biol. **177**(3), 515–525 (2007)
90. Schoenwaelder, S.M., Burridge, K.: Bidirectional signaling between the cytoskeleton and integrins. Curr. Opin. Cell Biol. **11**(2), 274–286 (1999)
91. Hotulainen, P., Lappalainen, P.: Stress fibers are generated by two distinct actin assembly mechanisms in motile cells. J. Cell Biol. **173**(3), 383–394 (2006)
92. Reinhart-King, C.A., Dembo, M., Hammer, D.A.: Endothelial Cell Traction Forces on RGD-Derivatized Polyacrylamide Substrata. Langmuir **19**(5), 1573–1579 (2003)
93. Plopper, G., Ingber, D.E.: Rapid induction and isolation of focal adhesion complexes. Biochem. Biophys. Res. Commun. **193**(2), 571–578 (1993)
94. Schmidt, C.E., et al.: Integrin-cytoskeletal interactions in migrating fibroblasts are dynamic, asymmetric, and regulated. J. Cell Biol. **123**(4), 977–991 (1993)
95. Gumbiner, B.M.: Cell adhesion: the molecular basis of tissue architecture and morphogenesis. Cell **84**(3), 345–357 (1996)
96. Spiegelman, B.M., Ginty, C.A.: Fibronectin modulation of cell shape and lipogenic gene expression in 3T3-adipocytes. Cell **35**(3 Pt 2), 657–666 (1983)
97. Chen, C.S., et al.: Geometric control of cell life and death. Science **276**(5317), 1425–1428 (1997)
98. McBeath, R., et al.: Cell shape, cytoskeletal tension, and RhoA regulate stem cell lineage commitment. Dev. Cell **6**(4), 483–495 (2004)
99. Vogel, V., Sheetz, M.: Local force and geometry sensing regulate cell functions. Nat. Rev. Mol. Cell. Biol. **7**(4), 265–275 (2006)
100. Lauffenburger, D.A., Horwitz, A.F.: Cell migration: a physically integrated molecular process. Cell **84**(3), 359–369 (1996)
101. Ridley, A.J., et al.: Cell migration: integrating signals from front to back. Science **302**(5651), 1704–1709 (2003)
102. Guo, W.H., Wang, Y.L.: Retrograde fluxes of focal adhesion proteins in response to cell migration and mechanical signals. Mol. Biol. Cell **18**(11), 4519–4527 (2007)
103. Friedl, P., Wolf, K.: Plasticity of cell migration: a multiscale tuning model. J. Cell Biol. **188**(1), 11–19 (2010)
104. Sheetz, M.P., Felsenfeld, D.P., Galbraith, C.G.: Cell migration: regulation of force on extracellular-matrix-integrin complexes. Trends Cell Biol. **8**(2), 51–54 (1998)
105. Paszek, M.J., Weaver, V.M.: The tension mounts: mechanics meets morphogenesis and malignancy. J Mammary Gland Biol. Neoplasia **9**(4), 325–342 (2004)
106. Bentley, S.A.: Bone marrow connective tissue and the haemopoietic microenvironment. Br. J. Haematol. **50**(1), 1–6 (1982)
107. Grigoriadis, A.E., Heersche, J.N., Aubin, J.E.: Differentiation of muscle, fat, cartilage, and bone from progenitor cells present in a bone-derived clonal cell population: effect of dexamethasone. J. Cell Biol. **106**(6), 2139–2151 (1988)
108. Howlett, A.R., Bissell, M.J.: The influence of tissue microenvironment (stroma and extracellular matrix) on the development and function of mammary epithelium. Epithelial Cell Biol. **2**(2), 79–89 (1993)
109. Malek, A.M., Izumo, S.: Mechanism of endothelial cell shape change and cytoskeletal remodeling in response to fluid shear stress. J. Cell Sci. **109** (Pt 4), 713–726 (1996)
110. Gregoire, F.M., Smas, C.M., Sul, H.S.: Understanding adipocyte differentiation. Physiol. Rev. **78**(3), 783–809 (1998)

111. Polte, T.R., et al.: Extracellular matrix controls myosin light chain phosphorylation and cell contractility through modulation of cell shape and cytoskeletal prestress. Am. J. Physiol. Cell Physiol. **286**(3), C518–C528 (2004)
112. Bissell, M.J., Rizki, A., Mian, I.S.: Tissue architecture: the ultimate regulator of breast epithelial function. Curr. Opin. Cell Biol. **15**(6), 753–762 (2003)
113. Drubin, D.G., Nelson, W.J.: Origins of cell polarity. Cell **84**(3), 335–344 (1996)
114. Gumbiner, B.M.: Regulation of cadherin-mediated adhesion in morphogenesis. Nat. Rev. Mol. Cell. Biol. **6**(8), 622–634 (2005)
115. Kass, L., et al.: Mammary epithelial cell: influence of extracellular matrix composition and organization during development and tumorigenesis. Int. J. Biochem. Cell Biol. **39**(11), 1987–1994 (2007)
116. Wozniak, M.A., et al.: ROCK-generated contractility regulates breast epithelial cell differentiation in response to the physical properties of a three-dimensional collagen matrix. J. Cell Biol. **163**(3), 583–595 (2003)
117. Moore, K.A., et al.: Control of basement membrane remodeling and epithelial branching morphogenesis in embryonic lung by Rho and cytoskeletal tension. Dev. Dyn. **232**(2), 268–281 (2005)
118. Wang, A.Z., Ojakian, G.K., Nelson, W.J.: Steps in the morphogenesis of a polarized epithelium. I. Uncoupling the roles of cell-cell and cell-substratum contact in establishing plasma membrane polarity in multicellular epithelial (MDCK) cysts. J. Cell Sci. **95**(Pt 1), 137–151 (1990)
119. Szauter, K.M., et al.: Lysyl oxidase in development, aging and pathologies of the skin. Pathol. Biol. (Paris) **53**(7), 448–456 (2005)
120. Padera, T.P., et al.: Pathology: cancer cells compress intratumour vessels. Nature **427**(6976), 695 (2004)
121. Baker, E.L., Bonnecaze, R.T., Zaman, M.H.: Extracellular matrix stiffness and architecture govern intracellular rheology in cancer. Biophys. J. **97**(4), 1013–1021 (2009)
122. Bellizzi, A., et al.: RhoA protein expression in primary breast cancers and matched lymphocytes is associated with progression of the disease. Int. J. Mol. Med. **22**(1), 25–31 (2008)
123. Burbelo, P., Wellstein, A., Pestell, R.G.: Altered Rho GTPase signaling pathways in breast cancer cells. Breast Cancer Res. Treat. **84**(1), 43–48 (2004)
124. Khaled, W., et al.: Palpation imaging using a haptic system for virtual reality applications in medicine. Stud. Health Technol. Inform. **98**, 147–153 (2004)
125. Park, C.C., et al.: Beta1 integrin inhibitory antibody induces apoptosis of breast cancer cells, inhibits growth, and distinguishes malignant from normal phenotype in three dimensional cultures and in vivo. Cancer Res. **66**(3), 1526–1535 (2006)
126. Kumar, S., Weaver, V.M.: Mechanics, malignancy, and metastasis: the force journey of a tumor cell. Cancer Metastasis Rev. **28**(1–2), 113–127 (2009)
127. Saez, A., et al.: Is the mechanical activity of epithelial cells controlled by deformations or forces? Biophys. J. **89**(6), L52–L54 (2005)
128. Califano, J.P., Reinhart-King, C.A.: Exogenous and endogenous force regulation of endothelial cell behavior. J. Biomech. **43**(1), 79–86
129. Fritz, G., Just, I., Kaina, B.: Rho GTPases are over-expressed in human tumors. Int. J. Cancer **81**(5), 682–687 (1999)
130. Kleer, C.G., et al.: WISP3 and RhoC guanosine triphosphatase cooperate in the development of inflammatory breast cancer. Breast Cancer Res. **6**(2), R110–R115 (2004)
131. Takaishi, K., et al.: Regulation of cell-cell adhesion by rac and rho small G proteins in MDCK cells. J. Cell Biol. **139**(4), 1047–1059 (1997)
132. Braga, V.M., et al.: The small GTPases Rho and Rac are required for the establishment of cadherin-dependent cell-cell contacts. J. Cell Biol. **137**(6), 1421–1431 (1997)
133. Levental, K.R., et al.: Matrix crosslinking forces tumor progression by enhancing integrin signaling. Cell **139**(5), 891–906 (2009)

134. Lee, J.M., et al.: The epithelial-mesenchymal transition: new insights in signaling, development, and disease. J. Cell Biol. **172**(7), 973–981 (2006)
135. Zaman, M.H., et al.: Migration of tumor cells in 3D matrices is governed by matrix stiffness along with cell-matrix adhesion and proteolysis. Proc. Natl Acad. Sci. USA **103**(29), 10889–10894 (2006)
136. Bos, J.L.: ras oncogenes in human cancer: a review. Cancer Res **49**(17), 4682–4689 (1989)
137. Ghosh, K., et al.: Tumor-derived endothelial cells exhibit aberrant Rho-mediated mechanosensing and abnormal angiogenesis in vitro. Proc. Natl Acad. Sci. USA **105**(32), 11305–11310 (2008)
138. Hida, K., Hida, Y., Shindoh, M.: Understanding tumor endothelial cell abnormalities to develop ideal anti-angiogenic therapies. Cancer Sci. **99**(3), 459–466 (2008)
139. Carmeliet, P.: Angiogenesis in health and disease. Nat. Med. **9**(6), 653–660 (2003)
140. Krishnan, L., et al.: Interaction of angiogenic microvessels with the extracellular matrix. Am. J. Physiol. Heart Circ. Physiol. **293**(6), H3650–H3658 (2007)
141. Sieminski, A.L., Hebbel, R.P., Gooch, K.J.: The relative magnitudes of endothelial force generation and matrix stiffness modulate capillary morphogenesis in vitro. Exp. Cell Res. **297**(2), 574–584 (2004)
142. Etienne-Manneville, S., Hall, A.: Rho GTPases in cell biology. Nature **420**(6916), 629–635 (2002)
143. Chien, S.: Mechanotransduction and endothelial cell homeostasis: the wisdom of the cell. Am. J. Physiol. Heart Circ. Physiol. **292**(3), H1209–H1224 (2007)
144. Levesque, M.J., Nerem, R.M.: The elongation and orientation of cultured endothelial cells in response to shear stress. J. Biomech. Eng. **107**(4), 341–347 (1985)
145. Ives, C.L., Eskin, S.G., McIntire, L.V.: Mechanical effects on endothelial cell morphology: in vitro assessment. In Vitro Cell Dev. Biol. **22**(9), 500–507 (1986)
146. Remuzzi, A., et al.: Orientation of endothelial cells in shear fields in vitro. Biorheology **21**(4), 617–630 (1984)
147. Galbraith, C.G., Skalak, R., Chien, S.: Shear stress induces spatial reorganization of the endothelial cell cytoskeleton. Cell Motil. Cytoskeleton **40**(4), 317–330 (1998)
148. Tzima, E.: Role of small GTPases in endothelial cytoskeletal dynamics and the shear stress response. Circ. Res. **98**(2), 176–185 (2006)
149. Davies, P.F., Robotewskyj, A., Griem, M.L.: Quantitative studies of endothelial cell adhesion. Directional remodeling of focal adhesion sites in response to flow forces. J. Clin. Invest. **93**(5), 2031–2038 (1994)
150. Tzima, E., et al.: Activation of integrins in endothelial cells by fluid shear stress mediates Rho-dependent cytoskeletal alignment. EMBO J. **20**(17), 4639–4647 (2001)
151. Li, S., et al.: Fluid shear stress activation of focal adhesion kinase. Linking to mitogen-activated protein kinases. J. Biol. Chem. **272**(48), 30455–30462 (1997)
152. Ishida, T., et al.: MAP kinase activation by flow in endothelial cells. Role of beta 1 integrins and tyrosine kinases. Circ. Res. **79**(2), 310–316 (1996)
153. Jalali, S., et al.: Integrin-mediated mechanotransduction requires its dynamic interaction with specific extracellular matrix (ECM) ligands. Proc. Natl Acad. Sci. USA **98**(3), 1042–1046 (2001)
154. Reyes-Reyes, M., et al.: Phosphatidylinositol 3-kinase mediates integrin-dependent NF-kappaB and MAPK activation through separate signaling pathways. J. Cell Sci. **114**(Pt 8), 1579–1589 (2001)
155. Wojciak-Stothard, B., Ridley, A.J.: Shear stress-induced endothelial cell polarization is mediated by Rho and Rac but not Cdc42 or PI 3-kinases. J. Cell Biol. **161**(2), 429–439 (2003)
156. Li, S., et al.: Distinct roles for the small GTPases Cdc42 and Rho in endothelial responses to shear stress. J. Clin. Invest. **103**(8), 1141–1150 (1999)
157. Kraynov, V.S., et al.: Localized Rac activation dynamics visualized in living cells. Science **290**(5490), 333–337 (2000)

158. Tzima, E., et al.: Activation of Rac1 by shear stress in endothelial cells mediates both cytoskeletal reorganization and effects on gene expression. EMBO J. **21**(24), 6791–6800 (2002)
159. Shiu, Y.T., et al.: Rho mediates the shear-enhancement of endothelial cell migration and traction force generation. Biophys. J. **86**(4), 2558–2565 (2004)
160. Seebach, J., et al.: Endothelial barrier function under laminar fluid shear stress. Lab. Invest. **80**(12), 1819–1831 (2000)
161. Shikata, Y., et al.: Differential effects of shear stress and cyclic stretch on focal adhesion remodeling, site-specific FAK phosphorylation, and small GTPases in human lung endothelial cells. Exp. Cell Res. **304**(1), 40–49 (2005)
162. Wojciak-Stothard, B., et al.: Rho and Rac but not Cdc42 regulate endothelial cell permeability. J. Cell Sci. **114**(Pt 7), 1343–1355 (2001)
163. Madri, J.A., Stenn, K.S.: Aortic endothelial cell migration. I. Matrix requirements and composition. Am. J. Pathol. **106**(2), 180–186 (1982)
164. Vyalov, S., Langille, B.L., Gotlieb, A.I.: Decreased blood flow rate disrupts endothelial repair in vivo. Am. J. Pathol. **149**(6), 2107–2118 (1996)
165. van der Meer, A.D., et al.: A microfluidic wound-healing assay for quantifying endothelial cell migration. Am. J. Physiol. Heart Circ. Physiol. **298**(2), H719–H725 (2010)
166. Chung, C.Y., et al.: Role of Rac in controlling the actin cytoskeleton and chemotaxis in motile cells. Proc. Natl Acad. Sci. USA **97**(10), 5225–5230 (2000)
167. Young, W.C., Herman, I.M.: Extracellular matrix modulation of endothelial cell shape and motility following injury in vitro. J. Cell Sci. **73**, 19–32 (1985)
168. Iba, T., Sumpio, B.E.: Morphological response of human endothelial cells subjected to cyclic strain in vitro. Microvasc. Res. **42**(3), 245–254 (1991)
169. Kalluri, R.: Basement membranes: structure, assembly and role in tumour angiogenesis. Nat. Rev. Cancer **3**(6), 422–433 (2003)
170. Singh, R.B., et al.: Pathogenesis of atherosclerosis: a multifactorial process. Exp. Clin. Cardiol. **7**(1), 40–53 (2002)
171. Choi, C.K., Helmke, B.P.: Short-term shear stress induces rapid actin dynamics in living endothelial cells. Mol. Cell. Biomech. **5**(4), 247–258 (2008)
172. Garin, G., Berk, B.C.: Flow-mediated signaling modulates endothelial cell phenotype. Endothelium **13**(6), 375–384 (2006)
173. Chiu, Y.J., et al.: Endothelial cell-cell adhesion and mechanosignal transduction. Endothelium **11**(1), 59–73 (2004)
174. Goldfinger, L.E., et al.: Localized alpha4 integrin phosphorylation directs shear stress-induced endothelial cell alignment. Circ. Res. **103**(2), 177–185 (2008)
175. Helmke, B.P.: Choosing sides in polarized endothelial adaptation to shear stress. Circ. Res. **103**(2), 122–124 (2008)

The Physical Mechanical Processes that Shape Tissues in the Early Embryo

Lance A. Davidson

Abstract The morphology of a multicellular organism and its internal organs is determined by interactions between an organism's genome and the physical properties of living matter. Recent successes in sequencing the genome have revived interest the generation of physical shape, or morphogenesis, the physical properties of living matter, and how biological and biophysical processes shape that living matter during development. One of the goals of modern developmental biology is to understand how tissues are shaped and how physiological function is initiated. Remarkable advances in cell and molecular biology have led to a wealth of data on the molecular mechanisms required during early development. More recently, developmental biologists have been turning to biophysical and bioengineering approaches to understand how embryos as well as organs are shaped by these molecular mechanisms. These studies are finding hints that mechanical processes may be playing novel roles in developing embryos in addition to their direct roles in shaping tissues. Many early molecular pathways regulating cell differentiation and embryonic morphogenesis are reused as tumors grow and metastasize and during the regeneration of injured or damaged tissues. These discoveries have attracted cancer biologists and tissue engineers to join developmental biologists in studying the mechanical processes that drive morphogenesis. In this review we will present a short primer for the engineer on developmental biology and embryonic morphogenesis and then describe experimental and theoretical approaches to investigate the physical principles of morphogenesis.

L. A. Davidson (✉)
Departments of Bioengineering and Developmental Biology, University of Pittsburgh, 3501 Fifth Avenue, 5059-BST3, Pittsburgh, PA 15213, USA
e-mail: lad43@pitt.edu

Stud Mechanobiol Tissue Eng Biomater (2011) 4: 71–97
DOI: 10.1007/8415_2010_29

Published Online: 30 October 2010

1 From Genome to Phenotype: Understanding the Physical Mechanisms of Morphogenesis

To understand the linkage between information in the genome and the phenotype of the organism we need to understand the physical mechanisms that shape tissues during morphogenesis and organogenesis. Classical embryologists from the late 1800s and early 1900s posed many questions about these processes but did not have tools to investigate them. Recently, the field has returned to these questions and made significant advances by developing new biophysical tools to mechanically manipulate tissues in vivo such as micromechanical testing [26, 66, 152, 176, 177, 179], laser-ablation [58, 146], and magnetic tweezers [33]. In addition to these experimental approaches sophisticated computer simulation techniques have been developed to help interpret the complex and often counter-intuitive findings that arise when studying physical processes in embryos [20, 30, 39, 75, 118]. Continued elucidation of the physical mechanisms of morphogenesis requires simultaneous development of new techniques and re-investigation of classical cell and developmental phenomena.

1.1 Three Roles that Mechanics may Play During Development

Ongoing investigations of morphogenesis as well as studies of single cell motility and cell shape change suggest three distinct roles for mechanics during development. First, mechanics can play a direct role through force-production and mechanical resistance to shape the body and organs. However, this direct role must account for both passive and active responses of tissues to applied forces as well as biological principles guiding tissue self-assembly. Cells within embryonic tissues are not shaped solely by externally applied forces but are responsible for generating forces that drive movements as well as maintaining the tissue mechanical properties such as the viscoelastic modulus that guide and mechanically constrain those movements.

A second role for mechanics may be to provide feedback on the progress of morphogenesis to enhance the robustness of these processes. Variable maternal contributions, environmental conditions such as temperature, and stochastic variation in gene expression can all work to destabilize the events of morphogenesis. In the worst cases these variations lead to birth defects. Evolutionary biologists and systems biologists have suggested redundant molecular mechanisms could adjust the activity of signaling pathways or gene expression of developmental processes to ensure morphogenetic movements succeed. We would suggest mechanosensing and dynamically adaptive mechanics may also play key roles in ensuring successful development. Mechanical adaptation could occur at over a range of scales from self-correcting changes in tissue anatomy to alterations in the levels of actin cross-linking. Circuits for mechanosensing may be mediated by

classical signal transduction pathways such as those observed at focal adhesions in cultured cell studies [128] but could be mediated directly through mechanical adaptation by physical changes in tissue anatomy or cell shapes. Experimental tests of this role for mechanics will require new biophysical and molecular techniques to measure and control cell and tissue mechanics and anatomy.

Another possible role for mechanics in providing positional information during patterning is coming to light from studies on the role of the physical cellular microenvironment in stem or progenitor cell differentiation. Evidence for such a role for mechanics during morphogenesis comes from studies on the induction of mesodermal cells in fruit fly [14, 33, 38]. Epithelial cells at the posterior end of the fly embryo require stimulation by mechanical strain to choose the mesodermal cell fate. Reductions in strain block mesodermal differentiation pathways and ectopic application of strain can drive a much larger number of cells down the mesodermal lineage. Another line of evidence comes from studies on factors that control stem cell differentiation [36, 37, 69]. These studies have found the stiffness of a progenitor cell's mechanical microenvironment can direct cell fate down a range of pathways toward bone, muscle, neuron, or adipose identities. The challenge comes in integrating these two lines of evidence. The first challenge is that stem cells appear to respond to stiffness that mimic those seen within adult tissues [36], however, the mechanical microenvironment within early mammalian embryos before overt differentiation takes place is unknown. Very little work has been done to reveal the spatial heterogeneity of cellular microenvironments but some studies on frog embryos from our own group have found large increases in tissue stiffness parallel development [179]. Furthermore, spatial variation in the mechanical microenvironment is present as tissues begin the process of specification and differentiation. For instance, Zhou et al. [179] found that cells within the dorsal side of the somite face stiff neural ectoderm whereas cells within the ventral leaflet face soft endoderm. Such variations in the microenvironment of the forming somite may play a role in directing neural-facing somitic cells toward dermomyotome fates and endoderm-facing somitic cells toward sclerotomal fates. Thus, spatial variations in the stiffness of embryonic tissues could provide positional information to guide cell differentiation in developing tissues.

In order to discuss the roles of physical mechanics in shaping the embryo this chapter will first review the historical background of the problem, topics in developmental biology that set the stage for the morphogenesis, and current efforts to understand the physical mechanics of morphogenesis using developmental, cell biological, and biophysical techniques.

2 Historical Perspective on the Role of Mechanics During Morphogenesis

The direct role of physical mechanics in shaping embryonic tissues has been recognized for more than a century [145] and has been the subject of considerable

theoretical modeling. Following suggestions that biological life was the consequence of chemical and physical processes [60] many embryologists began investigating the physical mechanics of morphogenesis. Before the successes of the modern chemical-molecular approaches, embryologists developed many mechanically-based hypotheses to explain the physical basis of epithelial morphogenesis. For instance, in his textbook on embryology Morgan [97] reviewed several of the earliest proposed mechanisms for driving epithelial buckling during gastrulation of the chordate *Amphioxus*. *Amphioxus* embryos gastrulate from a single cell layered hollow blastula and it was suggested that the forces driving invagination and involution in *Amphioxus* could originate in three different regions of the embryo [121]: (1) the epithelium could be pushed in by extrinsic forces, (2) the epithelium could be sucked in by a decrease in pressure within the blastocoel, or (3) increased pressure within the plate could force the center of the plate inward. Rhumbler demonstrated the physical plausibility of the third hypothesis with an analog model consisting of a set of elastic steel bands bent into rings and assembled with solid bars and string into the form of an *Amphioxus* blastula. By pulling a string strung through one half of the rings, representing the prospective ectoderm, the other half of the rings buckled, imitating the gastrulation movements. Later, Butschli [15] envisioned a driving force located within the buckling *Amphioxus* epithelium. He assembled a model of the blastula out of a strip of blotter paper and a thin strip of gelatin, forming a ring by connecting the two strips. Butschli's model mimicked the movements of invagination when a disk of filter paper soaked in hot water was placed next to the gelatin half. Based on observations from these qualitative models, Butschli argued against an earlier hypothesis by His [56], who proposed that increased growth in the center of the epithelium could cause the epithelium to roll inward. From observations on swelling gelatin sheets, Butschli recognized that differences in growth from one region to another would only cause local thickening of the epithelium, and that buckling required that growth on the basal surface (i.e. facing the blastocoel) exceeded growth on the apical surface (i.e. facing the sea water) of the epithelium. Spek [138] extended the one layer gelatin model of Butschli to include two layers of differentially swelling gels, agar and gelatin. Spek found that his model could mimic *Amphioxus* gastrulation as long as the basal half of the bilayered gel swelled more than the apical half. Based on better histology and with the recognition that subcellular structures could generate force, Lewis [85] developed analog mechanical models fabricated from brass bars to represent shared cell–cell boundaries, and rubber bands to mimic the apical and basal faces of the epithelium. Lewis' mechanical epithelia buckled only when there was a difference in tension between the two faces.

Over the last 30 years the simulation of epithelial bending using physical analogs has given way to numerically based computer simulations. These numerical simulations have begun to address more complex morphogenetic movements such as those driving elongation of the vertebrate axis. Models such as those developed by Odell et al. [104], Davidson et al. [30], and more recently by Miodownik and co-workers [24] are direct descendents of models of epithelial

sheets constructed by Lewis. Simulating the directed cell rearrangements that accompany vertebrate axis elongation requires detailed descriptions of the physical mechanics along with sets of rules that reflect the observed biological processes. For instance, rules are needed to dictate how cells establish polar behaviors, the nature of those behaviors, and how cells physically exchange cell–cell bonds when they exchange neighbors [28]. Several groups have succeeded in simulating axis elongation using different sets of mathematical equations and logical rules [11–13, 18, 105, 161, 174, 175, 180]. The general goal of these efforts have been to demonstrate the physical plausibility of those mechanical principles. As more experimental data becomes available simulations will more often be used to interpret kinematic and mechanical data, test the validity of particular hypotheses, and predict the physical requirements and critical rules required by those hypotheses. Such predictive and interpretive simulations will be needed soon since experimental tools used to study the mechanics of single cells (see reviews by [34, 109, 165]) are being adapted by cell biologists, biophysicists, and bioengineers to study 3-dimensional multicellular systems and morphogenesis.

3 Engineering Lessons: From Egg to Embryo

Early development is marked by establishment of dynamic domains of gene expression and growth factor signaling that begin the process of specifying cell identities and by large scale movements that re-position cells to build the basic body plan of the embryo. Initial domains of gene expression can be established by several processes, the earliest being the localization of determination factors in the egg within the mother. Proteins, mRNA, and even organelles such as mitochondria can be localized within the egg as it matures. This is a common strategy to establish a pre-pattern within invertebrate and vertebrate embryos, however, the role of such pre-pattern in mammals such as mouse and human have been debated and remains an open question (see review [43]). Once the egg is fertilized the unequal inheritance of these factors is made possible by asymmetric cell divisions during cleavage stages. All early embryos undergo rounds of rapid cell division where the number of cells increases and localized factors can be partitioned to regions where daughter cells have inherited greater or lesser amounts of these factors. In some cases such as the fruit fly *Drosophila melanogaster*, early rounds of cell division occur without completion of cytokinesis, however, determination factors are still not free to diffuse and contribute to gene expression patterns that initiate formation of the dorsal–ventral and anterior-posterior axes of the embryo. In embryos without localized factors or where localized factors establish some but not all axes subsequent interactions between the early embryo and external cues are thought to “break-the-symmetry” of the egg. For instance, the sperm entry point in amphibian embryos or the site where mammalian embryos first contact the uterine wall may provide cues that polarize the formation of additional axes in the embryo. In the case of amphibian embryos the sperm entry point establishes

the plane of left–right symmetry and the site of the primary lip where the anterior-most cell identities are established and gastrulation begins.

Once asymmetries are established in the embryo, gene regulatory networks and growth factor signaling cascades enable cells and tissues to acquire specific identities (Fig. 1). As the start of morphogenesis approaches, cells and tissues must establish identities that allow cells to adopt regional behaviors and tissues to spatially pattern mechanical properties. The number of cells within a tissue-type and the position of interfaces between tissues can play key roles in the course of later morphogenetic movements. Incorrect numbers of cells may produce too large or inadequate levels of force. Improperly positioned boundaries between tissues may alter the boundary conditions in such a way that subsequent tissue movements fail, for example, due to buckling. The pathways involved in cell–cell signaling and the factors and networks that control gene transcription are remarkably diverse and involve complex cell biology well beyond the simple diffusion–reaction processes that were originally suggested [79]. Rather than providing a summary we refer interested readers to recent reviews on the systems-biology of patterning [25, 78, 102, 112]. Cell identities and tissue boundaries generated at these early

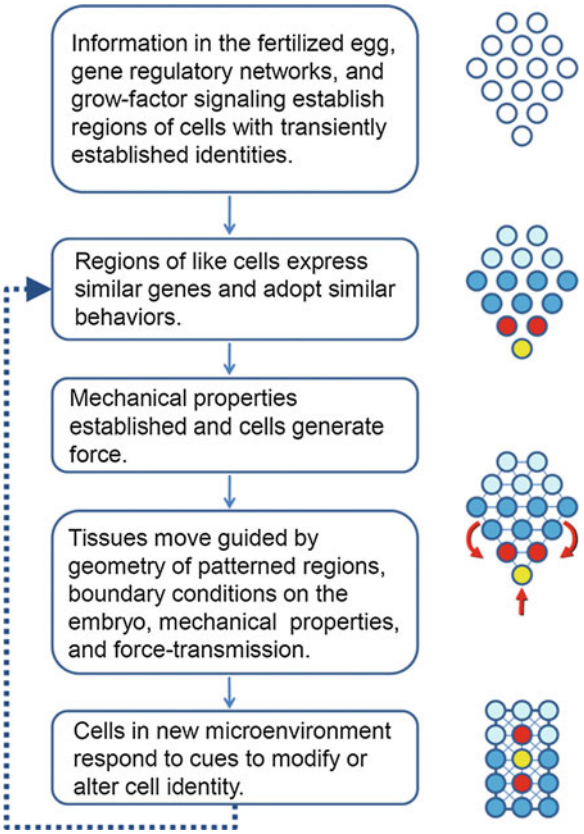

Fig. 1 Programming morphogenesis. The flow chart on the left breaks down the key steps involved in initially patterning cell identities, establishing tissue boundaries, installing cell behaviors and mechanical properties, and tissue movement. As cells move into new locations their microenvironment changes and another round of patterning, boundary formation, mechanics, and movement begins

stages are far from static and continue to shift as cell and tissue movements alter both the chemical and physical microenvironments in the embryo.

The tissue engineer can learn several lessons from the processes that shape the early embryo. The first of these, is that the processes that establish cell identities in embryos can inform the tissue engineer about the in vitro treatments that could be used to create specific cell types from progenitor or stem cells isolated from patients. By recapitulating the same steps of induction by growth factors, or by controlling gene expression to match those regulating specification of cell identity in the embryo the researcher or tissue engineer can produce cells that are only found in vivo during terminal stages of differentiation. However, in most cases the microenvironment of lab-cultured cells is lacking cues found in vivo, for instance, the supporting cells are missing or the complex extracellular matrix (ECM) is incomplete or missing completely. The tissue context or microenvironment of the cell in vivo can play a major role in the cell's capacity to carry out its physiological function and to maintain the size and structure of the organ of which it is a functioning part. In the jargon of developmental biology, the capacity of the cell to differentiate and functional can depend on autonomous factors such as the events that occur within the cell and non-cell autonomous factors that can include cues from the microenvironment that may include local and long-range signaling by growth-factors and ECM, organization of tissue polarity such as the presence of apical-basal polarity, and mechanical cues such as shear flow, cyclic strain, or compressive stress. These non-cell autonomous factors can result from mechanical processes that move blocks of cells and tissues within the embryo. These movements play critical role in creating complex organs composed of cells from different origins by exposing cells to complex microenvironments along the trajectory of their movements and bringing cells that originated distantly from each other into close proximity. Together these processes create a wide variety of structures and organs by generating diverse cell identities and complex microenvironments.

One of the key consequences of cell and tissue patterning events is the initiation of cell and tissue movements that shape the body plan. Targets of the gene regulatory and growth-factor signaling networks generate early spatial patterns of gene expression or protein activity of "effector proteins" such as cadherins and integrins as well as molecules that modulate the cytoskeleton such as the Rho-family of GTPases. These factors act within target cells to initiate programs of cell behavior which guide the assembly of local tissue blocks and the movement of these blocks to construct the body plan of the embryo. The precise biophysics and biomechanics that convert molecular scale regulation of effector proteins into cell behaviors are poorly understood [41] and the subject of ongoing research [90, 106].

We turn now to review the morphogenetic processes that shape embryonic tissues and leave the topics of gene regulation and grow-factor signaling. We direct readers interested in more in-depth reviews of the diverse forms of cell motility to Dennis Bray's and John Trinkaus' books [10, 147], readers interested in more in-depth accounts on comparative forms of gastrulation to Claudio Stern's book [140], readers interested in more in-depth reviews of cell biology to a textbook on

Molecular Cell Biology [4], and readers interested in more in-depth review of biophysics to Joe Howard's book on the mechanics of the cytoskeleton [57].

4 Converting Blueprints to Structures: How Cell Shape Change, Directed Cell Rearrangement, and Large Scale Tissue Movements Sculpt the Basic Vertebrate Body

From the engineer's perspective morphogenesis is a self-organizing mechanical process in which locally coordinated movement or shape change by individual cells direct deformation of the very tissues they inhabit. Cells can engage in a vast array of different behaviors to bring about directed cell rearrangement or change their shape. In the literature there is often little distinction made between the movement and shapes cells adopt actively and movements and shape changes adopted in response to applied stresses. For instance, as tissues bend and fold cells within them often adopt wedge shapes; the narrowest dimension of the cell faces the concave surface and the widest dimension faces the convex surface. However, cells are just as likely to adopt these shape passively as actively. Likewise, cell rearrangements are usually attributed to active cell traction forces but may be driven passively in response to shear stresses generated by more distance cells. To begin to address the question of whether cells are active or passive participants developmental biologists have coined the term *autonomy*. The autonomy of a particular cell behavior suggests that processes such as gene expression or signal transduction must operate *within* the cell exhibiting the behavior, e.g. cell autonomous, or whether processes *outside* the cell are driving the local movements, e.g. non-cell autonomous. Thus, non-cell autonomous processes influencing a cell's shape or behavior could include the effect of gene expression and signal transduction events in more distant cells. These events may be responsible for forces generated by neighboring cells or forces produced a great distance away. Non-cell autonomous processes could also include establishment of mechanical constraints such as boundary conditions or bulk properties of the tissue. In the sections below we will focus on tissue movements that are driven cell autonomously but will return to the role of non-cell autonomous processes later.

5 Cell-mechanics: Cell Behaviors Drive Embryonic Tissue Movements

In the follow sections we will review two distinct autonomous cell behaviors, *apical constriction* and *mediolateral cell intercalation*, which contribute to the bending of

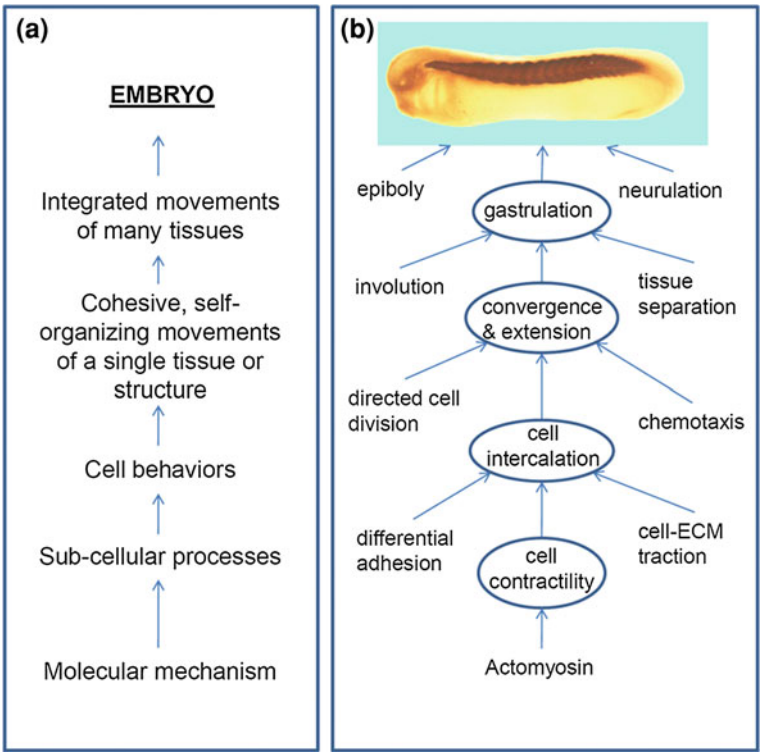

Fig. 2 Integrating events at multiple scales. **a** Processes at a variety of scales from the molecular to the cell- and tissue-level need to be coordinated to generate embryonic form. Mechanical forces are generated on molecular scale but mechanical resistance and boundary conditions may arise at any scale. Feed-back from large-scales may influence events on the molecular scale through mechanotransduction and cell-signaling. **b** Example of the processes thought to be involved in *Xenopus* gastrulation. At each level multiple processes may shape processes at the next larger scale

epithelial sheets and elongation of mesenchymal tissues, respectively. We conceptually break large-scale tissue movements down into sets of cell behaviors (Fig. 2). A variety of different cell behaviors can contribute to the same tissue movement. For instance, both apical constriction and basolateral cell shortening can contribute to the same tissue movement; in fact, they can even work together to bring about epithelial bending [30]. Similarly, a variety of cell behaviors operating locally within mesenchymal tissues can induce convergence and extension. It can be helpful to think of cell behaviors as force-generators and tissue movements as the deformations they generate. Just as multiple patterns of applied stress can produce the same deformation so too different patterns of cell behaviors can produce the same large scale tissue movements. One of the goals in studying the cellular mechanics of morphogenesis is to identify specific molecular pathways and the specific cell behaviors they regulate during the large-scale tissue movements of morphogenesis.

In the sections below we will review two key cell behaviors, mediolateral cell intercalation and apical constriction, that contribute to morphogenetic movements of convergent extension and epithelial bending, respectively.

5.1 Mediolateral Cell Intercalation by Mesenchymal Cells Causes Convergence and Extension

Mediolateral cell intercalation is a form of directed cell rearrangement that is responsible for the large-scale tissue movements of convergent extension that sculpt the basic vertebrate body plan of the frog [68]. In the frog *Xenopus laevis*, mesodermal cells are initially patterned as a ring of tissue in the early spherical embryo. Mesoderm cells form a compact tissue of mesenchymal cells that are connected with neighbors through transient adhesions. Mesenchymal cells do not have a strict apical-basal polarity like epithelial cells but often adopt some form of polarity after they associate with laminar sheets of ECM [48]. Mesoderm cells in the frog intercalate between their neighbors in an orchestrated manner causing shape changes in the surrounding tissues that approach 10–20% strain per hour. The onset of cell intercalation is accompanied by dramatic changes in the cell biology of mesodermal cells; prior to the onset of gastrulation cells barely recognize fibronectin substrates, adhere tightly to their neighbors, and show no bias in their shape or protrusive activity [119]. After gastrulation begins cells gain the ability to spread on fibronectin [119], loosen their attachment to neighbors [19, 178], and intercalate between mediolateral neighboring cells driving them apart in the anterior-posterior direction. This last process, known as mediolateral cell intercalation, spreads throughout the mesoderm medially, laterally, and posteriorly from the vegetal alignment zone (VAZ) in the early gastrula to include all of the mesoderm by the neurula stages [35, 80, 130]. Three to four rounds of mediolateral cell intercalation and the local stress this rearrangement creates drives dorsal tissues to elongate against the viscoelastic resistance of the embryo in a process known as convergent extension. Convergence and extension provides the frog embryo with a definitive vertebrate anatomy consisting of a head, elongated body, and tail. At the conclusion of convergence and extension the frog body plan includes forming blocks of muscle and a basic architecture ready for subsequent steps of organogenesis. Similar patterns of mediolaterally directed cell intercalation are thought to contribute to large-scale tissue movements in mouse [169], chick [150], and zebrafish embryos [172].

Proteins within the planar cell polarity (PCP) pathway are key regulators of mediolateral cell intercalation in frog and other vertebrates [157, 158]. New molecular components of the PCP pathway and their effects on mediolateral cell intercalation are identified every month and highlight linkages between signal transduction elements [170], cytoskeletal effectors [86], cell-adhesion [163], and ECM [47]. PCP components prickle and strabismus (van gogh) appear to regulate the assembly and use of the ECM during mediolateral cell intercalation

[47]. The roles of PCP and the ECM during convergence and extension is complicated since ECM is assembled by [29] by the same cell behaviors that drive mediolateral cell intercalation [31]. The PCP pathway in mesoderm cells regulates key effectors that regulate the actin cytoskeleton. Principle among these factors are the Rho-family GTPases [107], associated GTPase effectors (GEFs; [76, 144]) and GTPase activator proteins (GAPs; [61]). PCP regulation extends to elements of the actin-polymerization machinery [113] via formins and profilin [86, 124]. Balanced function of non-muscle myosin II, the main force-generating motor within the actin cytoskeleton, is also required for gastrulation and neurulation [123, 134, 160]. Cell protrusive activity, cellular mechanics, and the bulk forces generated by cell rearrangement are obvious targets of the PCP pathways yet we have only the most limited understanding of the mechanical role of the actin cytoskeleton in orienting cells or how the actin and myosin II drive cell intercalation.

Many researchers have induced developmental defects in convergent extension by perturbing the embryo's cytoskeleton. For instance, perturbing cytoskeletal myosin II in the frog [134] or myosin phosphatase in Zebrafish [160] disrupts convergent extension. Since the cytoskeleton underlies the mechanical properties of cells and force-production we must conclude that mechanics plays a major role in convergent extension. However, it is unclear how signaling pathways control the cytoskeleton within embryos to produce specific cell behaviors and how these processes regulate the mechanical properties of the embryo or how a cell's capacity to generate force is controlled. Recently, several groups working with *Drosophila* embryos have adapted quantitative approaches similar to ours to investigate the mechanical consequences of disrupting actomyosin contractility during germband elongation [120] and dorsal closure [111]. Furthermore, these new approaches have begun to identify new roles for mechanics in initiating morphogenetic movements and activating mesodermal genes [115]. Future work will be needed to test whether vertebrate homologs of the *Drosophila* genes are controlled in the same manner.

5.2 Apical Constriction in Epithelial Sheets Induces Bending

Apical constriction within epithelial sheets is a form of cell shape change that is responsible for folding and bending embryonic epithelial sheets to shape the neural tube, the tubular archenteron, and later branched epithelial organs [82, 117, 125]. Epithelia are sheets of cells connected into a tensile array at their apical ends. This tensile array provides mechanical continuity with forces transmitted through apical cell–cell junctions, lateral cell–cell adhesions, and basal attachments to neighboring cells or ECM [42]. The tight association of epithelial cells is reflected in the types of cell behaviors and tissue movements exhibited by epithelial tissues. Given their attachments to their microenvironment epithelial morphogenesis is more commonly driven by cell shape changes rather than directed cell rearrangement.

Cell contraction is a major contributor to the forces that regulate cell shape [165]. As groups of cells contract in epithelia they can narrow their apices to form wedge or bottle-shaped cells. Coordinated contraction has been proposed to drive a wide variety of morphogenetic events such as sea-urchin gastrulation [99], *Drosophila* ventral-furrow formation [84], and neurulation in vertebrates [135, 136]. Furthermore, cell contraction in single epithelial cells occurs during epithelial-to-mesenchymal transitions in gastrulating amniotes [131], dorsal closure in *Drosophila* [146], and wound healing in *X. laevis* [27]. Historically researchers have focused on apical constriction, but recent studies suggest a role for general cellular contractility, not restricted to the cell apex, in guiding several morphogenetic events [73, 165].

Cell and tissue contraction may be driven by a number of different cellular mechanisms including: (1) whole cell contraction, (2) apical-basal contraction, (3) circum-apical or circum-basal contraction, and (4) apical cortex contraction. Each of these cellular mechanisms depend critically on remodeling of the F-actin cytoskeleton (for instance see [83, 91, 146]). These developmentally programmed events form the basis of our understanding of the role of contraction and provide clues to the molecular mechanisms.

Studies on the molecular basis of epithelial morphogenesis focus on answering three basic questions: What triggers a cell to change shape? How is cell shape change guided by the cytoskeleton? and, How do cells transfer force to their surrounding to effect tissue movement? Many cases of epithelial morphogenesis appear to use a common molecular mechanism, the actomyosin "purse-string", to generate cell shape change [122] but add specialized molecular and biophysical mechanisms to transduce that force to surroundings. For instance, contractile cells along the midline of the vertebrate neural plate simultaneously contract their apices and adhere to underlying ECM producing short pyramidal cells at the "floorplate" of the neural tube [126, 127]. In contrast, contractile cells in the primitive streak of chick or mouse embryos contract their apices and extend protrusions from their basal ends producing large "bottle-shaped" cells before they ingress into the mesodermal layer [131]. Little is known about what triggers contraction but evidence is abundant that actomyosin is a principle generator of cell shape change and that the cell biological and biomechanical micro-environment dictates the course of tissue movement.

5.3 The Role of the Mechanics in Patterning and Establishing Cell Identity

New roles for mechanics have come to light from recent studies of cellular mechanics in cultured cells and within developing *Drosophila* embryos [34, 165]. These studies have revealed that mechanical cues within the microenvironment are capable of generating spatial information for the specification of cell types including

triggers for apoptosis, the differentiation of progenitor cells, pathways for specialized cell migration, and progression of cancer. The molecular pathways that sense mechanical properties within the microenvironment and the programmed cellular responses are termed *mechanotransduction.* Thus, as mechanotransduction joins other biophysical and biochemical processes that pattern gene expression and physically shape tissues we must consider the control of mechanical properties during these processes.

Due to the relative simplicity of epithelia in early embryos of the fruit fly *Drosophila*, a growing set of experimental studies are elucidating the mechanical principles of *Drosophila* epithelia (Hutson and Ma 2008) and beginning to probe the connection between genetics, cellular mechanics, and morphogenesis during ventral furrow formation [91], germ band elongation [7, 8, 120], dorsal closure [111, 146], and eye formation [51]. These approaches have not yet been applied to the mechanics of vertebrate epithelial tissues where the general principles of cell connectivity or how cells transmit force remain open questions.

5.4 Genetic Studies Provide Clues About the Cytoskeletal Regulators of Cell Behaviors and Mechanics of Morphogenesis

Many proteins associated with the actomyosin cytoskeleton have been identified in genetic screens in Mouse, *Drosophila*, *C. elegans*, and cell-culture systems but the precise biophysical details of contraction within embryonic tissues are not well understood. However, the regulation of F-actin dynamics, and control over myosin II contractility during early epithelial morphogenesis in *Drosophila* appear nearly identical to the pathways that regulate F-actin dynamics and myosin II contractility during cell migration. Pulsed contractions of actomyosin within the apical cortex are thought to drive morphogenetic movements of ventral furrow formation [91, 173], as well as closure of the amnioserosa in *Drosophila* [146]. Pulsed contractions typically occur within the actin-rich apical cortex, however, actomyosin dynamics within the circum-apical belt, along basolateral membranes, as well as microtubule dynamics along the apical basal axis of epithelial cells are all believed to play a role in generating forces of cell shape change within epithelial cells. Myosin contractility during ventral furrow formation is regulated through the Rho family of GTPases via Rho Kinase in a manner not unlike control of myosin II at the rear of migratory cells [168]. Without exception, these events can be inhibited by drugs such as blebbistatin, Y-27632, and ML-7 which inhibit myosin II mediated retrograde flow and retraction of the trailing edge in migratory cells. However, whereas cues that initiate new protrusions or redirect actin polymerization are known in migratory cells, there is less understanding of the cues that initiate these events during apical constriction in *Drosophila* [115].

6 Integrative Studies of Cell Mechanics and Morphogenesis

Questions concerning the role of cell mechanics during morphogenesis require attention to both cell autonomous mechanics and the non-cell autonomous mechanical properties of the surrounding tissues. Numerous studies point to interactions between cellular mechanics and nearly every aspect of the cell biology [62]. Many of these interactions are mediated by the cell's ability to sense its mechanical microenvironment. Mechanosensing of cellular substrates such as protein-conjugated polyacrylamide gels and arrays of microscopic posts reveal effects of substrate stiffness separate from the effects of the chemical composition of the substrate [5, 87, 98, 143]. Precise control of cell substrate geometry has revealed how cell shape controls cell behavior [17, 65, 166]. Such studies have shown that substrate stiffness is a major regulator of cell migration, cell shape and spreading, cell adhesion, proliferation and apoptosis, and gene expression [36, 109, 110, 159, 171]. Interestingly, the cellular microenvironment is shaped by the resident cells raising the likelihood of complex feedback loops where cells modulate their environment which then modifies the cells and so forth. Given the possibility of feedback and that cell behavior and cell identity can be guided by the mechanical environment there has been a critical need for tools capable of measuring mechanical properties and forces generated by tissue-, cellular-, and molecular-structures within the embryo.

Our group has focused on embryos of the frog *X. laevis* to investigate fundamental mechanical principles of morphogenesis. *Xenopus* embryos exhibit several large-scale morphogenetic movements during early development and the tissues involved are accessible to a wide variety of mechanical measurements [26, 152, 162, 179]. The frog model has a number of practical advantages for mechanical measurements. First, like most amphibians, eggs are fertilized external to the mother. Eggs contain all nutrients needed by the embryos until they begin to feed allowing access to embryos before cell divisions begin and allowing isolated cells and tissues to develop as they would if they remained in the embryo. Embryos in early cleavage stages can be injected with synthetic mRNA, DNA plasmids, proteins, or any other desired reagent [133]. Injections of mRNA at the single cell stage can result in even protein expression throughout the embryo while injections into single cells at the two-cell, four-cell, or later cleavage stages allow the preparation of embryos with patchy or mosaic expression. A second advantage of amphibian models is that they do not require complex environmental controls since they develop normally over a range of temperatures from 14 to 28°C and have no special CO_2 or O_2 requirements. Another advantage is that unlike cultured cells there is no strict requirement for sterile handling; amphibian embryos are typically cultured in media containing antibiotic and antimycotic. These are all practical aspects of amphibian models in general, however, *Xenopus* eggs and embryos have been the focus of cell biologists for many decades [67]. *Xenopus* eggs have been favorite model systems for cell biologists since their eggs provide abundant raw material and colonies of frogs are easy vertebrates to keep near

research labs. Thus, current and historical use of *Xenopus* to address cell biology questions provides a rich set of established methods and biochemical tools. A number of groups are working to develop new biophysical tools for mechanical analysis of developing embryos and to integrate these with traditional cell biological and embryological methods.

While amphibian embryos or embryonic tissues are highly adaptable to direct biophysical measurements, alternative model systems such as Mouse, Chicken, Zebrafish, *Drosophila*, and *C. elegans* embryos offer complementary advantages. For instance, human development is more closely represented in the mouse model system but mouse embryos are difficult to obtain and maintain in culture. Historically, chicken embryos have been amenable to microsurgical manipulation and develop at the center of a large sheet of extra-embryonic tissues in a fashion more similar to human development than the style of developing amphibians. Recent efforts are working to establish genetic models for studying amphibian [70] and avian [116] embryonic development, however, the lack of advanced genetic tools such as UAS-GAL4 driver systems, CRE-LOX, or abundant lines of mutant animals hamper the effectiveness of both avian and amphibian model systems.

Recent studies in *Drosophila* have spurred interest in the mechanics of epithelial morphogenesis. Early development in *Drosophila* is coordinated by large scale reorganization of an epithelial sheet that surrounds a syncytial yolk mass. In the first few hours of development several distinct morphogenetic movements of this epithelial sheet provide the opportunity to investigate epithelial bending, convergent extension, wound-like closure, and involution. Epithelial bending occurs during ventral furrow formation and invagination of the posterior mid-gut [142]. Convergent extension occurs during the early and late phases of germband elongation [63]. The dorsal closure of lateral epidermal cell sheets over extra-embryonic tissue of the amnioserosa [164] appears similar to tissue movements that accompany wound healing in vertebrate tissues [92]. Organogenesis at the end of the early phase of *Drosophila* development is marked by involution of an epidermal cell sheet to form the larva's salivary glands and trachea [88].

Complex regulation of the actomyosin cytoskeleton appears to underlie each of these movements in *Drosophila*. For instance, contractile actomyosin assemblies in the apical cortex of ventral cells appear to drive ventral furrow formation [91] and similar process are likely to drive posterior midgut invagination and segment folding. More localized contractility of actomyosin bundles at discrete cell–cell boundaries drives the early phase of germband elongation [7, 8, 40, 120]. Stochastic actomyosin contractions in the amnioserosa and a contractile actomyosin belt at the margins of the lateral epidermis produce forces that integrate to drive dorsal closure [137, 146]. Actomyosin contractility plays a key role in organogenesis as prospective salivary gland cells first form an invagination and then involute as a sheet into the forming gland [167]. In all instances these movements are made possible by imbalances in directed forces and the mechanical resistance of surrounding tissues. Sorting out the autonomous processes of force-production from the non-cell autonomous processes of mechanical resistance are challenging [59, 89]. In addition to the biophysical challenges, the use of embryos lacking

actin-binding or modulating proteins or carrying mutant forms may generate defects in both autonomous and non-cell autonomous processes. Advanced genetic tools using heat-shock controlled mutations, UAS/GAL4 driven constructs, or mosaic expression have been used to address the role of actomyosin in controlling cell behaviors and their mechanical environment but do not yet provide the precise control of cell behaviors and the cellular environment provided by cell culture systems. Genetic and biophysical approaches combined with live-cell imaging are revealing the pathways that pattern and control cell behaviors and revealing universal principles of epithelial morphogenesis.

Cell culture studies reveal how the biophysical events of cell movement and cell shape change depend critically on a dynamic actin cytoskeleton. Most cell movements depend on dynamic assembly and disassembly of the F-actin network [77] and actomyosin contractility [72, 168]. The dynamic cytoskeleton generates forces to shape and propel cells through their environment [81]. Biophysical principles have emerged that connect F-actin dynamics to cell shape change, cell protrusions, and cell traction [21, 49, 114]. For instance, the flow of moving F-actin networks over sites of cell adhesions appear to generate traction forces that direct cell movement [16]. Ultimately it is the mechanical properties of F-actin, microtubules, intermediate filaments and their associated proteins and motors that control these cellular processes. Mechanical properties such as stiffness are strongly dependent on the 3D conformation of the cytoskeleton, how filaments are bundled or cross-linked, and whether active motors, such as myosin II, remodel the polymer networks [46, 64, 71]. Many of these molecular factors are principle targets of gene regulatory networks that control the identity and function of differentiating cells [132]. Biophysical analyses of biopolymers suggest how the cytoskeleton may regulate mechanical properties and force production by multicellular tissues but these hypotheses have not yet been extensively tested.

7 Quantifying Mechanical Properties and Force-production in Shaping Tissues

Quantitative approaches to investigating the mechanics of morphogenesis have been challenging. The mechanical properties of paper, agar, gelatin, brass, and steel materials were crucial to the success of Rhumbler, Butschli, Spek, and Lewis' mechanical models. There has been much work on measuring the elastic modulus of many tissues and materials of adult organisms (e.g. [9, 44, 45, 149, 155]) as well as the properties of single cells (e.g. [1–3, 6, 139]), however, measurements of embryonic tissues, cultured tissue lines, or epithelia have been more rare. Consider our understanding of a relatively simple echinoderm embryo. Echinoderms, like humans, are members of the phylum Chordata. During gastrulation, one of the earliest morphogenetic movements in the echinoderm, a simple epithelial monolayer bends to form a pit that is then reshaped into a tube. Due to their relative

simplicity they have been the subject of biomechanical analysis. The mechanical properties of echinoderm oocytes and fertilized eggs have been studied extensively; Cole [22, 23] first compressed eggs with calibrated microneedles to determine the stiffness of the cell cortex of oocytes and eggs. Hiramoto [52] updated the apparatus and refined the analytical methods to measure changes of the cortical stiffness properties over the first cell cycle in several Japanese species of sea urchin. Hiramoto confirmed his results with three other methods: (1) applying pressure to the cortex with a micropipette [55]; (2) compressing eggs in a centrifuge microscope [53]; and (3) pulling beads against the cortex with a calibrated magnetic field [54]. Studies on the mechanics of late blastula sea urchin embryos used parallel plate compression [32] and found stiffness varied twofold from one clutch to another [151]. These studies on sea urchin embryos evaluated the altered mechanical properties of embryonic tissues after molecular perturbations of the cytoskeleton and the ECM and found the ECM contributed much of the bulk modulus to these marine invertebrate embryos.

While cell and tissue mechanical properties play key roles during embryonic morphogenesis, ultimately cell and tissue movements require the generation and transmission of force. There have been only a few direct measurements of the forces driving morphogenesis [95, 96, 129, 154]. While these studies provided some indication of the magnitude of forces driving morphogenesis, the force-driving role of individual cells is less clear. One study on vertebrate embryos by Waddington [153] attempted to mechanically stall the process of mesoderm movement during gastrulation in the newt. Waddington used small steel balls manipulated by external magnetic field and found approximately 3 Pa was sufficient to stall mesoderm. We can estimate from these studies how molecular-scale processes may be involved in the production and transmission of force by active cells. For instance, molecular motors like myosin and kinesin are capable of generating forces between 2 and 5 picoNewtons [93, 141, 148]. Motors anchored at low densities could easily generate such low stresses or pressures. For instance, two motor molecules properly coordinated with cytoskeletal elements aligned perpendicular to a surface of one square micron, could generate stresses equal to 4–25 pN/μm^2 (1 pN/μm^2 = 1 Pa). Thus, only two molecules of kinesin per square micron could generate the stall stress used by Waddington.

Another analysis of force production during gastrulation in invertebrate species by Moore [94] estimated the forces required to maintain primary invagination in the starfish embryo from the osmotic pressures needed to stall invagination. Moore found that pressures from 36 to 76 kPa could block further extension of the archenteron. In contrast to sparsely spread motor molecules, swelling of proteoglycans exocytosed from cells are capable of generating several orders of magnitude greater stresses [100]. Thus, high levels of force production sufficient to drive invagination of the starfish archenteron could be achieved by either densely concentrated motor proteins or swelling gels. Considerable effort will be needed to develop biophysical tools to measure force-production by embryonic cells and tissues and dissect the molecular and anatomical factors responsible.

8 Connecting Quantitative Models of Morphogenesis to Experimental Measurements

Given the challenges of measuring force-production by embryonic tissues many have turned to multi-scale modeling as a tool to investigate the mechanics of morphogenesis. Researchers have increasingly turned to computer modeling to make sense of the complex cell and tissue movements observed during invertebrate (e.g. [39]) and vertebrate morphogenesis (e.g. [18]). Modeling serves several distinct functions: (1) to help interpret biomechanical experiments, (2) to demonstrate the plausibility of hypotheses, and (3) to identify key physical parameters that are crucial to the success of morphogenetic movements. As genetic studies integrated with biomechanical analyses models will be key in testing the multiple roles of mechanics. Most models of morphogenesis until now have been concerned with testing the direct role of mechanics in shaping tissues but more complex models incorporating gene regulatory networks, cell–cell signaling via growth factors, and mechanotransduction will be needed. One of the goals of these models will be to illustrate and test cellular and molecular mechanisms that lead to redundancy, robustness, and mechanical adaptation during morphogenesis. Models will need to be flexible enough to test both deterministic events of morphogenesis as well as the stochastic and variable aspects. Closer collaborations between modelers and experimentalists will provide insights for interpretation of current experiments and guide future experiments that will lay bare developmental programs that ensure robust self-assembly of tissues and make possible the emergence of complex structures.

9 Conclusion

Research elucidating the physical and chemical mechanisms of morphogenesis will change the way congenital birth defects are viewed and studied. Congenital birth defects such as neural tube and chronic heart defects are present in nearly 1 in 130 live births and are principle causes of infant mortality in the first year of life [101]. Birth defects also cause immense personal suffering and have a high cost to society [156]. A major aim of modern developmental biology is to understand the root causes of these defects and provide tools for genetic counseling. Systematic efforts are underway to identify mutations in the mouse that parallel human congenital birth defects [181]. One of the major clusters of these mutations encode genes that interact with actin [50]. While actin mediates many cellular processes it is also a key element in the biomechanical processes of morphogenesis and organogenesis. Efforts to characterize the mechanical role of the cytoskeleton in controlling tissue mechanics and morphogenesis will provide valuable insights into biomechanical lesions that may be responsible for congenital birth defects and aid the identification of new factors that contribute to birth defects.

The significance of basic research on morphogenesis extends beyond its immediate impact to provide fundamental physical principles for future tissue engineers [103], and to understand the role of tissue mechanics in oncogenesis [74, 109]. Current engineered tissues must be biocompatible at the chemical, cellular, and tissue level. At the tissue level, engineered constructs are currently designed to match the mechanical conditions of their environment. At the cellular level, the mechanical environment seen by engineered cells plays an important role in controlling differentiation [36]. Thus, while there is widespread recognition of the importance of cell and tissue mechanics during morphogenesis there are few tools and little information on how local tissue microenvironments develop. For instance, recent work has found that the mechanical properties of tumors and surrounding healthy soma regulate the progression of metastasis [108]. During development and oncogenesis, and within engineered tissues, mechanics is regulated by factors such as Rho-GTPase through the actin cytoskeleton: modulating cell migration, cell mechanics, and assembly of the ECM [109]. By using model systems researchers studying the biomechanics of tissue formation may allow future tissue engineers to control aspects of tissue mechanics and characterize the consequences of alterations to tissue mechanics on cell behaviors that are outside the reach of conventional cell culture and tissue models. Future studies will provide novel insights into the coordination between bulk tissue mechanics and the fine scale cytoskeletal control of cell behaviors that are highly relevant to the regulation of cell behaviors in the diverse fields of oncology and tissue engineering.

Acknowledgments The work was supported by grants from the NSF (IOS-0845775) and the NIH (HD044750).

References

1. Akkas, N.: NATO advanced research workshop on biomechanics of cell division (1986: Istanbul, Turkey). In: NATO ASI series. Series A, Life Sciences, vol. 132. Plenum Press, New York (1987)
2. Akkas, N.: NATO advanced study institute on biomechanics of active movement and deformation of cells (1989: Istanbul, Turkey). In: NATO ASI series. Series H, Cell Biology, vol. 42. Springer, New York (1990)
3. Akkas, N.: Biomechanics of active cell movement and division of cells. In: NATO ASI series. Series H, Cell biology, vol. 84. Springer, New York (1994)
4. Alberts, B., Johnson, A., Lewis, J., Raff, M., Roberts, K., Walter, P.: Molecular biology of the cell. Garland Science, New York (2008)
5. Beningo, K.A., Dembo, M., Kaverina, I., Small, J.V., Wang, Y.L.: Nascent focal adhesions are responsible for the generation of strong propulsive forces in migrating fibroblasts. J. Cell Biol. **153**, 881–888 (2001)
6. Bereiter-Hahn, J., Anderson, O.R., Reif, W.-E.: Cytomechanics; the mechanical basis of cell form and structure, pp. 294. Springer, New York (1987)
7. Bertet, C., Sulak, L., Lecuit, T.: Myosin-dependent junction remodelling controls planar cell intercalation and axis elongation. Nature **429**, 667–671 (2004)
8. Blankenship, J.T., Backovic, S.T., Sanny, J.S., Weitz, O., Zallen, J.A.: Multicellular rosette formation links planar cell polarity to tissue morphogenesis. Dev. Cell **11**, 459–470 (2006)

9. Bolis, L., Maddrell, S.H.P., Schmidt-Nielsen, K.: Comparative physiology: functional aspects of structural materials. In: Proceedings of the International Conference on Comparative Physiology, Ascona 1974, pp. 268. North-Holland Publications, Amsterdam (1975)
10. Bray, D.: Cell movements: from molecules to motility. Garland Publications, New York (2001)
11. Brodland, G.W.: The Differential Interfacial Tension Hypothesis (DITH): a comprehensive theory for the self-rearrangement of embryonic cells and tissues. J. Biomech. Eng. **124**, 188–197 (2002)
12. Brodland, G.W.: Do lamellipodia have the mechanical capacity to drive convergent extension? Int. J. Dev. Biol. **50**, 151–155 (2006)
13. Brodland, G.W., Veldhuis, J.H.: Lamellipodium-driven tissue reshaping: a parametric study. Comput. Methods Biomech. Biomed. Eng. **9**, 17–23 (2006)
14. Brouzes, E., Farge, E.: Interplay of mechanical deformation and patterned gene expression in developing embryos. Curr. Opin. Genet. Dev. **14**, 367–374 (2004)
15. Butschli, O.: Bemerkungen zur mechanishen erklarung der gastrula-invagination, vol. 4, pp. 3–13. Sitzungsberichte Akademie Wissenschaffen, Heidelberg (1915)
16. Chan, C.E., Odde, D.J.: Traction dynamics of filopodia on compliant substrates. Science **322**, 1687–1691 (2008)
17. Chen, C.S., Mrksich, M., Huang, S., Whitesides, G.M., Ingber, D.E.: Geometric control of cell life and death. Science **276**, 1425–1428 (1997)
18. Chen, X., Brodland, G.W.: Multi-scale finite element modeling allows the mechanics of amphibian neurulation to be elucidated. Phys. Biol. **5**, 15003 (2008)
19. Chen, X., Gumbiner, B.M.: Crosstalk between different adhesion molecules. Curr. Opin. Cell Biol. **18**, 572–578 (2006)
20. Cheshire, A.M., Kerman, B.E., Zipfel, W.R., Spector, A.A., Andrew, D.J.: Kinetic and mechanical analysis of live tube morphogenesis. Dev. Dyn. **237**, 2874–2888 (2008)
21. Choi, C.K., Vicente-Manzanares, M., Zareno, J., Whitmore, L.A., Mogilner, A., Horwitz, A.R.: Actin and alpha-actinin orchestrate the assembly and maturation of nascent adhesions in a myosin II motor-independent manner. Nat. Cell Biol. (2008)
22. Cole, K.S.: Surface forces of the *Arbacia* egg. J. Cell Comp. Physiol. **1**, 1–9 (1932)
23. Cole, K.S., Michaelis, E.M.: Surface forces of fertilized *Arbacia* eggs. J. Cell. Comp. Physiol. **2**, 121–126 (1932)
24. Conte, V., Munoz, J.J., Baum, B., Miodownik, M.: Robust mechanisms of ventral furrow invagination require the combination of cellular shape changes. Phys. Biol. **6**, 016010 (2009)
25. Davidson, E.H., Levine, M.S.: Properties of developmental gene regulatory networks. Proc. Natl. Acad. Sci. USA **105**, 20063–20066 (2008)
26. Davidson, L., Keller, R.: Measuring mechanical properties of embryos and embryonic tissues. Methods Cell Biol. **83**, 425–439 (2007)
27. Davidson, L.A., Ezin, A.M., Keller, R.: Embryonic wound healing by apical contraction and ingression in *Xenopus laevis*. Cell Motil. Cytoskelet. **53**, 163–176 (2002)
28. Davidson, L.A., Joshi, S.D., Kim, H.Y., von Dassow, M., Zhang, L., Zhou, J.: Emergent morphogenesis: elastic mechanics of a self-deforming tissue. J. Biomech. **43**, 63–70 (2010)
29. Davidson, L.A., Keller, R., Desimone, D.W.: Assembly and remodeling of the fibrillar fibronectin extracellular matrix during gastrulation and neurulation in *Xenopus laevis*. Dev. Dyn. **231**, 888–895 (2004)
30. Davidson, L.A., Koehl, M.A., Keller, R., Oster, G.F.: How do sea urchins invaginate? Using biomechanics to distinguish between mechanisms of primary invagination. Development **121**, 2005–2018 (1995)
31. Davidson, L.A., Marsden, M., Keller, R., Desimone, D.W.: Integrin alpha5beta1 and fibronectin regulate polarized cell protrusions required for Xenopus convergence and extension. Curr. Biol. **16**, 833–844 (2006)

32. Davidson, L.A., Oster, G.F., Keller, R.E., Koehl, M.A.: Measurements of mechanical properties of the blastula wall reveal which hypothesized mechanisms of primary invagination are physically plausible in the sea urchin *Strongylocentrotus purpuratus*. Dev. Biol. **209**, 221–238 (1999)
33. Desprat, N., Supatto, W., Pouille, P.A., Beaurepaire, E., Farge, E.: Tissue deformation modulates twist expression to determine anterior midgut differentiation in Drosophila embryos. Dev. Cell **15**, 470–477 (2008)
34. Discher, D.E., Janmey, P., Wang, Y.L.: Tissue cells feel and respond to the stiffness of their substrate. Science **310**, 1139–1143 (2005)
35. Domingo, C., Keller, R.: Induction of notochord cell intercalation behavior and differentiation by progressive signals in the gastrula of *Xenopus laevis*. Development **121**, 3311–3321 (1995)
36. Engler, A.J., Sen, S., Sweeney, H.L., Discher, D.E.: Matrix elasticity directs stem cell lineage specification. Cell **126**, 677–689 (2006)
37. Even-Ram, S., Artym, V., Yamada, K.M.: Matrix control of stem cell fate. Cell **126**, 645–647 (2006)
38. Farge, E.: Mechanical induction of twist in the Drosophila foregut/stomodeal primordium. Curr. Biol. **13**, 1365–1377 (2003)
39. Farhadifar, R., Roper, J.C., Aigouy, B., Eaton, S., Julicher, F.: The influence of cell mechanics, cell-cell interactions, and proliferation on epithelial packing. Curr. Biol. **17**, 2095–2104 (2007)
40. Fernandez-Gonzalez, R., Simoes Sde, M., Roper, J.C., Eaton, S., Zallen, J.A.: Myosin II dynamics are regulated by tension in intercalating cells. Dev. Cell **17**, 736–743 (2009)
41. Forgacs, G., Newman, S.A.: Biological physics of the developing embryo. Cambridge University Press, Cambridge (2005)
42. Fristrom, D.: The cellular basis of epithelial morphogenesis: a review. Tissue Cell **20**(5), 645–690 (1988)
43. Fujimori, T.: Preimplantation development of mouse: a view from cellular behavior. Dev. Growth Differ. **52**, 253–262 (2010)
44. Fung, Y.C.: Biomechanics: mechanical properties of living tissues. Springer, Berlin (1981)
45. Fung, Y.C.: Biomechanics: motion, flow, stress, and growth. Springer, New York (1991)
46. Gardel, M.L., Nakamura, F., Hartwig, J.H., Crocker, J.C., Stossel, T.P., Weitz, D.A.: Prestressed F-actin networks cross-linked by hinged filamins replicate mechanical properties of cells. Proc. Natl. Acad. Sci. USA **103**, 1762–1767 (2006)
47. Goto, T., Davidson, L., Asashima, M., Keller, R.: Planar cell polarity genes regulate polarized extracellular matrix deposition during frog gastrulation. Curr. Biol. **15**, 787–793 (2005)
48. Green, J.B., Davidson, L.A.: Convergent extension and the hexahedral cell. Nat. Cell Biol. **9**, 1010–1015 (2007)
49. Gupton, S.L., Waterman-Storer, C.M.: Spatiotemporal feedback between actomyosin and focal-adhesion systems optimizes rapid cell migration. Cell **125**, 1361–1374 (2006)
50. Harris, M.J., Juriloff, D.M.: Mouse mutants with neural tube closure defects and their role in understanding human neural tube defects. Birth Defects Res. A Clin. Mol. Teratol. **79**, 187–210 (2007)
51. Hayashi, T., Carthew, R.W.: Surface mechanics mediate pattern formation in the developing retina. Nature **431**, 647–652 (2004)
52. Hiramoto, Y.: Mechanical properties of sea urchin eggs. II. Changes in the mechanical properties from fertilization to cleavage. Exp. Cell Res. **32**, 76 (1963)
53. Hiramoto, Y.: Observations and measurements of sea urchin eggs with a centrifuge microscope. J. Cell Physiol. **69**, 216–230 (1967)
54. Hiramoto, Y.: Mechanical properties of the surface of the sea urchin egg at fertilization and during cleavage. Exp. Cell Res. **89**(2), 320–326 (1974)
55. Hiramoto, Y.: Determination of mechanical properties of the egg surface by elastimetry. Methods Cell Biol. **27**, 435–442 (1986)

56. His, W.: Unsere korperform und das physiologische problem ihrer entstehung. F.C.W. Vogel, Leipzig (1874)
57. Howard, J.: Mechanics of motor proteins and the cytoskeleton. Sinauer Associates, Sunderland (2001)
58. Hutson, M.S., Tokutake, Y., Chang, M.S., Bloor, J.W., Venakides, S., Kiehart, D.P., Edwards, G.S.: Forces for morphogenesis investigated with laser microsurgery and quantitative modeling. Science **300**, 145–149 (2003)
59. Hutson, M.S., Veldhuis, J., Ma, X., Lynch, H.E., Cranston, P.G., Brodland, G.W.: Combining laser microsurgery and finite element modeling to assess cell-level epithelial mechanics. Biophys. J. **97**, 3075–3085 (2009)
60. Huxley, T.H.: On the physical basis of life. Conn, New Haven (1870)
61. Hyodo-Miura, J., Yamamoto, T.S., Hyodo, A.C., Iemura, S., Kusakabe, M., Nishida, E., Natsume, T., Ueno, N.: XGAP, an ArfGAP, is required for polarized localization of PAR proteins and cell polarity in Xenopus gastrulation. Dev. Cell **11**, 69–79 (2006)
62. Ingber, D.E.: Mechanical control of tissue morphogenesis during embryological development. Int. J. Dev. Biol. **50**, 255–266 (2006)
63. Irvine, K.D., Wieschaus, E.: Cell intercalation during Drosophila germband extension and its regulation by pair-rule segmentation genes. Development **120**, 827–841 (1994)
64. Janmey, P.A., Georges, P.C., Hvidt, S.: Basic rheology for biologists. Methods Cell Biol. **83**, 3–27 (2007)
65. Jiang, X., Bruzewicz, D.A., Wong, A.P., Piel, M., Whitesides, G.M.: Directing cell migration with asymmetric micropatterns. Proc. Natl. Acad. Sci. USA **102**, 975–978 (2005)
66. Kalantarian, A., Ninomiya, H., Saad, S.M., David, R., Winklbauer, R., Neumann, A.W.: Axisymmetric drop shape analysis for estimating the surface tension of cell aggregates by centrifugation. Biophys. J. **96**, 1606–1616 (2009)
67. Kay, B.K., Peng, H.B.: *Xenopus laevis*: practical uses in cell and molecular biology. Academic Press, New York (1991)
68. Keller, R., Davidson, L., Edlund, A., Elul, T., Ezin, M., Shook, D., Skoglund, P.: Mechanisms of convergence and extension by cell intercalation. Philos. Trans. R. Soc. Lond. B **355**, 897–922 (2000)
69. Kilian, K.A., Bugarija, B., Lahn, B.T., Mrksich, M.: Geometric cues for directing the differentiation of mesenchymal stem cells. Proc. Natl. Acad. Sci. USA **107**, 4872–4877 (2010)
70. Klein, S.L., Strausberg, R.L., Wagner, L., Pontius, J., Clifton, S.W., Richardson, P.: Genetic and genomic tools for Xenopus research: The NIH Xenopus initiative. Dev. Dyn. **225**, 384–391 (2002)
71. Koenderink, G.H., Dogic, Z., Nakamura, F., Bendix, P.M., MacKintosh, F.C., Hartwig, J.H., Stossel, T.P., Weitz, D.A.: An active biopolymer network controlled by molecular motors. Proc. Natl. Acad. Sci. USA **106**, 15192–15197 (2009)
72. Kolega, J.: The role of myosin II motor activity in distributing myosin asymmetrically and coupling protrusive activity to cell translocation. Mol. Biol. Cell **17**, 4435–4445 (2006)
73. Krieg, M., Arboleda-Estudillo, Y., Puech, P.H., Kafer, J., Graner, F., Muller, D.J., Heisenberg, C.P.: Tensile forces govern germ-layer organization in zebrafish. Nat. Cell Biol. **10**, 429–436 (2008)
74. Kumar, S., Weaver, V.M.: Mechanics, malignancy, and metastasis: the force journey of a tumor cell. Cancer Metastasis Rev. **28**, 113–127 (2009)
75. Kurpios, N.A., Ibanes, M., Davis, N.M., Lui, W., Katz, T., Martin, J.F., Belmonte, J.C., Tabin, C.J.: The direction of gut looping is established by changes in the extracellular matrix and in cell:cell adhesion. Proc. Natl. Acad. Sci. USA **105**, 8499–8506 (2008)
76. Kwan, K.M., Kirschner, M.W.: A microtubule-binding Rho-GEF controls cell morphology during convergent extension of *Xenopus laevis*. Development **132**, 4599–4610 (2005)
77. Lacayo, C.I., Pincus, Z., VanDuijn, M.M., Wilson, C.A., Fletcher, D.A., Gertler, F.B., Mogilner, A., Theriot, J.A.: Emergence of large-scale cell morphology and movement from local actin filament growth dynamics. PLoS Biol. **5**, e233 (2007)

78. Lander, A.D.: Morpheus unbound: reimagining the morphogen gradient. Cell **128**, 245–256 (2007)
79. Lander, A.D., Nie, Q., Wan, F.Y.: Do morphogen gradients arise by diffusion? Dev. Cell **2**, 785–796 (2002)
80. Lane, M.C., Keller, R.: Microtubule disruption reveals that Spemann's Organizer is subdivided into two domains by the vegetal alignment zone. Development **124**, 895–906 (1997)
81. Lauffenburger, D.A., Horwitz, A.F.: Cell migration: a physically integrated molecular process. Cell **84**, 359–369 (1996)
82. Lecuit, T., Lenne, P.F.: Cell surface mechanics and the control of cell shape, tissue patterns and morphogenesis. Nat. Rev. Mol. Cell Biol. **8**, 633–644 (2007)
83. Lee, J.Y., Harland, R.M.: Actomyosin contractility and microtubules drive apical constriction in Xenopus bottle cells. Dev. Biol. **311**, 40–52 (2007)
84. Leptin, M., Grunewald, B.: Cell shape changes during gastrulation in Drosophila. Development **110**(1), 73–84 (1990)
85. Lewis, W.H.: Mechanics of invagination. Anat. Rec. **97**, 139–56 (1947)
86. Liu, W., Sato, A., Khadka, D., Bharti, R., Diaz, H., Runnels, L.W., Habas, R.: Mechanism of activation of the Formin protein Daam1. Proc. Natl. Acad. Sci. USA **105**, 210–215 (2008)
87. Lo, C.M., Wang, H.B., Dembo, M., Wang, Y.L.: Cell movement is guided by the rigidity of the substrate. Biophys. J. **79**, 144–152 (2000)
88. Lubarsky, B., Krasnow, M.A.: Tube morphogenesis: making and shaping biological tubes. Cell **112**, 19–28 (2003)
89. Ma, X., Lynch, H.E., Scully, P.C., Hutson, M.S.: Probing embryonic tissue mechanics with laser hole drilling. Phys. Biol. **6**, 036004 (2009)
90. Mammoto, T., Ingber, D.E. Mechanical control of tissue and organ development. Development **137**, 1407–1420
91. Martin, A.C., Kaschube, M., Wieschaus, E.F.: Pulsed contractions of an actin-myosin network drive apical constriction. Nature **457**, 495–499 (2009)
92. Martin, P., Lewis, J.: Actin cables and epidermal movement in embryonic wound healing. Nature **360**(6400), 179–183 (1992)
93. Miyata, H., Yoshikawa, H., Hakozaki, H., Suzuki, N., Furuno, T., Ikegami, A., Kinosita, K., Jr., Nishizaka, T., Ishiwata, S.: Mechanical measurements of single actomyosin motor force. Biophys. J. **68**, 286S–289S (discussion 289S–290S) (1995).
94. Moore, A.R.: On the mechanics of gastrulation in Dendraster excentricus. J. Exp. Zool. **87**, 101–111 (1941)
95. Moore, S.W.: A fiber optic system for measuring dynamic mechanical properties of embryonic tissues. IEEE Trans. Biomed. Eng. **41**, 45–50 (1994)
96. Moore, S.W., Keller, R.E., Koehl, M.A.R.: The dorsal involuting marginal zone stiffens anisotropically during its convergent extension in the gastrula of *Xenopus leavis*. Development **121**, 3130–3140 (1995)
97. Morgan, T.H.: Experimental embryology: Columbia University Press, New York (1927)
98. Munevar, S., Wang, Y., Dembo, M.: Traction force microscopy of migrating normal and H-ras transformed 3T3 fibroblasts. Biophys. J. **80**, 1744–1757 (2001)
99. Nakajima, Y., Burke, R.D.: The initial phase of gastrulation in sea urchins is accompanied by the formation of bottle cells. Dev. Biol. **179**, 436–446 (1996)
100. Nanavati, C., Fernandez, J.M.: The secretory granule matrix: a fast-acting smart polymer. Science **259**, 963–965 (1993)
101. Nemer, M.: Genetic insights into normal and abnormal heart development. Cardiovasc. Pathol. **17**, 48–54 (2008)
102. Niehrs, C.: On growth and form: a Cartesian coordinate system of Wnt and BMP signaling specifies bilaterian body axes. Development **137**, 845–857 (2010)
103. NSTC: Strategies for advancing tissue science and engineering: foundation for the future, pp. 52. Washington, D.C. (2007)

104. Odell, G.M., Oster, G., Alberch, P., Burnside, B.: The mechanical basis of morphogenesis. Dev. Biol. **85**, 446–462 (1981)
105. Oster, G., Weliky, M.: Morphogenesis by cell rearrangement: a computer simulation approach. Semin. Dev. Biol. **1**, 313–323 (1990)
106. Paluch, E., Heisenberg, C.P.: Biology and physics of cell shape changes in development. Curr. Biol. **19**, R790–R799 (2009)
107. Park, T.J., Gray, R.S., Sato, A., Habas, R., Wallingford, J.B.: Subcellular localization and signaling properties of dishevelled in developing vertebrate embryos. Curr. Biol. **15**, 1039–1044 (2005)
108. Paszek, M.J., Weaver, V.M.: The tension mounts: mechanics meets morphogenesis and malignancy. J. Mammary Gland Biol. Neoplasia **9**, 325–342 (2004)
109. Paszek, M.J., Zahir, N., Johnson, K.R., Lakins, J.N., Rozenberg, G.I., Gefen, A., Reinhart-King, C.A., Margulies, S.S., Dembo, M., Boettiger, D. et al.: Tensional homeostasis and the malignant phenotype. Cancer Cell **8**, 241–254 (2005)
110. Pelham, R.J., Jr., Wang, Y.: Cell locomotion and focal adhesions are regulated by substrate flexibility. Proc. Natl. Acad. Sci. USA **94**, 13661–13665 (1997)
111. Peralta, X.G., Toyama, Y., Kiehart, D.P., Edwards, G.S.: Emergent properties during dorsal closure in Drosophila morphogenesis. Phys. Biol. **5**, 15004 (2008)
112. Peter, I.S., Davidson, E.H.: Modularity and design principles in the sea urchin embryo gene regulatory network. FEBS Lett. **583**, 3948–3958 (2009)
113. Pollard, T.D., Borisy, G.G.: Cellular motility driven by assembly and disassembly of actin filaments. Cell **112**, 453–465 (2003)
114. Ponti, A., Machacek, M., Gupton, S.L., Waterman-Storer, C.M., Danuser, G.: Two distinct actin networks drive the protrusion of migrating cells. Science **305**, 1782–1786 (2004)
115. Pouille, P.A., Ahmadi, P., Brunet, A.C., Farge, E.: Mechanical signals trigger Myosin II redistribution and mesoderm invagination in Drosophila embryos. Sci. Signal **2**, ra16 (2009)
116. Poynter, G., Huss, D., Lansford, R.: Japanese quail: an efficient animal model for the production of transgenic avians. CSH Protocol 2009, pdb emo112 (2009)
117. Quintin, S., Gally, C., Labouesse, M.: Epithelial morphogenesis in embryos: asymmetries, motors and brakes. Trends Genet. **24**, 221–230 (2008)
118. Ramasubramanian, A., Latacha, K.S., Benjamin, J.M., Voronov, D.A., Ravi, A., Taber, L.A.: Computational model for early cardiac looping. Ann. Biomed. Eng. **34**, 1655–1669 (2006)
119. Ramos, J.W., Whittaker, C.A., DeSimone, D.W.: Integrin-dependent adhesive activity is spatially controlled by inductive signals at gastrulation. Development **122**, 2873–2883 (1996)
120. Rauzi, M., Verant, P., Lecuit, T., Lenne, P.F.: Nature and anisotropy of cortical forces orienting Drosophila tissue morphogenesis. Nat. Cell Biol. **10**, 1401–1410 (2008)
121. Rhumbler, L.: Zur mechanik des gastrulationsvorganges insbesondere der invagination. Archiv Fur Entwicklungsmechanic **14**, 401–476 (1902)
122. Rodriguez-Diaz, A., Toyama, Y., Abravanel, D.L., Wiemann, J.M., Wells, A.R., Tulu, U.S., Edwards, G.S., Kiehart, D.P.: Actomyosin purse strings: renewable resources that make morphogenesis robust and resilient. HFSP J. **2**, 220–237 (2008)
123. Rolo, A., Skoglund, P., Keller, R.: Morphogenetic movements driving neural tube closure in Xenopus require myosin IIB. Dev. Biol. **327**, 327–338 (2009)
124. Sato, A., Khadka, D.K., Liu, W., Bharti, R., Runnels, L.W., Dawid, I.B., Habas, R.: Profilin is an effector for Daam1 in non-canonical Wnt signaling and is required for vertebrate gastrulation. Development **133**, 4219–4231 (2006)
125. Sawyer, J.M., Harrell, J.R., Shemer, G., Sullivan-Brown, J., Roh-Johnson, M., Goldstein, B.: Apical constriction: a cell shape change that can drive morphogenesis. Dev. Biol. **341**, 5–19 (2010)
126. Schoenwolf, G.C., Smith, J.L.: Epithelial cell wedging: a fundamental cell behavior contributing to hinge point formation during epithelial morphogenesis. Semin. Dev. Biol. **1**, 325–334 (1990)

127. Schroeder, T.E.: Neurulation in *Xenopus laevis*. An analysis and model based upon light and electron microscopy. J. Embryol. Exp. Morphol. **23**(2), 427–462 (1970)
128. Schwartz, M.A., DeSimone, D.W.: Cell adhesion receptors in mechanotransduction. Curr. Opin. Cell Biol. **20**, 551–556 (2008)
129. Selman, G.G.: The forces producing neural closure in amphibia. J. Embryol. Exp. Morphol. **6**, 448–465 (1958)
130. Shih, J., Keller, R.: Patterns of cell motility in the organizer and dorsal mesoderm of *Xenopus laevis*. Development **116**(4), 915–930 (1992)
131. Shook, D., Keller, R.: Mechanisms, mechanics and function of epithelial-mesenchymal transitions in early development. Mech. Dev. **120**, 1351–1383 (2003)
132. Sinner, D., Kirilenko, P., Rankin, S., Wei, E., Howard, L., Kofron, M., Heasman, J., Woodland, H.R., Zorn, A.M.: Global analysis of the transcriptional network controlling Xenopus endoderm formation. Development **133**, 1955–1966 (2006)
133. Sive, H.L., Grainger, R.M., Harland, R.M.: Early development of *Xenopus laevis*: a laboratory manual, pp. 338. Cold Spring Harbor Laboratory Press, Cold Spring Harbor (2000)
134. Skoglund, P., Rolo, A., Chen, X., Gumbiner, B.M., Keller, R.: Convergence and extension at gastrulation require a myosin IIB-dependent cortical actin network. Development **135**, 2435–2444 (2008)
135. Smith, J.L., Schoenwolf, G.C.: Neurulation: coming to closure. Trends Neurosci. **20**, 510–517 (1997)
136. Smith, J.L., Schoenwolf, G.C., Quan, J.: Quantitative analyses of neuroepithelial cell shapes during bending of the mouse neural plate. J. Comp. Neurol. **342**, 144–151 (1994)
137. Solon, J., Kaya-Copur, A., Colombelli, J., Brunner, D.: Pulsed forces timed by a ratchet-like mechanism drive directed tissue movement during dorsal closure. Cell **137**, 1331–1342 (2009)
138. Spek, J.: Differenzen im quellungszustand der plasmakolloide als eine ursache der gastrulainvagination, sowie der einstulpungen und faltungen von zellplatten uberhaupt. Kolloidchemische Beihefte **9**, 259–399 (1918)
139. Stein, W.D., Bronner, F.: Cell Shape: determinants, regulation, and regulatory role. Academic Press, San Diego (1989)
140. Stern, C.D.: Gastrulation: from cells to embryo. Cold Spring Harbor Laboratory Press, Cold Spring Harbor (2004)
141. Svoboda, K., Schmidt, C.F., Schnapp, B.J., Block, S.M.: Direct observation of kinesin stepping by optical trapping interferometry [see comments]. Nature **365**(6448), 721–727 (1993)
142. Sweeton, D., Parks, S., Costa, M., Wieschaus, E.: Gastrulation in *Drosophila*: the formation of the ventral furrow and posterior midgut invaginations. Development **112**(3), 775–789 (1991)
143. Tan, J.L., Tien, J., Pirone, D.M., Gray, D.S., Bhadriraju, K., Chen, C.S.: Cells lying on a bed of microneedles: an approach to isolate mechanical force. Proc. Natl. Acad. Sci. USA **100**, 1484–1489 (2003)
144. Tanegashima, K., Zhao, H., Dawid, I.B.: WGEF activates Rho in the Wnt-PCP pathway and controls convergent extension in Xenopus gastrulation. Embo. J. **27**, 606–617 (2008)
145. Thompson, D.A.W.: On growth and form. Cambridge University Press, London (1917)
146. Toyama, Y., Peralta, X.G., Wells, A.R., Kiehart, D.P., Edwards, G.S.: Apoptotic force and tissue dynamics during Drosophila embryogenesis. Science **321**, 1683–1686 (2008)
147. Trinkaus, J.P.: Cells into organs: the forces that shape the embryo. Prentice-Hall Inc., Englewood Cliffs (1984)
148. VanBuren, P., Guilford, W.H., Kennedy, G., Wu, J., Warshaw, D.M.: Smooth muscle myosin: a high force-generating molecular motor. Biophys. J. **68**, 256S–258S; 258S–259S (1995)
149. Vincent, J.V.: Structural biomaterials. Princeton University Press, Princeton (1990)

150. Voiculescu, O., Bertocchini, F., Wolpert, L., Keller, R.E., Stern, C.D.: The amniote primitive streak is defined by epithelial cell intercalation before gastrulation. Nature **449**, 1049–1052 (2007)
151. von Dassow, M., Davidson, L.A.: Variation and robustness of the mechanics of gastrulation: the role of tissue mechanical properties during morphogenesis. Birth Defects Res. C Embryo Today **81**, 253–269 (2007)
152. von Dassow, M., Davidson, L.A.: Natural variation in embryo mechanics: gastrulation in *Xenopus laevis* is highly robust to variation in tissue stiffness. Dev. Dyn. **238**, 2–18 (2009)
153. Waddington, C.H.: Order of magnitude of morphogenetic forces. Nature **144**(3649), 637 (1939)
154. Waddington, C.H.: Observations on the forces of morphogenesis in the amphibian embryo. J. Exp. Biol. **19**, 284–293 (1942)
155. Wainwright, S.A., Biggs, W.D., Currey, J.D., Gosline, J.M.: Mechanical design in organisms. Wiley, New York (1976)
156. Waitzman, N.J., Romano, P.S., Scheffler, R.M.: Estimates of the economic costs of birth defects. Inquiry **31**, 188–205 (1994)
157. Wallingford, J.B., Fraser, S.E., Harland, R.M.: Convergent extension: the molecular control of polarized cell movement during embryonic development. Dev. Cell **2**, 695–706 (2002)
158. Wallingford, J.B., Rowning, B.A., Vogeli, K.M., Rothbacher, U., Fraser, S.E., Harland, R.M.: Dishevelled controls cell polarity during *Xenopus* gastrulation. Nature **405**, 81–85 (2000)
159. Wang, H.B., Dembo, M., Wang, Y.L.: Substrate flexibility regulates growth and apoptosis of normal but not transformed cells. Am. J. Physiol. Cell Physiol. **279**, C1345–C1350 (2000)
160. Weiser, D.C., Row, R.H., Kimelman, D.: Rho-regulated Myosin phosphatase establishes the level of protrusive activity required for cell movements during zebrafish gastrulation. Development **136**, 2375–2384 (2009)
161. Weliky, M., Minsuk, S., Keller, R., Oster, G.: Notochord morphogenesis in *Xenopus laevis*: simulation of cell behavior underlying tissue convergence and extension. Development **113**(4), 1231–1244 (1991)
162. Wiebe, C., Brodland, G.W.: Tensile properties of embryonic epithelia measured using a novel instrument. J. Biomech. **38**, 2087–2094 (2005)
163. Witzel, S., Zimyanin, V., Carreira-Barbosa, F., Tada, M., Heisenberg, C.P.: Wnt11 controls cell contact persistence by local accumulation of Frizzled 7 at the plasma membrane. J. Cell Biol. **175**, 791–802 (2006)
164. Wood, W., Jacinto, A., Grose, R., Woolner, S., Gale, J., Wilson, C., Martin, P.: Wound healing recapitulates morphogenesis in Drosophila embryos. Nat. Cell Biol. **4**, 907–912 (2002)
165. Wozniak, M.A., Chen, C.S.: Mechanotransduction in development: a growing role for contractility. Nat. Rev. Mol. Cell Biol. **10**, 34–43 (2009)
166. Xia, N., Thodeti, C.K., Hunt, T.P., Xu, Q., Ho, M., Whitesides, G.M., Westervelt, R., Ingber, D.E.: Directional control of cell motility through focal adhesion positioning and spatial control of Rac activation. Faseb. J. **22**(6):1649–1659 (2008)
167. Xu, N., Keung, B., Myat, M.M.: Rho GTPase controls invagination and cohesive migration of the Drosophila salivary gland through Crumbs and Rho-kinase. Dev. Biol. **321**, 88–100 (2008)
168. Yam, P.T., Wilson, C.A., Ji, L., Hebert, B., Barnhart, E.L., Dye, N.A., Wiseman, P.W., Danuser, G., Theriot, J.A.: Actin-myosin network reorganization breaks symmetry at the cell rear to spontaneously initiate polarized cell motility. J. Cell Biol. **178**, 1207–1221 (2007)
169. Yamanaka, Y., Tamplin, O.J., Beckers, A., Gossler, A., Rossant, J.: Live imaging and genetic analysis of mouse notochord formation reveals regional morphogenetic mechanisms. Dev. Cell **13**, 884–896 (2007)

170. Ybot-Gonzalez, P., Savery, D., Gerrelli, D., Signore, M., Mitchell, C.E., Faux, C.H., Greene, N.D., Copp, A.J.: Convergent extension, planar-cell-polarity signalling and initiation of mouse neural tube closure. Development **134**, 789–799 (2007)
171. Yeung, T., Georges, P.C., Flanagan, L.A., Marg, B., Ortiz, M., Funaki, M., Zahir, N., Ming, W., Weaver, V., Janmey, P.A.: Effects of substrate stiffness on cell morphology, cytoskeletal structure, and adhesion. Cell Motil. Cytoskelet. **60**, 24–34 (2005)
172. Yin, C., Kiskowski, M., Pouille, P.A., Farge, E., Solnica-Krezel, L.: Cooperation of polarized cell intercalations drives convergence and extension of presomitic mesoderm during zebrafish gastrulation. J. Cell Biol. **180**, 221–232 (2008)
173. Young, P.E., Pesacreta, T.C., Kiehart, D.P.: Dynamic changes in the distribution of cytoplasmic myosin during Drosophila embryogenesis. Development **111**(1), 1–14 (1991)
174. Zajac, M., Jones, G.L., Glazier, J.A.: Model of convergent extension in animal morphogenesis. Phys. Rev. Lett. **85**, 2022–2025 (2000)
175. Zajac, M., Jones, G.L., Glazier, J.A.: Simulating convergent extension by way of anisotropic differential adhesion. J. Theor. Biol. **222**, 247–259 (2003)
176. Zamir, E.A., Taber, L.A.: Material properties and residual stress in the stage 12 chick heart during cardiac looping. J. Biomech. Eng. **126**, 823–830 (2004a)
177. Zamir, E.A., Taber, L.A. On the effects of residual stress in microindentation tests of soft tissue structures. J. Biomech. Eng. Trans. Asme **126**, 276–283 (2004b)
178. Zhong, Y., Brieher, W.M., Gumbiner, B.M.: Analysis of C-cadherin regulation during tissue morphogenesis with an activating antibody. J. Cell Biol. **144**, 351–359 (1999)
179. Zhou, J., Kim, H.Y., Davidson, L.A.: Actomyosin stiffens the vertebrate embryo during critical stages of elongation and neural tube closure. Development **136**, 677–688 (2009)
180. Ziherl, P.: Aggregates of two-dimensional vesicles: rouleaux, sheets, and convergent extension. Phys. Rev. Lett. **99**, 128102 (2007)
181. Zohn, I.E., Anderson, K.V., Niswander, L.: Using genomewide mutagenesis screens to identify the genes required for neural tube closure in the mouse. Birth Defects Res. A Clin. Mol. Teratol. **73**, 583–590 (2005)

Mechanobiology of Primary Cilia

Ronald Y. Kwon, David A. Hoey and Christopher R. Jacobs

Abstract Within many mechanosensitive tissues and organs such as vascular endothelium, renal and liver epithelium, and bone, the cells residing within them are exposed to fluid flow. The process by which flow-induced mechanical loads are sensed by these cells and transduced into a biochemical signal is mostly unknown. The primary cilium is a rod-like, microtubule-based structure that projects from the cell surface into the extracellular environment. By possessing (1) mechanical characteristics that allow it to deflect under fluid flow, and (2) a number of receptors, channels, and signaling molecules, the primary cilium is uniquely suited to function as a cellular "flow sensor". In our review of the primary cilium and its role in sensing of fluid flow, we consider ciliary mechanobiology from both biological and mechanical perspectives. The first part of this chapter focuses on comparing and contrasting ciliary flow sensing mechanisms in kidney epithelial cells, cardiovascular endothelial cells, bile duct epithelial cells, nodal cells, and bone cells. We demonstrate that ciliary sensation of fluid flow can involve molecular mechanisms that are shared across diverse cell types, yet can also uniquely differ between cell types as well. The second part of this chapter focuses on ciliary mechanics. In particular, we review the contribution of various ciliary components to the mechanical behavior of the cilium, and efforts to mechanically model cilium deflection under flow.

R. Y. Kwon (✉)
La Jolla Bioengineering Institute, 505 Coast Blvd South Ste 406, La Jolla, CA, USA
e-mail: rkwon@ljbi.org

D. A. Hoey
Royal College of Surgeons in Ireland, Dublin, Ireland

D. A. Hoey and C. R. Jacobs
Department of Biomedical Engineering, Columbia University, New York, NY, USA

Stud Mechanobiol Tissue Eng Biomater (2011) 4: 99–124
DOI: 10.1007/8415_2010_28

Published Online: 15 September 2010

1 Introduction

A number of tissues and organs critically depend on extrinsic and/or intrinsic mechanical signals for proper development, maintenance, and/or function. In most cases, the molecular mechanisms utilized by the cells within these tissues and organs to sense mechanical loads and transduce them into biochemical signals (i.e., the mechanisms involved in the process of cellular mechanotransduction) are unknown. A better understanding of these mechanisms is central to understanding the causes of diseases, disorders, and syndromes in which aberrant mechanotransduction contributes to their onset and/or progression [38].

The capacity for tissues and organs to be regulated by mechanical loads is dependent on the generation of one or more cell-level physical signals that alter cellular function. Within many mechanosensitive tissues and organs, the cells residing within them are exposed to fluid flow. For example, lumen-lining cells such as tubular kidney epithelial cells, epithelial cells of the liver, and endothelial cells lining blood vessels are subjected to flow of luminal fluid, bile, and blood, respectively. Within bone, cells residing within the mineralized matrix are subjected to interstitial fluid flow arising from loads imparted to the bone tissue [57, 81]. During development, flow of extra-embryonic fluid is transiently generated in the node, a structure on the surface of the mammalian embryo that appears during gastrulation [52]. Fluid flow subjects cells to variety of potential regulatory signals, such as enhanced transport of nutrients and/or signaling molecules [12], streaming potentials [92], and fluid shear stress. Given the vastly different functions of the cells described above, it is perhaps rather remarkable they all share the capacity to sense and respond to fluid flow utilizing a mechanism mediated by a common organelle, the primary cilium (or in the case of nodal cells, a primary cilium-like structure termed the nodal cilium). The primary cilium is a rod-like, solitary (i.e., each cell possesses one), non-motile (except for some nodal cilia, as will be discussed later), microtubule-based structure that projects from the surface of the plasma membrane into the extracellular environment. By extending into the extracellular space and possessing mechanical characteristics that allow flow-induced bending, it is uniquely suited to serve a mechanosensory role by deflecting under fluid flow. In addition, given that a number of receptors, channels, and signaling molecules localize within the cilium, it is biochemically suited to function as a cellular "flow sensor".

In this chapter, we review primary cilia mechanobiology with a focus on sensation of fluid flow. In our review, we take both biological and mechanical perspectives. The first part of this chapter focuses on comparing and contrasting ciliary flow sensing mechanisms in kidney epithelial cells, cardiovascular endothelial cells, bile duct epithelial cells, nodal cells, and bone cells. We demonstrate that sensation of fluid flow via the primary cilium can involve molecular mechanisms that are both shared across these diverse cell types, but can also uniquely differ between cell types as well. The second part of this chapter focuses on ciliary mechanics. In particular, we review the contribution of various ciliary components

to the mechanical behavior of the cilium. In addition, we review both experimental and theoretical efforts to characterize the mechanics of cilium deflection under flow.

1.1 Architecture, Formation, and Maintenance

1.1.1 Primary Cilia are Microtubule-Based Structures Distinct from Motile Cilia

We begin this chapter with a discussion of the architecture of primary cilia and the processes involved in their formation and maintenance. For more in depth information regarding these processes, the reader is directed to several excellent reviews [6, 10, 65, 88]. As briefly discussed earlier, the primary cilium is an antenna-like structure that projects from the surface of the plasma membrane into the extracellular environment. They are found on nearly every cell in the mammalian body [10]. Primary cilia are distinct from motile cilia (found, for example, on the surface of epithelial cells), particularly in regards to their motility, the number of cilia that cells possess, their molecular structure, and their function. For example, motile cilia are generally found in large groups, and beat in an orchestrated manner to facilitate fluid or cell movement [10]. In contrast, primary cilia are solitary and non-motile. Like motile cilia, primary cilia are microtubule-based structures with axoneme cores. The axonemes of primary cilia, which originate from basal bodies (microtubule-organizing centers that are derived from centrioles), are surrounded by a plasma membrane that joins with the plasma membrane of the cell body. The molecular architecture of the axonemes of primary cilia differs from that of motile cilia. In particular, the axonemes of motile cilia are made up of nine sets of microtubule doublets and a central pair of singlet microtubules. Thus, they are often described as having a 9+2 microtubule architecture. In contrast, while primary cilia also possess an axoneme composed of nine microtubule doublets, they do not posses the central pair (Fig. 1). Thus, they are described as having a 9+0 microtubule architecture. In addition, primary cilia are missing several molecular components found in motile cilia such as inner and outer dynein arms, and radial spokes [61].

1.1.2 Primary Cilium Formation and Maintenance Relies on Intraflagellar Transport

Primary cilia lack protein synthesis machinery, thus they require a coordinated process called intraflagellar transport (IFT) for delivery of ciliary components [35, 65]. Ciliary proteins such as receptors and channels are synthesized in the cell body, and transported along the axoneme by IFT. Proteins that are to be incorporated into the cilium assemble into complexes termed IFT particles [88], and are then transported along the axoneme. Transport occurs in a bidirectional manner,

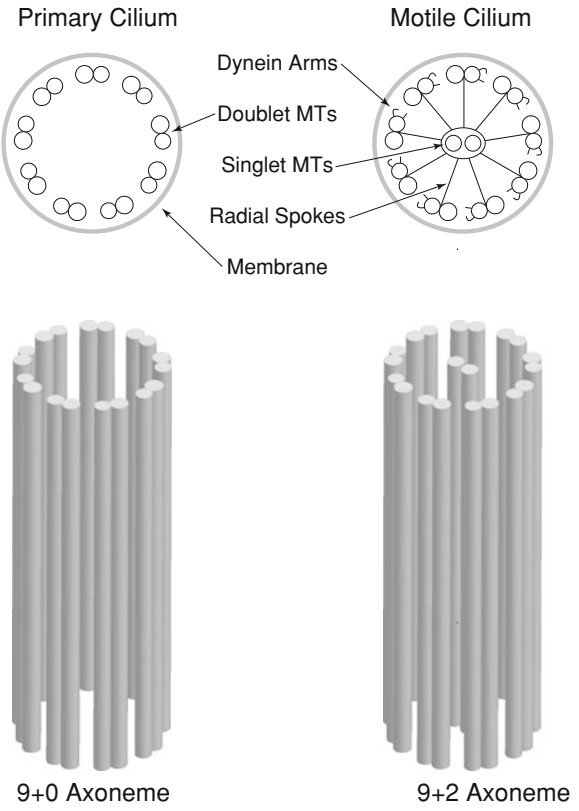

Fig. 1 Molecular architecture of the primary cilium (*left*) and motile cilium (*right*). The primary cilium axoneme is composed of nine doublet microtubules. The motile cilium axoneme additionally possesses a central pair of singlet microtubules. Figure adapted from [10]

with different molecular motors responsible for transport in different directions. Anterograde transport occurs via kinesin 2 [9], a heterotrimeric protein that is composed of three subunits, two of which have a motor function (Kif3a and Kif3b), and a third which does not. Retrograde transport occurs by cytoplasmic dynein 1B [55]. During ciliogenesis, axoneme elongation occurs distally from the basal body via addition of axoneme subunits at the ciliary tip [6].

1.2 Physiological Function of Primary Cilia

In recent years, primary cilia have become the focus of intense research efforts to elucidate their functions [10]. These efforts have revealed that these organelles are involved in remarkably diverse processes. For example, during embryonic development, nodal cilia have been found to be critical for the establishment of left–right asymmetry [52]. In addition, disruption of the IFT component polaris has been found to result in defects in skeletal patterning and endochondral bone formation [25], and other developmental abnormalities such as arrest in development

at mid-gestation, pericardial sac enlargement, and defects in neural tube closure [47]. Mutations in ciliary-associated genes have also been found to result in a broad range of non-developmental pathologies (see [6] for review). For example, ciliary dysfunction has been linked to polycystic kidney disease (PKD) and growth of cystic lesions in the liver and pancreas [10, 88]. It has also been associated with mental impairment, blindness, obesity, and diabetes, particularly in association with Bardet–Biedel syndrome (BBS), a genetic disorder linked to mutations in proteins that localize to the ciliary/centrosomal complex [6].

Although the specific role of primary cilia in regulating the diverse processes and pathologies described above has yet to fully elucidated, their function as sensory organelles of chemical and physical stimuli has been established [38]. For example, in addition to functioning as mechanosensors of fluid flow, they have been implicated in mediating sensation of tonicity [19] and temperature [34]. With regards to chemical stimuli, primary cilia have been shown to mediate sonic hedgehog signaling through a mechanism that involves the departure of Ptc1 from cilia upon Shh binding, and subsequent accumulation of Smo within the cilium [63]. Receptors for somatostatin and PDGF, which regulate cell proliferation, have also been found to localize to the cilium [23, 69]. Although the mechanisms by which cilia mediate the sensation of such diverse stimuli are still largely unknown, it is not unreasonable to believe that chemical signal transduction at the primary cilium involves common signaling components including those involved in ciliary mechanotransduction, which are reviewed in the next section.

2 Primary Cilia Mechanotransduction: Signaling Mechanisms

In this section, we compare and contrast ciliary signaling mechanisms involved in the sensation of fluid flow in kidney epithelial cells, cardiovascular endothelial cells, bile duct epithelial cells, nodal cells, and bone cells. These cells share a common trait in that they all possess the capacity to sense fluid flow via a mechanism involving the cilium, yet these cells have vastly different functions. Thus, perhaps it is not surprising that while these cells use some shared molecular machinery in transducing flow via the cilium, there are also key differences in their mechanosensing mechanisms.

2.1 Renal Primary Cilia

2.1.1 Renal Cilia Passively Bend Under Fluid Flow

We begin our review of ciliary mechanotransduction signaling pathways in kidney epithelial cells, since it is in these cells that a mechanosensory function for the primary cilium was first ascribed. Due to their wide distribution throughout the

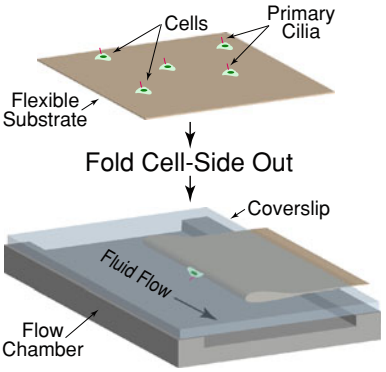

Fig. 2 Schematic of the flexible substrate technique of Roth et al. [66] for viewing cilium deflection under fluid flow from the side. Cells are cultured on flexible substrates, which are folded in half cell-side out, and positioned in a flow chamber so that the folded edge is parallel to the direction of flow

kidney and their projection from the cell surface, a sensory role for cilia within the kidney had long been speculated [3]. The first experimental evidence that they were mechanically suited to sense luminal flow was provided by Roth et al. [66] who used a flexible substratum technique to view perfused kidney epithelial cells in side view. In this technique, cells were grown on flexible substrates and folded cell-side out. The cells residing on the creased edge were then loaded into a flow chamber and placed under a microscope such that they could be viewed from the side (Fig. 2). When exposed to flow, Roth et al. observed that the renal cilia bent passively, and recoiled following cessation of flow, indicating that primary cilia were ideally suited to serve a mechanosensory function by passively bending under flow. Schwartz et al. [70] later demonstrated that a range of physiologically relevant levels of flow were sufficient to deflect renal cilia, and noted that such deflections would result in the generation of membrane tension that could serve to open stretch-activated ion channels.

2.1.2 Bending Renal Primary Cilia Induces Extracellular Ca^{2+}-Dependent Intracellular Ca^{2+} Release

The first direct evidence linking primary cilium deflection and biochemical signaling was provided by Praetorius and Spring [59, 60] who demonstrated that ciliary bending was sufficient to induce intracellular Ca^{2+} fluxes. In particular, these authors demonstrated that bending the cilium in MDCK cells, either by micropipette suction of individual cilia (Fig. 3), or by exposure to flow, resulted in a substantial increase in intracellular Ca^{2+} concentration [Ca^{2+}] [59]. Under both flow and micropipette bending, the intracellular Ca^{2+} mobilization was eliminated in the presence of Ca^{2+}-free media, Gd^{3+} (a putative blocker of mechanosensitive ion channels), or thapsigargin (which depletes intracellular Ca^{2+} stores), indicating that the intracellular Ca^{2+} flux was mediated by extracellular Ca^{2+}-dependent intracellular Ca^{2+} release. Interestingly, intracellular Ca^{2+} mobilization induced by poking of the apical membrane with a micropipette was not abrogated by removal of extracellular Ca^{2+}, indicating that renal epithelial cells possess both cilium-dependent and

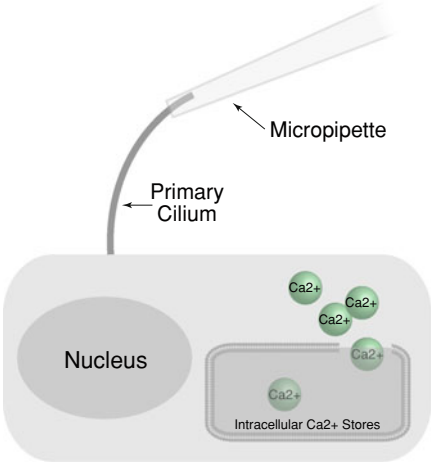

Fig. 3 Experimental setup of Praetorius and Spring [59] in which individual renal cilia were bent by micropipette suction. Pipette bending was demonstrated to induce release of Ca^{2+} from intracellular stores via a mechanism involving extracellular Ca^{2+} and Gd^{3+}-sensitive channels

cilium-independent mechanosensory mechanisms that can result in intracellular Ca^{2+} mobilization via distinct signaling pathways. In addition, these data suggest that the intracellular Ca^{2+} flux induced by ciliary bending was not due to deformation of the surrounding apical membrane [59], but rather deformations at or near the cilium. The hypothesis that ciliary bending is responsible for transducing luminal fluid flow in kidney was further supported by subsequent investigations by these authors indicating that pharmacological removal of the primary cilium by treatment with chloral hydrate abolished flow-induced increases in intracellular Ca^{2+}, despite the cells having normal intracellular microtubule organization [60].

2.1.3 Polycystin-1 and Polycystin-2 Mediate Flow-Induced Signaling Responses in Kidney

A link between renal flow sensing, primary cilia, and polycystic kidney disease (PKD) was established by Nauli et al. [48]. Autosomal dominant polycystic kidney disease (ADPKD), which is characterized by the formation of renal cysts, involves polycystin-1, a large, integral membrane protein [41] encoded by the gene Pkd1, and polycystin-2, a Ca^{2+}-permeable cation channel [18, 79] encoded by the gene Pkd2. In particular, mutations in either Pkd1 or Pkd2 results in ADPKD [50]. Prior to the studies of Nauli et al. the importance of primary cilia in the etiology of PKD had been established through several studies [4, 54, 89], such as investigations indicating that PC1 and PC2 are associated with the cilium, and the discovery that the Oak Ridge Polycystic Kidney (orpk) mutant mouse, which develops cystic lesions in the kidney, possessed a mutation in the gene that encoded for polaris, which is required for proper cilium formation [24, 76, 90].

Nauli et al. found that PC1 and PC2 co-distribute in renal cilia, and that kidney cells from transgenic mice lacking functional PC1 and wildtype cells treated with blocking antibodies against PC2 did not exhibit an increase in intracellular Ca^{2+}

when exposed to flow [48]. These data provided a molecular link between the apparent extracellular Ca^{2+}-dependent intracellular Ca^{2+} release and ciliary bending previously observed by Praetorius and Spring. Given the function of PC2 as a Ca^{2+}-permeable channel, the large extracellular domains of PC1, and the evidence that PC1 and PC2 could heterodimerize [11, 22, 48, 72], Nauli et al. proposed that PC1/2 form a mechanosensing complex in which bending of the cilium results in conformational changes in PC1, which subsequently activates PC2 [48] (Fig. 4). These authors also suggested that abnormal mechanosensing due to dysfunction in this complex may contribute to PKD pathogenesis.

Several investigations have identified additional signaling mechanisms involved in renal ciliary flow sensing that involve PC1 and/or PC2 and which may also be involved in the onset and progression of PKD. For example, Low et al. [41] demonstrated that the cytoplasmic tail of PC1 interacts with the transcription factor STAT6, and that PC1 can undergo proteolytic cleavage such that the PC1 tail translocates to the nucleus and activates STAT6-mediated gene expression. These authors also demonstrated that cessation of flow causes nuclear translocation of STAT6 from the cilium. Interestingly, they observed that expression of the human PC1 tail in zebrafish embryos resulted in the formation of kidney cysts, suggesting that overexpression of the cytoplasmic tail of PC1 is sufficient to induce the formation of renal cysts [41]. Besschetnova et al. [5] demonstrated that increased levels of cyclic adenosine monophosphate (cAMP) and subsequent activation of protein kinase A (PKA) increased ciliary length and anterograde intraflagellar transport. When exposed to flow, intracellular cAMP levels and ciliary length were decreased. These findings lead these authors to propose the presence of a negative feedback loop whereby flow leads to cilium bending-induced decreases in cAMP and subsequent shortening of the cilium and decreased

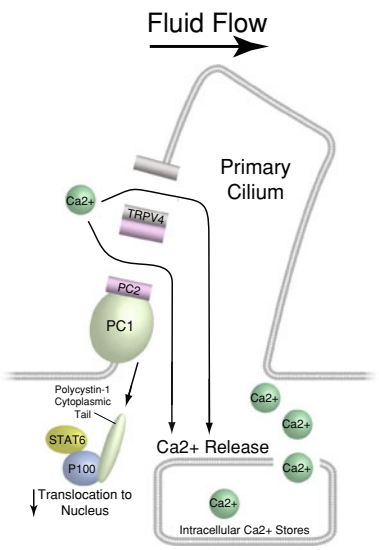

Fig. 4 Schematic demonstrating proposed renal ciliary flow sensing mechanisms [34, 41, 48]

mechanosensitivity. Interestingly, this response was blocked when PC1 and PC2 were reduced, suggesting that in PKD, disruption of this negative feedback loop may contribute to its pathology. Kottgen et al. [34] found that TRPV4, a member of the transient receptor potential (TRP) superfamily of cation channels, localizes to renal primary cilia and interacts with PC2. Further, these authors found that depletion of TRPV4 abolished flow-induced increases in intracellular Ca^{2+} [34]. Interestingly, they also found that morpholino-mediated knockdown of PC2, but not TRPV4, was sufficient to induce renal cysts in zebrafish larvae, suggesting that the disruption of renal flow sensing is not sufficient to induce renal cyst formation, and that PC2 may be involved in multiple processes that contribute to PKD pathology. For example, Siroky et al. [71] demonstrated that collecting duct principal cells obtained from the orpk mutant mouse exhibit abnormal PC2 localization and elevated levels of unstimluated apical Ca^{2+} entry. These findings suggest that in addition to being involved in flow sensing, PC2 may have other regulatory functions, such as mediating apical Ca^{2+} entry under tonic pressure [71].

2.2 Endothelial Primary Cilia

The capacity for endothelial cells lining blood vessels to sense fluid shear stresses arising from blood flow has been established, and the physiological role of fluid shear stress as an important regulator of endothelial cell function is well recognized. Abnormal mechanosensation has been implicated in vascular diseases such as hypertension and atherosclerosis [29]. For example, within regions of the vasculature that are susceptible to atherosclerotic plaques, there is a correlation between endothelial cell dysfunction and shear stress level and/or temporal profile [83]. The mechanisms by which endothelial cells transduce shear stresses arising from blood flow have yet to be fully revealed. However, given the role of primary cilia in mediating flow sensation in kidney cells, perhaps it is not surprising that a similar role for cilia has been speculated in endothelial cells.

2.2.1 Endothelial Primary Cilia Formation and Length are Flow Dependent

The presence of primary cilia in the vasculature was established by Bystrevskaya et al. [8] who detected them in adult and embryonic human aortic endothelial cells. Interestingly, unlike renal cilia which are found throughout most of the kidney, the presence of ciliated endothelial cells within the vasculature appears to be more limited (<25%) [58, 78]. In vivo investigations have revealed that the presence or absence of primary cilia is correlated with the level of fluid shear and/or temporal shear profile. For example, in chick embryonic endocardium, the presence of cilia was found to be inversely related to the presence of Kruppel-like factor 2 (KLF2), a marker of high shear stress [77]. Within the aortic arch and common carotid arteries of the adult mouse, primary cilia were found to preferentially distribute to

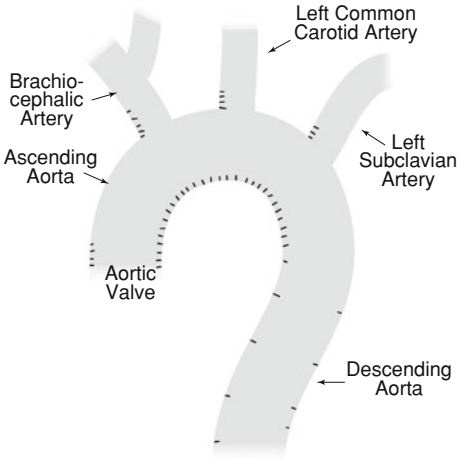

Fig. 5 Schematic demonstrating the distribution of endothelial cilia (represented as *short black line segments*) within the aortic arch. Ciliation occurs in regions of expected low or disturbed flow. Figure adapted from [78]

atherosclerosis-prone regions that are expected to experience disturbed blood flow [78] (Fig. 5). Interestingly, in mice deficient for apolipoprotein-E (which develop atherosclerosis spontaneously), ciliation was also found to frequently occur on or around lesions. Consistent with the notion that endothelial ciliation is responsive to blood flow-induced fluid shear stress, Iomini et al. [30] demonstrated that the primary cilia of cultured human endothelial cells disassembled when exposed to steady fluid flow. There is evidence that the absence of cilia desensitizes endothelial cells to fluid shear [26], suggesting the presence of a negative feed back loop in which cilium-induced bending leads to ciliary disassembly and reduced mechanosensitivity, similar to the mechanism proposed to occur in kidney [5].

2.2.2 A Potential Link Between Endothelial Primary Cilia Mechanosensing and Cardiovascular Defects in Patients with PKD

PKD is associated with the early presentation of hypertension and associated cardiovascular defects [1]. Given the role of PC1 in mediating primary cilia flow sensing in kidney, Nauli et al. [49] investigated whether primary cilia and PC1 may serve a similar role in endothelial mechanotransduction. These authors demonstrated that PC1 colocalized with primary cilia in cultured embryonic aortic endothelial cells, and that cells obtained from mice with disruptions in polaris and PC1 failed to exhibit flow-induced increases in intracellular Ca^{2+} and nitric oxide synthesis. Similar to kidney [59], the mechanosensory function of endothelial primary cilia was specific to flow, as increases in intracellular Ca^{2+} and NO in response to mechanical perturbation of the apical membrane were not abrogated in cells with dysfunctions in polaris or PC1. Interestingly, these authors also found that shear stress induced proteolytic cleavage of PC1, similar to kidney [41], which they speculated could play a role in desensitizing cells to further increases in shear

[49]. More recently, AbouAlaiwi et al. [1] showed that PC2 localizes to endothelial cilia within the mouse femoral artery, and that mouse endothelial cells with disruptions in PC2 fail to exhibit flow-induced increases in NO. These authors also showed that endothelial cells obtained from ADPKD patients lack ciliary PC2 and are insensitive to fluid flow, suggesting that abnormal endothelial mechanosensation of blood flow may underlie vascular defects associated with PKD [1].

2.3 Nodal Cilia

2.3.1 Nodal Cilia are Structurally Related to Primary Cilia

In this section, we shift our focus to the role of ciliary flow sensing during mammalian embryonic development. In particular, we will review the role of cilia in generating and sensing extra-embryonic fluid in cells of the node (a transient triangular indentation that appears on the embryo surface during gastrulation), the physiological role of this fluid generation, and mechanisms involved in flow sensing as they relate to the specification of left–right asymmetry. The solitary cilia on nodal cells are structurally similar to primary cilia in that the axonemes have a 9+0 microtubule arrangement [52]. However, unlike primary cilia, some nodal cilia are motile [52], thus they are often considered a distinct class of cilia in addition to primary cilia and motile cilia.

2.3.2 The Establishment of Left–Right Asymmetry Requires the Generation and Sensation of Flow by Nodal Cilia

Given that left–right defects were observed in humans with immotile cilia syndrome [2, 52] (left–right defects are also found in mouse embryos with immotile or abnormal cilia [43, 47, 80]), Nonaka et al. [52] investigated the role of nodal cilia in establishing left–right asymmetry. These authors found that the movements of nodal cilia consisted of a vortical motion that generated a leftward flow of fluid, referred to as nodal flow, and that embryos with disruption of nodal cilia and nodal flow exhibited left–right randomization. The physiological role of nodal flow in left–right axis determination was clearly demonstrated in subsequent investigations by Nonaka et al. where embryos were loaded in flow chambers and rightward flow applied. They found that superimposition of rightward flow such that the intrinsic leftward flow was reversed resulted in reversal of left–right asymmetry [51].

The importance of nodal cilia in generating nodal flow for proper left–right specification was established in the studies described above; McGrath et al. established a potential mechanism for the sensation of nodal flow soon thereafter. These authors observed that left–right dynein, an axonemal dynein that is required for nodal cilia motility, localizes to a subset of nodal cilia [46], and that in the presence of nodal flow, an asymmetric intracellular calcium signal appeared at the left margin

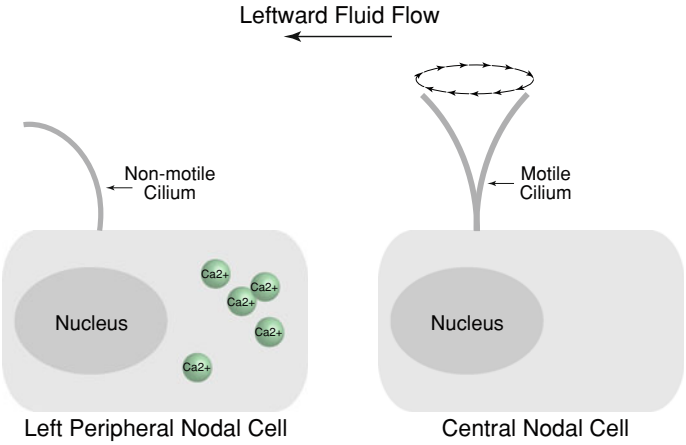

Fig. 6 Two-cilia hypothesis for the generation and sensation of nodal flow. Central nodal cells possess motile cilia and generate leftward nodal flow via vortical ciliary motions. Left peripheral nodal cells possess non-motile cilia and sense flow via ciliary bending and subsequent intracellular Ca^{2+} mobilization

of the node [46]. These observations led these authors to develop the *two-cilia* model where left–right asymmetry is established via a mechanism in which nodal cells expressing left–right dynein and possessing motile cilia generate nodal flow, and cells not expressing left–right dynein and possessing non-motile cilia sense and transduce this flow, resulting in asymmetric intracellular Ca^{2+} signaling (Fig. 6).

Although it is unknown whether the asymmetric signaling resulting from nodal flow is mediated by chemotransport (e.g., sensation of one or more signaling molecules transported to the left side of the node), or mechanical loading (e.g., mechanosensation of fluid shear stress), as noted by Nauli and Zhou [50], there are several reasons to believe that nodal cells transduce nodal flow via a mechanotransduction mechanism involving bending of the cilium and PC2. PC2 is expressed in both motile and non-motile nodal cilia, and McGrath et al. [46] found that embryos lacking functional PC2 failed to exhibit a perinodal Ca^{2+} response. Consistent with a role for PC2 in transducing nodal flow, mice with disruption of Pkd2 exhibit laterality defects [56]. Interestingly however, PC1-deficient mice do not exhibit laterality defects [50], suggesting that if nodal flow is transduced via a mechanism involving ciliary bending and PC2, the mechanism by which this occurs is not identical to that in kidney.

2.4 *Cholangiocyte Primary Cilia Integrate Chemical and Physical Signals*

We now shift our attention to the role of ciliary flow sensing in liver health and disease, with an emphasis on cholangiocytes, epithelial cells that line the lumen of

intrahepatic bile ducts. Cholangiocyte primary cilia extend into the lumen [28] in a manner such that their lengths are proportional with duct diameter [28]. The physiological significance of cholangiocyte primary cilia is still being elucidated, however, there is evidence suggesting that they play a key role in the onset and/or progression of liver disease. For example, polycystic liver disease occurs in combination with PKD [44]. In addition, nephronophthisis and BBS, which also result from mutations in ciliary-associated proteins, are associated with hepatic fibrosis [44].

2.4.1 Integration of Mechanical and Chemical Signals in Cholangiocytes via a Mechanism Involving Primary Cilia, PC1, PC2, cAMP, and AC6

Cholangiocytes are exposed to passive movement of fluid within the bile duct [44]. The physiological function of cholangiocyte cilia in sensing this flow was investigated by Masyuk et al. [45] who found that in perfused intrahepatic bile duct units, luminal flow induced intracellular Ca^{2+} mobilization in a manner that was dependent on primary cilia, PC1, PC2, extracellular Ca^{2+}, and intracellular Ca^{2+} stores, identical to kidney. These authors also investigated whether sensation of fluid flow involved cAMP, which has been implicated as a key signaling molecule in biliary epithelia [45]. When exposed to flow, no alteration in intracellular cAMP levels was detected. However, when cells treated with forskolin, a non-specific cAMP agonist, were exposed to flow, forskolin-stimulated levels of cAMP were significantly reduced in a PC1- and PC2-dependent manner. Interestingly, these authors found that adenylyl cyclase 6 (AC6), a Ca^{2+}-inhibitable isoform of adenylyl cyclase (the enzyme which catalyzes the synthesis of cAMP from ATP) localized to cholangiocyte cilia, and that inhibition of AC6 abrogated flow-induced decreases in cAMP in cholangiocytes treated with forskolin. These observations led these authors to propose a model in which receptor-mediated activation of AC6 is reduced by flow-induced ciliary bending, entry of extracellular Ca^{2+} via PC1/2, and subsequent inhibition of ciliary AC6 by this Ca^{2+} influx [45]. In this model, the cilium functions as a cellular nexus where chemical and mechanical signals are integrated. The capacity for the cilium to function similarly in other flow-sensitive cells (and in particular, in cells which demonstrate synergistic signaling in response to mechanical and chemical signals [73]) is an exciting possibility.

2.5 Bone Cell Primary Cilia

In the cells reviewed thus far, flow sensing via the primary cilium involved intracellular Ca^{2+} mobilization. We now review mechanisms mediating ciliary flow sensing in bone cells, which recent evidence suggests does not involve this response.

2.5.1 Bone Cell Cilia Bend Under Flow and Mediate Flow Sensation Independent of Extracellular Ca^{2+}-Mediated Intracellular Ca^{2+} Release

The capacity for bone to adapt its structure to its mechanical environment has been recognized for over 200 years [84]. When bone is mechanically loaded (such as under habitual loading), pressure gradients are generated that drive interstitial fluid within the lacunar–canalicular system (LCS) [57, 81]. The LCS is fluid-filled network of voids in which osteocytes reside called lacunae that are interconnected to one another via channels called canaliculi [36, 37]. This fluid movement is reversed when the load is removed, resulting in flow that is dynamic in nature [31]. A variety of responses have been documented in cultured bone cells exposed to dynamic fluid flow (see, for example, [38]), one of which is an intracellular Ca^{2+} flux [31] that depends on intact intracellular Ca^{2+} stores [91]. Given that bone cells possess primary cilia [14, 86] and that flow-induced intracellular Ca^{2+} signaling is mediated by primary cilia in kidney, we speculated that primary cilia may have a mechanosensory function in bone.

In our lab, we first sought to determine whether bone cell cilia were physically suited to serve a mechanosensory function by deflecting under flow. Using the flexible substratum technique [66] to view cells in side view, we found that bone cell primary cilia passively bent in response to sub-physiological fluid flow, and recoiled following flow cessation [42] (Fig. 7). In addition, we found that primary cilia mediate the capacity for bone cells to sense and respond to flow, as indicated by the loss of flow-induced transcriptional changes in osteopontin, OPG/RANKL, and COX-2 and release of PGE2 in cells with disrupted cilia [42]. Interestingly however, disruption of bone cell primary cilia did not abrogate flow-induced intracellular Ca^{2+} mobilization, whereas in renal cilia, under identical experimental conditions, this response was significantly reduced [42]. This indicated that primary cilia mediate flow sensing in bone cells independently of extracellular Ca^{2+}-dependent intracellular Ca^{2+} release [42].

2.5.2 Bone Cell Primary Cilia Transduce Flow via AC6 and cAMP

Building on the findings described above, we next investigated whether the primary cilium-dependent responses to flow in bone cells were mediated by a mechanism regulated by modulation of cAMP production rather than intracellular Ca^{2+} release. We found that bone cells exposed to flow exhibited a rapid decrease in intracellular levels of cAMP which was abrogated by cilia inhibition [38]. Interestingly, we also found that AC6, a Ca^{2+}-inhibitable isoform of adenylyl cyclase, preferentially localized to bone cell cilia, similar to cholangiocytes (Fig. 8), and that inhibition of AC6 eliminated flow-induced decreases in cAMP. Inhibiting Gd^{3+}-sensitive channels, but not emptying intracellular Ca^{2+} stores, also abrogated this response. This suggests that bone cell primary cilia may transduce fluid flow via a mechanism involving Ca^{2+} entry through Gd^{3+} sensitive channels

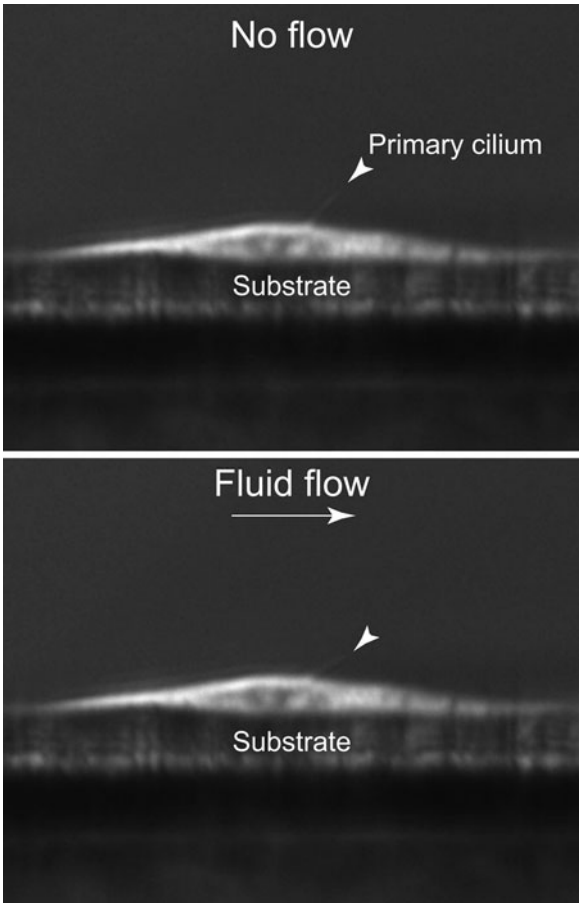

Fig. 7 Bone cells imaged under side view and exposed to a pulse of ~0.03 Pa steady flow. The primary cilium can be seen extending from the apical surface (*arrowhead*) before (*top*) and during (*bottom*) application of fluid flow (from *left* to *right*). For further details regarding experimental methods see [42]

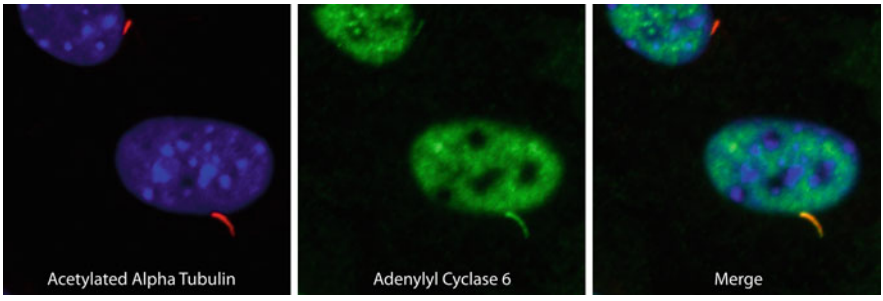

Fig. 8 MLO-Y4 bone cells immunostained for acetylated alpha tubulin (*left*, *red*) and adenylyl cyclase 6 (*middle*, *green*). Adenylyl cyclase six colocalizes with the cilium (*right*, *merge*)

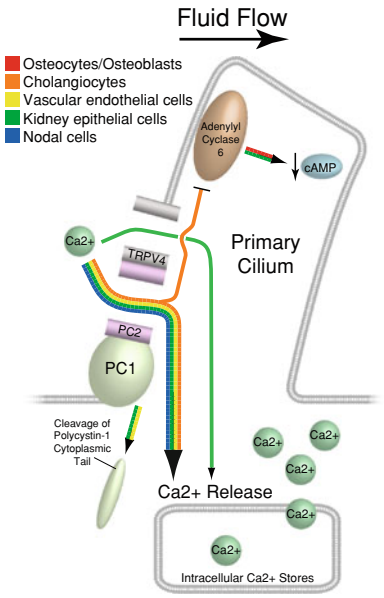

Fig. 9 Summary of proposed ciliary signaling mechanisms in different cell types. In comparing and contrasting these mechanisms, interesting questions arise such as whether ciliary flow sensing in bone involves molecules implicated in other tissues (such as PC1/2 and/or TRPV-4), or whether flow-induced decreases in cAMP occur in kidney cells via a mechanism involving AC6

at the cilium in response to flow-induced bending, Ca^{2+}-mediated inhibition of AC6, and subsequent decreases in intracellular levels of cAMP [38].

The findings described above clearly demonstrate that primary cilia mechanotransduction of fluid flow can involve different combinations of molecular machinery that may be shared among diverse cell types (Fig. 9 gives a schematic summarizing the pathways reviewed thus far). An intriguing question that arises by comparing and contrasting the mechanisms described in this section is whether the Gd^{3+}-sensitive ion channel(s) mediating primary cilia flow sensing in bone include molecules implicated in other tissues, such as PC1/2, which localizes to bone cell primary cilia [85], and/or TRPV-4 [34]. Another interesting question is whether flow-induced decreases in cAMP occur in kidney cells. Indeed, several animal models of PKD exhibit high levels of intracellular cAMP, possibly due to hyperactivity of Ca^{2+}-inhibitable ACs arising from low levels of Ca^{2+} [16, 38].

3 Ciliary Mechanotransduction: Mechanics

The mechanics of the primary cilium dictate how external forces translate into local cellular deformations that ultimately regulate cellular function. For example, as a primary cilium bends under fluid flow, the convex surface of the bent cilium experiences membrane tension, which may act to activate Ca^{2+}-permeable cation channels such as PC2. Despite the potential importance of ciliary mechanics in regulating cellular mechanosensation, little is known of the mechanical properties

and behavior of primary cilia. In this section we discuss efforts to mathematically model the mechanics of the primary cilium. In addition, we explore the structure of the cilium in more detail, with a focus on structural elements that appear to positively contribute to its mechanosensory function.

3.1 Mechanical Models

3.1.1 The Primary Cilium can be Modeled as a Cantilevered Beam

The bending behavior of the primary cilium was first modeled mathematically by Schwartz et al. [70]. These authors modeled the primary cilium under fluid shear as a cylindrical cantilevered beam subjected to a fluid drag force perpendicular to its long axis:

$$\frac{\mathrm{d}^2\varphi}{\mathrm{d}s^2} + k^2 \cos\varphi = 0$$

where s is the distance along the beam, $\varphi(s)$ is the angle of slope of the bent beam at each point s, and k is a constant dependent on a variety of factors such as applied load, and beam material properties, size, and shape. The fluid drag force per unit length (w) was calculated by assuming laminar flow around a cylinder as

$$w = \frac{4\pi\rho v^2 d}{Re[2.002 - 1\mathrm{n}(Re)]}$$

where ρ and v are the density and velocity of the fluid respectively, d is the cilium diameter, and Re is the Reynolds number.

Using the model described above Schwartz et al. accurately predicted the bending profile of kidney epithelial cilia observed experimentally under various physiological flow profiles. In addition, these authors were able to measure the flexural rigidity (EI) of the primary cilium ($3.1 \pm 0.8 \times 10^{-23}$ Nm^2). They found that the flexural rigidity was approximately one order of magnitude less than that of motile cilia, indicating that compared to motile cilia, primary cilia are much less rigid structures. Given that the model, which assumes the cilium has a fixed base, accurately predicted experimentally obtained bending profiles under flow, Schwartz et al. concluded that the cilium is firmly supported at its base.

3.1.2 Primary Cilium Length Regulates Mechanosensitivity

As discussed earlier in this chapter, there is a evidence suggesting the existence of a negative feedback loop in which primary cilia shorten their lengths under flow, resulting in less ciliary deflection and decreased mechanosensitivity [5, 30]. The dependence of ciliary bending on length has been explored using mechanical models. For example, using the cantilevered beam model described above,

Schwartz et al. demonstrated that within a given flow field, longer cilia will experience greater fluid drag and will bend more relative to shorter cilia. The relation between cilium deflection and length was further explored in the model of Liu et al. [40] who modeled flow around an array of primary cilia using a modified Stokes equation with a Darcy term. Interestingly, these authors demonstrated that due to hydrodynamic interactions between cilia, expected increases in fluid velocity and drag force were diminished relative to the case in which these interactions were ignored [40].

3.1.3 The Mechanical Properties of the Ciliary Membrane Dictate Transmittal of Forces Under Different Flow Profiles

Rydholm et al. recently investigated ciliary bending behavior and flow-induced calcium signaling in kidney epithelial cells under different flow profiles. Interestingly, these authors observed a time delay of $\sim$20 s from application of flow to the calcium flux. In addition, they found that high frequency flows did not elicit any calcium response. In order to gain insight into these findings the authors developed a finite element model of the primary cilium [67]. The ciliary axoneme was modeled as a cylindrical elastic beam that was fixed at its base. The axoneme surface consisted of a viscoelastic membrane that was continuous with the cell body plasma membrane. Utilizing this model, Rydholm et al. found that under flow, the stress in the ciliary membrane increased at a much slower rate than that of the axoneme itself. This may explain the lack of response under high frequency flow, since under such a flow profile the stress in the membrane may not reach sufficient levels to activate mechanosensitive channels. In this case, the primary cilium could act as a low pass filter by transferring loads to membrane channels under steady flow but not under flow in which rapid fluctuations in flow rate occur. These authors also observed that near the tip, the bending profile of the cilium observed experimentally differed to that predicted by the model. This suggests that unlike in the model, flexural rigidity may not remain constant along the length of the cilium. This could be due, for example, to increased disorganization of the circumferential arrangement of microtubule doublets towards the tip of the cilium [53, 87].

3.2 Structural Components

3.2.1 The Ciliary Axoneme is Optimally Suited to Resist Bending

In this section, we shift our attention from mathematical modeling of ciliary mechanics to a more in depth examination of ciliary structural components and their contribution to the mechanical properties and behavior of the cilium. The cilium possesses a unique molecular architecture that appears to increase or reinforce its structural integrity and thus facilitate its capacity to serve a

mechanosensory role. For example, we previously saw that the ciliary axoneme consists of a circumferential arrangement of nine doublet microtubules. Each individual doublet consists of one complete tubule containing 13 protofilaments and another adjoining incomplete tubule consisting of 10 protofilaments [13]. Since hollow cylindrical structures maximize bending resistance while minimizing mass, the structure of the individual doublets as well as the circumferential arrangement of the doublets can be both be considered optimal configurations that allow for a stiff structure. Interestingly, the complete tubule of the doublet is elongated in the radial direction of the axoneme which would further enhance ciliary resistance to bending [74]. Non-tubulin protein structures within the axoneme may also contribute to the mechanical integrity of the cilium. For example, Tektin A, B, and C, which share structural features with intermediate filament proteins, form protofilaments that associate with microtubules within the axoneme that my provide mechanical resistance to deformation [39]. In particular, the Tektin protofilaments appear to be ideally positioned to stabilize the partition between the two tubules.

3.2.2 The Ciliary Necklace May Act to Sensitize Membrane Associated Channels at the Base of the Cilium

While much of our attention thus far has been paid to the axoneme, the ciliary membrane may also play a key role in regulating mechanosensitivity. The ciliary membrane is continuous with the plasma membrane of the cell body but there are physiological differences between the two [64]. For example, the ciliary membrane does not precipitate pyroantimonate to the same extent as the cellular membrane, indicating that the ion-binding properties of the two differ [68]. Gilula and Satir [17] observed a unique feature of the ciliary membrane which they termed the ciliary necklace. The ciliary necklace is an intra-membrane structure consisting of a complex of membrane-associated particles located at the base of cilium. The particles are arranged in three strands and in scalloped rows, with each scallop coupled to a microtubule doublet. The physiological function of this structure has yet to be fully elucidated, however it is worth nothing that immunostaining studies have established the presence of ion channels and receptors localized at the base of the cilium [62, 93]. The ciliary necklace may function to increase membrane tension in this region, sensitizing membrane-associated proteins to cilium deflection.

3.2.3 The Base of the Primary Cilium Contains a Number of Stabilizing Structural Elements

As described previously, experimental observations of ciliary deflection in conjunction with mechanical models suggest that the base of the primary cilium is firmly anchored to the cell body. A number of structural elements extend from the basal body that may function to support this anchorage. For example, surrounding the

circumference of the basal body are conical structures known as basal feet, which function as points of attachment to cytoskeletal microtubules and thus allow the cytoskeletal microtubules to stabilize the base of the primary cilium. The number of basal feet is known to differ depending on whether the cilium is motile or non-motile. In motile cilia, only one basal foot is present and is orientated in the direction of motion [7]. In primary cilia, several (1–5) basal feet are present, orientated laterally in all directions. The variable number of basal feet in primary cilia suggests that within individual cells, the number of basal feet is not fixed, and it may be possible for a cell to reorient and possibly add basal feet in response to mechanical stimuli. Altering the number and/or orientation of basal feet could greatly impact the capacity of the cilium to transmit loads to the ciliary base and/or cell body.

Striated rootlets are collections of filamentous structures that radiate from the proximal end of the basal body into the cytoplasm. The exact function of these structures is unknown. However, based on their location, orientation, and structure, it has been hypothesized that similar to basal feet, striated rootlets anchor the basal body/primary cilium complex to the cell by interacting with the cytoskeleton [33]. Interestingly, the occurrence and orientation of striated rootlets depend on whether the cilium is motile or non-motile, similar to basal feet. For example, motile cilia have only one striated rootlet which is aligned in a direction running from the basal body to the nucleus [20]. In contrast, primary cilia have numerous striated rootlets which are orientated in all directions [21]. An intriguing change in the striated rootlets has been observed in post-menopausal women, appearing shortened and aligned perpendicular to the longitudinal axis of the cell [27]. An interesting question is whether these changes occur in other tissues/organs such as bone, and if they do, whether they result in aberrant mechanosensing, which has been implicated in contributing to post-menopausal osteoporosis [32].

3.2.4 Microtubule Acetylation May Affect Ciliary Stiffness

The microtubules of the ciliary axoneme undergo a variety of post-translational modifications such as acetylation [82]. While it is unknown whether acetylation changes the mechanics of microtubules (and hence primary cilia), the presence of microtubule associated proteins (MAPs) has been found to coincide with acetylation. The binding of MAPs to microtubules has been demonstrated to substantially increase their flexural rigidity [15, 75]. This suggests that cells may possess the capacity to reversibly stiffen primary cilia (and thus tune its mechanical sensitivity to its environment) via microtubule acetylation.

4 Conclusions

In recent years, the primary cilium has generated an extraordinary amount interest due to investigations identifying it as a chemo- and mechanosensing organelle that

mediates a remarkably diverse range of developmental processes and post-development disorders. A growing body of evidence indicates that the primary cilium is uniquely suited to serve a mechanosensory role due to its physical structure, its mechanical behavior under flow, and the localization of a number of receptors, channels, and signaling molecules at or near the cilium. The role of ciliary mechanics in regulating cellular mechanosensitivity is almost completely unknown. Future experimental investigations elucidating the mechanical behaviors of the cilium under load, and subsequent mathematical modeling of these behaviors, are critical to better understanding the relationship between ciliary mechanics and cellular mechanotransduction. In addition, future investigations elucidating signaling mechanisms involved in ciliary mechanosensing in a variety of tissues and organs are critical to advancing our understanding of how cellular mechanotransduction occurs. Such investigations may have a broad impact beyond the field of mechanobiology. In particular, given the evidence suggesting that the primary cilium serves as a cellular nexus where mechanical and chemical signals are integrated, and the likelihood that signal transduction at the primary cilium involves common signaling components, such studies would likely provide key insights into ciliary signaling and its role in a broad range of processes.

Acknowledgments This work was supported by a National Institutes of Health NRSA Post-doctoral Fellowship (F32 AR056934 to RYK), an IRCSET-Marie Curie International Mobility Fellowship in Science (to DAH), and a New York State Stem Cell Research Grant (N08G-210 to CRJ).

References

1. AbouAlaiwi, W.A., Takahashi, M., Mell, B.R., Jones, T.J., Ratnam, S., Kolb, R.J., Nauli, S.M.: Ciliary polycystin 2 is a mechanosensitive calcium channel involved in nitric oxide signaling cascades. Cell Biol. **104**(7), 860–869 (2009)
2. Afzelius, B.A.: A human syndrome caused by immotile cilia. Science **193**(4250), 317–319 (1976)
3. Andrews, P.M., Porter, K.R.: A scanning electron microscopic study of the nephron. Am. J. Anat. **140**(1), 81–115 (1974)
4. Barr, M.M., Sternberg, P.W.: A polycystic kidney-disease gene homologue required for male mating behaviour in *C. elegans*. Nature **401**(6751), 386–389 (1999)
5. Besschetnova, T.Y., Kolpakova-Hart, E., Guan, Y., Zhou, J., Olsen, B.R., Shah, J.V.: Identification of signaling pathways regulating primary cilium length and flow-mediated adaptation. Curr. Biol. **20**(2), 182–187 (2010)
6. Bisgrove, B.W., Yost, H.J.: The roles of cilia in developmental disorders and disease. Development **133**(21), 4131–4143 (2006)
7. Boisvieux-Ulrich, E., Sandoz, D.: Determination of ciliary polarity precedes differentiation in the epithelial cells of quail oviduct. Biol. Cell **72**(1–2), 3–14 (1991)
8. Bystrevskaya, V.B., Lichkun, V.V., Antonov, A.S., Perov, A.S.: An ultrastructural study of centriolar complexes in adult and embryonic human aortic endothelial cells. Tissue Cell **20**(4), 493–503 (1988)
9. Cole, D.G., Chinn, S.W., Wedaman, K.P., Hall, K., Vuong, T., Scholey, J.M.: Novel heterotrimeric kinesin-related protein purified from sea urchin eggs. Nature **366**(6452), 268–270 (1993)

10. Davenport, J.R., Yoder, B.K.: An incredible decade for the primary cilium: a look at a once-forgotten organelle. Am. J. Physiol. Renal Physiol. **289**(6), F1159–F1169 (2005)
11. Delmas, P., Nomura, H., Li, X., Lakkis, M., Luo, Y., Segal, Y., Fernández-Fernández, J.M., Harris, P., Frischauf, A.M., Brown, D.A., Zhou, J.: Constitutive activation of G-proteins by polycystin-1 is antagonized by polycystin-2. J. Biol. Chem. **277**(13), 11276–11283 (2002)
12. Donahue, T.L.H., Haut, T.R., Yellowley, C.E., Donahue, H.J., Jacobs, C.R.: Mechanosensitivity of bone cells to oscillating fluid flow induced shear stress may be modulated by chemotransport. J. Biomech. **36**(9), 1363–1371 (2003)
13. Downing, K.H., Sui, H.: Structural insights into microtubule doublet interactions in axonemes. Curr. Opin. Struct. Biol. **17**(2), 253–259 (2007)
14. Federman, M., Nichols, G.: Bone cell cilia: vestigial or functional organelles? Calcif. Tissue Res. **17**(1), 81–85 (1974)
15. Felgner, H., Frank, R., Schliwa, M.: Flexural rigidity of microtubules measured with the use of optical tweezers. J. Cell Sci. **109**(2), 509–516 (1996)
16. Gattone, V.H., Wang, X., Harris, P.C., Torres, V.E.: Inhibition of renal cystic disease development and progression by a vasopressin V2 receptor antagonist. Nat. Med. **9**(10), 1323–1326 (2003)
17. Gilula, N.B., Satir, P.: The ciliary necklace. A ciliary membrane specialization. J. Cell Biol. **53**(2), 494–509 (1972)
18. González-Perrett, S., Kim, K., Ibarra, C., Damiano, A.E., Zotta, E., Batelli, M., Harris, P.C., Reisin, I.L., Arnaout, M.A., Cantiello, H.F.: Polycystin-2, the protein mutated in autosomal dominant polycystic kidney disease (ADPKD), is a Ca^{2+}-permeable nonselective cation channel. Proc. Natl. Acad. Sci. USA **98**(3), 1182–1187 (2001)
19. Gradilone, S.A., Masyuk, A.I., Splinter, P.L., Banales, J.M., Huang, B.Q., Tietz, P.S., Masyuk, T.V., LaRusso, N.F.: Cholangiocyte cilia express TRPV4 and detect changes in luminal tonicity inducing bicarbonate secretion. Proc. Natl. Acad. Sci. USA **104**(48), 19138–19143 (2007)
20. Hagiwara, H., Aoki, T., Ohwada, N., Fujimoto, T.: Development of striated rootlets during ciliogenesis in the human oviduct epithelium. Cell Tissue Res. **290**(1), 39–42 (1997)
21. Hagiwara, H., Harada, S., Maeda, S., Aoki, T., Ohwada, N., Takata, K.: Ultrastructural and immunohistochemical study of the basal apparatus of solitary cilia in the human oviduct epithelium. J. Anat. **200**(1), 89–96 (2002)
22. Hanaoka, K., Qian, F., Boletta, A., Bhunia, A.K., Piontek, K., Tsiokas, L., Sukhatme, V.P., Guggino, W.B., Germino, G.G.: Co-assembly of polycystin-1 and -2 produces unique cation-permeable currents. Nature **408**(6815), 990–994 (2000)
23. Handel, M., Schulz, S., Stanarius, A., Schreff, M., Erdtmann-Vourliotis, M., Schmidt, H., Wolf, G., Hollt, V.: Selective targeting of somatostatin receptor 3 to neuronal cilia. Neuroscience **89**(3), 909–926 (1999)
24. Haycraft, C.J., Swoboda, P., Taulman, P.D., Thomas, J.H., Yoder, B.K.: The *C. elegans* homolog of the murine cystic kidney disease gene tg737 functions in a ciliogenic pathway and is disrupted in osm-5 mutant worms. Development **128**, 1493–1505 (2001)
25. Haycraft, C.J., Zhang, Q., Song, B., Jackson, W.S., Detloff, P.J., Serra, R., Yoder, B.K.: Intraflagellar transport is essential for endochondral bone formation. Development **134**(2), 307–316 (2007)
26. Hierck, B.P., Van der Heiden, K., Alkemade, F.E., Van de Pas, S., Van Thienen, J.V., Groenendijk, B.C.W., Bax, W.H., Van der Laarse, A., DeRuiter, M.C., Horrevoets, A.J.G., Poelmann, R.E.: Primary cilia sensitize endothelial cells for fluid shear stress. Dev. Dyn. **237**(3), 725–735 (2008)
27. Holley, M.C.: The ciliary basal apparatus is adapted to the structure and mechanics of the epithelium. Tissue Cell **16**(2), 287–310 (1984)
28. Huang, B.Q., Masyuk, T.V., Muff, M.A., Tietz, P.S., Masyuk, A.I., LaRusso, N.F.: Isolation and characterization of cholangiocyte primary cilia. Am. J. Physiol. Gastrointest. Liver Physiol. **291**(3), G500–G509 (2006)

29. Ingber, D.E.: Mechanobiology and diseases of mechanotransduction. Ann. Med. **35**(8), 564–577 (2003)
30. Iomini, C., Tejada, K., Mo, W., Vaananen, H., Piperno, G.: Primary cilia of human endothelial cells disassemble under laminar shear stress. J. Cell Biol. **164**(6), 811–817 (2004)
31. Jacobs, C.R., Yellowley, C.E., Davis, B.R., Zhou, Z., Cimbala, J.M., Donahue, H.J.: Differential effect of steady versus oscillating flow on bone cells. J. Biomech. **31**(11), 969–976 (1998)
32. Kelly, P.J., Pocock, N.A., Sambrook, P.N., Eisman, J.A.: Age and menopause-related changes in indices of bone turnover. J. Clin. Endocrinol. Metab. **69**(6), 1160–1165 (1989)
33. Kobayashi, N., Hirokawa, N.: Cytoskeletal architecture and immunocytochemical localization of fodrin in the terminal web of the ciliated epithelial cell. Cell Motil. Cytoskelet. **11**(3), 167–177 (1988)
34. Kottgen, M., Buchholz, B., Garcia-Gonzalez, M.A., Kotsis, F., Fu, X., Doerken, M., Boehlke, C., Steffl, D., Tauber, R., Wegierski, T., Nitschke, R., Suzuki, M., Kramer-Zucker, A., Germino, G.G., Watnick, T., Prenen, J., Nilius, B., Kuehn, E.W., Walz, G.: TRPP2 and TRPV4 form a polymodal sensory channel complex. J. Cell Biol. **182**(3), 437–447 (2008)
35. Kozminski, K.G., Johnson, K.A., Forscher, P., Rosenbaum, J.L.: A motility in the eukaryotic flagellum unrelated to flagellar beating. Proc. Natl. Acad. Sci. USA **90**(12), 5519–5523 (1993)
36. Kwon, R.Y., Frangos, J.A.: Quantification of lacunar-canalicular fluid flow through computational modeling of fluorescence recovery after photobleaching. Cell. Mol. Bioeng. doi:10.1007/s12195-010-0129-8 (2010)
37. Kwon, R.Y., Meays, D.R., Tang, W.J., Frangos, J.A.: Microfluidic enhancement of intramedullary pressure increases interstitial fluid flow and inhibits bone loss in hindlimb suspended mice. J. Bone Miner. Res. doi:10.1002/jbmr.74 (2010)
38. Kwon, R.Y., Temiyasathit, S., Tummala, P., Quah, C.C., Jacobs, C.R.: Primary cilium-dependent mechanosensing is mediated by adenylyl cyclase 6 and cyclic amp in bone cells. FASEB J. **24**(8), 2859–2868 (2010)
39. Linck, R.W., Goggin, M.J., Norrander, J.M., Steffen, W.: Characterization of antibodies as probes for structural and biochemical studies of tektins from ciliary and flagellar microtubules. J. Cell Sci. **88**(4), 453–466 (1987)
40. Liu, W., Xu, S., Woda, C., Kim, P., Weinbaum, S., Satlin, M.: Effect of flow and stretch on the $[Ca^{2+}]$i response of principal and intercalated cells in cortical collecting duct. Am. J. Physiol. Renal Physiol. **285**(5), F998–F1012 (2003)
41. Low, S.H., Vasanth, S., Larson, C.H., Mukherjee, S., Sharma, N., Kinter, M.T., Kane, M.E., Obara, T., Weimbs, T.: Polycystin-1, STAT6, and P100 function in a pathway that transduces ciliary mechanosensation and is activated in polycystic kidney disease. Dev. Cell **10**, 57–69 (2006)
42. Malone, A.M., Anderson, C.T., Tummala, P., Kwon, R.Y., Johnston, T.R., Stearns, T., Jacobs, C.R.: Primary cilia mediate mechanosensing in bone cells by a calcium-independent mechanism. Proc. Natl. Acad. Sci. USA **104**(33), 13325–13330 (2007)
43. Marszalek, J.R., Ruiz-Lozano, P., Roberts, E., Chien, K.R., Goldstein, L.S.: Situs inversus and embryonic ciliary morphogenesis defects in mouse mutants lacking the KIF3A subunit of kinesin-II. Proc. Natl. Acad. Sci. USA **96**(9), 5043–5048 (1999)
44. Masyuk, A.I., Masyuk, T.V., LaRusso, N.F.: Cholangiocyte primary cilia in liver health and disease. Dev. Dyn. **237**(8), 2007–2012 (2008)
45. Masyuk, A.I., Masyuk, T.V., Splinter, P.L., Huang, B.Q., Stroope, A.J., LaRusso, N.F.: Cholangiocyte cilia detect changes in luminal fluid flow and transmit them into intracellular Ca^{2+} and camp signaling. Gastroenterology **131**(3), 911–920 (2006)
46. McGrath, J., Somlo, S., Makova, S., Tian, X., Brueckner, M.: Two populations of node monocilia initiate left–right asymmetry in the mouse. Cell **114**(1), 61–73 (2003)
47. Murcia, N.S., Richards, W.G., Yoder, B.K., Mucenski, M.L., Dunlap, J.R., Woychik, R.P.: The Oak Ridge Polycystic Kidney (orpk) disease gene is required for left–right axis determination. Development **127**(11), 2347–2355 (2000)

48. Nauli, S.M., Alenghat, F.J., Luo, Y., Williams, E., Vassilev, P., Li, X., Elia, A.E., Lu, W., Brown, E.M., Quinn, S.J., Ingber, D.E., Zhou, J.: Polycystins 1 and 2 mediate mechanosensation in the primary cilium of kidney cells. Nat. Genet. **33**(2), 129–137 (2003)
49. Nauli, S.M., Kawanabe, Y., Kaminski, J.J., Pearce, W.J., Ingber, D.E., Zhou, J.: Endothelial cilia are fluid shear sensors that regulate calcium signaling and nitric oxide production through polycystin-1. Circulation **117**(9), 1161–1171 (2008)
50. Nauli, S.M., Zhou, J.: Polycystins and mechanosensation in renal and nodal cilia. Bio Essays **26**(8), 844–856 (2004)
51. Nonaka, S., Shiratori, H., Saijoh, Y., Hamada, H.: Determination of left–right patterning of the mouse embryo by artificial nodal flow. Nature **418**(6893), 96–99 (2002)
52. Nonaka, S., Tanaka, Y., Okada, Y., Takeda, S., Harada, A., Kanai, Y., Kido, M., Hirokawa, N.: Randomization of left–right asymmetry due to loss of nodal cilia generating leftward flow of extraembryonic fluid in mice lacking KIF3B motor protein. Cell **95**(6):829–837 (1998)
53. Odor, D.L., Blandau, R.J.: Observations on the solitary cilium of rabbit oviductal epithelium: its motility and ultrastructure. Am. J. Anat. **174**(4), 437–453 (1985)
54. Pazour, G.J., San Agustin, J.T., Follit, J.A., Rosenbaum, J.L., Witman, G.B.: Polycystin-2 localizes to kidney cilia and the ciliary level is elevated in orpk mutant mice with polycystic kidney disease. Curr. Biol. **12**(11), R378–R380 (2002)
55. Pazour, G.J., Wilkerson, C.G., Witman, G.B.: A dynein light chain is essential for the retrograde particle movement of intraflagellar transport (IFT). J. Cell Biol. **141**(4), 979–992 (1998)
56. Pennekamp, P., Karcher, C., Fischer, A., Schweickert, A., Skryabin, B.: The ion channel polycystin-2 is required for left–right axis determination in mice. Curr. Biol. **12**(11), 938–943 (2002)
57. Piekarski, K., Munro, M.: Transport mechanism operating between blood supply and osteocytes in long bones. Nature **269**(5623), 80–82 (1977)
58. Poelmann, R.E., Van der Heiden, K., Gittenberger-de Groot, A.C., Hierck, B.P.: Deciphering the endothelial shear stress sensor. Circulation **117**(9), 1124–1126 (2008)
59. Praetorius, H.A., Spring, K.R.: Bending the MDCK cell primary cilium increases intracellular calcium. J. Membr. Biol. **184**(1), 71–79 (2001)
60. Praetorius, H.A., Spring, K.R.: Removal of the MDCK cell primary cilium abolishes flow sensing. J. Membr. Biol. **191**(1), 69–76 (2003)
61. Praetorius, H.A., Spring, K.R.: A physiological view of the primary cilium. Annu. Rev. Physiol. **67**, 515–529 (2005)
62. Quarmby, L.: Ciliary ion channels: location, location, location. Curr. Biol. **19**(4), R158–R160 (2009)
63. Rohatgi, R., Milenkovic, L., Scott, M.P.: Patched1 regulates hedgehog signaling at the primary cilium. Science **317**(5836), 372–376 (2007)
64. Rohatgi, R., Snell, W.J.: The ciliary membrane. Curr. Opin. Cell Biol. **22**(4), 541–546 (2010)
65. Rosenbaum, J.L., Witman, G.B.: Intraflagellar transport. Nat. Rev. Mol. Cell Biol. **3**(11), 813–825 (2002)
66. Roth, K.E., Rieder, C.L., Bowser, S.S.: Flexible substratum technique for viewing cells from the side: some in vivo properties of primary (9+0) cilia in cultured kidney epithelia. J. Cell Sci. **89**(Pt. 4), 457–466 (1988)
67. Rydholm, S., Zwartz, G., Kowalewski, J.M., Kamali-Zare, P., Frisk, T., Brismar, H.: Mechanical properties of primary cilia regulate the response to fluid flow. Am. J. Physiol. Renal Physiol. **298**(5), 1096–1102 (2010)
68. Satir, P., Gilula, N.B.: The cell junction in a lamellibranch gill ciliated epithelium: localization of pyroantimonate precipitate. J. Cell Biol. **47**(2), 468–487 (1970)
69. Schneider, L., Clement, C.A., Teilmann, S.C., Pazour, G.J., Hoffmann, E.K., Satir, P., Christensen, S.T.: PDGFR-alpha-alpha signaling is regulated through the primary cilium in fibroblasts Curr. Biol. **15**(20), 1861–1866 (2005)
70. Schwartz, E.A., Leonard, M.L., Bizios, R., Bowser, S.S.: Analysis and modeling of the primary cilium bending response to fluid shear. Am. J. Physiol. Renal Physiol. **272**(41), F132–F138 (1997)

71. Siroky, B.J., Ferguson, W.B., Fuson, A.L., Xie, Y., Fintha, A., Komlosi, P., Yoder, B.K., Schwiebert, E.M., Guay-Woodford, L.M., Bell, P.D.: Loss of primary cilia results in deregulated and unabated apical calcium entry in ARPKD collecting duct cells. Am. J. Physiol. Renal Physiol. **290**(6), F1320–F1328 (2006)
72. Stayner, C., Zhou, J.: Polycystin channels and kidney disease. Trends Pharmacol. Sci. **22**(11), 543–546 (2001)
73. Sugiyama, T., Saxon, L.K., Zaman, G., Moustafa, A., Sunters, A., Price, J.S., Lanyon, L.E.: Mechanical loading enhances the anabolic effects of intermittent parathyroid hormone (1–34) on trabecular and cortical bone in mice. Bone **43**(2), 238–248 (2008)
74. Sui, H., Downing, K.H.: Molecular architecture of axonemal microtubule doublets revealed by cryo-electron tomography. Nature **442**(7101), 475–478 (2006)
75. Takemura, R., Okabe, S., Umeyama, T., Kanai, Y., Cowan, N.J., Hirokawa, N.: Increased microtubule stability and alpha tubulin acetylation in cells transfected with microtubule-associated proteins. J. Cell Sci. **103**(4), 953–964 (1992)
76. Taulman, P.D., Haycraft, C.J., Balkovetz, D.F., Yoder, B.K.: Polaris, a protein involved in left–right axis patterning, localizes to basal bodies and cilia. Mol. Biol. Cell **12**(3), 589–599 (2001)
77. Van der Heiden, K., Groenendijk, BCW., Hierck, B.P., Hogers, B., Koerten, H.K., Mommaas, A.M., Gittenberger-de Groot, A.C., Poelmann, R.E.: Monocilia on chicken embryonic endocardium in low shear stress areas. Dev. Dyn. **235**(1), 19–28 (2006)
78. Van der Heiden, K., Hierck, B.P., Krams, R., de Crom, R., Cheng, C., Baiker, M., Pourquie, M.J.B.M., Alkemade, F.E., DeRuiter, M.C., Gittenberger-de Groot, A.C., Poelmann, R.E.: Endothelial primary cilia in areas of disturbed flow are at the base of atherosclerosis. Atherosclerosis **196**(2), 542–550 (2008)
79. Vassilev, P.M., Guo, L., Chen, X.Z., Segal, Y., Peng, J.B., Basora, N., Babakhanlou, H., Cruger, G., Kanazirska, M., Ye, C., Brown, E.M., Hediger, M.A., J., Z.: Polycystin-2 is a novel cation channel implicated in defective intracellular Ca(2+) homeostasis in polycystic kidney disease. Biochem. Biophys. Res. Commun. **282**(1), 341–350 (2001)
80. Watanabe, D., Saijoh, Y., Nonaka, S., Sasaki, G., Ikawa, Y., Yokoyama, T., Hamada, H.: The left–right determinant inversin is a component of node monocilia and other 9+0 cilia. Development **130**(9), 1725–1734 (2003)
81. Weinbaum, S., Cowin, S.C., Zeng, Y.: A model for the excitation of osteocytes by mechanical loading-induced bone fluid shear stresses. J. Biomech. **27**(3), 339–360 (1994)
82. Westermann, S., Weber, K.: Post-translational modifications regulate microtubule function. Nat. Rev. Mol. Cell Biol. **4**(12), 938–947 (2003)
83. White, C.R., Frangos, J.A.: The shear stress of it all: The cell membrane and mechanochemical transduction. Philos. Trans. R. Soc. Lond. B. Biol. Sci. **362**(1484), 1459–1467 (2007)
84. Wolff, J.: Das gesetz der transformation der knocken. Berlin (1892)
85. Xiao, Z., Zhang, S., Magenheimer, B.S., Luo, J., Quarles, D.: Polycystin-1 regulates skeletogenesis through stimulation of the osteoblast-specific transcription factor runx2-ii. J. Biol. Chem. **283**(18), 12624–12634 (2008)
86. Xiao, Z., Zhang, S., Mahlios, J., Zhou, G., Magenheimer, B.S., Guo, D., Dallas, S.L., Maser, R., Calvet, J.P., Bonewald, L., Quarles, L.D.: Cilia-like structures and polycystin-1 in osteoblasts/osteocytes and associated abnormalities in skeletogenesis and runx2 expression. J. Biol. Chem. **281**(41), 30884–30895 (2006)
87. Yamamoto, M., Kataoka, K.: Electron microscopic observation of the primary cilium in the pancreatic islets. Arch. Histol. Jap. **49**(4), 449–457 (1986)
88. Yoder, B.K.: Role of primary cilia in the pathogenesis of polycystic kidney disease. J. Am. Soc. Nephrol. **18**(5), 1381–1388 (2007)
89. Yoder, B.K., Hou, X., Guay-Woodford, L.M.: 2002) The polycystic kidney disease proteins, polycystin-1 and polycystin-2, polaris, and cystin, are co-localized in renal cilia. J. Am. Soc. Nephrol. **13**(10), 2508–2516.

90. Yoder, B.K., Tousson, A., Millican, L., Wu, J.H., Bugg, C.E., Schafer, J.A., Balkovetz, D.F.: Polaris, a protein disrupted in orpk mutant mice, is required for assembly of renal cilium. Am. J. Physiol. Renal Physiol. **282**(3), F541–F552
91. You, J., Reilly, G.C., Zhen, X., Yellowley, C.E., Chen, Q., Donahue, H.J., Jacobs, C.R.: Osteopontin gene regulation by oscillatory fluid flow via intracellular calcium mobilization and activation of mitogen-activated protein kinase in MC3T3-E1 osteoblasts. J. Biol. Chem. **276**(16), 13365–13371 (2001)
92. Zeng, Y., Cowin, S.C., Weinbaum, S.: A fiber-matrix model for fluid-flow and streaming potentials in the canaliculi of an osteon. Ann. Biomed. Eng. **22**(3), 280–292 (1994)
93. Zhang, M.Z., Mai, W., Li, C., Cho, S.Y., Hao, C., Moeckel, G., Zhao, R., Kim, I., Wang, J., Xiong, H., Wang, H., Sato, Y., Wu, Y., Nakanuma, Y., Lilova, M., Pei, Y., Harris, R.C., Li, S., Coffey, R.J., Sun, L., Wu, D., Chen, X.Z., Breyer, M.D., Zhao, Z.J., McKanna, J.A., Wu, G.: PKHD1 protein encoded by the gene for autosomal recessive polycystic kidney disease associates with basal bodies and primary cilia in renal epithelial cells. Proc. Natl. Acad. Sci. USA **101**(8), 2311–2316 (2004)

Mechanical Response of Living Cells to Contacting Shear Forces

Alison C. Dunn, W. Gregory Sawyer, Malisa Sarntinoranont and Roger Tran-Son-Tay

Abstract Cells adjacent to implanted devices often experience stress in the form of shearing forces from relative motion with those devices. Cell response to contacting shear, specifically in the reorganization of the cytoskeletal actin fibrils, is not yet fully understood. Many techniques such as atomic force microscopy and micro-pipette aspiration are currently used to deform or stress cells in a controlled way. Assessments are typically measured changes in mechanical, fluid, or biochemical properties. Novel micro-friction measurements between a living cell monolayer and a hydrogel material with fluorescence microscopy analysis provide insight into the mechanotransduction of stresses, actin fibril densification in the contacted zone, and the time scales involved in the cellular stiffening response. This type of measurement is sensitive enough to cause an *in situ* response without killing the cells, and could be used to understand more about the nature of cellular response to applied stresses and wound healing.

1 Introduction

Since the first doctors treated the human body, they have recognized the fragility and sensitivity of cells and tissues, both in their destruction and in active healing.

A. C. Dunn, W. Gregory Sawyer, M. Sarntinoranont and R. Tran-Son-Tay (✉)
Department of Mechanical and Aerospace Engineering, University of Florida, Gainesville, FL 32611, USA
e-mail: rtst@ufl.edu

A. C. Dunn
e-mail: alisn@ufl.edu

M. Sarntinoranont and R. Tran-Son-Tay
J. Crayton Pruitt Family Department of Biomedical Engineering, University of Florida, Gainesville, FL 32611, USA

Stud Mechanobiol Tissue Eng Biomater (2011) 4: 125–141
DOI: 10.1007/8415_2010_23

Published Online: 9 November 2010

Cells actively respond to applied stresses of many types, whether chemical, physical, environmental, etc. This is particularly true of implanted prosthetic devices, which either support or replace biological organs. Often, the implantation of these devices causes a disruption in the local environment, whether damaged cells, re-routed circulatory system flows, or load support changes. Even now, no implant is guaranteed against rejection.

Cells respond to these newly implanted devices in a variety of ways: immune response, revascularization, and survival mechanisms of the adjacent cells. How do the cells sustain themselves against an applied force? How can the response be quantified and correlated to immune response or survival mechanisms? This paper will briefly review methods used to apply contacting forces to cells in order to characterize the mechanical properties, and then focus on micro-friction measurements with fluorescent microscopy analysis in order to quantify the shear response by actin filament reorganization in the cytoskeleton of corneal epithelial cells [1] (Fig. 1). Using a hydrogel counterface provides contemporary relevance because of the increasingly common use of hydrogel materials in medical devices. The example data provided here is the friction coefficient and cellular response from the relative motion between a silicone-based hydrogel contact lens and a monolayer of cells. Methods of applying forces to surfaces has been artfully reviewed by others in the past, with the exception of contacting applied shear stresses [2, 3]. Surface properties such as friction, adhesion, and limited mechanical response have been measured with macro-friction instruments and atomic force microscopy (AFM). Bulk properties like viscosity and complex modulus (elastic and loss) are measured with rheological techniques or single-cell methods like micro-pipette aspiration. Indirect shear stresses have been provided in fluid flow instruments. Physiological stresses by controlled tension and compression of the substrate, micro-bead tracking, or magnetic or laser trapping provide specialized information regarding the response of organelles or the cytoplasm. Micro-friction measurements are uniquely suited to stress living cells and produce a physiological response because the cells are not isolated, sacrificial,

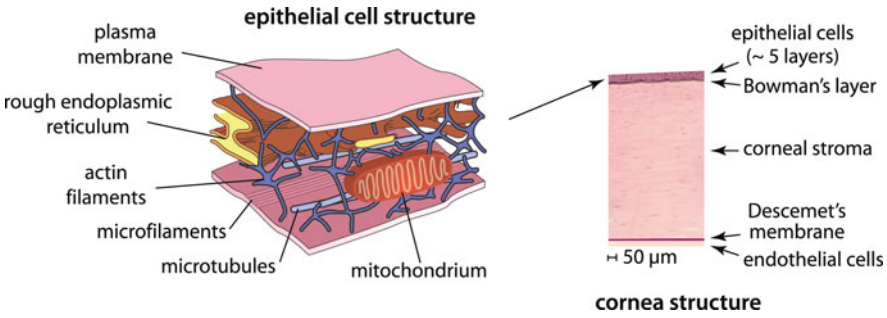

Fig. 1 Schematic of the structure of an epithelial cells (*left*) including the structural elements such as the actin filaments (*blue*), microfilaments (*light blue*), and microtubules (lining the bottom plasma membrane). The location of epithelial cells in the multilayered corneal structure (*right*)

or disguised among other types of cells in a bulk tissue. This review distinguishes micro-friction measurements among the types mentioned above, but is limited to quantitative friction measurements and the qualitative analysis of cytoskeletal actin densification in the peripheral regions to the friction track.

The difficulties presented by the above techniques are dictated by the fragility of living cells and the tight ranges of applied load and speed which have a measurable effect without causing traumatic cell necrosis. Macro-scale instruments tend to be overly destructive while nano-scale forces do not elicit a detectable spectroscopic change in the cytoskeletal actin density.

Mechanotransduction of information and specifically forces is not yet fully understood, but could be aided by controlled application of shearing forces in the form of micro-friction experiments. From this, the forces can be correlated to pressure and elastic mechanical properties such as elastic modulus, shear modulus, and Poisson ratio. Also, the time response of transduction between cells and actin filament reorganization could follow from this work.

2 Overview of Contacting Force Measurements on Biological Samples

2.1 Macro-tribology

Shear forces have been applied to biological entities from cells to tissues in order to assess properties related to mechanics, surface science, lubrication, and chemical changes. The first friction tests on biological materials were designed to mimic classical friction tests on engineering materials (steel, ceramic), which are carried out at high loads and speeds not typically seen in biological situations. The traditional setup for a friction tests is four steel balls rotating on a flat plate [4]. Forces are measured with strain gauges, or more recently by multiaxial load cells [5]. The friction coefficient μ is defined as the frictional force F_f divided by the normal applied force, F_n as shown in Eq. 1. Motion is provided by a motor-driven stage geared to produce a rotary, linear reciprocating, or other motion path. The results of such a test are reliable at fairly high loads and with known force application materials (steel, in this case).

$$\mu = \frac{F_f}{F_n}. \tag{1}$$

However, this setup is too aggressive to meet the requirements of low load applications and measurements. Thus, tribometer designs have evolved to more closely mimic *in vivo* loading conditions of bone, tissue, or cellular surfaces.

The first modification to the standard tribometer design was to change the materials. Soft fixed tissues with a particular surface of interest have been glued to the ball or pin with cyanoacrylate [6]. This is fairly common for crude soft tissue

testing, but it becomes hard to justify when more sensitive techniques are both necessary and available. Chemical changes and substrate mechanics, for example, can be hard to distinguish from the voltage noise floor of such an instrument. Even more, the sample may experience unintended shear forces on the non-glued surface, as only the back side is fixed by the glue. This method is limited to fixed tissues. The water content of these porous tissues is variable and tunable depending on the method of fixation and subsequent treatments, such that measured friction coefficients could be tunable as well [7].

The second modification that experimentalists often make is to tailor the tribometer geometry to the application for which they need to quantify the friction response. For example, friction of catheters has been quantified by a mechanism which runs the catheter between rollers; normal load is applied by tensioning the catheter tube between the rollers, and friction force is determined by load cells attached to the rollers [8]. This method may be sensitive enough to differentiate the types of materials used in catheters, but for testing of surface modifications, water-based applied lubricants, the noise levels of the measured signal from the load cell may overwhelm the frictional differences.

In these modified friction testing setups, the temperature and hydration at the point of contact are difficult to match to biological conditions [9]. In more sensitive instruments, sample hydration can be achieved through the use of submersion baths, dosing of lubricant at known intervals, and an uptake and diffusion scheme, all coupled with an environment chamber and temperature control (humidity as regulated by temperature).

When these instruments are started in motion, measurement handling is of critical importance. For example, it is possible that the steady-state friction coefficients of a certain type of tissue sample do not differ, but the transient response between the static friction point and the steady-state friction coefficient exhibits a rate-dependent change [10]. The three modes of lubrication as defined by the Stribeck curve [11] are boundary lubrication, hydrodynamic lubrication, and a mixed regime of the two. Boundary lubrication is typically characterized by slow sliding speeds, low lubricant viscosity, and high applied loads. The lubricant is located between the two surfaces, but not necessarily between all asperity contacts. Hydrodynamic lubrication is characterized by a separation between the surfaces due to increased lubricant viscosity, higher sliding speeds, and lower applied loads. Confusion of the types of friction and lubrication phases (boundary, mixed, and hydrodynamic) can lead to incorrectly designed experiments and inappropriate interpretation of results.

2.2 Shear Flow and Rheological Techniques

Prokaryotic cells can exist as both anchorage-dependent cells such as corneal epithelial cells, and suspended cells such as white blood cells. Shear flow techniques are abundant and versatile in the ability to apply a known shear stress to a

monolayer of cultured cells on a particular substrate, and to analyze a response. Dangaria and colleagues [12] found that cells can respond to such a shear flow in as little as 30 s. Dr. Chien [13] gives a compact overview of laminar and pulsatile flows used to apply shear stress.

Rheological techniques can be used to assess the mechanical properties of suspended cells and other biological components. The most popular technique for measuring the mechanical properties of a single blood cell is the micropipette technique [14, 15] which is widely used in the study of mammalian cells. This manipulation technique has been used for studying liquid drops, cells, and aggregates, as well as to investigate the effects of diseases and treatments [16, 17]. Two typical types of experiment, aspiration and recovery, are usually performed to determine the mechanical properties of individual cells. For example, passive leukocytes (white blood cells) are aspirated at a constant pressure into a micropipette. The length of the aspirated cell is measured over time to generate an aspiration curve. Assuming that cells behave as liquid drops, the viscosity values can be derived from the slope of the aspiration curves [18]. As for recovery, white blood cells are drawn by a small suction pressure into a micropipette, held, and quickly expelled out. Again, assuming that cells behave as liquid drops, the changing length of the cell as it recovers its spherical shape is recorded as a function of time, t, and is described by a polynomial [19]. Rheology can also be a more general term applied to the study of viscoelasticity in the cytoskeleton while the cells are subject to an external fluid shear flow [20].

To allow direct observation of suspended cells during shear stress application, a modified cone-plate viscometer, called a rheoscope, has been developed in which the cone and plate counter-rotate. The advantage of the rheoscope is that both suspended and anchorage dependent cells can be observed and studied under flow [21–23]. A particle midway between the cone and plate is subjected to a well defined shear stress field and remains nearly stationary in the laboratory frame of reference so that it can be studied without the help of high speed cinematography.

2.3 Atomic Force Microscopy (AFM)

Measuring forces by the displacement of a flexure of known stiffness is one of the best ways to get high precision and resolution on the micro- and nano-scale. This is the method used by the AFM which measures forces between a sharp silicon probing tip attached to a cantilever spring and a sample surface. Topographical images are obtained by probing the sample with a tip in tapping or scanning modes, and measuring the deflection of the cantilever. Typically, the deflection is measured using a laser spot reflected from the top of the cantilever onto an array of photodiodes. Probe spring constants range 0.001–100 N/m, and displacements from microns down to $\sim$0.1 Å are measured by the deflection array. Typical forces between the probe tip and the sample range from 10^{-11} up to 10^{-6} N.

It is presently one of the prime tools for imaging, measuring and manipulating matter at the nanoscale.

Valuable results of the evolution of cellular structures have been done using AFM, as well as adhesion probing [24–26]. Some groups have attached a single cell to the tip of the probe and suspended specific proteins down to the surface in order to measure the binding properties [27]. This method can provide complex shear modulus $G^*(\omega)$ of single cells by applying oscillatory indentations to the cell with a microtip attached to a cantilever flexure of known stiffness and then measuring the resulting force [28]. A popular technique used in the estimation of the rheological properties of cells with AFM and rheometers is the dynamic (oscillatory) testing method. These testing methods can provide information not only on the cell plasma membrane but also on the intracellular contents. The dynamic testing method consists of imposing an applied force on a marker (cell or body) and measuring its displacement, or vice versa. The force/indentation relationship is a characterization of the cell (cellular component) properties. These methods are usually done under small oscillatory deformations so that the simpler linear viscoelastic theory can be applied [29]. This technique stems from foundational studies of the effect of pressure on cell membranes [30, 31].

Another dynamic technique similar to AFM and micro-tribology is the 'cell poking' technique [32, 33]. It measures the force required to indent the surface of a cell, or the relaxation time of the cell membrane after perturbation by the glass stylus (indenter). It provides similar information about both the mechanical properties of adherent cells and the internal cytoskeleton based on a linear viscoelasticity theory.

Errors in these methods are typically introduced by tolerances of the AFM flexure beam(s). A single beam flexure made of silicon can rotate as well as translate in two axes. The measured deflection should be carefully resolved in order to get accurate force values and understand their meaning.

2.4 Substrate Strain and Other Techniques

While AFM is typically a single-cell technique, bulk deformation of a single cell or layer of cells by other techniques can probe the internal reorganization of cellular components and average properties of the cellular layer. Shear stress is in fact necessary for homeostasis of bearing tissues [34], and specifically for fibroblasts to develop properly [35]. However, guided cell motion along prescribed nano-etched tracks in the substrate may be dominated by cell–cell interactions rather than adherence to the substrate by individual cells at a given time [36]. Sniadecki et al. [37] have used magnetic posts to deform the substrate of a layer of cells in order to compare the sensitivity of mouse fibroblasts to external forces and the subsequent traction response by the cells themselves. Moving from measurements on the cell surface to those inside, magnetic or laser trapping of intercellular particles (cytometry) is emerging as a versatile technique [38–40].

2.5 Custom Micro-tribology

Many of the techniques above operate on isolated cells or fixed tissues that retain some of their mechanical properties; this cannot illustrate the active response of a confluent layer of cells adhered to each other and to a substrate. Due to the fragile nature of cells, they must be stressed in such a manner that they do not die immediately, become completely rigid, or undergo apoptosis. Most traditional force applications do not work in this situation because the forces must be on the order of 0.5 mN or lower, depending on the cell substrate and degree of adhesion.

Custom micro-tribometry is a highly appropriate way to probe the response of cells to a mechanical applied force (both normally loaded and shear). The probe can be chosen to contact as few as tens of cells up to hundreds, and then can be assessed by a variety of optical techniques, and even by more sensitive techniques such as AFM. Due to the custom nature of the contact zone, this technique can be applied to small tissues samples, cell multi-layers, or confluent single layers of cells. Comparisons between fixed samples, added solutions, treatments, etc., are easily achieved.

These cantilevered flexures along with the accompanying instrumentation have been described in detail as related to biotribology, gas surface interactions of hard coating's and carbon nanotube film properties by a number of authors [41–46].

3 Micro-tribology on Living Cells

3.1 Capabilities and Motivation

Micro-friction studies are suited to applications requiring controlled application and measurement of small forces, but this technique has been used extensively to understand the surface force interactions on soft hydrogel polymers [43, 47]. Aqueous test conditions, adhesion, and meniscus effects on the measurement probe all contribute to the complex nature of the experiments, and must be quantified and subtracted as necessary. For example, the force of the meniscus pulling the probe tip toward the sample should not be an addition to the prescribed force; the measured force while the pin is submerged (but not yet in contact with the sample) can be subtracted.

Epithelial cells are of particular interest due to their functionality and quantity; the epithelium is one of four primary body tissues, and its functions include secretion, absorption, protection, sensation detection, and selective permeability. The response of these cells to mechanical stimuli has been investigated in a variety of ways including cultured substrate stretch and *in vivo* animal studies. There is a stiffening of human alveolar epithelial cells when strained in an equibiaxial fashion as reported by Trepat et al. [48]. In addition, the application of mechanical pressure to oral epithelia of rats with orthodontic elastic bands causes the cells to

proliferate more slowly, possibly a mechanism to ensure survival under adverse conditions [49]. Though the epithelium of human corneas is designed to thrive under a variety of environmental changes, these cells can be abraded away in response to contact lens design and materials, as well as tear fluid and immune response. The data reported provide insight as to how biological surfaces (cell layers) react to direct contact and sliding against contact lens hydrogel materials. This differs from prior proof-of-concept experiments carried out by Dunn et al. [42] with endothelial cells that were tested against glass pins in that the contacting counter-material is compliant and hydrated. Under similar loads the contact pressures should be substantially lower, but may not be as low as the forecasted pressures during blinking.

For this later study, human corneal epithelial cells were cultured in Dulbecco's Modified Eagle's Medium and Ham's F12 media (DMEM/F12). The cells were subcultured within special holders for approximately 24 h so that 100% confluency was reached before friction testing was performed. The cultured cell density as measured optically was 2,750 cells/mm^2.

Cell holders were constructed using a polydimethylsiloxane ring fitted onto a cover glass of diameter $D = 25$ mm, which provided a small bath of $\sim$2 mL growth media on top of the cell layer during the culture period and lubrication during frictional testing. Detailed information on the construction of the cell holders and methods for culturing cells in the holders can be found in Cobb et al. [41].

Before and after testing, cells were submerged in 10% trypan blue for 1 min and then observed under a 10$\times$ objective in a Leica DMLM microscope using the DIC/Nomarski mode. Damage is assessed immediately before testing and after testing to assure that only cells affected by friction tests are included in the analysis. The hydrogel pins were assessed before and after testing at 20$\times$ to assure that no ripping or bunching of the lens material occurred during setup or transit. A pristine lens has small surface features that range from 0 to 5 μm in size. Photo analysis software was used to quantify confluent cell density, amount of cell necrosis (number of cells), and areas where cells detached.

3.2 Mechanical Design for Small Force Application and Measurement

The small forces required for meaningful application to cells must be applied and measured in the relevant scale. This is best done with a flexure of known geometry and motion measured by high-resolution optical sensors.

Currently, the most appropriate way to apply small direct forces to such a layer is with a thin-beam dual cantilevered flexure. As the flexure displaces, the distance change is measured with a high-resolution optical probe. This is then correlated to a force through the calibrated stiffness of the cantilevered flexure. AFM probe tips operate in this way, but without the advantage of displacement limited to the

vertical and horizontal directions. AFM tips can rotate and change the precise location of contact on the pin tip, whereas the nature of the dual cantilevered flexure limits the rotation without adding undue resistance. The size of pin on the microtribometer is an order of magnitude larger than a typical AFM tip, but the most appropriate scale over which to measure collective cellular response is precisely that size. As of now, these dual cantilevered flexures can resolve displacements down to <1 μm. Spread over a wide area of contact, pressures applied can reach an order of magnitude lower than reported values for pressure applied by eyelids during blinking [50].

The compliant and hydrated nature of soft contact lenses does not allow them to be clamped in traditional fixation devices or glued with cyanoacrylate. Thus, the hydrogel must be lightly clamped on the perimeter of the area of interest; this prevents wrinkling while holding the area still. The flexure assembly and the pin holder for the hydrogels are shown in Fig. 2. The applied normal loads and sliding cycles were varied from either 500 μN or 2 mN and 2–20 cycles, respectively. The experimental apparatus used to run these friction tests was the customized microtribometer previously described. It was modified to achieve submerged sample capability, lower applied normal loads (100 μN to 1 N), and straightforward data acquisition and processing.

Kinetic coefficients of friction were calculated, as in more classical friction measurements, as the ratio of F_t to F_n. Normal force feedback was achieved by adjusting a vertical piezoelectric cell according to the difference between the desired average normal load and the average normal load from the previous sliding

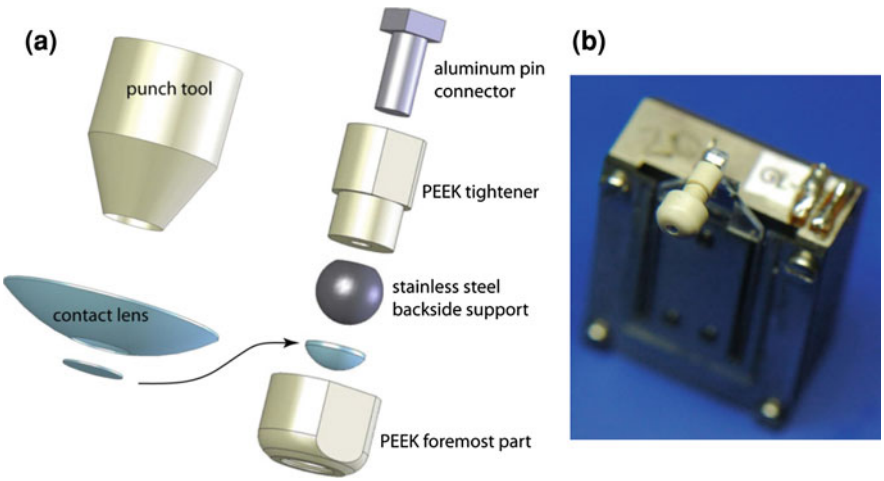

Fig. 2 A Schematic (**a**) and photograph (**b**) of the pin holder designed to hold a thin circular section of hydrogel material. Samples are taken from the central region of commercially available contact lenses. The sample holder is mounted onto a calibrated glass flexure that is used to make lateral and normal force measurements

cycle. The sliding for these reciprocating friction tests were provided by a precision piezo-driven stage with maximum displacement of 600 μm. For a silicone-based hydrogel sliding against a confluent layer of HCE-T cells, the friction coefficient started at $\mu = 0.03$ and rose to a value of $\mu = 0.05$ (Fig. 3).

Although nanoindenters such as that made by Hysitron can apply and measure these kind of high-resolution light forces, the type of pin and cost of standoffs tips make it ill-suited to samples submerged in fluid baths.

3.3 Discussion and Applications

Previously it was reported that there exists a threshold normal load of about 0.7 mN above which the endothelial cells would detach [42], presumably, due to the friction forces across the top interface. One of the challenges with this work was the difficulty in maintaining low contact pressures on the cell layer; this motivated the use of a compliant hydrogel pin as the countersurface to the cell layer. Previous work modeling hydrogels in tribology has used a viscous damped elastic foundation [43] that was necessary due to the cyclic deformation of a

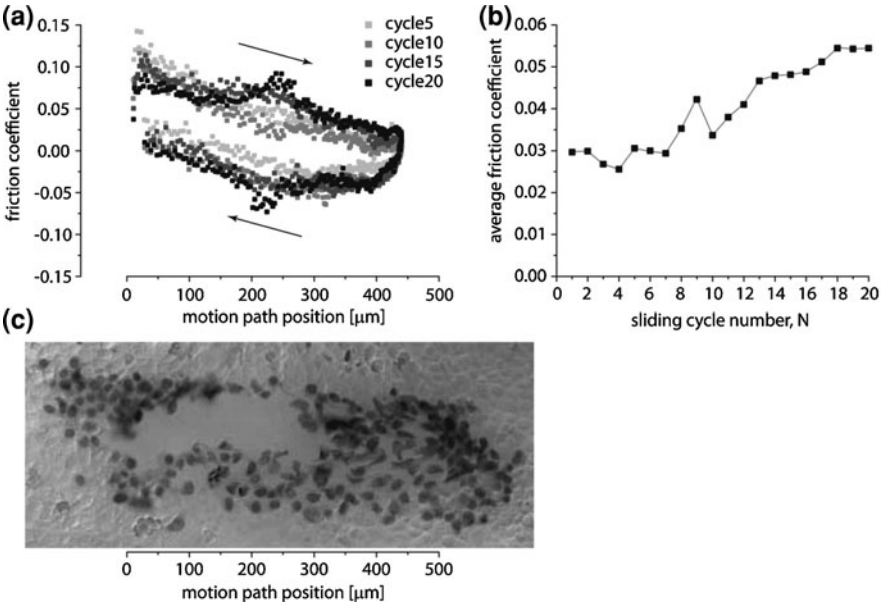

Fig. 3 **a** Friction loops for cycles 5, 10, 15, and 20 of a silicone-based hydrogel running on a layer of human corneal epithelial cells (HCE-T) under a normal load of 500 μN. **b** Average values of friction coefficient over the 20 cycles shows a monotonic increase presumably correlated with a monotonic increase in cell damage **c** A post-test micrograph reveals gross cell damage in the center of the wear track and cell death throughout

hydrogel foundation. Here the hydrogel pin is statically compressed, and a relatively simple elastic foundation solution to the maximum pressure (P_{max}), the average pressure (P_0), and the contact half width (a) are given in the following equations. The radius of the hydrogel pin (R) is assumed to conform to the stainless steel back support, and the thickness of the hydrogel (t) is on the order of 100 μm. Any additional compliance from the cell layer is neglected in this analysis, thus the expectation is that the computed pressures represent and upper bound and the computed areas a lower. The equation for the pressure distribution of the elastic foundation is given by Eq. 2, where the effective elastic modulus (E') is given by Eq. 3, and the symbol δ represents the local deformation.

$$P = \frac{E}{(1-\nu^2)}\frac{\delta}{t} \tag{2}$$

$$E' = \frac{E}{(1-\nu^2)}. \tag{3}$$

The contact geometry has a maximum central deformation (δ_{max}) approximated by Eq. 4, which assumes that the half width of the contact area (a) is less than the radius of the spherical support (R).

$$\delta_{max} \cong \frac{a^2}{2R}. \tag{4}$$

The relationship between the deformation and the normal load (F_n) for this type of a contact can be found by integrating the pressure distribution given in Eq. 2, and is given by Eq. 5, along with the approximate solution.

$$F_n = \int_0^{2\pi}\int_0^{a} \mathrm{Pr}\ \mathrm{d}r\,\mathrm{d}\theta = \int_0^{2\pi}\int_0^{a} \frac{E'\delta}{t} r\,\mathrm{d}r\,\mathrm{d}\theta \cong \frac{\pi E' a^4}{4tR}. \tag{5}$$

Using the approximate solution, the contact half width (a), the maximum contact pressure (P_{max}), and the average contact pressure (P_0) are given in Eq. 6–8 respectively.

$$a = \sqrt[4]{\frac{4F_n tR}{\pi E'}} \tag{6}$$

$$P_{max} = \sqrt{\frac{F_n E'}{\pi tR}} \tag{7}$$

$$P_0 = \frac{1}{2}P_{max} = \frac{1}{2}\sqrt{\frac{F_n E'}{\pi tR}} \tag{8}$$

Using the material and geometry conditions given in Table 1, the maximum contact pressures at normal loads of 0.5 and 2 mN are 23 and 45 kPa respectively.

These contacts have corresponding predicted contact widths of 240 and 340 μm for the 0.5 and 2 mN loads. Using a measured cell density of 2,750 cells/mm^2 calculations suggests that ~125 cells are under the contact at the 0.5 mN load. These computations agree favorably with the measured damage zones observed on the cell layers as shown in Fig. 4.

4 Closure

Here the tribology of a well described epithelial system against a hydrogel pin is described during sliding. Mechanics of the cell layer have not yet thoroughly been investigated. The hydrogel pin was soaked in growth media for 5 min prior to testing to provide equilibrium with respect to swelling and protein adsorption, which is known to occur rapidly on submerged material surfaces [51–53]. In fact, material surface properties affect composition and functional activity of adsorbed proteins, modulating cellular adhesive responses [54–56]. Friction tests were carried out in complete growth medium that contains 5% serum and the hydrogel pin used in this study is expected to be coated with serum proteins (e.g. vitronectin, albumin, and fibronectin). While protein adsorption would be expected to differ if carried out in the presence of human tear fluid, standard culturing conditions were used for these preliminary experiments. Future developments will include a light CO_2 gas partial pressure for continued cell viability over long testing times and provide regulated temperature for uninterrupted culture during testing. Optics will be added to the micro-tribometer to record the in situ cell response to mechanically-applied forces. Additionally, the contact pressure must be further reduced to reach clinically relevant levels.

The immunofluorescent stain seen in Fig. 5 can provide some insight as to the cell cytoskeleton response to applied forces. Regions within the friction testing zone (black, where many cells were removed), show a higher density of actin filaments than the control regions outside of the friction testing zone. The cells began to adapt to a harsh shear environment, though this response is not yet completely understood or quantified. Information about the rate at which actin filaments align and densify can be used in understanding the process of wound healing. Careful future studies may be able to differentiate the cellular response to applied forces in a variety of conditions such as single-direction shear in the

Table 1 Tribological conditions for cellular testing

Condition	Values	Application note
Forces	0.5–1,000 uN	Applied and monitored using a piezo-electric stage
Pressure	50–5,000 kPa	Estimated using material properties and contact zone
Temperature	25–37°C	Applied using a heated bath, monitored with a thermocouple
Environment	Aqueous	Up to 8 mL of test solution

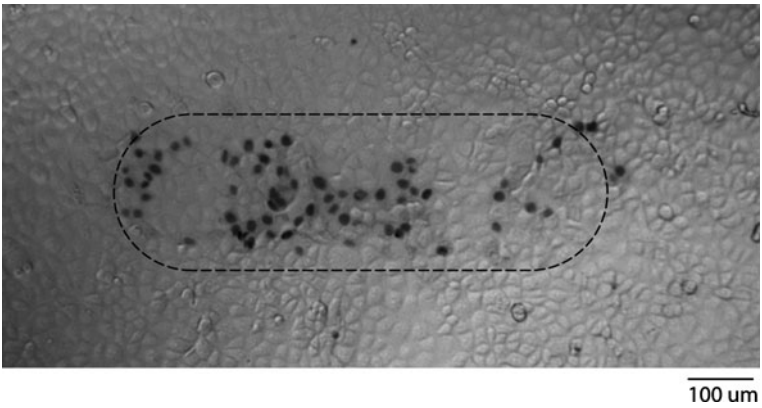

Fig. 4 A microscope image of a wear track after five cycles of sliding under a silicone-based hydrogel at 500 μN of normal load. The dark cells were stained by Typan blue and indicate cells that have been damaged during the experiment. The analytical solution to the contact problem and a 550 μm sliding track gives a dashed region of contact area that corresponds to an average contact pressure of approximately 12 kPa

presence of a strained cell substrate, etc. It has been shown that articular cartilage development is promoted by use of the surrounding musculature, but the specific cellular transduction and response methods are yet unknown.

One emerging way to assess cellular stress response is through the use of spectroscopy [57], though this is complicated by the high number of elements present in, for example, the proteins of a tear film. Krafft et al. [58] have mapped nucleic acid intensity bands using Raman spectroscopy in order to image lung fibroblast cells, and specifically their response to stress, with the major findings detailing the progress of organelle breakdown in late-stage apoptosis. Chan et al. [59] have also used Raman spectroscopy to provide a highly reproducible biomolecular fingerprint of normal cells vs. adjacent neoplastic (tumor) cells.

One direction that signal transduction may progress is toward more fundamental cell responses such as gene expression. Cells could be stressed in a known manner, and then analyzed via gene micro-array [60, 61]. This would give information as to how the genetic material in the cell nucleus interprets the applied forces, and then which response markers are expressed. This, coupled with knowledge of the protein transport and transduction systems of prokaryotic cells, could assemble a more complete map of cellular response to applied stress.

When does cellular stress response indicate healing, a survival mechanism, or apoptosis? The qualitative nature of cell fluorescence microscopy and the complexities of actin fibril formation must be overcome by carefully-designed studies and new analysis techniques. Quantifying cellular response to shear forces, in the form of actin fibril orientation or density for example, could help to define the critical threshold between productive cell stimulation and destructive stimulation.

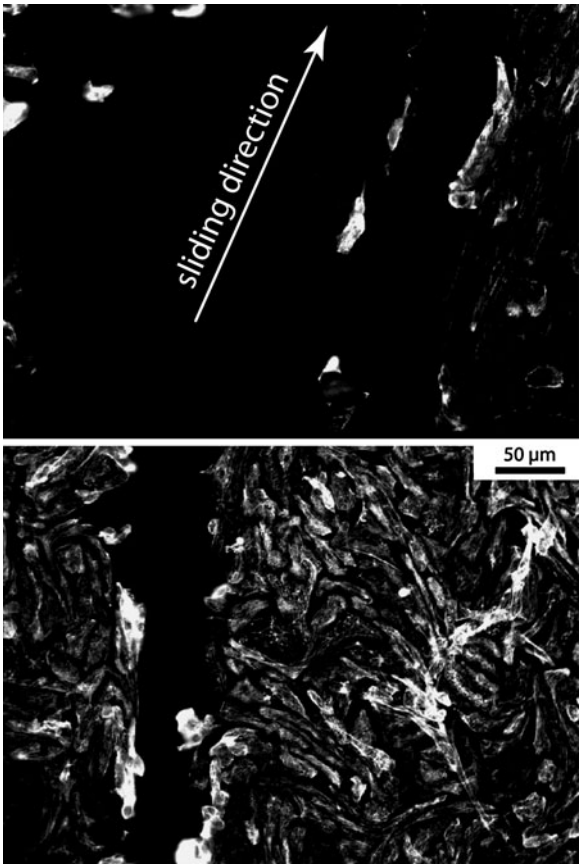

Fig. 5 Immunofluorescence staining of actin stress fibers at the edge region of the sliding tests where some cells were detached. Bright regions indicate bundling of structural actin fibers and alignment along the sliding direction within the cells (actin fibers have been stained and show up white). Solid black regions are void of cells. This is illustrated both in friction tests where all the cells were removed (*top*) and on smaller scratches (*bottom*)

Acknowledgments Dr. Daniel J. Dickrell III, Dr. Jessica A. Cobb, Alina Kozinda, Ana N. Kantzios, Dr. Pamela L. Dickrell, Dr. Benjamin Keselowsky, Toral Zaveri, and Natalia Dolgova have provided foundational work and valuable advice.

References

1. Dunn, A.C., Cobb, J.A., Kantzios, A.N., Lee, S.J., Sarntinoranont, M., Tran-Son-Tay, R., Sawyer, W.G.: Friction coefficient measurement of hydrogel materials on living epithelial cells. Tribol. Lett. **30**(1), 13–19 (2008)
2. Brown, T.D.: Techniques for mechanical stimulation of cells in vitro: a review. J. Biomech. **33**, 3–14 (2000). doi:10.1016/S0021-9290(99)00177-3
3. Huang, H.D., Kamm, R.D., Lee, R.T.: Cell mechanics and mechanotransduction: pathways, probes, and physiology. Am. J. Physiol. Cell Physiol. **287**(1), C1-C11 (2004). doi: 10.1152/ajpcell.00559.2003
4. Vainshtok, V.V., Gureev, A.A., Fuks, I.G.: Improvement of lubricity of greases. Khimiya i Tekhnologiya Topliv i Masel **16**(7), 465–470 (1980)

5. Schmitz, T.L., Action, J.E., Ziegert, J.C., Sawyer, W.G.: The difficulty of measuring low friction: uncertainty analysis for friction coefficient measurements. J. Tribol. Trans. Asme **127**(3), 673–678 (2005)
6. Dokos, S., LeGrice, I.J., Smaill, B.H., Kar, J., Young, A.A.: A triaxial-measurement sheer-test device for soft biological tissues. J. Biomech. Eng. Trans. Asme **122**(5), 471–478 (2000)
7. Chen, X.M., Dunn, A.C., Sawyer, W.G., Sarntinoranont, M.: A biphasic model for micro-indentation of a hydrogel-based contact lens. J. Biomech. Eng. Trans. Asme **129**(2), 156–163 (2007). doi:10.1115/1.2472373
8. Kazmierska, K., Szwast, M., Ciach, T.: Determination of urethral catheter surface lubricity. J. Mater. Sci. Mater. Med. **19**(6), 2301–2306 (2008)
9. Drobek, T., Spencer, N.D.: Nanotribology of surface-grafted peg layers in an aqueous environment. Langmuir **24**(4):1484–1488 (2008)
10. Meyer, A.E., Baier, R.E., Chen, H.G., Chowhan, M.: Differential tissue-on-tissue lubrication by ophthalmic formulations. J. Biomed. Mater. Res. B **82B**(1), 74–88 (2007)
11. Heshmat, H.: Tribology of Interface Layers. CRC Press, Boca Raton (2010)
12. Dangaria J.H., Butler P.J.: Macrorheology and adaptive microrheology of endothelial cells subjected to fluid shear stress. Am. J. Physiol. Cell Physiol. **293**(5), C1568–C1575 (2007). doi:10.1152/ajpcell.00193.2007
13. Chien, S.: Mechanotransduction and endothelial cell homeostasis: the wisdom of the cell. Am. J. Physiol. Heart Circ. Physiol. **292**(3), H1209–H1224 (2007). doi:10.1152/ajpheart.01047.2006
14. Tran-Son-Tay, R., Nash, G.: Mechanical properties of leukocytes and their effects on the circulation. In: Baskurt, O.G., Hardeman, M.R., Meiselman, H.J., Rampling, M.W. (eds.) Handbook of Hemorheology and Hemodynamics, pp. 127–152. IOS Press, Amsterdam (2007)
15. Sato, M., Ohshima, N., Nerem, R.M.: Viscoelastic properties of cultured porcine aortic endothelial cells exposed to shear stress. J. Biomech. **29**(4), 461–467 (1996)
16. Thomas, S., Bolch, W., Kao, K.J., Bova, F., Tran-Son-Tay, R.: Effects of X-ray radiation on the rheologic properties of platelets and lymphocytes. Transfusion **43**(4), 502–508 (2003)
17. Perrault, C.M., Bray, E.J., Didier, N., Ozaki, C.K., Tran-Son-Tay, R.: Altered rheology of lymphocytes in the diabetic mouse. Diabetologia **47**(10), 1722–1726 (2004)
18. Needham D., Hochmuth R.M.: Rapid flow of passive neutrophils into a 4 mu-m pipette and measurement of cytoplasmic viscosity. J. Biomech. Eng. Trans. Asme **112**(3), 269–276 (1990)
19. Tran-Son-Tay, R., Needham, D., Yeung, A., Hochmuth, R.M.: Time-dependent recovery of passive neutrophils after large deformation. Biophys. J. **60**(4), 856–866 (1991)
20. del Alamo, J.C., Norwich, G.N., Li, Y.S.J., Lasheras, J.C., Chien, S.: Anisotropic rheology and directional mechanotransduction in vascular endothelial cells. Proc. Natl Acad. Sci. USA **105**(40), 15411–15416 (2008). doi:10.1073/pnas.0804573105
21. Tran-Son-Tay, R., Sutera, S.P., Rao, P.R.: Determination of red-blood-cell membrane viscosity from rheoscopic observations of tank-treading motion. Biophys. J. **46**(1), 65–72 (1984)
22. Tran-Son-Tay, R., Nash, G.B., Meiselman, H.J.: Oscillatory viscometry of red-blood-cell suspensions—relations to cellular viscoelastic properties. J. Rheol. **30**(1), 231–249 (1986)
23. Tran-Son-Tay, R., Sutera, S.P., Zahalak, G.I., Rao, P.R.: Membrane stress and internal-pressure in a red-blood-cell freely suspended in a shear-flow. Biophys. J. **51**(6), 915–924 (1987)
24. Henderson, E.: Imaging of living cells by atomic-force microscopy. Prog. Surf. Sci. **46**(1), 39–60 (1994)
25. Sato, M., Nagayama, K., Kataoka, N., Sasaki, M., Hane, K.: Local mechanical properties measured by atomic force microscopy for cultured bovine endothelial cells exposed to shear stress. J. Biomech. **33**(1), 127–135 (2000). doi:10.1016/S0021-9290(99)00178-5
26. Darling, E.M., Zauscher, S., Block, J.A., Guilak, F.: A thin-layer model for viscoelastic, stress-relaxation testing of cells using atomic force microscopy: do cell properties reflect metastatic potential? Biophys. J. **92**(5), 1784–1791 (2007). doi:10.1529/biophysj.106.083097

27. Helenius, J., Heisenberg, C.P., Gaub, H.E., Muller, D.J.: Single-cell force spectroscopy. J. Cell Sci. **121**(11), 1785–1791 (2008). doi:10.1242/Jcs.030999
28. Alcaraz, J., Buscemi, L., Grabulosa, M., Trepat, X., Fabry, B., Farre, R., Navajas, D.: Microrheology of human lung epithelial cells measured by atomic force microscopy. Biophys. J. **84**(3), 2071–2079 (2003)
29. Mahaffy, R.E., Park, S., Gerde, E., Kas, J., Shih, C.K.: Quantitative analysis of the viscoelastic properties of thin regions of fibroblasts using atomic force microscopy. Biophys. J. **86**(3), 1777–1793 (2004)
30. Rand, R.P., Burton, A.C.: Mechanical properties of red cell membrane: I. Membrane stiffness and intracellular pressure. Biophys. J. **4**(2), 115–135 (1964)
31. MacDonald, A.G.: The effects of pressure on the molecular-structure and physiological functions of cell-membranes. Philos. Trans. R. Soc. Lond. B Biol. Sci. **304**(1118), 47–68 (1984)
32. Duszyk, M., Schwab, B., Zahalak, G.I., Qian, H., Elson, E.L.: Cell poking—quantitative-analysis of indentation of thick viscoelastic layers. Biophys. J. **55**(4), 683–690 (1989)
33. Petersen, N.O., Mcconnaughey, W.B., Elson, E.L.: Dependence of locally measured cellular deformability on position on the cell, temperature, and cytochalasin-*b*. Proc. Natl Acad. Sci. USA Biol. Sci. **79**(17), 5327–5331 (1982)
34. Yeung, T., Georges, P.C., Flanagan, L.A., Marg, B., Ortiz, M., Funaki, M., Zahir, N., Ming, W.Y., Weaver, V., Janmey, P.A.: Effects of substrate stiffness on cell morphology, cytoskeletal structure, and adhesion. Cell Motil. Cytoskeleton **60**(1), 24–34 (2005). doi:10.1002/Cm.20041
35. Hirata, H., Tatsumi, H., Sokabe, M.: Mechanical forces facilitate actin polymerization at focal adhesions in a zyxin-dependent manner. J. Cell Sci. **121**(17), 2795–2804 (2008). doi:10.1242/Jcs.030320
36. Clark, P., Connolly, P., Curtis, A.S.G., Dow, J.A.T., Wilkinson, C.D.W.: Cell guidance by ultrafine topography invitro. J. Cell Sci. **99**, 73–77 (1991)
37. Sniadecki, N.J., Anguelouch, A., Yang, M.T., Lamb, C.M., Liu, Z., Kirschner, S.B., Liu, Y., Reich, D.H., Chen, C.S.: Magnetic microposts as an approach to apply forces to living cells. Proc. Natl Acad. Sci. USA **104**(37), 14553–14558 (2007). doi:10.1073/pnas.0611613104
38. Ashkin, A., Dziedzic, J.M.: Internal cell manipulation using infrared-laser traps. Proc. Natl Acad. Sci. USA **86**(20), 7914–7918 (1989)
39. Dembo, M., Wang, Y.L.: Stresses at the cell-to-substrate interface during locomotion of fibroblasts. Biophys. J. **76**(4), 2307–2316 (1999)
40. Kumar, S., Maxwell, I.Z., Heisterkamp, A., Polte, T.R., Lele, T.P., Salanga, M., Mazur, E., Ingber, D.E.: Viscoelastic retraction of single living stress fibers and its impact on cell shape, cytoskeletal organization, and extracellular matrix mechanics. Biophys. J. **90**(10), 3762–3773 (2006). doi:10.1529/biophysj.105.071506
41. Cobb, J.A., Dunn, A.C., Kwon, J., Sarntinoranont, M., Sawyer, W.G., Tran-Son-Tay, R.: A novel method for low load friction testing on living cells. Biotechnol. Lett. **30**(5), 801–806 (2008). doi:10.1007/s10529-007-9623-z
42. Dunn, A.C., Zaveri, T.D., Keselowsky, B.G., Sawyer, W.G.: Macroscopic friction coefficient measurements on living endothelial cells. Tribol. Lett. **27**(2), 233–238 (2007). doi:10.1007/s11249-007-9230-0
43. Rennie, A.C., Dickrell, P.L., Sawyer, W.G.: Friction coefficient of soft contact lenses: Measurements and modeling. Tribol. Lett. **18**(4), 499–504 (2005). doi:10.1007/s11249-005-3610-0
44. Dickrell, P.L., Sinnott, S.B., Hahn, D.W., Raravikar, N.R., Schadler, L.S., Ajayan, P.M., Sawyer, W.G.: Frictional anisotropy of oriented carbon nanotube surfaces. Tribol. Lett. **18**(1), 59–62 (2005). doi:10.1007/s11249-004-1752-0
45. Dickrell, P.L., Pal, S.K., Bourne, G.R., Muratore, C., Voevodin, A.A., Ajayan, P.M., Schadler, L.S., Sawyer, W.G.: Tunable friction behavior of oriented carbon nanotube films. Tribol. Lett. **24**(1), 85–90 (2006)

46. Scherge, M., Stanislav, G.N.: Microscale test equipment. In: Biological Micro- and Nanotribology: Nature's Solutions. Nanoscience and Technology, pp 153–178. Springer-Verlag, Heidelberg (2001)
47. Young, R., Tighe, B.J.: Frictional characteristics of contact lenses and ophthalmic solutions. Cornea **19**(6), S139 (2000)
48. Trepat, X., Grabulosa, M., Puig, F., Maksym, G.N., Navajas, D., Farre, R.: Viscoelasticity of human alveolar epithelial cells subjected to stretch. Am. J. Physiol. Lung Cell. Mol. Physiol. **287**(5), L1025–L1034 (2004). doi:10.1152/ajplung.00077.2004
49. Grunheid, T., Zentner, A., Heaney, T.G.: Cell kinetics of mechanically stimulated rat oral epithelia. Arch. Oral Biol. **50**(9), 829–835 (2005). doi:10.1016/j.archoralbio.2005.01.005
50. Shaw, A.J., Collins, M.J., Davis, B.A., Carney, L.G.: Eyelid pressure: inferences from corneal topographic changes. Cornea **28**(2):181–188 (2009)
51. Andrade, J.D., Hlady, V.: Protein adsorption and materials biocompatibility—a tutorial review and suggested hypotheses. Adv. Polym. Sci. 79, 1–63 (1986)
52. Brash, J.L.: Protein interactions with solid-surfaces following contact with plasma and blood. Biol. Chem. Hoppe Seyler **368**(7), 736 (1987)
53. Ratner, B.D., Bryant, S.J.: Biomaterials: where we have been and where we are going. Annu. Rev. Biomed. Eng. **6**, 41–75 (2004)
54. Keselowsky, B.G., Collard, D.M., Garcia, A.J.: Integrin binding specificity regulates biomaterial surface chemistry effects on cell differentiation. Proc. Natl Acad. Sci. USA **102**(17), 5953–5957 (2005). doi:10.1073/pnas.0407356102
55. Keselowsky, B.G., Collard, D.M., Garcia, A.J.: Surface chemistry modulates focal adhesion composition and signaling through changes in integrin binding. Biomaterials **25**(28), 5947–5954 (2004). doi:10.1016/j.biomaterials.2004.01.062
56. Keselowsky, B.G., Collard, D.M., Garcia, A.J.: Surface chemistry modulates fibronectin conformation and directs integrin binding and specificity to control cell adhesion. J. Biomed. Mater. Res. A **66A**(2), 247–259 (2003). doi:10.1002/Jbm.A.10537
57. Lim, C.T., Zhou, E.H., Li, A., Vedula, S.R.K., Fu, H.X.: Experimental techniques for single cell and single molecule biomechanics. Mater. Sci. Eng. C-Bio S **26**(8), 1278–1288 (2006)
58. Krafft, C., Knetschke, T., Funk, R.H.W., Salzer, R.: Studies on stress-induced changes at the subcellular level by raman microspectroscopic mapping. Anal. Chem. **78**(13), 4424–4429 (2006). doi:10.1021/Ac060205b
59. Chan, J.W., Taylor, D.S., Zwerdling, T., Lane, S.M., Ihara, K., Huser, T.: Micro-raman spectroscopy detects individual neoplastic and normal hematopoietic cells. Biophys. J. **90**(2), 648–656 (2006). doi:10.1529/biophysj.105.066761
60. Sanzari, J.K., Nuth, M., Kennedy, A.R.: Induction of cytokine gene expression in human thyroid epithelial cells irradiated with HZE particles (iron ions). Radiat. Res. **172**(4), 437–443 (2009)
61. Kusanagi, R., Umemoto, T., Yamato, M., Matsuzaki, Y., Nishida, K., Kobayashi, Y., Fukai, F., Okano, T.: Nectin-3 expression is elevated in limbal epithelial side population cells with strongly expressed stem cell markers. Biochem, Biophys. Res. Commun. **389**(2), 274–278 (2009)

Part II
Experimental Methods

Microfabricated Devices for Studying Cellular Biomechanics and Mechanobiology

Christopher Moraes, Yu Sun and Craig A. Simmons

Abstract Recognition of the cell as being a mechanical entity has strongly influenced our conceptual model of biology. Measuring the mechanical properties of the cell, including stiffness, adhesion, and contractility, and understanding how cells respond to mechanical factors has prompted the development of a variety of experimental tools and techniques. Microfabrication-based approaches to study these phenomena can result in substantial advantages in providing the requisite capability, utility, precision, and throughput for such experiments. However, mainstream use of these technologies remains to be realized. This chapter aims to survey and summarize recent developments in using microfabricated technologies to address experimental challenges in the fields of cellular biomechanics and mechanobiology, while critically assessing the advantages and disadvantages of such techniques over conventional platforms.

1 Introduction

The mechanical behaviour of biological cells dynamically changes in response to chemical stimulation [1], mechanical forces [2] and cell to cell contacts [3].

C. Moraes, Y. Sun and C. A. Simmons (✉)
Department of Mechanical and Industrial Engineering, University of Toronto, 5 King's College Road, Toronto ON, M5S 3G8, Canada
e-mail: simmons@mie.utoronto.ca

C. Moraes, Y. Sun and C. A. Simmons
Institute of Biomaterials and Biomedical Engineering, University of Toronto, 164 College Street, Toronto ON, M5S 3G9, Canada

C. A. Simmons
Faculty of Dentistry, University of Toronto, 124 Edward Street, Toronto ON, M5G 1G6, Canada

Stud Mechanobiol Tissue Eng Biomater (2011) 4: 145–175
DOI: 10.1007/8415_2010_24

Published Online: 2 November 2010

The cytoskeleton provides mechanical support to the cell, reflects cell phenotype [4–6], has been shown to play a pivotal role in transducing mechanical stimuli in the environment [7], and may be a critical determinant of cell fate and function [8, 9]. The cytoskeleton is instrumental in regulating processes including programmed cell death [10]; differentiation [11]; adhesion, polarity, contractility and migration [12, 13]; and gene uptake, protein expression, secretion and metabolic activity [14, 15]. Furthermore, disease progression can be dependent on alteration of the cytoskeleton: metastatic cancer cells become more compliant to facilitate motility [16, 17]; red blood cells in patients infected with the malaria parasite become stiff and more adherent, preventing re-entry into the liver [18]; and red blood cells in patients with sickle cell anemia have difficulty flowing in capillaries, causing circulatory problems [19, 20]. Hence, the importance of recognizing the cell as being a *mechanical* entity, both in terms of its behaviour in the surrounding environment, and in being responsive to surrounding mechanical conditions is becoming more apparent in various biological studies.

This increasing recognition of the critical role played by mechanics in regulating biological form and function has given rise to two distinct areas of research: biomechanics and mechanobiology [21, 22]. *Biomechanics* is "the application of the principles of mechanics to study living organisms and their components" [21]. The application of biomechanics at the cellular scale continues to be ripe with challenges and opportunities. This includes both understanding the intrinsic mechanical properties of a cell, and determining how the cell mechanically interacts with the external microenvironment. Mechanical behaviour of the cell is quite complex, and cannot be isolated to a specific structural component, but rather arises from the collective mechanical interactions of multiple filamentous proteins [8]. The mechanical properties of cells reflect [4–6] and forecast [8, 9] cell phenotype, and can be used as a marker for disease progression [23]. Adhesion, migration and contractility of cells are mechanically-oriented processes through which cells manipulate and remodel the environment, and are hence of critical importance in wound healing [24], progression of certain diseases [25] and developmental biology [26]. Thus, cytoskeletal changes may indicate or even trigger pathogenic responses, and the ability to probe the mechanical nature of the cell could provide insight into how cells receive and integrate regulatory signals from the surrounding environment.

In contrast to biomechanics, *mechanobiology* is "the application or analysis of the role of mechanical forces in eliciting a molecular response, leading to a quantifiable change in form and/or function" [21, 22]. The importance and influence of environmental mechanical conditions on cell fate and function has been thoroughly established and is the subject of multiple reviews [27–29]. Mechanobiology is a key component in pathobiology [25, 30, 31]; development and morphogenesis [32]; and in many specialized tissues such as bone [33], tendon [34], heart valves [35], intervertebral disc [36] and cartilage [37, 38]. The ability to precisely manipulate the mechanical microenvironment to understand the mechanisms and processes by which mechanical forces regulate cell function will also require novel experimental platforms and techniques.

Microfabricated technologies can provide viable solutions to some of the problems associated with understanding both cell biomechanics and mechanobiology. Applications of these microtechnologies in this field have prompted a few recent reviews on the subjects [39–41]. In this book chapter, we aim to provide a categorical summary of how emerging microfabricated technologies can be used to study various aspects of biomechanics and mechanobiology; and to critically appraise these technologies in terms of their advantages and disadvantages over more conventional macroscale techniques.

2 Advantages at the Microscale

Microfabricated systems yield a number of advantages that are applicable in working with cells. First and foremost, microfabricated features can span the range of sub-cellular (<1 μm) to tissue (>1 mm) dimensions, making them ideally suited to study a range of biological systems. The ability to fabricate on this length scale enables the development of arrayed structures, which can greatly increase experimental throughput. Given the inherent heterogeneity of biological systems, the need for higher throughput experimental techniques becomes immediately apparent [42]. This is particularly true when studying single cells, where ensemble averaging of population response can wash out single cell dynamics [43]. Likewise for rare cell populations (such as primary stem cells), in which only a few cells from a mixed population are relevant to the study at hand. Furthermore, the synergistic response of cells to multiple environmental parameters necessitates high-throughput systems to screen for the effects of combinatorial stimuli. Hence, one of the critical advantages and strong attractions of microfabricated systems in biomechanics and mechanobiology is the ability to provide increased throughput to probe more samples under more experimental conditions.

Microfabricated technologies also allow the integration and consolidation of multiple functional components on a robust, single-piece chip. Actuation and sensing mechanisms can be integrated directly onto a single chip, and this concept of having a “lab-on-a-chip” results in extremely portable and versatile systems. The reduction of pieces of equipment can substantially improve the usability of an experimental technique, and the ability to fabricate batches of arrays means that microfabricated systems will eventually be low-cost and disposable.

Control of displacements and features at the microscale allows highly accurate control over experimental parameters and conditions. For example, replacement of fluid in a microchannel requires only a few microliters, and laminar flow in the channels ensures that the resident liquid is expelled without contamination of the incoming fluid. This also allows for very rapid switching of experimental culture conditions, enabling the maintenance of a steady-state environment, and highly accurate control of mass transport, both in terms of time and space. The ability to reliably fabricate features at the microscale can also greatly simplify experimental setups and procedures, without relying on sensitive and expensive equipment to

control environmental parameters over large areas or volumes. Often, this is a result of favourable physics that arise from operating at the microscale, which can be used to create conditions not possible at larger scales.

Lastly, materials used in microfabricated systems, such as the ubiquitous poly(dimethylsiloxane) (PDMS), are generally biocompatible, and easily integrated with most other techniques and equipment used in traditional wetlabs, including inverted microscopes, fluorescent labeling and imaging techniques, and autoclave sterilizers, making these technologies relatively simple to incorporate into a standard wetlab's infrastructure.

3 Measurement and Biomechanics

Microfabricated techniques to measure the mechanical aspects of cell form and function can be broadly categorized as either passive measurement of the mechanical properties of a cell, or measurements of forces actively exerted by cells on their surrounding environments. Both passive and active measurements are strongly dependent on cell type and environment. In this section, we first survey the various microfabricated techniques used to characterize the passive mechanical properties of a cell. Second, we categorize the large number of micro-scale approaches to this problem based on the practical advantages gained by designing and using microtechnologies. We then survey microdevices designed to measure mechanical interactions with the surrounding environment, including adhesion strength and traction forces. In general, microfabricated measurement approaches to these problems can provide substantial improvements in sensing resolutions and throughput, as compared to more conventional macroscale systems.

3.1 Mechanical Characterization

Biological cells are typically considered to have elastic moduli ranging in magnitude from 1 to 10,000 Pa, and are complex enough that different measurement techniques produce disparate results on the same cell population [44]. The length scale of features fabricated using microtechnologies is particularly well-suited to characterizing single cells ($\sim$20 μm in diameter) and improving measurement throughput in a cell population. Further, the actuation and sensing technologies available are promising in terms of increasing sensitivity and resolution by precise application and measurement of forces and deformations.

When a biological cell is modeled as a linear elastic solid, the parameter typically used to describe its mechanical properties is the Young's modulus, which relates applied stresses and cell deformation. Mechanical characterization given this assumption merely requires the application of a known force and measurement of a resulting displacement, or vice versa. However, the mechanical behaviour of

cells is often more complex than a linear elastic solid, and so is often characterized using a dynamic frequency-dependent shear modulus. This modulus is independent of frequency for normal solids, and is linearly proportional to frequency for liquids. The material behaviour of cells is between the characteristics of solids and liquids, displaying a non-linear, frequency-dependent response in shear modulus. This is due to the complicated deformation of various constituents of the mechanical structure supporting the cell. Mathematical models including the liquid drop, viscoelastic, and tensegrity based models developed for single cell biomechanics have been thoroughly reviewed by others [45, 46], but the issue is briefly mentioned here to elucidate some of the complexities that arise in designing systems to characterize these mechanical properties.

The spatial resolution of systems designed to probe cell biomechanics is a critical design parameter, as some techniques such as platen-based compressive measurement assume a biological cell to be a homogenous body and characterize the 'whole-cell' deformation in response to an applied force, while others are capable of spatially resolving mechanical properties in different regions of the cell.

3.1.1 Traditional Tools to Characterize Cell Biomechanics

Standard techniques to probe the mechanics of single cells have been previously reviewed [45, 47, 48], and the most common are briefly recapitulated here (Fig. 1). Lumped mechanical properties of single cells can be probed by several methods. Microplate compression consists of applying a known force to plates sandwiching an adherent cell, and observing the resulting deflection [49, 50]. Optical stretching [23, 51] involves using opposed laser beams to apply a stretching force to a cell in suspension, and the resulting deformation is observed through a microscope. In micropipette aspiration [52, 53] a controlled suction pressure is applied to a cell via a micropipette, and the resulting distention of the cell into the pipette can be

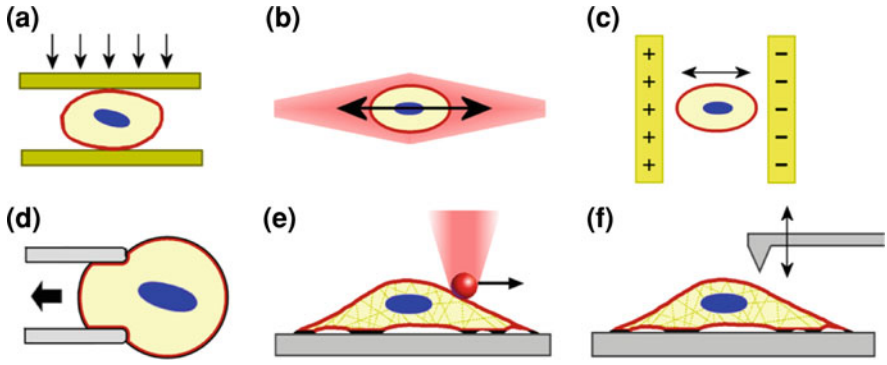

Fig. 1 Key experimental techniques in cell biomechanics. **a** Microplate compression; **b** optical stretching; **c** electrodeformation; **d** micropipette aspiration; **e** Use of optical tweezers or magnetic force on a cell-attached bead; and **f** atomic force microscopy

used to calculate the mechanical properties of the cell, using analytical or computational models. Micropipette aspiration is a versatile technique in that it can be conducted on both adherent and suspended cells and spatial resolution can be controlled by changing the pipette diameter, enabling characterization of the whole cell or of sub-cellular cell segments. Magnetic twisting cytometry [54], gradients [55] and bead manipulation in an optical trap [56, 57] can be used to measure sub-cellular material properties, by applying precise forces to beads attached to receptors on the cell membrane, via a magnetic field or a laser-based optical tweezer system. Alternatively, atomic force microscopy [58] can be used to create a "stiffness map" of the cell, by rastering a vibrating cantilever across the surface and observing the deflection of the cantilever resulting from the applied force.

The key limitation to each of these techniques is in equipment complexity. Each of the experimental setups is challenging to operate, and requires skilled and trained operators. Peripheral equipment can be expensive and is rarely portable, making measurements outside a lab environment quite challenging. These techniques are also typically limited in throughput. Given the heterogeneity inherent in cell biology, and the number of environmental conditions that influence the cytoskeletal structure and the mechanical nature of the cell, high-throughput approaches are necessary to provide a better understanding of mechanical behaviour in various microenvironments. Though an ideal solution to probe single cell mechanics does not yet exist, microfabricated approaches have been designed to alleviate some of these issues.

3.1.2 Microfabricated Approaches in Mechanical Characterization of Cells

We categorize the surveyed microdevice systems by advantages over currently available techniques: increased system integration, reduction in experimental complexity, improved usability, and increases in throughput.

Component integration and miniaturization

Integrating actuation and sensing components into a single chip can reduce the number of peripheral and external components required to perform a characterization experiment. This could lead to more robust, compact, efficient and accurate systems. To illustrate this point, magnetic bead cytometry is an excellent case study. Functionalized magnetic microspheres are bound to integrins on the cell surface. External magnets can then be used to apply a well-characterized force to the integrins, and to the attached cytoskeleton. Magnetic actuation is particularly appealing because it is a non-contact method. The force at a distance created by a magnetic dipole is inversely proportional to the cube of the distance, and hence small positioning errors in systems in which the magnetic dipole is manually positioned could result in large errors in applied force. De Vries et al. [59] successfully integrated three and four micromagnetic poles on a glass substrate, which conduct magnetic flux into a sharp tip, precisely patterned in relation to each other. This scheme allows for 120 pN of force to be delivered to a magnetic microsphere,

and by adding force vectors for each pole, a force can be applied along any vector in two dimensions. Though De Vries et al. did not use this system to conduct mechanical characterization studies, they did manipulate particles within live cells, and so the principle is sound.

Conducting parallel experiments in such a magnetic scheme would be limited, as mechanical characterization would require continuous optical monitoring of the single cell and deforming bead. The requirement for optical observation is a significant barrier to parallelization in most experiments in cell mechanics. The integration of electrical displacement or strain sensors directly into the platform would resolve such issues, and one such approach is to design electrostatically interacting silicon surfaces, across which a small voltage is applied. Measured capacitance between the interlocking comb structures can then be used to infer separation of the combs. Hence measurement of applied displacements can be automated, increasing throughput of such characterization systems.

The interlocking structures can also be used as actuators, by applying a voltage between the combs. This actuation scheme has been employed in a silicon-based MEMS device capable of applying precisely controlled forces to separate two [60] and four [61] adjoining plates. A single cell cultured across both plates would resist the applied uniaxial and biaxial loads, and plate displacement can be tracked visually to characterize viscoelastic cell response (Fig. 2). Capacitance-based force sensors can be incorporated into this fabrication process to automatically track deformations. A similarly themed device makes use of electrothermal deformation as the actuation strategy, in which electrical current causes heating in a resistive V-shaped suspended silicon structure, attached to a plunger. On heating, the actuator bends, and the plunger compresses a cell in a dielectrophoretic trap [62].

Measurements of cell mechanics using the electrostatic actuation technique were not reported, possibly because of (1) the difficulties in precisely positioning a

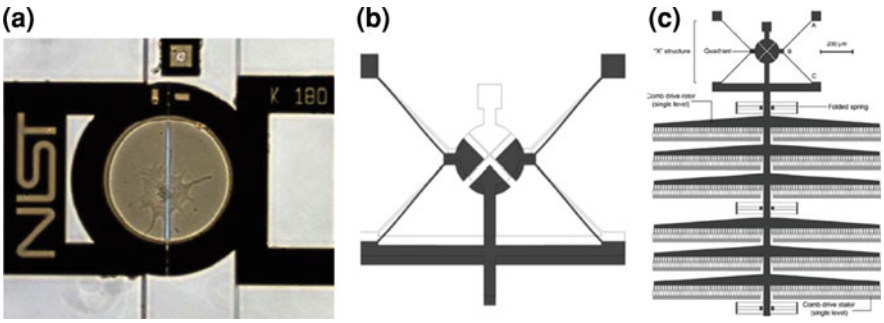

Fig. 2 Silicon-based devices for mechanical characterization of cells. **a** Separated plates across which a cell is cultured (Source: Serrell et al. [63], with permission from Springer). **b** Biaxial stretching mechanism for a cell cultured in the center of the gap; and **c** the electrostatic comb drive required to actuate such a structure (Source: Scuor et al. [61] with permission from Springer)

single cell on a single point over a large area; or (2) the need to maintain cells under conductive liquid media, which leads to current-induced heating, charge shielding, and electrochemical reactions in the media [64]. More recent finding that the use of high-frequency actuation voltages in electrostatic actuation eliminates electrochemical reactions does suggest that this problem is solvable [65]. However, in spite of demonstrated maintenance of cell viability, the impact of such electric fields on biological function is still to be determined. The thermal actuator developed in [62] was used to compress a cell, but the authors did not provide results for the mechanical characterization. Thermally actuated systems may not cause electrochemical problems in cell culture media, but do have a related disadvantage in terms of maintaining local temperatures, to which cells are exquisitely sensitive [66]. Furthermore, the size of the actuation structure in the electrostatic and electrothermal actuation systems requires a large device area, limiting the scalability and throughput of such systems. In addition, the challenging and expensive silicon fabrication process typically results in a low-device yield, further reducing possibilities for increased throughput and parallelization.

Directly applying electrostatic forces to cells in suspension may be more feasible for mechanical characterization, but analysis is limited to non-adherent cells. The use of dielectrophoretic forces for biomedical applications such as cell sorting, identification and manipulation are covered in other reviews [64], but this idea was first applied to mechanical characterization in 1984, when Engelhardt et al. [67] characterized the viscoelastic response of erythrocytes placed in a high-frequency electric field. The original experimental setup consisted of two razor blade electrodes immersed in culture media, between which the cell was trapped by the dielectrophoretic forces. More recent studies [68, 69] have used more robust approaches with electrodes micropatterned directly onto glass substrates to apply the requisite electric field. However, this method still requires the application of strong electric fields, which may influence cell biology, and which may be further exacerbated by the requirement for ionically conductive media. Additionally, analytical methods to relate raw data (voltage-cell deformation) to the mechanical properties of cells need to be developed.

An alternative approach has been to use an external precision stage to apply a known displacement to the biological sample and using electrostatic combs as capacitative sensors [70] or visually observing lateral cantilever deflection [63, 71–74], to measure the reaction force of the sample. Such systems were used to determine the viscoelastic response of a cell to an applied step displacement. Although this approach does reduce the degree of on-chip integration, the use of the external motion system provides a strong actuation force over a long stroke length; and eliminates the issue of electrochemical reactions in the culture media.

One key issue that affects all the devices outlined in this section is that of cell positioning. In all the mentioned devices, a single cell has to be placed in a precise location in order to measure their mechanical properties. The use of robotic micromanipulation tools or micropatterning techniques [75, 77] may alleviate this issue, but does make the experimental process more complicated and challenging.

Reduction in Complexity

Microfabricated structures can be used to either measure or apply biologically relevant forces and displacements, attaining high levels of precisions with a mechanism simpler than a commercial force transducer. Silicon and polymeric cantilevers are particularly useful as force sensors, as deformation can be visually tracked and related back to applied force using a simple analytical equation for cantilever bending.

Integrated sensors to measure post displacement via electrical resistance changes in an attached strain gauge have been developed [78, 79], and these could be utilized in high throughput applications. In current approaches to cell biomechanics, post deformation is more easily measured optically, and microfabricated cantilevers are able to provide the size and force resolution necessary for mechanical characterization of single cells. Though the atomic force microscope (AFM) is based on a similar concept, the ability to customize microfabricated posts has enabled parallelization and probing cell mechanics in complex conditions. Sasoglu et al., used a micromanipulator to maneuver an array of PDMS sensing posts designed to measure the stiffness of an array of cells patterned on extracellular matrix-coated spots on a glass substrate. Though they successfully fabricated and characterized a device with suitable accuracy and resolution requirements [80], and have also developed computer methods for parallel analysis of the array [81], experiments probing cell mechanics have been proposed but not performed as yet.

Sun and co-workers [82] leveraged the concept of force-sensing cantilevers to mechanically characterize oocytes during microinjection. A robotically-controlled micromanipulator was used to puncture the cell membrane under displacement control, and deflection of surrounding micropillars was monitored to assess forces required for injection. The ability to produce large arrays of cantilevers enabled the authors to observe previously unknown differences in stiffness between young and old mouse oocytes.

Improved Usability and Throughput

Microfabricated systems can also improve the usability and applicability of more standard techniques, by using microstructures to precisely control cell position. For example, optical stretching requires suspended non-adherent cells to be positioned at the correct location between two focused beams of laser light. Guck and coworkers used microfluidics to improve the usability of their technology, and developed a capillary based microfluidic system which integrates fiber optic cables delivering the laser beams to cells positioned by microfluidic flow [83]. The integrated system can measure the viscoelastic signature of 50–100 cells/h in a rapid, serial process. In this demonstration, the group was able to compare the distribution of deformability between a normal epithelial cell line and a cancerous one, and found significant differences between the two.

Similarly, AFM is commonly used to measure applied forces under load control across a cell surface, but is challenging to use with non-adherent cell populations. Rosenbluth et al. [84] made use of microfabricated wells to physically trap non-adherent leukocytes, for rapid measurement with an AFM. The microwell system was able to trap cells in defined locations during the testing process, greatly speeding up measurements. The AFM applies a compressive load at a point, but alternatives exist to apply platen-like compressive loads to cells in culture. On the macroscale, microplate compression techniques [49] are cumbersome and delicate, but microfluidic compressive testing systems require relatively fewer pieces of supporting equipment. These devices consist of a thin suspended layer of PDMS in a multilayer PDMS device [85], pressurized to come in contact with cells cultured on a surface [86, 87]. Viscoelasticity of the cells under compression can be determined by observing cell deformation under a microscope after a known pressure is applied. Kim et al. [88] used such a device to demonstrate differences in viscoelasticity between cancerous and normal cells.

Micropipette aspiration is another technique which is inherently slow and requires extensive operator training. In order to eliminate the need for a skilled operator, Moraes et al. [89] integrated the micropipette into a microfluidic channel, to allow cells to be localized close to the pipette tip, where a suction pressure draws them towards the pipette tip. The resulting experimental procedure was simple enough to be performed by untrained and minimally supervised undergraduate students as part of a teaching course. The same group has also investigated the use of parallel channels in PDMS for high-throughput micropipette aspiration of suspended cells [90].

3.2 Force Measurement

Microengineered systems to measure the mechanical interactions between cells and the substrate to which they are adhered can substantially improve force and spatial resolution over conventional techniques. In this section we review microfabricated systems to measure cell adhesion and cell-generated traction forces.

3.2.1 Adhesion

Traditional techniques used to measure cell adhesion include atomic force microscopy, in which a cantilever tip is used to ‘scrape’ a cell off a substrate, while observing the force required to do so [91], and an extended micropipette aspiration technique in which a second pipette is used to place a bead in contact with a cell, and pull them apart using suction at various pressures [92]. Adhesion assays can also be conducted in parallel plate flow chamber (PPFC) systems [93], in which cells are allowed to attach onto a substrate, and a shear profile is applied to determine the fraction of cells remaining on the substrate at each shear level.

The low throughput of these techniques limits the practical use of these tools in understanding the effects of multiple environmental parameters on cell adhesion.

Microfabricated approaches provide higher throughput by applying precisely controlled shear forces to detach cells from a substrate within a microfabricated channel. Work in the Griffiths and Jensen labs demonstrated a shear device that enables both short- and long-term culture of cells in PDMS microchannels, with separated fluid channels to perfuse nutrients and to apply shear stresses to the cells in culture (Fig. 3a). They determined the fraction of cells remaining adhered as a function of time and shear magnitude, and demonstrated differences in adhesion between cells cultured with and without epidermal growth factor. By manipulating the width of fluidic channels on the same chip, the group was able to use a single pressure differential to create a variety of shear magnitudes in different regions of

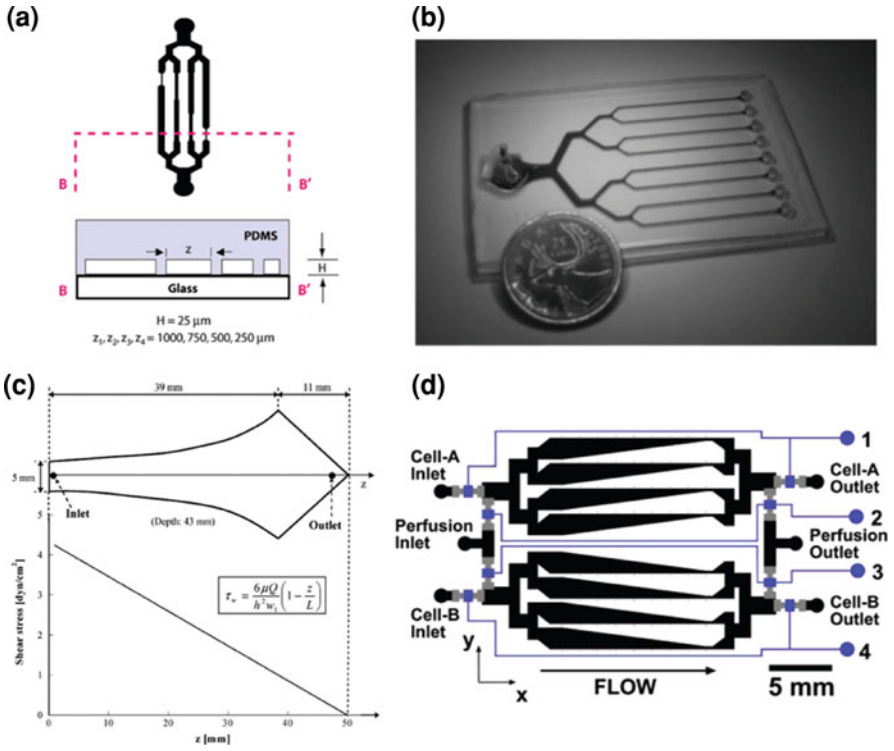

Fig. 3 Microfluidic devices to test adhesion of cells to various substrates. **a** Varying channel dimensions enables multiple shear forces to be applied simultaneously on a single chip (Source: Lu et al. [94] with permission from American Chemical Society). **b** Use of multiple flow channels enables higher-throughput testing of adhesion on multiple matrix protein coatings (Source: Young et al. [95], reproduced by permission of The Royal Society of Chemistry). **c** Logarithmic design used to apply a linearly increasing shear stress along the microchannel length (Source: Plouffe et al. [101], with permission from the American Chemical Society); and **d** Channels with varying shear stress profiles along each channel (Source: Gutierrez et al. [102], with permission from the American Chemical Society)

the device [94]. Young et al. [95] used a simpler device (Fig. 3b) with uniform channels, but leveraged the ability to increase experimental throughput to conduct experiments involving eight culture conditions simultaneously on a single chip. They compared adhesion strengths of closely related but functionally distinctive vascular and valvular endothelial cells, on glass substrates coated with six different concentrations of the extracellular matrix proteins fibronectin and collagen, demonstrating matrix and cell-type dependent adhesion patterns.

Adhesion differences between cell types can also be maximized by manipulating the physical features of the substrate on which cells are grown. Kwon et al. [96] demonstrated the use of nanotopographically patterned substrates integrated in microfluidic shear channels to selectively control adhesion of cancerous cells. More complex studies of detachment in microchannels have also been conducted, including measurement of cell-substrate contact area over time and under shear; fluorescence-based analysis of focal adhesion formation; and development of models to calculate the adhesive stresses exerted at each point of contact [97, 98].

The concept of using the fraction of cells remaining under shear as a defining feature for the subpopulation has also been exploited to enrich rare cell populations by depleting unwanted, adherent cells [99, 100]. Widening single channels designed to produce a linearly increasing shear stress profile along the channel length clearly show the shear level at which cell detachment occurs [101] (Fig. 3c). More complex devices operating on the same basic principles have been developed by Guiterrez and Groisman, who integrated valves into the microfluidic chip, enabling greater precision and automated control of applied adhesion assays [102] (Fig. 3d).

3.2.2 Traction Forces

Traction forces are typically measured by examining deformations of the surrounding microenvironment. The wrinkling of thin, compliant films in response to cells exerting traction forces at the surface can be used to determine cell traction force fields [103]. Automated image tracking procedures can be used to track deformation fields for textured materials [104] or to image the displacement of embedded fiduciary markers in the underlying substrate [105], which can then be deconvolved to calculate traction forces.

Deconvolving displacement vector fields to calculate applied forces is a computationally intensive process. More critically however, each of these techniques are limited to relatively soft systems, where it is difficult to isolate the effects of substrate stiffness (and hence cell spreading) on cell behaviour. Microfabricated silicon cantilevers were able to partially address these issues. Cells cultured on separated adhesive pads exert mechanical forces as they migrate, which bends the silicon cantilever along one direction. Tracking cantilever deflection allowed the use of simple analytical models to calculate traction forces, and altering cantilever size provided force sensors of different stiffness [106, 107]. This approach was

extended to a two-dimensional substrate by Chen and coworkers, who developed a bed of polymer microneedles, on top of which cells were cultured. Microneedle deflection in response to cell-generated traction forces were monitored, and a simple analytical model (Sect. 3.1.2) can be used to determine the forces required for those deformations, providing a computationally simple and spatially-defined 'map' of force generation [108]. Matrix proteins patterned on the micropost tips can also be used to test cell traction forces under various matrix protein stimuli, limit cell adhesion to specific areas, and study traction forces arising from these decoupled parameters. To improve the usability of this system, image processing techniques to improve the accuracy and speed of microneedle displacement measurements have been developed [109]. Several novel biological mechanisms have been identified using this system of force measurement, and have been covered thoroughly in recent reviews [40].

The microfabricated polymer cantilever approach has been recently extended to cells cultured in a three-dimensional culture system. Legant et al. developed a modified micropost system, embedded within a polymerizable cell-laden hydrogel biomaterial. As cells in the hydrogel exert contractile forces and the matrix undergoes deformation, the force with which the hydrogel contracts can be measured by deflection of the posts [110]. Interestingly, the group found that the force of contraction increased with stiffness of the post. This suggests that cells 'feel' the increased stiffness of the posts by transmission of mechanical stiffness through the gel, and undergo increased contractility as a result of the change of stiffness.

This complex behaviour suggests that the line drawn between cell biomechanics and cell mechanobiology has shades of gray. There exists a complex and exquisitely sensitive feedback mechanism between internal forces generated by the cell, and forces applied to the cell [111]. Hence, although the experiments described in this section are designed to merely *measure* passive cytoskeletal mechanics and the active forces generated, the forces required to probe the system could change the results, further emphasizing the need for multiple measurements in a high-throughput format.

4 Manipulating the Mechanical Microenvironment

In this section, we survey microengineered approaches to manipulating mechanical cues in the cellular environment, in order to: (1) control the microenvironment in ways that are not possible with conventional technologies; and (2) use high-throughput systems to study the effects of parametric or combinatorial mechanobiological stimuli on cell function. Surveyed technologies are categorized based on the engineering approach taken to manipulating the mechanical cues. These include spatially-defined surface features; systems to apply stimulation to cells by direct manipulation of liquids; and systems that interact with cells using forces applied through a solid structure (Fig. 4).

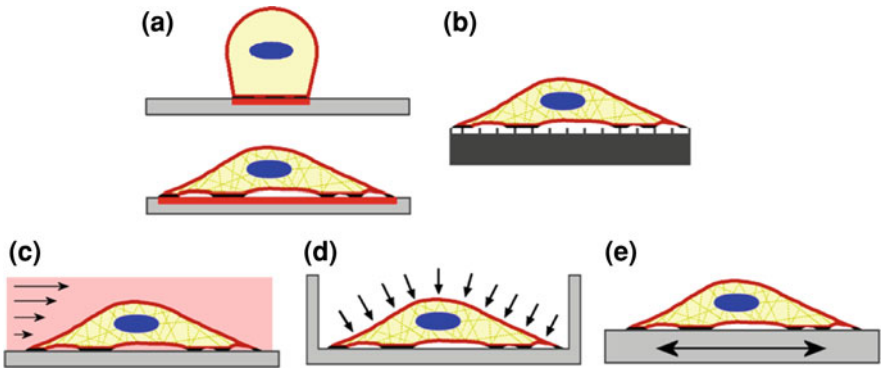

Fig. 4 Key experimental techniques in cell mechanobiology: **a** adhesion patterning; **b** surface topography; **c** fluid shear; **d** hydrostatic compression; **e** substrate deformation

4.1 … via Surface Features

Critical mechanobiological cues can be provided by designing the interface between culture materials and the cell itself. Surfaces can be engineered with natural or synthetic matrix proteins to control cell adhesion with sub-cellular resolution in length, enabling fundamental studies of the relationships between mechanical cell spreading area, matrix composition and cell fate and function. The surface topography is also a critical component, and both micro- and nano-patterned surfaces play a key role in modulating cell behaviour. The development of model systems for these studies would not be possible without microfabricated approaches.

4.1.1 Spatial Control of Adhesion

A variety of techniques are available to pattern two-dimensional culture surfaces, restricting cell attachment to specific regions (reviewed elsewhere [75, 112]). Briefly, adhesive proteins can be spatially patterned on a substrate using a number of different techniques, and the remaining areas are rendered non-adhesive to cell attachment using a suitable chemical or physical method. One of the most commonly used techniques to precisely pattern protein features on a surface is microcontact printing [113, 114], in which a PDMS stamp with microfabricated features is used to transfer patterns of proteins onto the desired substrate, much like a carved-potato stamp. Alternatively, a PDMS stencil can be fabricated with through-holes at the regions to be patterned. Adhesive proteins deposited on top of the stencil come in contact with the underlying substrate only at specific regions. Removal of the stencil results in the formation of a pattern of adhesive proteins or cells [115]. Alternatively, this method can be used to selectively activate the surface by plasma treatment, before subsequent deposition of the matrix proteins

and blocking agents [116, 117]. Removable microfluidic channels can also be used to deliver adhesive molecules to specific regions on a substrate [118]. These techniques enable the study of cells that are mechanically confined to specific regions or allowed to spread; and cells that are shaped such that they generate different cytoskeletal tension fields in different parts of a pattern. These techniques can also be coupled with other fabrication paradigms to create more complex microenvironments, including substrate-bound protein gradients [119] and designing temporally-manipulated matrix environments [120, 121] with electrically programmable adhesive surfaces [122]. Such approaches are promising in their ability to determine the temporal aspect of mechanobiology, but have not yet been used to directly manipulate the mechanical microenvironment.

Controlling available cell spreading area results in the mechanical structure of the cell being altered. Cells patterned on sub-cellular adhesive regions remained balled up on the substrate, while cells patterned on larger adhesive regions spread out over the available area. This geometric control of cell shape was found to regulate life and death: a large percentage of cells that were not allowed to spread underwent apoptosis, while spread cells maintained healthy phenotypes [123]. Regulation of cell spreading area was found to play a critical role in cell differentiation. Constrained mesenchymal stem cells (MSCs) differentiate to adipocytes, while MSCs that were allowed to spread underwent osteogenesis [11] (Fig. 5).

Pattern shape has also been shown to have a substantial impact on how cells function. Cells patterned on square islands have been shown to develop increased traction forces, as opposed to cells patterned on round islands [124], demonstrating oriented control of cytoskeletal tension. Cell orientation also direct lamellipodia extension [125] and migration [126], as cells migrate towards the blunt end of a

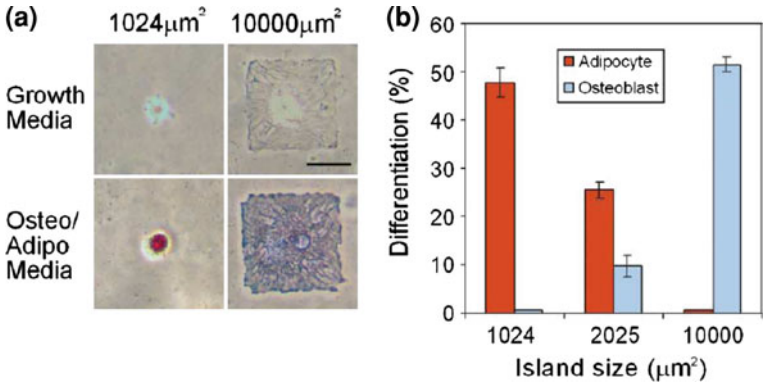

Fig. 5 Control of cell adhesion area directs stem cell differentiation (Source: adapted from McBeath et al. [11], with permission from Elsevier). **a** Cells cultured on patterns of increasing size cause, **b** increased osteogenic and reduced adipogenic differentiation, independent of chemical stimulation

tear-drop shaped pattern [127]. Differentiation of stem cells is also related to cytoskeletal tension, as demonstrated in a study by Ruiz et al. [128] in which MSCs at the edge of multicellular islands undergo osteogenic differentiation, while those in the center become adipocytes. More recently, Kilian et al. [129] have demonstrated this phenomena in single cells: high-aspect ratio patterns increased acto-myosin contractility in the cell, and promoted osteogenic MSC differentiation, whereas more rounded patterns form fewer stress fibers and differentiate towards an adipocyte lineage. Three-dimensional control of cell adhesion and spreading within a homogenous material remains to be attained, but shaped microwells have been successfully used to manipulate cell geometries [130].

The development of sub-cellular micropatterning techniques has enabled precise control over mechanical constraints applied to cells, and has resulted in a substantially better understanding of how cells behave in complex environments. Hence, controlling adhesion on two-dimensional substrates is an indispensable tool in cell mechanobiology.

4.1.2 Physical Topography

Cells are able to sense physical topography at a number of different scales: curvatures in the underlying substrate [131], micro-scaled ridges and grooves [132], nanoscale topographies [133], and anisotropic gradients in topography [134]. The effects of physical topography have been shown to be more influential on cell alignment and function than patterned chemical cues [135], and have been shown to better recapitulate in vivo cell behaviour [136, 137]. These substantial mechanobiological effects on cell adhesion, alignment and migration [138] have been well-established since the 1990s [132], particularly on substrates consisting of micropatterned grooves of varying heights and widths. As such, we will not review the standard techniques and methods in detail here, but interested readers are referred to a number of relevant reviews on the subject [40, 139, 140]. Recent novel contributions to this existing field include the use of a PDMS platform to produce a substrate with reconfigurable microtopographies. Compression of a PDMS substrate results in 550–800 nm high features, spaced $\sim$6 μm apart, and cells repeatably switched orientations in response to the applied topographical cues [141]. Other recent studies have shown that nanoscale topographies have a profound influence on cell function. MSCs differentiate to osteoblasts under the influence of nanopatterned substrates, without osteogenic components in the nutrient media [142]. Cell geometry, action potential conduction velocity and cell-to-cell coupling in nanopatterned cardiac tissue constructs are extraordinarily sensitive to the underlying patterns [143]. Likewise, neurons are able to sense nanometer scaled roughness [144]. Thus, both micro- and nano-topographies can play important roles in cellular response to the mechanical microenvironment, and can be eventually used to manipulate migration and matrix production in tissue engineering applications.

4.2 … via Fluid Control

Fluid flow is a defining component of the in vivo mechanical environment, and is particularly relevant to endothelial cells [145], which are exposed to both continuous and pulsatile shear stresses in vivo. Fluid shear stress plays a critical role in development and differentiation, and a large number of temporal and spatial shear stress patterns and magnitudes exist in vivo [33, 146]. Hydrostatic pressures are also known to play a role in cell biology, particularly in cartilage [28] and ocular tissues [31]. Macroscale equipment used to apply fluid shear stress, such as parallel plate flow chambers and cone-and-plate systems are reviewed elsewhere, as are systems to apply hydrostatic forces to cells in culture [147]. Miniaturizing these systems allows for greater throughput in creating multiple experimental conditions, device usability and portability, and precise control and uniformity in applied stimulation stresses.

4.2.1 Shear Stress

The use of artificial microfabricated channels is a suitable approach to mimic many in vivo environments as the reduction in scale enables well-controlled laminar flow in *n*th channels. Simple PDMS channels can be used in combination with passive pumping [148], pressure-driven flows or syringe pumps to apply shear to cultured cells. For example, Higgins et al. [20] used a single microfluidic channel to study the behaviour of sickle-type red blood cells in a physiologically relevant environment. Pressure (gravity)-driven flow was used to drive the defective red blood cells through a channel, to study the effects of geometric, physical, and biological factors in vascular occlusion and rescue.

Various design considerations need to be factored into scaling such simple channel systems up for higher-throughput studies, and one of the key criterion is the method for driving fluid flow through the system. External connections to various devices can often hinder scalability, and passive pumping is one technique which does not require these external connectors. In passive pumping, surface tension differences between droplets of different sizes at either end of a microfluidic channel drive fluid flow [148]. Although passive pumping has not yet been used to apply physiologically relevant shear stresses to cells, the authors suggest that this is one possible application of the technique [149]. Beebe and co-workers [149] have used this principle to demonstrate an automated high-throughput microfluidic system, in which a robotic system deposits and removes droplets across an array of microfluidic channels. Syringe pump and pressure-driven flows are harder to implement in high-throughput systems, but serve adequately for devices designed for lower-throughput experiments. Careful design of the microfluidic channels can be used to maintain increased throughput while minimizing the world-to-chip interface connection issues that arise: connections are typical sources of device failure. Channels with varying widths connected to a

single fluid delivery source can be used to generate a range of fluid velocities, and hence applied shear stresses across a single device [94]. Channel bends and curves can also be used to apply spatially distinctive shear stresses [150]. Carefully designed channels of increasing width can also be used to apply linearly increasing shear stresses across a single channel [151].

More complex technologies have also been developed to further miniaturize such systems. The development of the 'Quake valve' [85] enabled the large-scale integration of multiplexed microfluidic valves on a single chip [152]. Using a multilayered PDMS microfluidic system, the valves consist of a pressure control channel which deforms thin PDMS films to block flow in fluidic channels—much like stepping on a garden hose. The valves can be used to direct fluid flow or drive it by operating as a peristaltic pump. Using these valves, an automated, high-throughput microfluidic cell culture system was developed, in which 96 culture chambers could be individually addressed [153]. Such systems have not as yet been used to explicitly explore the effects of shear stress on cultured cells, but can do so in principle.

Use of the Quake system of valves still requires an undesirably large number of world-to-chip interfaces. Technology developed in the Takayama lab may address this concern: commercially available Braille displays are used to deform the base of a flexible microfluidic channel [154]. Pin actuation can be independently and automatically controlled to manipulate fluid within the microchannels. Although it is not as scalable, it is simpler to implement and has been used to apply shear stress to endothelial cells in culture [155].

Microengineered technologies for fluid shear can also improve functionality in a variety of ways. In situ measurements of shear stresses can be made using MEMS-based 'hair' sensors, incorporated directly into the shear channels [79]. Direct readouts can also be integrated into the microfluidic devices, for example, Tolan et al. [156] have developed an integrated luminescence detection system in which fluorescent reagents react with erythrocyte lysates to simultaneously monitor various biochemicals produced by erythrocytes under shear in underlying channels.

4.2.2 Hydrostatic Pressure

Classification of hydrostatic pressure as "mechanical" stimulation is somewhat contentious: increases in external pressure cause increases in internal pressure, presumably resulting in no net cell deformation. Changes in cell function may instead be due to differences in gas solubility at different pressures, if gas concentrations are not controlled independently of the applied pressure. The only presently reported microfabricated system designed to apply hydrostatic pressures to cells was developed by Sim et al. [157] who used a single pressure source to create a range of deflections in suspended PDMS membranes of various diameters. The differing deflections cause different pressures in isolated culture chambers, enabling the high-throughput evaluation of MSC response to a range of hydrostatic pressures.

4.3 … via Solid Deformation

Mechanical cues presented to cells by way of deformations of the external environment are critical factors in cell regulation. Depending on the stiffness of the surrounding matrix, cell-generated traction forces generate large or small deflections, which are then sensed and dictate cell fate and function [158]. Similarly, cells sense deformations in their surroundings caused by *externally* applied deformations, and respond accordingly [28, 147].

4.3.1 Substrate Stiffness

Substrate (two-dimensional) and matrix (three-dimensional) stiffness is generally manipulated by means of differentially crosslinked polymer substrates. Polyacrylamide (PA) systems are perhaps the best established biomaterial substrate for this purpose, and was first used in the 1990s to study cell locomotion and focal adhesion formation as a function of substrate stiffness [159]. Engler et al. more recently used PA gels to show that substrate stiffness directs stem cell lineage differentiation. MSCs differentially displayed neurogenic, myogenic and osteogenic differentiation on substrates with modulus increasing from 0.1 to 40 kPa [160]. More recently, poly(ethylene) glycol (PEG) has shown promise as a "blank slate" fully customizable matrix material with a considerable range of formulation-dependent mechanical modulus values [161]. PEG hydrogels are particularly interesting in terms of microfabrication, as they have been integrated into microfluidic devices, using molding [162] and photopatterning [163–165] techniques. Direct molding of PEG hydrogels has resulted in a high-throughput combinatorial screening system for stiffness, adhesive ligands and chemical cues [166, 167].

In addition to the possible increases in throughput due to miniaturization, two further advantages are gained in microfabricated environments to study substrate stiffness. First, micropatterned mechanical gradients can be defined in both two- [168, 169] and three-dimensional [170] culture systems to study the effects of non-uniform substrate stiffness. Photopolymerizable hydrogels with varying concentrations of crosslinker are flushed into a microfluidic channel, and a standard gradient generator channel scheme and UV lamp are used to create polymerizable hydrogel structures with a stiffness gradient [139, 168], in order to study adhesion, spreading and migration in complex environments.

Second, when working on the length scale of tens of microns, spacing between hydrogel surfaces and adhesive structures can be used to modulate effective stiffness experienced by cells. Though not ostentatiously a "microfabricated device", Yip et al. report a culture technique by which cells cultured on thick ($\sim$1 mm) collagen gels experience lower stiffness than thin ($\sim$10 μm) gels firmly attached to a glass coverslip [171]. As is the case with the fictional princess who is able to feel a hard pea beneath several mattresses [172], cells 'feel' the stiffer substrate through the thin, compliant hydrogel. This effect is also seen in the

microfabricated three-dimensional culture platform developed by Legant et al. (previously reviewed in Sect. 3.2.2), in which PDMS posts of different dimensions anchor a cell-laden collagen hydrogel. Cell contractility is influenced by posts of different dimensions, as cells experience the differing stiffness through the matrix material [110]. This approach to manipulating mechanical stiffness avoids complicating factors in changing concentrations of crosslinking agents, such as an increase in adhesion sites with increasing crosslink density.

4.3.2 Externally Applied Strains

Although in vivo mechanical strain modes are quite complex, the effects and underlying mechanisms can be studied using simplified in vitro models. Strains can be applied to cells cultured on substrates by uniaxial, biaxial, equibiaxial, compressive and tensile loading, in both two- and three-dimensional materials [173]. Cells are sensitive to strain magnitude [174], applied strain field [175] and stimulation frequency [176]; and response to these mechanical parameters are modulated by the other features of the microenvironment. Current platforms for mechanical stimulation [147] are limited in throughput, and are hence unable to probe combinations of mechanobiological parameters.

A few microfabricated systems have been developed for these applications. Kurpinski et al. [177] and Wang et al. [178] aligned MSCs and fibroblasts along topographically patterned stretchable substrates, before applying uniaxial strains in a macroscale bioreactor. They demonstrated that mechanical stimulation influences gene expression, protein expression and proliferation differentially dependent on the direction of strain to the aligned patterns. Tan et al. [179] used a similar topographical patterning approach to align cells along specific orientations, but applied a pressure differential across circular patterned diaphragms. The pressure differential caused the diaphragm to bulge, creating non-uniform anisotropic biaxial strains in different regions of the device. Gopalan et al. [180] followed a similar approach, except the diaphragms were distended by a loading post in a manually actuated screw-type system.

Each of these systems were relatively limited in throughput. To address this, Takayama and co-workers used a commercial Braille display system to apply non-uniform substrate deformations to cells cultured on thin films (Fig. 6). The films were distended by the hemispherical-headed pin, applying non-uniform strains. The automated Braille displays enabled screening for various cyclic loading frequencies ranging from 0.2 to 5 Hz, and differences were found in degree of alignment of various cell types in response to frequency and stimulation duration [176].

In order to address the need to apply well-characterized uniform strains to cultured cells, Moraes et al. [174] developed a microfabricated array-based bioreactor system, in which a circular loading post is vertically actuated to distend a culture diaphragm, producing an equibiaxial uniform strain applied to cells on the diaphragm surface (Fig. 7). By varying geometry of the individual units, a single

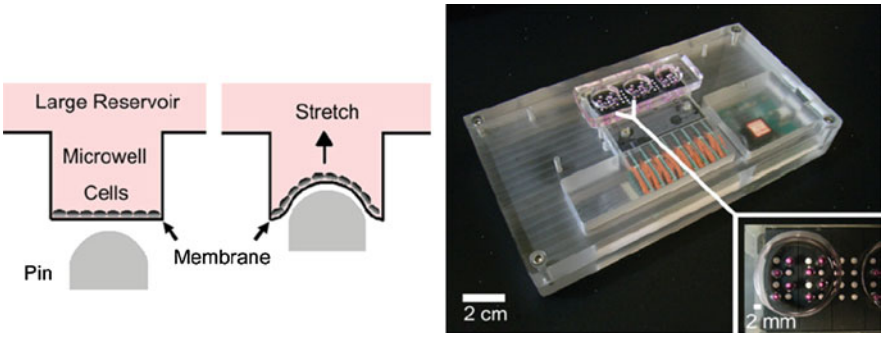

Fig. 6 A Braille display integrated into microfabricated well system, in which the displacement pin creates biaxial strains on the cell surface (Source: Kamotani et al. [189], with permission from Elsevier)

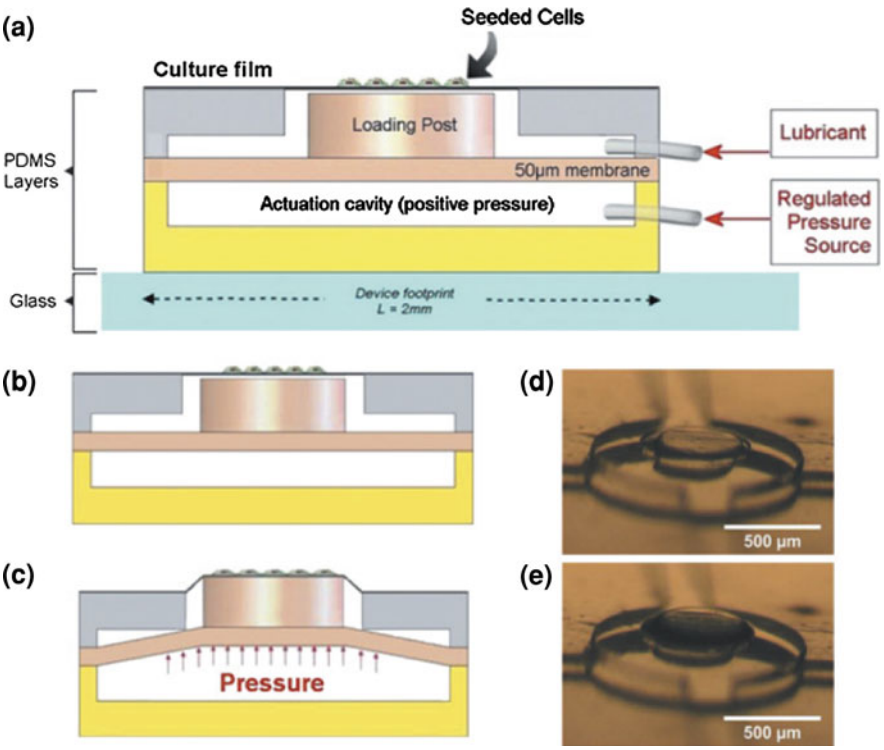

Fig. 7 A microfabricated array designed to apply cyclic uniform mechanical strains to cells cultured on the device surface. **a** Schematic overview of device operation; and device at (**b**, **d**) rest and (**c**, **e**) under load (Source: Moraes et al. [174], reproduced by permission of the Royal Society of Chemistry)

pressure source was used to simultaneously produce mechanical strains ranging from 2 to 15% across the array. Strains were characterized over 100,000 loading cycles, and negligible changes were observed. This is in contrast to commercially available equipment, which has been shown to reduce strain levels over several thousand cycles of loading [181]. The advantage is likely due to mechanical properties arising from using a thin (<15 μm) microfabricated culture diaphragm. Using the high-throughput system, the group identified a novel time- and strain magnitude-dependent relationship in translocation of the β-catenin protein into the cell nucleus.

Moraes et al. [163] also extended their technology to apply compressive stimuli to cells in three-dimensional biomaterials (Fig. 8). Cell-laden hydrogels were photopatterned between similar loading posts and a rigid glass substrate. Raising the posts simultaneously applied compressive strains ranging from 2 to 25%, and the group observed a non-linear relationship between matrix and cell deformation,

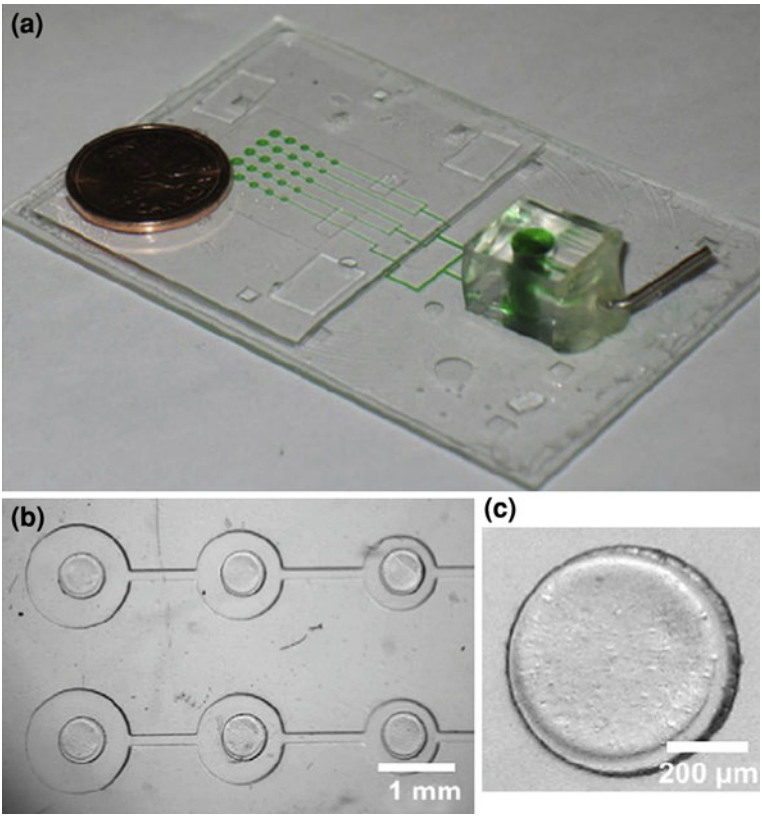

Fig. 8 Microfabricated array designed to apply cyclic compressive strains to cells cultured within a photopolymerized three-dimensional biomaterial. (Source: Moraes et al. [163], with permission from Elsevier)

further emphasizing the need for high-throughput mechanobiological screening platforms.

5 Discussion and Conclusions

The development and use of microfabricated tools for experiments in biomechanics and mechanobiology can have a profound impact on understanding the relationship between mechanics and cellular form and function. Increases in experimental throughput and experimental simplicity can substantially improve our understanding of rare cell populations, and how these cells respond to varied parameters. Microfabrication also allows designers to combine multiple stimulation and measurement techniques. Sniadecki et al. [182] linked biomechanics and mechanobiology in developing a system designed to measure traction forces in response to an externally applied deformation. Combinatorial stimulation with a variety of mechanical cues is also possible. To date, this has included combining topography with shear [183] and with substrate strain [177, 179, 180]. Work in evaluating combinatorial sensitivity of cells to other forms of mechanical cues is ongoing.

However, recent findings have suggested that the use of certain microfabricated systems in studying biological cells may have under-appreciated and substantial side effects. Beebe and coworkers have determined that PDMS, used ubiquitously in microfabricated devices, sequesters small bioactive molecules and releases small chain polymers into surround media, which is then incorporated into the cell membrane [184, 185]. This suggests that alternative techniques such as hot embossing, to create microfluidic channels using generally accepted materials for cell culture, such as polystyrene would be a more acceptable approach. Alternatively, others have investigated using coating films of polyurethane on PDMS materials, to provide cell adhesion sites and improve biological compatibility [186]. In general, better characterization of the effects of microdevice materials and cell culture techniques on biological function is needed, before such techniques can be broadly adopted into mainstream wetlabs.

There is also a substantial divide to cross in terms of expertise: device design, fabrication and validation require specific and detailed skill sets, and it is difficult for experts in microdevice design to thoroughly understand the relevant biology, and vice versa. Devices can often be complicated to operate in practice, and are frequently unable to provide a reliable platform to study biological systems. Simplifying device designs may aid in solving these issues of usability, but more generally, bridging the gap between microdevice engineers and cell biologists will require interdisciplinary collaborations, or integrative thinkers in both areas developing tools to understand and answer specific biological questions. The promise of such techniques is powerful, and successful research programs integrating these disciplines will produce new insights and advances in both.

References

1. Ridley, A.J., Hall, A.: The small Gtp-binding protein Rho regulates the assembly of focal adhesions and actin stress fibers in response to growth-factors. Cell **70**, 389–399 (1992)
2. Smith, P.G., Deng, L.H., Fredberg, J.J., et al.: Mechanical strain increases cell stiffness through cytoskeletal filament reorganization. Am. J. Physiol. Lung Cell. Mol. Physiol. **285**, L456–L463 (2003)
3. Chen C.S., Tan J., Tien J.: Mechanotransduction at cell-matrix and cell-cell contacts. Annu Rev Biomed Eng. **6**, 275–302 (2004).
4. Darling, E.M., Topel, M., Zauscher, S., et al.: Viscoelastic properties of human mesenchymally-derived stem cells and primary osteoblasts, chondrocytes, and adipocytes. J. Biomech. **41**, 454–464 (2008)
5. Huang, H.D., Kamm, R.D., Lee, R.T.: Cell mechanics and mechanotransduction: pathways, probes, and physiology. Am. J. Physiol. Cell Physiol. **287**, C1–C11 (2004)
6. Titushkin, I., Cho, M.: Modulation of cellular mechanics during osteogenic differentiation of human mesenchymal stem cells. Biophys. J. **93**, 3693–3702 (2007)
7. Janmey, P.A., McCulloch, C.A.: Cell mechanics: integrating cell responses to mechanical stimuli. Annu. Rev. Biomed. Eng. **9**, 1–34 (2007)
8. Fletcher, D.A., Mullins, R.D.: Cell mechanics and the cytoskeleton. Nature **463**, 485–492 (2010)
9. Treiser, M.D., Yang, E.H., Gordonov, S., et al.: Cytoskeleton-based forecasting of stem cell lineage fates. Proc. Natl. Acad. Sci. USA **107**, 610–615 (2010)
10. Hsieh, M.H., Nguyen, H.T.: Molecular mechanism of apoptosis induced by mechanical forces. Int. Rev. Cytol. **245**, 45–90 (2005)
11. McBeath, R., Pirone, D.M., Nelson, C.M., et al.: Cell shape, cytoskeletal tension, and RhoA regulate stem cell lineage commitment. Dev. Cell. **6**, 483–495 (2004)
12. Ridley, A.J., Schwartz, M.A., Burridge, K., et al.: Cell migration: integrating signals from front to back. Science **302**, 1704–1709 (2003)
13. Kaibuchi, K., Kuroda, S., Amano, M.: Regulation of the cytoskeleton and cell adhesion by the Rho family GTPases in mammalian cells. Annu. Rev. Biochem. **68**, 459–486 (1999)
14. Ingber, D.E.: Cellular mechanotransduction: putting all the pieces together again. FASEB J. **20**, 811–827 (2006)
15. Orr, A.W., Helmke,B.P., Blackman, B.R., et al.: Mechanisms of mechanotransduction. Dev Cell. **10**, 11–20 (2006)
16. Ward, K.A., Li, W.I., Zimmer, S., et al.: Viscoelastic properties of transformed cells: role in tumor cell progression and metastasis formation. Biorheology. **28**, 301–313 (1991)
17. Suresh, S.: Biomechanics and biophysics of cancer cells. Acta Biomater. **3**, 413–438 (2007)
18. Suresh, S., Spatz, J., Mills, J.P. et al.: Connections between single-cell biomechanics and human disease states: gastrointestinal cancer and malaria. Acta Biomater. **1**, 15–30 (2005)
19. Lee, G.Y, Lim, C.T.: Biomechanics approaches to studying human diseases. Trends Biotechnol. **25**, 111–118 (2007)
20. Higgins, J.M., Eddington, D.T., Bhatia, S.N., et al.: Sickle cell vasoocclusion and rescue in a microfluidic device. Proc. Natl. Acad. Sci. USA **104**, 20496–20500 (2007)
21. Merryman, W.D., Engler, A.J.: Innovations in cell mechanobiology. J. Biomech. **43**, 1–1 (2010)
22. Stoltz, J.F., Wang, X.: From biomechanics to mechanobiology. Biorheology **39**, 5–10 (2002)
23. Guck J., Schinkinger S., Lincoln B., et al.: Optical deformability as an inherent cell marker for testing malignant transformation and metastatic competence. Biophys. J. **88**, 3689–3698 (2005)
24. Desai, R.A., Gao, L., Raghavan, S., et al.: Cell polarity triggered by cell-cell adhesion via E-cadherin. J. Cell Sci. **122**, 905–911 (2009)
25. Ingber, D.E.: Mechanobiology and diseases of mechanotransduction. Ann. Med. **35**, 564–577 (2003)

26. Wozniak, M.A., Chen, C.S.: Mechanotransduction in development: a growing role for contractility. Nat. Rev. Mol. Cell Biol. **10**, 34–43 (2009)
27. van der Meulen M.C., Huiskes, R.: Why mechanobiology? A survey article. J. Biomech. **35**, 401–414 (2002)
28. Wang, J.H., Thampatty, B.P.: An introductory review of cell mechanobiology. Biomech. Model Mechanobiol. **5**, 1–16 (2006)
29. Bao, G., Suresh, S.: Cell and molecular mechanics of biological materials. Nat. Mater. **2**, 715–725 (2003)
30. Makale M.: Cellular mechanobiology and cancer metastasis. Birth Defects Res. C Embryo Today. **81**, 329–343 (2007)
31. Jaalouk, D.E., Lammerding, J.: Mechanotransduction gone awry. Nat. Rev. Mol. Cell Biol. **10**, 63–73 (2009)
32. Ingber D.E.: Mechanical control of tissue morphogenesis during embryological development. Int. J. Dev. Biol. **50**, 255–266 (2006)
33. Chen, J.H., Liu, C., You, L., et al.: Boning up on Wolff's Law: mechanical regulation of the cells that make and maintain bone. J. Biomech. **43**, 108–118 (2010)
34. Wang, J.H.: Mechanobiology of tendon. J. Biomech. **39**, 1563–1582 (2006)
35. Butcher, J.T., Simmons, C.A., Warnock, J.N.: Mechanobiology of the aortic heart valve. J. Heart Valve Dis. **17**, 62–73 (2008)
36. Setton, L.A., Chen, J.: Cell mechanics and mechanobiology in the intervertebral disc. Spine **29**, 2710–2723 (2004)
37. Lammi, M.J.: Current perspectives on cartilage and chondrocyte mechanobiology. Biorheology **41**, 593–596 (2004)
38. Huselstein, C., Netter, P., de Isla, N., et al.: Mechanobiology, chondrocyte and cartilage. Biomed. Mater. Eng. **18**, 213–220 (2008)
39. Loh, O., Vaziri, A., Espinosa, H.D.: The potential of MEMS for advancing experiments and modeling in cell mechanics. Exp. Mech. **49**, 105–124 (2009)
40. Kim, D.H., Wong, P.K., Park J., et al.: Microengineered platforms for cell mechanobiology. Annu. Rev. Biomed. Eng. **11**, 203—233 (2009)
41. Vanapalli, S.A., Duits, M.H., Mugele, F.: Microfluidics as a functional tool for cell mechanics. Biomicrofluidics **3**, 12006 (2009)
42. Sims, C.E., Allbritton, N.L.: Analysis of single mammalian cells on-chip. Lab Chip **7**, 423–440 (2007)
43. Ferrell, J.E., Jr., Machleder, E.M.: The biochemical basis of an all-or-none cell fate switch in Xenopus oocytes. Science **280**, 895–898 (1998)
44. Ethier, C.R., Simmons, C.A.: Introductory Biomechanics: from Cells to Organisms. Cambridge University Press, London (2007)
45. Hoffman, B.D., Crocker, J.C.: Cell mechanics: dissecting the physical responses of cells to force. Annu. Rev. Biomed. Eng. **11**, 259–288 (2009)
46. Lim, C.T., Zhou, E.H., Quek, S.T.: Mechanical models for living cells—a review. J. Biomech. **39**:195–216 (2006)
47. Pelling, A.E., Horton, M.A.: An historical perspective on cell mechanics. Pflugers Arch. **456**, 3–12 (2008)
48. Lim, C.T., Zhou, E.H., Li, A., et al.: Experimental techniques for single cell and single molecule biomechanics. Mater. Sci. Eng. C Biomim. Supramol. Syst. **26**, 1278–1288 (2006)
49. Thoumine, O., Ott, A., Cardoso, O., et al.: Microplates: a new tool for manipulation and mechanical perturbation of individual cells. J. Biochem. Biophys. Methods **39**, 47–62 (1999)
50. Peeters, E.A., Bouten, C.V., Oomens, C.W., et al.: Monitoring the biomechanical response of individual cells under compression: a new compression device. Med. Biol. Eng. Comput. **41**, 498–503 (2003)
51. Guck, J., Ananthakrishnan, R., Mahmood, H., et al.: The optical stretcher: a novel laser tool to micromanipulate cells. Biophys. J. **81**, 767–784 (2001)

52. Mitchison, J.M., Swann, M.M.: The mechanical properties of the cell surface .1. The cell elastimeter. J. Exp. Biol. **31**, 443–460 (1954)
53. Hochmuth, R.M.: Micropipette aspiration of living cells. J. Biomech. **33**, 15–22 (2000)
54. Wang, N., Ingber, D.E.: Probing transmembrane mechanical coupling and cytomechanics using magnetic twisting cytometry. Biochem. Cell Biol. **73**, 327–335 (1995)
55. Bausch, A.R., Ziemann, F., Boulbitch, A.A., et al.: Local measurements of viscoelastic parameters of adherent cell surfaces by magnetic bead microrheometry. Biophys. J. **75**, 2038–2049 (1998)
56. Li, J., Dao, M., Lim, C.T. et al.: Spectrin-level modeling of the cytoskeleton and optical tweezers stretching of the erythrocyte. Biophys. J. **88**, 3707–3719 (2005)
57. Mills, J.P., Qie, L., Dao, M., et al.: Nonlinear elastic and viscoelastic deformation of the human red blood cell with optical tweezers. Mech. Chem. Biosyst. **1**, 169–180 (2004)
58. Costa, K.D.: Single-cell elastography: probing for disease with the atomic force microscope. Dis Markers. **19**, 139–154 (2003)
59. de Vries, A.H., Krenn, B.E,, van Driel, R., et al.: Micro magnetic tweezers for nanomanipulation inside live cells. Biophys. J. **88**, 2137–2144 (2005)
60. Panchawagh, H.V., Serrell, D., Finch, D.S., et al.: Design and characterization of a BioMEMS device for in vitro mechanical stimulation of single adherent cells. Micro-Electro-Mechanical Syst. **7**, 19–25 (2005)
61. Scuor, N., Gallina, P., Panchawagh, H.V, et al.: Design of a novel MEMS platform for the biaxial stimulation of living cells. Biomed. Microdevices **8**, 239–246 (2006)
62. Zhang, W.Y., Gnerlich, M., Paly, J.J., et al.: A polymer V-shaped electrothermal actuator array for biological applications. J. Micromech. Microeng. **18**, 075020 (2008)
63. Serrell, D.B., Law, J., Slifka, A.J., et al.: A uniaxial bioMEMS device for imaging single cell response during quantitative force-displacement measurements. Biomed. Microdevices **10**, 883–889 (2008)
64. Voldman, J.: Electrical forces for microscale cell manipulation. Annu. Rev. Biomed. Eng. **8**, 425–454 (2006)
65. Mukundan, V., Pruitt, B.L.: MEMS electrostatic actuation in conducting biological media. J. Microelectromech. Syst. **18**, 405–413 (2009)
66. Waugh, R., Evans, E.A.: Thermoelasticity of red blood cell membrane. Biophys. J. **26**, 115–131 (1979)
67. Engelhardt, H., Gaub, H., Sackmann, E.: Viscoelastic properties of erythrocyte membranes in high-frequency electric fields. Nature. **307**, 378–380 (1984)
68. Korlach, J., Reichle, C., Muller, T. et al.: Trapping, deformation, and rotation of giant unilamellar vesicles in octode dielectrophoretic field cages. Biophys. J. **89**, 554–562 (2005)
69. Wong, P.K., Tan, W., Ho, C.M.: Cell relaxation after electrodeformation: effect of latrunculin A on cytoskeletal actin. J. Biomech. **38**, 529–535 (2005)
70. Kim, K., Cheng, J., Liu, Q. et al.: Investigation of mechanical properties of soft hydrogel microcapsules in relation to protein delivery using a MEMS force sensor. J. Biomed. Mater. Res. Part A **92A**, 103–113 (2010)
71. Serrell, D.B., Oreskovic, T.L., Slifka, A.J., et al.: A uniaxial bioMEMS device for quantitative force-displacement measurements. Biomed. Microdevices **9**, 267–275 (2007)
72. Yang, S., Saif, T.: Reversible and repeatable linear local cell force response under large stretches. Exp. Cell Res. **305**, 42–50 (2005)
73. Yang, S., Saif, M.T.: Force response and actin remodeling (agglomeration) in fibroblasts due to lateral indentation. Acta Biomater. **3**, 77–87 (2007)
74. Yang, S., Saif, M.T.A.: Microfabricated force sensors and their applications in the study of cell mechanical response. Exp. Mech. **49**, 135–151 (2009)
75. Falconnet, D., Csucs, G., Grandin, H.M., et al.: Surface engineering approaches to micropattern surfaces for cell-based assays. Biomaterials **27**, 3044–3063 (2006)
76. Fink, J., Thery, M., Azioune, A., et al.: Comparative study and improvement of current cell micro-patterning techniques. Lab Chip **7**, 672–680 (2007)

77. Lu, Z., Moraes, C., Zhao, Y., et al.: A micromanipulation system for single cell deposition. In: IEEE International Conference on Robotics and Automation (ICRA2010), Alaska, 3–8 May 2010
78. Chen, N.N., Tucker, C., Engel, J.M., et al.: Design and characterization of artificial haircell sensor for flow sensing with ultrahigh velocity and angular sensitivity. J. Microelectromech. Syst. **16**, 999–1014 (2007)
79. Liu, C.: Micromachined biomimetic artificial haircell sensors. Bioinspir. Biomim. **2**, S162–S169 (2007)
80. Sasoglu, F.M., Bohl, A.J., Layton, B.E.: Design and microfabrication of a high-aspect-ratio PDMS microbeam array for parallel nanonewton force measurement and protein printing. J. Micromech. Microeng. **17**, 623–632 (2007)
81. Sasoglu, F.M., Bohl, A.J., Allen, K.B., et al.: Parallel force measurement with a polymeric microbeam array using an optical microscope and micromanipulator. Comput. Methods Programs Biomed. **93**, 1–8 (2009)
82. Liu, X.Y., Fernandes, R., Jurisicova, A., et al.: In situ mechanical characterization of mouse oocytes. Lab Chip **10**, 2154–2161 (2010)
83. Lincoln, B., Schinkinger, S., Travis, K., et al.: Reconfigurable microfluidic integration of a dual-beam laser trap with biomedical applications. Biomed. Microdevices **9**, 703–710 (2007)
84. Rosenbluth, M.J., Lam, W.A., Fletcher, D.A.: Force microscopy of nonadherent cells: a comparison of leukemia cell deformability. Biophys. J. **90**, 2994–3003 (2006)
85. Unger, M.A., Chou, H.P., Thorsen, T., et al.: Monolithic microfabricated valves and pumps by multilayer soft lithography. Science. **288**, 113–116 (2000)
86. Kim, Y.C., Kang, J.H., Park, S.J., et al.: Microfluidic biomechanical device for compressive cell stimulation and lysis. Sens. Actuators B Chem. **128**, 108–116 (2007)
87. Hohne, D.N., Younger, J.G., Solomon, M.J.: Flexible microfluidic device for mechanical property characterization of soft viscoelastic solids such as bacterial biofilms. Langmuir **25**, 7743–7751 (2009)
88. Kim, Y.C., Park, S.J., Park, J.K.: Biomechanical analysis of cancerous and normal cells based on bulge generation in a microfluidic device. Analyst **133**, 1432–1439 (2008)
89. Moraes, C., Wyss, K., Brisson, E., et al.: An Undergraduate lab (on-a-chip): probing single cell mechanics on a microfluidic platform. Cell. Mol. Bioeng. (2010). doi:10.1007/s12195-010-0124-0.
90. Moraes, C., Tong, J.H., Liu, X.Y., et al.: Parallel micropipette aspirator arrays for high-throughput mechanical characterization of biological cells. In: Proceedings of the Micro Total Analysis Systems Conference, pp. 751–753 (2007)
91. Sagvolden, G., Giaever, I., Pettersen, E.O., et al.: Cell adhesion force microscopy. Proc. Natl. Acad. Sci. USA **96**, 471–476 (1999)
92. Shao, J.Y., Xu, J.B.: A modified micropipette aspiration technique and its application to tether formation from human neutrophils. J. Biomech. Eng. Trans. ASME **124**, 388–396 (2002)
93. Fu, G., Milburn, C., Mwenifumbo, S., et al.: Shear assay measurements of cell adhesion on biomaterials surfaces. Mater. Sci. Eng. C-Biomimetic Supramol. Syst. **29**, 1293–1301 (2009)
94. Lu, H., Koo, L.Y., Wang, W.C.M., et al.: Microfluidic shear devices for quantitative analysis of cell adhesion. Anal. Chem. **76**, 5257–5264 (2004)
95. Young, E.W.K., Wheeler, A.R., Simmons, C.A.: Matrix-dependent adhesion of vascular and valvular endothelial cells in microfluidic channels. Lab Chip **7**, 1759–1766 (2007)
96. Kwon, K.W., Choi, S.S., Lee, S.H., et al.: Label-free, microfluidic separation and enrichment of human breast cancer cells by adhesion difference. Lab Chip **7**, 1461–1468 (2007)
97. Couzon, C., Duperray, A., Verdier, C. Critical stresses for cancer cell detachment in microchannels. Eur. Biophys. J. Biophys. Lett. **38**, 1035–1047 (2009)
98. Wankhede, S.P., Du, Z.Q., Berg, J.M., et al.: Cell detachment model for an antibody-based microfluidic cancer screening system. Biotechnol. Prog. **22**, 1426–1433 (2006)

99. Plouffe, B.D., Radisic, M., Murthy, S.K: Microfluidic depletion of endothelial cells, smooth muscle cells, and fibroblasts from heterogeneous suspensions. Lab Chip **8**, 462–472 (2008)
100. Plouffe, B.D., Brown, M.A., Iyer, R.K., et al.: Controlled capture and release of cardiac fibroblasts using peptide-functionalized alginate gels in microfluidic channels. Lab Chip **9**, 1507–1510 (2009)
101. Plouffe, B.D., Njoka, D.N., Harris, J., et al.: Peptide-mediated selective adhesion of smooth muscle and endothelial cells in microfluidic shear flow. Langmuir **23**, 5050–5055 (2007)
102. Gutierrez, E., Groisman, A.: Quantitative measurements of the strength of adhesion of human neutrophils to a substratum in a microfluidic device. Anal. Chem. **79**, 2249–2258 (2007)
103. Harris, A.K., Wild, P., Stopak, D.: Silicone rubber substrata: a new wrinkle in the study of cell locomotion. Science **208**, 177–179 (1980)
104. Vanni, S., Lagerholm, B.C., Otey, C., et al.: Internet-based image analysis quantifies contractile behavior of individual fibroblasts inside model tissue. Biophys. J. **84**, 2715–2727 (2003)
105. Dembo, M., Oliver, T., Ishihara, A., et al.: Imaging the traction stresses exerted by locomoting cells with the elastic substratum method. Biophys, J. **70**, 2008–2022 (1996)
106. Galbraith, C.G., Sheetz, M.P.: A micromachined device provides a new bend on fibroblast traction forces. Proc. Natl. Acad. Sci. USA **94**, 9114–9118 (1997)
107. Galbraith, C.G., Sheetz, M.P.: Forces on adhesive contacts affect cell function. Curr. Opin. Cell Biol. **10**, 566–571 (1998)
108. Tan, J.L., Tien, J., Pirone, D.M., et al.: Cells lying on a bed of microneedles: an approach to isolate mechanical force. Proc. Natl. Acad. Sci. USA **100**, 1484–1489 (2003)
109. Li, B., Xie, L., Starr, Z.C., et al.: Development of micropost force sensor array with culture experiments for determination of cell traction forces. Cell Motil. Cytoskeleton **64**, 509–518 (2007)
110. Legant, W.R., Pathak, A., Yang, M.T., et al.: Microfabricated tissue gauges to measure and manipulate forces from 3D microtissues. Proc. Natl. Acad. Sci. USA **106**, 10097–10102 (2009)
111. Chen, C.S.: Mechanotransduction—a field pulling together? J. Cell Sci. **121**, 3285–3292 (2008)
112. Barbulovic-Nad, I., Lucente, M., Sun, Y. et al.: Bio-microarray fabrication techniques—a review. Crit. Rev. Biotechnol. **26**, 237–259 (2006)
113. Schmalenberg, K.E., Buettner, H.M., Uhrich, K.E.: Microcontact printing of proteins on oxygen plasma-activated poly(methyl methacrylate). Biomaterials **25**, 1851–1857 (2004)
114. Bernard, A., Renault, J.P., Michel, B., et al.: Microcontact printing of proteins. Adv. Mater. **12**, 1067–1070 (2000)
115. Ostuni, E., Kane, R., Chen, C.S., et al.: Patterning mammalian cells using elastomeric membranes. Langmuir **16**, 7811–7819 (2000)
116. Langowski, B.A., Uhrich, K.E.: Microscale plasma-initiated patterning (muPIP). Langmuir **21**, 10509–10514 (2005)
117. Rhee, S.W., Taylor, A.M., Tu, C.H., et al.: Patterned cell culture inside microfluidic devices. Lab Chip **5**, 102–107 (2005)
118. Takayama, S., McDonald, J.C., Ostuni, E., et al.: Patterning cells and their environments using multiple laminar fluid flows in capillary networks. Proc. Natl. Acad. Sci. USA **96**, 5545–5548 (1999)
119. Jiang, X., Xu, Q., Dertinger, S.K., et al.: A general method for patterning gradients of biomolecules on surfaces using microfluidic networks. Anal. Chem. **77**, 2338–2347 (2005)
120. Yeo, W.S., Yousaf, M.N., Mrksich, M.: Dynamic interfaces between cells and surfaces: electroactive substrates that sequentially release and attach cells. J. Am. Chem. Soc. **125**, 14994–14995 (2003)
121. Yeo, W.S., Mrksich, M.: Electroactive self-assembled monolayers that permit orthogonal control over the adhesion of cells to patterned substrates. Langmuir **22**, 10816–10820 (2006)
122. Fan, C.Y., Tung, Y.C., Takayama, S., et al.: Electrically programmable surfaces for configurable patterning of cells. Adv. Mater. **20**, 1418 (2008)

123. Chen, C.S., Mrksich, M., Huang, S., et al.: Geometric control of cell life and death. Science **276**, 1425–1428 (1997)
124. Wang, N., Ostuni, E., Whitesides, G.M., et al.: Micropatterning tractional forces in living cells. Cell Motil Cytoskeleton **52**, 97–106 (2002)
125. Parker, K.K., Brock, A.L., Brangwynne, C., et al.: Directional control of lamellipodia extension by constraining cell shape and orienting cell tractional forces. FASEB J. **16**, 1195–1204 (2002)
126. Brock, A., Chang, E., Ho, C.C., et al.: Geometric determinants of directional cell motility revealed using microcontact printing. Langmuir **19**, 1611–1617 (2003)
127. Jiang, X., Bruzewicz, D.A., Wong, A.P., et al.: Directing cell migration with asymmetric micropatterns. Proc. Natl. Acad. Sci USA **102**, 975–978 (2005)
128. Ruiz, S.A., Chen, C.S.: Emergence of patterned stem cell differentiation within multicellular structures. Stem Cells **26**, 2921–2927 (2008)
129. Kilian, K.A., Bugarija, B., Lahn, B.T., et al.: Geometric cues for directing the differentiation of mesenchymal stem cells. Proc. Natl. Acad. Sci. USA **107**, 4872–4877 (2010)
130. Ochsner, M., Dusseiller, M.R., Grandin, H.M., et al.: Micro-well arrays for 3D shape control and high resolution analysis of single cells. Lab Chip **7**, 1074–1077 (2007)
131. Park, J.Y., Lee, D.H., Lee, E.J., et al.: Study of cellular behaviors on concave and convex microstructures fabricated from elastic PDMS membranes. Lab Chip **9**, 2043–2049 (2009)
132. Curtis, A., Wilkinson, C.: Topographical control of cells. Biomaterials **18**, 1573–1583 (1997)
133. Kim, D.H., Lee, H.J., Lee, Y.K., et al.: Biomimetic nanopatterns as enabling tools for analysis and control of live cells. Adv. Mater. (2010, in press)
134. Kim, D.H., Han, K., Gupta, K., et al.: Mechanosensitivity of fibroblast cell shape and movement to anisotropic substratum topography gradients. Biomaterials **30**, 5433–5444 (2009)
135. Charest, J.L., Eliason, M.T., Garcia, A.J., et al.: Combined microscale mechanical topography and chemical patterns on polymer cell culture substrates. Biomaterials **27**, 2487–2494 (2006)
136. Motlagh, D., Hartman, T.J., Desai, T.A., et al.: Microfabricated grooves recapitulate neonatal myocyte connexin43 and N-cadherin expression and localization. J. Biomed. Mater. Res. A **67**, 148–157 (2003)
137. Wang, L., Murthy, S.K., Fowle, W.H., et al.: Influence of micro-well biomimetic topography on intestinal epithelial Caco-2 cell phenotype. Biomaterials **30**, 6825–6834 (2009)
138. Mai, J.Y., Sun, C., Li, S., et al.: A microfabricated platform probing cytoskeleton dynamics using multidirectional topographical cues. Biomed. Microdevices **9**, 523–531 (2007)
139. Wong, J.Y., Leach, J.B., Brown, X.Q.: Balance of chemistry, topography, and mechanics at the cell-biomaterial interface: Issues and challenges for assessing the role of substrate mechanics on cell response. Surf. Sci. **570**, 119–133 (2004)
140. Lim, J.Y., Donahue, H.J.: Cell sensing and response to micro- and nanostructured surfaces produced by chemical and topographic patterning. Tissue Eng. **13**, 1879–1891 (2007)
141. Lam, M.T., Clem, W.C., Takayama, S.: Reversible on-demand cell alignment using reconfigurable microtopography. Biomaterials. **29**, 1705–1712 (2008)
142. Dalby, M.J., Gadegaard, N., Tare, R., et al.: The control of human mesenchymal cell differentiation using nanoscale symmetry and disorder. Nat. Mater. **6**, 997–1003 (2007)
143. Kim, D.H., Lipke, E.A., Kim, P., et al.: Nanoscale cues regulate the structure and function of macroscopic cardiac tissue constructs. Proc. Natl. Acad. Sci. USA **107**, 565–570 (2010)
144. Brunetti, V., Maiorano, G., Rizzello, L., et al.: Neurons sense nanoscale roughness with nanometer sensitivity. Proc. Natl. Acad. Sci. USA **107**, 6264–6269 (2010)
145. Young, E.W., Simmons, C.A.: Macro- and microscale fluid flow systems for endothelial cell biology. Lab Chip **10**, 143–160 (2010)
146. van der Meer, A.D., Poot, A.A., Duits, M.H., et al.: Microfluidic technology in vascular research. J. Biomed. Biotechnol. **2009**, 823148 (2009)

147. Brown, T.D.: Techniques for mechanical stimulation of cells in vitro: a review. J. Biomech. **33**, 3–14 (2000)
148. Walker, G.M., Beebe, D.J.: A passive pumping method for microfluidic devices. Lab Chip **2**, 131–134 (2002)
149. Meyvantsson, I., Warrick, J.W., Hayes, S., et al.: Automated cell culture in high density tubeless microfluidic device arrays. Lab Chip **8**, 717–724 (2008)
150. Green, J.V., Kniazeva, T., Abedi, M., et al.: Effect of channel geometry on cell adhesion in microfluidic devices. Lab Chip **9**, 677–685 (2009)
151. Usami, S., Chen, H.H., Zhao, Y.H., et al.: Design and construction of a linear shear-stress flow chamber. Ann. Biomed. Eng. **21**, 77–83 (1993)
152. Melin, J., Quake, S.R.: Microfluidic large-scale integration: the evolution of design rules for biological automation. Annu. Rev. Biophys. Biomol. Struct. **36**, 213–231 (2007)
153. Gomez-Sjoberg, R., Leyrat, A.A., Pirone, D.M., et al.: Versatile, fully automated, microfluidic cell culture system. Anal. Chem. **79**, 8557–8563 (2007)
154. Gu, W., Zhu, X.Y., Futai, N., et al.: Computerized microfluidic cell culture using elastomeric channels and Braille displays. Proc. Natl. Acad. Sci. USA **101**, 15861–15866 (2004)
155. Song, J.W., Gu, W., Futai, N., et al.: Computer-controlled microcirculatory support system for endothelial cell culture and shearing. Anal. Chem. **77**, 3993–3999 (2005)
156. Tolan, N.V., Genes, L.I., Subasinghe, W., et al.: Personalized metabolic assessment of erythrocytes using microfluidic delivery to an array of luminescent wells. Anal. Chem. **81**, 3102–3108 (2009)
157. Sim, W.Y., Park, S.W., Park, S.H. et al.: A pneumatic micro cell chip for the differentiation of human mesenchymal stem cells under mechanical stimulation. Lab Chip **7**, 1775–1782 (2007)
158. Discher, D.E., Janmey, P., Wang, Y.L.: Tissue cells feel and respond to the stiffness of their substrate. Science **310**, 1139–1143 (2005)
159. Pelham, R.J., Wang, Y.L.: Cell locomotion and focal adhesions are regulated by substrate flexibility. Proc. Natl. Acad. Sci. USA **94**, 13661–13665 (1997)
160. Engler, A.J., Sen, S., Sweeney, H.L., et al.: Matrix elasticity directs stem cell lineage specification. Cell **126**, 677–689 (2006)
161. Peyton, S.R., Raub, C.B., Keschrumrus, V.P., et al.: The use of poly(ethylene glycol) hydrogels to investigate the impact of ECM chemistry and mechanics on smooth muscle cells. Biomaterials **27**, 4881–4893 (2006)
162. Khademhosseini, A., Yeh, J., Jon, S., et al.: Molded polyethylene glycol microstructures for capturing cells within microfluidic channels. Lab Chip **4**, 425–430 (2004)
163. Moraes, C., Wang, G., Sun, Y., et al.: A microfabricated platform for high-throughput unconfined compression of micropatterned biomaterial arrays. Biomaterials **31**, 577–584 (2010)
164. Liu, V.A., Bhatia, S.N.: Three-dimensional photopatterning of hydrogels containing living cells. Biomed.Microdevices **4**, 257–266 (2002)
165. Liu J., Gao D., Li, H.F., et al.: Controlled photopolymerization of hydrogel microstructures inside microchannels for bioassays. Lab Chip **9**, 1301–1305 (2009)
166. Jongpaiboonkit, L., King, W.J., Lyons, G.E., et al.: An adaptable hydrogel array format for 3-dimensional cell culture and analysis. Biomaterials **29**, 3346–3356 (2008)
167. Jongpaiboonkit, L., King, W.J., Murphy, W.L.: Screening for 3D environments that support human mesenchymal stem cell viability using hydrogel arrays. Tissue Eng. Part A **15**, 343–353 (2009)
168. Zaari N., Rajagopalan, P., Kim, S.K. et al.: Photopolymerization in microfluidic gradient generators: microscale control of substrate compliance to manipulate cell response. Adv. Mater. **16**, 2133–2137 (2004)
169. Gray, D.S., Tien, J., Chen, C.S.: Repositioning of cells by mechanotaxis on surfaces with micropatterned Young's modulus. J. Biomed. Mater. Res.A. **66A**, 605–614 (2003)
170. Du, Y., Hancock, M.J., He, J. et al.: Convection-driven generation of long-range material gradients. Biomaterials **31**, 2686–2694 (2010)

171. Yip, C.Y., Chen, J.H., Zhao, R. et al.: Calcification by valve interstitial cells is regulated by the stiffness of the extracellular matrix. Arterioscler Thromb Vasc Biol. **29**, 936–942 (2009).
172. Buxboim, A., Rajagopal, K., Brown, A.E.X., et al. How deeply cells feel: methods for thin gels. J. Phys. Condens. Matter. **22**, 194116 (2010)
173. Bilodeau, K., Mantovani, D. Bioreactors for tissue engineering: focus on mechanical constraints. A comparative review. Tissue Eng. **12**, 2367–2383 (2006)
174. Moraes, C., Chen, J.H., Sun, Y. et al. Microfabricated arrays for high-throughput screening of cellular response to cyclic substrate deformation. Lab Chip **10**, 227–234 (2010)
175. Geddes-Klein, D.M., Schiffman, K.B., Meaney, D.F. Mechanisms and consequences of neuronal stretch injury in vitro differ with the model of trauma. J. Neurotrauma. **23** 193–204 (2006)
176. Kamotani, Y., Bersano-Begey, T., Kato, N., et al. Individually programmable cell stretching microwell arrays actuated by a Braille display. Biomaterials **29**, 2646–2655 (2008)
177. Kurpinski, K., Chu, J., Hashi, C., et al. Anisotropic mechanosensing by mesenchymal stem cells. Proc. Natl. Acad. Sci. USA **103**, 16095–16100 (2006)
178. Wang, J.H., Yang, G., Li, Z.: Controlling cell responses to cyclic mechanical stretching. Ann. Biomed. Eng. **33**, 337–342 (2005)
179. Tan, W., Scott, D., Belchenko, D., et al.: Development and evaluation of microdevices for studying anisotropic biaxial cyclic stretch on cells. Biomed.Microdevices **10**, 869–882 (2008)
180. Gopalan, S.M., Flaim, C., Bhatia, S.N., et al.: Anisotropic stretch-induced hypertrophy in neonatal ventricular myocytes micropatterned on deformable elastomers. Biotechnol. Bioeng. **81**, 578–587 (2003)
181. Bieler, F.H., Ott, C.E., Thompson, M.S., et al.: Biaxial cell stimulation: a mechanical validation. J. Biomech. **42**, 1692–1696 (2009)
182. Sniadecki, N.J., Anguelouch, A., Yang, M.T. et al.: Magnetic microposts as an approach to apply forces to living cells. Proc. Natl. Acad. Sci. USA **104**, 14553–14558 (2007)
183. Vartanian, K.B., Kirkpatrick, S.J., Hanson S.R., et al.: Endothelial cell cytoskeletal alignment independent of fluid shear stress on micropatterned surfaces. Biochem. Biophys. Res. Commun. **371**, 787–792 (2008)
184. Toepke, M.W., Beebe, D.J.: PDMS absorption of small molecules and consequences in microfluidic applications. Lab Chip **6**, 1484–1486 (2006)
185. Regehr, K.J., Domenech, M., Koepsel, J.T., et al.: Biological implications of polydimethylsiloxane-based microfluidic cell culture. Lab Chip **9**, 2132–2139 (2009)
186. Moraes, C., Kagoma, Y.K., Beca, B.M., et al.: Integrating polyurethane culture substrates into poly(dimethylsiloxane) microdevices. Biomaterials **30**, 5241–5250 (2009)

Nanotechnology Usages for Cellular Adhesion and Traction Forces

Sangyoon J. Han and Nathan J. Sniadecki

Abstract Cell mechanobiology studies have incorporated micro- and nanotechnology-based tools to understand the interaction between cells and their surrounding environment. These tools have helped to uncover findings that physical factors in the extracellular matrix can strongly affect important cell functions like proliferation, migration, differentiation, and survival. Here, we review the nanotechnologies that have been used for cellular adhesions and traction forces and the findings that have come at the molecular and protein level.

1 Introduction

Prior to revolutions in the life sciences, there have been innovations in technology that helped unlock the limitations in scientific understanding. For example, development of the microscope led to the discovery of cells and automated DNA sequencing and information storage has both made it possible to map and better understand the human genome. Likewise, adoption of nanotechnology in cell biology has led to a new era where it is now possible to control the physical interactions between a cell and its surroundings. A typical eukaryotic cell has a diameter that can range between 10 and 100 μm, but the protein structures inside it are even smaller. Understanding the mechanics of a cell is critical because it plays a role in orchestrating cell function. It is now possible to use approaches that have

S. J. Han and N. J. Sniadecki (✉)
Department of Mechanical Engineering, University of Washington, Seattle, WA, USA
e-mail: nsniadec@uw.edu; syhan@u.washington.edu

N. J. Sniadecki
Department of Bioengineering, University of Washington, Seattle, WA, USA

Stud Mechanobiol Tissue Eng Biomater (2011) 4: 177–200
DOI: 10.1007/8415_2010_26

Published Online: 22 September 2010

the same length scale as the structures of interest in a cell to learn how they work in the overall system. In particular, it has become apparent that spatial domains, structural compositions, and mechanical forces influence the adhesive binding interactions between cells and their underlying substrates.

The environment that surrounds a cell is its extracellular matrix (ECM). It is composed of matrix proteins such as collagen and elastin that serve as tension-bearing structures. These proteins form strong fibers that are mixed with a gel-like substance that consists of proteoglycans. By their affinity with water, proteoglycans provide resistance against compressive forces as well as regulate cell behavior through interactions with other enzymes. The structure of the ECM can also take a sheet-like mesh, referred to as the basement membrane, which consists of laminin and collagen networks. In addition to these proteins, there are others such as fibronectin and vitronectin that help cells adhere by having binding sites for adhesions receptors. Mechanical and structural features of the ECM such as stiffness, content, and density of available ligands can influence cellular functions through mechanosensation at integrins [40].

Integrins are heterodimeric, transmembrane receptors that bind to ligands found in the ECM [48]. In particular, integrins $\alpha_v\beta_3$ and $\alpha_5\beta_1$ bind to a short peptide sequence (Arg-Gly-Asp, RGD) found in ECM proteins. They have a width of 10 nm and are 10–100 times more abundant on a cell's surface than other receptor types [2]. Integrins are freely dispersed within a cell's membrane, but become tightly bound when they encounter a ligand. A conformational change occurs upon binding within the cytoplasmic domains of integrins that allow for the recruitment of proteins at the cytoplasmic side of the membrane. These proteins are known as focal adhesion proteins and they link integrins to the actin cytoskeleton. At the same time, these focal adhesion proteins can act as signaling transducers that interpret the cell's environment and influence cellular decisions like migration, apoptosis, proliferation, or differentiation. As more focal adhesion proteins and integrins are recruited, the size, strength and signaling activity of the structure becomes larger. These aggregated clusters are known as focal complexes and have are approximately a 100 nm in diameter and contain over a 100 different proteins that associate within the adhesion site [4, 18, 39]. Focal complexes are transient structures that can vanish or develop into mature focal adhesions. Although the molecular nature of ligand binding is relatively well-established, the changes that allow the focal complex to transition into a focal adhesion remain elusive. Yet, the size, strength, assembly, and disassembly of focal adhesions appear to be key mediator of many cellular functions.

One aspect of focal adhesion maturation is that mechanical forces acting on the structure are essential for its regulation. Focal adhesions are elongated and localized at the terminating end of fiber bundles containing actin, myosin, II, and α-actinin, which are known as stress fibers [81]. Interestingly, the formation and growth of focal adhesions relies on myosin, II, especially its isoform myosin IIA [33, 101, 102]. It is increasingly evident that traction forces from the actin–myosin contractile machinery mediate the assembly and disassembly of focal adhesions [36, 88]. Traction forces are generated by the cross-bridge cycling between myosin and actin and allow a cell to spread, migrate, and maintain its shape. Since focal adhesions act as points

where tension in stress fibers are transmitted to the surrounding microenvironment, they are essential for a cell's ability to migrate, but also to pull and rearrange proteins in the ECM or reshape tissue during morphogenesis [59, 74, 75, 96].

While cells can perform many functions by applying traction forces at their focal adhesions, much interest has been focused on how cells sense and respond to forces. In vivo, mechanical forces are transmitted to cells through the tissue during physiological events: For example, hemodynamic shear forces acts on endothelial cells in the vasculature and fibroblasts experience loads during the movement of tendons and ligaments. These forces that cells experience are of great importance in tissue formation, maintenance, and growth [3, 49]. Cells use traction forces to respond to their surroundings [27, 93]. In particular, cells can sense and respond to rigidity of a substrate by using traction forces to probe the elasticity and by using feedback from mechanosignaling at the focal adhesions [27]. The stiffness of the ECM can change if the tissue has reached a severe diseased state. Increased stiffness of mammary gland tissue can promote malignancy by increasing focal adhesions, Rho activity, traction forces, and migration [64, 79]. On the other hand, the geometry of a cell's spread area affects differentiation in human mesenchymal stem cells (MSCs) by driving osteogenesis or adipogenesis [55, 73]. Matrix rigidity is also found to be a key factor that directs stem cell differentiation [30]. Since both substrate stiffness and spread area of a cell change a state of cellular function (e.g. differentiation) through Rho-mediated cytoskeletal contractility [8, 73, 86], there has been a growing number of tools developed for studying traction forces which we highlight in this chapter.

The binding interactions between cells and their surroundings have been investigated over the last half-century through the development of micro- and nano-engineered tools and techniques. The first representative example is the internal reflection microscopy which enabled a closer scrutiny of the cell–substrate contact area [100]. Chick heart fibroblasts were observed to have non-uniform, discrete adhesion points at their peripheral regions of contact, whereas the center of cell was separated from the substrate by a distance up to a few hundred nanometers [22]. This observation of the existence of focal adhesions was also later confirmed by electron microscopy [1]. Micropatterning of ECM proteins on a surface is the second example. By spatially controlling the available area of ligand on which a cell can spread, it was found that whether a cell proliferates or dies can be strongly influenced [17]. As mentioned previously, the same technique was used to discover that cells differentiate into specific lineages depending on available area [73]. As a last example, optical tweezers trap nanosize objects with focused light and have been used to study the formation and maturation of focal adhesions by trapping ECM-coated beads at a cell's surface where integrins can bind [19]. It was found that by increasing the trapping force of the optical tweezer, the adhesion strength between a cell and a bead also grew stronger. This strengthening of the adhesion site implicates that cells can sense forces at their integrins and recruit additional focal adhesion proteins to reinforce the connection. Together, these examples underline that with the advent of new technology, the fundamental mechanism behind a cell's behavior can be revealed.

In this chapter, we review nanotechnology-based tools that have been used for cell–surface interactions, major discoveries through using the tools, and the needed areas for new technology. Specifically, we will examine achievements attained by surface control over the chemical presentation of the ECM and tools for measuring and analyzing cellular traction forces.

2 Surface Control

Cell adhesion is the essential mechanism that guarantees the structural and functional integrity of tissue. It involves different biochemical signaling pathways that mediate the integrin-ligand transduction response [111]. However, knowledge has been somewhat limited by the biochemical composition of a substrate used for cell culture, which is typically a polystyrene dish. There have been efforts to tailor the surface chemistry of polystyrene for better attachment of cells by modulating the ability of the surface of polystyrene to capture soluble ECM proteins in culture media [23, 43]. It was found that the surface that promotes the best adhesion of cultured cells had a contact angle of 40° with water, which is relatively hydrophobic. By forming a gradient of the wettability on a surface using a nano-film of metal, it was observed that cells migrated toward regions of higher adhesivity, a process referred to as haptotaxis [14, 15]. Likewise, cells have been found to spread to a larger extent when in contact with a hydrophobic surface [44]. Moreover, by adjusting the adhesivity of a surface by applying a hydrophilic hydrogel coating of poly(2-hydroxyethyl methacrylate), it was found that spread area, DNA synthesis, and proliferation of cells increased with the degree of surface adhesivity [34]. These early findings on adhesion, migration, and proliferation established a framework that has been used to engineer surfaces that control the geometrical area, spacing, and density of ligands.

Self-assembled monolayers (SAMs) of alkanethiols on gold have become a model surface to study cell adhesion due to its fine control over protein adsorption and its ability to spatially pattern regions of adhesion. Alkanethiols have a general structure of $SH(CH_2)_nX$ in which the sulfur atom coordinates with a gold atom of underlying film, n is the length of the hydrocarbon spacers, and X is the terminal group that is presented on the surface (Fig. 1a). Alkanethiols self-assemble on gold surface in a side-by-side fashion that is dense, stable, and highly ordered, creating a semi-crystalline monolayer that is approximately 2–3 nm in thickness (Fig. 1b). The terminal group (X) and the length of alkyl chain spacer ($(CH_2)_n$) can be tailored to control the surface properties of the monolayer [7]. If the terminal group is hydrophobic such as methyl or carboxyl, it readily adsorbs a number of ECM proteins, whereas terminal groups such as poly(ethylene glycol) (PEG) prevent protein adsorption [83]. Furthermore, the adhesivity of the model surface can be also tuned by altering the ratio of terminal groups between methyl and PEG.

Using SAMs, different densities and gradients of ECM ligands could be made to study cell growth and migration. By controlling the adsorption time of carboxyl

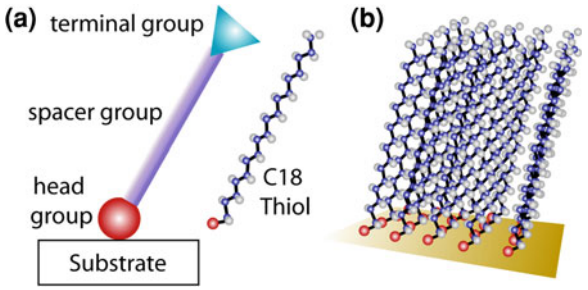

Fig. 1 Typical alkanethiol molecules on a gold substrate form self-assembled monolayers (SAMs). **a** Simplified illustration of a single C18 thiol molecule shows a head group (sulfuric atom), spacer group (alkyl chain), and terminal group. **b** Alkanethiols form a tightly-packed SAM on a gold substrate that can be used to study cell adhesion by tailoring the degree of protein adsorption. Refer to the electronic version of this chapter, DOI: 10.1007/8415_2010_26, for viewing color version of this figure

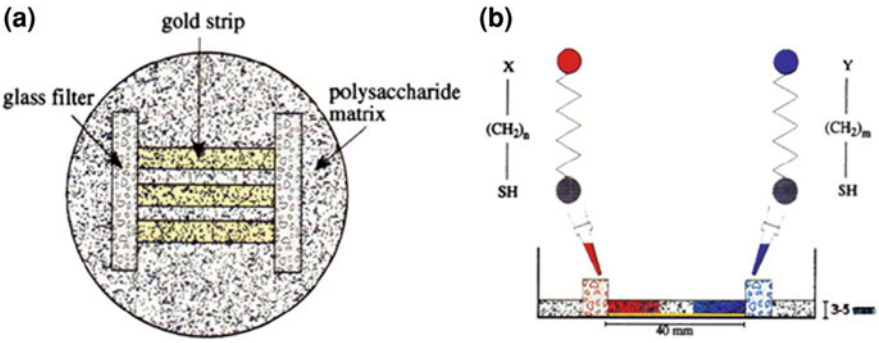

Fig. 2 Cross-diffusion device used for the preparation of the ligand gradients: **a** top view and **b** side view. The polysaccharide matrix is used to diffuse different alkanethiol solutions from either end to create a concentration gradient on top of a gold strip. Adapted from [66]. Refer to the electronic version of this chapter, DOI: 10.1007/8415_2010_26, for viewing color version of this figure

terminal group that had been conjugated with RGD, it was found that more cells attached to the surface and had larger spread areas [50]. Likewise, on gradients of fibronectin, it was observed that cells migrated faster in the direction of the highest gradient [91, 92]. To make the gradients, a cross-diffusion method was used (Fig. 2), where inert and reactive alkanethiols were simultaneously added to either end of filtration gel and allowed to diffuse across the gel to produce a gradient of carboxyl terminal groups on a gold-coated surface. In addition to studying the haptotactic migration speed of cells, it was also found that cells polarized their morphological structure in the direction of the steepest gradient. Previously, cells had been seen to migrate in the direction of steepest gradient of chemo-attractants, a process known as chemotaxis. Interestingly, when haptotaxis was compared against chemotaxis by preparing a gradient of fibronectin in a direction

perpendicular to a gradient of VEGF, it was found that directional migration was influence by both factors, but the influence of chemotaxis was stronger [67]. This result supports that insoluble factors like ligand density gradients have a role in cell migration, but may not be as dominant as soluble factors.

A powerful advantage of using SAMs has been the ability to incorporate microscale spatial control by microcontact printing. Here, an elastomeric stamp is coated with alkanethiols and placed in contact with a gold substrate to form regions of SAMs (Fig. 3a). The region that did not contact the stamp was treated subsequently with PEG-based alkanethiols to block cell adhesion. The stamp is made from a silicone rubber and formed with features as small as 0.2 μm through a technique known as soft lithography [76, 106]. By having square patterns of different area on a stamp (Fig. 3b), it was found that spread area determines whether cells proliferate or undergo apoptosis [17]. Different patterns of small dots were also used to limit the available ECM area for a cell, but still allow them to spread to the same area as the square patterns. It was found that whether a cell proliferations or commits suicide did not depend on the extent of its cell–ECM contact area but on the extent of its projected spread area. Cell spreading was also found to control whether stems cells undergo osteogenesis or adipogenesis [73]. Since then, it has been observed that cells patterned onto a wider variety of shapes such as triangles, pentagons, hexagons, and trapezoids formed lamellipodial extensions used for migration at the sharp corners of each pattern (Fig. 3c) [11]. Similar patterns have been found to play a role in stem cell differentiation [55]. The work on cell polarity has progressed beyond the use of symmetric geometries

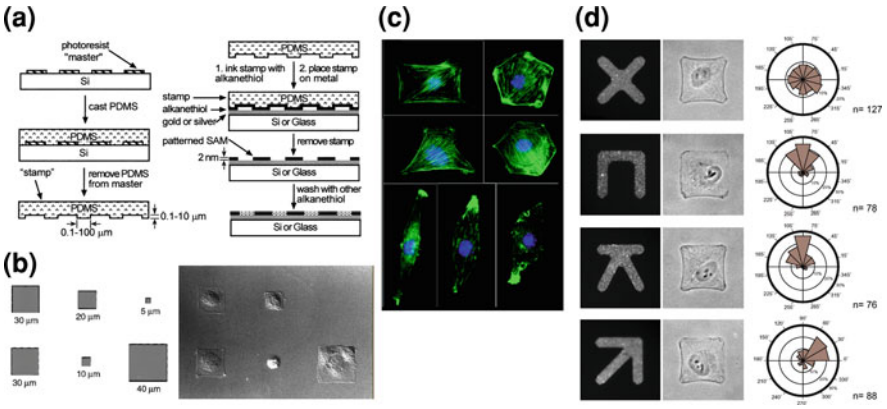

Fig. 3 Microcontact printing of SAMs. **a** Schematic showing microcontact printing procedure of alkanethiol molecules. Reproduced from [105]. **b** Cells attached and spread on printed islands of square patterns (shown in phase image at *right*) with several different areas. Adapted from [17]. **c** Patterned cells on various shapes have more actin filaments at the sharp corners. *Green* actin, *blue* nucleus. Reproduced from [11]. **d** Cells (*middle column*) were plated on anisotropic adhesive ligands (*left column*). Polarity vectors from nucleus–centrosome locations were plotted as angular distribution (*right column*). Reproduced from [99]. Refer to the electronic version of this chapter, DOI: 10.1007/8415_2010_26, for viewing color version of this figure

by patterning anisotropic shapes (X, C, K and arrows), which all had the same projected area for the cells (Fig. 3d) [99]. It was found that cells defined their polarity by positioned their centrosomes in the direction of greatest adhesivity. These works suggest that projected spread area determines cell fate in both growth and differentiation and adhesive geometry determines cell polarity and migration, but there may be cross-interactions between the two.

Microcontact printing typically confines a cell from migrating, but using electrochemistry, however, it is possible to switch a non-adhesive surface to an adhesive one by electrically desorbing PEG-terminated SAMs from a surface. This approach has been used to patterned cells of two different cell types to look at co-culture interactions [109]. The switchable SAMs also allowed cells to migrate out of confined region after a voltage pulse, providing a nondestructive alternative to scratch-wound assays to study cell migration [53]. With this electrochemical approach, it was possible to study the effect of cell polarization on the direction of migration. Fibronectin was printed onto a substrate in an asymmetric, teardrop shape (Fig. 4a, top left) [54]. Before release, the lamellipodia of the cells preferentially formed at the blunt end, but with a lesser degree at the sharp end (Fig. 4a, bottom left). After release, the cells migrated in the same direction as their blunt ends (Fig. 4a, right), suggesting that asymmetry of lamellipodia extension induced biased migration. Building from this work, the persistence of biased migration was studied with arrays of teardrop patterns formed in a ring (Fig. 4b, top) [57]. When blunt ends of the teardrops were adjacent to the sharp ends of the next pattern, cells preferentially migrated in the direction of the blunt

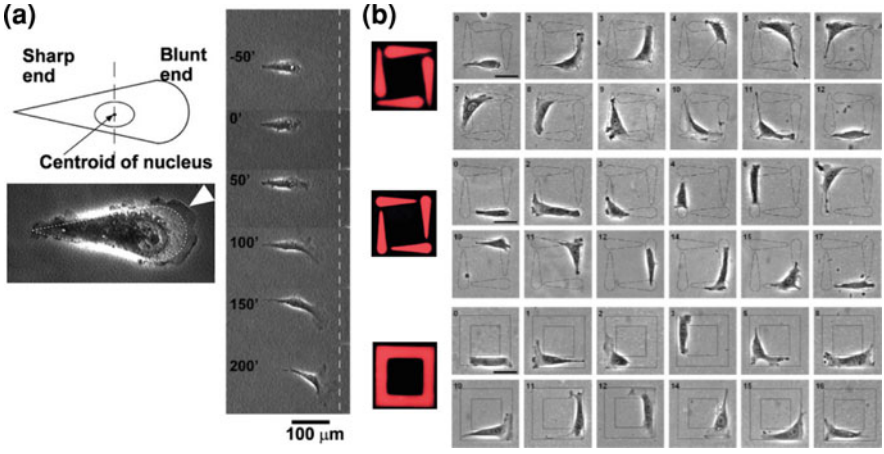

Fig. 4 Cells show directed migration on micropatterned surfaces. **a** A 3T3 fibroblast patterned by a teardrop shape (*top left*) showed ruffling activity of lamellipodia (*arrowhead*, *bottom left*) and migration in the direction of the blunt end upon release of confinement (*right*). Adapted from [54]. **b** Arrays of teardrop patterns direct cell migration. NIH 3T3 fibroblasts migrate from the blunt ends to the sharp ends of the next island (*top*). In contrast, cells migrate from the sharp end to the blunt end of an adjacent island (*middle*). Cells on continuous rectangular islands (*bottom*) showed no preferential orientation of cell migration. Adapted from [57]

ends. However, when the sharp ends were adjacent to blunt ends, the direction of migration was reversed (Fig. 4b, middle). These works demonstrate that directional migration depends on the polarity of the cell, but also on the availability of ECM in the direction of lamellipodia formation.

Cell polarization from geometric anisotropy and migration along the polarized direction implicates that cells are polarized before migration. Since haptotaxis was observed on gradients of ECM ligand, cells might be polarized in a confined, but gradient condition. This question was evaluated using microfluidic networks and SAMs [82]. To prepare the surface, SAMs were deposited as patterned strips using an arrangement of parallel microfluidic channels (Fig. 5A, a,b). A Y-shaped microfluidic serpentine channel was placed on top of the treated surface and active RGD peptide and inactive RDG peptide were flowed over the SAMs from two entrance ports to form a diffusion-based gradient (Fig. 5A, c). The remaining unexposed regions were also blocked in a solution of nonadhesive peptides, rendering square patterns in which there was a gradient in adhesivity (Fig. 5A, d). Cells formed focal adhesions predominantly in the direction of the gradient (Fig. 5A, e). Interestingly, despite the presence of a gradient, the geometric effect of sharp corners persisted in these cells, which indicates that nanoscale geometries may have a stronger effect than adhesive gradients.

Instead of using continuous confinement of a certain pattern shape, microcontact printing at the length scale of focal adhesions can provide more insight into

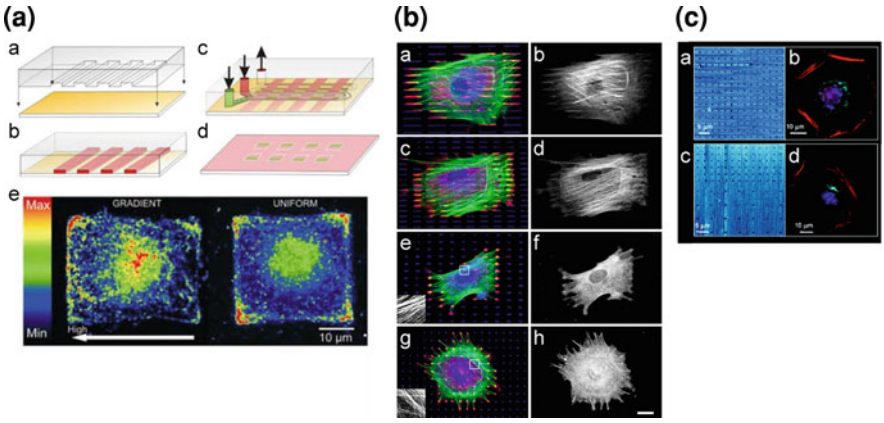

Fig. 5 Various micropatterning approaches. **A** Micropatterning combined with microfluidics creates a pattern with gradient (*a–d*). Vinculin heat maps (*e*) of stacked images of cells on gradient islands and uniform islands show focal adhesion density distribution. Reproduced from [82]. **B** Myofibroblasts plated on arrays of islets of different lengths (*a*, *b* 20 μm, *c*, *d* 10 μm, *e*, *f* 6 μm, and *g*, *h* 2 μm). *Green* F-actin, *red* vinculin, *blue* fibronectin, *right column image* α-SMA. Reproduced from [42]. **C** Dip-pen nanolithography was used to form symmetric (*a*) and asymmetric (*c*) nanoarrays. Images of the patterns were observed under lateral force microscopy (*a*, *c*). Fibroblasts attached to asymmetric nanoarrays (*d*) showed polarized cytoskeletal structure whereas those on the symmetric pattern showed no polarity. *Green* Golgi apparatus, *red* actin, *blue* nuclei. Refer to the electronic version of this chapter, DOI: 10.1007/8415_2010_26, for viewing color version of this figure

how cells sense and respond to the ECM environment. Cells plated onto substrates micropatterned with arrays of fibronectin islets were used to verify the hypothesis that only large focal adhesion can support high tension from stress fibers [42]. Incorporation of α-smooth muscle actin (α-SMA) into stress fibers was the hallmark used to indicate a high cytoskeletal tension. Cells plated on the long islets arrays formed "supermature" focal adhesions and only those cells showed stress fibers that had α-SMA (Fig. 5B, a,d). In contrast, cells grown on the small islet arrays showed no α-SMA incorporation in their stress fibers (Fig. 5B, e,h). Furthermore, when the cells were stretched mechanically, their focal adhesions grew in size, allowing α-SMA to be recruited to the stress fibers, but this response only occurred for adhesions that were stretch above a critical size to support the higher cytoskeletal tension.

Dip-pen nanolithography (DPN) is another approach to patterned adhesive islands on which cells can form focal adhesions. DPN uses an atomic force microscope tip that is inked with SAMs or proteins to deposit these molecules at defined locations on a surface [61]. Although there have been few studies that used this powerful tool to study cell–ECM interaction, one was conducted on how asymmetric peptide nanoarray affect cell polarization [47]. Cells were plated on either symmetric arrays having 3 μm pitch and 500 nm RGD peptide spots (Fig. 5C, a) or asymmetric arrays consisting of two regions—high density (3 μm pitch) and low density (6 μm pitch) regions with the same 500 nm spot size (Fig. 5C, c). Cells on the asymmetric array were observed to be polarized toward the higher density region as evidenced by the relative position of Golgi apparatus with respect to the nucleus (Fig. 5C, d). Cells on the symmetric arrays showed non-uniform distribution of their Golgi, indicating they were not polarized (Fig. 5C, b). Although this polarization result is in agreement with the result found in ligand gradients using microfluidics, the DPN study demonstrated that nanotechnology affords the opportunity to conduct more quantitative studies by tailoring the spatial pattern—ligand size, spacing between adhesive islands, aspect ratios, and shapes.

Efforts to study how individual integrins interact with each other in mechanosensing have led to the development multidomain colloidal gels to control spacing between individual integrin receptors. The colloidal gels are made from a large polymer molecule that has a brush-like structure (Fig. 6A, a) [51]. Poly(methyl methacrylate) (PMMA) forms the backbone of the molecule and polyethylene oxide (PEO) forms the side chains. A portion of the ends of the side chains are functionalized with RGD peptides to allow cells to adhere, but those side chains without peptides block cell adhesion. The diameter of the brush-like molecule was approximately 32 nm and the spacing between RGD peptides varied between 14 and 25 nm, which depended upon the number of peptides bound to the molecule (Fig. 6A, b). The nanoscale spacing between RGD peptides allowed for control over integrin clustering, independent of the overall RGD surface density. For colloidal gels with small spacing between RGD peptides, the clustering of integrins permitted the cells to remain attached to the surface when subjected to a centrifugal detachment force. This result indicates that integrin clustering is more essential for the mechanical stability of cell adhesion than ligand surface density. Similar colloidal

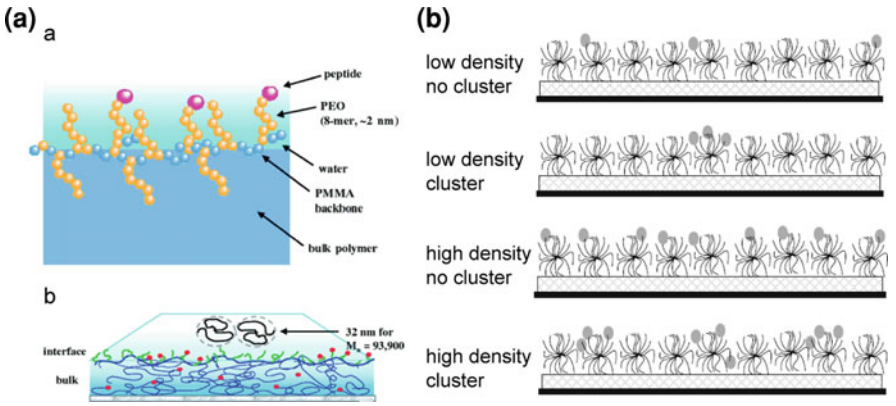

Fig. 6 Multidomain peptide colloidal gel system. **A** Schematic of RGD-comb structure (*a*) shows RGD peptides attached on short PEO side chains that are tethered to the PMMA backbone. RGD islands (*b*) are formed in a quasi-2D configuration at the water–polymer interface. Reproduced from [56]. **B** On a film of star polymers, ligands (*shaded oval*) are tethered with controlled density and degree of spacing to control integrin clustering. Adapted from [71]

gels were used to study how integrin clustering affects cell migration [71]. Cells were plated on PEO gel substrates that either permitted or restricted clustering and had either high or low density of RGD peptide (Fig. 6B). As expected, cells on substrates that had high RGD surface density had increased motility. However, migration speeds were significantly reduced if the integrins were restricted from clustering. Furthermore, ligand clustering reduced the average ligand density required for cell migration and also allowed more stress fibers to form. In contrast, non-clustered integrin did not allow full spreading or motility, but only weak adhesion. Together, the studies using colloidal gels implicate that integrin clustering enables recruitment of cytoplasmic regulatory and structural proteins at focal adhesion to activate signaling pathway that regulate cell motility and traction forces.

Patterning gold nanodots is a technique that corroborates the findings that used colloidal gels to investigate integrin clustering, but affords a higher degree of spatial control and precision in the placement of the adhesion sites. Each gold nanodot has a diameter of 6–8 nm whereas that of the integrin head domain is 9 nm [107], resulting in only a single integrin binding to a deposited gold particle. Arrays of gold nanodots were made by self-assembled polymer micelles, which contained a single gold particle at their center (Fig. 7A, top). The micelles form a monolayer on a substrate that begins the seeding process for the gold particle arrays. When the micelle-coated substrate is exposed to oxygen plasma, the polymer capsule is removed and only the naked gold particles are left on the surface (Fig. 7A, bottom). By using different diameters of micelles, the spacing between the particles could be varied between 30 and 140 nm [95]. Examples of gold nanodot patterns with 50 and 90 nm inter-particle spacing are shown in Fig. 7B. Gold particles are biofunctionalized with RGD-containing peptide, and rest of the region on a substrate is covered with PLL-g-PEG to prevent integrin adhesion to the glass. Taking

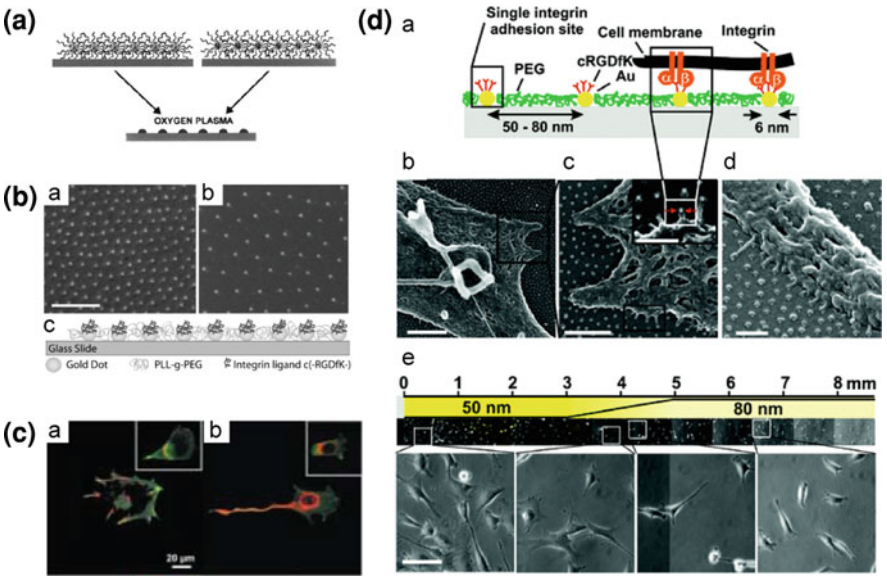

Fig. 7 Gold dots for controlling integrin interactions and clustering. **A** Gold clusters (*bottom*) are formed via oxygen plasma treatment by degrading copolymer micelles completely (*top*). Reproduced from [95]. **B** Nanopatterned glass substrates have hexagonally arranged gold particles with inter-particle spacings of 50 nm (*left*) and 90 nm (*right*). The illustration on the *bottom* shows the schematic of a nanopatterned substrate with gold particles coated with RGD peptide for integrin adhesion and space between the gold dots filled with PLL-g-PEG for integrin blocking. **C** Cells on 58-nm spaced RGD-coated nanodots (*a*) showed β_3-integrins (*green*) colocalized with focal adhesion kinase (FAK, *red*) whereas cells on 73-nm spaced nanopattern (*b*) showed poor spreading and no colocalization with FAK. Reproduced from [5]. **D** Schematic (*a*) and SEM images (*b–d*) of cells on a gradient of nanodots across an 8-mm long substrate (*e*). Reproduced from [6]. Refer to the electronic version of this chapter, DOI: 10.1007/8415_2010_26, for viewing color version of this figure

advantage of the nanoscale control over ligand spacing, it was found that cells on substrates with adhesive spacing greater than 73 nm showed poor adhesion and spreading, whereas cells on smaller spacings spread as well as they do on glass surfaces coated uniformly with RGD peptide [5]. Cells on nanodots with 58 nm spacings (Fig. 7C, a) were observed to have focal complexes that were well formed because β_3 integrin and focal adhesion kinase (FAK) co-localized with each other. On the other hand, cells on 73 nm spacing (Fig. 7C, b) had poor spreading because β_3 integrin and FAK failed to co-localize. These results demonstrate that the distance between ligands can restrict the ability for integrin to cluster together and thus prevent the maturation of an adhesion. Interestingly, integrin clustering was found to be more important than the amount of ligand deposited on a surface. Cells spread better on hybrid arrays of $2 \times 2\ \mu m^2$ squares, where each square consisted of 58-nm spaced gold dots, than on uniform arrays of 73-nm spaced dots that had more ligand content. The influence of ligand spacing on focal adhesion formation was further confirmed by a study where integrins that formed on 108-nm spaced

nanodots showed rapid turnover of focal adhesions and reduced amounts of zyxin at the focal adhesions, which is a protein that is recruited to the adhesion complex upon mechanical force [16, 62]. In addition to cell spreading, studies on cell polarization have benefitted from this nanopatterning technique. A gradient of nanodot spacings from 50 to 80 nm (Fig. 7D, e) was used to find that cells reorient their polarization towards closer spaced patterns and are able to sense spatial differences as small as 1 nm in spacing [6]. Cells on gradients of gold dots also showed membrane protrusions toward individual gold particles at the nanometer scale, which suggests that membrane protrusion activity is essential for restructuring the polarity of a cell (Fig. 7D, b,d).

3 Force Measuring Tools

Use of surface control techniques at the nanoscale has helped to reveal the structure and underlying mechanisms that influences cell adhesion, polarization, and migration. However, the same intracellular proteins involved in adhesion are also essential for actin–myosin generated traction forces that are transmitted at focal adhesions. For this reason, traction forces can strongly contribute to cellular responses such as adhesion strength, cytoskeletal morphology, and cell motility. During cell migration, for example, cells need to pull themselves forward to move. Traction forces had been hypothesized to drive cell migration due to actin–myosin cross-bridges, but they had been difficult to measure at the nanoscale. Development of deformable substrates has provided approaches to observe and quantify cellular traction forces by the extent of physical distortion in a substrate.

The first method for measuring traction forces was to use a thin film of silicone rubber that wrinkled under the load from traction forces exerted on them [45].

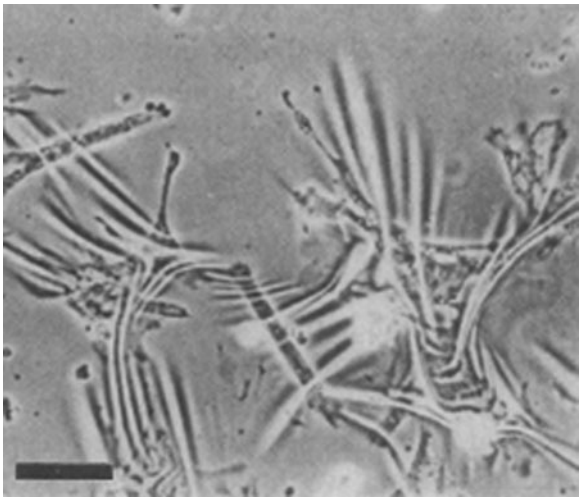

Fig. 8 Silicone rubber membrane wrinkles due to the traction forces from several chick heart fibroblasts. Reproduced from [45]. *Bar* 100 μm

This wrinkling substrate was made by briefly exposing silicone fluid to a flame that crosslinked only the surface of the silicone, creating a skin of 1 μm thickness. When cells were plated on the surface, they spread out and pulled tangentially on the rubber sheet, producing visible wrinkles in the rubber (Fig. 8). This result was significant in that traction forces could be observed and compared for the first time. Wrinkling membranes were used to confirm that signaling pathways such as the small GTPase RhoA or Ca^{2+}/calmodulin pathways regulate traction forces through stress fiber formation and focal adhesion formation [20, 46]. Despite the immense significance of this technique to the field, it provided a limited measurement because it could only be used to assess cells by the number of wrinkles they produced and not the exact amount of force. Some improvements have been made to provide a semi-quantitative measurement of the traction forces using wrinkling membranes [12, 13]. The mechanics of wrinkling however is nonlinear in its relationship between force and deformation so it is inherently inaccurate to find an exact force measurement. Moreover, wrinkles are formed rather chaotically so there is limited temporal and spatial resolution possible to measure forces acting at individual focal adhesions [25].

The first, non-wrinkling, but still deformable substrate was made by crosslinking the silicone rubber in a glass chamber using a glow discharge device (Fig. 9a) [60]. Small beads that were a micrometer in diameter were embedded on the elastomer surface. As a cell produced traction forces, the position of the beads on the silicone

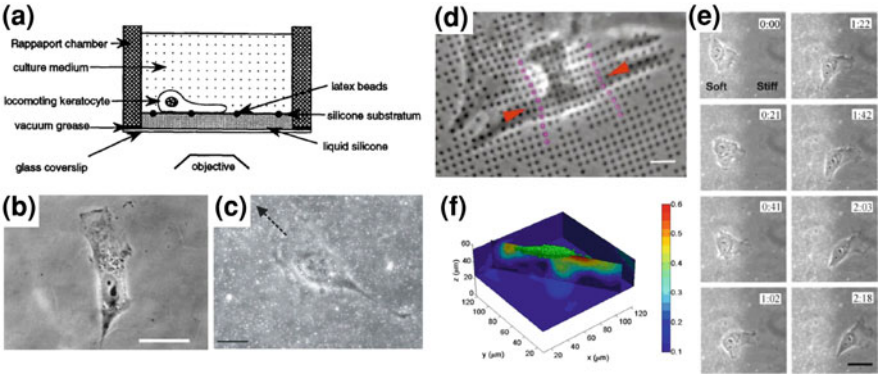

Fig. 9 Traction force microscopy (TFM) is used to measure cellular forces. **a** Silicone rubber-based traction force microscopy has latex beads embedded on the surface of silicone film to report the distortion from traction forces. Reproduced from [60]. **b** A fibroblast on a compliant polyacrylamide (PA) gel. Reproduced from [80]. *Bar* 10 μm. **c** Traction forces of a fibroblast migrating in the direction of the *arrow* were measured by the displacement of fluorescent nanobeads (0.2 μm diameter) which are seen as *white dots* embedded in the gel. Reproduced from [77]. *Bar* 20 μm. **d** Regular array of micropatterned dots on an elastomeric substrate shows contraction of a fibroblast (indicated by *arrowheads*). Reproduced from [8]. *Dots pitch* 2 μm, *bar* 6 μm. **e** A fibroblast plated on a soft region of a gel migrated towards the rigid region. Reproduced from [69]. *Bar* 40 μm. **f** 3D forces of a cell are measured by the displacement contour slice along the depth of a gel. *Color bar* Magnitude of total 3D displacement. Reproduced from [72]. Refer to the electronic version of this chapter, DOI: 10.1007/8415_2010_26, for viewing color version of this figure

rubber changed due to deformation of the film. From the bead displacements, the force vectors of cells could be measured. At first, the local traction force was assumed to be linearly related to bead displacement. This incorrect assumption was later rectified by using elasticity theory about the deformation of a compliant film [24]. This technique was only able to measure traction forces for highly contractile cells and so a limited range of cultured cells were able to be studied. Nonetheless, there were interesting findings on the migration of fish keratocytes using this early elastic film. These cells are highly motile and had been studied extensively to understand the mechanisms and mechanics of cell migration. Using the non-wrinkling silicone films, small bead displacements were observed at the leading edge of the cells and larger bead displacements at the rearward region.

The introduction of polyacrylamide gel to measure traction forces was a breakthrough in addressing the limitations of silicone film substrates by providing a way to control the stiffness by varying the mixing ratios between the acrylamide monomer and bisacrylamide cross-linker (Fig. 9b) [80, 104]. The technique measured the movement of fluorescent nanobeads embedded in the gel and was referred to as traction force microscopy (TFM) (Fig. 9c). The displacement vectors are calculated by subtracting the positions of beads as they are deformed by a cell's traction forces from their original, undeformed positions once the cell has been removed. The traction stress field is then calculated from the displacement vectors using elasticity theory [10, 58]. Since the beads are randomly seeded into the gels, there can be uncertainty in solving for the appropriate traction forces at regions of low bead density. To address this, orthogonal arrays of fluorescent beads were made by electron beam lithography and then patterned onto an elastomeric substrate (Fig. 9d) [8]. Due to the even distribution of the bead markers, the number of possible solutions for the traction force vector field for a measured displacement field was significantly reduced.

Despite some of the difficulties in analyzing traction forces using TFM, it has become widely used to study cells during migration and contraction. The traction stress distribution of migrating fibroblasts was found to have high forces at the leading edge of a cell whereas the middle and posterior of a cell had lower forces (Fig. 9c) [25]. This non-uniform distribution of forces indicates that cells are pulled forward by contractile forces at the front of a cell. The role of high forces at the leading edge were also found to determine the change in direction during migration [77]. Since the gels can have finely controlled stiffness, this has led to an important finding that cells sense and respond to the rigidity of the ECM [27]. Cells on soft gels have less spread area, increased rates of motility and lamellipodia extension, small focal adhesions, and less phosphorylation of focal adhesion proteins as compared to those on rigid gels [80]. Building from this finding, gels were created that contained both soft and rigid regions that were adjacent to each other [69]. Cells were able to migrate from the soft region to the rigid region (Fig. 9e). However, cells refused to cross from the rigid region into the soft region because they had higher traction forces and more spreading on the rigid side. This phenomenon of directed migration due to substrate rigidity is called durotaxis. It was later found that durotaxis, like haptotaxis and chemotaxis, is sensitive to

gradients in substrate stiffness [52]. In addition, ECM stiffness has been found to affect the contractile development of cardiomyocytes [31], differentiation of stem cells [30], and invasiveness of breast tumor cells [64, 79].

TFM has also been used to study the effect of ligand density and the involvement of traction forces in spreading. The spread areas of cells were tightly influenced by the ligand density on a surface, but had different increasing relationships depending on cell type and ECM ligand type [29, 38, 84]. Interestingly, traction forces also increased with spread area and ligand density, indicating that traction forces play a role in a cell's ability to extend its structure and maintain stable contact with a surface [84, 85]. These findings are in agreement with those from previous studies using surface adhesivity control, where cell spreading and adhesion strength were enhanced with increased ligand density [5, 44, 50]. Since integrins need high ligand density in order to cluster, it is likely that ligand density allows focal adhesions to stabilize in such a way that multiple integrins work together to support a larger degree of traction force. Furthermore, focal adhesion size, a measure of the degree of recruitment of cytoplasmic proteins and integrins, was found to increase with the local traction force acting at an individual adhesion [8]. In light of these findings, it is likely that the high force required to detach cells on colloidal gels and gold nanodots is because these surfaces promote integrin clustering so that large focal adhesions are able to form [71, 89].

TFM has elucidated the two-dimensional (2D) distribution of cellular contractility, but cells often reside in a three-dimensional (3D) context. Cell motility in 3D is slower and the molecular composition of focal adhesions are smaller as compared to those in 2D [21, 32, 110]. Thus, traction forces of cells are expected to be different in 3D environments. Some early works into measuring traction forces in 3D have been implemented using TFM, but have not found dramatic differences are compared to traction forces in 2D [9, 72]. One approach was to overlay a second TFM gel on top of a cell to look at tangential traction forces on the dorsal and ventral surfaces [9]. It was found that the strength of these traction forces were similar to those observed in 2D culture. To analyze traction forces that were normal to a surface, the distortion of beads in a gel underneath a cell were measured in all three directions using confocal microscopy [72]. Interestingly, the normal displacements were similar to or slightly greater than tangential displacements for the cells (Fig. 9f). The forces that cells generate in 3D imply that they can use them to explore or remodel their microenvironment using both normal and tangential forces. Although these works provided an early framework to analyze 3D traction forces, there are still many challenges and obstacles to create a feasible and analyzable assay to study the physical interactions of cells in 3D [26, 32].

Continuous, deformable substrates such as silicone membranes or TFM gels have an inherent disadvantage in that a local force at a focal adhesion can cause a wide distortion of the substrate, which can in turn cause weaker, secondary forces that act externally at adjacent focal adhesions. Thus, the continuous nature of the substrates makes it difficult to isolate the local force at each focal adhesion. The need for tools to measure the local traction force in an independent manner brought about the development of the microfabricated cantilevers [28, 35, 36, 97]. The first cantilever

used for a traction force study was a horizontal cantilever which was fabricated on a silicon wafer using surface micromachining fabrication (Fig. 10a) [35]. The cantilever is deflected laterally when a cell pulls on the tip of the cantilever. The local traction force can be determined by multiplying the displacement of the tip by the stiffness of the cantilever. Interestingly, a migrating cell showed much larger force at its tail than those found at the front [35]. This result is similar to traction forces of keratocytes measured on silicone rubber [60], but somewhat different from findings by TFM [25, 77]. Nonetheless, the study with this micromachined device provided deeper understanding that forces at the front of the cell need to overcome those at the rear in order for a cell to migrate [90].

One of the limitations of the horizontal cantilever was a fixed, single location of force sensing which only allowed for a force measurement across a straight-line trajectory of a migrating cell. Unlike TFM, it did not provide a 2D map of traction forces acting at all adhesions of a cell. To address this issue, vertical arrays of elastomeric cantilevers were developed through a soft lithography and replica casting with a silicone rubber [28, 97]. Cells could spread out by attaching to the tips of individual posts (Fig. 10b) [63, 97]. Like the horizontal cantilever, posts deflect independent of each other and thus could report the local traction force based upon the stiffness of the posts. The use of this array of vertical cantilevers has helped confirm that RhoA signaling and focal adhesion size affect the strength of traction forces, as seen previously with wrinkling silicone membranes and TFM [97]. Moreover, the stiffness of a post can be easily tuned by tailoring dimensions of a post, so traction forces of a cell could be tested in response to different stiffness. As seen with 2D TFM, traction forces increased with the stiffness of the posts in an array, which indicates that the displacement at a focal adhesion is constant, but the local force increases in accordance to the stiffness of the

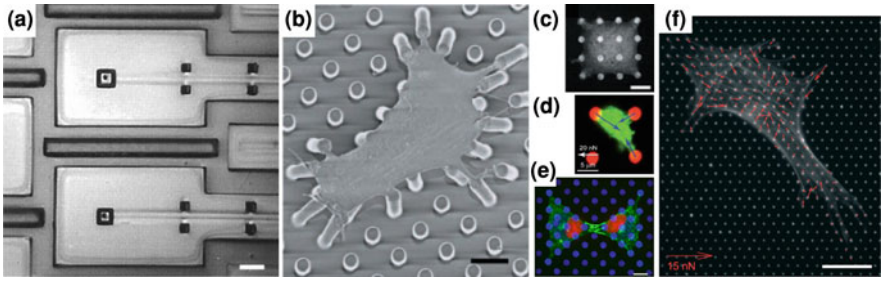

Fig. 10 Microfabricated cantilevers for traction force study. **a** MEMS-based horizontal cantilever force sensor. The end of the cantilever is positioned below the *square* opening in the surface of the substrate. Reproduced from [35]. *Bar* 10 μm. **b** Scanning electron micrograph of a smooth muscle cell attached on tips of vertical post arrays. **c** Microcontact printing can be used to confine cell spreading. **b** and **c** reproduced from [97]. *Scales bars* 10 μm. **d** Platelets in a clot (*green*) deflect the microposts (*red*). Reproduced from [65]. **e** Two cells patterned in a bow-tie shape apply a tugging force against each other. *Green β*-catenin, *red* DAPI, *blue* DiI. Reproduced from [68]. *Bar* 10 μm. **f** Cell on nanopost arrays showing force vectors (*red*). Reproduced from [108]. *Bar* 20 μm. Refer to the electronic version of this chapter, DOI: 10.1007/8415_2010_26, for viewing color version of this figure

environment [27, 41, 88]. It is worth noting that in 3D, TFM has shown that the magnitude of bead displacements were constant for different gel stiffness [72]. It may be likely that a cell has an integrin-associated mechanosensory feedback system that regulates the overall strain that actin and myosin produce within a cell.

One advantage of using silicone rubber for the posts is its availability to be functionalized by microcontact printing [98]. Cells can be patterned on the posts with different sized square patterns to pattern single cells, pairs of cells, or monolayers (Fig. 10c) [68, 78, 87, 97]. It has been seen that cells with more spreading exerted higher traction forces than those that are less spread, which agrees with findings from TFM studies. Confinement of spread area on a force sensor can allow one to rule out the effect of spread area and focus on the influences of other factors on traction forces. For example, cells have been observed to exert more force on stiffer substrates, but at the same time, they also spread more on stiffer environments so the effect on traction forces may be confounded by cell spreading [29, 69, 84, 85, 88]. Techniques to isolate the roles of cell spreading and stiffness would be beneficial to understand how cells regulate their adhesion strength and traction forces. Microcontact printing can also be used to examine intercellular forces of cells in a monolayer or adjacent to one another (Fig. 10e) [68, 78]. It has been seen that cells transmit tugging forces through their adherens junctions and the length of the junctions can determine the strength of force that can be withstood.

As the contractile and adhesion biomechanics of different cell types become of wider interest, post arrays with micrometer dimensions may not provide enough spatial resolution. In particular, platelets are amongst the smallest cells in the human body and have adhesion and contractile properties that are essential for clotting and vascular healing. The contractility of aggregated platelets on different ligands have been tested with the microscale post arrays (Fig. 10d) [65]. Moving forward, measuring the contractility of individual platelets would be valuable for evaluating the strength of platelet–platelet versus platelet–ECM interactions. One approach that could be helpful is nanopost arrays. Nanoposts have sub-micrometer dimensions and can be fabricated using projection lithography and reactive ion etching [108]. Cells plated on these posts showed similar spreading area and morphology as those found on continuous substrates (Fig. 10f). Further development of nanoposts might also elucidate the contractile mechanics of cells during migration and spreading. In particular, the lamellipodium and lamellum regions at the leading edge of a cell have different molecular players involved in their extension and contraction [102]. It would be beneficial to use the improved spatial resolution of nanoposts to examine the different strengths of traction forces at each of these regions.

4 Conclusions

Cells respond to many aspects of their surrounding ECM—from chemical presentations such as adhesivity, ligand density, and nanoscale ligand spacing to mechanical presentations such as stiffness and spreadable area. Surface

characterization techniques have provided a platform to find that cell adhesion requires integrin clustering, focal adhesion strengthening, and stress fiber formation. At the same time, studies with force measurement tools have revealed that myosin-based traction forces are necessary for the stability of cell adhesions. As new nanotechnology-based tools are developed, however, it is worth noting that a cell contains a complex network of interactions that combine receptor signaling, protein conformational changes, ion gradients, and transport along the cytoskeleton, which are all integrated to determine the activity of a cell. Particularly for the cell–ECM interactions, there is a reciprocal relationship between the cell and the ECM that involves mechanical forces. Specifically, the structure of the ECM can affect the adhesion, morphology, contractility and motility of cells, and at the same time, those cellular activities can also cause the restructuring of the surrounding ECM. When developing and applying new technology, one should consider secondary causes and maintain a degree of guarded skepticism when interpreting the results from the data. Moreover, it would be a vast improvement if there were approaches to study the different chemical and mechanical factors independently and in combination with each other.

We have highlighted the tools for studying the adhesions and traction forces of cells in response to changes in the microenvironment. It is worth noting that there are tools that can be used to applying nanoscale forces to a cell, which help understand the sensation and response involved in mechanotransduction [93]. These tools use magnetic forces, optical forces, or atomic force microscopy to test the local adhesion strengthening and cytoskeletal connection to focal adhesion [19, 37, 70, 89, 94, 103]. One common finding from these tools was that in response to external force, cells strengthen the connections between their adhesions and the ECM by recruiting additional focal adhesion proteins. Interestingly the same adhesion strengthening occurred in response to internally generated traction forces, which implicates that cells respond to forces acting internally or externally. A number of questions on the molecular nature of mechanosensing, focal adhesion maturation, cytoskeletal connectivity, membrane extension, and release of adhesions remain unaddressed. The tools to address these questions are emerging and with them will likely be the answers to important questions in stem cell and cancer biology.

Acknowledgments The authors are grateful for support in part from grants from the National Institutes of Health (HL097284) and the National Science Foundation's CAREER Award.

References

1. Abercrombie, M., Heaysman, J.E., Pegrum, S.M.: The locomotion of fibroblasts in culture. IV. Electron microscopy of the leading lamella. Exp. Cell Res. **67**(2), 359–367 (1971)
2. Alberts, B.: Molecular Biology of the Cell, 4th ed. Garland Science, New York (2002)
3. Alenghat, F.J., Ingber, D.E.: Mechanotransduction: all signals point to cytoskeleton, matrix, and integrins. Sci STKE **2002**(119), pe6 (2002)
4. Alexandrova, A.Y., Arnold, K., Schaub, S., Vasiliev, J.M., Meister, J.J., Bershadsky, A.D., Verkhovsky, A.B.: Comparative dynamics of retrograde actin flow and focal adhesions:

formation of nascent adhesions triggers transition from fast to slow flow. PLoS One **3**(9), e3234 (2008)
5. Arnold, M., Cavalcanti-Adam, E.A., Glass, R., Blummel, J., Eck, W., Kantlehner, M., Kessler, H., Spatz, J.P.: Activation of integrin function by nanopatterned adhesive interfaces. Chemphyschem **5**(3), 383–388 (2004)
6. Arnold, M., Hirschfeld-Warneken, V.C., Lohmuller, T., Heil, P., Blummel, J., Cavalcanti-Adam, E.A., Lopez-Garcia, M., Walther, P., Kessler, H., Geiger, B., Spatz, J.P.: Induction of cell polarization and migration by a gradient of nanoscale variations in adhesive ligand spacing. Nano Lett **8**(7), 2063–2069 (2008)
7. Bain, C.D., Whitesides, G.M.: Formation of 2-component surfaces by the spontaneous assembly of monolayers on gold from solutions containing mixtures of organic thiols. J. Am. Chem. Society **110**(19), 6560–6561 (1988)
8. Balaban, N.Q., Schwarz, U.S., Riveline, D., Goichberg, P., Tzur, G., Sabanay, I., Mahalu, D., Safran, S., Bershadsky, A., Addadi, L., Geiger, B.: Force and focal adhesion assembly: a close relationship studied using elastic micropatterned substrates. Nat. Cell Biol. **3**(5), 466–472 (2001)
9. Beningo, K.A., Dembo, M., Wang, Y.L.: Responses of fibroblasts to anchorage of dorsal extracellular matrix receptors. Proc. Natl. Acad. Sci. U.S.A. **101**(52), 18024–18029 (2004)
10. Bernardo, J.M., Smith, A.F.M.: Bayesian Theory. Wiley, Chichester (2000)
11. Brock, A., Chang, E., Ho, C.C., LeDuc, P., Jiang, X.Y., Whitesides, G.M., Ingber, D.E.: Geometric determinants of directional cell motility revealed using microcontact printing. Langmuir **19**(5), 1611–1617 (2003)
12. Burton, K., Taylor, D.L.: Traction forces of cytokinesis measured with optically modified elastic substrata. Nature **385**(6615), 450–454 (1997)
13. Burton, K., Park, J.H., Taylor, D.L.: Keratocytes generate traction forces in two phases. Mol. Biol. Cell **10**(11), 3745–3769 (1999)
14. Carter, S.B.: Principles of cell motility: the direction of cell movement and cancer invasion. Nature **208**(5016), 1183–1187 (1965)
15. Carter, S.B.: Haptotaxis and the mechanism of cell motility. Nature **213**(5073), 256–260 (1967)
16. Cavalcanti-Adam, E.A., Volberg, T., Micoulet, A., Kessler, H., Geiger, B., Spatz, J.P.: Cell spreading and focal adhesion dynamics are regulated by spacing of integrin ligands. Biophys. J. **92**(8):2964–2974 (2007)
17. Chen, C.S., Mrksich, M., Huang, S., Whitesides, G.M., Ingber, D.E.: Geometric control of cell life and death. Science **276**(5317), 1425–1428 (1997)
18. Choi, C.K., Vicente-Manzanares, M., Zareno, J., Whitmore, L.A., Mogilner, A., Horwitz, A.R.: Actin and alpha-actinin orchestrate the assembly and maturation of nascent adhesions in a myosin II motor-independent manner. Nat. Cell Biol. **10**(9), 1039–1050 (2008)
19. Choquet, D., Felsenfeld, D.P., Sheetz, M.P.: Extracellular matrix rigidity causes strengthening of integrin-cytoskeleton linkages. Cell **88**(1), 39–48 (1997)
20. Chrzanowska-Wodnicka, M., Burridge, K.: Rho-stimulated contractility drives the formation of stress fibers and focal adhesions. J. Cell Biol. **133**(6), 1403–1415 (1996)
21. Cukierman, E., Pankov, R., Stevens, D.R., Yamada, K.M.: Taking cell-matrix adhesions to the third dimension. Science **294**(5547), 1708–1712 (2001)
22. Curtis, A.S.: The mechanism of adhesion of cells to glass. A study by interference reflection microscopy. J. Cell Biol. **20**, 199–215 (1964)
23. Curtis, A.S., Forrester, J.V., McInnes, C., Lawrie, F.: Adhesion of cells to polystyrene surfaces. J. Cell Biol. **97**(5 Pt 1), 1500–1506 (1983).
24. Dembo, M., Oliver, T., Ishihara, A., Jacobson, K.: Imaging the traction stresses exerted by locomoting cells with the elastic substratum method. Biophys. J. **70**(4), 2008–2022 (1996)
25. Dembo, M., Wang, Y.L.: Stresses at the cell-to-substrate interface during locomotion of fibroblasts. Biophys. J. **76**(4), 2307–2316 (1999)

26. Discher, D., Dong, C., Fredberg, J.J., Guilak, F., Ingber, D., Janmey, P., Kamm, R.D., Schmid-Schonbein, G.W., Weinbaum, S.: Biomechanics: cell research and applications for the next decade. Ann. Biomed. Eng. **37**(5), 847–859 (2009)
27. Discher, D.E., Janmey, P., Wang, Y.L.: Tissue cells feel and respond to the stiffness of their substrate. Science **310**(5751), 1139–1143 (2005)
28. du Roure, O., Saez, A., Buguin, A., Austin, R.H., Chavrier, P., Silberzan, P., Ladoux, B.: Force mapping in epithelial cell migration. Proc. Natl. Acad. Sci. U.S.A. **102**(7), 2390–2395 (2005)
29. Engler, A., Bacakova, L., Newman, C., Hategan, A., Griffin, M., Discher, D.: Substrate compliance versus ligand density in cell on gel responses. Biophys. J. **86**(1), 617–628 (2004)
30. Engler, A.J., Sen, S., Sweeney, H.L., Discher, D.E.: Matrix elasticity directs stem cell lineage specification. Cell **126**(4), 677–689 (2006)
31. Engler, A.J., Carag-Krieger, C., Johnson, C.P., Raab, M., Tang, H.Y., Speicher, D.W., Sanger, J.W., Sanger, J.M., Discher, D.E.: Embryonic cardiomyocytes beat best on a matrix with heart-like elasticity: scar-like rigidity inhibits beating. J. Cell Sci. **121**(Pt 22), 3794–3802 (2008)
32. Even-Ram, S., Yamada, K.M.: Cell migration in 3D matrix. Curr. Opin. Cell Biol. **17**(5), 524–532 (2005)
33. Even-Ram, S., Doyle, A.D., Conti, M.A., Matsumoto, K., Adelstein, R.S., Yamada, K.M.: Myosin IIA regulates cell motility and actomyosin-microtubule crosstalk. Nat. Cell Biol. **9**(3), 299–309 (2007)
34. Folkman, J., Moscona, A.: Role of cell shape in growth control. Nature **273**(5661), 345–349 (1978)
35. Galbraith, C.G., Sheetz, M.P.: A micromachined device provides a new bend on fibroblast traction forces. Proc. Natl. Acad. Sci. U.S.A. **94**(17), 9114–9118 (1997)
36. Galbraith, C.G., Sheetz, M.P.: Forces on adhesive contacts affect cell function. Curr. Opin. Cell Biol. **10**(5), 566–571 (1998)
37. Galbraith, C.G., Yamada, K.M., Sheetz, M.P.: The relationship between force and focal complex development. J. Cell Biol. **159**(4), 695–705 (2002)
38. Gaudet, C., Marganski, W.A., Kim, S., Brown, C.T., Gunderia, V., Dembo, M., Wong, J.Y.: Influence of type I collagen surface density on fibroblast spreading, motility, and contractility. Biophys. J. **85**(5), 3329–3335 (2003)
39. Geiger, B., Bershadsky, A., Pankov, R., Yamada, K.M.: Transmembrane crosstalk between the extracellular matrix—cytoskeleton crosstalk. Nat. Rev. Mol. Cell Biol. **2**(11), 793–805 (2001)
40. Geiger, B., Spatz, J.P., Bershadsky, A.D.: Environmental sensing through focal adhesions. Nat. Rev. Mol. Cell Biol. **10**(1), 21–33 (2009)
41. Ghibaudo, M., Saez, A., Trichet, L., Xayaphoummine, A., Browaeys, J., Silberzan, P., Buguin, A., Ladoux, B.: Traction forces and rigidity sensing regulate cell functions. Soft Matter **4**(9), 1836–1843 (2008)
42. Goffin, J.M., Pittet, P., Csucs, G., Lussi, J.W., Meister, J.J., Hinz, B.: Focal adhesion size controls tension-dependent recruitment of alpha-smooth muscle actin to stress fibers. J. Cell Biol. **172**(2), 259–268 (2006)
43. Grinnell, F.: Cellular adhesiveness and extracellular substrata. Int. Rev. Cytol. **53**, 65–144 (1978)
44. Harris, A.: Behavior of cultured cells on substrata of variable adhesiveness. Exp. Cell Res. **77**(1), 285–297 (1973)
45. Harris, A.K., Wild, P., Stopak, D.: Silicone rubber substrata: a new wrinkle in the study of cell locomotion. Science **208**(4440), 177–179 (1980)
46. Helfman, D.M., Levy, E.T., Berthier, C., Shtutman, M., Riveline, D., Grosheva, I., Lachish-Zalait, A., Elbaum, M., Bershadsky, A.D.: Caldesmon inhibits nonmuscle cell contractility and interferes with the formation of focal adhesions. Mol. Biol. Cell **10**(10), 3097–3112 (1999)

47. Hoover, D.K., Chan, E.W., Yousaf, M.N.: Asymmetric peptide nanoarray surfaces for studies of single cell polarization. J. Am. Chem. Soc. **130**(11), 3280–3281 (2008)
48. Hynes, R.O.: Integrins: versatility, modulation, and signaling in cell adhesion. Cell **69**(1), 11–25 (1992)
49. Ingber, D.E.: Mechanobiology and diseases of mechanotransduction. Ann. Med. **35**(8), 564–577 (2003)
50. Inoue, S., Iida, Y., Otani, Y., Hirano, Y., Tabata, Y.: Adhesion behavior of human adipo-stromal cells on self-assembled monolayers with different surface densities or gradients of RGD peptide. J. Biomater. Sci. Polym. Ed. **20**(4), 495–510 (2009)
51. Irvine, D.J., Mayes, A.M., Griffith, L.G.: Nanoscale clustering of RGD peptides at surfaces using Comb polymers. 1. Synthesis and characterization of Comb thin films. Biomacromolecules **2**(1), 85–94 (2001)
52. Isenberg, B.C., Dimilla, P.A., Walker, M., Kim, S., Wong, J.Y.: Vascular smooth muscle cell durotaxis depends on substrate stiffness gradient strength. Biophys. J. **97**(5), 1313–1322 (2009)
53. Jiang, X., Ferrigno, R., Mrksich, M., Whitesides, G.M.: Electrochemical desorption of self-assembled monolayers noninvasively releases patterned cells from geometrical confinements. J. Am. Chem. Soc. **125**(9), 2366–2367 (2003)
54. Jiang, X., Bruzewicz, D.A., Wong, A.P., Piel, M., Whitesides, G.M.: Directing cell migration with asymmetric micropatterns. Proc. Natl. Acad. Sci. U.S.A. **102**(4), 975–978 (2005)
55. Kilian, K.A., Bugarija, B., Lahn, B.T., Mrksich, M.: Geometric cues for directing the differentiation of mesenchymal stem cells. Proc. Natl. Acad. Sci. U.S.A. **107**(11), 4872–4877 (2010)
56. Koo, L.Y., Irvine, D.J., Mayes, A.M., Lauffenburger, D.A., Griffith, L.G.: Co-regulation of cell adhesion by nanoscale RGD organization and mechanical stimulus. J. Cell Sci. **115**(Pt 7), 1423–1433 (2002)
57. Kumar, G., Ho, C.C., Co, C.C.: Guiding cell migration using one-way micropattern arrays. Adv. Mater. **19**(8), 1084–1090 (2007)
58. Landau, L.D., Lifshits, E.M., Kosevich, A.d.M., Pitaevskii, L.P.: Theory of Elasticity, 3rd English ed. Pergamon Press, Oxford (1986)
59. Lee, G.M., Loeser, R.F.: Cell surface receptors transmit sufficient force to bend collagen fibrils. Exp. Cell Res. **248**(1), 294–305 (1999)
60. Lee, J., Leonard, M., Oliver, T., Ishihara, A., Jacobson, K.: Traction forces generated by locomoting keratocytes. J. Cell Biol. **127**(6 Pt 2), 1957–1964 (1994)
61. Lee, K.B., Park, S.J., Mirkin, C.A., Smith, J.C., Mrksich, M.: Protein nanoarrays generated by dip-pen nanolithography. Science **295**(5560), 1702–1705 (2002)
62. Lele, T.P., Pendse, J., Kumar, S., Salanga, M., Karavitis, J., Ingber, D.E.: Mechanical forces alter zyxin unbinding kinetics within focal adhesions of living cells. J. Cell. Physiol. **207**(1), 187–194 (2006)
63. Lemmon, C.A., Sniadecki, N.J., Ruiz, S.A., Tan, J.L., Romer, L.H., Chen, C.S.: Shear force at the cell–matrix interface: enhanced analysis for microfabricated post array detectors. Mech. Chem. Biosyst. **2**(1), 1–16 (2005)
64. Levental, K.R., Yu, H., Kass, L., Lakins, J.N., Egeblad, M., Erler, J.T., Fong, S.F., Csiszar, K., Giaccia, A., Weninger, W., Yamauchi, M., Gasser, D.L., Weaver, V.M.: Matrix crosslinking forces tumor progression by enhancing integrin signaling. Cell **139**(5), 891–906 (2009)
65. Liang, X.M., Han, S.J., Reems, J.A., Gao, D., Sniadecki, N.J.: Platelet retraction force measurements using flexible post force sensors. Lab Chip **10**(8), 991–998 (2010)
66. Liedberg, B., Tengvall, P.: Molecular gradients of omega-substituted alkanethiols on gold—preparation and characterization. Langmuir **11**(10), 3821–3827 (1995)
67. Liu, L., Ratner, B.D., Sage, E.H., Jiang, S.: Endothelial cell migration on surface-density gradients of fibronectin, VEGF, or both proteins. Langmuir **23**(22), 11168–11173 (2007)

68. Liu, Z., Tan, J.L., Cohen, D.M., Yang, M.T., Sniadecki, N.J., Ruiz, S.A., Nelson, C.M., Chen, C.S.: Mechanical tugging force regulates the size of cell–cell junctions. Proc. Natl. Acad. Sci. U.S.A. **107**(22), 9944–9949 (2010)
69. Lo, C.M., Wang, H.B., Dembo, M., Wang, Y.L.: Cell movement is guided by the rigidity of the substrate. Biophys. J. **79**(1), 144–152 (2000)
70. Mack, P.J., Kaazempur-Mofrad, M.R., Karcher, H., Lee, R.T., Kamm, R.D.: Force-induced focal adhesion translocation: effects of force amplitude and frequency. Am. J. Physiol. Cell Physiol. **287**(4), C954–C962 (2004)
71. Maheshwari, G., Brown, G., Lauffenburger, D.A., Wells, A., Griffith, L.G.: Cell adhesion and motility depend on nanoscale RGD clustering. J. Cell Sci. **113**(Pt 10), 1677–1686 (2000)
72. Maskarinec, S.A., Franck, C., Tirrell, D.A., Ravichandran, G.: Quantifying cellular traction forces in three dimensions. Proc. Natl. Acad. Sci. U.S.A. **106**(52), 22108–22113 (2009)
73. McBeath, R., Pirone, D.M., Nelson, C.M., Bhadriraju, K., Chen, C.S.: Cell shape, cytoskeletal tension, and RhoA regulate stem cell lineage commitment. Dev. Cell **6**(4), 483–495 (2004)
74. Meshel, A.S., Wei, Q., Adelstein, R.S., Sheetz, M.P.: Basic mechanism of three-dimensional collagen fibre transport by fibroblasts. Nat. Cell Biol. **7**(2), 157–164 (2005)
75. Montell, D.J.: Morphogenetic cell movements: diversity from modular mechanical properties. Science **322**(5907), 1502–1505 (2008)
76. Mrksich, M., Dike, L.E., Tien, J., Ingber, D.E., Whitesides, G.M.: Using microcontact printing to pattern the attachment of mammalian cells to self-assembled monolayers of alkanethiolates on transparent films of gold and silver. Exp. Cell Res. **235**(2), 305–313 (1997)
77. Munevar, S., Wang, Y., Dembo, M.: Traction force microscopy of migrating normal and H-ras transformed 3T3 fibroblasts. Biophys. J. **80**(4), 1744–1757 (2001)
78. Nelson, C.M., Jean, R.P., Tan, J.L., Liu, W.F., Sniadecki, N.J., Spector, A.A., Chen, C.S.: Emergent patterns of growth controlled by multicellular form and mechanics. Proc. Natl. Acad. Sci. U.S.A. **102**(33), 11594–11599 (2005)
79. Paszek, M.J., Zahir, N., Johnson, K.R., Lakins, J.N., Rozenberg, G.I., Gefen, A., Reinhart-King, C.A., Margulies, S.S., Dembo, M., Boettiger, D., Hammer, D.A., Weaver, V.M.: Tensional homeostasis and the malignant phenotype. Cancer Cell **8**(3), 241–254 (2005)
80. Pelham, R.J., Jr., Wang, Y.: Cell locomotion and focal adhesions are regulated by substrate flexibility. Proc. Natl. Acad. Sci. U.S.A. **94**(25), 13661–13665 (1997)
81. Pellegrin, S., Mellor, H.: Actin stress fibres. J. Cell Sci. **120**(Pt 20), 3491–3499 (2007)
82. Petty, R.T., Li, H.W., Maduram, J.H., Ismagilov, R., Mrksich, M.: Attachment of cells to islands presenting gradients of adhesion ligands. J. Am. Chem. Soc. **129**(29), 8966–8967 (2007)
83. Prime, K.L., Whitesides, G.M.: Self-assembled organic monolayers: model systems for studying adsorption of proteins at surfaces. Science **252**(5010), 1164–1167 (1991)
84. Rajagopalan, P., Marganski, W.A., Brown, X.Q., Wong, J.Y.: Direct comparison of the spread area, contractility, and migration of balb/c 3T3 fibroblasts adhered to fibronectin- and RGD-modified substrata. Biophys. J. **87**(4), 2818–2827 (2004)
85. Reinhart-King, C.A., Dembo, M., Hammer, D.A.: The dynamics and mechanics of endothelial cell spreading. Biophys. J. **89**(1), 676–689 (2005)
86. Riveline, D., Zamir, E., Balaban, N.Q., Schwarz, U.S., Ishizaki, T., Narumiya, S., Kam, Z., Geiger, B., Bershadsky, A.D.: Focal contacts as mechanosensors: externally applied local mechanical force induces growth of focal contacts by an mDia1-dependent and ROCK-independent mechanism. J. Cell Biol. **153**(6), 1175–1186 (2001)
87. Ruiz, S.A., Chen, C.S.: Emergence of patterned stem cell differentiation within multicellular structures. Stem Cells **26**(11), 2921–2927 (2008)
88. Saez, A., Buguin, A., Silberzan, P., Ladoux, B.: Is the mechanical activity of epithelial cells controlled by deformations or forces? Biophys. J. **89**(6), L52–L54 (2005)

89. Selhuber-Unkel, C., Erdmann, T., Lopez-Garcia, M., Kessler, H., Schwarz, U.S., Spatz, J.P.: Cell adhesion strength is controlled by intermolecular spacing of adhesion receptors. Biophys. J. **98**(4), 543–551 (2010)
90. Sheetz, M.P., Felsenfeld, D.P., Galbraith, C.G.: Cell migration: regulation of force on extracellular-matrix-integrin complexes. Trends Cell Biol. **8**(2), 51–54 (1998)
91. Smith, J.T., Tomfohr, J.K., Wells, M.C., Beebe, T.P., Jr., Kepler, T.B., Reichert, W.M.: Measurement of cell migration on surface-bound fibronectin gradients. Langmuir **20**(19), 8279–8286 (2004)
92. Smith, J.T., Elkin, J.T., Reichert, W.M.: Directed cell migration on fibronectin gradients: effect of gradient slope. Exp. Cell Res. **312**(13), 2424–2432 (2006)
93. Sniadecki, N.J., Desai, R.A., Ruiz, S.A., Chen, C.S.: Nanotechnology for cell–substrate interactions. Ann. Biomed. Eng. **34**(1), 59–74 (2006)
94. Sniadecki, N.J., Anguelouch, A., Yang, M.T., Lamb, C.M., Liu, Z., Kirschner, S.B., Liu, Y., Reich, D.H., Chen, C.S.: Magnetic microposts as an approach to apply forces to living cells. Proc. Natl. Acad. Sci. U.S.A. **104**(37), 14553–14558 (2007)
95. Spatz, J.P., Mossmer, S., Hartmann, C., Moller, M., Herzog, T., Krieger, M., Boyen, H.G., Ziemann, P., Kabius, B.: Ordered deposition of inorganic clusters from micellar block copolymer films. Langmuir **16**(2), 407–415 (2000)
96. Stopak, D., Wessells, N.K., Harris, A.K.: Morphogenetic rearrangement of injected collagen in developing chicken limb buds. Proc. Natl. Acad. Sci. U.S.A. **82**(9), 2804–2808 (1985)
97. Tan, J.L., Tien, J., Pirone, D.M., Gray, D.S., Bhadriraju, K., Chen, C.S.: Cells lying on a bed of microneedles: an approach to isolate mechanical force. Proc. Natl. Acad. Sci. U.S.A. **100**(4), 1484–1489 (2003)
98. Tan, J.L., Liu, W., Nelson, C.M., Raghavan, S., Chen, C.S.: Simple approach to micropattern cells on common culture substrates by tuning substrate wettability. Tissue Eng. **10**(5–6), 865–872 (2004)
99. Thery, M., Racine, V., Piel, M., Pepin, A., Dimitrov, A., Chen, Y., Sibarita, J.B., Bornens, M.: Anisotropy of cell adhesive microenvironment governs cell internal organization and orientation of polarity. Proc. Natl. Acad. Sci. U.S.A. **103**(52), 19771–19776 (2006)
100. Verschueren, H.: Interference reflection microscopy in cell biology: methodology and applications. J. Cell Sci. **75**, 279–301 (1985)
101. Vicente-Manzanares, M., Zareno, J., Whitmore, L., Choi, C.K., Horwitz, A.F.: Regulation of protrusion, adhesion dynamics, and polarity by myosins IIA and IIB in migrating cells. J. Cell Biol. **176**(5), 573–580 (2007)
102. Vicente-Manzanares, M., Ma, X., Adelstein, R.S., Horwitz, A.R.: Non-muscle myosin II takes centre stage in cell adhesion and migration. Nat. Rev. Mol. Cell Biol. **10**(11), 778–790 (2009)
103. Wang, N., Butler, J.P., Ingber, D.E.: Mechanotransduction across the cell surface and through the cytoskeleton. Science **260**(5111), 1124–1127 (1993)
104. Wang, Y.L., Pelham, R.J., Jr.: Preparation of a flexible, porous polyacrylamide substrate for mechanical studies of cultured cells. Methods Enzymol. **298**, 489–496 (1998)
105. Whitesides, G.M., Ostuni, E., Takayama, S., Jiang, X.Y., Ingber, D.E.: Soft lithography in biology and biochemistry. Ann. Rev. Biomed. Eng. **3**, 335–373 (2001)
106. Xia, Y., Whitesides, G.M.: Soft lithography. Annu. Rev. Mater. Sci. **28**, 153–184 (1998)
107. Xiong, J.P., Stehle, T., Diefenbach, B., Zhang, R.G., Dunker, R., Scott, D.L., Joachimiak, A., Goodman, S.L., Arnaout, M.A.: Crystal structure of the extracellular segment of integrin alpha V beta 3. Science **294**(5541), 339–345 (2001)
108. Yang, M.T., Sniadecki, N.J., Chen, C.S.: Geometric considerations of micro- to nanoscale elastomeric post arrays to study cellular traction forces. Adv. Mater. **19**(20), 3119–3123 (2007)
109. Yousaf, M.N., Houseman, B.T., Mrksich, M.: Using electroactive substrates to pattern the attachment of two different cell populations. Proc. Natl. Acad. Sci. U.S.A. **98**(11), 5992–5996 (2001)

110. Zaman, M.H., Trapani, L.M., Sieminski, A.L., Mackellar, D., Gong, H., Kamm, R.D., Wells, A., Lauffenburger, D.A., Matsudaira, P.: Migration of tumor cells in 3D matrices is governed by matrix stiffness along with cell–matrix adhesion and proteolysis. Proc. Natl. Acad. Sci. U.S.A. **103**(29), 10889–10894 (2006)
111. Zamir, E., Geiger, B.: Molecular complexity and dynamics of cell-matrix adhesions. J. Cell Sci. **114**(Pt 20), 3583–3590 (2001)

The Mechanical Environment of Cells in Collagen Gel Models

Global and Local Effects in Three-dimensional Biological Hydrogels

Kristen L. Billiar

Abstract It is becoming increasingly clear that cells behave differently in two-dimensional (2D) culture than in three-dimensional (3D) tissues, and that 3D culture models and new tools for probing them are needed for advancing our knowledge of mechanobiology. Cells physically interact with their surrounding extracellular matrix; they are able to sense the local stiffness, tension, and deformation within the matrix and, in turn, are able to remodel the matrix and generate forces with long-range effects. In tissues with sufficiently high cell density, the cells interact and generate coordinated forces which can be regulated by controlling the macroscopic mechanical boundary conditions. Understanding this dynamic reciprocity between the cells, matrix, and external environment is critical for determining how the cells sense, transduce, and respond to their mechanical surroundings. However, even in simplified models of 3D tissues, quantification of local (non-linear viscoelastic) mechanical properties is problematic, and the transfer of strain and stress to the cells is complicated by non-affine, non-uniform deformation of the cell/matrix composite. This review focuses on methods for characterizing and modulating the mechanical environment of cells cultured within reconstituted collagen gels, the most extensively utilized in vitro models of native 3D tissue.

K. L. Billiar (✉)
Worcester Polytechnic Institute, Worcester, MA 01602, USA
e-mail: kbilliar@wpi.edu

Stud Mechanobiol Tissue Eng Biomater (2011) 4: 201–245
DOI: 10.1007/8415_2010_30

Published Online: 27 November 2010

1 Introduction

The mechanical environment surrounding cells guides the development, remodeling and pathogenesis of tissues in vivo. For example, blood vessels remodel with hypertension, muscles atrophy when a limb is placed in a cast, and skin contracture is reduced with splinting following injury. The need for more quantitative study of the effects of mechanical cues on cell behavior, i.e., mechanobiology, has lead to the development of a broad range of tools as highlighted in this volume. Although our knowledge of the mechanisms behind mechanotransduction have increased dramatically in recent years, the majority of the powerful new methods used to study cells are applicable only to two-dimensional (2D) cultures.

Cells have repeatedly been shown to behave differently in 2D culture than in three-dimensional (3D) models and tissues [100, 102]. For example, the "pancake" cell shape characteristic of 2D culture is not found in 3D gels, rather stellate, bipolar, or rounded cells are observed. Further, cell proliferation and protein biosynthesis are generally suppressed in cells entrapped in protein-based gels relative to culture on 2D tissue culture surfaces, and cell motility, an important means of reorganization of the surrounding matrix, is not limited to in-plane migration. In some cases, contradictory responses to mechanical stimuli are observed 2D and 3D systems. For example, in 2D motility is maximal on higher stiffness substrates in contrast to faster tumor cell movement in 3D matrices of lower protein concentration (and lower stiffness) [139]. In cyclically stretched 2D systems, adherent cells generally align along directions of minimal stretch [68], whereas cells cultured within uniaxially stretched 3D protein gels generally align in the direction of stretch along with the fibrous proteins [113]. As a final example, breast epithelial cells develop like tumor cells when cultured on 2D surfaces, but in 3D basal lamina protein gels (Matrigel) they revert to normal growth behavior [101].

Reasons for discrepancies in cell behavior between 2D and 3D environments are undoubtedly complex and include differences in stiffness (3D models are generally compliant compared to standard 2D culture) [100], the alignment [54] and microstructure [43] of fibrous structures in protein-based 3D systems, concentration of ligands available for binding, specialized cell–matrix adhesions [28], and more symmetric adhesions over surface of cell [44]. Differences may arise due to "dimensionality" itself as the cells are surrounded by fluid in 2D and simply adhered to the surface of a material in contrast to being entirely encased in the material in 3D. Imagine the difference of walking on a carpet compared to trying to walk through a massive tangle of yarn. To separate these effects which confound the study of mechanobiology, controlled manipulation of the physical environment of cells cultured within 3D tissue models is necessary while keeping the biochemical environment constant. This review focuses on methods for modulating the mechanical environment of cells cultured within reconstituted collagen gels, the most highly utilized in vitro model systems for the study of cell behavior in 3D.

Collagen is the major structural protein in connective tissues. Self-assembly of acid soluble collagen at 37°C to form a "stiff" gel was first observed approximately 40 years ago [53, 64]. Under these conditions collagen molecules and aggregates of molecules spontaneously assemble. Reconstituted collagen gel models populated with cells were developed by Bell et al. [10] in the late 1970s and utilized for the basis of tissue engineered skin and blood vessels. Although successful for wound healing treatments (Apligraf®, Organogenesis Inc.), collagen gels have not been successfully utilized for substitution of blood vessels or other load bearing tissues as collagen gels neither obtain the stiffness and strength of mature tissue nor the native collagen hierarchy, even with long-term mechanical conditioning (months). Primarily, these biopolymer gels are utilized as model systems to study cell behavior such as cell contraction and migration in simulated "developmental" or "healing" environments (depending upon boundary conditions) [50].

Cells cultured within collagen gels are surrounded by "native" extracellular matrix (ECM) proteins and can remodel their surrounding fibrous matrix. This remodeling is modulated by local and global physical cues, and it results in changes to the mechanical properties. This "dynamic reciprocity" between the cells and matrix resembles that which occurs in vivo [50]. Remodeling of ECM (reviewed by Daley et al. [29]) is a key aspect of tissue development and fibrosis, is critical for "functional tissue engineering," and is a major advantage of utilizing the collagen gel model system. Synthetic polymeric hydrogels fail to capture this fibrillar structure and remodeling, although synthetic hydrogels can be engineered to degrade with ECM production by the cells filling in the gaps [62]. Structural guidance and anisotropy can also be engineered into collagen gels by alignment of collagen fibrils via pre-processing (magnetically or mechanically) which provide additional physical cues that are difficult to incorporate into synthetic systems.

Despite many studies of the mechanics of collagen fibrillation [119] and the use of collagen gels for understanding cell–matrix behavior in 3D [108], issues remain in the use of this popular in vitro model for the controlled study of mechanobiology. This brief review is not meant to cover the "3D mechanobiology" literature exhaustively, rather we aim to clarify the terminology of the field and highlight how collagen gels can be used both in short- and long-term studies for different purposes, and how changes in global boundary conditions can be used to alter local cell behavior.

In the next section, we introduce the creation of collagen gel models with detailed discussion of the effects of collagen concentration, cell density, collagen sources, and extraction methods on the gel. Then in Sect. 3, the structure and physical properties of collagen gels are discussed. We describe methods for altering the mechanical environment using various static and dynamic boundary conditions in Sects. 4 and 5, respectively. The local environment of the cell within the fibrous matrix and calculation of cell-generated forces are discussed in Sect. 6. Finally, Sect. 7 provides a general discussion and look to the future use of 3D collagen gel model systems.

2 Composition and Creation of ECM Models

2.1 Creation of a Cell-populated Collagen Gel: The Basics

Cell-populated collagen gels are created by mixing together concentrated solutions of purified collagen, cells, and media. The solution is "cast" (poured into a mold), allowed to "gel" (fibrillate by self-assembly), and cultured under a variety of mechanical and chemical environments. Typically, they are cultured either attached to a dish/surface or gently released from the surface following gelation and allowed to culture free floating (see Sect. 4). *Compaction* of the gel by the resident cells is most striking in free floating gels where traction forces generated by migration of the cells results in reorganization of the gel and expulsion of unbound water which reduces the gel volume by an order of magnitude and increases the collagen density. The *compaction* process is often termed *contraction* of the gel, although it is best to reserve the term *contraction* for cell contractile behavior which utilizes muscle-like cell machinery (see grey terminology box below).

Typically, cell-populated collagen gels are produced by rapidly combining *stock solutions* of purified monomeric collagen (collagen extraction discussed in Sect. 2.4), cells, and concentrated cell culture medium. The stock collagen solution is stored in chilled weak acid to avoid premature fibrillation thus NaOH (typically 0.1 M) is used to neutralize pH of the solution. Concentrated medium (e.g., 5× DMEM) and serum are utilized to obtain a normo-osmotic solution with the desired serum concentration for culture. For example, for 10 ml of an initial solution with 2 mg/ml collagen, 0.5 million cells/ml, and 10% serum, stock solutions of the following volumes can be utilized: 4 ml of 5 mg/ml collagen, 5 ml of 1 million cells/ml with 20% serum, and 1 ml of 5× concentrated medium (the NaOH volume is minimal) [13]. The solution is quickly pipetted into a culture dish with desired shape, placed in a warm stable location, and allowed to gel for 30–60 min before further manipulation.

Compaction and Concentration Terminology

Compaction: short-term cell-mediated reorganization of protein fibers in a hydrogel where the majority of the fluid is expelled resulting in a dramatic reduction of gel volume.
Contraction: active exertion of tension on the protein matrix by stationary cells (distinct from forces imposed during migration during compaction).
Stock concentration: concentration of in the stock solution before forming a hydrogel.
Initial concentration: protein concentration in the cast hydrogel which including dilution by media and cells.
Final concentration: protein concentration at end of culture duration (post compaction, remodeling, stretching, etc.)

2.2 Effects of Protein Concentration

The initial concentration of the protein alters both the mechanics of the gel and the ligand presentation (number of sites for cell adhesion). Typical concentrations range from 0.3 to 5 mg/ml collagen (although some report up to 30 mg/ml) [37, 58, 94, 142]. These hydrogels typically contain <1% protein and are >99% water since water is 1,000 mg/ml and the gels typically contain <10 mg collagen per ml solution. For comparison, most native connective tissues have hundreds of mg/ml protein and 70–80% water; a table of values for gels and various tissues can be found in [100]. When comparing studies, one must be careful to differentiate between stock concentration, initial concentration, and final concentration (see terminology text box), as many groups use "final" concentration for the protein concentration in the gel after it is cast, before the start of culture. The cells within the gels interact with the collagen fibrils (Fig. 1a) and remodel, crosslink, and synthesize ECM proteins. Thus, after standard culture duration (>6 h) the initial protein concentration does not represent the local environment of the cell accurately which confounds the study of mechanobiology as the stiffness and collagen (and thus ligand) density change over time. Further, the protein concentration is higher around the cell due to local densification (see Fig. 1b).

Interestingly, the degree of compaction decreases with an increase in initial concentration, and the average final concentration of a collagen gel is actually higher for gels with lower initial concentration [58, 94, 142]. For example, Zhu

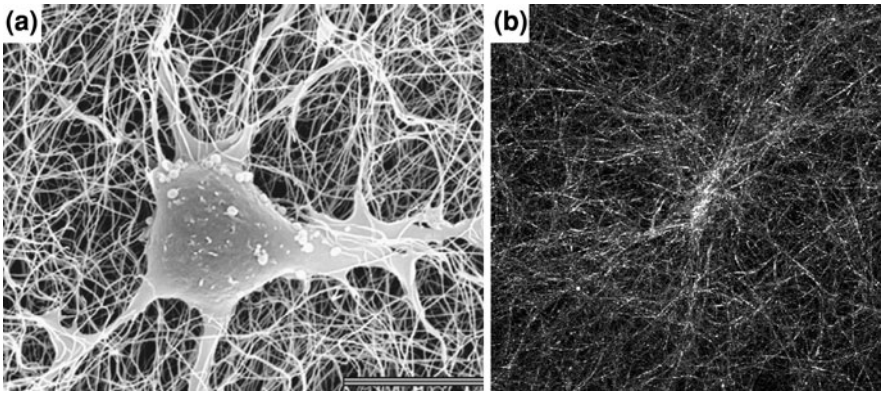

Fig. 1 **a** Scanning electron micrograph of a human fibroblast within a collagen gel demonstrating the multiple adhesions to the collagen fibers. Note the small size of the fibers and pores relative to the cell size and the penetration and entanglement of cell extensions and collagen matrix. Reprinted from Ref. [108] with permission from Elsevier. Bar, 10 μm **b** Confocal reflectance image of the collagen network surrounding a fibroblast cultured within a collagen gel after 4 h in culture showing the local densification produced by fibroblast-mediated compaction. Low passage neonatal human dermal fibroblasts (5×10^4 cells/ml) and 2% FBS were utilized; shear storage modulus ~50 Pa. Image width = 180 μm. Image generously provided by Dr. Sherry Voytik-Harbin

et al. [142] varied the initial collagen concentration from 0.75 to 2.5 mg/ml and after 21 days compaction by human fetal lung fibroblasts measured final collagen concentrations of ~50 mg/ml to ~8 mg/ml, respectively; Helary et al. [58] found similar a monotonic relationship between initial and final collagen concentration for human dermal fibroblasts (0.66–3 mg/ml initial concentration resulting in 37–11 mg/ml final concentration, respectively). Evans and Barocas [37] found this pattern only with initial cell density >0.15 million cells/ml; they also found the final mechanical properties could not be predicted by the final collagen concentration alone (see Sect. 3.2) although they only cultured the gels for 24 h. Collagen degradation occurs during culture due to matrix metalloproteinase (MMP) secretion, although total collagen after substantial culture duration (>2 weeks) is relatively constant [142] even with a high initial cell density (2×10^6 cells/ml) [1]. The collagen in the gel inhibits collagen synthesis by the resident cells [25] but some collagen is secreted along with other proteins and polysaccharides, notably fibronectin and hyaluronic acid.

2.3 *Effects of Cell Density and Activity*

The cells entrapped within collagen gels (Fig. 2a) have striking dendritic morphology not observed in those cultured on the surface of collagen-coated coverslips (Fig. 2b). The morphology of the cells is also dependent upon the cell density, an indication that the cells actively interact and can sense the traction and/or soluble factors from adjacent cells (compare Fig. 2c, d with low and high cell density, respectively).

A wide range of initial cell densities are utilized in collagen gels depending upon the application from $<10^4$ [10] to $>10^6$ cells/ml [1]. As with stock, initial, and final protein concentrations, definitions of cell density can differ between studies in a similar manner. At low initial density (e.g., 10^4 cells/ml) the cells do not initially interact with each other as there is, on average, approximately 500 μm between cells (assuming even distribution of cells and cuboidal volume elements). At high density (e.g., 10^6 cells/ml with approximately 100 μm between cells) the cells can sense their neighbors and interact even at short culture durations; a more extended cell morphology can be observed 1–4 h after casting than seen in cells seeded at low density. In general, the final cell density is determined by the extent of gel compaction by the cells as proliferation is very slow in 3D gels compared to standard (stiff) 2D culture. For example, it is commonly reported that fibroblast cell doubling time is on the order of a week in a standard density collagen gel compared to 12–14 h on tissue culture plastic. Grinnell [50] suggests that proliferation is inhibited by increased collagen fibril-cells contacts; however, in compliant 2D systems the regulation of cell proliferation is strongly controlled by matrix stiffness [32] and recent studies demonstrate that cell proliferation increases with initial collagen concentration (at high concentrations, which correlates to initial stiffness) [56, 58]. Alternatively, Simmons and colleagues [138] recently

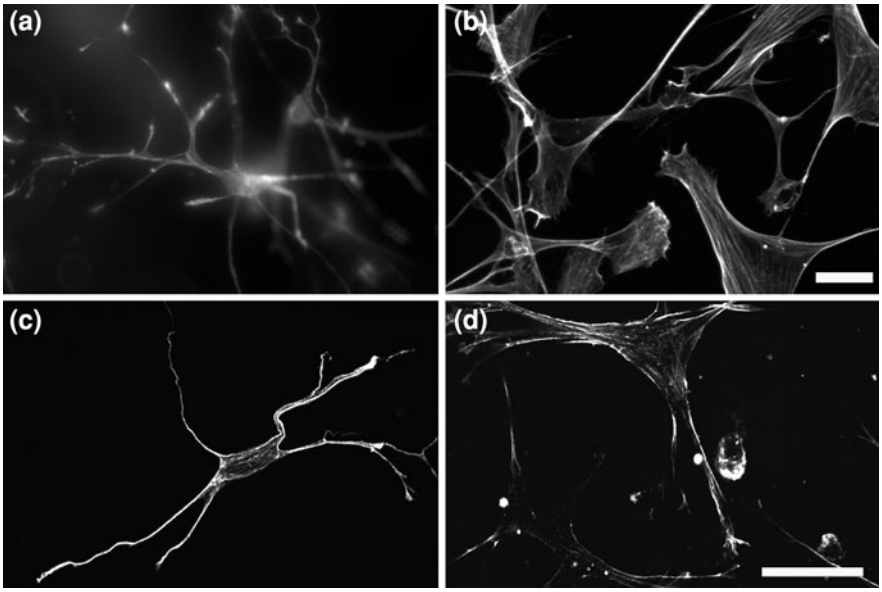

Fig. 2 Fluorescent images of human fibroblasts cultured within collagen gels (**a**, **c**, **d**) show dendritic shapes compared to the flat, extended morphology of cells on collagen-coated glass (**b**). Cells within gels cultured at low density (10^5 cells/ml) have shorter extensions when gels are unrestrained (**a**) than when anchored (**c**). The cells more closely resemble the stiff glass control when cultured at high density (10^6 cells/ml) where they interact heavily (**d**). All cells stimulated with PDGF for robust development of stress fibers in a short time period (1 h for **a** and **b** and 4 h for **c** and **d**) and visualized by phalloidin staining of the actin cytoskeleton. *Scale bars* indicate 25 μm; images in *same row* have same magnification. Images generously provided by Frederick Grinnell and reprinted from Mol Biol Cell, 13, Tamariz, E. and Grinnell, F. Modulation of fibroblast morphology and adhesion during collagen matrix remodeling, 3915–3929, 2002 (**a** and **b**) and from Ref. [51] (**c** and **d**) with permission from the American Society for Cell Biology

report that valvular interstitial cells proliferated more rapidly on compliant matrices (thick collagen gels) than stiff matrices (thin gels on glass). Regardless, the cell density increases with culture duration as the cells compact the matrix resulting in increased cell–cell interactions and collective behavior even with low initial density and slow proliferation. Thus, if it is desired to study how an individual cell is affected by its local mechanical environment in a 3D gel, e.g., the effect of matrix stiffness on migration speed [118], low cell density and short culture duration should be chosen. Although collagen gels are used for these types of "single cell" studies, models with higher initial cell density are utilized in the majority of research, and the collective response of the cells to chemical and physical stimuli are studied with extended culture duration.

Not surprisingly, the extent and rate of compaction is strongly affected by cell density. In their seminal paper, Bell et al. [10] demonstrated dose-dependent increases in free gel compaction from 10^4 to 10^5 fibroblasts/ml, with differences

being most prominent at low cell densities and little difference in final compaction at higher cell densities (4×10^4 to 1×10^5). Allen and Schor [4] observed a linear increase in the initial (2 h) rate of compaction with cell density from 5×10^4 to 5×10^5 fibroblasts/ml. In collagen gels rigidly attached to an isometric force transducer (a.k.a. culture force monitor), the force during compaction has been shown to increase monotonically with cell density although the relationship can be complex [31]. These trends have been confirmed in further systematic studies by others [37, 58, 94, 106]. Further, a high degree of compaction which occurs with free gel boundaries and low initial collagen concentration leads to higher final cell density but also apoptosis [142]. If higher initial collagen concentration or an anchored configuration is used, lower levels of apoptosis are observed, apparently due to the cells' ability to generate tension against the matrix. However, due to the complex interaction between the cells and collagen (including increasing collagen density with compaction), more work is needed to determine if cells alter their behavior (phenotype) as the cell density increases during compaction due to soluble factors, cell contact, or mechanical factors.

2.4 Collagen: Types, Sources, and Extraction Methods

Collagen constitutes one quarter of the total protein mass of animals and is thus the most abundant protein in vertebrates [3]. Procollagen is secreted from the cell and is soluble under physiological conditions and able to diffuse through intercellular space. The ends are enzymatically cleaved, leaving triple-helical rod-like tropocollagen monomer [3]. Collagen monomers fibrillate outside of the cell laterally then aggregate further laterally and longitudinally to form interconnected branching fibrillar networks. The creation of collagen gels exploits this self-assembly process (described in Sect. 3.1), and the ability to recapitulate this native process in vitro provides rationale for utilizing collagen gels as models of tissue development and healing.

However, when adopting a collagen gel model for mechanobiology, it is important to understand that all collagen is not equal. Most obviously, there are many types of collagen (29 at last count [47]) which are tissue specific, e.g. type II predominates in cartilage, type IV is found in basal lamina and blood vessels, and large amounts of type III (relative to type I) are observed in healing wounds and developing skin [3, 47]. Of these, type I collagen is the major collagen type found in skin and bones, and it accounts for about 90% of the collagen present in the body. Accordingly, type I is most often used for creating collagen gels and is the focus of this review. Yet it is important to note that the collagen type will likely alter gel physical and biochemical properties, and what is sold as "type I collagen" may include a significant portion of other collagen types, most likely type III when young animals are utilized. Further, the animal source, method of extraction, purity, and processing of the collagen all have major impacts on the fibrillation and resulting mechanics of collagen gels.

Purified type I collagen is most often obtained from tendons due to its high collagen content and relative purity, although reticular dermis is also a popular source. For lab research, collagen is often obtained from rat tail tendons (RTT) which are abundant in many laboratory settings and are readily soluble under acidic conditions (processing described below). But for commercial scale, calf hide (dermis), bovine Achilles tendon, or porcine skin are most often used. Collagen undergoes crosslinking over an animal's life-time, thus, unlike tail tendons from young rats, the extraction efficiency using dilute acid alone is very low for mature bovine tissues and enzymes are often utilized. Dilute acid extracts only recently synthesized collagen as aldimine type inter-molecular crosslinks can be dissociated by dilute acids, but not the keto-imine type which form with age. Thus, the age of the animal is an important determinant of the quality and amount of the collagen and an important consideration of choice of collagen source [141].

To extract the collagen, tendons are dissected from surrounding fascia, washed in cold neutral salt solution, frozen, minced with ice to keep cold, and finally suspended in weak acid (e.g., 1–10 mM HCl) for a few days at 4°C. The collagen slurry is then filtered (e.g., through a 1 mm nylon screen) to separate the "soluble" (acid-extractable) and insoluble fractions (see Zeugolis et al. [140, 141] for a clear flow chart of the entire process). The acid-extracted collagen fraction is purified by repeated salt precipitation and centrifugation then dialyzed ($\sim$8,000 Mw cut-off filter) against weak acid (0.01–0.05 M). To obtain a usable solution of collagen from the insoluble fraction, the insoluble fraction is treated with pepsin under acidic conditions for a few days, filtered, then purified by salt precipitation, centrifugation, and dialysis as described above to yield pepsin-extracted collagen. It is important that all steps, including mincing, centrifugation, and storage, are performed cold (4°C) to preserve the native (triple-helical) structure of the collagen molecules. The remaining insoluble residue cannot be used to form collagen gels as defined herein; it contains large aggregates of crosslinked collagen fibrils. Despite apparently similar processing, the purity of the resulting "monomeric" collagen solutions can be variable and may contain a substantial fraction of oligomers (more with acid-soluble than pepsin-soluble collagen) which significantly alters fibrillation kinetics [42].

Acid- and pepsin-extracted collagen are both commonly utilized for creating collagen gel models. They are often used interchangeably, yet there are substantial differences in the fibrillation kinetics and the resulting physical properties. Pepsin cleaves the telopeptide region of collagen, which, in addition to allowing high extraction efficiency (>90% from calf tendon as opposed to <5% of wet weight for dilute acid alone [75]) also alters the ability to form a collagen gel by self-assembly. The telopeptide region is important for the rate and extent of fibrillation and crosslinking both in vivo [24] and in vitro [75]. For example, the strength of gels made from acid-extracted collagen is >10-fold higher than for pepsin-extracted collagen [75], and the stiffness of gels made from acid-extracted collagen [110] are significantly higher than that of gels made from pepsin-extracted collagen [96]. On the nano-scale, extruded collagen fibers (similar to gels) created from acid-extracted collagen contain thick quarter-staggered fibrils, whereas

pepsin-extracted collagen fibers have both thin non-banded and thick banded fibrils [141]

Acid-extracted, pepsin-extracted, and relatively unprocessed "fibrous" collagen extracted from skin and tendons from cows and pigs are available packaged either in dilute acid or freeze dried for long-term storage. Acid-extracted versions include "DM6 Bovine Dermal Collagen Acid Soluble" from Devro Medical (3 mg/ml, pH 2). Pepsin-extracted bovine dermal collagen products ($\sim$3 mg/ml in $\sim$0.01 N HCl) include "Purcol" from Advanced Biomatrix (previously named "Vitrogen 100" from Inamed/Cohesion/Collagen Corporation), "Collagen from Calf Skin" from Sigma–Aldrich, "Collagen 04902" from Stem Cell Technologies (Canada), "DM1 Atelo" from Devro (USA), and "Porcogen" from Sunmax (Taiwan), the latter being porcine-derived. Freeze-dried pepsin-extracted bovine dermal collagen products are supplied by Kensy Nash (US), Koken (Japan), and Symatese Biomateriaux (France). Freeze-dried non-purified collagen products are also available including "Calf Skin Collagen" from Sigma–Aldrich, "Bovine Achilles Tendon Collagen" from Fluka, and "Bovine Achilles Tendon Collagen" from Yi Erkang (China). As they are largely unprocessed, they are less expensive though they must be purified as described above to obtain acid- and pepsin-extracted type I collagen for making collagen gels. The subsequent processing and storage of collagen for distribution can also alter the collagen material without changing its composition, e.g., by rendering it insoluble with poor temperature control during freeze drying [140]. More recently, recombinant human collagen has become available, developed in large part to avoid interspecies disease transmission but also to reduce lot-to-lot variability and provide higher purity, albeit at a high cost [95].

Further, other proteins, such as the components in serum, are generally considered necessary for the cells to adhere to the matrix, actively generate forces, and remodel the collagen. The need for serum is shown quantitatively using culture force monitoring [31, 71], although some researchers report compaction of gels by fibroblasts in the absence of serum [6, 66]. Thus, serum proteins further complicate the biochemical environment, and simple "one-component" collagen gels generally contain a small fraction of other collagen types, e.g., "Semed S" contains $\sim$5% type III collagen. Some consider this a benefit since native collagen fibers are heterotypic to varying extents [47]. Finally, it is important to remember that even with the purest collagen material, cells will create their own surrounding matrix when allowed to culture for sufficient time which complicates the composition of the gel.

Collagen Source Terminology

Acid-extracted collagen: collagen fraction that can be extracted by dilute acid alone; a.k.a. "telo collagen" as the non-helical telopeptide regions remain intact. It is also called "acid-soluble," but this terminology is not specific since pepsin-extracted collagen is also soluble in weak acid.

Pepsin-extracted collagen: the collagen fraction that can be extracted by pepsin treatment in dilute acid (~0.5 M). Also termed pepsin-soluble collagen and atelocollagen since pepsin solubilization cleaves the telopeptide region.
Soluble collagen: both "acid-extracted" and "pepsin-extracted" collagen are termed "soluble" collagen in the literature. Both are extracted by weak acid and are insoluble under physiologic conditions.
Insoluble collagen: collagen that is not soluble in dilute acid; most appropriately used to refer to residue remaining following acid extraction with or without pepsin treatment. Raw collagen before extraction is sometimes referred to as "insoluble" although a small fraction of this collagen is soluble in acid and should be termed "fibrous collagen."

3 Characterization: Structure and Physical Properties of Collagen Gels

3.1 Collagen Self-assembly and Architecture

The in vitro progression of collagen fibril formation is similar to the native process in the extracellular environment, and thus collagen gels have been used extensively to study this process [11, 39, 69, 105, 119]. Acid-soluble collagen self-assembles into fibrils and bundles of fibrils (fibers) by an entropy-driven process; that is, collagen molecules exclude water and lower surface energy by aggregating [119]. The monomers (~1.5 nm diameter and 300 nm long) first form aggregates of 5–17 molecules, so called subfibrils 4–5 nm in diameter and 2–3 molecules long, which further simultaneously assemble both linearly and laterally into fibrils (20–300 nm wide). These fibrils bundle into fibers to form a 3D interpenetrating and interconnected fibrillar network [23, 119, 137]. The sigmoidal shape of standard turbidity and rheometric measurements with time during gelation suggests that a nucleation-and-growth mechanism consistent with percolation theory governs collagen fibril assembly [39].

The monomer backbone of the fibrils is stabilized by noncovalent, hydrophobic bonds and electrostatic interactions which results in a physical gel. The importance of noncovalent interactions has been demonstrated by the modification of the self-assembly process by the addition of ions, alcohols and other substances [23]. Further, covalent bonds (crosslinks) can form between the helical crosslinking sites and nonhelical monomer ends; however, these crosslinks are sparse compared to those contributed by cell-mediated crosslinks. Further, in pepsin-extracted collagen the nonhelical (telopeptide) region is removed thus this crosslinking mechanism is lost resulting in a slowing of aggregation and wider fibers [119]. Incubation of self-assembled collagen solutions for long periods (up to 150 days) increases mechanical and thermal stability [30] possibly due to an increase in the number of

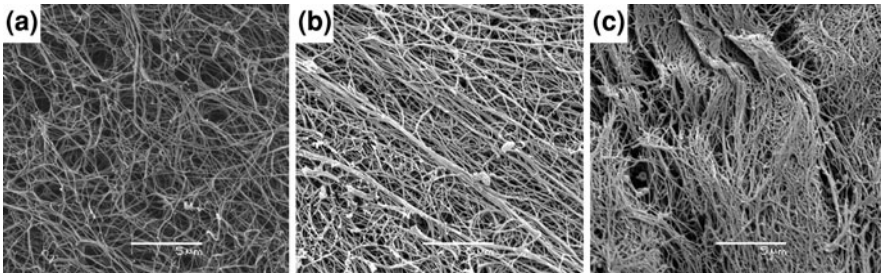

Fig. 3 Scanning electron micrographs of the collagen gel fibrous structure showing the aggregation and decrease in pore size which occurs with fibroblast-mediated compaction over one (*left*), two (*middle*) and three (*right*) weeks in floating culture. Initial concentrations: 3.4×10^4 cells/ml human dermal fibroblasts; 5% FBS; 0.66 mg/ml collagen. Images generously provided by Dr. Christophe Helary; see [58] for methods. *Scale bars* 5 μm

crosslinks that form spontaneously over time. In the absence of cells, the fibrils mainly interact by entanglement resulting in a physical gel rather than crosslinked gel, despite the lack of thermal reversibility characteristic of physical gels [39].

Cells entrapped in the matrix further condense and bundle the fibrils into larger structures and provide additional stabilization methods, most notably lysyl-oxidase-mediated crosslinks [61]. Contraction by fibroblasts gives rise to bundles of collagen fibrils; the collagen network becomes heterogeneous and large fibril bundles (~5 μm fibers) appear from initial small fibrils (~50 nm) with time in culture (Fig. 3). Condensation of collagen is observed around cells locally (shown clearly in Fig. 1b) creating local heterogeneity with contraction [98]. Yet even without cells, the initial gel is shown to be very inhomogeneous both in structure and local mechanical properties [83].

The parameters of the 3D fibrillar network (fiber diameter, spacing, length, etc.) are dependent upon the initial collagen density, pH, and temperature [110]. In general, lower temperature and pH lead to larger fibers as they affect the balance of forces (hydrophobic, electrostatic, and hydrogen bond) between fibrillating collagen monomers and fibrils. Lower temperature weakens attractive hydrophobic forces favoring lateral fibril and fiber growth [105]. Despite the wide range of these variables studied in acellular preparations, the pH and temperature ranges are quite limited when utilizing cells.

Electron microscopy is the most common imaging modality for characterization of the collagen fibrillar network structure, although confocal reflectance microscopy and second harmonic generation (SHG) with two-photon microscopy are proving to be useful techniques for visualizing the fibril architecture in the hydrated state [105, 110]. The latter techniques allow direct visualization of the evolution of collagen fibrils with gelation and have the advantage of being non-invasive (Fig. 4). Recently, SHG and two-photon excited fluorescence (TPF) have been combined and correlated with mechanical properties; SHG reflects fibril, monomer and α-chain configurations whereas TPF is created by fluorescent crosslinks which offers superior correlation to mechanical properties than either

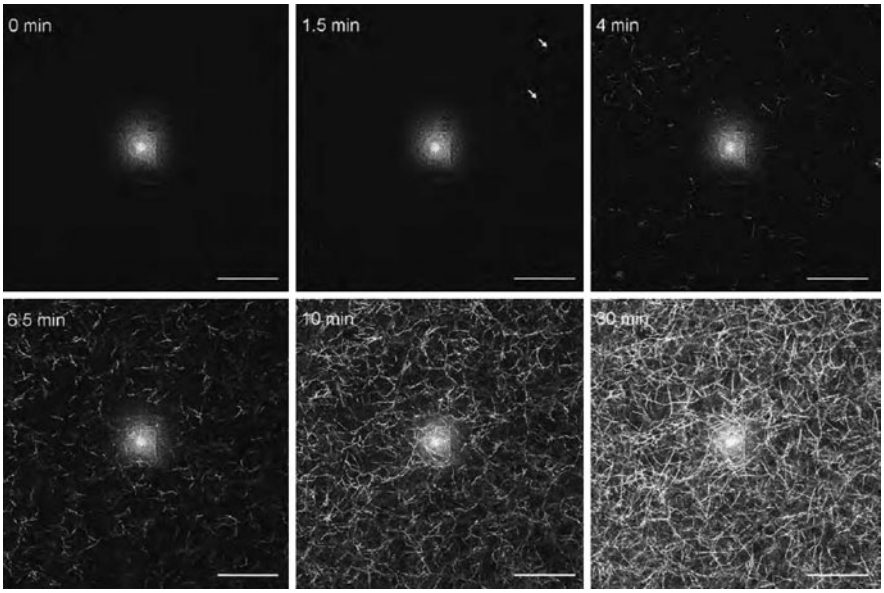

Fig. 4 Time-lapse confocal reflectance images showing the evolution of collagen fibrillation (1 mg/ml collagen at 37°C). The first fibers can be visualized at 1.5 min with more fibers evolving with time and clear interconnections at longer times. *Bright spot* at center is due to reflection off of optical elements. *Scale bar* 50 μm. Reprinted from Ref. [137] with permission from the Biophysical Society

modality alone [105]. With standard SEM and TEM, the fibrillar network collapses with drying and application of vacuum [4], thus the fiber spacing, pore structure, and interconnections between fibers are difficult to quantify accurately with these techniques. Fiber diameters observed by SHG have recently been reported to be an order of magnitude larger than observed by SEM [105]. Despite the processing limitations, electron microscopy remains the standard for measuring fibril size due to its high spatial resolution ($\sim$5–10 nm). For comparison, the lower limit of confocal is $\sim$200 nm [100], the Rayleigh resolution limit for SHG images is $\sim$415 nm [105], and the effective lateral resolution is $\sim$1 μm in many standard confocal systems. Estimating pore size remains even more problematic than fibril size; from a combination of modeling and microscopic measurements, pore sizes in collagen gels appear to be on the order of 5–10 μm [81].

3.2 Mechanical Properties

3.2.1 Micromechanics of Acellular Gels

Due to the similarity of the collagen self-assembly process in vitro and in vivo, the mechanics of acellular collagen gel models have been studied extensively for a

better understanding of native collagen fibrillogenesis and self-organization, e.g. [119]. As with matrix architecture, and due to this architecture in large part, the mechanical properties of collagen gels are dependent upon a number of parameters including collagen density, pH, and temperature, but one must not forget the profound effects of cell remodeling. Even with low cell density and short culture duration (minutes to hours) cells profoundly alter their local environment leading to pronounced densification of the surrounding gel which undoubtedly alters mechanical signaling. With higher cell density and longer term culture (hours to days), the cells alter the global properties dramatically with greater than 10-fold compaction, reorganization (bundling of fibrils), and crosslinking of fibers. Thus, when describing mechanobiology in collagen gels, it is useful to consider separately short-term (hours) and long-term (hours-days) studies. In the short-term, the initial properties of the gel are similar to those of an acellular gel and are critical as cells apply traction to migrate through and reorganize the matrix—processes which are mechanically regulated. Over the long-term, it is useful to characterize the mechanics of the gel both to better understand the mechanical environment of the cell and to assess the cell-mediated remodeling and resulting changes in the functional mechanical properties of the more tissue-like material. In this section we first examine the general features of collagen gel mechanics gleaned from combined uniaxial stretch, confocal imaging, and modeling. Changes in the mechanics with cell-mediated remodeling are then considered. Finally, we discuss more general mechanical characterization of gels with a focus on terminology, methods, and the effects of initial parameters to aid the reader in selection of a test and comparison between studies.

As mentioned previously, in the short-term collagen gels can be considered physical gels with few crosslinks and >90% water. In terms of bulk behavior, a collagen gel can be considered an entropic spring such as an elastomeric polymer, being extended from its highest entropy state and losing organizational entropy (and excluding water) when stretched [100]. Although collagen monomers are not rigid as originally thought and have been shown to be flexible in bending [119], they are very long and axially stiff ($\sim$1 GPa) compared to globular proteins (e.g., albumin) and thus do not uncoil when loaded, but rather rotate and bend. In their pioneering work combining confocal reflectance imaging with uniaxial stretching, Voytik-Harbin and colleagues [109, 110, 133] describe the collagen fibril matrix to be an interconnected network of tensile elements (collagen fibrils connected by hinges). In response to low levels of loading, the fibrils within a gel reorient, slide, bend and buckle, rather than becoming extended themselves. This non-affine fibril behavior (discussed in Sect. 6.1) leads to an increase in density and consolidation of fibrils locally, high distensibility, low stiffness, and surprisingly large decreases in transverse dimensions ("Poisson's ratio" >2). Models predict bending predominates over slipping at intersections of collagen fibrils, at least for confined compression [20], and this is supported by confocal reflectance imaging observations of buckling of fibrils perpendicular to uniaxial tensile direction [111]. The relative proportion of each mechanism of fibril deformation likely depends upon collagen concentration and crosslinking. Whether slipping or bending, collagen

fibrils align in the loading direction and as the applied strain increased a "scissoring" effect of the "hinged" fibrils resulting in a reduction in angle between fibrils [111]. Understanding failure mechanisms in collagen gels is even more complex than analysis of sub-failure mechanics, and little is known. Observed correlations between tensile strength and fibril length in acellular gels suggests that the strength of self-assembled collagen is dependent on the presence of end-to-end crosslinks between molecules [119], although in non-aligned gels failure is likely due to inter fibril slippage between fiber entanglements.

While study of acellular collagen gels with combined stretch and imaging modalities provides substantial insight into collagen fiber kinematics, small fibrils and bundles (<200 nm) surrounding the cells cannot be observed, and with cell compaction the mechanical environment surrounding the cells changes substantially. Utilizing quantitative measurements and mathematical modeling, Evans and Barocas [37] show that the equilibrium modulus after 1 day of reorganization by cells in culture cannot be explained by final collagen concentration; gels that start at a low collagen concentration remain less stiff than higher initial-concentration gels. The initial cell density is an important determinant of final properties due to extreme densification near cells (Fig. 1b) leading to a heterogeneous final gel structure that can be modeled more accurately as stiff inclusions within a soft matrix than by standard composite models of stiff fibers in parallel with a soft matrix. The effects of both non-affine and non-uniform deformation on transfer of stress and strain to embedded cells are discussed in Sect. 6.

Mechanics terminology

Strain: deformation normalized to the sample dimensions; typically change in length divided by initial length. Less than 10% strain is considered "infinitesimal" or small strain.
Stiffness: slope of stress–strain curve typically referred to as Young's modulus E, for linear elastic materials; often defined in low and high stress regions for nonlinear (J-shaped) stress–strain curves.
Storage modulus: elastic part of the dynamic stiffness, typically defined in shear as G' which can be related to E assuming linear elastic behavior.
Loss modulus: shear loss modulus, G'', which indicates the proportion of the viscous behavior of the gel.
Compliance: inverse of stiffness, also functional measure for tubes (e.g., % change in diameter per change in pressure).
Strength: the maximum stress the gel can withstand, generally peak force normalized to initial cross-sectional area and termed ultimate tensile strength (UTS).
Elasticity: stress and strain are uniquely related thus loading and unloading curves are identical regardless of time and strain level.

Elastic return: ability to regain initial (prior to stretch) dimensions.
Hysteresis: energy lost between loading and unloading. Calculated as difference between loading and unloading curves.
Plastic deformation: non elastic return, note different mechanism than metals since fibrous—can often return with rehydration but with long time constant.
Viscoelasticity: time-dependent properties due to both elastic and viscous behaviors being present.
Preconditioning: cyclic loading before representative stress–strain behavior is recorded; it is necessary for repeatable stress–strain curves.

3.2.2 Terminology

Due to the complex network behavior described above, collagen gels do not behave as linear elastic solids but rather non-linear viscoelastic materials. To avoid confusion when describing the properties of collagen gels, it is important to utilize precise terminology especially considering the broad range of backgrounds of researchers utilizing collagen gel models. A grey text box with definitions of the terms most commonly used is provided. The most common misunderstandings are between stiffness and strength, between linearity and elasticity, and between plastic deformation and long-term viscoelastic behavior. Stiffness and strength are entirely separate concepts. *Stiffness* can be broadly defined as the change in stress for a given change in strain. Due to non-linearity in the stress–strain response different moduli are often reported for the "low stress" region and for the "high stress" region, e.g., maximum tangent modulus (MTM). A gel with a low modulus is often termed "soft." The "Young's modulus" (E) obtained from uniaxial testing can be related to the shear modulus (G) obtained from shear testing using the Poisson's ratio (v, ratio between axial and transverse strain) by $E = 2(1 + v)G$, with the caveat that this relationship assumes linear elasticity only remotely justified at small strain. *Strength* relates only to the maximum force per unit material (usually initial cross-sectional area) that the gel can withstand before breaking. Although these definitions are very basic, "strong" is often incorrectly used to describe a "stiff" gel. *Elasticity* refers to deformation that is reversible, that is, the unloading curve follows the loading curve. Elasticity does not imply linearity or a minimal level of stiffness, it precludes viscous behavior and plastic deformation. Due to the mobility of the collagen fibrils, collagen gels do not have particularly good elastic return (to original dimensions) following loading, thus elastic supports are generally needed for use in mechanobiological studies involving cyclic loading as discussed in Sect. 5. The proportion of the applied deformation that is not recovered following stretch is often termed plastic deformation or permanent set, but may also be due to long time-constant viscoelastic (i.e., time dependent) behavior. Plastic deformation may arise from sliding, reorientation, and buckling of fibers into new configurations; however, if allowed to equilibrate in a stress-free state for long enough, rehydration can often provide a sufficient restoring force to

recover much of the original configuration if the deformation was not excessive. Due to the high water content, collagen gels also exhibit other viscoelastic behavior including stress relaxation when held at constant strain, creep under constant or cyclic load, and hysteresis between loading and unloading. Gels are also loaded with sequential rapid ramps separated by relaxation periods to obtain both an instantaneous modulus (E_0) and an equilibrium modulus (E_∞). When cyclic loading is utilized, the stress–strain relationship is complex (literally), and the complex modulus can be separated into a storage modulus (real part, G' in shear) and loss modulus (imaginary part, G'' in shear). To obtain stable stress–strain behavior in tensile or compressive testing, cyclic preconditioning for 3–8 cycles is needed. Finally, due to their fibrous nature, collagen gels can exhibit anisotropy, i.e., different behavior along different directions. Although not often taken advantage of in studies of mechanobiology, the anisotropy of collagen gels represents a major advantage over other polymer systems towards understanding mechanical regulation of cell migration and orientation in three dimensions.

3.2.3 Mechanical Testing Methodologies

Many mechanical testing methods have been employed to study collagen gel mechanics, each with its own benefits and limitations. The choice of method depends and test parameters depend upon what information is needed. The strain or stress magnitude, strain rate, and test duration should be based on expected external and internal (cell-generated) loading, but the most relevant ranges of values are under debate. Methods used to characterize bulk and local gel properties are highlighted below. A table of values for key mechanical parameters is provided in Table 1.

Shear rheometry: Due to the high sensitivity of commercial instruments (seven orders of magnitude of torque) and the low stiffness of collagen solutions during and immediately after fibrillation, rotational rheometers have been utilized extensively to study collagen fibrillation kinetics and the bulk viscoelastic properties of collagen gels (see Table 1). Specifically, collagen fibrillation has been shown to start with a lag phase during nucleation in which turbidity and shear modulus are constant (with $G'' > G'$), followed by a growth phase in which turbidity and G' rapidly increase (with G' crossing over G''), and finally reaching a plateau where the available collagen monomers are fully incorporated into assemblies [39]. Strain, stress, and frequency sweeps over a range of values can be performed relatively easily without having to manually handle the gels, and most commercial rheometers are equipped with Peltier plates to accurately control temperature. From strain sweeps, the response is roughly linear under small strain (<5%) [105]. Typically the applied strain is very small (<1%) and the frequency set to 1 Hz to avoid slippage. Upon gelation, the storage modulus greatly exceeds the loss modulus ($G' > 10G''$) for collagen networks [137], thus the gel is considered predominantly elastic (rather than viscous). Due to the high water content the gels are often assumed incompressible and $\nu = 0.5$ is used to calculate Young's modulus. The mechanics of cell-populated collagen gels are not often

Table 1 Mechanical properties of collagen gels from rheometry, uniaxial loading, and biaxial loading

Test method	Metric (units)	Typical range	Min/max values	Collagen (mg/ml)	Strain (%)	Comments
Shear rheometry						
	G' (Pa)	0.3–50[a–i]	0.1[a]/290[g]	0.4–5.0[a–i]	0.1–5%[a–i]	See 1
	G'' (Pa)	1–29[a–i]	0.02[a]/44[g]			
Uniaxial						
Acellular	E_{low} (kPa)	0.5–33[j–z]	0.32[k]/60[n]	1–4[j–z] (0.3, 200[p])	5–50%[j–z] (2%[j], 70%[l])	See 2
	MTM (kPa)	42–1,805[p]	42[p]/1,805[p]			
Cell-populated	E_{low} (kPa)	100[z]–500[r]	25[z]/2,100[w]	0.32–2[j–z] (0.065[q])	26–38%[q,t]	
	MTM (kPa)	23–1,800[j-z]	16[u]/3,400[w]			
	UTS (kPa)	8–240[j–z]	6[z]/380[w]			
Biaxial						
Cell-populated	E_{low} (kPa)	5.6[c′]	0.2[c′]/3,000[b′]	1.92–2.2[a′–c′]	5–30%[a′–c′]	See 3
	MTM (kPa)		46.9[a′]/ 9,000[b′]			

G' shear storage modulus, G'' shear loss modulus, E_{low} tensile or compressive modulus in low stress region, *MTM* maximum tangent modulus in high stress region, *UTS* ultimate tensile stress. Outliers are listed in *parentheses* and references are *superscripted*

Comment 1 G' generally increases with concentration and strain; cell-populated [118]; [86]; microrheology [58]; [118]

Comment 2 Dogbone, rectangle, cylindrical, and ring shapes all used; plastic compression [56]; rings used for all cases except for one linear shape [116]; 0.2 to 2×10^6 cells/ml typical; dynamic conditioning used [113], [114]

Comment 3 Circular samples inflated to failure [13]; varying sized cruciform samples [65]; square samples [124]

[a] [81]; [b] [76]; [c] [131]; [d] [99]; [e] [105]; [f] [137]; [g] [58]; [h] [118]; [i] [86]; [j] [96]; [k] [76]; [l] [110]; [m] [104]; [n] [80]; [o] [136]; [p] [56]; [q] [21]; [r] [61]; [s] [6]; [t] [113]; [u] [46]; [v] [114]; [w] [63]; [x] [38]; [y] [116]; [z] [45]; [a′] [13]; [b′] [65]; [c′] [124]

studied by rheometry as extended culture within a rheometer is problematic in terms of sterility, metabolite availability, and cost of machine time. It is also difficult to utilize a rotational rheometer to study gels remodeled by cells in standard culture dishes due to slipping of gels not polymerized in situ and non-uniform strain in the parallel-plate configuration (strain is zero at the center and maximum at the outer edge for parallel plates, whereas a cone-and-plate configuration would compress the sample unevenly). Specialized microrheometric methods have been developed for cell-populated gels as described below under "Local Property Characterization." As seen in Table 1, there is approximately a 1,000-fold difference between shear and tensile moduli which may be attributed to the difference in strain applied in the two modalities. At low strains fiber motility and rearrangement precludes substantial transfer of tension to the larger bundles of

fibrils as evidenced by the strong dependence of shear modulus on crosslinking which reduces fiber mobility [123].

Uniaxial testing: Uniaxial testing in various configurations is the most utilized testing modality for large deformation analysis and characterization of cell-remodeled collagen gels. As previously discussed, much of our knowledge of fiber kinematics during loading comes from uniaxial stretch experiments of "dogbone"-shaped specimens in concert with confocal reflectance microscopy [109]. Due to the time needed to obtain images, these studies utilize quasistatic loading, but for general mechanical characterization a range of strain levels and rates have been utilized and many studies include mechanical preconditioning [113]. Cyclic preconditioning is needed to obtain a stable state with water and to accurately assess stored energy. The "dogbone" sample shape is used to minimize the effect of stress concentrations at the grips as rectangular specimens invariably rip at the grips. An aspect ratio of at least 5:1 is required for homogeneous strain. For cell-remodeled gels, researchers generally utilize ring configurations, either made as rings [70, 134, 135] or cultured as tubes and cut into rings [113, 120], as they are relatively easy to make and to mount between pins for mechanical testing. Collagen gels tested under uniaxial tension generally exhibit a more linear response, lower stiffness, and less elastic return than native collagenous tissues likely due to a less mature and complex fiber architecture. Under uniaxial confined compression, the fluid phase is much more pronounced and extrusion of fluid through the matrix dominates early behavior [76]. Unconfined compression has been utilized to obtain structural stiffness, a relative measure of collagen gel properties (force/distance) but not intrinsic properties [6, 138].

Tube inflation: Inflation of tubular-shaped collagen gels is a popular method for obtaining "functional" properties (burst pressure and compliance) of tissue engineered blood vessels [46, 82]. This testing modality applies multiaxial stress to the gel which results in approximately pure uniaxial (strip biaxial) deformation in the absence of the application of axial stress and/or torsion which are controlled only in more sophisticated devices, e.g., Vorp et al. [132]. To obtain material properties, the dimensions of the sample including diameter and wall thickness must be known. As ring testing is easier and cheaper it is more popular.

Planar biaxial testing: To characterize remodeling of planar collagen gel samples, a few research groups have employed biaxial testing. Holmes and colleagues [124] hung weights of increasing mass from the edges of square samples to obtain the quasistatic mechanical properties and found anisotropic behavior in gels cultured under uniaxial constraint. More recently, cruciform sample geometry have been used to minimize edge effects and biaxial testing has been combined with powerful optical microscopy techniques to examine structure–function relationships in collagen gels [60, 65]. Tranquillo and colleagues [65] combined planar biaxial testing with polarized light microscopy to demonstrate that the initial prescribed fiber alignment of cell-remodeled collagen gels strongly affects the mechanical anisotropy of cruciform-shaped samples. Hu et al. [60] combined biaxial stretch with second harmonic generation to characterize development of the collagen architecture in planar gels.

Membrane inflation: Due to the fragility of collagen gels, it is difficult to assess their failure properties (strength, extensibility) accurately. Even with "dogbone" samples and rings, the samples often fail at the grips due to the high stress concentration and crushing. We have developed a fluid inflation method to characterize the biaxial mechanical properties of planar samples [13]. It is important to note that the burst pressure which is sometimes reported [75] is not a measure of the intrinsic strength of the gel due to the dependence on clamp diameter. The tension must be calculated from the radius of curvature and pressure.

Local property characterization: Indentation using an atomic force microscope probe is becoming a popular method for measuring the local properties of tissues and thin soft gels used for 2D cell culture, e.g., see table of values in Reilly and Engler [107]; however, this technique has not, to our knowledge, been applied to characterize the local properties of collagen gels (with the exception of glutaraldehyde-treated gels [36]). We have recently measured the surface stiffness of isoelectrically focused collagen gels using a microsphere-tipped AFM probe (unpublished data) and found little difference between fibrillated and non-fibrillated gels; however, such measurements only probe the top 500 nm of the gel and ignore the anisotropy of the material. Recently, Baaijens and colleagues [27] successfully combined deep microindentation and digital image correlation (DIC) to measure the resulting non-uniform strain field to assess the anisotropic stiffness of cell-remodeled collagen/matrigel composite gels. To measure local properties within collagen gels during cell-mediated remodeling, Tschumperlin and colleagues [86] developed an innovative microrheometric approach based on the rotation of ferromagnetic microbeads cast within the gel, and the authors utilized this method to demonstrate TGF-β1 and interleukin-1β enhanced matrix stiffness cooperatively. Optical tweezers have been used to probe the properties at the level of a single microbead deep within a collagen gel. The researchers show that the gels are highly inhomogeneous due to the gel having very low density areas locally, even in the absence of non-uniform cell-mediated compaction [83]. Two-dimensional laser traps have been employed to study local collagen gel anisotropy [98]. The latter three particle-based techniques for probing the mechanical environment surrounding cells during mechanical loading and cell-mediated remodeling hold tremendous promise for increasing our understanding of cell mechanobiology in 3D gels and tissues.

3.2.4 Effects of Fibrillation Parameters on Mechanical Properties of Collagen Gels

As mentioned at the start of this section, the mechanical properties of collagen gels are dependent upon a number of parameters including collagen density, pH, and temperature—not to mention cell compaction. It is instructive to examine a few of these dependencies to better understand reasons behind the large range of mechanical properties for collagen gels listed in Table 1.

Concentration: In a recent well-controlled study, Helary et al. [58] show the dependence of acellular gel stiffness on initial collagen concentration clearly with G' values of 13, 50, 290, and 189 Pa for 0.66, 1.5, 3, and 5 mg/ml, respectively at 2% strain. In this study the highest initial concentration hydrogels (5 mg/ml) tended to creep and to be thus less stiff due to non-homogeneity of these hydrogels (dense and loose regions scattered within), a condition that has since been rectified by handling the stock solutions at 20°C rather than 4°C to reduce viscosity (Christophe Helary, personal communication). For collagen gels "plastically compressed" to obtain extremely high density collagen the modulus by uniaxial tensile testing ranges from 42 to 1,805 kPa for 0.4–20% collagen (4–200 mg/ml hydrated) [56].

pH: In terms of solution acidity during fibrillogenesis, fibril diameters increase as pH decreases. Silver and colleagues [23] found that fibril diameter correlates positively with the low strain modulus (increasing from 0.5 to 5.5 MPa with pH decreasing from 8.5 to 6 at 37°C) but not with either the ultimate tensile strength or the high strain modulus. These studies were completed with extruded gels thus the modulus values are higher than found in isotropic cast collagen gels. For cast gels, the relaxation modulus measured by uniaxial compression has been found to correlate with pH; gelation pH between 5 and 8 alters stiffness from 5 to 25 kPa [136].

Temperature: The storage modulus has been shown to increase roughly two orders of magnitude with polymerization temperature within reasonable limits, from a G' of 0.3 Pa for collagen gels polymerized at 4°C to 22.7 Pa for 37°C-polymerized gels [105]. This finding is surprising since the mean fiber diameter for these gels, as measured by SHG using a two-photon microscope, were 216 and 62 nm for the 4 and 37°C groups, respectively, and larger fibers have been found to correlate with higher stiffness (e.g., with pH as discussed above). The authors attribute the higher stiffness in the 37°C group to a higher volume fraction of interconnected fibers; larger pore structures were observed in the low temperature group and a more interconnected and continuous network with higher fibril density was observed in the 37°C group. Interestingly, the loss modulus was approximately twofold higher than the storage modulus in this study indicating a more viscous than elastic response, an uncommon finding for collagen gels.

4 Static Boundary Conditions: Modulating the Effective Stiffness of the Gel

The stiffness of a material is related to the amount of force needed to deform a material a given amount, normalized to appropriate dimensions. To generate tension, cells require their surroundings to have a minimal level of resistance to deformation (effective stiffness). There are multiple ways to alter the ease by which cells deform the surrounding collagen matrix for a given amount tension generated by the cells. As discussed above, pH and temperature affect the stiffness, but ideally, the collagen gels should be polymerized with entrapped cells under

physiological conditions (neutral pH and 37°C). Collagen crosslinking and increases in collagen density can also be utilized to modulate the stiffness of the gel, yet it is generally held that the collagen gel should present the same ligand density (collagen concentration) to the cells and only the mechanical stimuli should vary between treatment groups. Thus, despite the range of stiffness values reported for collagen gels, we have quite little control over the initial intrinsic properties of collagen gel models when trying to isolate mechanical stimuli for mechanobiological studies. As an alternative approach, many researchers have capitalized on the fact that the mechanical environment of the cells within collagen gels is strongly dependent upon the external boundary conditions of the gel; many innovative approaches have been developed to alter these conditions. This section begins with a short discussion of approaches for modulating the intrinsic stiffness of collagen gels then focuses on means of modulating the effective stiffness of the gel by controlling the boundary conditions.

4.1 Concentration and Crosslinking

The intrinsic stiffness of a collagen gel can be directly modulated by crosslinking the collagen molecules. Biochemical additives including ribose glycation [46], genipin fixation [123], photo-crosslinking [14], and non-enzymatic nitrite modification [97] have all been used to increase the matrix stiffness. Both the stiffness of the collagen fibrils themselves and the strength and number of inter-fibrillar bonds (reducing slippage) likely increase with crosslinking and contribute to the stiffening, although the specific influence of each factor has not been elucidated. At low concentrations, these treatments effectively increase the matrix stiffness by twofold or greater and have been shown to be minimally cytotoxic (unlike glutaraldehyde treatment). However, such exogenous crosslinkers also modify the collagen biochemistry and are likely to alter the cell interaction with and remodeling of the matrix, confounding the assessment of the effects of mechanical factors. As such, they have not been widely adopted for mechanobiological studies.

The intrinsic stiffness can also be directly modulated by altering the collagen concentration (as described in the previous section), and this method has been widely adopted. When cells compact a collagen gel, the collagen concentration increases dramatically (10 to 20-fold increases are typical), and the stiffness rises with the collagen density. Although somewhat counterintuitive, with cell compaction lower initial collagen concentration actually leads to higher final concentration [142] although the final stiffness does not rise proportionally [37]. To obtain higher collagen concentration and reduce compaction, Helary et al. [58] created concentrated collagen hydrogels at up to 5 mg/ml initial concentration which, unlike the “normal” concentration of 0.66 mg/ml, favored cell growth that reached about 10 times the initial cell number at day 21. The concentrated gels had lower compaction in vitro and enhanced neovascularization in vivo. Brown et al. [16] have developed a method for “plastically compressing” gels and wicking the

excess fluid from gels to greatly increase collagen concentration (up to 200 mg/ml with only ~15% cell death). The compression results in a >40-fold increase in Young's modulus and correlates with increased fibroblast proliferation. This method is gaining popularity with the technology licensed and semi-automated devices available commercially (RAFT system, Automation Partnership, UK). A dense skin (collagen membrane) is formed on the surface of the mechanically compacted gels whereas the inner region is relatively uniform. Examination of differences between cell-compacted and mechanically compacted gels of equivalent final concentration may provide clues towards the importance of cell-generated structures (crosslinks, bundles, local densifications) in cell mechanobiology. Although the collagen biochemistry is essentially the same in these high-concentration preparations, the cells are presented with altered ligand density (Nemir and West 2010) and differences in pore size. As collagen fibrils are not covalently bound, at low concentration the cells are able to migrate through the interfibrillar spaces, whereas motility in high concentration gels may require enzymatic degradation.

4.2 Floating, Anchored, and Released Gels

The most common means for examining the effect of the mechanical environment of cells within a collagen gel is to compare cells cultured in gels attached to a rigid culture dish with those released from the dish following polymerization and cultured freely floating in media. Altering the external boundary conditions has profound impact on the cell mechanical environment if cells are seeded at sufficient density to interact in a concerted manner (e.g., $>10^4$ cells/ml and >4 h). The terminology for these culture conditions is varied and the names used are often imprecise and/or misnomers. For example, anchored gels are often termed "loaded" since the cells can generate macroscopically measureable tension (see terminology text box for more precise terminology).

Regardless of terminology, cell phenotype and activity in the gels are strongly modulated by the boundary conditions of the gel shown schematically in Fig. 5. If the gel is cultured unconstrained and floating (zero force boundary condition), the matrix cannot sufficiently resist cell-generated tractional forces which results in slow compaction of the matrix. Concerted mechanical stress is not generated, the matrix remains highly compliant, the cell morphology becomes rounded and dendritic, and fibroblastic cells do not differentiate into myofibroblasts even in the presence of TGF-β1, a known stimulant of myofibroblast activation for fibroblasts cultured on stiff substrates [15, 126]. If the gel is anchored around its periphery (zero displacement boundary condition), the matrix is able to resist the cell-generated tension, mechanical stress develops within the matrix, cell-mediated matrix remodeling occurs, and the matrix becomes relatively stiff [6]. Inside anchored matrices, fibroblasts initially and at low cell density appear similar to cells in floating matrices (personal communication, Fred Grinnell), and at short times

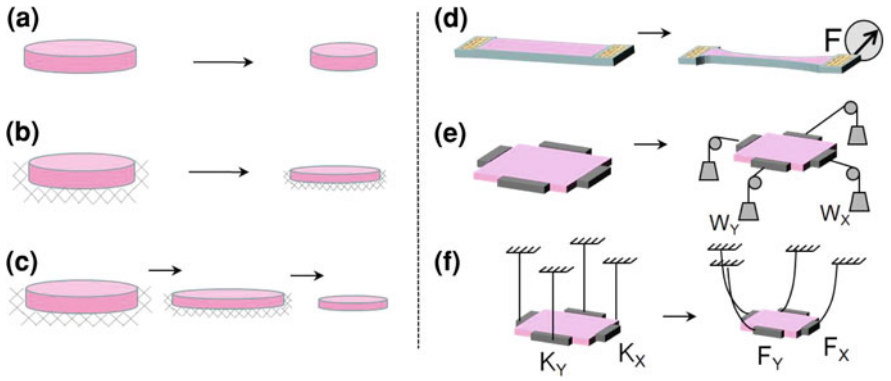

Fig. 5 Schematic diagrams of different static boundary conditions used to modulate the mechanical environment of the cells cultured within collagen gels. The standard culture conditions are shown on the *left* and include **a** floating gel, **b** anchored gel, and **c** released gel (following being anchored). More quantitative and specialized systems shown on the right include **d** the culture force monitor with an isometric force transducer, **e** the isotonic force device with calibrated hanging weights, and **f** the compliant anchor device with controlled stiffness springs at the boundaries

(<24 h) migratory forces dominate contractile forces [35]. At longer times (days), with cooperative cell remodeling of the gel, the cells become extended and stellate or bipolar [15, 51]. In the presence of TGF-β1, after a few days in culture, the cells in anchored gels differentiate into myofibroblasts manifested by increased αSMA expression, remodeling, and force of contraction [6, 59].

To abruptly alter the mechanical environment of the cells within a gel, an anchored gel may be released after a period time (generally 3–5 days). This experimental condition is thought to represent an accelerated transition between active tissue repair and healed tissue where the cells are shielded from extrinsic stress [48]. Following release, the cells contract the matrix rapidly by a smooth muscle-like mechanism [127], profound changes in cell morphology occur, cell proliferation and collagen synthesis decline rapidly, and the cells appear to switch from an active to a quiescent phenotype [91]. Release of collagen gels has also been shown to trigger apoptosis of fibroblasts and myofibroblasts, although the factors that regulate this phenomenon are unclear [52]. Pre-compacted (floating) gels have also been "nested" within acellular gels to examine the migratory behavior across boundaries of different stiffness [90]. Cells are able to migrate out of the relatively stiff compacted gels and into the soft acellular gels. Time-lapse microscopic observations demonstrate "flow" of collagen fibrils from the acellular gel towards the compacted gel which is attributed to the forces associated with cell migration. Further characterization of the mechanics of this system may yield interesting information about mechanical regulation of migration in 3D.

Collagen gels are generally circular due to the shape of common cell culture dishes and for uniformity of the boundary attachment and thus compaction. Tubular

specimens are similarly symmetric and utilized extensively for the formation of "media equivalents" and for ease of mechanical stimulation and testing, although they require a mold for preparation. The use of different shapes (square, rectangular and annular gels) and mixed boundary conditions (some edges free, some anchored) highlights the importance of boundary conditions on cell-mediated remodeling of the gels as shown elegantly by Costa et al. [26]. Anchoring the ends of long rectangular samples and culturing annular gels results in a high degree of alignment (both cells and collagen fibrils) parallel to the free surfaces. Tranquillo and colleagues [65] further demonstrate that the degree of alignment can be controlled by the relative width (anisotropy) of the arms of cruciform gels.

In addition to the periphery, the bottom and top surface of anchored planar gels have very different boundary conditions (usually free on top and fixed below), although the effects of this asymmetry is generally ignored as most of the cells are sufficiently far from the surfaces in thick gels (>1 mm) and coordinated tension is assumed to be in the plane of the gel. Reducing the gel thickness substantially can be used to alter the effective stiffness of the gel. Simmons and colleagues [138] demonstrate that very thin gels have substantially higher compressive structural stiffness than thick gels (6,000 N/m for $\sim$10 μm vs. 2,000 N/m for $\sim$2.5 mm) and show mechanical modulation of calcification potential by valve interstitial cells using these gels. The authors further demonstrate the relative difference in shear deformation between the thin and thick gels using finite element analysis. This analysis is focused on the cells cultured on the surface of these gels, and cells cannot be cultured in ultrathin gels; however, with further development this relatively simple but powerful method for mechanically manipulating the effective stiffness of the cell environment may prove useful for 3D mechanobiology.

Static Boundary Conditions Terminology

Floating gel: collagen is allowed to gel then released after 30 min–1 h (a.k.a. "free" or "unloaded gels")—a zero force boundary condition.
Anchored gel: held rigidly along outer perimeter and generally lower surface as well (a.k.a., "fixed," "loaded," "restrained" or "stressed" gels)—a zero displacement boundary condition.
Released gel: cultured in anchored state (1–5 days generally), then released to free floating state (a.k.a. "stress relaxed" gel).
Isotonically loaded gel: weights are suspended (via pulleys) on the edges; these are generally square whereas other types are typically circular.
Controlled boundary stiffness: gels are cultured suspended by springs of known stiffness.

4.3 Other Isotonic and Isometric Boundary Conditions

Utilizing an innovative device involving hanging weights to produce constant force along each edge of a gel [78], researchers have recently demonstrated that different isotonic boundary conditions can be imposed on each axis of a collagen gel to control the anisotropy of the remodeled gel [124]. An additional advantage of this system is the ability to asses biaxial tensile properties by the use of optical tracking of fiduciary markers used to monitor deformation. Using this system, Costa and colleagues [84] demonstrate realignment of collagen with static loading (Fig. 6) and studied the mechanical regulation of cell alignment in 3D gels. The authors demonstrate that cell realignment precedes collagen realignment when the direction of load is altered. This finding indicates that the cells, when acting in concert at sufficiently high density, actively sense the external boundary and overcome the local contact guidance of the aligned collagen in which they reside.

Prestretching a gel 5–10% uniaxially has been described as a method for effectively increasing the stiffness of a collagen gel without altering the matrix biochemistry. Specific values of stiffness are not described in the development of the method [72], and it is unclear if the proposed increase in stiffness is due to moving to a higher modulus portion of a non-linear stress–strain curve (i.e., past the "toe-region"), or if the effective stiffness increase is analogous to that of a pre-stressed drum or guitar string. However, interesting changes in cell contraction and matrix remodeling are observed in this system [72, 73].

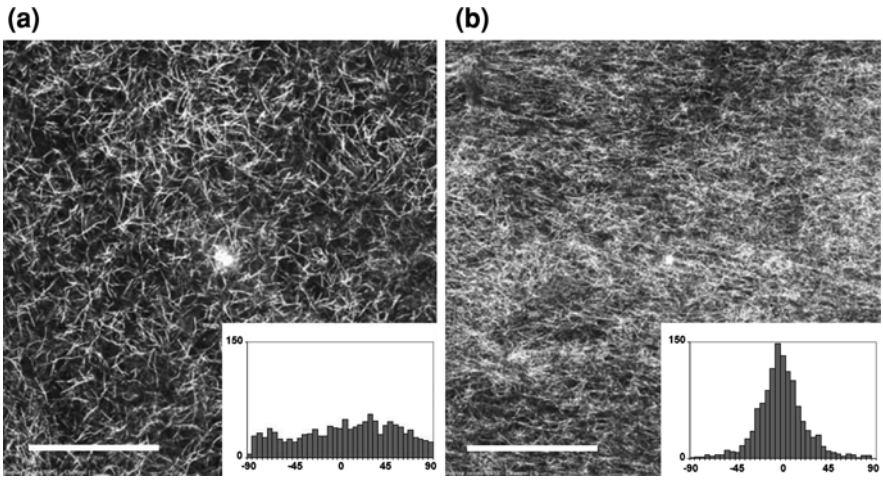

Fig. 6 Confocal reflectance images demonstrating collagen fibril alignment due to remodeling under static uniaxial constraint in the isotonic force device for 72 h. With kind permission from Springer Science + Business Media: from Ref. [84], Fig. 5a and b

4.4 Compliant Boundaries: Springs as Anchors

To modulate the effective stiffness that the cells experience in a graded and controlled manner without altering the physiochemical properties of the extracellular matrix, we have developed a method utilizing compliant anchors (0.048–0.64 N/m) to tune the boundary stiffness of suspended collagen gels (Fig. 7f) [67]. Using this system we find that increased boundary stiffness elicits enhanced basal tension and potassium-stimulated active contractile force from fibroblasts. Remodeling of the collagen matrix is also increased with boundary stiffness indicating stiffness-dependent phenotypic regulation of the cells. TGF-β1 acts synergistically with boundary stiffness to enhance remodeling and αSMA expression (Fig. 7). A similar concept has been developed by Chen and colleagues [85] to study the effect of boundary stiffness on small collagen gel "microtissues" utilizing soft lithography methods. The authors report that mechanical stress increases with increased boundary stiffness, but decreases with increased collagen density (used to increase intrinsic stiffness); a finding that highlights the complex relationship between generation of tension and compaction of collagen matrices.

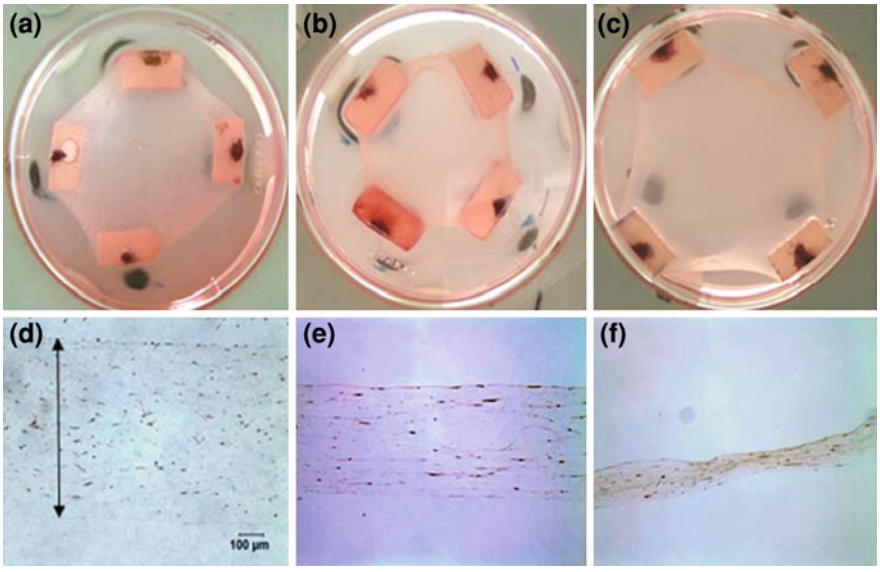

Fig. 7 Compaction of collagen gels after culturing for 3 days in the controlled boundary stiffness device with (**a**, **d**) compliant beams ($K = 0.048$ N/m) without 10 ng/ml TGF-β1 (**b**, **e**) compliant beam with TGF-β1 and (**c**, **f**) in presence of stiff beam ($K = 0.57$ N/m) and TGF-β1. The diameter of the dish is 60 mm and original magnification is 200× (**d**–**f**). With kind permission from Springer Science + Business Media: Ref. [67], Fig. 8

5 Dynamic Boundary Conditions: Cyclic Loading and Stretch

Whereas modulating the effective stiffness of the matrix can be used to probe "inside-out" cellular mechanotransduction, stretching the cells can be used to investigate "outside-in" signaling [32]. Dynamically stretching fibroblasts within collagen gels has been shown to regulate myriad aspects of cell behavior including alignment [70], morphology [34], altered MMP synthesis [114]. It has also been shown to modulate cell phenotype [2, 5] and gene regulation including those encoding for collagen [19] and matrix proteases [103]. Many systems have been developed to stretch collagen gel models as described below and schematically illustrated in Fig. 8.

5.1 Uniaxial Loading

The majority of studies of mechanobiology in collagen gels utilize cyclic uniaxial stretch. Samples are generally cast into either long rectangular molds with porous anchors at each of the ends to affix the samples to the stretch device [117], or into short tubular molds to create ring-shaped specimen [70, 134, 135]. Rectangular specimens become cord-like due to cellular compaction with larger area at the

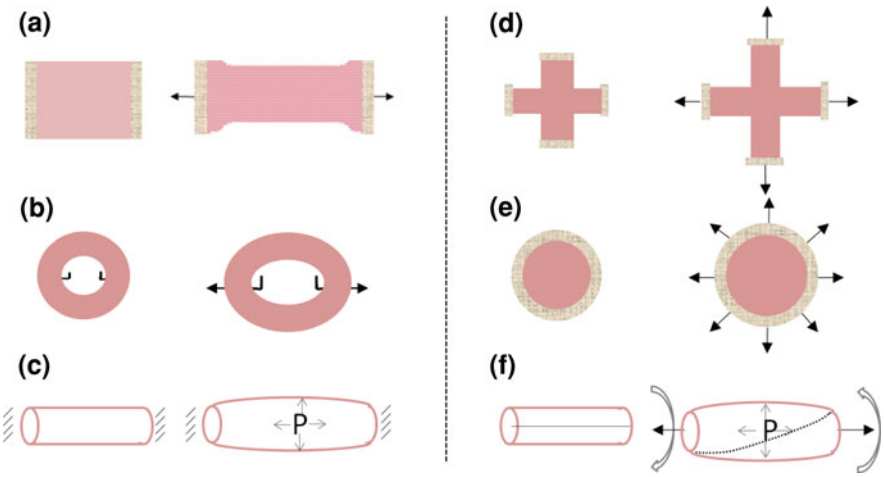

Fig. 8 Schematic diagrams of different dynamic boundary conditions used to modulate the mechanical environment of the cells cultured within collagen gels. The uniaxial culture conditions are shown on the *left* and include (**a**) rectangular-, **b** ring-, and **c** tube-shaped gels (note that the tube is inflated resulting in roughly pure-uniaxial circumferential stretch with little transverse contraction). The biaxial culture conditions are shown on the *right* and include **d** cruciform-shaped samples pulled along orthogonal axes, **e** circular samples stretched on silicone membranes, and **f** tube-shaped samples simultaneously inflated, stretched, and twisted

anchors which, similar to a "dogbone" shape, minimizes stress concentration. Rings have the advantage of being easy to stretch between pins without the need to grip the samples, thus not relying on integration into porous anchors and avoid crushing the ends. Using these systems, researchers have found that 10% stretch at 1 Hz results in increased contractile apparatus within smooth muscle cells relative to static controls [70], and that the mechanical effect is augmented when combined with growth factors including PDGF and TGF-β1 [120]. Uniaxial stretch has also been combined with twist to simulate tendon loading and found to direct mesenchymal progenitor cell differentiation towards a ligament cell lineage [5].

If wide rectangular samples are utilized as is often the case with culture force monitors, the transverse compaction is minimized; in the center of the sample the strain field is pure uniaxial [15, 34]. In short-term stretching experiments Brown et al. [15] found that fibroblast populations within collagen gels have a homeostatic contractile force set point; when a gel is decreased in length and the tension removed, the fibroblasts contract the gel and increase the tension in the gel back to the previous level.

For long-term cycling, Flexcell International has developed a modification to their cell stretching device to apply uniaxial stretch to collagen gels (Tissue Train; Flexcell). In this commercial device, the silicone membrane provides elastic return to the attached ends, but lack of elastic return of the collagen gel itself may lead to buckling of the cord-like collagen gel especially at high frequency cycling (personal observation). Recently, collagen gels have been cast into macroporous elastic polymer substrates to provide local elastic return [128]. Cells within the collagen can be imaged and the authors report lung fibroblast-to-myofibroblast differentiation in the device (30% strain at 0.1 Hz) by αSMA-positive staining; however, the cell-remodeled collagen gel cannot be removed to assess functional remodeling or cell contractile force.

Tube inflation is also a popular method for applying cyclic stretch to collagen gels [63, 113, 120]. Due to the high permeability of the gels, a silicone support is generally utilized. Inflation of the silicone tube with fixed ends results in almost pure uniaxial (circumferential) stretch to the gel if it is well adhered to the silicone tube. For sufficient attachment, the silicone tubes can be pre-treated with acid to etch the surface and a thin pre-coating of collagen and/or chitosan can be dried onto the tube [113]. Without proper adherence to the silicone, the collagen gel lacks sufficient elastic recoil to follow the cyclic inflation and little dynamic strain is applied to the cells. Further, without adherence, the cells freely compact the gel laterally resulting in a short dense tube, although pulling off of the membrane can occur even with good adhesion if the contraction is strong, e.g., with TGF-β1 stimulation combined with stretch [120]. Using tube inflation of rat smooth muscle cell-populated gels, Seliktar et al. [113] observed pronounced alignment of the collagen and cells (Fig. 9) and found that the stiffness and strength increased more than twofold after 8 days of 10% stretch at 1 Hz relative to static controls. In a similar study, the same group reports an increase in the production of MMP-2 and activation of latent MMP-2 with 4 days of dynamic culture and, importantly, that

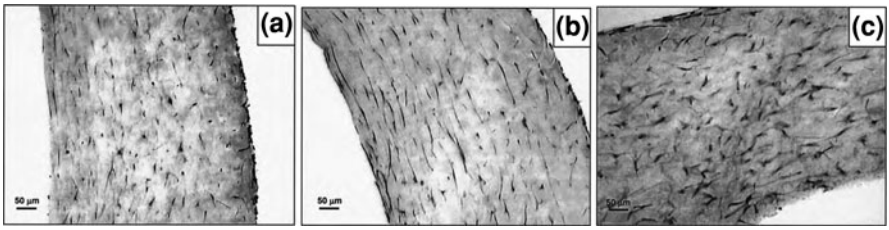

Fig. 9 Cross-sections of rat smooth muscle cell-populated collagen gel tubes following 4 days of **a** static culture on a rigid mandrel, **b** 10% cyclic uniaxial stretch, and **c** floating culture. Comparison of **a** and **b** illustrates the circumferential alignment of the cells and collagen with dynamic stretch and the complete lack of orientation in gels following floating culture. The collagen stains light and the cells dark with the hematoxylin and eosin stain in the histological sections. With kind permission from Springer Science + Business Media: from Ref. [113], Fig. 5

nonspecific inhibition of MMPs completely mitigate the stretch-induced changes in mechanical properties [114].

It is difficult to determine the precise effect of uniaxial stretch on alignment since, even in the absence of stretch, uniaxial samples become cord-like with a high degree of cell and collagen alignment due to the lack of resistance to cell traction along the free transverse boundary [26, 61, 135]. This limitation has lead to the development of controlled biaxial stretch methodologies.

Dynamic Boundary Conditions Terminology

Uniaxial loading: loaded on only one axis (whether force or displacement controlled), with other two axes free to deform with zero stress at the boundaries.
Strip biaxial stretch: deformation restricted to only one direction, with the transverse strain held to zero (3rd axis free to deform) a.k.a. pure uniaxial strain.
Biaxial loading: controlled loading or stretch along two axes generally without shear (strip biaxial is a special case with zero transverse strain).
Shear loading: loading perpendicular to the axis of interest e.g., applying a lateral (x-direction) force on the upper (z) face of a gel; shear stresses and strains are also present in cases of non-uniform loading, e.g., near clamps, tethers, or rigid inclusions.

5.2 Biaxial Loading

For fibrous gels, equibiaxial stretch has the advantage that the overall fiber alignment in the plane of the sample does not change with stretch and fiber

realignment in the direction of stretch does not overshadow other remodeling events (compaction, protein accumulation, and crosslinking). Similar to uniaxial methods, biaxial methods are hindered by the poor elastic return of collagen gels and difficulty in attaching the gels to elastic polymeric substrates. We have utilized equibiaxial stretch of fibrin gels, taking advantage of the adhesive property of fibrin and utilizing anchors around the perimeter of the gel, and shown dramatic strain magnitude-dependent compaction and strengthening [8]; however, similar large magnitude dynamic stretch of collagen gels has proven unsuccessful with the Flexcell system. Considering the difficulty in keeping collagen gels adhered to static culture plates against the substantial cell traction during compaction, it is not surprising that external stretch causes the gels to detach from silicone membranes. Nerem and colleagues [17] report that small hemispherical collagen gel layers can be adhered to acid-etched silicone membranes with Cell-Tak, and that they can withstand being stretched to 10% area strain at 1 Hz for up to 2 days. The authors report that smooth muscle cells in these very thin stretched gels become less elongated and shift to a more synthetic phenotype.

Grande-Allen and colleagues [55] developed a device to equibiaxially stretch cruciform-shaped collagen gels populated with valvular interstitial cells up to 10% at $\sim$1 Hz for 2 days and demonstrated that glycosaminoglycan and proteoglycan synthesis of these cells is regulated by cyclic stretching in a magnitude-dependent fashion. With minor modifications, this device has the potential to apply non-equibiaxial strain as well, although the sample dimensions are quite large (30 mm maximum dimension) and thus expensive. The goal of this and most other test systems has been to obtain a strain field that is as homogeneous as possible.

We have created a system to apply repeatable non-uniform strain fields to cells by utilizing rigid inclusions affixed to circular membranes that are pulled uniformly and radially [9]. In this system, there is a gradient of strain anisotropy from pure uniaxial near the inclusion to equibiaxial at the outer edge. Our preliminary results with dermal fibroblasts cultured within fibrin gels indicate that cells orient perpendicular to the direction of stretch in the pure uniaxial stretch region, in contrast to findings of alignment along the uniaxial stretch direction in systems described in the previous subsection. Additional work is needed with collagen gels in these biaxial systems to investigate cell responses to a range of strain anisotropy (not just pure uniaxial and equibiaxial) as well as cell responses to gradients of strain within a 3D environment.

6 Cell Environment

6.1 Transfer of Stress and Strain to Cells within a Collagen Gel

For the study of cell mechanobiology in collagen gels, it is important (and non-trivial) to determine the forces and deformations experienced by the cells.

The transfer of stress and strain to the cells within a collagen gel (and native tissue) depends not only upon the fibril microstructure immediately surrounding the cell and the how the cell is attached to the matrix elements [100, 109, 126], but also the matrix architecture far from the cells. Due to non-affine fiber behavior and non-uniform stiffness within collagen gels, local strains experienced by cells are generally lower than global (applied) strains as demonstrated by confocal microcopy [100, 111]. Collagen gels are inherently non-affine as they are made up of discrete fibers tangled together in a physical gel. These fibrils are also able to exhibit local reorientation, scissoring, and buckling as predicted by multiscale models [112] and confirmed experimentally [111]. We have quantified similar non-affine behavior of collagen fibers within native tissues [12], and bucking behavior has been observed in collagen/GAG sponges due contraction of single cells [57]. With affine fiber kinematics, all elements are stretch to the same degree as the bulk applied strain (Fig. 10a, b). With non-affine behavior, as shown in

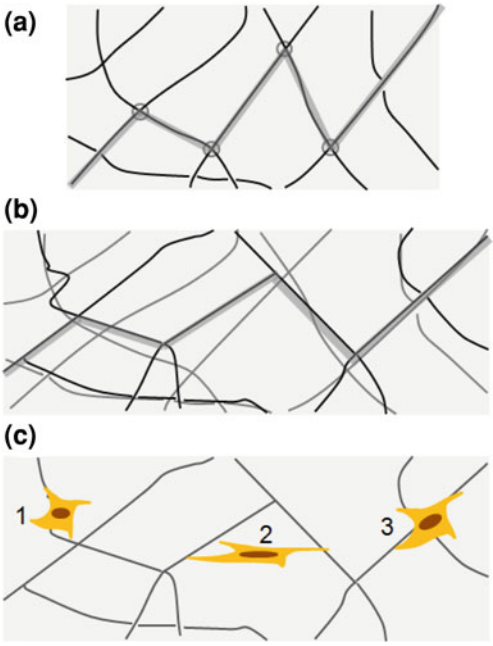

Fig. 10 Schematics of a hypothetical fiber arrangement within a collagen gel. **a** Undeformed state showing entanglements (*circled*) and highlighting one fiber path (*wide grey lines*). **b** Following 30% pure uniaxial stretch, the difference between affine (*light grey lines*) and non-affine (*black lines*) fiber kinematics is shown. In the affine case, all points in the material follow the bulk deformation. In the exaggerated non-affine case, the fiber segments between entanglements rotate and are not stretched at all (*wide grey lines* are the same length in **a** and **b**). **c** Depending upon how a cell is attached to the fibrous matrix, the cell can experience *1* unloading, *2* greater than bulk stretch, or *3* zero stretch. In a collagen gel, cells actually span many fibrils as shown in Fig. 1a, and thus the transfer to the cells is more likely similar to the affine case than the exaggerated non-affine case shown in schematic above

Fig. 10c, a fiber can remain unstretched due to rotational freedom, even with large bulk strains. Even with pure uniaxial applied strain, cells attached to a non-affine fiber matrix may experience a range of strains from compressive to highly tensile or no strain at all (cells 1, 2, and 3, respectively in Fig. 10c). Although these strains are theoretically possible, in collagen gels the fibrils are much smaller than the cells and are relatively dense (see Fig. 1a), thus these extreme cases are not likely to occur. Further, the relative impact of non-affine fiber kinematics on strain and stress transfer likely decreases in relative importance in very dense and/or highly crosslinked gels (e.g., after extensive cell-mediated remodeling) since the relative mobility of the fibers is low compared to sparse gels prior to compaction. As the gel is stretched to higher levels of strain, the impact of non-affine behavior is also reduced as the fibrils are reordered and lose entropy [20].

Under physiological loading levels and following localized remodeling, heterogeneous material properties likely dominate non-affine fibril behavior in governing the (lack of) strain and stress transfer to the cells. Although non-uniform deformation due to heterogeneous mechanical properties is by definition non-affine deformation (local deformation does not follow bulk deformation in a one-to-one manner), here we consider material heterogeneity separately from non-affine fiber kinematics in terms of their effects on strain non-uniformity within the collagen gel. Cells in a collagen gel are not necessarily attempting to "shield themselves" from the external loading, but rather they simply can reorganize their local matrix which leads to heterogeneous material properties. A few simplified cases shown schematically in Fig. 11 demonstrate the impact of heterogeneous material properties on stress and strain transfer. Figure 11a shows a material with alternating dark and light regions in series. Upon loading, the (engineering) stress in all locations is the same and if the material properties of the regions are similar the strains are similar (Fig. 11b), whereas if the dark material is twice as stiff as the light region, the strain is ½ that of the light region (Fig. 11c). Alternatively, if the alternating regions are arranged in parallel as shown in Fig. 11d, when loaded the strain is the same in both materials regardless of stiffness (Fig. 11e) but the stress is higher in the more stiff material. This parallel arrangement is analogous to fibrous native tissues where stiff surrounding fibers bear the external loads and cells surrounded by softer matrix (e.g., proteoglycans) are stress shielded and can remain quiescent. With transection of the stiff bundles upon injury (Fig. 11f) the stress from external loading is transferred to the cells. Neither of these simplified structures are representative of collagen gels where local remodeling around each cell creates roughly spherical stiff inclusions within a compliant bulk matrix [37]. This heterogeneous structure leads to both strain and stress shielding of the cells as shown by preliminary measurements [100]. Regardless of the structure of a material, it is important to remember that the deformation must be conserved with the local deformations adding up to the overall applied displacement, thus low stiffness areas in series with stiff cell-remodeled areas must undergo exaggerated deformation (Fig. 11c). Simply stated, although strains measured locally within

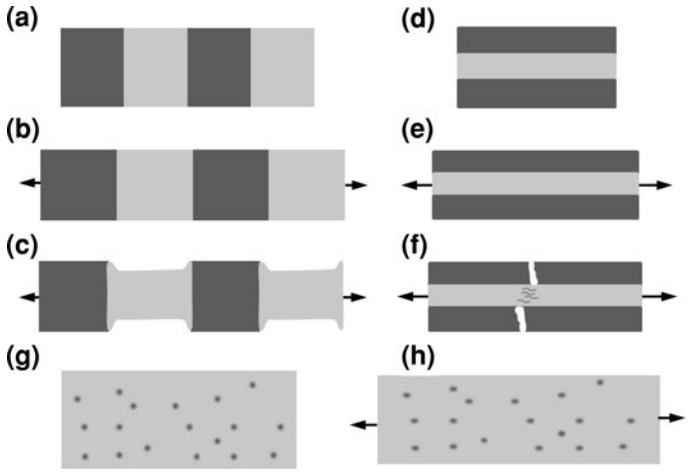

Fig. 11 Schematics of a hypothetical material with alternating regions arranged in series (**a**) demonstrating the resulting deformation if the regions have the (**b**) same stiffness ($E_1 = E_2$) or (**c**) different stiffness ($E_1 = 2E_2$). Schematic of parallel arrangement of materials (**d**) is analogous to native fibrous tissues with stiff fibrous bands (*dark region*) and cells within soft GAGs (*light region*). With stretch (**e**) cells experience the bulk stretch but are stress shielded by the stiff fibers. If the stiff "fibers" are transected to simulate injury, the soft regions are exposed to high stresses (**f**). The stiff inclusions (*dark*) in a soft matrix (*light*) show in (**g**) are more realistic for collagen gels. Cells within the stiff inclusions are shielded from both stress and strain applied externally

collagen gels have been shown to underpredict applied strain levels, the local strain of the matrix cannot be lower than the global strain in all locations.

The previous discussion considers the local strain and stress on the fibrils surrounding the cell rather than strain of the cell itself, and the cell is assumed to be attached to the local fibrils. Clearly, if a cell is not adhered to the collagen matrix it will not be strained, and no force transfer can occur to or from the cell. Due to the natural binding sites on the collagen molecule, adherent cells generally attach well to the fibrils (via integrins; see recent reviews [7, 22, 74]). Elson and colleagues [134] demonstrate, by treating cell-populated gels with cytochalasin-D, that active cell tension has a large impact on the overall stress–strain response under cyclic uniaxial extension. These results indicate that cells can be assumed to be attached firmly to the collagen fibrils in the absence of excessive forces or inhibited attachment, e.g., by blocking integrin subunits.

6.2 Calculation of Cell-generated Forces

In addition to external loading that is transferred to the cells through the matrix, the cells also exert tension on the matrix and on each other. Cell-generated tension

propagates through the matrix surprisingly far in soft collagen gels, hundreds of microns [130]. Propagation of cell tension is especially evident when combined with remodeling of the collagen fibers along lines of stress [121]. When cells are present in sufficiently high density and the matrix is sufficiently compliant, the force can be measured externally [15]. Most commonly, a culture force monitor (CFM) is utilized [33]. Similar to a blood vessel myograph, a CFM consists of a highly sensitive isometric force transducer attached to one end of a compacting collagen gel submerged in media while the other end is rigidly anchored. The force of compaction may also be measured simply by the deflection of compliant beams uniaxially [40] or biaxially [67], which also modulates the effective stiffness of the collagen gel system, or by measuring the frequency and damping of a mechanically pulsed gel cultured on a flexible membrane [129].

The measured force of compaction rises exponentially over the course of approximately 24 h due to the cells migrating through the matrix and compacting the collagen fibrils [87]. The force then levels out at a homeostatic level of basal cell tension which can be eliminated by a variety of agents such as cytochalasin-D. The cells can also be stimulated to contract more vigorously by various agents, the simplest being potassium chloride [67]. In long-term culture, the cells "shorten" the matrix and residual stress is developed within the matrix as evidenced by residual matrix tension following cytochalasin-D treatment.

The force per cell is generally estimated by dividing the total (uniaxial) contractile force measured by the number of cells in the gel [31, 33]. Using this calculation, dermal and cardiac fibroblasts generate 0.1–10 mN/million cells (i.e., 0.1–10 nN/cell) in uniaxial [31, 33] and biaxial [67, 78] systems. Although straightforward, this calculation assumes all cells act in parallel (see schematic, Fig. 12a) which is clearly inaccurate. Assuming that all of the cells act in series, the total force measured would be equal to the force generated by a single cell which is similarly flawed (Fig. 12b). Since the cells are distributed approximately uniformly throughout a cell-populated collagen gel, cells act in parallel with some cells and in series with others (Fig. 12c). Kolodney and Wysolmerski [79] divide the measured uniaxial force by the cell cross-sectional area measured from histological cross-sections which is an improvement for uniaxially constrained gels but not for biaxial configurations. As a simple solution for (equi)biaxially restrained gels, we utilize a representative volume element (RVE) containing one cell and the surrounding volume of ECM (Fig. 12c, inset), and integrate over the RVEs in the perpendicular cross-section and assume a uniform distribution of cell orientations to calculate the total force along each axis. Using this method, dermal fibroblasts generate 17–100 nN/cell for low to high stiffness boundary conditions, respectively, after 3 days in standard media. Comparable values have been reported by Chen and colleagues [85] for NIH 3T3 cells cultured within collagen gels attached to micro-pillars of different stiffness (14 and 24 nN/cell for low and high boundary stiffness, respectively. To more accurately estimate the force per cell in collagen gels, a computational model such as the anisotropic biphasic theory

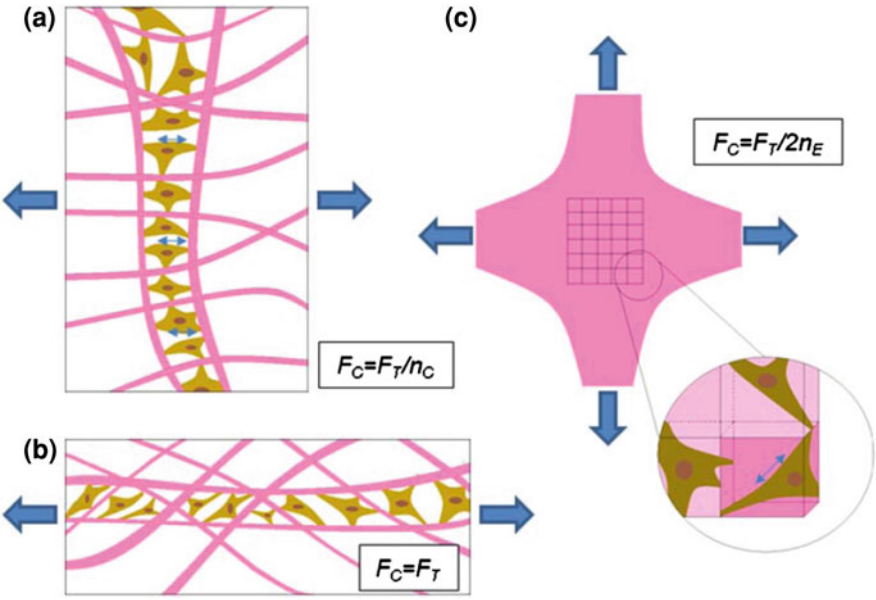

Fig. 12 Schematics representing idealized arrangements of cells in a collagen gels in **a** parallel and **b** series formations for the purpose of estimating the force per cell F_C, assuming uniaxial restraint. **c** Shows a biaxial configuration subdivided into representative volume elements (RVEs) with each RVE containing a single fibroblast in random orientation; n_C number of cells, n_E number of RVEs in parallel in a given cross section. Note that F_C is lowest in (**a**), highest in (**b**), and in between in (**c**). With kind permission from Springer Science + Business Media: from Ref. [67], Fig. 10

[77] would be superior, yet current models rely on assumptions of cell–ECM interactions that are not valid for long culture times.

For collagen-GAG sponges, Gibson and colleagues [57] developed an innovative method involving analysis of the bending of ECM "struts" by individual fibroblasts and found similar values as reported above (26 nN/cell average, maximum 450 nN). These forces are substantially higher than estimated by dividing force by total cell number in earlier studies using the same system ($\sim$3 nN/cell) [41]. Unfortunately the pore and strut size are too small in collagen gels to apply this method. Ideally, the cell force would be determined on a per cell basis using optical measurements of displacements combined with computational methods similar to traction force microscopy used extensively for 2D cell studies on compliant gels. Although not straightforward, 3D traction force microscopy is showing promise with preliminary results indicating that carcinoma cells (human breast) generate forces in excess of 100 nN (unpublished data described in [89]). It is only a matter of time, with new microscopy techniques and computational power, before researchers will be able to image bead/fibril displacements in 3D with sufficient resolution for accurate, routine quantification of cell forces in collagen gels.

7 Discussion

While it is clear that a 3D culture environment is necessary to study cell behavior in a biofidelic manner, there are many aspects that need to be considered when using the collagen gel model system. Collagen gels are complex compared to 2D substrates due to dynamic reciprocity, yet highly simplified both biochemically and structurally compared to native tissues. Dynamic reciprocity between cells and matrix confounds analysis of the specific effects of mechanical cues, e.g., stiffness of the gel changes with cell-mediated remodeling and gels become heterogeneous. Yet the interaction between the matrix and cells in collagen gels can be used to our advantage by measuring functional changes in cooperative cell behavior upon external modulation of the mechanical environment. These metrics, including contractile force and matrix remodeling, can be measured in collagen gels more readily than in standard 2D culture. Further, in 2D systems mechanical cues have been shown to alter gene expression for both ECM synthesis and degradation. Collagen gel models allow researchers to determine the functional outcome of a given set of physical stimuli, i.e., on balance, does the tissue grow or is it resorbed? While we limited our focus to mesenchymal cells entrapped within collagen gels and the effects of stiffness and stretch, it is important to note that interstitial flow within collagen gels is also a strong mechanical signal which alters both fiber alignment and cell behavior [93]. Further, epithelial cells (endothelial cells, keratinocytes, airway epithelial cells, etc.) which reside at the solid/fluid interface have been cultured on collagen gels (i.e., in 2D environment), and the interaction between cell types (e.g., endothelial and interstitial) can be studied in collagen gels as well [18].

This review only touches on complex combinations of proteins; for these the reader is referred to reviews and works regarding fibrin gels [100], Matrigel [139], and decellularized cell-derived matrix [28]. Many of same tools (modulation of boundaries) could potentially be applied to these protein gel models systems to study mechanotransduction in more biochemically relevant matrices. For specific aspects of fibroblast biology in collagen gels, the reader is also referred to excellent reviews by Grinnell and colleagues [49, 50, 108] which include discussions of cell migration, matrix remodeling, and cell morphology in collagen gels. Biomaterial-related reviews for matrices produced with higher order structures such as electrospun biopolymers [88, 115], extruded collagen microfibers [119], and crosslinked collagen sponges, e.g., lyophilized and crosslinked collagen/GAG scaffolds [41] are also available.

Finally, although extensively utilized for studies of cell response to substrate rigidity in 2D (mainly polyacrylamide-based substrates) and beginning to be used for 3D studies (mainly PEG-based gels) to afford independent control of mechanical and biochemical parameters, synthetic polymers are beyond the scope of this review. Their use is described in an excellent review by Nemir and West [92] which includes informative tables with stiffness ranges of tissues and model systems utilized, and future prospects are reviewed by Tibbitt and Anseth [125].

In the future, the field would benefit from a more quantitative and evidence-based analysis of stress transfer and strain shielding in collagen gels. At present, it is unclear if cells are able to sufficiently remodel the collagen matrix to shield themselves from external loading and become quiescent as occurs in native (uninjured) tissues; this important issue should be addressed with additional models and combined microscopic/mechanical studies. Clearly, quantitative measurements of cell and matrix deformations are needed for better understanding of strain transfer to the cells, and these are difficult to visualize in 3D. Although powerful microscopy tools are becoming available, the resolution limit is generally above that of the collagen fibrils and the time required for imaging is long for viable cell studies. A few local methods are described herein, but there is a clear need for additional methods for assessing mechanics of the collagen gel at the cell level including viscoelastic effects. Further, nonlinear collagen stiffness may make local stiffness much higher than bulk stiffness in 3D collagen [122], thus there is a need for large deformation measurements near the cells as well. Better understanding how cell populations are governed by boundary stiffness is also essential, as this condition involves a complex interplay between the boundary and the cells similar to that which occurs in vivo.

The collagen gel remains a powerful model for studying mechanobiology in a three-dimensional environment. Knowledge gained from mechanically controlled and properly characterized systems have had, and will continue to have, a significant impact on fields as diverse as physiotherapy, wound and fracture healing, hypertension, or tissue engineering.

Acknowledgments I would like to thank Drs. Sherry Voytik-Harbin, Frederick Grinnell and Christophe Helary for the generous confocal, fluorescent, and electron micrographs. I also extend my thanks to Heather Cirka for her help with drawing schematics and configuring the table. Finally, I would like to acknowledge the Fulbright Commission in Ireland and the NIH (1 R15 HL087257) for their financial support of this work.

References

1. Ahlfors, J.E., Billiar, K.L.: Biomechanical and biochemical characteristics of a human fibroblast-produced and remodeled matrix. Biomaterials **28**(13), 2183–2191 (2007)
2. Akhouayri, O., Lafage-Proust, M.H., Rattner, A., Laroche, N., Caillot-Augusseau, A., Alexandre, C., Vico, L.: Effects of static or dynamic mechanical stresses on osteoblast phenotype expression in three-dimensional contractile collagen gels. J. Cell Biochem. **76**(2), 217–230 (1999)
3. Alberts, B., Johnson, A., Lewis, J., Raff, M., Roberts, K., Walter, P.: Molecular Biology of the Cell. Garland Science, New York (2002)
4. Allen, T.D., Schor, S.L.: The contraction of collagen matrices by dermal fibroblasts. J. Ultrastruct. Res. **83**(2), 205–219 (1983)
5. Altman, G.H., Horan, R.L., Martin, I., Farhadi, J., Stark, P.R., Volloch, V., Richmond, J.C., Vunjak-Novakovic, G., Kaplan, D.L.: Cell differentiation by mechanical stress. FASEB J. **16**(2), 270–272 (2002)

6. Arora, P.D., Narani, N., Mcculloch, C.A.: The compliance of collagen gels regulates transforming growth factor-beta induction of alpha-smooth muscle actin in fibroblasts. Am. J. Pathol. **154**(3), 871–882 (1999)
7. Baker, E.L., Zaman, M.H.: The biomechanical integrin. J. Biomech. **43**, 38–44 (2010)
8. Balestrini, J.L., Billiar, K.L.: Magnitude and duration of stretch modulate fibroblast remodeling. J. Biomech. Eng. **131**, 051005 (2009)
9. Balestrini, J.L., Skorinko, J.K., Hera, A., Gaudette, G.R., Billiar, K.L.: Applying controlled non-uniform deformation for in vitro studies of cell mechanobiology. Biomech. Model Mechanobiol. **9**(3), 329–344 (2010)
10. Bell, E., Ivarsson, B., Merril, C.: Production of a tissue-like structure by contraction of collagen lattices by human fibroblasts of different proliferative potential in vitro. Proc. Natl. Acad. Sci. U.S.A. **76**(3), 1274–1278 (1979)
11. Berg, R., Birk, D., Silver, F.: Physical characterization of type I procollagen in solution: evidence that the propeptides limit self-assembly. Int. J. Biol. Macromol. **8**(3), 177–182 (1986)
12. Billiar, K.L., Sacks, M.S.: A method to quantify the fiber kinematics of planar tissues under biaxial stretch. J. Biomech. **30**(7), 753–756 (1997)
13. Billiar, K.L., Throm, A.M., Frey, M.T.: Biaxial failure properties of planar living tissue equivalents. J. Biomed. Mater. Res. A **73A**(2), 182–191 (2005)
14. Brinkman, W.T., Nagapudi, K., Thomas, B.S., Chaikof, E.L.: Photo-cross-linking of type I collagen gels in the presence of smooth muscle cells: mechanical properties, cell viability, and function. Biomacromolecules **4**(4), 890–895 (2003)
15. Brown, R.A., Prajapati, R., Mcgrouther, D.A., Yannas, I.V., Eastwood, M.: Tensional homeostasis in dermal fibroblasts: mechanical responses to mechanical loading in three-dimensional substrates. J. Cell. Physiol. **175**(3), 323–332 (1998)
16. Brown, R.A., Wiseman, M., Chuo, C.-B., Cheema, U., Nazhat, S.N.: Ultrarapid engineering of biomimetic materials and tissues: fabrication of nano- and micro-structures by plastic compression. Adv. Funct. Mater. **15**, 1762–1770 (2005)
17. Butcher, J.T., Barrett, B.C., Nerem, R.M.: Equibiaxial strain stimulates fibroblastic phenotype shift in smooth muscle cells in an engineered tissue model of the aortic wall. Biomaterials **27**(30), 5252–5258 (2006)
18. Butcher, J.T., Nerem, R.M.: Valvular endothelial cells regulate the phenotype of interstitial cells in co-culture: effects of steady shear stress. Tissue Eng. **12**, 905–915 (2006)
19. Carver, W., Nagpal, M.L., Nachtigal, M., Borg, T.K., Terracio, L.: Collagen expression in mechanically stimulated cardiac fibroblasts. Circ. Res. **69**(1), 116–122 (1991)
20. Chandran, P.L., Barocas, V.H.: Affine versus non-affine fibril kinematics in collagen networks: theoretical studies of network behavior. J. Biomech. Eng. **128**(2), 259–270 (2006)
21. Chapuis, J.F., Agache, P.: A new technique to study the mechanical properties of collagen lattices. J. Biomech. **25**, 115–120 (1992)
22. Chiquet, M., Renedo, A.S., Huber, F., Fluck, M.: How do fibroblasts translate mechanical signals into changes in extracellular matrix production? Matrix Biol. **22**(1), 73–80 (2003)
23. Christiansen, D.L., Huang, E.K., Silver, F.H.: Assembly of type I collagen: fusion of fibril subunits and the influence of fibril diameter on mechanical properties. Matrix Biol. **19**(5), 409–420 (2000)
24. Chung, H.J., Steplewski, A., Chung, K.Y., Uitto, J., Fertala, A.: Collagen fibril formation. A new target to limit fibrosis. J. Biol. Chem. **283**(38), 25879–25886 (2008)
25. Clark, R.A., Nielsen, L.D., Welch, M.P., Mcpherson, J.M.: Collagen matrices attenuate the collagen-synthetic response of cultured fibroblasts to tgf-beta. J. Cell. Sci. **108**(Pt 3), 1251–1261 (1995)
26. Costa, K.D., Lee, E.J., Holmes, J.W.: Creating alignment and anisotropy in engineered heart tissue: role of boundary conditions in a model three-dimensional culture system. Tissue Eng. **9**(4), 567–577 (2003)

27. Cox, M.A.J., Gawlitta, D., Driessen, N.J.B., Oomens, C.W.J., Baaijens, F.P.T.: The non-linear mechanical properties of soft engineered biological tissues determined by finite spherical indentation. Comput. Methods Biomech. Biomed. Eng. **11**(5), 585–592 (2008)
28. Cukierman, E., Pankov, R., Stevens, D.R., Yamada, K.M.: Taking cell–matrix adhesions to the third dimension. Science **294**(5547), 1708–1712 (2001)
29. Daley, W.P., Peters, S.B., Larsen, M.: Extracellular matrix dynamics in development and regenerative medicine. J. Cell. Sci. **121**(Pt 3), 255–264 (2008)
30. Danielsen, C.C.: Reconstituted collagen fibrils. Fibrillar and molecular stability of the collagen upon maturation in vitro. Biochem. J. **222**, 663–668 (1984)
31. Delvoye, P., Wiliquet, P., Leveque, J.L., Nusgens, B.V., Lapiere, C.M.: Measurement of mechanical forces generated by skin fibroblasts embedded in a three-dimensional collagen gel. J. Invest. Dermatol. **97**(5), 898–902 (1991)
32. Discher, D.E., Janmey, P., Wang, Y.L.: Tissue cells feel and respond to the stiffness of their substrate. Science **310**(5751), 1139–1143 (2005)
33. Eastwood, M., Mcgrouther, D.A., Brown, R.A.: A culture force monitor for measurement of contraction forces generated in human dermal fibroblast cultures: evidence for cell-matrix mechanical signalling." Biochim. Biophys. Acta (BBA) Gen. Subj. **1201**(2), 186–192 (1994)
34. Eastwood, M., Mudera, V.C., Mcgrouther, D.A., Brown, R.A.: Effect of precise mechanical loading on fibroblast populated collagen lattices: morphological changes. Cell Motil. Cytoskeleton **40**(1), 13–21 (1998)
35. Eastwood, M., Porter, R., Khan, U., Mcgrouther, G., Brown, R.: Quantitative analysis of collagen gel contractile forces generated by dermal fibroblasts and the relationship to cell morphology. J. Cell. Physiol. **166**, 33–42 (1996)
36. Engler, A., Bacakova, L., Newman, C., Hategan, A., Griffin, M., Discher, D.: Substrate compliance versus ligand density in cell on gel responses. Biophys. J. **86**(1 Pt 1), 617–628 (2004)
37. Evans, M.C., Barocas, V.H.: The modulus of fibroblast-populated collagen gels is not determined by final collagen and cell concentration: experiments and an inclusion-based model. J. Biomech. Eng. **131**, 101014 (2009)
38. Feng, Z., Yamato, M., Akutsu, T., Nakamura, T., Okano, T., Umezu, M.: Investigation on the mechanical properties of contracted collagen gels as a scaffold for tissue engineering. Artif. Organs **27**(1), 84–91 (2003)
39. Forgacs, G., Newman, S., Hinner, B., Maier, C., Sackmann, E.: Assembly of collagen matrices as a phase transition revealed by structural and rheologic studies. Biophys. J. **84**, 1272–1280 (2003)
40. Freyman, T.M., Yannas, I.V., Yokoo, R., Gibson, L.J.: Fibroblast contraction of a collagen-gag matrix. Biomaterials **22**(21), 2883–2891 (2001)
41. Freyman, T.M., Yannas, I.V., Yokoo, R., Gibson, L.J.: Fibroblast contractile force is independent of the stiffness which resists the contraction. Exp. Cell Res. **272**(2), 153–162 (2002)
42. Friess, W.: Collagen—biomaterial for drug delivery. Eur. J. Pharm. Biopharm. **45**, 113–136 (1998)
43. Ghibaudo, M., Trichet, L., Le Digabel, J., Richert, A., Hersen, P., Ladoux, B.: Substrate topography induces a crossover from 2d to 3d behavior in fibroblast migration. Biophys. J. **97**, 357–368 (2009)
44. Gieni, R.S., Hendzel, M.J.: Mechanotransduction from the ECM to the genome: are the pieces now in place? J. Cell. Biochem. **104**, 1964–1987 (2008)
45. Gildner, C.D., Lerner, A.L., Hocking, D.C.: Fibronectin matrix polymerization increases tensile strength of model tissue. Am. J. Physiol. Heart Circ. Physiol. **287**(1), H46–H53 (2004)
46. Girton, T.S., Oegema, T.R., Grassl, E.D., Isenberg, B.C., Tranquillo, R.T.: Mechanisms of stiffening and strengthening in media-equivalents fabricated using glycation. J. Biomech. Eng. **122**(3), 216–223 (2000)

47. Gordon, M.K., Hahn, R.A.: Collagens. Cell Tissue Res. **339**, 247–257 (2010)
48. Grinnell, F.: Fibroblasts, myofibroblasts, and wound contraction. J. Cell. Biol. **124**(4), 401–404 (1994)
49. Grinnell, F.: Fibroblast–collagen–matrix contraction: growth-factor signalling and mechanical loading. Trends Cell Biol. **10**(9), 362–365 (2000)
50. Grinnell, F.: Fibroblast biology in three-dimensional collagen matrices. Trends Cell Biol. **13**(5), 264–269 (2003)
51. Grinnell, F., Ho, C.H., Tamariz, E., Lee, D.J., Skuta, G.: Dendritic fibroblasts in three-dimensional collagen matrices. Mol. Biol. Cell **14**(2), 384–395 (2003)
52. Grinnell, F., Zhu, M., Carlson, M.A., Abrams, J.M.: Release of mechanical tension triggers apoptosis of human fibroblasts in a model of regressing granulation tissue. Exp. Cell Res. **248**(2), 608–619 (1999)
53. Gross, J., Highberger, J.H., Schmitt, F.O.: Some factors involved in the fibrogenesis of collagen in vitro. Proc. Soc. Exp. Biol. Med. **80**(3), 462–465 (1952)
54. Guido, S., Tranquillo, R.T.: A methodology for the systematic and quantitative study of cell contact guidance in oriented collagen gels. Correlation of fibroblast orientation and gel birefringence. J. Cell. Sci. **105**(Pt 2), 317–331 (1993)
55. Gupta, V., Tseng, H., Lawrence, B.D., Grande-Allen, K.J.: Effect of cyclic mechanical strain on glycosaminoglycan and proteoglycan synthesis by heart valve cells. Acta Biomater. **5**, 531–540 (2009)
56. Hadjipanayi, E., Mudera, V., Brown, R.A.: Close dependence of fibroblast proliferation on collagen scaffold matrix stiffness. J. Tissue Eng. Regen. Med. **3**, 77–84 (2009)
57. Harley, B.A., Freyman, T.M., Wong, M.Q., Gibson, L.J.: A new technique for calculating individual dermal fibroblast contractile forces generated within collagen-gag scaffolds. Biophys. J. **93**(8), 2911–2922 (2007)
58. Helary, C., Bataille, I., Abed, A., Illoul, C., Anglo, A., Louedec, L., Letourneur, D., Meddahi-Pellé, A., Giraud-Guille, M.M.: Concentrated collagen hydrogels as dermal substitutes. Biomaterials **31**, 481–490 (2010)
59. Hinz, B., Gabbiani, G.: Mechanisms of force generation and transmission by myofibroblasts. Curr. Opin. Biotechnol. **14**(5), 538–546 (2003)
60. Hu, J.-J., Humphrey, J.D., Yeh, A.T.: Characterization of engineered tissue development under biaxial stretch using nonlinear optical microscopy. Tissue Eng. Part A **15**, 1553–1564 (2009)
61. Huang, D., Chang, T.R., Aggarwal, A., Lee, R.C., Ehrlich, H.P.: Mechanisms and dynamics of mechanical strengthening in ligament-equivalent fibroblast-populated collagen matrices. Ann. Biomed. Eng. **21**(3), 289–305 (1993)
62. Hubbell, J.A.: Biomaterials in tissue engineering. Biotechnology **13**, 565–576 (1995)
63. Isenberg, B.C., Tranquillo, R.T.: Long-term cyclic distention enhances the mechanical properties of collagen-based media-equivalents. Ann. Biomed. Eng. **31**(8), 937–949 (2003)
64. Jackson, D.S., Fessler, J.H.: Isolation and properties of a collagen soluble in salt solution at neutral pH. Nature **176**(4471), 69–70 (1955)
65. Jhun, C.S., Evans, M.C., Barocas, V.H., Tranquillo, R.T.: Planar biaxial mechanical behavior of bioartificial tissues possessing prescribed fiber alignment. J. Biomech. Eng. **131**(8), 081006 (2009)
66. Jiang, H., Rhee, S., Ho, C.H., Grinnell, F.: Distinguishing fibroblast promigratory and procontractile growth factor environments in 3-d collagen matrices. FASEB J. **22**, 2151–2160 (2008)
67. John, J., Quinlan, A.T., Silvestri, C., Billiar, K.: Boundary stiffness regulates fibroblast behavior in collagen gels. Ann. Biomed. Eng. **38**, 658–673 (2010)
68. Jungbauer, S., Gao, H., Spatz, J.P., Kemkemer, R.: Two characteristic regimes in frequency-dependent dynamic reorientation of fibroblasts on cyclically stretched substrates. Biophys. J. **95**, 3470–3478 (2008)
69. Kadler, K.E., Hojima, Y., Prockop, D.J.: Assembly of collagen fibrils de novo by cleavage of the type I pc-collagen with procollagen c-proteinase. Assay of critical concentration

demonstrates that collagen self-assembly is a classical example of an entropy-driven process. J. Biol. Chem. **262**, 15696–15701 (1987)
70. Kanda, K., Matsuda, T., Oka, T.: Mechanical stress induced cellular orientation and phenotypic modulation of 3-d cultured smooth muscle cells. ASAIO J. **39**(3), M686–M690 (1993)
71. Karamichos, D., Brown, R.A., Mudera, V.: Complex dependence of substrate stiffness and serum concentration on cell-force generation. J. Biomed. Mater. Res. A **78**(2), 407–415 (2006)
72. Karamichos, D., Brown, R.A., Mudera, V.: Collagen stiffness regulates cellular contraction and matrix remodeling gene expression. J. Biomed. Mater. Res. A **83**(3), 887–894 (2007)
73. Karamichos, D., Skinner, J., Brown, R., Mudera, V.: Matrix stiffness and serum concentration effects matrix remodelling and ECM regulatory genes of human bone marrow stem cells. J. Tissue Eng. Regen. Med. **2**(2–3), 97–105 (2008)
74. Katsumi, A., Orr, A.W., Tzima, E., Schwartz, M.A.: Integrins in mechanotransduction. J. Biol. Chem. **279**(13), 12001–12004 (2004)
75. Kemp, P., Falco, L., Regan, K., Bell, E.: Collagen Compositions and Methods for Preparation Thereof. Organogenesis Inc., USA (1992)
76. Knapp, D.M., Barocas, V.H., Moon, A.G., Yoo, K., Petzold, L.R., Tranquillo, R.T.: Rheology of reconstituted type I collagen gel in confined compression. J. Rheol. **4**(15), 971–993 (1997)
77. Knapp, D.M., Tower, T.T., Tranquillo, R.T., Barocas, V.H.: Estimation of cell traction and migration in an isometric cell traction assay. AIChE J. **45**, 2628–2640 (1999)
78. Knezevic, V., Sim, A.J., Borg, T.K., Holmes, J.W.: Isotonic biaxial loading of fibroblast-populated collagen gels: a versatile, low-cost system for the study of mechanobiology. Biomech. Model. Mechanobiol. **1**, 59–67 (2002)
79. Kolodney, M.S., Wysolmerski, R.B.: Isometric contraction by fibroblasts and endothelial cells in tissue culture: A quantitative study. J. Cell. Biol. **117**(1), 73–82 (1992)
80. Krishnan, L., Weiss, J.A., Wessman, M.D., Hoying, J.B.: Design and application of a test system for viscoelastic characterization of collagen gels. Tissue Eng. **10**(1–2), 241–252 (2004)
81. Kuntz, R., Saltzman, W.: Neutrophil motility in extracellular matrix gels: mesh size and adhesion affect speed of migration. Biophys. J. **72**, 1472–1480 (1997)
82. L'heureux, N., Paquet, S., Labbe, R., Germain, L., Auger, F.A.: A completely biological tissue-engineered human blood vessel. FASEB J. **12**(1), 47–56 (1998)
83. Latinovic, O., Hough, L.A., Daniel Ou-Yang, H.: Structural and micromechanical characterization of type I collagen gels. J. Biomech. **43**, 500–505 (2010)
84. Lee, E.J., Holmes, J.W., Costa, K.D.: Remodeling of engineered tissue anisotropy in response to altered loading conditions. Ann. Biomed. Eng. **36**(8), 1322–1334 (2008)
85. Legant, W.R., Pathak, A., Yang, M.T., Deshpande, V.S., Mcmeeking, R.M., Chen, C.S.: Microfabricated tissue gauges to measure and manipulate forces from 3d microtissues. Proc. Natl. Acad. Sci. U.S.A. **106**(25), 10097–10102 (2009)
86. Leung, L.Y., Tian, D., Brangwynne, C.P., Weitz, D.A., Tschumperlin, D.J.: A new microrheometric approach reveals individual and cooperative roles for tgf-beta1 and IL-1beta in fibroblast-mediated stiffening of collagen gels. FASEB J. **21**(9), 2064–2073 (2007)
87. Marenzana, M., Wilson-Jones, N., Mudera, V., Brown, R.A.: The origins and regulation of tissue tension: identification of collagen tension-fixation process in vitro. Exp. Cell Res. **312**(4), 423–433 (2006)
88. Mauck, R.L., Baker, B.M., Nerurkar, N.L., Burdick, J.A., Li, W.-J., Tuan, R.S., Elliott, D.M.: Engineering on the straight and narrow: the mechanics of nanofibrous assemblies for fiber-reinforced tissue regeneration. Tissue Eng. Part B **15**(2), 171–193 (2009)
89. Mierke, C.T., Rösel, D., Fabry, B., Brábek, J.: Contractile forces in tumor cell migration. Eur. J. Cell. Biol. **87**, 669–676 (2008)

90. Miron-Mendoza, M., Seemann, J., Grinnell, F.: Collagen fibril flow and tissue translocation coupled to fibroblast migration in 3d collagen matrices. Mol. Biol. Cell **19**(5), 2051–2058 (2008)
91. Mochitate, K., Pawelek, P., Grinnell, F.: Stress relaxation of contracted collagen gels: disruption of actin filament bundles, release of cell surface fibronectin, and down-regulation of DNA and protein synthesis. Exp. Cell Res. **193**(1), 198–207 (1991)
92. Nemir, S., West, J.L.: Synthetic materials in the study of cell response to substrate rigidity. Ann. Biomed. Eng. **38**, 2–20 (2009)
93. Ng, C.P., Hinz, B., Swartz, M.A.: Interstitial fluid flow induces myofibroblast differentiation and collagen alignment in vitro. J. Cell. Sci. **118**(Pt 20), 4731–4739 (2005)
94. Nishiyama, T., Tominaga, N., Nakajima, K., Hayashi, T.: Quantitative evaluation of the factors affecting the process of fibroblast-mediated collagen gel contraction by separating the process into three phases. Coll. Relat. Res. **8**(3), 259–273 (1988)
95. Olsen, D., Yang, C., Bodo, M., Chang, R., Leigh, S., Baez, J., Carmichael, D., Perälä, M., Hämäläinen, E.-R., Jarvinen, M., Polarek, J.: Recombinant collagen and gelatin for drug delivery. Adv. Drug Deliv. Rev. **55**, 1547–1567 (2003)
96. Ozerdem, B., Tozeren, A.: Physical response of collagen to gels to tensile strain. J. Biomech. Eng. **117**, 397–401 (1995)
97. Paik, D.C., Saito, L.Y., Sugirtharaj, D.D., Holmes, J.W.: Nitrite-induced cross-linking alters remodeling and mechanical properties of collagenous engineered tissues. Connect. Tissue Res. **47**(3), 163–176 (2006)
98. Parekh, A., Velegol, D.: Collagen gel anisotropy measured by 2-d laser trap microrheometry. Ann. Biomed. Eng. **35**(7), 1231–1246 (2007)
99. Parsons, J.W., Coger, R.N.: A new device for measuring the viscoelastic properties of hydrated matrix gels. J. Biomech. Eng. **124**(2), 145–154 (2002)
100. Pedersen, J.A., Swartz, M.A.: Mechanobiology in the third dimension. Ann. Biomed. Eng. **33**(11), 1469–1490 (2005)
101. Petersen, O.W., Rønnov-Jessen, L., Howlett, A.R., Bissell, M.J.: Interaction with basement membrane serves to rapidly distinguish growth and differentiation pattern of normal and malignant human breast epithelial cells. Proc. Natl. Acad. Sci. U.S.A. **89**, 9064–9068 (1992)
102. Peyton, S.R., Ghajar, C.M., Khatiwala, C.B., Putnam, A.J.: The emergence of ECM mechanics and cytoskeletal tension as important regulators of cell function. Cell. Biochem. Biophys. **47**(2), 300–320 (2007)
103. Prajapati, R.T., Chavally-Mis, B., Herbage, D., Eastwood, M., Brown, R.A.: Mechanical loading regulates protease production by fibroblasts in three-dimensional collagen substrates. Wound Repair Regen. **8**(3), 226–237 (2000)
104. Pryse, K.M., Nekouzadeh, A., Genin, G.M., Elson, E.L., Zahalak, G.I.: Incremental mechanics of collagen gels: new experiments and a new viscoelastic model. Ann. Biomed. Eng. **31**(10), 1287–1296 (2003)
105. Raub, C.B., Suresh, V., Krasieva, T., Lyubovitsky, J., Mih, J.D., Putnam, A.J., Tromberg, B.J., George, S.C.: Noninvasive assessment of collagen gel microstructure and mechanics using multiphoton microscopy. Biophys. J. **92**, 2212–2222 (2007)
106. Redden, R.A., Doolin, E.J.: Collagen crosslinking and cell density have distinct effects on fibroblast-mediated contraction of collagen gels. Skin Res. Technol. **9**(3), 290–293 (2003)
107. Reilly, G.C., Engler, A.J.: Intrinsic extracellular matrix properties regulate stem cell differentiation. J. Biomech. **43**, 55–62 (2010)
108. Rhee, S., Grinnell, F.: Fibroblast mechanics in 3d collagen matrices. Adv. Drug Deliv. Rev. **59**, 1299–1305 (2007)
109. Roeder, B.A., Kokini, K., Robinson, J.P., Voytik-Harbin, S.L.: Local, three-dimensional strain measurements within largely deformed extracellular matrix constructs. J. Biomech. Eng. **126**, 699–708 (2004)
110. Roeder, B.A., Kokini, K., Sturgis, J.E., Robinson, J.P., Voytik-Harbin, S.L.: Tensile mechanical properties of three-dimensional type I collagen extracellular matrices with varied microstructure. J. Biomech. Eng. **124**(2), 214–222 (2002)

111. Roeder, B.A., Kokini, K., Voytik-Harbin, S.L.: Fibril microstructure affects strain transmission within collagen extracellular matrices. J. Biomech. Eng. **131**, 031004 (2009)
112. Sander, E.A., Stylianopoulos, T., Tranquillo, R.T., Barocas, V.H.: Image-based multiscale modeling predicts tissue-level and network-level fiber reorganization in stretched cell-compacted collagen gels. Proc. Natl. Acad. Sci. U.S.A. **106**, 17675–17680 (2009)
113. Seliktar, D., Black, R.A., Vito, R.P., Nerem, R.M.: Dynamic mechanical conditioning of collagen-gel blood vessel constructs induces remodeling in vitro. Ann. Biomed. Eng. **28**(4), 351–362 (2000)
114. Seliktar, D., Nerem, R.M., Galis, Z.S.: The role of matrix metalloproteinase-2 in the remodeling of cell-seeded vascular constructs subjected to cyclic strain. Ann. Biomed. Eng. **29**(11), 923–934 (2001)
115. Sell, S.A., Mcclure, M.J., Garg, K., Wolfe, P.S., Bowlin, G.L.: Electrospinning of collagen/biopolymers for regenerative medicine and cardiovascular tissue engineering. Adv. Drug Deliv. Rev. **61**, 1007–1019 (2009)
116. Shi, Y., Vesely, I.: Characterization of statically loaded tissue-engineered mitral valve chordae tendineae. J. Biomed. Mater. Res. A **69**(1), 26–39 (2004)
117. Shi, Y., Vesely, I.: A dynamic straining bioreactor for collagen-based tissue engineering. In: Chaudhuri, J.B., Al-Rubeai, M. (eds.) Bioreactors for Tissue Engineering, pp. 209–219. Springer, Dordrecht (2005)
118. Shreiber, D.I., Barocas, V.H., Tranquillo, R.T.: Temporal variations in cell migration and traction during fibroblast-mediated gel compaction. Biophys. J. **84**(6), 4102–4114 (2003)
119. Silver, F.H., Freeman, J.W., Seehra, G.P.: Collagen self-assembly and the development of tendon mechanical properties. J. Biomech. **36**(10), 1529–1553 (2003)
120. Stegemann, J.P., Nerem, R.M.: Phenotype modulation in vascular tissue engineering using biochemical and mechanical stimulation. Ann. Biomed. Eng. **31**(4), 391–402 (2003)
121. Stopak, D., Harris, A.K.: Connective tissue morphogenesis by fibroblast traction. I. Tissue culture observations. Dev. Biol. **90**(2), 383–398 (1982)
122. Storm, C., Pastore, J.J., Mackintosh, F.C., Lubensky, T.C., Janmey, P.A.: Nonlinear elasticity in biological gels. Nature **435**, 191–194 (2005)
123. Sundararaghavan, H.G., Monteiro, G.A., Lapin, N.A., Chabal, Y.J., Miksan, J.R., Shreiber, D.I.: Genipin-induced changes in collagen gels: correlation of mechanical properties to fluorescence. J. Biomed. Mater. Res. A **87**(2), 308–320 (2008)
124. Thomopoulos, S., Fomovsky, G.M., Holmes, J.W.: The development of structural and mechanical anisotropy in fibroblast populated collagen gels. J. Biomed. Eng. **127**(5), 742–750 (2005)
125. Tibbitt, M.W., Anseth, K.S.: Hydrogels as extracellular matrix mimics for 3d cell culture. Biotechnol. Bioeng. **103**, 655–663 (2009)
126. Tomasek, J.J., Gabbiani, G., Hinz, B., Chaponnier, C., Brown, R.A.: Myofibroblasts and mechano-regulation of connective tissue remodelling. Nat. Rev. Mol. Cell Biol. **3**(5), 349–363 (2002)
127. Tomasek, J.J., Haaksma, C.J., Eddy, R.J., Vaughan, M.B.: Fibroblast contraction occurs on release of tension in attached collagen lattices: dependency on an organized actin cytoskeleton and serum. Anat. Rec. **232**(3), 359–368 (1992)
128. Tomei, A.A., Boschetti, F., Gervaso, F., Swartz, M.A.: 3d Collagen cultures under well-defined dynamic strain: a novel strain device with a porous elastomeric support. Biotechnol. Bioeng. **103**, 217–225 (2009)
129. Trzewik, J., Artmann-Temiz, A., Linder, P.T., Demirci, T., Digel, I., Artmann, G.M.: Evaluation of lateral mechanical tension in thin-film tissue constructs. Ann. Biomed. Eng. **32**(9), 1243–1251 (2004)
130. Vanni, S., Lagerholm, B.C., Otey, C., Taylor, D.L., Lanni, F.: Internet-based image analysis quantifies contractile behavior of individual fibroblasts inside model tissue. Biophys. J. **84**, 2715–2127 (2003)
131. Velegol, D., Lanni, F.: Cell traction forces on soft biomaterials. I. Microrheology of type I collagen gels. Biophys. J. **81**(3), 1786–1792 (2001)

132. Vorp, D.A., Severyn, D.A., Steed, D.L., Webster, M.W.: A device for the application of cyclic twist and extension on perfused vascular segments. Am. J. Physiol. **270**, H787–H795 (1996)
133. Voytik-Harbin, S.L., Roeder, B.A., Sturgis, J.E., Kokini, K., Robinson, J.P.: Simultaneous mechanical loading and confocal reflection microscopy for three-dimensional microbiomechanical analysis of biomaterials and tissue constructs. Microsc. Microanal. **9**, 74–85 (2003)
134. Wakatsuki, T., Kolodney, M.S., Zahalak, G.I., Elson, E.L.: Cell mechanics studied by a reconstituted model tissue. Biophys. J. **79**(5), 2353–2368 (2000)
135. Wille, J.J., Elson, E.L., Okamoto, R.J.: Cellular and matrix mechanics of bioartificial tissues during continuous cyclic stretch. Ann. Biomed. Eng. **34**(11), 1678–1690 (2006)
136. Yamamura, N., Sudo, R., Ikeda, M., Tanishita, K.: Effects of the mechanical properties of collagen gel on the in vitro formation of microvessel networks by endothelial cells. Tissue Eng. **13**(7), 1443–1453 (2007)
137. Yang, Y.-L., Kaufman, L.J.: Rheology and confocal reflectance microscopy as probes of mechanical properties and structure during collagen and collagen/hyaluronan self-assembly. Biophys. J. **96**, 1566–1585 (2009)
138. Yip, C.Y., Chen, J.H., Zhao, R., Simmons, C.A.: Calcification by valve interstitial cells is regulated by the stiffness of the extracellular matrix. Arterioscler. Thromb. Vasc. Biol. **29**(6), 936–942 (2009)
139. Zaman, M.H., Trapani, L.M., Sieminski, A.L., Siemeski, A., Mackellar, D., Gong, H., Kamm, R.D., Wells, A., Lauffenburger, D.A., Matsudaira, P.: Migration of tumor cells in 3d matrices is governed by matrix stiffness along with cell–matrix adhesion and proteolysis. Proc. Natl. Acad. Sci. U.S.A. **103**, 10889–10894 (2006)
140. Zeugolis, D.I., Li, B., Lareu, R.R., Chan, C.K., Raghunath, M.: Collagen solubility testing, a quality assurance step for reproducible electro-spun nano-fibre fabrication. A technical note. J. Biomater. Sci. Polym. Ed. **19**, 1307–1317 (2008)
141. Zeugolis, D.I., Paul, R.G., Attenburrow, G.: Factors influencing the properties of reconstituted collagen fibers prior to self-assembly: animal species and collagen extraction method. J. Biomed. Mater. Res. A **86**, 892–904 (2008)
142. Zhu, Y.K., Umino, T., Liu, X.D., Wang, H.J., Romberger, D.J., Spurzem, J.R., Rennard, S.I.: Contraction of fibroblast-containing collagen gels: Initial collagen concentration regulates the degree of contraction and cell survival. In Vitro Cell. Dev. Biol. Anim. **37**(1), 10–16 (2001)

Biomechanical Characterization of Single Chondrocytes

Johannah Sanchez-Adams and Kyriacos A. Athanasiou

Abstract Normal cartilage functions to cushion and distribute loads throughout the joint. The tissue's constitutive cells, chondrocytes, experience a variety of stresses as a result of these functional aspects, but the effects of these stresses on the individual cells are largely unknown. To understand the mechanical integrity of chondrocytes and how these properties change in response to various stimuli, mechanical testing systems for single cells have been developed. These systems are able to apply a wide variety of load types to characterize cellular biomechanics, and must rely on complex mathematical models to calculate these properties. This chapter reviews the five major mechanical testing systems that are used to test single chondrocytes, their distinct advantages, and discusses the salient results they have produced relating to chondrocyte mechanics and mechanosensitivity. Using these testing systems, it is clear that mechanical signals play a major role in chondrocyte gene expression, and these changes are essential to understand when developing functional cartilage replacements.

1 Introduction

Beginning with Aristotle's book *On the Movement of Animals*, biomechanics has sought to explain the complex processes of locomotion. As our understanding of the inner workings of the human body increased, a subset of the field emerged to

J. Sanchez-Adams (✉)
Department of Bioengineering, Rice University, Houston, TX, USA
e-mail: js5@rice.edu

K. A. Athanasiou
Department of Biomedical Engineering, UC Davis, Davis, CA, USA
e-mail: athanasiou@ucdavis.edu

Stud Mechanobiol Tissue Eng Biomater (2011) 4: 247–266
DOI: 10.1007/8415_2010_20

Published Online: 9 November 2010

closely investigate the mechanical role of individual tissues and cells. By focusing in on smaller and smaller subcomponents, biomechanics is able to explain how mechanical perturbations affect the normal and diseased states of tissues and how these stimuli can be employed in tissue engineering strategies. Employing this micro-scale approach is especially useful in studying tissues such as articular cartilage, given its major mechanical role in the body, inability to self-repair following injury, and need for functional replacement therapies.

1.1 The Mechanical Role of Cartilage

Lining the ends of bones in articulating joints such as the knee, articular cartilage facilitates smooth joint movement as well as bearing and distributing mechanical loads. Within the knee joint, cartilage routinely experiences compressive loads of three times body weight depending on the joint flexion angle and activity. Shear forces in the knee are also significant, and can reach a third of body weight at a knee flexion angle of 40° [1]. These forces are further magnified during activities such as running or jumping. As the articular cartilage lining is only between 1 and 2.55 mm thick in the joints of the lower limb, the tissue must be highly specialized to withstand its mechanical environment [2].

To achieve mechanical integrity, articular cartilage relies on a network of collagen and proteoglycans produced by its constitutive cells, chondrocytes. The collagen present in the tissue is mainly type II and provides tensile strength, while negatively charged proteoglycans such as aggrecan attract water molecules and resist tissue compression. Containing mostly water and proteins, the tissue can be modeled as biphasic material [3–6]. Mechanical testing of the tissue reveals that the tensile and compressive moduli of articular cartilage vary with depth and joint type, with the aggregate compressive modulus ranging from 0.8 to 2 MPa, and tensile modulus between 5 and 25 MPa [7–13]. But as mechanically robust as cartilage is, injury and disease can compromise its integrity and, lacking vasculature, the tissue is unable to self-repair. In response to this problem, tissue engineering strategies and biomechanical characterization techniques have emerged to further understand the role of chondrocytes in cartilage and to apply this knowledge to cartilage replacement and repair strategies.

1.2 Functional Tissue Engineering

Due to the aforementioned forces it must bear, engineered cartilage must reflect the native tissue's functional characteristics, especially its compressive and tensile integrity. To this end, the field of functional tissue engineering has emerged and spurred the creation of mechanical stimulation bioreactors to produce mechanically robust engineered tissue, and enhance purely biochemical approaches to

tissue engineering cartilage. These bioreactors use hydrostatic pressure, direct compression, shear, and combinations thereof to recapitulate the native mechanical environment in vitro and cause engineered constructs to become more like native cartilage [14–18]. While these mechanical stimulation strategies have improved matrix deposition and mechanical strength, the exact mechanisms of their action are ill-understood and optimal parameters for stimulation have yet to be determined. It is clear, however, that construct changes in response to mechanical stimuli are caused by cells, the most basic functional unit of any engineered tissue. Therefore, by studying individual cells it is possible to tease out the microscopic phenomena that, in combination, give rise to macroscopic changes in engineered constructs.

Applying the functional unit approach to understand the effects of mechanical stimulation begins with mechanically characterizing single cells. By determining the mechanical properties of single chondrocytes, the material limitations of the cells can be used to define the upper and lower limits of stimulation. Using these limits, the effects of various mechanical perturbations on the gene expression of single cells can be studied. And finally, mechanical stimulation parameters resulting in ideal gene expression changes can be applied to more complex arrangements of cells in tissue engineered constructs. Thus, understanding the response of the single cell to various mechanical stimuli can provide useful information for developing tissue engineering strategies.

2 Mechanical Testing of Single Cells

A variety of techniques have been developed to study the unique mechanical characteristics of single chondrocytes. Because the chondrocyte's diameter is on the order of 10 μm, mechanical testing machines must be especially sensitive to small changes in force and displacement. For compressive and shear testing, this is often achieved by the use of a cantilever to probe the cell and some mechanism to detect the cantilever's position over time. To test the tensile properties of chondrocytes, micropipette aspiration is the most common method and relies on pressure differentials to deform the cell. The following sections will explore in more detail the most prominent techniques used to elucidate single chondrocyte compressive, shear, and tensile mechanics.

2.1 Compression

Physiologically, cartilage tissue undergoes compressive forces on a regular basis. According to its viscoelastic nature, compressive loads are initially borne by the fluid within the tissue, but over time this load transfers to the solid portion of the matrix as the fluid is forced out [3]. Trapped within their collagen and proteoglycan

matrix, chondrocytes also deform under the load. Three major tools have been used to test the compressive properties of single chondrocytes: the cytocompressor, cytoindenter, and the atomic force microscope. The basic principles of these three apparatuses will be detailed in this section.

2.1.1 Cytocompressor

The cytocompressor device is a tool to determine the compressive properties of single cells, and has been used extensively to characterize the bulk mechanical behavior of chondrocytes. In this setup, unconfined compression is applied to single cells seeded on a glass slide via a large, flat, nonporous probe of around 50 μm in diameter. This probe is attached to the end of a cantilever beam, which is controlled by a piezoelectric actuator (Fig. 1).

For each test, the probe is positioned directly over the cell which is determined by concurrent focusing of the cell and probe in the microscope. With the probe positioned over the cell, the piezoelectric actuator moves the cantilever a set distance toward the cell surface, causing the probe to compress it. This position is held until the cell reaches equilibrium. The cantilever is then retracted from the cell surface, and the volume recovery of the cell is observed. The entire compression event is recorded via a CCD camera. Video post-processing of each compression event allows for the measurement of key parameters, namely the initial, compressed, and recovery geometries of the cell at different time points, and the position of the probe. These measurements allow for the determination of the cell's compressive modulus, Poisson's ratio, and recovered volume fraction, among others.

To determine the compressive modulus of the cell, the relationship between stress and strain must be known. The following equations are used to determine the cell's stress (σ) from a cytocompression experiment:

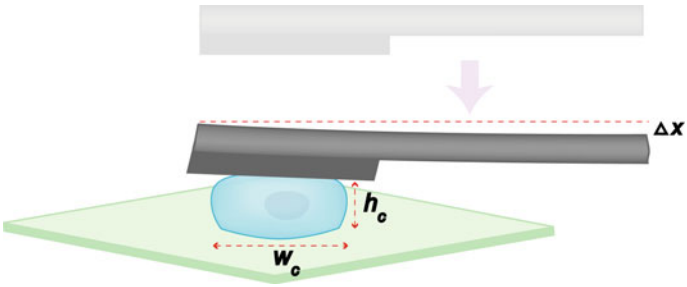

Fig. 1 *Schematic diagram of the cytocompressor.* To test single cells under unconfined compression, the cytocompressor uses a cantilever beam with a wide probe attached to its end. A piezoelectric actuator precisely moves the cantilever probe assembly toward the cell surface, and compresses the cell a set amount. Compression events are recorded via a CCD camera, and cell height (h_c) and width (w_c) are determined from extracted frames

$$\sigma = \frac{3EI(\Delta x)}{L^3 A}$$

where E and I are the Young's modulus and moment of inertia of the cantilever, L is the length of the cantilever, Δx is the difference between actual and prescribed translation of the cantilever, and A is the contact area of the cell and probe. The strain can be written as:

$$\varepsilon = \frac{h_i - h_f}{h_i}$$

where h_i is the initial height of the cell, and h_f is the height of the cell at maximum compression. Using the cytocompressor, a range of strains can be applied to single cells, and the resultant stresses can be calculated from the deformation of the cantilever beam and the contact area of the probe with the cell. These stresses and strains can then be plotted and fitted with a line, the slope of which gives the compressive modulus of the cell [19–22].

In addition to the modulus of the cell, the geometric data during the compression event allow for the determination of the cell's compressibility and recovery behavior over time. The apparent Poisson's ratio (v) for the cell can be calculated as follows [23]:

$$v = \frac{\frac{w_f}{w_i} - 1}{1 - \frac{h_f}{h_i}}$$

where w_i and h_i are the cell's initial width and height, and w_f and h_f are the cell's width and height at equilibrium compression. Recovery behavior can be determined by tracking the volumetric changes of the cell over time, and can indicate whether the cell was permanently changed as a result of the applied force. For chondrocytes, which remain mostly rounded after initial seeding, cell volume can be approximated as an ellipsoid with two identical axes. Approximating the cell's volume initially and after it has recovered from the compression, a measure of recovered volume fraction (V_r) can be determined as follows:

$$V_r = \frac{V_i - V_f}{V_i}$$

where V_i and V_f are the cell's initial and final volume, respectively.

By measuring the compressive stiffness, apparent Poisson's ratio, and recovered volume fraction, the cytocompressor is able to provide quantitative data to help understand not only the mechanical behavior of cells themselves, but also their ability to recover from mechanical stresses. It is a system that is capable of applying varying stresses to cells, at varying rates, and can even be programmed to apply dynamic strain. This system is also unique in that it performs unconfined compression on single cells. This test is particularly relevant to chondrocytes, as these cells live in a tissue that is regularly compressed.

It is important to note, however, that the cytocompressor has some limitations. Because its mechanism tests cells in a semi-rounded morphology, for cells that do not normally exist in this geometry the data may not be as relevant. Moreover, teasing out the mechanical characteristics of cells using this setup requires that some approximations in geometrical models be made. These approximations undoubtedly introduce error into the calculations, and careful measurements must be made in order to minimize this error.

2.1.2 Cytoindenter

Closely related to the cytocompressor is the cytoindenter (Fig. 2). This apparatus applies many of the same principles as the cytocompressor, but there are a few key differences. Like the cytocompressor, the cytoindenter uses a probe attached to a cantilever beam controlled by a piezoelectric actuator for load application, but here the probe is much smaller than the cell (approximately one quarter of its diameter). Unlike the cytocompressor, the cytoindenter does not rely on video capture to determine probe position and deflection. Originally these measurements were made using a dual photodiode detector, a technique that is used in the cytodetacher apparatus and will be discussed in more detail later [24, 25]. The current system, however, monitors the displacement of the cantilever via a laser reflected off the free end of the cantilever [26]. This information is transmitted to the control system and integrated with the displacement data of the

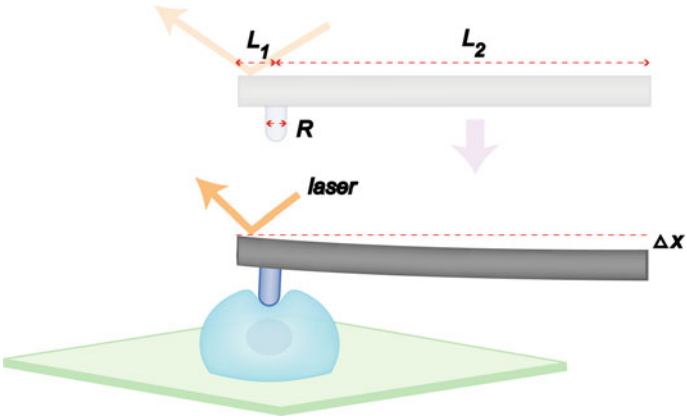

Fig. 2 *Schematic diagram of the cytoindenter.* The cytoindenter tests cells under creep indentation, using a thin probe of radius R attached to a cantilever beam. Like the cytocompressor, the cantilever-probe assembly is controlled by a piezoelectric actuator. The probe placement on the cantilever (described by lengths L_1 and L_2), material properties of the cantilever, and data from the laser micrometer allow for the application of constant force to the cell surface. Probe displacement data over time are recorded and used to extract viscoelastic material properties of the cell

piezoelectric actuator. Together, the laser displacement meter and piezoelectric actuator are able to keep constant the force applied to the cell, resulting in creep indentation testing.

As the system does not measure force outright, it must be calculated based on the measured cantilever displacement by the laser and the intrinsic geometry of the apparatus. This is achieved by combining laser displacement data with the force equation for a cantilever beam, as shown below [26]:

$$F = \frac{3EI\Delta x}{\left(L_1^3 + \frac{3}{2}L_1^2 L_2\right)}$$

where E is the Young's modulus of the cantilever, I is its moment of inertia, L_1 and L_2 add up to the length of the cantilever and are determined by the position of the probe, and Δx is the deflection of the cantilever beam, as measured by the laser micrometer. This equation is similar to that for pure end-loading of a cantilever, but is complicated by the fact that the force is applied a short distance from the end and the laser micrometer measures the displacement of the beam at its end. Nevertheless, using this equation the force can be monitored in real time and used to apply creep indentation to single chondrocytes.

Once a creep curve is produced, it must be analyzed using a mathematical model in order to obtain the material properties of the cell. To model cell indentation, the punch problem can be used in which the cell is assumed to be a linearly elastic, isotropic, and homogeneous half-space which is indented with a flat, rigid punch. The basic equations for this model have been adapted by Koay et al. [26] to account for viscoelasticity in the cell. The resultant equations from this analysis can define three material properties of the cell: the apparent viscosity (μ), instantaneous modulus (E_0), and relaxed modulus (E_∞). These properties are determined by fitting the following equation to the displacement versus time curve from each experiment:

$$\Delta x(t) = \frac{3F}{8RE_0}\left(-\frac{E_0}{E_x}e^{\frac{-E_x t}{3\mu}} + \frac{E_0}{E_x} + 1\right)$$

where R is the radius of the indenting probe and E_x is an elastic constant. The relaxed modulus can then be calculated from the following equation:

$$E_\infty = \frac{E_0 E_x}{E_0 + E_x}$$

where the variables are as mentioned previously.

The cytoindentation apparatus possesses several advantages that allow it to characterize the mechanical behavior of individual chondrocytes. Most importantly, it is capable of performing creep indentation on single cells, a test that is able to elucidate the viscoelastic properties of single cells. Due to the simplicity of

sample preparation in this setup, any type of anchorage dependent cell type may be tested. The system may also be adapted to use different shaped probes to apply different types of load to the cell. These characteristics all contribute to the system's versatility and applicability.

Along with its many advantages, there are some limitations that must be considered when using the cytoindenter. As with the cytocompressor, assumptions about the geometry and homogeneity of the material must be made in order to solve for material properties. In the case of indentation of single cells, the assumption of cell homogeneity may not be accurate as the mechanical properties of subcellular components can vary. Additionally, this system is unable to record recovery data for mechanical tests due to inherent noise in the system. Cell analysis using cytoindentation must be therefore be combined with recovery data from the cytocompressor.

2.1.3 Atomic Force Microscopy

Atomic force microscopy (AFM) has a wide variety of applications including scanning material surfaces, measuring intermolecular forces, and testing the mechanical properties of single cells. This technology relies on the use of a cantilever beam, similar to the cytocompressor and cytoindenter, but the tip of the cantilever on the AFM is much smaller (Fig. 3). For use in testing single chondrocytes, a 5 μm diameter spherical tip is attached to AFM cantilevers and used for indentation of the cell surface [27, 28]. The deflection of the cantilever as it

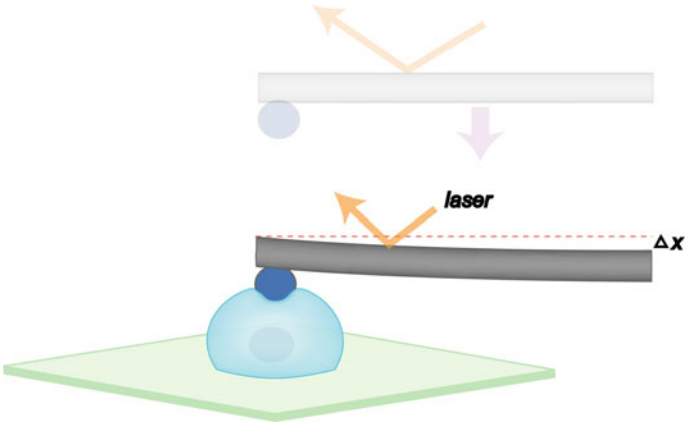

Fig. 3 *Schematic diagram of the atomic force microscope*. In this setup, stress relaxation experiments on single chondrocytes are performed by using a spherical probe attached to a cantilever beam. The probe displacement throughout the experiment is monitored by reflecting a laser off the cantilever and monitoring the angle of reflection over time. This information is then fed back into the actuator system that moves the cantilever to apply a constant strain on the cell. The resultant force versus time graph is then used to determine cellular mechanical properties

indents the cell is monitored via a laser reflecting off the cantilever into a photodiode detection system. Small changes in the position of the laser beam on the photodiodes indicate how far the cantilever is deflected, thereby allowing for the calculation of applied strain on the cell. For stress–relaxation testing using the AFM, a feedback loop is used to apply a set strain and measure the deflection of the beam over time. Using the appropriate model to fit the data, it is possible to gain both stress and strain data from these tests, and ascertain single cell mechanical properties.

Taking into account the shape and hardness of the indenting probe, and viscoelastic nature of cells, Darling et al. [27] developed a model to fit the data obtained from AFM stress–relaxation tests of single chondrocytes. Beginning with a modified Hertz equation for the force of a rigid sphere on a deformable substrate, the elastic and viscoelastic stress–strain relationships are derived assuming the cell surface is isotropic and incompressible. Combining the viscoelastic and elastic responses and specifying a step displacement for the stress–relaxation test, the following force equation can be obtained:

$$F(t) = \frac{4R^{1/2}\delta_0^{3/2}E_R}{3(1-\nu)}\left(1 + \frac{\tau_\sigma - \tau_\varepsilon}{\tau_\varepsilon}e^{-t/\tau_\varepsilon}\right)$$

where R is the relative radius of the probe tip and cell, E_R is the relaxed modulus of the cell, δ_0 is the prescribed step displacement, ν is the cell's Poisson's ratio, and τ_ε and τ_σ are relaxation time constants under constant deformation and load. This equation can then be fit to a force displacement curve to obtain viscoelastic properties such as the instantaneous and Young's moduli of the cell. The equations for these properties are as follows:

$$E_0 = E_R\left(1 + \frac{\tau_\sigma - \tau_\varepsilon}{\tau_\varepsilon}\right)$$

$$E_Y = \frac{3}{2}E_R$$

where E_0 is the instantaneous modulus, and E_Y is the Young's modulus of the cell.

AFM technology allows for very precise measurement of forces, and has been used to study many types of materials and surfaces [29, 30]. The system is capable of testing in a variety of modalities including scanning, tapping, and controlled displacement, and can accommodate many tip geometries including conical and spherical. The tips have even been functionalized to study interaction forces between molecules, demonstrating the AFM's ability to study nanoscale events on a cell's surface or between a cell and a substrate [31–33]. Indenting cells with the AFM can produce data that, when combined with an appropriate mathematical model, is a powerful characterization tool.

The development of a mathematical model to describe single cell testing with the AFM can be a challenging task. As all variables cannot be controlled, assumptions about the cell's geometry, homogeneity, and compressibility must be

made in order to solve the constitutive equations involved. Because the cell contains organelles and cytoskeleton, and may assume different shapes when attached to a surface, these assumptions may introduce error in calculating the mechanical properties. Careful consideration must be made, therefore, to ensure the applicability of various models to single cell AFM mechanics data.

2.2 Shear

In addition to compressive forces, chondrocytes also experience shear as loads are distributed within the joint space. Understanding the shear characteristics of single chondrocytes will allow for a better understanding of their contribution to the tissue as a whole. In this section, two related systems will be reviewed that are able to measure cell adhesion and the apparent shear modulus of single chondrocytes.

2.2.1 Cytodetacher and Cytoshear

The cytodetacher was first developed to measure adhesion forces of cells to various substrates, and has since broadened its applications to measure the bulk shear properties of chondrocytes and other cells [24]. The system consists of a 75 μm diameter horizontal cantilever probe attached at the top to a piezoelectric actuator setup (Fig. 4).

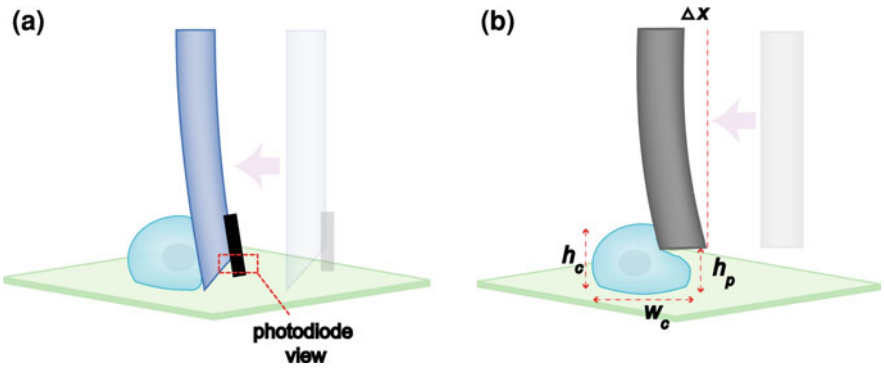

Fig. 4 *Schematic diagrams of the cytodetacher and cytoshear devices.* Both the cytodetacher (**a**) and cytoshear (**b**) systems rely on a piezoelectric actuator to move the probe toward the cell and cause deformation. The cytodetacher system uses a glass probe with an attached carbon filament positioned at the base of the cell, and monitors the carbon filament displacement via a dual photodiode. Attachment force is then calculated using cantilever beam theory. The cytoshear device records each event using a CCD camera, and positions its probe some distance above the base of the cell. Shear properties of the cell are then determined using the cell width (w_c) and height (h_c) over time combined with the knowledge of the probe height (h_p) and probe displacement (Δx)

Once the horizontal cantilever is positioned at the edge of a cell attached to a flat vertical substrate, the piezoelectric actuator moves a precise distance across the cell-seeded surface, detaching the cell from its substrate. The displacement of the probe is measured by a dual photodiode which detects small changes in the transmitted light in the microscope's view field resulting from the movement of a carbon filament attached to the side of the vertical probe. Using the displacement data from the photodiode, and the mechanical properties of the cantilever probe itself, it is possible to calculate the reaction force of the cell during detachment. From cantilever beam theory, this force can be written as:

$$F = \frac{3EI\Delta x}{L^3}$$

where E is the material stiffness of the horizontal probe, I is the probe's moment of inertia, Δx is the difference between the actual displacement of the probe and its prescribed displacement, and L is the length of the probe.

While the elements of data analysis remain the same, this system has been modified to allow for cells to be seeded on a horizontal surface [34]. This modification was achieved by rotating the probe 90° while maintaining the carbon filament horizontal to the cell seeded surface for photodiode detection. This provided a significant improvement in the system's ease of use, and initiated further modifications to enhance its ability to measure cell stresses and strains.

This system has most recently been modified to measure the shear properties of cells [35]. In this modification, the vertical probe is represented by a 50.8 μm diameter tungsten wire and displacement measurements are made by analyzing individual frames from video-captured shear events. As in the first iteration of this system, cantilever beam theory is used to calculate applied force from the apparent and prescribed displacements. In the case of cell shearing, however, the probe is placed a set distance from the substrate and translated resulting in shearing of the cell rather than simple detachment. The necessary data for the cellular deformation are also provided via analyzing frames extracted from video-captured events. Throughout the shearing event the cell's leading edge, trailing edge, and the probe are tracked providing data to calculate the cell-probe contact area (needed to calculate stress), and the cell's elongation. The contact area of the probe on the cell can be calculated by assuming the area is a half-ellipse:

$$A = \frac{1}{4}\pi(w_c)\left(h_c - h_p\right)$$

where w_c represents the width of the cell, and $h_c - h_p$ denotes the difference in height of the cell and probe from the surface, respectively. Using this contact area and the applied force from cantilever beam theory, a measure of the applied stress can be calculated using the relation:

$$\sigma = \frac{F}{A}$$

To calculate the shear strain (ε) experienced by the cell throughout the shearing event, the following relationship can be used:

$$\varepsilon = \frac{w_i}{w_c}$$

where w_i denotes the indentation depth of the probe into the cell, and w_c is the initial cell width as before. By plotting the stress versus strain curve and fitting a line to the data, it is possible to calculate the apparent shear modulus of the cell.

All of the modifications of the cytodetacher have provided some improvement in the ability to quantify cell adhesion forces and shear properties. As chondrocytes rapidly de-differentiate in monolayer, adhesiveness of these cells to various substrates can provide a quantitative measure of phenotypic changes over time. Adhesion forces of chondrocytes to various substrates is also an important measure of the cell's interaction with materials used in tissue engineering strategies. The modification of the cytodetacher for measurement of the apparent shear modulus of chondrocytes also provides a useful tool to measure the biomechanical properties of the cell itself. This method allows for measurement of the apparent shear modulus, which can be used to ascertain characteristics of the cell under a biomechanically relevant load.

The cytodetacher, while useful for studying anchorage-dependent cells, was not designed to study floating cells given that its setup necessitates cell adhesion to a substrate. Additionally, care must be taken to apply the correct geometrical model to each experiment as different cell types may appear more rounded than others when adhered to a surface.

2.3 Tension

Chondrocytes also experience tensile forces from matrix proteins around them pulling in the direction of local compressive or frictional loads. Tensile forces may also be generated in mechanical stimulation of tissue engineered cartilage constructs. In this section, the use of micropipette aspiration will be examined as it relates to chondrocyte biomechanics.

2.3.1 Micropipette Aspiration

Micropipette aspiration uses pressure differentials to calculate the force the cell experiences, and relates that to the observed strain, as seen in Fig. 5.

To perform this type of experiment, a cell is suspended in fluid of pressure p_1 and a micropipette is placed on the cell membrane. The pressure within the pipette is then reduced to p_0 and the cell membrane extends into the pipette at a distance l_p. Given the radius of the micropipette, r_p, the relationship between stiffness and pressure differential for an infinite homogeneous half-space aspirated into a pipette is:

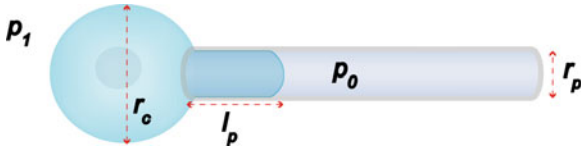

Fig. 5 *Schematic diagram of micropipette aspiration.* In this setup, the cell is suspended in fluid of pressure p_1 and a micropipette of radius r_p is placed on the cell membrane. The pressure inside of the pipette is then lowered to p_0 and the resulting deformation of the cell membrane, l_p, into the pipette is measured. This information, along with the radius of the cell outside of the pipette (r_c), can be used to determine the cell's tensile modulus and viscosity

$$\Delta P = \frac{2\pi}{3} E \frac{r_p}{l_p} \phi$$

where ΔP is the pressure differential between p_o and p_1, E is the Young's modulus of the cell, and φ is approximately 2.1 and depends on the geometric properties of the pipette itself [36]. Solving for the Young's modulus, and substituting for φ, this equation reduces to:

$$E = 0.22\left(\frac{r_p \Delta P}{l_p}\right).$$

Another useful parameter to gain from micropipette aspiration experiments is the viscosity of the cell. Given that cells are viscoelastic materials, cell viscosity can be a useful measure of its phenotype. Modeling the cell as a homogeneous, semi-infinite half-space, to calculate cell viscosity (μ) in this setup the following equation may be used [37]:

$$\mu = \frac{r_p \Delta P}{6\frac{dl_p}{dt}\left(1 - \frac{r_p}{r_c}\right)}$$

where ΔP, r_p, and l_p are the same as before, and r_c is the radius of the cell outside of the micropipette. In this equation, the rate of change of membrane extension into the pipette (dl_p/dt) must also be measured, and can be attained by varying the pressure within the micropipette and recording the resulting deformation with time. This method can also be used to obtain the instantaneous and relaxed modulus of the cell [27].

Micropipette aspiration can be used on both anchorage dependent and floating cells, making it a widely useful mechanical testing tool. It can produce forces between 10 pN and 10^4 nN, and can reach pressures as low as 0.1 pN/μm^2 [38]. This method can also determine whether a cell behaves as a liquid drop or a solid, which becomes useful when deciding on a model for further analysis of cell biomechanics. Mechanical parameters drawn from micropipette aspiration tests can be used to characterize cells and understand their mechanical role in the body.

Along with the many attributes to this method, there are some important considerations that must be made when analyzing its resulting data. Due to the nature of the experiment, measures of viscosity and stiffness are heavily influenced by the mechanical properties of the cell membrane, and thus may not reflect the bulk properties of the cell. Given the microenvironment of the chondrocyte, and that its deformation occurs mostly in compression, testing a portion of the cell in tension will provide some indication of cell properties, but those properties may not be as physiologically relevant.

3 Chondrocyte Biomechanics

All of the aforementioned single cell mechanical testing systems have been used to mechanically characterize chondrocytes, providing information on a wide variety of previously unknown cellular properties. Considering the mechanical properties of chondrocytes can help to understand the mechanical limitations of the cells within their native environment.

3.1 Mechanical Properties of Single Chondrocytes

Often, the same mechanical property can be obtained using a variety of different testing methods. The properties that do overlap, however, do not always match between systems. For example, the instantaneous modulus of chondrocytes using the AFM is around 0.29 kPa, while the same parameter measured using cytoindentation is around 8 kPa [26, 27]. Similar disparities are observed in relaxed modulus, viscosity, and equilibrium time constant measurements between systems. From Table 1, it is apparent that the AFM measures relatively low viscosity compared to measurements from micropipette aspiration, while the viscosity measured by cytoindentation falls between the two. Moreover, equilibrium time constants, when measured with micropipette aspiration can be more than an order of magnitude higher than values obtained from cytoindentation. This wide range could be a result of many different factors, including the constitutive model used, geometric assumptions, biological variability, the source of the tested chondrocytes, and of course the fact that the cell may or may not be anchored during testing.

Perhaps the biggest contributor to these apparent inconsistencies, however, is the type of test performed on the cell. Though literature for chondrocyte mechanics may report the same cellular properties, the particularities of each apparatus and the mathematical model used to calculate those values may only yield a certain aspect of those properties. For example, while the cell's instantaneous modulus can be obtained by AFM and cytoindentation, the different probe geometries and testing modalities may be testing different areas of the cell. More research must be done to better understand these differences, which will inevitably be helped by more rigorous mathematical models for the approximation of the cell.

Table 1 Reported mechanical properties of articular chondrocytes using various testing devices

Mechanical testing device	Modulus (kPa)[a]	Viscosity (μ, kPa·s)	Time constant (τ, s)	References
Cytocompressor	1.63 ± 0.31 (E)	–	1.6 ± 1.3 (recovery)	[20–22]
Cytoindenter	8.0 ± 4.41(E_0) 1.09 ± 0.54 (E_∞)	1.5 ± 0.92	1.32 ± 0.65	[26]
AFM	0.29 ± 0.14 (E_0) 0.17 ± 0.9 (E_∞)	0.61 ± 0.69	9 ± 6.2	[27]
Cytoshear	4.1 ± 1.3 (*low*) 2.6 ± 1.1 (*med*) 1.7 ± 0.8 (*high*)	–	–	[35]
Micropipette aspiration	0.41 ± 0.17 (E_0) 0.24 ± 0.11 (E_∞)	3 ± 0.18	33 ± 20	[44]
	0.45 ± 0.14 (E_0) 0.14 ± 0.05 (E_∞) 0.2 ± 0.07 (E_Y)	2.57 ± 1.83	37 ± 26	[27]

[a] Modulus abbreviations: instantaneous (E_0), relaxed (E_∞), compressive (E), Young's (E_Y), shear (*low, med, high* probe positions)

3.2 Contributors to Chondrocyte Mechanics

Though comparing properties from different mechanical testing modalities may not yield meaningful results, comparing cells tested in one modality is a powerful tool and has been used to understand the source of chondrocyte mechanical integrity. Using the cytocompressor, Ofek et al. [20–22] showed that knocking out different cytoskeletal components within the chondrocyte can vary the mechanical properties of the cell. Specifically, actin filaments emerged as the greatest contributor to compressive stiffness as actin disruption decreased the compressive modulus of the cell by nearly 40%. Additionally, absence of any of the cytoskeletal components doubled the residual strain of the cell following compression, indicating that the cell's cytoskeleton is important for recovery from mechanical perturbation. This study also showed that cytoskeletal components greatly influence the apparent Poisson's ratio. The results indicate that at a certain strain threshold, the microtubules that normally serve as rods holding the cell shape are broken down, reducing cell volume and Poisson's ratio. Termed the critical-strain threshold, this change in mechanical behavior of the cell with applied strain may indicate modifications in gene expression and matrix production in response to, or as a result of, cellular deformation.

Along with the cytoskeleton, the nucleus can contribute largely to the overall mechanical integrity of the cell. Chondrocytes, because they exist in a rounded morphology, also have rounded nuclei which respond to loading by changing volume and modifying gene expression [39]. Therefore, nuclear deformation may be necessary for the cell to respond to mechanical load, and the determination of its stiffness could play a major role in identifying effective cartilage stimulation regimens. Nuclear mechanical properties have been measured with a few different

methods. Using micropipette aspiration, the free-floating nucleus appears to be three to four times stiffer than the cell, while modeling techniques used to fit chondrocyte cytocompression data indicate that the nucleus may be only about 1.4 times stiffer than the rest of the cell [20–22, 40]. Despite the inconsistencies between micropipette aspiration data and theoretical modeling of nuclear stiffness, the methods do agree that the nucleus is somewhat stiffer than the rest of the cell, and therefore can affect its overall mechanics. With more investigation, nuclear mechanics data may prove to be a powerful tool in understanding the underlying mechanotransduction of stimulated chondrocytes.

3.3 Chondrocyte Mechanosensitivity

Chondrocytes are known to modify gene expression patterns in response to both biochemical and mechanical perturbations. While research in the area of chondrocyte mechanosensitivity is still in its early stages, the present data indicate that these cells are particularly sensitive to mechanical loading.

Both loading type and loading duration can cause shifts in gene expression of single chondrocytes. When subjected to varying forces applied in unconfined creep compression, chondrocytes display a dose-dependent decrease in collagen type II expression with increasing load, and aggrecan gene expression decreases sharply when force is increased from 25 to 50 nN of load. Accompanying the decrease in matrix protein expression with load, an increase in tissue inhibitor of metalloproteinase-1 (TIMP-1) gene expression levels is observed [39]. Together, these data indicate that when loaded in this manner, chondrocytes adapt their gene expression profiles from matrix production to matrix maintenance. Similar results are observed when chondrocytes are statically loaded with forces of 50 and 100 nN, but these forces applied dynamically result in matrix molecule gene expression recovered to control states [41]. These results suggest that the way a load is applied (static or dynamic) can profoundly affect the chondrocyte gene expression, and can provide valuable insight into useful modes of engineered cartilage stimulation.

Gene expression and mechanics of loaded chondrocytes are also affected by the biomolecules present. In the same creep compression experiment, Leipzig and Athanasiou [39] showed that the application of transforming growth factor beta-1 (TGF-β1) or insulin-like growth factor-I (IGF-I) throughout the experiment significantly decreased the strain experienced by the cell, and resulted in differing gene expression profiles than stimulated cells without growth factors. Applying TGF-β1 increased aggrecan gene expression over controls in most cases, while adding IGF-I kept TIMP-1 levels relatively constant for all loads. It has also been shown that these two biomolecules are able to stiffen cells significantly, resulting in altered deformation patterns under the same loading conditions [19, 42]. Biomolecules are therefore important regulators of chondrocyte mechanosensitivity. In fact, as chondrocytes in the presence of growth factors such as IGF-I are known to both stiffen the cells and increase gene expression for collagen type II and

aggrecan, they can provide a mechano-protective effect by inhibiting both deformation and gene expression changes caused by mechanical loading [19, 43]. More studies need to be performed to determine the precise ways biomolecules and mechanical stimulation can combine to affect chondrocyte gene expression and mechanics. This information will inevitably prove useful when designing cartilage engineering strategies such that they can harness the synthetic capabilities of chondrocytes.

4 Conclusions

The mechanical integrity of cartilage is extremely important to its normal function in the body. Due to its lack of reparative potential, damage to this tissue is usually permanent and can lead to further musculoskeletal complications. Therefore, a functional cartilage replacement is a valuable prospect, and tissue engineering continues to develop new and exciting answers to this problem. Achieving functionality in tissue engineered constructs, however, requires knowledge of the intrinsic biomechanics of cartilage and its cells. By first characterizing the biomechanics of individual chondrocytes, informed decisions can be made regarding the most effective biochemical and mechanical stimulation methods to use in more complex arrangements of these cells.

Healthy cartilage experiences many different types of loads on a daily basis, including compression, shear, and tension. How these forces are transmitted to individual chondrocytes and their effect on the cell's genotype, however, is not well understood. To study this, a number of mechanical testing and stimulation systems have been developed which are able to characterize not only cellular mechanics, but the effect mechanical loading has on gene expression. Additionally, these devices have been able to resolve the effects of growth factors on individual cell biomechanics, showing that chondrocytes become stiffer in the presence of certain biomolecules.

As chondrocyte mechanical properties obtained from different systems do not always agree with one another, it is important to understand each individual system and the type of test it performs. Small differences in load application and the type of model used to fit the data can magnify the discrepancies between mechanical testing systems. Bulk properties of individual chondrocytes are best tested using the cytocompressor and cytoshear devices because non-homogeneities are diminished by the probe being much larger than the cell. In devices where the probe is smaller than the cell, namely the cytoindenter, AFM, and micropipette aspiration systems, these non-homogeneities may be measured, and can provide information about cytoskeletal arrangement and local cell properties. With an understanding of these differences, the mechanical properties of single chondrocytes can be determined and this information can be used to inform tissue engineering strategies. As more information is available about cellular responses to mechanical and biochemical factors, more directed efforts can be made to combine cells with various stimuli to

create functional engineered cartilage. Cellular biomechanics testing and stimulation systems like the ones described here are beginning to make this possible.

5 Future Directions

With the recent advances in chondrocyte biomechanics testing and evaluation, some interesting questions have emerged which deserve further investigation. First, understanding the mechanosensitivity of subcellular components can elucidate the major players in the mechanosensitivity of the cell as a whole. As it is known that the actin cytoskeleton is an important component of cellular stiffness, it may be important in transducing mechanical signals from the cell membrane to the nucleus. Moreover, nuclear mechanical properties are known to differ from the rest of cell, but the importance of this difference in signal mechanotransduction is unknown. These same principles can be applied to any number of chondrocyte subcellular components, and may lead to a more complete understanding of the machinery of chondrocyte mechanotransduction. These types of experiments can be facilitated by the use of targeted fluorescent molecules to track subcellular components throughout a loading regimen, providing graphic evidence of their response to mechanical stresses.

Another area that should be expanded is the application of these cellular mechanical testing devices to other cell types. At present, aside from the AFM, many of these devices have only been used with a few cell types. Mechanical characterization of cells from other mechanically functional tissues such as tendon, ligament, bone, meniscus, and muscle can provide the same benefits as chondrocyte characterization. As most of these systems are highly adaptable, it would be a natural extension of the technology and would provide interesting comparative values for use in reconstructive therapies.

These future applications can add utility to cellular mechanical testing systems, and allow for a more complete understanding of mechanotransduction pathways of single chondrocytes.

Acknowledgments We would like to acknowledge the Rice-Houston Alliance for Graduate Education and the Professoriate (AGEP) program for their support and funding of this work. We would also like to acknowledge the former lab members who helped develop, test, and validate the cytocompressor, cytoindenter, and cytoshear systems from this lab: Dr. Adrian Shieh, Dr. Nic Leipzig, Dr. Eugene Koay, Dr. Gidon Ofek, Sriram Eleswarapu, and Dena Wiltz.

References

1. Kaufman, K. R., An, K. N., Litchy, W. J., Morrey, B. F., Chao, E. Y.: Dynamic joint forces during knee isokinetic exercise. Am. J. Sports Med. **19**(3), 305–316 (1991)
2. Shepherd, D. E., Seedhom, B. B.: Thickness of human articular cartilage in joints of the lower limb. Ann. Rheum. Dis **58**(1), 27–34 (1999)

3. Mow, V. C., Kuei, S. C., Lai, W. M. Armstrong, C. G. Biphasic creep and stress relaxation of articular cartilage in compression? Theory and experiments. J. Biomech. Eng. **102**(1), 73–84 (1980)
4. Mow, V. C., Gibbs, M. C., Lai, W. M., Zhu, Athanasiou, K. A.: Biphasic indentation of articular cartilage—II. A numerical algorithm and an experimental study. J. Biomech. **22**(8–9), 853–861 (1989)
5. Mak, A. F., Lai, W. M., Mow, V. C.: Biphasic indentation of articular cartilage—I. Theoretical analysis. J. Biomech. **20**(7), 703–714 (1987)
6. Spilker, R. L., Suh, J. K., Mow, V. C.: A finite element analysis of the indentation stress–relaxation response of linear biphasic articular cartilage. J. Biomech. Eng. **114**(2), 191–201 (1992)
7. Kempson, G. E., Freeman, M. A., Swanson, S. A.: Tensile properties of articular cartilage. Nature **220**(5172), 1127–1128 (1968)
8. Woo, S. L., Lubock, P., Gomez, M. A., Jemmott, G. F., Kuei, S. C., Akeson, W. H.: Large deformation nonhomogeneous and directional properties of articular cartilage in uniaxial tension. J. Biomech. **12**(6), 437–446 (1979)
9. Akizuki, S., Mow, V. C., Muller, F., Pita, J. C., Howell, D. S., Manicourt, D. H.: Tensile properties of human knee joint cartilage: I. Influence of ionic conditions, weight bearing, and fibrillation on the tensile modulus. J. Orthop. Res. **4**(4), 379–392 (1986)
10. Athanasiou, K. A., Rosenwasser, M. P., Buckwalter, J. A., Malinin, T. I., Mow V. C.: Interspecies comparisons of in situ intrinsic mechanical properties of distal femoral cartilage. J. Orthop. Res. **9**(3), 330–340 (1991)
11. Athanasiou, K. A., Niederauer, G. G., Schenck, Jr. R. C.: Biomechanical topography of human ankle cartilage. Ann. Biomed. Eng. **23**(5), 697–704 (1995)
12. Athanasiou, K. A., Liu, G. T., Lavery, L. A., Lanctot, D. R., Schenck, Jr. R. C.: Biomechanical topography of human articular cartilage in the first metatarsophalangeal joint. Clin. Orthop. Relat. Res. **348**, 269–281 (1998)
13. Schinagl, R. M., Gurskis, D., Chen, A. C., Sah, R. L.: Depth-dependent confined compression modulus of full-thickness bovine articular cartilage. J Orthop Res **15**(4), 499–506 (1997)
14. Smith, R. L., Rusk, S. F., Ellison, B. E., Wessells, P., Tsuchiya, K., Carter, D. R., Caler, W. E., Sandell, L. J., Schurman, D. J.: In vitro stimulation of articular chondrocyte mRNA and extracellular matrix synthesis by hydrostatic pressure. J. Orthop. Res. **14**(1), 53–60 (1996)
15. Davisson, T., Kunig, S., Chen, A., Sah, R., Ratcliffe, A.: Static and dynamic compression modulate matrix metabolism in tissue engineered cartilage. J. Orthop. Res. **20**(4), 842–848 (2002)
16. Kisiday, J. D., Jin, M., DiMicco, M. A., Kurz, B., Grodzinsky, A. J.: Effects of dynamic compressive loading on chondrocyte biosynthesis in self-assembling peptide scaffolds. J. Biomech. **37**(5), 595–604 (2004)
17. Stoddart, M. J., Ettinger, L., Hauselmann, H. J.: Enhanced matrix synthesis in de novo, scaffold free cartilage-like tissue subjected to compression and shear. Biotechnol. Bioeng. **95**(6), 1043–1051 (2006)
18. Elder, B. D., Athanasiou, K. A.: Effects of temporal hydrostatic pressure on tissue-engineered bovine articular cartilage constructs. Tissue Eng. Part A **15**(5), 1151–1158 (2009)
19. Koay, E. J., Ofek, G., Athanasiou, K. A.: Effects of TGF-beta1 and IGF-I on the compressibility, biomechanics, and strain-dependent recovery behavior of single chondrocytes. J. Biomech. **41**(5), 1044–1052 (2008)
20. Ofek, G., Natoli, R. M., Athanasiou, K. A.: In situ mechanical properties of the chondrocyte cytoplasm and nucleus. J. Biomech. **42**(7), 873–877 (2009)
21. Ofek, G., Willard, V. P., Koay, E. J., Hu, J. C., Lin, P., Athanasiou, K. A.: Mechanical characterization of differentiated human embryonic stem cells. J. Biomech. Eng. **131**(6), 061011 (2009)
22. Ofek, G., Wiltz, D. C., Athanasiou, K. A.: Contribution of the cytoskeleton to the compressive properties and recovery behavior of single cells. Biophys. J. **97**(7), 1873–1882 (2009)

23. Shieh, A. C., Athanasiou, K. A.: Biomechanics of single zonal chondrocytes. J. Biomech. **39**(9), 1595–1602 (2006)
24. Athanasiou, K. A., Thoma, B. S., Lanctot, D. R., Shin, D., Agrawal, C. M., LeBaron, R. G.: Development of the cytodetachment technique to quantify mechanical adhesiveness of the single cell. Biomaterials **20**(23–24), 2405–2415 (1999)
25. Shin, D., Athanasiou, K.: Cytoindentation for obtaining cell biomechanical properties. J. Orthop. Res. **17**(6), 880–890 (1999)
26. Koay, E. J., Shieh, A. C., Athanasiou, K. A.: Creep indentation of single cells. J Biomech Eng **125**(3), 334–341 (2003)
27. Darling, E. M., Zauscher, S., Guilak, F.: Viscoelastic properties of zonal articular chondrocytes measured by atomic force microscopy. Osteoarthritis Cartilage **14**(6), 571–579 (2006)
28. Darling, E. M., Zauscher, S., Block, J. A., Guilak, F.: A thin-layer model for viscoelastic, stress–relaxation testing of cells using atomic force microscopy: do cell properties reflect metastatic potential? Biophys. J. **92**(5), 1784–1791 (2007)
29. Neuman, K. C., Nagy, A.: Single-molecule force spectroscopy: optical tweezers, magnetic tweezers and atomic force microscopy. Nat. Methods **5**(6), 491–505 (2008)
30. Ikai, A.: A review on: atomic force microscopy applied to nano-mechanics of the cell. Adv. Biochem. Eng. Biotechnol. [Epub ahead of print] (2009)
31. Lal, R., Joh, S.A.: Biological applications of atomic force microscopy. Am. J. Physiol. **266**(1 Pt 1), C1–C21
32. Ushiki, T., Hitomi, J., Ogura, S., Umemoto, T., Shigeno, M.: Atomic force microscopy in histology and cytology. Arch. Histol. Cytol. **59**(5), 421–431 (1996)
33. You, H. X., Yu, L.: Atomic force microscopy imaging of living cells: progress, problems and prospects. Methods Cell Sci. **21**(1), 1–17 (1999)
34. Hoben, G., Huang, W., Thoma, B. S., LeBaron, R. G., Athanasiou, K. A.: Quantification of varying adhesion levels in chondrocytes using the cytodetacher. Ann. Biomed. Eng. **30**(5), 703–712 (2002)
35. Ofek, G., Dowling, E. P., Raphael, R. M., McGarry, J. P., Athanasiou, K. A.: Biomechanics of single chondrocytes under direct shear. Biomech. Model Mechanobiol. **9**(2), 153–162 (2010)
36. Theret, D. P., Levesque, M. J., Sato, M., Nerem, R. M., and Wheeler, L. T.: The application of a homogeneous half-space model in the analysis of endothelial cell micropipette measurements. J. Biomech. Eng. **110**(3), 190–199 (1988)
37. Needham, D., Hochmuth, R. M.: Rapid flow of passive neutrophils into a 4 microns pipet and measurement of cytoplasmic viscosity. J Biomech Eng **112**(3), 269–276 (1990)
38. Hochmuth, R. M.: Micropipette aspiration of living cells. J. Biomech. **33**(1), 15–22 (2000)
39. Leipzig, N. D., Athanasiou, K. A.: Static compression of single chondrocytes catabolically modifies single-cell gene expression. Biophys. J. **94**(6), 2412–2422 (2008)
40. Guilak, F., Tedrow, J. R., Burgkart, R.: Viscoelastic properties of the cell nucleus. Biochem. Biophys. Res. Commun. **269**(3), 781–786 (2000)
41. Shieh, A. C., Athanasiou, K. A.: Dynamic compression of single cells. Osteoarthritis Cartilage **15**(3), 328–334 (2007)
42. Leipzig, N. D., Eleswarapu, S. V., Athanasiou, K. A.: The effects of TGF-beta1 and IGF-I on the biomechanics and cytoskeleton of single chondrocytes. Osteoarthritis Cartilage **14**(12), 1227–1236 (2006)
43. Eleswarapu, S. V., Leipzig, N. D., Athanasiou, K. A.: Gene expression of single articular chondrocytes. Cell Tissue Res. **327**(1), 43–54 (2007)
44. Trickey, W. R., Lee, G. M., Guilak, F.: Viscoelastic properties of chondrocytes from normal and osteoarthritic human cartilage. J. Orthop. Res. **18**(6), 891–898 (2000)

Mechanics of Airway Smooth Muscle Cells and the Response to Stretch

Geoffrey N. Maksym

Abstract Airway smooth muscle (ASM) cells are continuously exposed to stretching as we breathe, and this stretching regulates the cell contractility that is ultimately responsible for making breathing difficult. The past dozen years have led to major advances in our understanding of the rheology of the ASM and of the mechanical response to imposed stretch. This review covers the highly adaptable ability of cell function to be maintained over large length changes and reviews characteristic softening and lengthening behaviors. It covers foundations of theoretical interpretations based on myosin dynamics to recent findings that have lead to redefining much of the acute mechanics of the ASM as a soft glassy material. ASM is far from equilibrium, crowded with jostling, interacting molecules with mechanics that are fragile and easily disrupted by large stretches, yet which easily and slowly recover from each stretch. Chronic stretching leads to further changes as contractile phenotype becomes altered. The response to stretch has become one of the most important characteristics of ASM mechanics and defines its function, and ultimately may underlie dysfunction in airway diseases such as asthma.

1 Introduction

This report reviews the fundamental behavior of airway smooth muscle (ASM) in response to acute or continuous oscillatory changes in length or stretches and reviews the current state of the art of our understanding of the mechanical behavior

G. N. Maksym (✉)
School of Biomedical Engineering, Dalhousie University, Halifax,
NS, B3H 1W2, Canada
e-mail: Geoff.maksym@dal.ca

Stud Mechanobiol Tissue Eng Biomater (2011) 4: 267–293
DOI: 10.1007/8415_2010_34

Published Online: 18 September 2010

of ASM in response to stretch. Recent results demonstrate that the ASM displays a rich response to stretch, adapting, stiffening or softening, and altering its constitutive elements. The following briefly introduces the basic "dys-" function of ASM in the lung and introduces the importance of understanding the role of stretch in airway pathology in asthma.

ASM is found in small bundles that encircle the airways of the lungs from the level of the trachea through the cartilaginous larger airways to the smallest airways leading to the alveoli. In humans and animals the ASM is always slightly activated as small amounts of bronchodilator or blocking vagal tone lead to measureable decreases in airflow resistance [18]. When the smooth muscle is activated to constrict, it can do so with substantial force, sufficient to impair airway function leading to death. Indeed, when individual airways are treated with methacholine, an airway can completely close [11]. The function of ASM is thus unlike other smooth muscle organs. In all other organs, organ function is dependent on proper and regulated function responsible for: maintaining tone in the vasculature, motility of the gut, contraction of the bladder and of the endocrine glands. However, the role of ASM in health is mysterious, and may be non-essential and has been the matter of much debate [24, 53, 56, 57, 62].

Its most obvious function is pathological and acts to narrow the airway in asthma with associated features of airway hyperresponsiveness. Airway hyperresponsiveness is present when ASM constricts too much and too easily in response to inhaled allergen or agonists [82]. Said another way, the airways of a healthy non-asthmatic individual require a large dose of inhaled bronchoconstrictor to narrow airways while an asthmatic requires a very small dose and the airways of an asthmatic narrow to a greater extent.

However, if the healthy individual takes a deep breath following an inhaled bronchoconstricting agent, the large stretch beneficially acts to dilate the airways in such a way that after the deep breath a portion of the dilation persists as much as some minutes, despite the ongoing activation of the ASM. This effect is termed bronchodilatory effect of a deep inspiration. The effect is reduced or absent in asthma and in more severe asthma the deep inspiration can lead to further narrowing, and the failure of this mechanism is not well understood [48, 49]. Deep inspirations are also bronchoprotective as a deep inhalation prior to inhaled challenge reduces the effect of the challenge, in healthy subjects, but again this effect is absent or limited in asthma [39, 61].

These differences in response to a stretch during constriction are thought to reside at the level of the ASM. In the following we review several key discoveries and principal behaviors of ASM mechanics in response to stretch or length change and we discuss their interpretations.

2 Length Adaptation

The force–length curve of ASM was once thought to be a fairly stable reproducible curve. That is, there was a unique force–length curve both for passive stretching

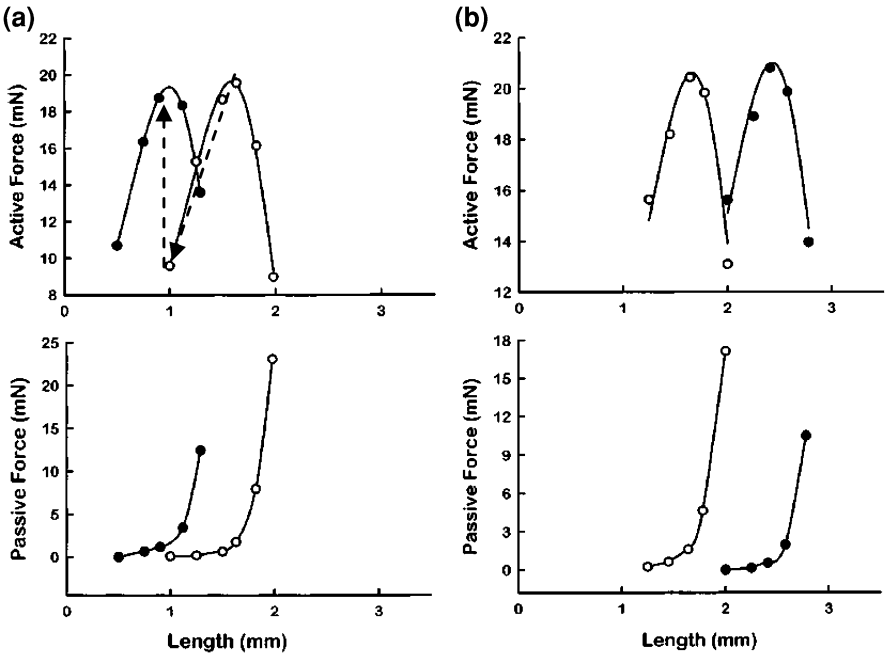

Fig. 1 Length–tension curves from rabbit trachealis. For each trace, active force (*top panels*) exhibits a maximum but when added to passive force (*lower panels*), the total force is always increasing with length (not shown). In situ length-tension curves (*open circles*) are compared with adapted curves (*solid circles*). On the left muscle is adapted to a shorter length while on the right it is adapted to a longer length. Adapted from [80] with permission

and active tension generation. The passive curve increased monotonically with stretch with a non-linear relationship becoming very stiff at large extensions. The active force length curve, created from subtracting the passive curve from total force–length curve, was an inverted parabola with a maximum known as the optimal length. Figure 1 shows passive length-tension curves for smooth muscle in the lower panels and active curves in the upper panels. Several investigators demonstrated that the force length curve in ASM was not immutable, but highly adaptable, and changes in force development depending on length-tension history were demonstrated [32, 59, 80].

It is now recognized that ASM can shift its force length curve over a remarkably wide range. Pratusevich et al. [59] demonstrated that repeated activation of the smooth muscle interspersed with relaxations could adapt the smooth muscle to generate similar force at lengths approximately 50% less and 50% more than the in situ length of the muscle. This adaptation to different lengths is best demonstrated by Wang et al. [80] shown in Fig. 1.

Length adaptation has been demonstrated in several different muscle types including bladder [1, 72], gut [31], and vascular smooth muscle [76] demonstrating the behavior is not unique to ASM.

As an example using Fig. 1, starting at maximal force, if a length change is imposed, the force decreases following the active length-tension curve. This is indicated by the downward dashed arrow in the top of panel A in Fig. 1. If the muscle is kept at this length, force development will gradually increase at this new length to the previous level of force development as indicated by the upward dashed arrow. The muscle has adapted to a new length and subsequent changes in length will explore the force along the new shifted curve (solid curves, Fig. 1). Remarkably, both the active and passive force–length curves are altered.

Length adaptation can be achieved in tens of minutes to several hours depending on the protocol, and this has implications for how it may occur in vivo. The data in Fig. 1 were simply obtained 24 h following a passive change in length. More rapid length adaptation is demonstrated experimentally with repeated intermittent activation, usually by electrical field stimulation, producing similar results to that shown in Fig. 1 [59, 80]. The time course of length adaptation with repeated activation is single time-constant exponential adaptation with a time constant estimated to be approximately 10 min [80]. While these examples of adaptation occurred with relaxed muscle or relaxed muscle with intermittent activation, adaptation has also been demonstrated with continuous sub maximal activation, which does have physiological implication since in vivo ASM is partially activated by basal tone [52].

The mechanisms for length adaptation are beginning to be understood. It is well established that the dramatic change in length-tension curves are accompanied by a change in the organization of both the contractile and passive force maintenance machinery within the smooth muscle cell, although the mechanisms underlying these changes are not clear. Also there are some clues as to what is happening from changes in other functional measures of muscle contraction. Despite no change in force once adapted to the new length, velocity and power are altered. That is, when muscle is adapted to a longer length, shortening velocity is increased in proportion to the change in length, and similarly when adapted to a shorter length velocity is decreased. Power also tracks these changes in velocity, as would be predicted since power is defined by force multiplied by velocity and adapted force is unchanged. These changes can only occur for lengthening adaptation if the contractile lattice is reorganizing with contractile units that were once in parallel becoming units arranged in series [42, 59]. The reverse process would occur for shortening adaptation.

To support this, there is strong evidence that myosin filaments depolymerize and repolymerize with repeated contractions. Using electron microscopy of separate samples at particular times during force recovery, it can be quantifiably observed that following a length change, thick filament density is first decreased but then recovers tracking force recovery and both myosin density and force recover to their prior level before the length change [9, 43]. That is, following a length change as force recovers, myosin filament numbers increase to suggesting that while isometric, the actin–myosin filament overlap is not changed during the adaptation, but force is increased from a change in filament organization. Indeed

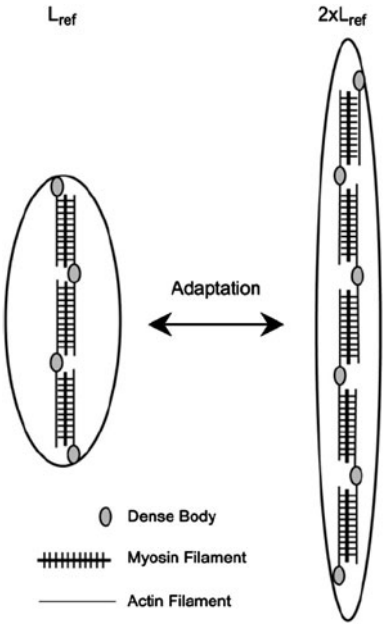

Fig. 2 During length adaptation the actin and myosin filament lattice is thought to reorganize adding contractile units in series. Only one filament is shown for simplicity, and the muscle contains hundreds or more filaments arrange in parallel. The longer muscle has greater shortening velocity but identical maximal force. Used with permission of the American Thoracic Society. Copyright© American Thoracic Society [9]

the myosin filament density is restored such that the number of filaments in parallel after length adaptation is maintained (Fig. 2).

What about actin to which the myosin heads must bind? Some of the myosin is always in filament form, while the remaining myosin is depolymerized, but available for polymerization such that there is ongoing myosin filament turnover during adaptation [60]. Actin turnover is well established during changes in cell shape, and it is well established that actin filament polymerization is induced during contraction and reduced during relaxation [34, 54]. Thus both actin and myosin filaments must be depolymerizing during each rest period and repolymerizing during contraction and in a manner that preserves maximal force and stiffness generation capabilities. How this is orchestrated at a filament level to optimize and attain nearly identical force development over a wide range of lengths is not understood.

2.1 Physiological Implications of Length Adaptation

The ability of ASM to adapt to different lengths, shifting its length–tension curve has profound physiological implications. It can facilitate function over wide changes in organ size, such as occurs in bladder, but in ASM, this ability is potentially harmful. In asthma, inflammation increases contractile activation due to neurological activation of ASM or directly via the presence of a variety of ASM agonists. This would lead to slightly narrower airways which, if the activation

persisted, could lead to length adaptation of the muscle to a shorter length. The adaptation means that the muscle will be able to generate greater force when stimulated, as might occur during exacerbation, and ultimately lead to greater narrowing than would otherwise occur. Further, once adapted to a shorter airway diameter, the muscle can generate larger force and stiffness, reducing the ability of large stretch such as a deep inspiration to reverse the effects of bronchoconstriction, potentially explaining why a deep inspiration fails to provide relief and maintained airway dilation in asthma [2]. Thus length adaptation to a shorter length could help explain this characteristic feature of asthma.

This mechanism also implies a potential treatment to reduce airway hyperresponsiveness. If the muscle could be adapted to a larger length, then airway constriction would be reduced. The same degree of narrowing could occur, but from a larger starting diameter, meaning the resistance to airflow would be much less affected. This is especially true since airway resistance is inversely dependent on the fourth power of airway diameter, implying for the same diameter change at twice the original diameter, the resistance increase would only be 1/16th. Indeed this hypothesis is beginning to be tested. Using continuous positive airway pressure to dilate the airways of ferrets during breathing, Xue et al. [83] showed that airway hyperresponsiveness could be reduced. While they showed this was due in part to reductions in ASM contractility through decreases in contractile proteins, they also demonstrated an increase in relaxed airway diameter which would be consistent with adaptation to an increased ASM length, although this was not directly confirmed.

3 Force Adaptation

Not only does the ASM have a profound ability to adapt to different lengths, but recently it has been described that ASM can increase its force generation ability beyond the usual maximum force [7, 8]. While there has been limited investigation of this behavior to date, it is established that if repeated electric field stimulation is applied to muscle that is also continuously and partially activated with acetylcholine, that the maximal force generated by electric field stimulation in the presence of acetylcholine increases perhaps about 15% [7]. This is not to say that there is a 15% increase in total force, as this represents only that electric field stimulation induced force above the acetylcholine induced tone; however, total force does increase nearly 5% at all doses. Further investigation is required to see if this is the limit of force adaptation achievable in vitro, and if this can occur in vivo. Also it would be important to investigate if repeated contraction by different agonists in combination, rather than electric field stimulation in combination with a contractile agonist would elicit the same change in mechanical force generation. Despite the small effect, the implication is significant, as repeated activation together with elevated baseline tone is characteristic of asthma, and if this mechanism is present in vivo, this would contribute to enhanced airway narrowing in asthma.

4 Fluctuation Induced Softening and Lengthening: Perturbed Equilibrium of Myosin Binding

Not only is the force–length curve mutable, but it is now well established that oscillations in muscle length can more rapidly and dramatically affect muscle force and length in fully contracted muscle. Gunst [33] had demonstrated that when subjected to length oscillations, smooth muscle force decreased well below the static isometric force. Subsequently detailed studies by Fredberg and colleagues [25, 26] showed that oscillations led to dramatic decreases in force and muscle stiffness or increases in length or both depending on oscillation protocol [44].

Two of these results are demonstrated in Figs. 3 and 4, and will be described more fully in the following paragraphs. As will be seen, some but not all of the behavior can be described by a theory based on actin–myosin dynamics referred to here as perturbed equilibrium of myosin binding, and some but not all the behavior can also be explained in a more general abstract theory known as soft glassy rheology described even further below. We first describe the fundamental behavior of the effect of oscillatory stretching on the mechanical properties of ASM, and summarize its interpretation here by actin–myosin dynamics as it was first described. We later return to the same data with respect to the later model of soft glassy rheology.

Similar to the experiments demonstrating length-adaptation, fluctuation induced softening and lengthening are demonstrated using excised muscle strips or suspended single cells. A muscle strip is placed in a tissue bath, then incrementally lengthened using short (1.5 ms) electric field stimulation pulses to discover (and possibly adapt) the peak in the force–length curve. The muscle is then maximally stimulated with a contractile agonist, and oscillations near breathing frequency (0.3 Hz) but of different amplitudes are applied following development of maximal force (Fig. 3).

Muscle force and stiffness decrease dramatically in an amplitude dependent manner decreasing to less than 30% of maximal contracted force, despite maximal activation [25]. Muscle hysteresivity, η, is the ratio of energy dissipated largely via friction-like processes to energy stored elastically during oscillations. It is largely proportional to the rate of turnover of actin–myosin attachment and detachment [27].

Interestingly, after the large amplitude fluctuations when they are reduced to a minimal 0.25% strain, the muscle appears to be in a different state and muscle force and stiffness are depressed at the end of the protocol lower than the maximal force and stiffness that occur when 0.25% strain fluctuations follow isometric contraction. This may be very important physiologically, as it may represent the effect of a large breath on contracted narrowed airways explaining the bronchodilatory effect of a deep inspiration.

A natural counter experiment to the above demonstration of loss of force and stiffness with fixed mean length oscillations is instead to impose oscillations with

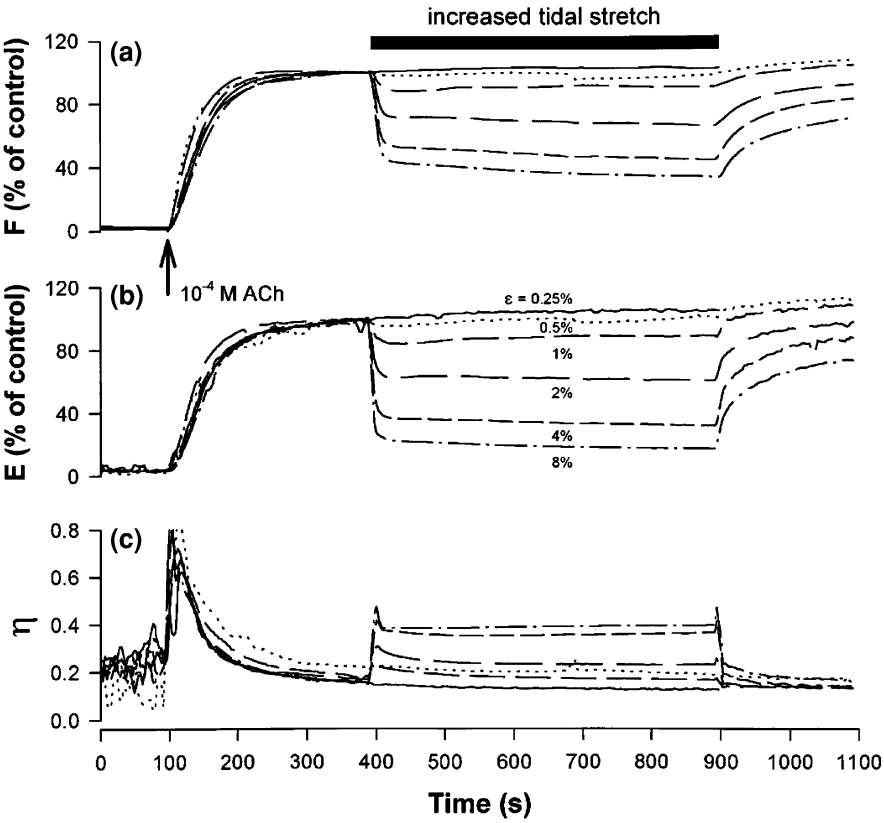

Fig. 3 Imposed oscillations of increasing amplitude from 0.25 to 8% lead to amplitude dependent decreases in force (F), stiffness (E) and increases in hysteresivity (η) on a representative ASM tissue strip. η is the ratio of energy dissipated by frictional forces to energy stored elastically during each oscillatory cycle. Mean muscle length is fixed during the protocol and F depicts mean force per oscillation cycle. Used with permission of the American Thoracic Society. Copyright© American Thoracic Society [25]

fixed mean force allowing mean length to change freely. This experiment is important, since in vivo airway diameter can change, and airway diameter determines resistance to airflow in the lung. When muscle mean length is free to vary, oscillations in muscle force (and of course length) lead to an increase in the average length of the muscle relative to its contracted length, lengthening completely as far as initial pre-contracted length. The muscle is maximally contracting, yet while the oscillations are applied, the muscle lengthens remarkably to the length of fully relaxed muscle. It is as if the muscle were not contracting at all. Importantly, while the amplitude of oscillations in force is 32% of maximal force, the actual amplitude of length oscillations to achieve this lengthening is only 1–2% (2–4% peak-peak) of initial length (Fig. 4).

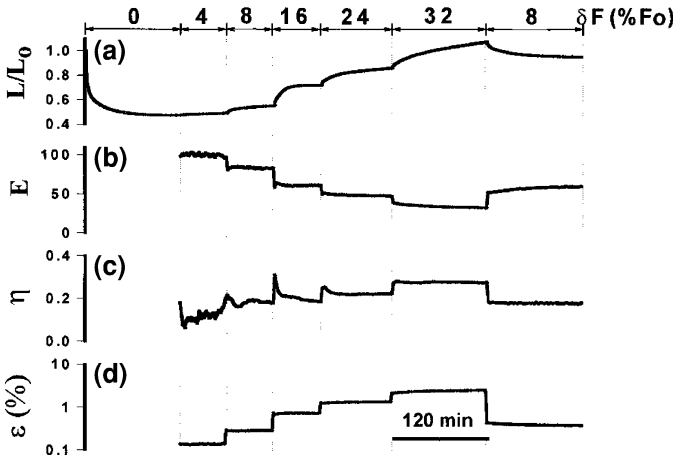

Fig. 4 A single tissue strip shortening following acetylcholine contraction and then lengthening as much as the uncontracted length with increasing amplitude of imposed force oscillations. Muscle stiffness *E* decreases and hysteresivity increases. Note imposed oscillatory strains are quite modest, actually only reaching 2% of Lo. Used with permission of the American Thoracic Society. Copyright© American Thoracic Society [26]

Similar to the fixed mean length, force reduction behavior, fluctuations around a fixed mean force lead to an apparent different length–tension state of the smooth muscle following the large amplitude oscillations. After fluctuations are reduced to minimal levels, the length is much longer than after isotonic contraction (end of length trace in Fig. 4). As described above this has important implications and may explain why after a deep breath in healthy individuals, airway resistance is reduced for a time despite prior airway narrowing due to inhalation of contractile agonists.

Of course, in vivo, neither mean length nor mean force is fixed, but both move according to the force balance between muscle force, hoop stress of the airway wall and parenchymal tethering transmitting lung transpulmonary pressure. Latourelle et al. [44] exposed excised smooth muscle strips to a computationally modeled and experimentally recreated physiological loading condition including these contributions. They demonstrated that both of the above behaviors decreasing force and increasing length with imposed tidal oscillations occurred together. Since some of the lengthening of the muscle lessened the stretch experienced by the parenchyma, this diminished the loading experienced by the muscle decreasing force, and for physiological levels, both force and stiffness decreased to a lesser degree than Fig. 3 and length increased, but again to a lesser degree than Fig. 4.

4.1 Cross-Bridge Dynamics

About a decade ago, it was found that the above fluctuation induced decrease in force (Fig. 3) and increases in length (Fig. 4) or their combinations, could be

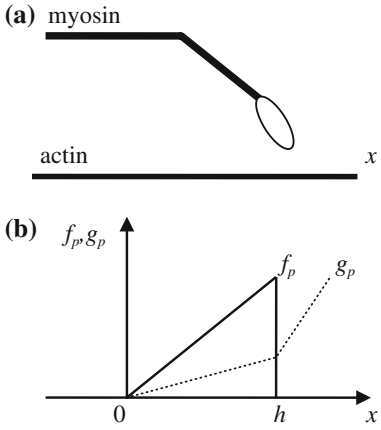

Fig. 5 **a** Depiction of unattached myosin head near actin filament with **b** associated probability for phosphorylated myosin to attach $f_p(x)$ (*solid line*) and detach $g_p(x)$ (*dashed line*), with subscript p denoting the rapidly cycling (phosphorylated) cross-bridge. The slower detachment probability function for unphosphorylated myosin has the same shape as $g_p(x)$ but is much less (not shown). These are functions of the relative location of sliding myosin filament to optimal actin attachment site, h (adapted from [55]). The probability to attach $f_p(x)$ is greater than zero for x between 0 and h, and zero everywhere else, and that the probability to detach $g_p(x)$, is very high for $x < 0$, is zero for $x = 0$, and increases with increasing x. With stretch the actin–myosin filaments slide and myosin heads can be convected out of this region where detachment is highly likely and attachment impossible. When oscillations are imposed, as amplitude of oscillation is increased, myosin heads spend less time within the region 0 to h, leading to less myosin heads bound to actin and less force

predicted from the Hai and Murphy model of actin–myosin cross-bridge dynamics, which is an extension of the Huxley model of cross-bridge dynamics [38, 26]. While not all of smooth muscle dynamic behavior can be explained by this model, as will be discussed below, its strengths lie in predicting several aspects of smooth muscle mechanics, its connection to actin and myosin filament structural organization, and its basis on independently established rate constants. But it does have weaknesses as will be discussed.

To explain maintained force with decreased ATP utilization in smooth muscle, Hai and Murphy included in their model a slowly cycling cross-bridge or ‘latch bridge’ which detached far more slowly than normal, and they developed a four state cross-bridge model based on the Huxley two state model to include this novel state [35]. Application of the this model to oscillatory perturbation of muscle was developed by Dr. S. Mijailovich in the laboratory of Dr. J. Fredberg and details can be found in [55]. At the heart of the Huxley model and thus the Hai and Murphy model is the strain dependence of actin–myosin attachment and detachment. That is, the probability for myosin to bind to actin depends on the physical location of the myosin head relative to the actin binding site (Fig. 5).

In Fig. 5, the model assumes an unattached cross-bridge has a finite increasing probability to attach as long as the sliding filament places the myosin head

between 0 and h. If the myosin head is outside this range, the probability to attach is zero, and the next attachment site is far away. When attached the probability to detach is zero at $x = 0$, and increases linearly until $x = h$ but then changes slope by a factor of 3 increasing thereafter, while for $x < 0$ the probability to detach is very large at 20 times this corner value [55].

The most obvious feature from Fig. 5 is the sensitivity to stretch built into the model. If the myosin head is pulled outside the binding region from 0 to h then the probability to attach is zero. If an attached cross-bridge is pulled outside this region the probability to detach is very high, regardless of whether the cross-bridge is slowly cycling or rapidly cycling. The implications for oscillations in length of the cross-bridge are that as the amplitude of the oscillation is increased, the myosin head spends less time in the binding region and the number of bound myosin heads to actin will be reduced. This is amplitude dependent and in large part explains the decrease in force or lengthening with increased amplitude of oscillation at a fixed frequency of oscillation shown in Figs 3 and 4.

What happens with different rates of oscillation is more complex, and reveals some of the limitations of this model. The mechanics predicted by the cross-bridge model depends on the rate of oscillation relative to the nearest rate constant for actin myosin binding in the model, and thus should show changes in slope when steady-state mean force or stiffness is plotted versus oscillation frequency. However data from ASM tissue strips is limited to a very short frequency range, and as we shall see below, data from a wider rage of frequencies from cultured cells does not reveal any kinks in the frequency dependence of cell stiffness.

5 Scale-Free Rheology

In the last decade, evidence has been rapidly mounting that much of the mechanics of ASM cells and that of adherent cells, qualitatively, and in some cases precisely quantitatively, follows behavior like that of a class of materials known as soft glasses. The recent attention to this behavior was first explored in Fabry et al. [21] who established that the rheological properties of the cytoskeleton were scale-free, with the elastic and loss moduli exhibiting weak power-law dependence in response to small oscillatory perturbations (Fig. 6).

They used ferromagnetic 4.5 μm beads that were bound to the cytoskeleton of adherent cultured cells. By manipulating the beads in magnetic fields they could be rotated, or pivoted in an oscillatory manner, and the mechanical properties of the cytoskeleton could be probed over a very broad frequency range. Over a broad range of frequencies, from 0.01 Hz to high frequencies to 1,000 Hz, the elastic or storage modulus of the cytoskeleton exhibited a weak power-law, f^{x-1} with the slope x depending on the pharmacological intervention (Fig. 6). The loss modulus exhibits the same power-law exponent demonstrated by an identical slope for each condition until 30 Hz when it begins to increase and approaches an asymptote value of $x = 1$.

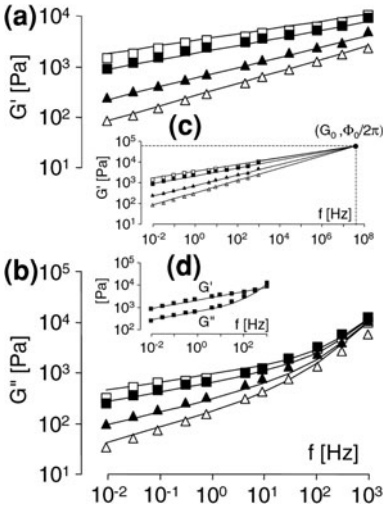

Fig. 6 Power law and scale free oscillatory mechanics of the cytoskeleton of adherent ASM cells. G' and G'' are the storage **a** and loss modulus **b** as measured by OMTC for different drug treatments histamine (*unfilled squares*), untreated (*filled squares*), db-cAMP (*filled triangles*), and cytochalasin D (*open triangles*). **c** Extrapolation of the storage modules converges on a single point given G_o, $\Phi/2\pi$. **d** The loss moduli is a fixed fraction of the storage moduli up until the effects of a small Newtonian viscosity at about 30 Hz when the loss modulus curves upwards with asymptote $G'' = \mu\omega$. Used with permission [21]

For a given treatment condition, the lack of any change of slope or resonance in the frequency dependence indicates there is no dominant resonance or material relaxation time in this frequency range, which is a characteristic of soft glassy materials [71]. Thus the material properties are described by

$$G*(\omega) = \frac{G_o}{\Gamma(x)}\left(\frac{i\omega}{\Phi_o}\right)^{x-1} + i\mu\omega, \tag{1}$$

where G_o and Φ_o being scale factors for stiffness and frequency, respectively, Γ being the gamma function and $\omega = 2\pi f$ and i is $\sqrt{-1}$. An alternative expression that evaluates the bracketed argument of Eq. 1 gives the relation provided in Fabry [21] that separates real and imaginary parts is,

$$G*(\omega) = G_o\left(\frac{\omega}{\Phi_o}\right)^{x-1}(1 + i\eta_s)\Gamma(2-x)\cos\frac{\pi}{2}(x-1) + i\mu\omega \tag{2}$$

which includes an easily accessible frequency independent parameter $\eta_s = \tan[\pi/2(x-1)]$, where the subscript s is used to differentiate this term from the very similar hysteresivity described earlier, and for completeness, $\delta = \pi/2(x-1)$ is the phase angle. Although here η_s is used, it is identical to η at low frequencies when the Newtonian viscosity, which contributes to additional energy dissipation at high

frequencies, can be neglected. For each of the four different treatments, only x changed, with slope decreased for histamine (10^{-4} M), and increased for db-cAMP (10^{-3} M) and cytochalasin D (2×10^{-6} M).

This equation and the behavior in Fig. 6 describes a complex modulus with real part as an elastic term which can be taken to represent a storage modulus, G', and an imaginary part which can be taken to represent a loss modulus G'' containing a dissipative part in proportion to G' in combination with a Newtonian viscosity term $\mu\omega$. The storage and loss moduli follow identical power-laws until about 30 Hz, after which the loss modulus begins to curve upwards and asymptotes to the viscosity term $\mu\omega$ with a slope of 1. Note that up until the effects of the Newtonian viscosity, G'' is a fixed fraction of G' (inset d, Fig. 6), and this is true for each treatment and this fraction is given by the factor η_s (Eq. 2). Further η_s is defined by x, meaning that the dissipative portion (excluding μ) and elastic portion of the model are enforced to be coupled via η_s, and thus also via x.

Fabry et al. [21] noted that over a broad range of treatments, within the ASM cell type G_o and Φ_o were unchanged and only the slope, $x - 1$, changed depending on treatment as indicated in Fig. 6. Thus, at any frequency within the range tested, the change in x enforced a change in both storage and loss modulus, such that an increase in x led to a decrease in the mechanical moduli.

If oscillatory excitations fall within a linear regime, then transforming equation 1 to the time domain reveals the instantaneous step response that follows a very simple power law

$$J(t) = J_o\left(\frac{t}{t_o}\right)^{x-1}, \tag{3}$$

where J_o is a scaling factor at an arbitrary time t_o [12, 51]. Indeed it was found that in response to step functions, the response of the cytoskeleton very closely followed this power law over the full range of time-scales examined from 3 ms to 3.2 s [12]. Furthermore changes in the power-law exponent x for different pharmacological treatments were well predicted from the oscillatory behavior (Eqs. 1 and 2). Further although creep responses were slightly better fit allowing different J_o for each treatment, the differences were small and for all intents and purposes, like G_o in Fig. 6, J_o could be considered a constant.

This finding verified the remarkable finding that the dynamic mechanical properties of the cytoskeleton were both linear and scale free over the full broad range of frequencies and time-scales that were tested. These findings are limited to the linear deformation range, but this is fairly broad, up to approximately 25%, estimated from motions of up to 1 μm that can occur for a 4.5 μm diameter bead pivoting on a cell used in this technique.

Scale free mechanical behavior is not unique to the cytoskeleton of ASM. To a similar accuracy this behavior also fits a variety of other cell types [21], with G_o and x differing somewhat depending on cell types [22]. Further, scale free mechanical behavior is a robust finding among many measurement methods with

similar results being obtained from optical tweezers [4, 13], magnetic tweezers [5], and atomic force microscopy [47, 77].

5.1 Structural Damping

Scale free power-law behavior as described in Eq. 1 or 2 has been previously described by an empirical behavior known as structural damping [28, 29, 70]. Structural damping is an empirical behavior coupling dissipative forces to elastic forces. As such, structural damping is not easily described using viscous dissipation that would occur from fluid flows, but more easily via frictional processes that might occur with sliding or perhaps other irreversible processes that might occur in proportion to the elastic deformation. This behavior was first described as structural damping because it was identified in solid materials in composite structures such as airplane wings [28]. Coupling of dissipative stresses to elastic stresses occurs when the moduli share the same slope $(x - 1)$ versus frequency and this is enforced in Eq. 2. G'' is a constant fraction of G' often expressed using the quantity hysteresivity, $\eta = G''/G'$ as a constant. It is apparent that the empirical theory of structural damping is well described within Eq. 2 and thus is consistent with the theory of soft glassy rheology, which attempts to provide some insights to this empirical relation described below.

6 Soft Glassy Rheology

The scale-free rheology exhibited in Figs. 6 and 7 is well described by an abstract model developed by Sollich [70, 71] for a broad class of materials known as soft glasses. Soft glasses include slurries, pastes and colloids that are solid until shaken or disrupted by mechanical energy upon which they flow like liquids. Familiar soft glasses include ketchup which is easier to pour after the bottle is shaken, toothpaste and granular soils which no longer supports buildings during earthquakes. Soft glasses have weak elastic moduli, feature structural reorganizations that are slow and inelastic, and with mechanical disruption their properties become more fluid-like, but recover slowly becoming more solid.

The theory Sollich developed for soft glassy rheology is based on an earlier model [10] and is a semi-empirical theory. The model is based on the physical properties of colloids where the structural elements are in close contact with each other but weakly interacting. The elements are often portrayed as particles jostling among each other, and for elements to move in the model, they must attain sufficient energy to 'hop' from one location into a nearby gap. One abstract component within the model is that the elements are distributed within energy wells of finite height according to an exponential distribution and in order for the system to deform, the elements must hop out of their energy wells. At any given instant in time, the elements or particles are in a state that is far from equilibrium.

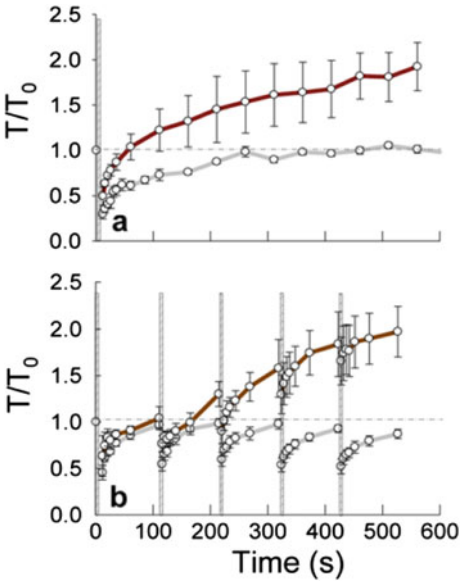

Fig. 7 **a** Contractile moment normalized to unstretched baseline value (To) versus time after stretch cessation. In response to both homogenous biaxial stretch (gray, 10%) and non-homogenous stretch (brown ranging to 5%), both cells exhibited prompt fluidization and recovery was back to baseline in the homogenous case but exceeded recovery when stretch was inhomogeneous indicating stiffening or reinforcement. **b** The response to inhomogeneous repeated stretches was similar to the single stretch, but repeated homogenous stretches resulted in significantly decreased contractile moment [40]

That is, they are in a metastable state with particles located in local minima. An in depth mathematical treatment can be found in Sollich [70] which is further explored in later works for the rheology of the cytoskeleton in [51, 78].

When such a system receives sufficient mechanical shear to cause the particles to rearrange inelastically, this provides energy to the elements, and the system moves further from equilibrium. When the shear ceases, the system begins to evolve to a lower energy configuration, as elements hop to wells of deeper height from which higher energies are needed to escape. The material becomes less fluid and more solid as elements become more trapped, and the material increases in mechanical stiffness. Perturbation of the material that causes a shift in metastable state leads to a shift either to more solid or more fluid-like state are defined by the slope parameter x. When $x = 1$, the material is an elastic solid and when $x = 2$, the material is a viscous Newtonian fluid.

However the rheology of the cytoskeleton of ASM cells never achieves these extremes, and under the steady state conditions as explored in Fig. 6, x ranges from between $x = 1.17$ and 1.33 depending on interventional treatment and is thus decidedly more solid than fluid [21]. Because via Eq. 1 or 2, at frequencies other than G_o, x defines G' and G'', this range of x values corresponds to a change in cytoskeletal stiffness or G' of more than one order of magnitude at low frequencies, and a smaller difference at higher frequencies.

In the model, x represents a quantity like a temperature that represents the level or magnitude of jostling of the structural elements within the model. It does not correspond to an actual temperature as changes in cell temperature lead to changes in x in opposite direction to the imposed change in temperature [75]. However it has been reasonably suggested that ATP consumption within the cell may

ultimately be the energy source within the cell that governs the jostling at steady state and maintains the cytoskeleton far from equilibrium [20, 45].

However numerous factors contribute to changes in x that are not well understood. A decrease in x represents less jostling of structural elements within the Sollich model and the material is more frozen. While an increase in x represents more jostling among the structural elements and the material is in a more fluid state. Factors that decrease x also increase the cytoskeletal tensions set by the prestress [73, 74, 81] and factors that increase x also decrease the cytoskeletal tension set by the prestress. Indeed it would appear that the prestress sets the stiffness, G', and thus sets x. For example activating the contractile apparatus via histamine leads to an increase in prestress, an increase in G', and a corresponding decrease in x, all coupled via the scale free relations in Eqs. 1–3.

6.1 Fluidization

The rheology of Fig. 6 and 7 are the steady state physical properties of the cytoskeleton of adherent cells including ASM cells and are well described by the theory of scale-free dynamics within soft glassy rheology. However the theory predicts that when not in steady state, large deformations cause fluidization of the soft glass, with a predicted decrease in moduli and increase in x. Indeed Trepat et al. [78] demonstrated this using a transient biaxial stretch and return protocol ranging from 2.5 to 10% stretch of ASM cultured cells plated on flexible substrates. They showed that stiffness decreased with the stretch and slowly recovered. They further showed that the behavior was robust to changes in the initial baseline state of the cell. Stretch decreased stiffness with pretreatments of (1) Jasplakinolide that stabilized the actin cytoskeleton, with (2) depolymerization of the actin cytoskeleton by latrunculin-A, (3) inhibition of contractile function by the myosin light chain kinase inhibitor ML-7, (4) chelation of calcium by EGTA to prevent calcium influx via stretch activated calcium channels, and (5) ATP depletion. The decrease in cell stiffness in each case was not however due to cell damage, because in each case, the cells would recover stiffness following the quick stretch despite ongoing presence of the mediator. Since in all cases the stretch led to similar fluidization despite different pretreatments indicates that the mechanism for the decrease was very likely not dependent on a triggered signaling cascade, but was highly likely to be simple and general, and simply caused by mechanical disruption of the lattice. Indeed the behavior was consistent with fluidization of soft glasses, much like the colloid examples of ketchup and granular materials mentioned above [78].

6.1.1 Evidence of Jostling, Motions at the Nanoscale

If the theory of soft glasses applies to the ASM cell, and if the underlying structural elements correspond to elements of the cytoskeleton and proteins

jostling within the cell, then there should be evidence for this jostling at the nanoscale. Trepat [78] examined the nanomotions of the cytoskeleton prior to the stretch by tracking the spontaneous nanoscale motions of cytoskeleton bound beads. This was done, by quantifying the mean squared displacement of the beads over different and increasing interval times at different times following the quick stretch. They found that the rate of remodeling inferred by the bead motion jumped by more than an order of magnitude following the quick stretch, and slowly recovered, more slowly than any exponential process. This provides further evidence that even during non-steady state conditions, the material properties of the ASM cell are well predicted by that of a soft glass.

6.2 Fluidization Versus Reinforcement

The large decrease in cytoskeletal stiffness in response to a transient stret is in sharp contrast to the better known increase in cytoskeletal stiffening or reinforcement in response to small localized deformations of the cytoskeleton. In response to small deformation of a focal adhesion of an adherent cell it is established that the cytoskeleton responds to strengthen the adhesion, such that the stress through the focal adhesion is a constant [3, 13, 30]. This response to localized stretch depends on complex stretch triggered signaling cascades, and constitutes a build-up of adhesion proteins at the site of the localized deformation and polymerization of actin filaments, among other signaling events. Indeed that the growth depends on cell signaling is demonstrated in the ASM cell as stress induced focal adhesion growth and localized actin polymerization response can be inhibited by depression of cellular contractile state [15, 16].

Thus we have on the one hand reinforcement which acts to build up and resist deformation and fluidization where the material acquiesces and permits large deformation. Krishnan et al. [40] asked, what determines which response will occur? From their experiments, it is now clear that reinforcement occurs when the deformation is localized and inhomogeneous. Fluidization occurs when the cell stretch is cell wide [40, 78]. To show this, Krishnan et al. [40] grew ASM cells on deformable substrates and tracked their contractile moments through specially designed deformation procedures. The contractile moment is a scalar value that quantifies contractile traction force exerted by the cell on the substrate.

They demonstrated that a rapid fluidization response always occurred with deformations that were either homogeneous and isotropic (biaxial), homogeneous and anisotropic (uniaxial), or inhomogeneous. In each case, in response to similar magnitudes of applied stretch, the cells promptly and similarly fluidized. However, following the stretch, the force slowly recovered. In the case of either cell-wide homogenous isotropic or anisotropic stretch, the recovery was to the pre-stretch value, but in the case of non-homogeneous stretch where stretch was localized, the recovery significantly exceeded the pre-stretch values, indicating that following fluidization in this case, the recovery was accompanied by reinforcement (Fig. 7).

These findings are important as it establishes that in the case of adherent cells in response to cell-wide strains, that the predominant response to stretch is fluidization with slow recovery to baseline values. The reinforcement response to localized strains can be thought of as a protective mechanism for the cell which responds to additional load by firming up, building and polymerizing filaments to bear the added force, thereby reducing cytoskeletal stress. However in response to cell-wide strains, the cell has a different basic response that permits the cell to deform without damage, by immediately weakening structurally and recovering only that contractile tension that was lost during the applied stretch. Krishnan et al. [40] proposes that the fluidization response acts as a balancing or compensatory mechanism to reinforcement, and is essential for permitting cell function in the face of cell-wide deformations. This is particularly important for cells within organs that are repeatedly deformed such as cells of the lung including ASM and cells of the bladder, gut and heart. Only when deformation is anisotropic does the effect of the stretch lead to a persistent change in the mechanics of the cell, where the cell strengthens and becomes stiffer. This may have implications to ASM pathology as increased persistent stiffness would potentially impair the ability of a stretch to overcome and fluidize the 'frozen' state of the ASM, leading to stiffer, narrowed airways.

6.3 Fluidization via Soft Glassy Rheology Versus Perturbed Equilibrium of Myosin Binding

Perturbed equilibrium of myosin binding described above is a quantitative model with excellent predictive ability for the decrease in force and stiffness following length oscillation. This behavior is also well described by the more general behavior of fluidization, a property of soft glassy rheology. As described above, perturbed equilibrium of myosin binding is a quantitative model based on independently measured actin–myosin dynamics established by Huxley [38] and modified by Hai and Murphy [35]. By comparison, the soft glassy model is more abstract, and is semi-empirical albeit based on realistic but nevertheless postulated features of colloids. Which is the correct model for ASM? For that we are currently guided by two notable differences. Perturbed equilibrium of myosin binding can predict both the rapid softening in response to stretches, and importantly, the equilibrium values for ASM lengthening in response to force fluctuations (Fig. 4). However it is not apparent that soft glassy rheology can predict lengthening, at least quantitatively. Although soft glassy rheology predicts fluidization and thus greater deformability with applied shear, the model does not have a preferred orientation thus the material does not have a preferred direction to lengthen, also the model does not yet have quantitative prediction regarding the magnitude of lengthening demonstrated by Fig. 4. These are limitations of the more abstract model and possibly its current state of development. On the other hand, perturbed equilibrium of myosin binding is limited in that at its heart are the dynamic rate

constants that govern actin–myosin phosphorylation and dephosphorylation reactions. As described earlier, these rate constants would be expected to show themselves as resonances or changes in slope in the ASM cell rheological properties versus frequency, but over a wide range the rheology follows a power-law and is scale free (Fig. 6). However, kinks are observed in freshly isolated (non-adherent) smooth muscle cells but these are attributed to transition from soft glassy rheology at slow times to fluctuations in semiflexible polymers thought to govern purified actin networks [17]. To date intact smooth muscle strips have not been probed over a wide frequency range. ASM rheology profoundly exhibits scale-free rheology that is consistent with soft glassy rheology but appears to be at odds with perturbed equilibrium of myosin binding in this aspect.

Thus force generation may be more mechanistically tied to actin and myosin dynamics through the Hai and Murphy model of smooth muscle contraction, and more abstractly through soft glassy rheology. Also to date only perturbed equilibrium of myosin binding predicts ASM tissue strip lengthening. However, for understanding the fluidization response to acute large stretches, ASM as a soft glass is a compelling hypothesis. Indeed soft glassy rheology contains several mechanistic predictions. It predicts qualitatively and quantitatively to an order of magnitude, fluidization and recovery, scale-free rheology, and the tightly coupled relationship between stiffness G' and tangent angle present in ASM. Further Bursac et al. [12] finds good evidence for aging and rejuvenation, two additional soft glassy phenomena not covered in this review.

While soft glassy rheology provides a good basis for understanding cytoskeletal rheology, there are still discrepancies and open questions. Currently the nature of the mechanistic basis for the energy barriers described in the model is not well understood. Reasonable assumptions described in the supplement 8 of Trepat et al. [78] find the barriers cannot correspond to the work required to move single molecules of the order 100 kDa (30 nm^3) expected to be the colloidal like fundamental particles in a material with modulus on the order established for ASM cells of 100 s of Pa. Possible resolutions are that the barriers are several orders of magnitude larger for some unknown reason, or is the effective relevant mechanical stiffness at the scale of the hopping structural elements several orders larger? In any case, the evidence to date supports the remarkable and perhaps surprising finding that soft glassy rheology is an attractive framework to describe a large part of ASM mechanics and indeed the mechanics of all adherent cells. Trepat et al. [78] proposes that where soft glassy rheology fails, this is where it serves us best as a useful tool, pointing the way to where new theories are yet to be developed.

6.3.1 Physiological Implications for ASM as a Soft Glass

If fluidization and freezing are predominant mechanisms governing ASM contractile function in the lung, then this has profound implications to airway hyperresponsiveness and asthma [41]. For example it means that the normal function of ASM may be sufficient to lead to impaired dilation through inhibited

fluidization. This would occur in the case of increases in ASM contractile function, interpreted as shifts in x from fluid to solid, for any reason., Or would occur without any change in ASM function at the cellular level, if accompanied by an increase in number of ASM cells. An increase in ASM cell number with no change in cell function would increase the stiffness of the ASM layer relative to the surrounding parenchyma and much of the stretch that occurs during inflation would be taken up by the parenchyma rather than the airway, and the ASM would receive a small stretch insufficient to fluidize and dilate the airway. Indeed this was suggested and simulated by Oliver et al. [58]. and is well supported by the evidence indicating increases in ASM mass in asthma [2, 19].

7 Stretch, Tone and ASM Phenotype

If stretching of ASM cells persists longer than minutes or hours and extends to several days, this provides the opportunity for longer mechanotransduced signaling processes leading to alteration of gene expression such as those leading to shifts in cell phenotype. Smith et al. [67, 68] demonstrated that in response to continuous stretching in culture over a period from 7 to 11 days, canine ASM cells increase their contractile function by increasing the contractile force, increasing the capacity to shorten, and increasing the velocity of shortening. These changes were accompanied by changes in contractile proteins myosin heavy chain and myosin light chain kinase and the intermediate filament desmin [66]. In response to stretch the cells reoriented transverse to the directions of the applied stretch and the cytoskeleton demonstrated increased organization and also increased stiffness and contractility [64]. These cells clearly were becoming more contractile, yet during this period of reorganization and increased contractile proteins, the cells also exhibited a small increase in proliferation [65]. This is at odds with the established transition for smooth muscle between either (1) a proliferative-synthetic phenotype capable of enhanced matrix molecule production and (2) a contractile phenotype which is non- or low-proliferative, and has low synthetic abilities and strong contractile function [36, 37]. However the increase in proliferation rate is modest and no information is available about secretory behavior. Thus the predominant effect of chronic and anisotropic stretch on ASM is an increase in contractile phenotype with increased contractile function.

It is interesting to note that these results were all from ASM cells exposed to chronic periods of nearly uniform but uniaxial stretch with a slight gradient stretch [50]. In a study examining uniform stretching of ASM cells, Wang et al. [79] found results that are not consistent with increased proliferation, although the same markers and function were not measured. They found that in response to biaxial strain, ASM cells do not align, there is no change in proliferation, SM22 and smMHC promoter decrease by 50%, and filamentous to globular actin ratio decreases. They reported that these were consistent with decreased Rho activation in contrast to increased Rho activation in uniaxially strained cells [69]. This

difference between uniform biaxial application of strain is similar to the reinforcement found in Krishnan et al. [40] with cells exposed to acute, but anisotropic stretch. Together, these data clearly indicate that strain profile is an important factor in determining either short-term acute responses to stretch as well as longer term phenotypic changes in contractility.

We have recently demonstrated that contractile tone is a very important factor affecting the response to stretch. We noted above that lowering contractile tone inhibits reinforcement in response to localized stretch [15]. However when tone is decreased by twice daily treatments of human cultured ASM by low-dose forskolin, contractility measured by the increase in stiffness in response to KCl is decreased as is MLCK content. Similarly, the elevation of contractile tone by twice daily low-dose histamine treatment increases contractility and increases MLCK content [23]. In preliminary data we have recently found that chronic uniaxial stretch with either chronic tone depression by forskolin or tone elevation by histamine revealed a tone dependent change in MLCK and myosin light chain phosphatase [14]. That is, with increased tone and stretch, there was greater MLCK leading to enhanced phosphorylation of myosin light chain and less myosin light chain phosphatase which would have led to reduced dephosphorylation of myosin light chain. These were associated with higher recovery rates from large stretch [14]. That is, we demonstrated that while fluidization response to stretch was not altered, the recovery from stretch was enhanced when cells were cultured with a combination of mechanical strain and elevated contractile tone.

These findings may be important in asthma, where both stretch from breathing and enhanced tone and periodic contraction of the ASM are present. Indeed while some studies have found no change in mRNA or protein of contractile markers in ASM form subjects with asthma, some studies have found an increase [6, 46, 63]. Thus it is conceivable that airway hyperresponsiveness may be associated with an enhanced recovery from stretch that is induced by phenotypic changes in ASM.

8 Summary

Our understanding of the mechanical properties of the ASM cell has been largely revised in the past dozen years. The smooth muscle cell can readily adapt to a new length and produce the same force over a broad range of lengths, termed length adaptation. This has positive consequences for function in organs that must span a wide range of distensions such as the bladder and gut, but in the lung the ramifications could be harmful if the adaptation were to occur to a short length which could lead to enhanced airway resistance during exacerbations and narrowed airways that would resist distension.

When ASM is exposed to acute stretches and the response tracked from milliseconds to hours, the stretch acts to soften activated smooth muscle reducing both force and stiffness more effectively than any bronchodilator. This state is now recognized as a disrupted fluidized high-energy metastable state which slowly

recovers to the initial lower energy less fluid metastable state. Both actin–myosin dynamics incorporated in the model for perturbed equilibrium of myosin binding, and soft glassy rheology can describe this behavior. But soft glassy rheology also accounts for observed scale free linear rheology whereas perturbed equilibrium of myosin binding does not. Several features of the mechanical properties of the ASM cell are consistent with soft glasses. These include a low modulus, scale-free rheology and enforced coupling between elastic and dissipative stresses. Further, the structure of the cytoskeleton and its components can be considered to be composed of many jostling, weakly interacting constituents, also required by soft glasses. However, the Sollich model for soft glassy rheology applied to the cytoskeleton is not without its limitations. The source for jostling within the cell is not known, the size and nature of the elements corresponding to colloid-like particles in the model are unclear, and the barriers corresponding to energy wells are not known. It is an abstract model and is not yet developed to quantitatively predict force development or lengthening in response to fluidization. It nevertheless is a powerful tool to guide further investigations of ASM cell mechanical behavior.

The rapid fluidizing effect of cell-wide applied large stretches may be providing a protective mechanism against airway narrowing even in the face of induced constriction. A failure of large stretches to fluidize ASM may explain the failure of deep inspirations to dilate airways in asthma, providing a second mechanism to length adaptation for this characteristic pathology in asthma. The ASM in asthma could be ‘frozen’ in a state that is too stiff relative to the parenchyma of the lung, leading to a failure to dilate airways and no relief for the asthmatic. This can arise solely from increases in ASM mass with no change in the contractile function of ASM at the cell level, but any enhancement in ASM contractile function would amplify this mechanism for impaired airway dilation, including changes in contractile phenotype to a stiffer, stronger, more rapidly recovering ASM cell.

In summary, we now understand the cell to be highly adaptable over time sales of minutes to days, with an ability to adapt to length changes, a stiffness and force generating capacity that depends on the fluidizing effect of the stretching it receives, and an ability to alter its phenotype in response to chronic elevations of tone during stretching. In each case, each of these mechanisms suggests an antidote; a means to improve airway function.

To reduce adaptation to shorter lengths, airways could potentially be adapted to longer lengths as is currently being investigated by Drs. R. Tepper and S. Gunst of Indiana University [83]. To enhance fluidization of the ASM during stretch this implies seeking mechanisms to increase x, or to delay its recovery. Both of these responses already occur with the administration of ASM relaxant agents or inhibitors of ASM contraction, such as common bonrchodilators are coincidentally being explored development of novel approaches to relax ASM, but other mediators could be sought evaluated based on their potency in promoting fluidization or delaying recovery assessed at the ASM level. Finally mechanisms to reduce the effect of chronic tone on stretch induced promotion of contractile phenotype could

be sought. Indeed, the chronic use of long acting beta-agonists may not only act to dilate airways, but may perhaps be functioning to reverse or prevent changes in ASM phenotype and ASM remodeling in asthma.

Acknowledgments Work conducted by the author included in this report was supported by the Canadian Institutes of Health Research, the Nova Scotia Health Research Foundation and the Lung Association of Nova Scotia.

References

1. Almasri, A.M., Ratz, P.H., Speich, J.E.: Length adaptation of the passive-to-active tension ratio in rabbit detrusor. Ann. Biomed. Eng. **38**, 2594–2605 (2010)
2. An, S.S., Bai, T.R., Bates, J.H., Black, J.L., Brown, R.H., Brusasco, V., Chitano, P., Deng, L., Dowell, M., Eidelman, D.H., Fabry, B., Fairbank, N.J., Ford, L.E., Fredberg, J.J., Gerthoffer, W.T., Gilbert, S.H., Gosens, R., Gunst, S.J., Halayko, A.J., Ingram, R.H., Irvin, C.G., James, A.L., Janssen, L.J., King, G.G., Knight, D.A., Lauzon, A.M., Lakser, O.J., Ludwig, M.S., Lutchen, K.R., Maksym, G.N., Martin, J.G., Mauad, T., McParland, B.E., Mijailovich, S.M., Mitchell, H.W., Mitchell, R.W., Mitzner, W., Murphy, T.M., Pare, P.D., Pellegrino, R., Sanderson, M.J., Schellenberg, R.R., Seow, C.Y., Silveira, P.S., Smith, P.G., Solway, J., Stephens, N.L., Sterk, P.J., Stewart, A.G., Tang, D.D., Tepper, R.S., Tran, T., Wang, L.: Airway smooth muscle dynamics: a common pathway of airway obstruction in asthma. Eur. Respir. J. **29**, 834–860 (2007)
3. Balaban, N.Q., Schwarz, U.S., Riveline, D., Goichberg, P., Tzur, G., Sabanay, I., Mahalu, D., Safran, S., Bershadsky, A., Addadi, L., Geiger, B.: Force and focal adhesion assembly: a close relationship studied using elastic micropatterned substrates. Nat. Cell.Biol. **3**, 466–472 (2001)
4. Balland, M., Desprat, N., Icard, D., Fereol, S., Asnacios, A., Browaeys, J., Henon, S., Gallet, F.: Power laws in microrheology experiments on living cells: Comparative analysis and modeling. Phys. Rev. E Stat. Nonlin Soft Matter Phys. **74**, 021911 (2006)
5. Bausch, A.R., Moller, W., Sackmann, E.: Measurement of local viscoelasticity and forces in living cells by magnetic tweezers. Biophys. J. **76**, 573–579 (1999)
6. Benayoun, L., Druilhe, A., Dombret, M.C., Aubier, M., Pretolani, M.: Airway structural alterations selectively associated with severe asthma. Am. J. Respir. Crit. Care Med. **167**, 1360–1368 (2003)
7. Bosse, Y., Chin, L.Y., Pare, P.D., Seow, C.Y.: Adaptation of airway smooth muscle to basal tone: relevance to airway hyperresponsiveness. Am. J. Respir. Cell. Mol. Biol. **40**, 13–18 (2009)
8. Bosse, Y., Chin, L.Y., Pare, P.D., Seow, C.Y.: Chronic activation in shortened airway smooth muscle: a synergistic combination underlying airway hyperresponsiveness? Am. J. Respir. Cell. Mol. Biol. **42**, 341–348 (2010)
9. Bosse, Y., Sobieszek, A., Pare, P.D., Seow, C.Y.: Length adaptation of airway smooth muscle. Proc. Am. Thorac. Soc. **5**, 62–67 (2008)
10. Bouchaud, J. P.: Weak ergodicity breaking and aging in disordered systems. J. Phys. I France **2**, 1705–1713 (1992)
11. Brown, R.H., Mitzner, W.: The myth of maximal airway responsiveness in vivo. J. Appl. Physiol. **85**, 2012–2017 (1998)
12. Bursac, P., Lenormand, G., Fabry, B., Oliver, M., Weitz, D.A., Viasnoff, V., Butler, J.P., Fredberg, J.J.: Cytoskeletal remodelling and slow dynamics in the living cell. Nat. Mater. **4**, 557–561 (2005)

13. Choquet, D., Felsenfeld, D.P., Sheetz, M.P.: Extracellular matrix rigidity causes strengthening of integrin-cytoskeleton linkages. Cell **88**, 39–48 (1997)
14. Connolly, S.C., Fairbank, N.J., Mackinnon, J.D., Maksym, G.N.: Increased contractile function in airway smooth muscle without a phenotypic shift: role of stretch, tone, MLCK and ROCK. Am. J. Respir. Crit. Care Med. **179**, A6136 (2009)
15. Deng, L., Fairbank, N.J., Cole, D.J., Fredberg, J.J., Maksym, G.N.: Airway smooth muscle tone modulates mechanically induced cytoskeletal stiffening and remodeling. J. Appl. Physiol. **99**, 634–641 (2005)
16. Deng, L., Fairbank, N.J., Fabry, B., Smith, P.G., Maksym, G.N.: Localized mechanical stress induces time-dependent actin cytoskeletal remodeling and stiffening in cultured airway smooth muscle cells. Am. J. Physiol. Cell. Physiol. **287**, C440–C448 (2004)
17. Deng, L., Trepat, X., Butler, J.P., Millet, E., Morgan, K.G., Weitz, D.A., Fredberg, J.J.: Fast and slow dynamics of the cytoskeleton. Nat. Mater. **5**, 636–640 (2006)
18. Douglas, N.J., Sudlow, M.F., Flenley, D.C.: Effect of an inhaled atropinelike agent on normal airway function. J. Appl. Physiol. **46**, 256–262 (1979)
19. Ebina, M., Takahashi, T., Chiba, T., Motomiya, M.: Cellular hypertrophy and hyperplasia of airway smooth muscles underlying bronchial asthma. A 3-D morphometric study. Am. Rev. Respir. Dis. **148**, 720–726 (1993)
20. Fabry, B., Fredberg, J.J.: Remodeling of the airway smooth muscle cell: are we built of glass? Respir. Physiol. Neurobiol. **137**, 109–124 (2003)
21. Fabry, B., Maksym, G.N., Butler, J.P., Glogauer, M., Navajas, D., Fredberg, J.J.: Scaling the microrheology of living cells. Phys. Rev. Lett. **87**, 148102 (2001)
22. Fabry, B., Maksym, G.N., Butler, J.P., Glogauer, M., Navajas, D., Taback, N.A., Millet, E.J., Fredberg, J.J.: Time scale and other invariants of integrative mechanical behavior in living cells. Phys. Rev. E Stat. Nonlin. Soft. Matter Phys. **68**, 041914 (2003)
23. Fairbank, N.J., Connolly, S.C., Mackinnon, J.D., Wehry, K., Deng, L., Maksym, G.N.: Airway smooth muscle cell tone amplifies contractile function in the presence of chronic cyclic strain. Am. J. Physiol. Lung Cell.Mol. Physiol. **295** L479–L488 (2008)
24. Fredberg, J.J.: Counterpoint: airway smooth muscle is not useful. J. Appl. Physiol. **102**, 1709–1710 (2007)
25. Fredberg, J.J., Inouye, D., Miller, B., Nathan, M., Jafari, S., Raboudi, S.H., Butler, J.P., Shore, S.A.: Airway smooth muscle, tidal stretches, and dynamically determined contractile states. Am. J. Respir. Crit. Care Med. **156**, 1752–1759 (1997)
26. Fredberg, J.J., Inouye, D.S., Mijailovich, S.M., Butler, J.P.: Perturbed equilibrium of myosin binding in airway smooth muscle and its implications in bronchospasm. Am. J. Respir. Crit. Care Med. **159**, 959–967 (1999)
27. Fredberg, J.J., Jones, K.A., Nathan, M., Raboudi, S., Prakash, Y.S., Shore, S.A., Butler, J.P., Sieck, G.C.: Friction in airway smooth muscle: mechanism, latch, and implications in asthma. J. Appl. Physiol. **81**, 2703–2712 (1996)
28. Fredberg, J.J., Stamenovic, D.: On the imperfect elasticity of lung tissue. J. Appl. Physiol. **67**, 2408–2419 (1989)
29. Fung, Y.C.: Biomechanics, mechanical properties of living tissues. Springer-Verlag, New York (1984)
30. Galbraith, C.G., Yamada, K.M., Sheetz, M.P.: The relationship between force and focal complex development. J. Cell. Biol. **159**, 695–705 (2002)
31. Gregersen, H., Emery, J.L., McCulloch, A.D.: History-dependent mechanical behavior of guinea-pig small intestine. Ann. Biomed. Eng. **26**, 850–858 (1998)
32. Gunst, S.J.: Effect of length history on contractile behavior of canine tracheal smooth muscle. Am. J. Physiol. **250**, C146–C154 (1986)
33. Gunst, S.J.: Contractile force of canine airway smooth muscle during cyclical length changes. J. Appl. Physiol. **55**, 759–769 (1983)
34. Gunst, S.J., Zhang, W.: Actin cytoskeletal dynamics in smooth muscle: a new paradigm for the regulation of smooth muscle contraction. Am. J. Physiol. Cell. Physiol. **295**, C576–C587 (2008)

35. Hai, C.M., Murphy, R.A.: Cross-bridge phosphorylation and regulation of latch state in smooth muscle. Am. J. Physiol. **254**, C99–C106 (1988)
36. Halayko, A.J., Camoretti-Mercado, B., Forsythe, S.M., Vieira, J.E., Mitchell, R.W., Wylam, M.E., Hershenson, M.B., Solway, J.: Divergent differentiation paths in airway smooth muscle culture: induction of functionally contractile myocytes. Am. J. Physiol. Lung Cell. Mol. Physiol. **20**, L197–L206 (1999)
37. Halayko, A.J., Salari, H., Ma, X.F., Stephens, N.L.: Markers of Airway Smooth Muscle Cell Phenotype. Am. J. Physiol. Lung Cell. Mol. Physiol. **14**, L1040–L1051 (1996)
38. Huxley, A. F.: Muscle structure and theories of contraction. Prog. Biophys. Biophys. Chem. **7**, 255–318 (1957)
39. King, G.G., Moore, B.J., Seow, C.Y., Pare, P.D.: Airway narrowing associated with inhibition of deep inspiration during methacholine inhalation in asthmatics. Am. J. Respir. Crit. Care Med. **164**, 216–218 (2001)
40. Krishnan, R., Park, C.Y., Lin, Y.C., Mead, J., Jaspers, R.T., Trepat, X., Lenormand, G., Tambe, D., Smolensky, A.V., Knoll, A.H., Butler, J.P., Fredberg, J.J.: Reinforcement versus fluidization in cytoskeletal mechanoresponsiveness. PLoS One **4**, e5486 (2009)
41. Krishnan, R., Trepat, X., Nguyen, T.T., Lenormand, G., Oliver, M., Fredberg, J.J.: Airway smooth muscle and bronchospasm: fluctuating, fluidizing, freezing. Respir. Physiol. Neurobiol. **163**, 17–24 (2008)
42. Kuo, K.H., Herrera, A.M., Wang, L., Pare, P.D., Ford, L.E., Stephens, N.L., Seow, C.Y.: Structure-function correlation in airway smooth muscle adapted to different lengths. Am. J. Physiol. Cell. Physiol. **285**, C384–C390 (2003)
43. Kuo, K.H., Wang, L., Pare, P.D., Ford, L.E., Seow, C.Y.: Myosin thick filament lability induced by mechanical strain in airway smooth muscle. J. Appl. Physiol. **90**, 1811–1816 (2001)
44. Latourelle, J., Fabry, B., Fredberg, J.J.: Dynamic equilibration of airway smooth muscle contraction during physiological loading. J. Appl. Physiol. **92**, 771–779 (2002)
45. Lau, A.W., Hoffman, B.D., Davies, A., Crocker, J.C., Lubensky, T.C.: Microrheology, stress fluctuations, and active behavior of living cells. Phys. Rev. Lett. **91**, 198101 (2003)
46. Leguillette, R., Laviolette, M., Bergeron, C., Zitouni, N., Kogut, P., Solway, J., Kachmar, L., Hamid, Q., Lauzon, A.M.: Myosin, transgelin, and myosin light chain kinase: expression and function in asthma. Am. J. Respir. Crit. Care Med. **179**, 194–204 (2009)
47. Leporatti, S., Sczech, R., Riegler, H., Köhler, G.K.B., Hauschildt, S., Donath, E.: Elasticity and adhesion of resting and lipopolysaccharide-stimulated macrophages. FEBS Lett. **580**, 450–454 (2006)
48. Lim, T.K., Ang, S.M., Rossing, T.H., Ingenito, E.P., Ingram Jr., R. H.: The effects of deep inhalation on maximal expiratory flow during intensive treatment of spontaneous asthmatic episodes. Am. Rev. Respir. Dis. **140**, 340–343 (1989)
49. Lim, T.K., Pride, N.B., Ingram Jr., R. H.: Effects of volume history during spontaneous and acutely induced air-flow obstruction in asthma. Am. Rev. Respir. Dis. **135**, 591–596 (1987)
50. Maksym, G. N., Deng, L., Fairbank, N. J., Connolly, S. C., (2005). Beneficial and harmful effects of oscillatory mechanical strain on airway smooth muslce. Can. J. Physiol. Pharmacol.
51. Mandadapu, K.K., Govindjee, S., Mofrad, M.R.: On the cytoskeleton and soft glassy rheology. J. Biomech. **41**, 1467–1478 (2008)
52. McParland, B.E., Tait, R.R., Pare, P.D., Seow, C.Y.: The role of airway smooth muscle during an attack of asthma simulated in vitro. Am. J. Respir. Cell. Mol. Biol. **33**, 500–504 (2005)
53. Mead, J.: A further comment on point:counterpoint "airway smooth muscle is/is not useful". J. Appl. Physiol. **103**, 412 (2007)
54. Mehta, D., Gunst, S.J.: Actin polymerization stimulated by contractile activation regulates force development in canine tracheal smooth muscle. J. Physiol. Lond. **519**, 829–840 (1999)
55. Mijailovich, S.M., Butler, J.P., Fredberg, J.J.: Perturbed equilibria of myosin binding in airway smooth muscle: bond-length distributions, mechanics, and ATP metabolism. Biophys. J. **79**, 2667–2681 (2000)

56. Mitzner, W.: Airway smooth muscle: the appendix of the lung. Am. J. Respir. Crit. Care Med. **169**, 787–790 (2004)
57. Mitzner, W.: A further comment on Point:Counterpoint "Airway smooth muscle is/is not useful". J. Appl. Physiol. **104**, 902 (2008)
58. Oliver, M.N., Fabry, B., Marinkovic, A., Mijailovich, S.M., Butler, J.P., Fredberg, J.J.: Airway hyperresponsiveness, remodeling, and smooth muscle mass: right answer, wrong reason? Am. J. Respir. Cell. Mol. Biol. **37**, 264–272 (2007)
59. Pratusevich, V.R., Seow, C.Y., Ford, L.E.: Plasticity in canine airway smooth muscle. J. Gen. Physiol. **105**, 73–94 (1995)
60. Qi, D., Mitchell, R.W., Burdyga, T., Ford, L.E., Kuo, K.H., Seow, C.Y.: Myosin light chain phosphorylation facilitates in vivo myosin filament reassembly after mechanical perturbation. Am. J. Physiol. Cell. Physiol. **282**, C1298–C1305 (2002)
61. Scichilone, N., Pyrgos, G., Kapsali, T., Anderlind, C., Brown, R., Permutt, S., Togias, A.: Airways hyperresponsiveness and the effects of lung inflation. Int. Arch. Allergy Immunol. **124**, 262–266 (2001)
62. Seow, C.Y.: Comments on point: counterpoint: "airway smooth muscle is/is not useful". J. Appl. Physiol. **102**, 1712 (2007)
63. Seow, C.Y., Schellenberg, R.R., Pare, P.D.: Structural and functional changes in the airway smooth muscle of asthmatic subjects. Am. J. Respir. Crit. Care Med. **158**, S179–S186 (1998)
64. Smith, P.G., Deng, L., Fredberg, J.J., Maksym, G.N.: Mechanical strain increases cell stiffness through cytoskeletal filament reorganization. Am. J. Physiol. Lung Cell. Mol. Physiol. **285**, L456–L463 (2003)
65. Smith, P.G., Janiga, K.E., Bruce, M.C.: Strain increases airway smooth muscle cell proliferation. Am. J. Respir. Cell. Mol. Biol. **10**, 85–90 (1994)
66. Smith, P. G., Moreno, R., Ikebe, M., (1997). Strain increases airway smooth muscle contractile and cytoskeletal proteins in vitro. Am. J. Physiol. **272**.
67. Smith, P.G., Roy, C., Dreger, J., Brozovich, F.: Mechanical strain increases velocity and extent of shortening in cultured airway smooth muscle cells. Am. J. Physiol. Lung Cell. Mol. Physiol. **21**, L343–L348 (1999)
68. Smith, P.G., Roy, C., Fisher, S., Huang, Q.Q., Brozovich, F.: Selected contribution: mechanical strain increases force production and calcium sensitivity in cultured airway smooth muscle cells. J. Appl. Physiol. **89**, 2092–2098 (2000)
69. Smith, P.G., Roy, C., Zhang, Y.N., Chauduri, S.: Mechanical stress increases RhoA activation in airway smooth muscle cells. Am. J. Respir. Cell. Mol. Biol. **28**, 436–442 (2003)
70. Sollich, P.: Rheological constitutive equation for a model of soft glassy materials. Phys. Rev. E Stat. Nonlin. Soft. Matter Phys. **58**, 738–759 (1998)
71. Sollich, P., Lequeux, F., Hébraud, P., Cates, M.E.: Rheology of Soft glassy materials. Phys. Rev. Lett. **78**, 2020–2023 (1997)
72. Speich, J.E., Almasri, A.M., Bhatia, H., Klausner, A.P., Ratz, P.H.: Adaptation of the length-active tension relationship in rabbit detrusor. Am. J. Physiol. Renal Physiol. **297**, F1119–F1128 (2009)
73. Stamenovic, D.: Effects of cytoskeletal prestress on cell rheological behavior. Acta Biomater. **1**, 255–262 (2005)
74. Stamenovic, D., Suki, B., Fabry, B., Wang, N., Fredberg, J.J.: Rheology of airway smooth muscle cells is associated with cytoskeletal contractile stress. J. Appl. Physiol. **96**, 1600–1605 (2004)
75. Sunyer, R., Trepat, X., Fredberg, J.J., Farre, R., Navajas, D.: The temperature dependence of cell mechanics measured by atomic force microscopy. Phys. Biol. **6**, 025009 (2009)
76. Syyong, H., Cheung, C., Solomon, D., Seow, C.Y., Kuo, K.H.: Adaptive response of pulmonary arterial smooth muscle to length change. J. Appl. Physiol. **104**, 1014–1020 (2008)
77. Trache, A., Trzeciakowski, J.P., Gardiner, L., Sun, Z., Muthuchamy, M., Guo, M., Yuan, S.Y., Meininger, G.A.: Histamine effects on endothelial cell fibronectin interaction studied by atomic force microscopy. Biophys. J. **89**, 2888–2898 (2005)

78. Trepat, X., Deng, L., An, S.S., Navajas, D., Tschumperlin, D.J., Gerthoffer, W.T., Butler, J.P., Fredberg, J.J.: Universal physical responses to stretch in the living cell. Nature **447**, 592–595 (2007)
79. Wang, L., Liu, H.W., McNeill, K.D., Stelmack, G., Scott, J.E., Halayko, A.J.: Mechanical strain inhibits airway smooth muscle gene transcription via protein kinase C signaling. Am. J. Respir. Cell. Mol. Biol. **31**, 54–61 (2004)
80. Wang, L., Pare, P.D., Seow, C.Y.: Selected contribution: effect of chronic passive length change on airway smooth muscle length-tension relationship. J. Appl. Physiol. **90**, 734–740 (2001)
81. Wang, N., Tolic-Norrelykke, I.M., Chen, J., Mijailovich, S.M., Butler, J.P., Fredberg, J.J., Stamenovic, D.: Cell prestress. I. Stiffness and prestress are closely associated in adherent contractile cells. Am. J. Physiol. Cell. Physiol. **282**, C606–C616 (2002)
82. Woolcock, A.J., Salome, C.M., Yan, K.: The shape of the dose-response curve to histamine in asthmatic and normal subjects. Am. Rev. Respir. Dis. **130**, 71–75 (1984)
83. Xue, Z., Zhang, L., Liu, Y., Gunst, S.J., Tepper, R.S.: Chronic inflation of ferret lungs with CPAP reduces airway smooth muscle contractility in vivo and in vitro. J. Appl. Physiol. **104**, 610–615 (2008)

Part III
Computational Modeling

Biomechanical Modelling of Cells in Mechanoregulation

Alexander B. Lennon, Hanifeh Khayyeri, Feng Xue and Patrick J. Prendergast

Abstract Many cells are mechanoregulated; their activities are performed at a rate partly determined by the biophysical stimulus acting on them. Computer simulations that would capture this could be used to predict the effect of physical exercise on tissue health. They could also be used to simulate how the tissues surrounding a medical device would respond to the placement of that device. Since cells are the actors within tissues, such simulations require models of how cells themselves are mechanoregulated. In this chapter, we review how mechanoregulation simulations may be built up from models in three ways: cells as simple points, cells as multiple points, cells as structures. In particular, a computer simulation method for tissue differentiation using cells as points is also given, and an approach for extending it to include cells as multiple points is presented. Cells as structures in the form of a hybrid tensegrity-continuum model is presented, and its potential for use in mechanoregulation simulations is discussed.

1 Introduction

According to the Oxford English dictionary, mechanics has two definitions; it is concerned with the explanation of the functioning of machines, or it deals with the motion and equilibrium of bodies and the action of forces. In addressing the biomechanical modelling of cells, both definitions are relevant because the human body behaves, in many respects, like a machine and yet the action of mechanical

A. B. Lennon (✉), H. Khayyeri, F. Xue and P. J. Prendergast
Trinity Centre for Bioengineering, School of Engineering, Trinity College, Parsons Building, Dublin 2, Ireland
e-mail: alex.lennon@gmail.com

Stud Mechanobiol Tissue Eng Biomater (2011) 4: 297–329
DOI: 10.1007/8415_2010_32

Published Online: 30 October 2010

forces maintains equilibrium of the tissues through the action of various cell populations. Cells regulate the tissues by responding to stimuli they receive through the extracellular matrix, including both biochemical and biophysical stimuli—it is because of this very regulation of cells that the 'machine' can grow, adapt, and remodel itself.

There are a multitude of possible approaches to biomechanical modelling of cells. Generally speaking, the approaches can be categorised as follows:

(i) Cells may be modelled as single points in space (often within a regular lattice or grid), with cell properties such as phenotype, age, etc., recorded as properties of the point. Cell activities are modelled as movements of the point (migration), creating new points (mitosis), removal of points (apoptosis), or change in the properties of a point (differentiation). Because the cell is represented as a point, the internal structure of the cell is not modelled explicitly, and therefore the complexities of the biophysical rearrangements internally in response to an external mechanical stimulus are not modellable with this method. In the limit, this approach models cells as points in the continuum, for example where cell dispersal is modelled using diffusion, e.g. [1, 2].

(ii) Cells may span several points in a lattice and thereby acquire volume and a surface membrane. The associated volume and surface energies may be computed and used to model more sophisticated aspects of migration, proliferation, and differentiation. For example, the Cellular Potts method attempts to simulate the most probable movements of a cell by selecting those movements that tend to minimise the energies associated with surface and volume changes of the cell [3, 4].

(iii) Structural cell models that explicitly account for the cell's internal components [membrane, cytosol, nucleus, etc.], including more intricate structural models such as tensegrity models [5, 6], and models using confocal microscopy images of cells [7]. Given the computational expense of these models they are only used for single cells at present. Obviously such models are far more intricate than modelling the cell as a simple point, or collection of points, and allow the analyst to answer questions relating to how internal stimuli may regulate cell activities. The simplest analyses consist of computing a quasi static response with the cell modelled as a passive structure. Accounting for the dynamic structure of the cell is a more complex task but some studies are beginning to address such processes, e.g. for actin [8] and microtubule cytoskeletal structures [9].

Questions relating to how mechanical stimulation affects tissue growth, adaptation and disease can be investigated using computer simulation with cells represented in all three of the above listed ways. We have used lattice modelling with cells represented as points to simulate mechanoregulated cellular processes; in doing so we have found it useful to think of simulations as being built from distinct algorithms [10]. Each algorithm is designed to simulate a certain cell activity, e.g. an algorithm for cell migration takes as input the cell distribution at one time point

and returns the distribution at the next time point due to cells 'jumping' from one lattice point to another either in a random manner, or along a biochemical gradient (chemotaxis) [11]. Similarly an algorithm may be written to transform the cell distribution due to cell division, or any other cellular activity. Algorithms can be corroborated separately against experiment and knitted together to create very complex simulations [12, 13]. In the future it will be possible to incorporate cell models of the third kind listed above (i.e. structural cell models) into such iterative simulations of the behaviour of cell populations—but for now it seems like a dream—in the meantime many researchers are developing such models for analysis of individual cells.

In this chapter we present research on biomechanical models of cells based on all of these approaches listed in (i) to (iii) above. We are driven in our research by the desire to know how cells respond to mechanical forces, and to use that knowledge to create computer simulations of tissue repair and regeneration under mechanical loading. This research is described in detail in the rest of the Chapter, which concludes with a discussion of where we see the frontiers in research for biomechanical modelling of cells.

2 Multi-Scale Modelling of Tissue Mechanoregulation

Cells and tissues are organised in a hierarchical way across several length scales, from molecular structures at the intra-cellular level to microscopic composite structures of cells interspersed in extracellular matrix (ECM) at the tissue level. Duration of characteristic events at each level also occur at different time scales, with intracellular processes tending to be very rapid molecular events and tissue level processes occurring relatively slowly due to the time it takes for cells to move and remodel ECM. Modelling activity at these different levels is a difficult task, made more complex by coupling between length and time scales and the need to use different scientific approaches at different scales (e.g. molecular dynamics, cell biology and biochemistry, and fluid and structural mechanics) [14]. Computational approaches also vary depending on the analytical technique—while assumptions of continuity and the application of differential equations may suit a given application, the use of structured or unstructured discretisation and the application of rule-based methods may be more suitable for others [15].

In the following sections we describe some approaches to modelling cell and tissue behaviour at different length and time scales and introduce some aspects of their implementation using a programming tool kit, the MechanoBiology Toolkit (MBTK) currently being developed within Trinity Centre for Bioengineering. MBTK is an object oriented C++ library designed to ease construction of mechanobiology simulations that require explicit modelling of cells and interaction (interpolation/extrapolation of biophysical stimuli) with mechanical simulations carried out at different length scales. It uses the Visualisation Toolkit (VTK, Kitware Inc., USA) to interact with both structured and unstructured meshes and

their associated data, for computational geometry methods (e.g. point-in-element tests), and for efficient spatial-searching data structures (e.g. octrees and kd-trees).

2.1 Lattice-Based Models for Populations of Cells

Cells are discrete entities and, with simplification of their structure and behaviour, can be treated using agent based modelling methods. A key decision is the choice of spatial discretisation, which can be either structured (e.g. voxel datasets) or unstructured (e.g. irregular finite element meshes). A lattice is a structured grid in which cells can occupy one or several points and can jump between points. It is most frequently comprised of isotropic orthogonal arrangements of points (Fig. 1) but other arrangements are also possible (e.g. hexagonal).

A major benefit of lattices is that they are computationally simple (e.g. point coordinates can be computed using the point number and the lattice spacing, thereby reducing some of the storage burden associated with a large unstructured mesh). Another benefit is that their structure provides a limited number of local neighbour locations, which simplifies the implementation of random walk processes and the computational burden of computing probabilities as a function of possible outcomes [16].

2.2 Interaction with the Tissue/Implant Scale

A key issue in addressing multiple length scales is transferring data between computational grids used for each length scale. For instance, in a typical mechanoregulation simulation, a cell lattice may be discretised with a 10 μm spacing while the typical element size within the corresponding finite element mesh used

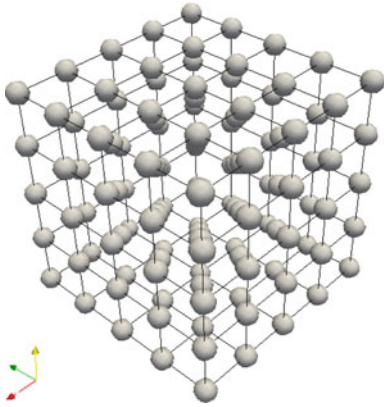

Fig. 1 Example of a $5 \times 5 \times 5$ orthogonal lattice. The *spheres* represent the points of the lattice that can be occupied by cells

to compute biophysical stimuli of strain and fluid flow may be of the order of 0.1–10 mm. In general, two-way communication is needed between these grids: (i) biophysical stimuli are mapped from the finite element mesh to the lattice to influence cell behaviour and (ii) ECM properties are mapped from the lattice to the relevant elements of the finite element mesh to update their material properties and influence subsequent mechanical behaviour.

Thus, methods of probing data from one grid type to another are an essential requirement within a modelling framework aimed at simulating the multiple length scales frequently investigated with mechanoregulation theory. Typical methods of probing include using the coordinates of points, voxels, or elements to query the corresponding region of the other grid and then either averaging, interpolating, or extrapolating the data associated with the relevant grid entities from one grid to the other. Geometric search trees, such as octrees and kd-trees, are used to speed up these spatial queries so that an entire pass through each grid is not needed to locate the required entities in the partner grid. Point container tests, e.g. point-in-triangle or point-in-hexahedron, can be used to refine the correspondence between entities in each grid. Finally, averaging, interpolation, or extrapolation schemes (e.g. linear, quadratic, Gaussian) can be used to actually transfer the data between the grids. In MBTK this functionality is achieved by including the VTK libraries within the framework. These not only provide the computational geometry and grid handling utilities required to achieve data mapping between length scales but also contain numerous classes to import/export grid data from/to many popular simulation codes, in addition to providing the ability to visualise this data as well as that produced by MBTK simulations.

3 Single Point Representation of Cells

Probably the most simple approach to representing a cell within a lattice is to assume that a cell can be represented by a single lattice point. Compared to differential equations (e.g. diffusion), the lattice approach provides a simple platform for introducing cell activity (such as migration, proliferation, and apoptosis) and more complex biological phenomena such as angiogenesis [17], anisotropy [18] and release of growth factors (directed growth). Furthermore, the approach enables non-deterministic simulations of cell processes where mechanoregulation theories can be implemented based on a set of rules.

Random number generation and activity-specific probabilities are the basic methods needed to implement the fundamental cellular activities of cell migration, proliferation, and apoptosis. Random walk can be implemented orthogonally (6-neighbour) by random selection of a coordinate direction, including a zero condition indicating no movement (Fig. 2). Diagonal movement within a $3 \times 3 \times 3$ neighbourhood (26-neighbour) can be achieved by random selection of a relative position vector to one of the 26 neighbouring points plus a zero vector indicating no movement from the cell's current location.

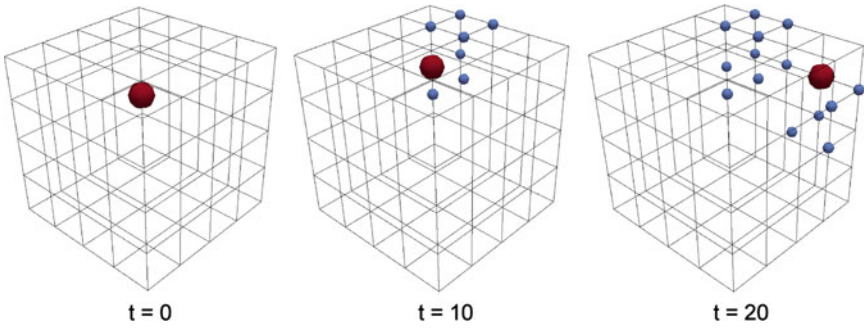

Fig. 2 Example of orthogonal random migration of an individual cell represented at three time points during 20 iterations of a random walk simulation in a 5 × 5 × 5 cubic lattice. The larger sphere (*red*) represents a cell and the smaller spheres (*blue*) represent the path history of the cell (for colour references see the electronic version of the text)

Similarly, cell division can be implemented as random selection of two locations from the neighbourhood (including the origin) from either the 6-neighbour or 26-neighbour case. Apoptosis can be achieved by simply removing the cell ID from a dynamic list of cells within the lattice, updating subsequent cell IDs to account for the removal of the lower numbered cell, and resetting the variables of the lattice point at which apoptosis occurred to the appropriate non-cell values. Deciding which process a cell undergoes in any given iteration can be achieved using a probability, p_i, for that process. Assuming that this probability is related to a discrete set of possible outcomes, N, the classical definition of probability ($p_i = n/N$) allows calculation of a threshold number, $n = p_i N$, representing the number of opportunities of generating an unsigned integer less than n from a uniform distribution with range (0, N). This approach is used frequently in the MechanoBiology Toolkit using a Mersenne Twister random number generator [19] from the Boost C++ Libraries (http://www.boost.org).

This single point representation of cells is computationally simple and efficient and can be used to quickly assemble simulations combining several cell behaviours, such as migration, proliferation, and apoptosis (Fig. 3).

3.1 Application of Single Point Representation of Cells to Modelling Mechanoregulation of Tissue Differentiation

As described in Sect. 5 later in this chapter, structural modelling of a single cell is a complex task which is not ideal for modelling cellular behaviour in larger scales such as tissue level. For modelling cellular behaviour in tissue processes, like tissue differentiation, lattice-based approaches are more suitable where the discrete entities can represent the cell, their biological activities and their mechanical behaviours. This section presents an application of the lattice-based approach to the process of mechanoregulated tissue differentiation.

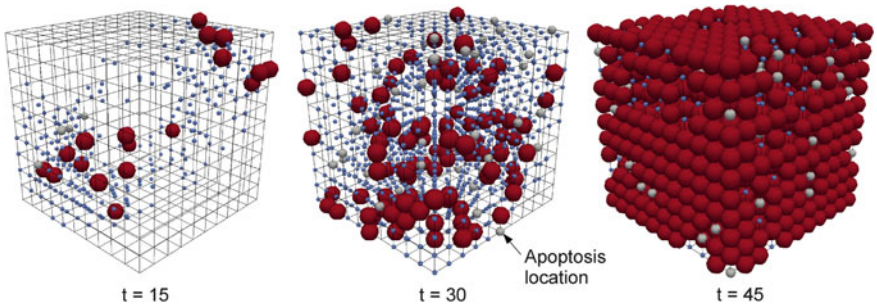

Fig. 3 Example of migration, proliferation, and apoptosis for a population of cells represented at three time points during 45 iterations of a simulation for a cubic lattice. The *larger* (*red*) spheres represent active cells, the *mid-sized* (*grey*) spheres indicate locations where a cell has recently undergone apoptosis, and the *smallest* (*blue*) spheres represent the path history of migrating cells (for colour references see the electronic version of the text)

3.1.1 Rule Based Modelling of Mechanoregulation

Mesenchymal stem cells (MSCs) are pluripotent cells that have the ability to differentiate along different cell lineages in response to an appropriate stimulus [20]. These cells can be found in the bone marrow and can differentiate into cells such as osteoblasts (bone), chondrocytes (cartilage), adipocytes (fat), myoblasts (muscle), fibroblasts (tendon) and neural cells [21]. Quiescent and uncommitted MSCs become active during repair and remodelling through regulation by external chemical and mechanical signals that control their proliferation, migration, and differentiation [22, 23]. Once the mesenchymal stem cells commit to a cell lineage they become fast-growing cells that can divide and mature in the process of becoming functional tissues [21]. Due to their pluripotency MSCs are ideal for tissue regenerative applications. Understanding the activation of MSCs and the mechanical stimulation they require to differentiate into tissues like bone and cartilage is fundamental to tissue engineering and regenerative medicine.

Towards this goal several mechanoregulatory theories, each using different mechanical stimuli, have been proposed for describing the influence of the mechanical environment on tissue differentiation. The earliest are those of Pauwels, in 1960, who proposed a combination of hydrostatic pressure and shear strain [24], Carter et al. who proposed compressive stress and tensile strain history [25], Claes and Heigele, who suggested local stress and hydrostatic pressure [26], and Prendergast et al. who proposed a combination of shear strain and fluid flow [27] to regulate mesenchymal stem cell differentiation. These theories have been compared using an identical computational model of healing in an osteotomy [28]. All models were able to predict the process of normal fracture healing; however when applying torsional loading, the biophysical stimulus proposed by Prendergast et al. [27] was able to simulate the failure of healing patterns closest to that observed in the animal experiments. This finding was further corroborated in a distraction osteogenesis study by Hayward and Morgan [29] that showed that the theory

presented in Prendergast et al. was able to also predict the differentiation patterns of inhibited healing due to bending. Geris et al. [30] applied the models of Prendergast et al. [27] and Claes and Heigele [26] to simulate an in vivo bone chamber experiment. It was concluded that although both models were able to describe the process of tissue regeneration in the chamber qualitatively, more qualitative and quantitative experimental results are necessary for corroborating the predictive capacities of the mechanoregulatory models. Although these theories have been able to predict some of the main aspects of the tissue regeneration process in cases such as fracture healing [28, 29, 31, 32], tissue engineering [33, 34], bone/implant interfaces [30, 35, 36] or distraction osteogenesis [37–40]; most of these mechanobiological models use differential equations in form of diffusion equations to describe the precursor cell migration and proliferation at the site of injury [28, 41–43], which makes the models deterministic and allows them to be criticised due to their lack of corroboration.

To improve the corroboration of models, and to implement a rule based mechanoregulation of MSC fate, the tissue domain may be represented by a grid of lattice points where each point depicts a position which a cell and its extracellular matrix can occupy. Cells in this lattice may then be given the capability to stochastically migrate, proliferate, apoptose, differentiate, form new capillaries and synthesize new extracellular matrices, depending on the mechanical environment surrounding the cells.

Following the mechanoregulation theory of Prendergast et al., mesenchymal stem cells within this domain can differentiate according to a biophysical stimulus (S) which consists of a combination of fluid flow (v) and octahedral shear strain (γ) and is described as $S = \gamma/a + v/b$, where $a = 0.0375$ and $b = 3$ μm/s are experimentally defined constants [35]. Depending on the level of biophysical stimulus, the cells differentiate into fibroblasts, chondrocytes or osteoblasts [35] according to,

$$\begin{aligned} S < 1 &\quad \text{Osteoblasts} \\ 1 < S < 3 &\quad \text{Chondrocytes} \\ S > 3 &\quad \text{Fibroblasts} \end{aligned}$$

The MSCs differentiate with a specific rate [44], which means that each day 30% of the MSCs, chosen at random, will differentiate into new cell phenotypes.

3.1.2 Angiogenesis

Another key factor that regulates tissue differentiation is the process of angiogenesis, i.e. formation of blood vessels. Newly formed blood vessels provide cells with oxygen and nutrients which are essential for cell proliferation and survival. Since the diffusion of oxygen is limited to a few hundred micrometers from the capillaries, the vascular morphology at the site may play a significant role in determining tissue differentiation patterns [45].

In the lattice model implemented by Checa and Prendergast [45] capillaries are described as a sequence of endothelial cells. Capillary tips can extend either in the previous direction (persistence), a random direction, or along a concentration gradient (e.g., VEGF that acts as an angiogenic factor and is assumed to be released by hypertrophic chondrocytes). Each vessel has a possibility to branch with a probability determined by the length of the vessel, where longer vessels have a higher probability. The growth of the vessels is restricted by anastomosis (the fusion of two sprouts) and a high mechanical stimulus ($S > 7$).

The modelled angiogenesis affects cell differentiation based on a set of rules such that low levels of mechanical stimulation ($S < 1$) favour osteoblastic differentiation but only in well vascularised areas where oxygen tension was high; whereas mesenchymal stem cells (MSCs) in regions under a mechanical stimulus favourable for osteoblast differentiation but with poor vascularity follow the chondrogenic pathway rather than the osteogenic.

3.1.3 Mechanobiological Modelling of Cells in an In Vivo Bone Chamber

Bone chamber experiments constitute a well suited environment for the corroboration of tissue differentiation theories. They provide a controlled mechanical environment which allows the application of different known loads. The predetermined geometry of the chambers constitutes a definitive advantage in using the experiments to corroborate the simulations. Several bone chambers have been developed and tested on different animals to investigate processes relating to mechanobiology and tissue engineering [30, 46, 47]. Among these, Tägil and Aspenberg's bone chamber experiments on rats [47] are ideal for corroboration of tissue differentiation simulations, since there is a defined loading and because very considerable experimental work has been reported [47–49]. This bone chamber consists of a hollow screw with two in-growth openings at the bottom of the implant from which mesenchymal progenitor cells can penetrate and fill the chamber. In the experiments, mechanical loading was applied via a piston, which the chamber is equipped with and which, when loaded, exerted a pressure on the in-growing tissues (Fig. 4). Their results indicate a strong influence of the mechanical environment on the tissue differentiation process and report a great variability among the animals (see Table 1).

More interestingly, the outcomes of the bone chamber show two different differentiation pathways (Fig. 5); one where differentiation of cartilage can be observed (in 4 out of 7 of the specimens, see Fig. 5b) and another with no cartilage but more fibrous tissue formation (found in 3 out of 7 of the specimens, see Fig. 5c); this clear dichotomy of outcome has not been reported in other in vivo bone chamber experiments.

In our computational analysis, we aim to implement the mechanoregulation theory by Prendergast et al. [27] in a computer simulation of the bone chamber experiments by Tägil and Aspenberg [47]. The results from the simulations will be

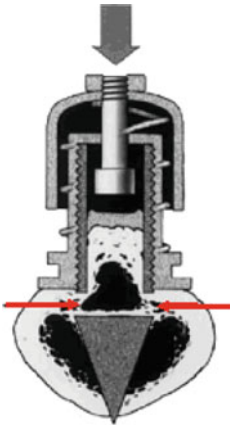

Fig. 4 Cross-section of the bone chamber, where the thin *horizontal* (*red*) *arrows* point at the ingrowth openings and the *thick vertical arrow* (*grey*) points at the piston and the direction of loading (for colour reference see the electronic version of the text)

Table 1 Experimental results: percentage of different tissue types differentiated in a cross-section of each bone chamber (7 specimens unloaded and 7 loaded)

Specimen	1	2	3	4	5	6	7	E	σ
Unloaded									
Bone marrow (%)	32.9	42.3	31.6	44.4	22.3	37.3	59.3	38.6	11.7
Bone (%)	28.1	25.7	40.5	31.2	37.3	26.3	28.0	31.0	5.7
Fibrous tissue (%)	39.0	31.9	27.9	24.4	40.4	36.4	12.6	30.4	9.8
Cartilage (%)	0	0	0	0	0	0	0	0	0
Necrotic tissue (%)	0	0	0	0	0	0	0	0	0
Loaded									
Bone marrow (%)	0	57.0	57.5	14.6	8.6	37.7	38.6	30.6	23.1
Bone (%)	0	25.9	31.4	26.8	20.8	38.7	21.3	23.5	12.7
Fibrous tissue (%)	94.0	5.0	5.6	46.0	55.1	15.3	25.5	35.2	32.7
Cartilage (%)	0	8.2	5.5	0	0	3.1	6.2	3.3	3.4
Necrotic tissue (%)	6.0	3.9	0	12.6	15.7	5.2	8.4	7.4	5.3

The mean areas (E) and the standard deviations (σ) were calculated for each tissue phenotype in the chamber

directly compared to the histological sections obtained during the animal experiments. We adopt a three-dimensional lattice approach [33] (Fig. 6) to model cell activities and a random walk theory [50] to describe cell dispersal; two biophysical stimuli (fluid flow and shear strain) are used to regulate tissue differentiation.

We are interested to know whether or not the stochastic nature of the lattice model together with changes in the environment that is likely to occur during the conduction of the animal experiments will capture the variability observed in the experiment. Different mechanical and biological parameters which could represent a source of variability during the experiments or anticipated to have a great impact on simulation outcomes are therefore studied to establish their relevance in explaining the variability observed among the animals. We hypothesise that simulations of this bone chamber experiment can corroborate mechanoregulation

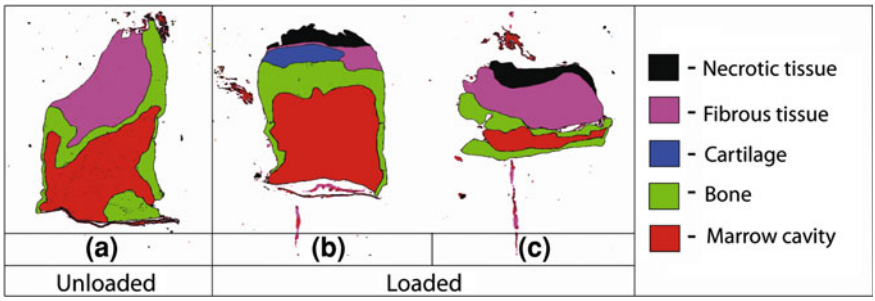

Fig. 5 Simplified results of the histology: **a** unloaded bone chamber after 9 weeks and **b** loaded bone chambers after 9 weeks, with a developed marrow cavity and cartilage on a well developed bone layer and **c** loaded bone chamber after 9 weeks with under-developed marrow cavity and no cartilage layer

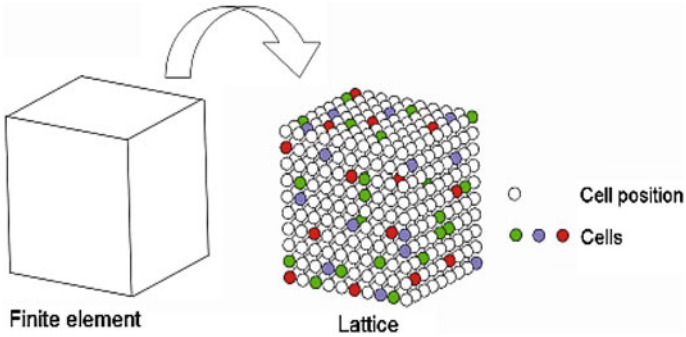

Fig. 6 A finite element consisting of 10 × 10 × 10 lattice points

theories, and if that is confirmed, the computational model of the bone chamber will be a useful virtual tool in orthopaedic research, particularly for further investigations of the effect of mechanical factors in tissue differentiation.

Methods

A finite element model of the cylindrical interior space of the bone chamber was developed and the lattice modelling approach was implemented in order to describe cell activities. In this lattice cells migrated, proliferated, differentiated, apoptosed and synthesized new extracellular matrices, based on the mechanical environment surrounding the cells. Cells differentiated depending on a biophysical stimulus (based on fluid flow and shear strain) into fibroblasts, chondrocytes or osteoblasts [35].

The interior of the bone chamber was modelled using 14,200 eight-node hexahedral finite elements with 1,000 lattice points inside each element, i.e. 14.2×10^6 lattice points in total. All elements were modelled to be of an equal

size of 0.1 mm, thus giving spacing around each lattice point of 10 μm [51]. The chamber wall and the two openings were modelled as boundary conditions allowing solid deformation and fluid flow through the nodes defining the ingrowth openings and the small area enclosed by the piston and the chamber wall (Fig. 7), which corresponded to conditions in the chamber experiments. All tissues were modelled as linear poroelastic homogeneous materials (see Table 2).

Following the experimental protocol, two groups of simulations were conducted; unloaded and loaded chambers. The unloaded chambers were not subjected to any manually applied loading for 9 weeks, whilst the loaded chambers were kept unloaded for 3 weeks and then manually loaded for another 6 consecutive weeks. The mechanical stimulus was created by applying a pressure load on the top surface of the growing tissues, with the area of the piston of the chamber. It was considered that the blood pressure and the daily activity of the animal contribute to low levels of strain and fluid flow inside the chamber during the

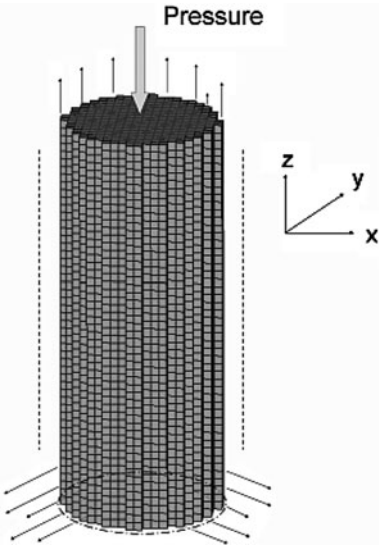

Fig. 7 FE model of the bone chamber with boundary conditions as follows; ↑↑↑↑ free fluid flow; ——: $u_x = u_y = 0$; - - - -: $u_x = u_y = u_z = 0$

Table 2 List of material parameters for tissue phenotypes that can exist in the model

	Granulation tissue	Fibrous tissue	Cartilage	Immature bone	Mature bone
Young's modulus (MPa)	0.2	2	10	1,000	6,000
Permeability ($m^4/N\ s \times 10^{-14}$)	1	1	0.5	10	37
Poisson's ratio	0.167	0.167	0.3	0.3	0.3
Porosity	0.8	0.8	0.8	0.8	0.8
Solid bulk modulus (MPa)	2,300	2,300	3,400	13,920	13,920
Fluid bulk modulus (MPa)	2,300	2,300	2,300	2,300	2,300

unloaded periods. Thus given that the normal systolic blood pressure for Sprague–Dawley rats, as used in the animal experiments, is 120–160 mmHg [52, 53], the unloaded time period was modelled as if the tissues were subjected to an intermediate pressure load of 0.02 MPa, applied with the piston. The mechanical loading (for the loaded simulations) was modelled based on the loading conditions applied during the loaded bone chamber experiments where tissues within the chamber were exerted to a pressure of 2 MPa, every 12 h. The load was modelled as a linear ramp from 0 to 2 MPa in 0.3 s and held constant at 2 MPa for another 2.7 s. The fluid velocity and the strains created by the mechanical loading were calculated using poroelastic analysis in Abaqus v 6.7-1.

Tissue regeneration inside the chamber was modelled as an iterative process (Fig. 8), where each iteration represents 12 h. The bone chamber was assumed to be filled with granulation tissue at the start of the simulations and a number of lattice points at the ingrowth openings were seeded with mesenchymal stem cells (MSCs) (30%), representing the MSC density in the bone marrow [44], that were allowed to disperse into the chamber. In every iteration, randomly chosen mature

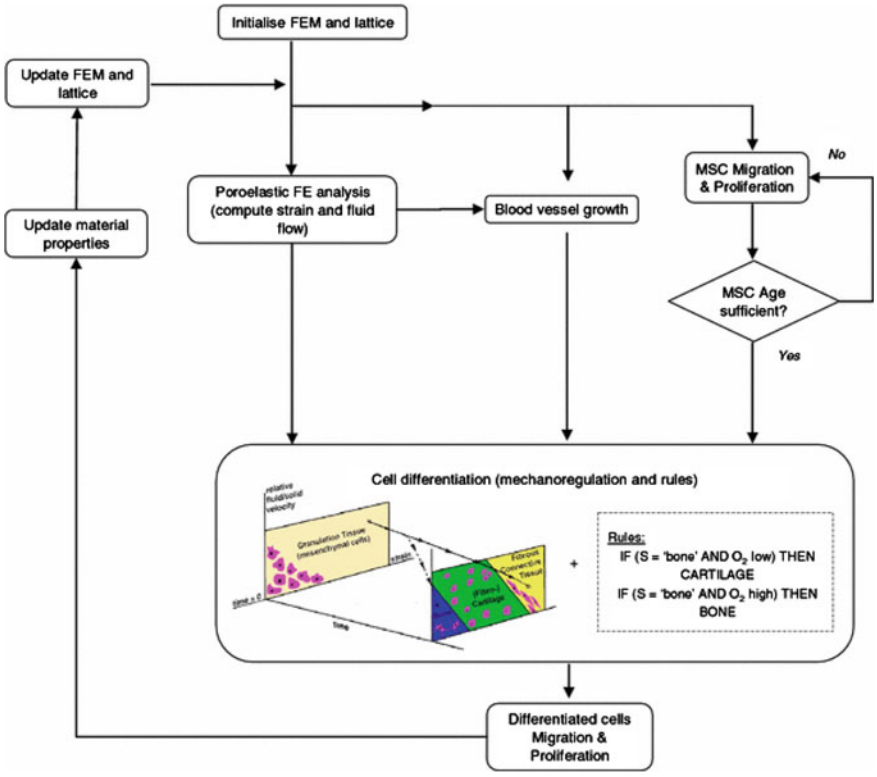

Fig. 8 Schematic representation of the computational algorithm to model tissue regeneration

Table 3 Cell phenotype specific rates

Cell type	Proliferation rate (1/2 day^{-1})	Apoptosis rate (1/2 day^{-1})	Differentiation rate (1/2 day^{-1})	Migration rate (μm/h)
Stem cells	0.30[a]	0.025[a]	0.15[a]	26.6[b]
Fibroblasts	0.27[a]	0.025[a]	–	26.6[b]
Chondrocytes	0.10[a]	0.05[a]	–	–
Osteoblasts	0.15[a]	0.08[a]	–	–

[a] Perez and Prendergast [50]
[b] Isaksson et al. [44]

MSCs (after 6 days in this model) differentiated with a defined rate (see Table 3) into fibroblasts, chondrocytes or osteoblasts based on the local mechanical stimulus. However, since the bone chamber is subjected to very low loading conditions initially, the formation of new capillaries in the chamber is unrestricted and does not have a significant effect on the simulation outcomes; this process is therefore omitted in the simulations presented in this chapter.

Since chondrocytes and osteoblasts are less motile, only the migration of fibroblasts and MSCs were considered in this model. Due to the similar morphology of fibroblasts and MSCs [54, 55] both phenotypes were assumed to migrate at an equal speed (Table 3). Cell phenotype specific rates were adopted for proliferation and apoptosis of the cells (Table 3). Since different cell phenotypes that synthesize different extracellular matrices with different material parameters could exist in an element, a rule of mixtures was used to calculate the material properties in each element [35], in every iteration. In order to prevent an unphysiological rapid change in material properties of the elements, the values were averaged over ten previous iterations [33].

In an attempt to understand the variability found among the animals of the experiment, the following environmental parameters were investigated:

1. *Load magnitude*: Throughout the animal experiments the pressure load was applied manually and a certain variability due to human manipulation of the loading device is expected. The effect of low (1 MPa), baseline (2 MPa) and high (3 MPa) load on the tissue regeneration in the chamber was investigated.
2. *Implant positioning*: During the surgical procedure the bone chamber is screwed into the epiphyseal cortex and the in-growth openings become placed at the level of the cortical bone and the pointed end of the implant is engaged through the opposite cortical bone. Although the largest area of the in-growth openings are in a region where there is bone marrow, the positioning of the implant may be such that some parts of the ingrowth openings are blocked by the cortical bone and thus restricting MSC access into the chamber. The effect of partial blocking (1/3 of the height) of the in-growth openings was investigated.
3. *Blood pressure*: During the unloaded period, the cells were assumed to be under a load caused by the blood pressure of the animal. The effect of low (0.01 MPa), baseline (0.02 MPa) and high (0.04 MPa) blood pressure was investigated.

4. *MSC density at the ingrowth openings*; the density of MSCs in the bone marrow may be different between animals. The access and the amount of MSCs in the bone chamber could affect the strain and fluid flow relationships and thus the tissue differentiation outcome. The effect of a low, baseline and a high density of cells (20, 30 and 50%, respectively) at the ingrowth openings was investigated.

Results

The simulation of the unloaded bone chamber experiment shows that intramembraneous ossification gradually fills the chamber with bone whereas very little bone is formed in the loaded chamber (Fig. 9).

After 9 weeks of simulation, no cartilage was observed in the unloaded chamber whereas a small amount of cartilage appears in the loaded bone chamber (Fig. 9). Due to the higher fluid flows and shear strains, a large amount of fibrous tissue was found at the base of the loaded chamber, whilst no fibrous tissue was observed in the unloaded simulation (Fig. 9).

Due to the stochastic nature of cell activity, different results are expected for each run of the algorithm when using the same parameter values. Five identical baseline simulations were compared and although there was a difference in the point to point correlation of lattice points neither of the results from the five baseline simulations showed a difference in histology. The percentages of each cell phenotype were calculated for each run of the algorithm for the loaded simulations (see Table 4) and the means of chondrocyte, fibroblast and osteoblast differentiation were 4.6, 86.2 and 9.2%, respectively. Standard deviations for each differentiated cell phenotype, explaining the variability in the outcome, were calculated as 1.7% for chondrocyte differentiation, 1.8% for fibroblast differentiation and 0.2% for osteoblast differentiation.

A low load magnitude (1 MPa) showed less fibrous tissue formation compared to the baseline simulation, due to lower strains and fluid flows, but promoted differentiation of chondrocytes and osteoblasts. Under higher loading (3 MPa) the chamber was mainly filled with fibroblasts with less chondrocytes and osteoblasts (Fig. 10).

Partial blocking of the ingrowth openings caused a lower tissue height in the loaded chamber and more chondrocyte differentiation, with less osteoblasts and fibroblasts (Fig. 11). The blockage restricted the MSC access into the chamber so that the cells with access had to migrate further in order to fill the chamber.

An environment exposed to high blood pressure (0.04 MPa) promoted differentiation of chondrocytes in the unloaded chamber, as a result of increased strain and fluid flow (Fig. 12). In the simulations where the MSC density at the ingrowth openings was varied, neither the loaded nor the unloaded bone chamber showed a significant change in the tissue outcome.

Discussion

The bone chamber constitutes a relatively reproducible and mechanically controlled environment which is, in principle, well suited for corroboration of mechanobiological simulations of tissue differentiation. In this study, partial corroboration of the mechanoregulation algorithm, based on shear strain and fluid flow, was achieved by simulating the bone chamber experiments developed by Tägil and Aspenberg [47]. The presence of cartilaginous tissue predicted in the loaded chamber agreed with the histology in terms of both layout and amount. The non-deterministic behaviour of the model due to random parameters also showed a higher variability in the loaded simulations compared to the unloaded simulations,

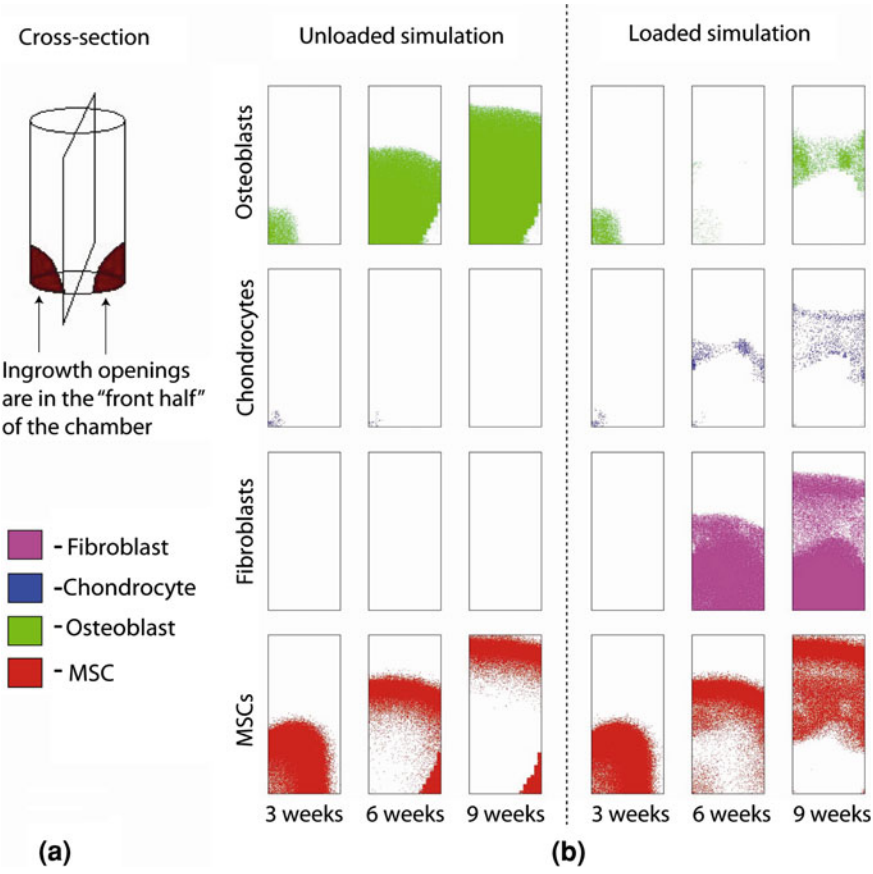

Fig. 9 **a** Cross-section of the bone chamber in which the results are presented. The section corresponds with the histological sections of the animal experiments. **b** Simulation results after 3, 6, and 9 weeks for the unloading and loading cases. The *rectangle* illustrates the cross-section of the bone chamber with the ingrowth holes located at the bottom left. The coloured lattice points show the differentiated cell phenotypes due to mechanical stimulus and MSCs

Table 4 Summary of the amount of the different cell phenotypes after 9 weeks in the simulations of the loaded bone chamber experiment

	Osteoblasts (%)	Fibroblasts (%)	Chondrocytes (%)
Baseline simulation 1	9.1	87.6	3.3
Baseline simulation 2	9.2	87.6	3.2
Baseline simulation 3	9.3	84.4	6.3
Baseline simulation 4	9.1	87.6	3.3
Baseline simulation 5	9.5	84.0	6.5
Load magnitude 1 MPa	28.6	62.3	9.1
Load magnitude 3 MPa	5.6	89.6	4.8
Blocking parts of the openings	8.9	84.8	6.3
20% MSCs at ingrowth openings	10.1	83.3	6.6
50% MSCs at ingrowth openings	7.6	86.7	5.7

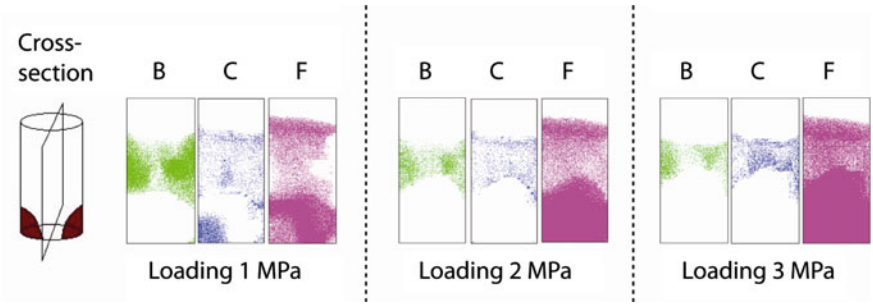

Fig. 10 Simulation results for varied loading on the piston, after 9 weeks. The phenotypes presented are osteoblasts (B) chondrocytes (C) and fibroblasts (F)

as seen in the histology; however the case where no cartilage formed in the loaded experiments (Fig. 5c) was never predicted by the simulations. For the simulations of the unloaded bone chambers, only a qualitative corroboration could be achieved.

The model contains many parameters that are taken from literature data and has several simplifications in relation to the biological reality. Model parameters, such as rates for different cell processes and material parameters that vary a great deal in the literature can have a significant effect on simulation outcomes. Furthermore, only differentiation of MSCs is considered in this model—processes such as de-differentiation and transdifferentiation have been omitted. Also, the genetic variability that exists in an animal population has not been taken account of, as one might expect the parameters related to cell activity (e.g. migration and proliferation rates) to be variable in the population. It is intriguing to speculate that this is why the experimentally observed variability is not predicted in the simulations.

The computer simulation of the unloaded experiments has not been able to capture the fibrous layer on top of the bone which is found in all specimens of the histology (Fig. 5a). This layer of fibrous tissue could be the periosteum that covers

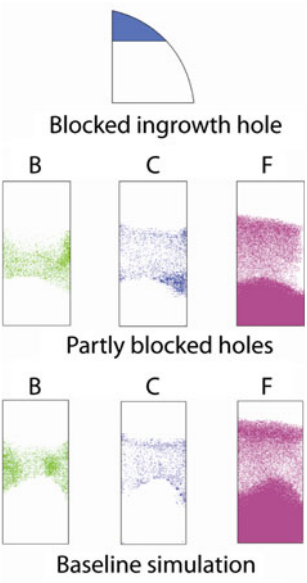

Fig. 11 An illustration of a blocked ingrowth opening, where the shaded region in the top right schematic represents the blocked region. Simulation results from the blocked and original loaded simulation after 9 weeks. The results show the differentiated cell phenotypes, osteoblasts (B), chondrocytes (C) and fibroblasts (F)

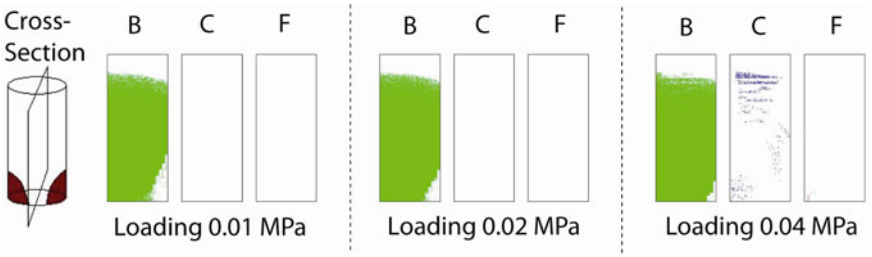

Fig. 12 Results from unloaded simulations where a variation in blood pressure was assumed to create different load magnitudes in the unloaded bone chamber simulation. The phenotypes illustrated are osteoblasts (B), chondrocytes (C) and fibroblasts (F), for all three simulations

the outer surface of all bones in vertebrates and is, most probably, chemically and not mechanically induced. Simulations of neither the unloaded nor the loaded experiments captured the formation of a marrow cavity, which is often seen in the specimens (Fig. 5). One explanation could be that the marrow cells found in the bone chamber are mesenchymal fat cells whose differentiation pathway is not included in the mechanoregulation algorithm or absent because transdifferentiation is not accounted for in the model. Since cell death due to necrosis was not included in the model, the necrotic tissue found in the animal experiments was not predicted by the simulations.

Despite these limitations, the computer simulations of the bone chamber experiments capture many of the trends seen in the histological results. In the unloaded experiment, no cartilaginous tissue is found in either the simulation (Fig. 10) or the histology (Fig. 5a). Simulation of the loaded experiment (Fig. 10)

captures the phenomena seen in some animals where a layer of cartilage has formed between the fibrous tissue and the bone interface (Fig. 5) which clearly points out the effect of mechanical loading on the process of tissue differentiation.

In the histology of the loaded bone chamber experiment, one of the specimens shows neither bone nor cartilage formation but only fibrous tissue throughout the entire chamber. However, the application of higher loading on the tissues could not simulate the complete lack of bone and cartilage in the bone chamber. Interestingly, when assuming that the position of the implant is such that part of the ingrowth openings is blocked, the height of the tissues formed inside the chamber was lower. The fact that the bone chamber does not get entirely filled with tissues has previously been explained by chemical signals; saying that they only reach a limited diffusion distance into the chamber [47]. The result of the simulations where the ingrowth openings were partly blocked points out that the tissue height in the chamber could also be influenced and subjected to a variability that is due to the surgical procedure.

The investigations of different MSC densities at the ingrowth openings did not contribute to a significant change in the predicted tissue distribution. This indicates that parameters such as migration and proliferation rates dominate over the initial conditions, in that they control the amount of MSCs in the chamber and hence the differentiation process. When simulating different blood pressures in the unloaded experiment, the results of the simulation with high blood pressure (0.04 MPa) shows chondrocyte differentiation which is never found in the histology. This indicates the sensitivity of our assumption regarding blood pressure and the importance of the magnitude of initial loading at the site of injuries; in this case, caused by the implantation of the bone chamber. Our investigations show that the variability in tissue distribution and amount is larger in the loaded simulation than the unloaded, which is also seen in the animal experiments.

In summary, the goal of this study was to create a computational model of a mechanically controlled bone chamber experiment for corroboration of mechanoregulation theories for tissue differentiation. The results of this study show that by modelling the cellular activities as stochastic processes using a lattice model, the mechanoregulatory algorithm compelled by fluid flow and shear strain [27] makes it feasible to predict the differentiated tissue distribution found in the bone chamber experiments. Contrary to other tissue differentiation simulations, which model cell migration as a diffusion process, this model adopts the random walk approach to capture the process in a more explicit manner [56]. Simulations performed in this study indicate that the role of human factors during the bone chamber experiment, such as loading and surgery, is significant and could perhaps explain some of the differences observed in the experimental tissue outcome. Although attempts on simulating the observed variability among the specimens of the experiment were made, the model did not capture the full extent of the differences such that quantitative corroborations could be made; in fact the source of the variability in experimental outcome remains unsolved. This raises the question whether or not mechanobiological models need to be yet more complex to achieve experimental corroboration.

4 Multi-Point Representation of Cells

In some cases it may be necessary to simulate cell movement in more detail or, alternatively, it may be necessary to simulate a combination of cell types of considerably different size or shape. In such cases it is no longer valid to assume that all cells correspond to individual lattice points and it becomes necessary to allow cells to occupy a region of the lattice. In MBTK this is done using a voxel-based approach based on the Cellular Potts model (CPM) [3, 4, 57].

Cells are allowed to occupy a connected set of voxels within the lattice and are assumed to have an effective energy (or Hamiltonian), H, that is a function of adhesion energy to neighbouring voxels surrounding the cell, volumetric energy, H_{volume}, arising from the deviation from a characteristic (target) volume for the cell type, and surface energy, $H_{surface}$, arising from deviation from the cell's characteristic surface area:

$$H_{cell} = H_{adhesion} + H_{volume} + H_{surface} \tag{1}$$

Adhesion energy, $H_{adhesion}$, is defined as

$$H_{adhesion} = \sum_{i=1}^{n_{surfVox}} J_{cell:neighbour} \Delta A \tag{2}$$

where $J_{cell:neighbour}$ is the contact energy between the cell and the neighbouring material, ΔA is an increment of contact area between the cell and its neighbour (in this case the area of a voxel face), and $n_{surfVox}$ is the number of surface voxels in the cell. Possible neighbours are other cells, ECM, biofluids, or biomaterials. Each surface voxel of the cell is checked against its external neighbour and added to the effective adhesion energy of the cell. Volume energy, H_{volume}, is defined as:

$$H_{volume} = \lambda_{vol}\left(V_{current} - V_{target}\right)^2 \tag{3}$$

where λ_{vol} is a constant for a given cell type, $V_{current}$ is the cell's current volume, and V_{target} is the target volume for the cell. This term is analogous to strain energy since it expresses a minimum energy in an unstretched state (i.e. when the cell achieves it's target volume) and increases as the cell expands/shrinks from this size; thus λ_{vol} is often referred to as a volumetric elasticity parameter. Surface (membrane) energy, $H_{surface}$, is analogously defined as

$$H_{surface} = \lambda_{surf}\left(A_{current} - A_{target}\right)^2 \tag{4}$$

where λ_{surf} is a constant for a given cell type, $A_{current}$ is the cell's current area, and A_{target} is the target area for the cell. This is the surface equivalent of Eq. 3. To summarise, $H_{adhesion}$ dictates attachment behaviour of the cell by favouring attachment to neighbours with lower contact energies while both H_{volume} and $H_{surface}$ impose energy penalties on deviations from the characteristic size and shape of a given cell type.

In the classical CPM trial movements (pairs of lattice sites representing either cell extension to an external voxel or retraction to an interior or neighbouring surface voxel within the cell) are selected at random from the entire lattice and the change in the Hamiltonian, ΔH, that would result from the movement is calculated locally within the site neighbourhood. Probability of accepting the movement, $P(\Delta H)$ is calculated as

$$\begin{aligned} P(\Delta H) &= 1 & \Delta H \leq 0 \\ &= e^{-\Delta H/T} & \Delta H > 0 \end{aligned} \tag{5}$$

where T represents the effective cytoskeletal fluctuation amplitude of cells in the simulation in units of energy [58]. This procedure is repeated to create a particular form of Monte Carlo simulation, known as a Metropolis algorithm [59], in which one trial is composed of as many movement attempts as there are sites within the lattice and a global Hamiltonian for the entire lattice is calculated by summing the contribution from all movements accepted according to Eq. 5. Since random selection of lattice sites frequently selects pairs of interior voxels within cells there is a high rejection rate of trial movements. A modification of this approach, known as the Random-Walker algorithm [60], only selects voxel pairs at the cell boundaries and can considerably speed up the simulation. Another approach, proposed by van Oers et al. [61], evaluates all movement options for the cell surface and computes a weight for each option using an equation similar to Eq. 5 for $\Delta H > 0$. Probability of a particular movement option is then calculated as the ratio of that option's weight divided by the sum of all options' weights for the cell.

Although the Hamiltonian decreases the probability of energetically expensive movements, the probabilistic and local nature of the calculations can result in unrealistic deformations of the cell. A particular problem is occasional fragmentation or splitting of the cell into disconnected patches by an accepted retraction movement. Merks et al. [62] have proposed a cyclic neighbourhood connectivity check in 2D but no equivalent of this algorithm has been proposed in 3D. CompuCell [63] uses a relatively expensive breadth first search algorithm in 3D for a cell that compares calculated volume with actual cell volume [64]. In MBTK a digital image processing technique known as "connected component labelling" [65] is used to check local connectivity during retraction movements. Briefly, the algorithm is described in Fig. 13.The tree representation of label equivalences can be implemented using a data structure called disjoint-sets [66]. An array-based implementation is used in MBTK to store the equivalences between labels and a technique known as Union-Find is used to merge and check label equivalences using methods proposed by Wu et al. [67]. This algorithm can be implemented for different types of connectivity, e.g. face connected (i.e. 6-neighbour) or vertex connected (26-neighbour) connectivities.

Up to this point only cell migration has been discussed in relation to multi-point cells. However, other cell processes can also be implemented in a straightforward manner. For instance, a simple implementation of cell division can be achieved by

```
Initialise component label variable
Iterate through voxels in neighbourhood
    If it is a same-cell voxel (i.e. if it belongs to the cell under consideration)
      then
        find prior neighbours with same-cell status.
        If no same-cell neighbour exists then
            a new label is created and assigned to the current voxel.
        Else,
            the minimum label from the prior neighbours is applied and an
            equivalence between the active label and the applied label is
            stored with a label tree (a parent-child data structure
            indicating if a connection exists between two labels).
If two or more label trees are generated after a complete pass through the
neighbourhood then the component labels are disjoint and there is no local
connectivity within the neighbourhood.
```

Fig. 13 Algorithm to check for fragmentation of a cell using connected component labelling

selection of a surface voxel (Fig. 14; t = 10), assigning it a new cell ID, and updating the relevant lattice arrays to account for the appearance of a new cell. Application of several migration trials before the next global timestep will cause the cell to grow quickly towards its target volume, resulting in two cells of similar size after the division (Fig. 14; t = 11). An example of this algorithm, applied several times, is shown in Fig. 14. After each division the cells are allowed to migrate within the lattice until the next division is signalled (in this conceptual example the next cell flagged for division was chosen at random from the current cell list). Apoptosis can be achieved by setting the target volume of a cell to zero and allowing the cell to retract over several timesteps until it needs to be deleted from the list of cells within the lattice, after which the appropriate lattice arrays are updated to reflect its removal.

Obviously, this multi-point cell approach is considerably more computationally expensive to implement than a single point cell representation. However, it provides a useful framework for incorporating specific cell behaviours that can make the extra complexity worthwhile for particular applications and provides the flexibility to investigate cell behaviour at different length scales. One of the immediate applications envisaged in our laboratory is to mix cell types of different size within a single simulation, i.e. to maintain a single point representation for existing mechanoregulation algorithms dealing with MSC derived cells and adding a multi-point representation for larger cells, such as osteoclasts, to investigate their influence on tissue differentiation processes.

5 Structural Models Using a Hybrid Continuum-Tensegrity Approach

Lattice based models of cells are well suited to modelling populations of cells. However, certain aspects of cell composition and structure are not easily

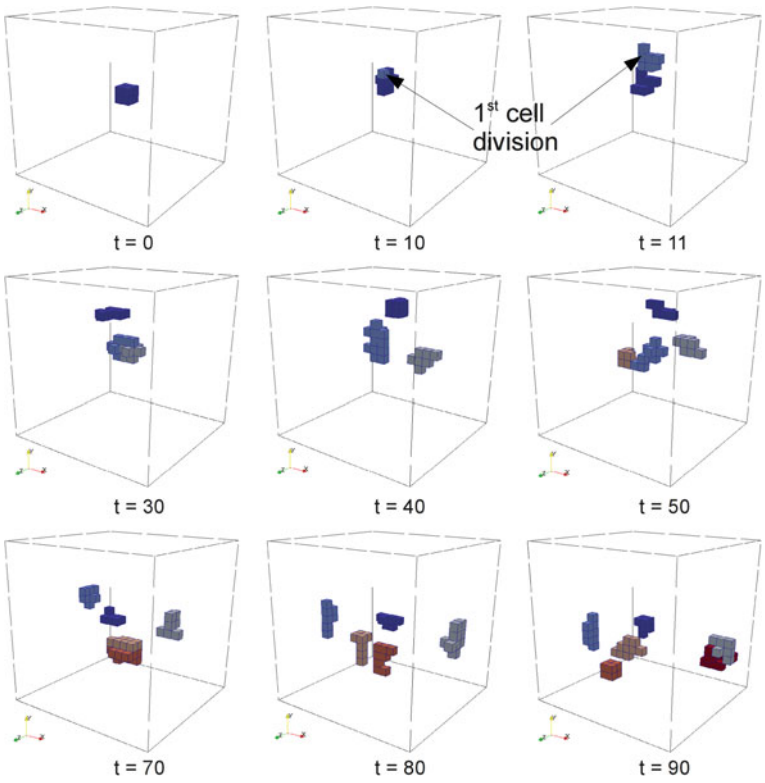

Fig. 14 Migration and division of multi-voxel cells. Cell division occurs at t = 10, 30, 50, 70, and 90 global iterations. In the intervening periods cells can be seen to migrate randomly within the lattice

incorporated into a lattice modelling scheme, e.g. the cytoskeleton of a cell or nonlinear material behaviour of cell constituents such as the nucleus. While molecular dynamics ultimately offers the possibility of detailed analysis of intracellular structure and function, it remains too computationally expensive for investigation at the level of a complete individual cell. We have developed models of individual cells on a hybrid concept of combining continuum finite element models (representing the membrane, cytoplasm, and nucleus) with tensegrity-based finite element models (representing the cytoskeleton) [68]. The following sections describe the current implementation of these models being used to investigate phenomena such as mechanosensing and mechanotransduction in cells.

5.1 Continuum Representation of Cell Components/Organelles

McGarry and Prendergast [68] first introduced the hybrid continuum tensegrity approach using linear elastic material properties for all cellular components with

the cytoskeleton modelled as a 6-strut tensegrity structure. A similar approach was used by De Santis et al. [69] with an improvement of implementing a 12-strut tensegrity structure representing the cytoskeleton. Since then further developments have been made to the solid constituents including the assignment of viscoelastic properties to both the cytoplasm and nucleus using a standard linear solid model; i.e. the shear modulus $G(t)$ and the bulk modulus $K(t)$ at time t are represented as:

$$\begin{aligned} G(t) &= G(\infty)\left(1 - g^p\left(1 - e^{t/\tau}\right)\right)\Big/(1 - g^p) \\ K(t) &= K(\infty)\left(1 - k^p\left(1 - e^{t/\tau}\right)\right)\Big/(1 - k^p) \end{aligned} \tag{6}$$

where the parameters g^p, k^p and relaxation time τ are viscoelastic material constants. G_∞ and K_∞ are the long-term shear and bulk moduli, respectively. Values for these parameters were selected according to previous studies [70, 71]. The cell membrane and nuclear envelope are modelled as linear elastic using membrane elements (i.e. with no bending stiffness) and the nucleus and cytoplasm are modelled with solid finite elements, e.g. linear hexehedra/tetrahedra depending on the geometric complexity of the cell configuration. Bonded (displacement compatible) interfaces are assumed at the interfaces between solid and membrane meshes for both the cell membrane-cytoplasm interface and the cytoplasm-nuclear envelope-nucleoplasm interfaces.

5.2 Cytoskeletal Representation Using Tensegrity Structures

Different levels of cytoskeletal complexity have been modelled since the hybrid continuum-tensegrity approach was first used by McGarry and Prendergast [68]. Our most recent development is the incorporation of multiple tensegrity structures for both the nucleus and the cytoskeleton and the addition of intermediate filaments connecting the cytoskeleton to the nucleus.

The nucleoskeleton is formed by 3 sets of 6-strut tensegrity structures, with the second and third rotated relative to the first, the relative rotation being 120° to ensure symmetry (Fig. 15, top left). Struts of the nuclear tensegrity structures are assumed to represent DNA strands while cables are assumed to correspond to nuclear lamina; this assumption is based on observations that DNA explodes outward (implying it is being released from compression) when the lamin protein lattice is cleaved [72]. Similarly, the cytoskeleton is formed by 3 sets of larger 6-strut tensegrity structures similarly rotated relative to each other (Fig. 15, top right). Struts in this case are assumed to correspond to compressed microtubules (MTs) [73] and cables are assumed to correspond to pre-stressed actin filament bundles (AFs) [74]. Further cables, representing intermediate filaments, connect the nuclear tensegrity structure to the cytoskeletal tensegrity structure (Fig. 15, bottom) [72]. Direct linkage is assumed between cytoskeleton and nucleoskeleton at the nuclear envelope, motivated by a study carried out by Dahl et al. [75]. Beam elements are used for struts and tension-only connector elements are used to model

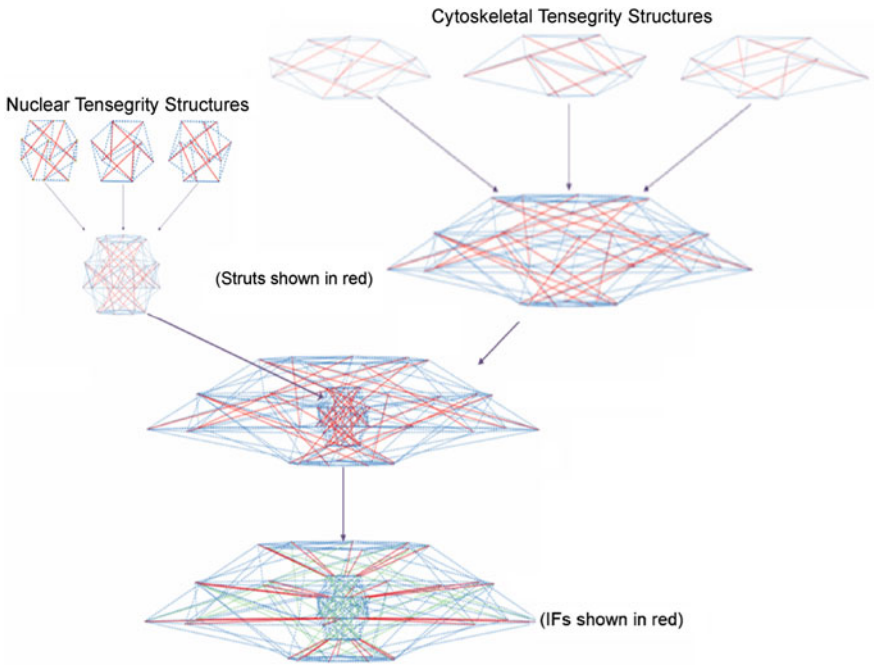

Fig. 15 Schematic of tensegrity structures used to represent both the nucleus and cytoskeleton. The *top row* shows the basic unit of the tensegrity structures used for both the nucleus and cytoskeleton; each unit consists of 6 struts and is rotated relative to its neighbour. The *next row* illustrates the combined structures for each case [note that microtubules (struts) are darker than the actin filaments (cables)]. These structures are combined into a single cell (row 3) and connected to each other using intermediate filaments (IFs) represented with cable elements (*bottom row*) with the IFs now *darkest* with all other components indicated in (*lighter shades*). For colour references in image, see the electronic version of the text

the cables in the cytoskeletal structures. Locations where the tensegrity structure meet the membrane are coupled to the membrane using connectors and are intended to represent focal adhesion complexes connecting the microtubule–actin junctions to integrin sites. Prestress can be assigned to actin filaments by assigning a reference length to each of the cables. The size and approximate geometry of the cell model are based on confocal images of mesenchymal stem cells taken in our laboratory and can be adapted using the rules described by McGarry and Prendergast [68]. Vertical displacements of the basal surface of the cell are restrained to mimic contact with the substrate while tangential displacements are free to move to mimic frictionless sliding.

5.3 Application to Biomechanics of Individual Cells

Combining the continuum and tensegrity structures into one model enables biomechanical investigation of several features of cell behaviour, such as the

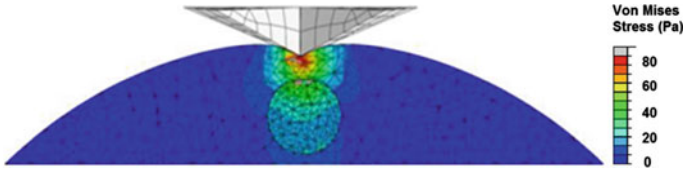

Fig. 16 Example of indentation structural model of a cell (in the form of a hybrid continuum-tensegrity representation) of a mesenchymal stem cell. A close-up cross-sectional view of the cell nucleus and the surrounding cytoplasm is shown on the right

interaction of the cytoskeleton with other organelles of a cell during AFM indentation. AFM indentation was simulated on the apex of the cell giving an internal stress transfer (Fig. 16). The stress also transfers into the nucleus (Fig. 17).

Looking at the stresses computed in the cell membrane under indentation (Fig. 18) shows local maxima where the microtubules connect with the membrane; in reality these stresses may dissipate due to cytoskeletal rearrangements under loading. Other applications using variations of the modelling approach described above include study of the effect of cell membrane stiffening in aged MSCs due to lipid peroxidation [76], comparison of strain and fluid flow as biophysical stimuli [77] and potential mechanisms of mechanosensation of extracellular matrix elasticity by cells [78].

These studies all exemplify the utility of a hybrid continuum-tensegrity representation of a cell. A particular strength of the approach is the ability to separate the potential load transfer mechanisms within a cell due to externally applied stimuli. For example, in the study of membrane stiffening, the effect of applying force directly to cytoskeleton receptor sites produces a much stiffer response than is predicted for indentation at other locations on the membrane [79–81]. Nevertheless, even this relatively complex tensegrity representation of the cytoskeleton does not capture the true complexity and dynamic behaviour observed in real cells and should therefore be considered a tool to understand the aggregate behaviour of cytoskeletal mechanics at instants of time rather than an accurate representation of cytoskeleton structure and mechanics under all circumstances.

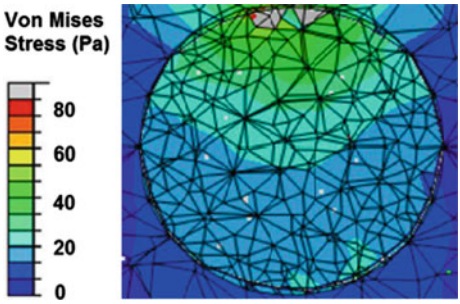

Fig. 17 A close-up cross-sectional view of the stress computed in a cell nucleus and the surrounding cytoplasm

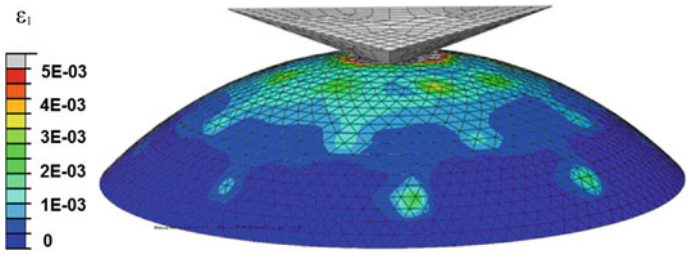

Fig. 18 Maximum principal strain distribution in cell membrane during indentation simulation on a mesenchymal stem cell. Local peaks of strain are predicted to occur where microtubule/actin complexes connect with the membrane. In reality these may dissipate quickly if microtubules respond to the forces acting on them by remodelling

6 Discussion

All cells are subjected to mechanical stimuli, whether it be a fluid pressure because it is suspended in a fluid, a stretch because it is tethered to a deforming substrate, or a shear stress because fluid flows over its membrane. Cells must resist these customary stimuli without disintegrating—but more, if they are mechanosensitive they should respond by regulating their environment through altered gene expression. It is discovering the relationship between mechanical stimulus and cell/tissue phenotype that motivates computational models for biomechanical modelling of cells in mechanoregulation. The brief review presented in this chapter shows that diverse approaches have been taken as follows:

– Cells as a point
– Cells as multiple points
– Structural models of cells

We have used the cells-as-a-point method to successfully simulate mechanoregulation of tissue differentiation. However, the cells-as-multiple-points method has definite advantages in better modelling migration and proliferation activities, and has often been successfully used by others. Structural modelling of cells has not yet been used in mechanoregulation, but it could easily be done when computational power allows it. One could imagine structural cells distributed throughout an extra cellular matrix (ECM) represented as a continuum. Each cell might have a different shape reflecting the diversity of the shapes occurring in vivo. Imaging techniques will eventually allow images of cells distributed in tissues to be generated automatically. A global force would stimulate each cell somewhat differently setting up a self-organising process that would remodel the ECM to an equilibrium configuration. In this regard, the use of computational models in biology can be thought of as creating virtual environments where ‘experiments’ can be performed.

In biomechanics, virtual environments are often envisaged for the testing of medical devices, such as orthopaedic implants, vascular devices, or tissue

engineered constructs/strategies. Computational modelling work is partly motivated by the difficulty in using animal models as environments for testing devices [82]. However, this approach of creating virtual or numerical environments is not always accepted as there is no guarantee that the fidelity to the reality in the particular circumstances of the validation is sufficient to allow for testing of the medical device [83, 84]. Indeed in this regard the attempt to create a virtual physiological human is the ultimate in creating a computational environment for the testing of interventional strategies. A less encompassing attitude is that computational models are created to test specific hypotheses regarding the behaviour of a system; when used to test specific hypotheses the validation can be focused on a limited set of features of the system. Taking forward this latter point, how can biomechanical models of cells in mechanoregulation be validated—or corroborated—by experiment. The approach we have taken to developing computer simulations of tissue differentiation is to devise algorithms for cell activities, and to use these algorithms as the building-blocks of the simulation. Each algorithm describes a mechanoregulated cell activity—migration, mitosis, apoptosis, or differentiation. In principle with this approach each algorithm can be validated separately against an in vitro cell experiment. Many researchers have attempted to establish quantitative relationships between biophysical stimuli and the regulation of cell activities [85]; for example we have done experiments to validate a relationship between stimulus and apoptosis [22], and between stimulus and differentiation [23]. However, the approach of separating the various processes into individual algorithms assumes a degree of modularity in the various cell activities.

When it comes to the biomechanical modelling of cells, two types of virtual environment exist: the environment of the individual patient and the environment of the population (clinical trials). Reviews of what happened in modelling in biomechanics since the 1980s [86, 87] show that these were not distinctly separated until recently; up to then most modellers aimed to create models representative of an average of the population. More recently however medical imaging of the patient has allowed patient-specific models to be generated, sometimes with a great degree of accuracy, for example in the cardiovascular system [88], or the skeletal system [89–91]; however in these instances to date patient-specificity relates to geometry, material properties, and/or loading and not yet to mechano-biological processes. Do patients have different mechanoresponsiveness in their cells and, if so, how does that inform the creation of virtual environments? Yes, would be the answer to the above question. Biomechanical modelling of cells will need to, ultimately, account for the variable nature of the response of cells to mechanical stimuli. In recent work [92] we have found that, if the experiment described in Sect. 3.1 above is simulated with a variation in the parameters then the outcome encompasses variability similar to that obtained in the experiment.

In conclusion, biomechanical modelling of cells for mechanoregulation simulations is in its infancy as a topic of investigation. A range of approaches is being taken, each becoming more sophisticated with increases in computational power and associated improved functionality of imaging systems. In the future their potential will be realised when structural models of cells are linked with organ

level models where patient-specific loading can be applied—this linking has the potential to generate 'virtual environments' where patient-specific mechanoregulation can be simulated. There is a long road to travel in experimental and computational mechanobiology before this can be achieved.

Acknowledgments Our research reported in this chapter has been funded in recent years by a Principal Investigator grant from Science Foundation Ireland to Prof. P. J. Prendergast (Grant No. 06/IN.1/B86) and by a Research Frontiers Grant (No. 08/RFP/ENM1361).

References

1. Lacroix, D., Prendergast, P.J., Li, G., Marsh, D.: Biomechanical model to simulate tissue differentiation and bone regeneration: application to fracture healing. Med. Biol. Eng. Comput. **40**, 14–21 (2002)
2. Geris, L., Gerisch, A., van der Sloten, J., Weiner, R., Oosterwyck, H.V.: Angiogenesis in bone fracture healing: a bioregulatory model. J. Theor. Biol. **251**, 137–158 (2008)
3. Graner, F., Glazier, J.A.: Simulation of biological cell sorting using a two-dimensional extended Potts model. Phys. Rev. Lett. **69**(13), 2013 (1992)
4. Ouchi, N., Glazier, J., Rieu, J., Upadhyaya, A., Sawada, Y.: Improving the realism of the cellular Potts model in simulations of biological cells. Physica A **329**(3–4), 451–458 (2003)
5. Kamm, R.D., McVittie, A.K., Bathe, M.: On the role of continuum models in mechanobiology. In: Casey, J., Bao, G. (eds.) Mechanics in Biology, pp. 1–11 (2000)
6. Ingber, D.E.: Tensegrity: the architectural basis of cellular mechanotransduction. Annu. Rev. Physiol. **59**, 575–599 (1997)
7. Slomka, N., Gefen, A.: Confocal microscopy-based three-dimensional cell-specific modeling for large deformation analyses in cellular mechanics. J. Biomech. **43**(9), 1806–1816 (2010)
8. McGarry, J.P., Fu, J., Yang, M.T., Chen, C.S., McMeeking, R.M., Evans, A.G., Deshpande, V.S.: Simulation of the contractile response of cells on an array of micro-posts. Philos. Transact. A Math. Phys. Eng. Sci. **367**(1902), 3477–3497 (2009)
9. Maurin, B., Cañadas, P., Baudriller, H., Montcourrier, P., Bettache, N.: Mechanical model of cytoskeleton structuration during cell adhesion and spreading. J. Biomech. **41**(9), 2036–2041 (2008)
10. Prendergast, P.J.: What Matters in Bioengineering, An Inaugral Lecture for the Chair of Bioengineering. Trinity College Dublin School of Engineering, Dublin (2008)
11. Prendergast, P.J., Checa, S., Lacroix, D.: Computational models of tissue differentiation. In: De, S., Guilak, F., Mofrad, R. (eds.) Computational Modeling in Biomechanics, pp. 335–372. Springer, New York (2010)
12. Checa, S., Byrne, D.P., Prendergast, P.J.: Predictive modelling in mechanobiology: combining algorithms for cell activities in response to physical stimuli using a lattice-modelling approach. In: Computer Methods in Mechanics, pp. 423–435. Springer (2010)
13. Checa, S., Sandino, C., Byrne, D.P., Kelly, D.J., Lacroix, D., Prendergast, P.J.: Computational techniques for selection of biomaterial scaffolds for tissue engineering. In: Fernandes, P.R., Bártolo, p. (eds.) Advances of modeling in Tissue Engineering. Springer (2010, in press)
14. Sloot, P.M.A., Hoekstra, A.G.: Multi-scale modelling in computational biomedicine. Brief. Bioinform. **11**(1), 142–152 (2010)
15. Boyle, C., Lennon, A., Early, M., Kelly, D., Lally, C., Prendergast, P.: Computational simulation methodologies for mechanobiological modelling: a cell-centred approach to neointima development in stents. Philos. Trans. R. Soc. A Math. Phys. **368**(1921), 2919–2935 (2010)

16. Codling, E.A., Plank, M.J., Benhamou, S.: Random walk models in biology. J. R. Soc. Interface **5**(25), 813–834 (2008)
17. Checa, S., Prendergast, P.J.: A mechanobiological model for tissue differentiation that includes angiogenesis: a lattice-based modeling approach. Ann. Biomed. Eng. **37**(1), 129–145 (2009)
18. Pérez, M.A., Prendergast, P.J.: Random-walk models of cell dispersal included in mechanobiological simulations of tissue differentiation. J. Biomech. **40**(10), 2244–2253 (2007)
19. Matsumoto, M., Nishimura, T.: Mersenne twister: a 623-dimensionally equidistributed uniform pseudo-random number generator. ACM Trans. Model. Comput. Simul. **8**(1), 3–30 (1998)
20. Chen, F., Song, L., Mauck, R.L., Li, W.J., Tuan, R.S.: Mesenchymal stem cells. In: Lanza, R., Langer, R.S., Vacanti J. (eds.) Principles of Tissue Engineering, 3rd edn. Elsevier Academic Press, Burlington (2007)
21. Minguell, J.J., Erices, A., Conget, P.: Mesenchymal stem cells. Exp. Biol. Med. **226**, 507–520 (2001)
22. Kearney, E.M., Prendergast, P.J., Campbell, V.A.: Mechanisms of strain-mediated mesenchymal stem cell apoptosis. J. Biomech. Eng. **130**, 061004 (2008)
23. Kearney, E.M., Farrell, E., Prendergast, P.J., Campbell, V.A., Tensile.: Strain as a regulator of Mesenchymal stem cell osteogenesis. Ann. Biomed. Eng. **38**(5), 1767–1779 (2010)
24. Pauwels, F.: A new theory of the influence of mechanical stimuli on the differentiation of supporting tissue. The tenth contribution to the functional anatomy and causal morphology of the supporting structure. Zeitschrift für Anatomie und Entwicklungsgeschichte, pp. 478–515 (1960)
25. Carter, D., Blenman, P., Beaupre, G.: Correlations between mechanical stress history and tissue differentiation in initial fracure healing. J. Orthop. Res. **6**, 736–748 (1988)
26. Claes, L.E., Heigele, C.A.: Magnitudes of local stress and strain along bony surfaces predict the course and type of fracture healing. J. Biomech. **32**, 255–266 (1999)
27. Prendergast, P.J., Huiskes, R., Soballe, K.: ESB Research Award 1996. Biophysical stimuli on cells during tissue differentiation at implant interfaces. J. Biomech. **30**, 539–548 (1997)
28. Isaksson, H., van Donkelaar, C.C., Huiskes, R., Ito, K.: Corroboration of mechanoregulatory algorithms for tissue differentiation during fracture healing: comparison with in vivo results. J. Orthop. Res. **24**, 898–907 (2006)
29. Hayward, L.N., Morgan, E.F.: Assessment of a mechano-regulation theory of skeletal tissue differentiation in an in vivo model of mechanically induced cartilage formation. Biomech. Model. Mechanobiol **8**(6), 447–455 (2009)
30. Geris, L., Vandamme, K., Naert, I., Vander Sloten, J., Duyck, J., Van Oosterwyck, H.: Application of mechanoregulatory models to simulate peri-implant tissue formation in an in vivo bone chamber. J. Biomech. **41**, 145–154 (2008)
31. Carter, D.R., Beaupre, G.S., Giori, N.J., Helms, J.A.: Mechanobiology of skeletal regeneration. Clin. Orthop. Relat. Res. **355** Suppl. S41–S55 (1998)
32. Lacroix, D., Prendergast, P.J.: A mechano-regulation model for tissue differentiation during fracture healing: analysis of gap size and loading. J. Biomech. **35**, 1163–1171 (2002)
33. Byrne, D.P., Lacroix, D., Planell, J.A., Kelly, D.J., Prendergast, P.J.: Simulation of tissue differentiation in a scaffold as a function of porosity, Young's modulus and dissolution rate: application of mechanobiological models in tissue engineering. Biomaterials **28**, 5544–5554 (2007)
34. Kelly, D.J., Prendergast, P.J.: Prediction of the optimal mechanical properties for a scaffold used in osteochondral defect repair. Tissue Eng. **12**, 2509–2519 (2006)
35. Huiskes, R., Van Driel, W.D., Prendergast, P.J., Soballe, K.: A biomechanical regulatory model for periprosthetic fibrous-tissue differentiation. J. Mater. Sci.: Mater. Med. **8**, 785–788 (1997)
36. Ambard, D., Swider, P.: A predictive mechano-biological model of the bone-implant healing. Eur. J. Mech. A Solids **25**, 927–937 (2006)

37. Isaksson, H., Comas, O., van Donkelaar, C.C., Mediavilla, J., Wilson, W., Huiskes, R., Ito, K.: Bone regeneration during distraction osteogenesis: mechano-regulation by shear strain and fluid velocity. J. Biomech. **40**, 2002–2011 (2007)
38. Loboa, E.G., Fang, T.D., Parker, D.W., Warren, S.M., Fong, K.D., Longaker, M.T., Carter, D.R.: Mechanobiology of mandibular distraction osteogenesis: finite element analyses with a rat model. J. Orthop. Res. **23**, 663–670 (2005)
39. Morgan, E.F., Longaker, M.T., Carter, D.R.: Relationships between tissue dilatation and differentiation in distraction osteogenesis. Matrix Biol. **25**, 94–103 (2006)
40. Boccaccio, A., Prendergast, P.J., Pappalettere, C., Kelly, D.J.: Tissue differentiation and bone regeneration in an osteotomized mandible: a computational analysis of the latency period. Med. Biol. Eng. Comput. **46**, 283–298 (2008)
41. Geris, L., Van Oosterwyck, H., Vander Sloten, J., Duyck, J., Naert, I.: Assessment of mechanobiological models for the numerical simulation of tissue differentiation around immediately loaded implants. Comput. Methods Biomech. Biomed. Eng. **6**, 277–288 (2003)
42. Gomez-Benito, M.J., Garcia-Aznar, J.M., Kuiper, J.H., Doblare, M.: Influence of fracture gap size on the pattern of long bone healing: a computational study. J. Theor. Biol. **235**, 105–119 (2005)
43. Liu, X., Niebur, G.L.: Bone ingrowth into a porous coated implant predicted by a mechano-regulatory tissue differentiation algorithm. Biomech. Model. Mechanobiol. **7**, 335–344 (2008)
44. Isaksson, H., van Donkelaar, C.C., Huiskes, R., Ito, K.: A mechano-regulatory bone-healing model incorporating cell-phenotype specific activity. J. Theor. Biol. **252**, 230–246 (2008)
45. Checa, S., Prendergast, P.J.: A mechanobiological model for tissue differentiation that includes angiogenesis: a lattice-based modeling approach. Ann. Biomed. Eng. **37**, 129–145 (2009)
46. Guldberg, R.E., Caldwell, N.J., Guo, X.E., Goulet, R.W., Hollister, S.J., Goldstein, S.A.: Mechanical stimulation of tissue repair in the hydraulic bone chamber. J. Bone Miner. Res. **12**, 1295–1302 (1997)
47. Tagil, M., Aspenberg, P.: Cartilage induction by controlled mechanical stimulation in vivo. J. Orthop. Res. **17**, 200–204 (1999)
48. de Rooij, P.P., Siebrecht, M.A., Tagil, M., Aspenberg, P.: The fate of mechanically induced cartilage in an unloaded environment. J. Biomech. **34**, 961–966 (2001)
49. Hannink, G., Aspenberg, P., Schreurs, B.W., Buma, P.: Development of a large titanium bone chamber to study in vivo bone ingrowth. Biomaterials **27**, 1810–1816 (2006)
50. Perez, M.A., Prendergast, P.J.: Random-walk models of cell dispersal included in mechanobiological simulations of tissue differentiation. J. Biomech. **40**, 2244–2253 (2007)
51. Lanza, R., Thomas, E., Thomson, J., Gearhart, J., Hogan, B., Melton, D., Pederson, R., Wilmut, I. (eds.) Essentials of Stem Cell Biology. Elsevier Academic Press, San Diego (2009)
52. Fletcher, E.C., Lesske, J., Qian, W., Miller, C.C., Unger, T.: Repetitive episodic hypoxia causes diurnal elevation of blood pressure in rats. Hypertension **19**, 555–561 (1992)
53. Hulman, S., Falkner, B.: The effect of excess dietary sucrose on growth, blood pressure, and metabolism in developing Sprague–Dawley rats. Pediatr. Res. **36**, 95–101 (1994)
54. Grinnell, F.: Fibroblasts myofibroblasts, and wound contraction. J. Cell Biol. **124**, 401–404 (1994)
55. Tamariz, E., Grinnell, F.: Modulation of fibroblast morphology and adhesion during collagen matrix remodeling. Mol. Biol. Cell **13**, 3915–3929 (2002)
56. Fisher, J.P., Mikos, A.G., Bronzino, J.D. (eds.) Tissue Engineering. CRC Press, Boca Raton (2007)
57. Glazier, J.A., Graner, F.: Simulation of the differential adhesion driven rearrangement of biological cells. Phys. Rev. E **47**(3), 2128 (1993)
58. Chen, N., Glazier, J.A., Izaguirre, J.A., Alber, M.S.: A parallel implementation of the Cellular Potts Model for simulation of cell-based morphogenesis. Comput. Phys. Commun. **176**(11–12), 670–681 (2007)

59. Metropolis, N., Rosenbluth, A.W., Rosenbluth, M.N., Teller, A.H., Teller, E.: Equation of state calculations by fast computing machines. J. Chem. Phys. **21**(6), 1087 (1953)
60. Gusatto, É., Mombach, J.C.M., Cercato, F.P., Cavalheiro, G.H.: An efficient parallel algorithm to evolve simulations of the cellular potts model. Parallel Process. Lett. **15**(1/2), 199–208 (2005)
61. van Oers, R.F.M., Ruimerman, R., Tanck, E., Hilbers, P.A.J., Huiskes, R.: A unified theory for osteonal and hemi-osteonal remodeling. Bone **42**(2), 250–259 (2008)
62. Merks, R.M., Brodsky, S.V., Goligorksy, M.S., Newman, S.A., Glazier, J.A.: Cell elongation is key to in silico replication of in vitro vasculogenesis and subsequent remodeling. Dev. Biol. **289**(1), 44–54 (2006)
63. Izaguirre, J.A., Chaturvedi, R., Huang, C., Cickovski, T., Coffland, J., Thomas, G., Forgacs, G., Alber, M., Hentschel, G., Newman, S.A., Glazier, J.A.: CompuCell, a multi-model framework for simulation of morphogenesis. Bioinformatics **20**(7), 1129–1137 (2004)
64. Swat, M.H., Hester, S.D., Heiland, R.W., Zaitlen, B.L., Glazier, J.A., Shirinifard, A.: CompuCell3D Manual and Tutorial, Version 3.4.1. Biocomplexity Institute and Department of Physics, Indiana University, Bloomington (2009)
65. Rosenfeld, A., Pfaltz, J.L.: Sequential operations in digital picture processing. J. ACM **13**(4), 471–494 (1966)
66. Cormen, T.H., Leiserson, C.E., Rivest, R.L., Stein, C.: Introduction to Algorithms. MIT Press, MIT USA (2001)
67. Wu, K., Otoo, E., Shoshani, A.: Optimizing connected component labeling algorithms (2005)
68. McGarry, J.G., Prendergast, P.J.: A three-dimensional finite element model of an adherent eukaryotic cell. Eur. Cell Mater. **7**, 27–33 (2004). discussion 33-34
69. De Santis, G., Boschetti, F., Lennon, A.B., Prendegast, P.J., Verdonck, P., Verhegghe, B.: How an eukaryotic cell senses the substrate stiffness? An exploration using a finite element model with cytoskeleton modelled as tensegrity structure. In: Proceedings of the ASME 2009 Summer Bioengineering Conference, American Society of Mechanical Engineers (ASME), Lake Tahoe, CA, USA (2009)
70. McGarry, J.P., Murphy, B.P., McHugh, P.E.: Computational mechanics modelling of cell-substrate contact during cyclic substrate deformation. J. Mech. Phys. Solids **53**(12), 2597–2637 (2005)
71. Guilak, F., Tedrow, J.R., Burgkart, R.: Viscoelastic properties of the cell nucleus. Biochem. Biophys. Res. Commun. **269**(3), 781–786 (2000)
72. Ingber, D.: Tensegrity I. Cell structure and hierarchical systems biology. J. Cell Sci. **116**(7), 1157–1173 (2003)
73. Brangwynne, C.P., MacKintosh, F.C., Kumar, S., Geisse, N.A., Talbot, J., Mahadevan, L., Parker, K.K., Ingber, D.E., Weitz, D.A.: Microtubules can bear enhanced compressive loads in living cells because of lateral reinforcement. J. Cell Biol **173**(5), 733–741 (2006)
74. Kumar, S., Maxwell, I., Heisterkamp, A., Polte, T., Lele, T., Salanga, M., Mazur, E., Ingber, D.: Viscoelastic retraction of single living stress fibers and its impact on cell shape, cytoskeletal organization, and extracellular matrix mechanics. Biophys. J. **90**(10), 3762–3773 (2006)
75. Dahl, K.N., Booth-Gauthier, E.A., Ladoux, B.: In the middle of it all: mutual mechanical regulation between the nucleus and the cytoskeleton. J. Biomech. **43**(1), 2–8 (2010)
76. Xue, F., McKayed, K., Lennon, A.B., Campbell, V.A., Prendergast, P.J.: Computational investigation of influence of age on biomechanics of mesenchymal stem cells. In: Proceedings of the 9th international symposium on computer methods in biomechanics and biomedical engineering 2010, Valencia, Paper 154, CDROM (2010, in press)
77. McGarry, J.G., Klein-Nulend, J., Mullender, M.G., Prendergast, P.J.: A comparison of strain and fluid shear stress in stimulating bone cell responses—a computational and experimental study. FASEB J. **19**(3), 482–484 (2005)
78. De Santis, G., Lennon, A.B., Boschetti, F., Verhegghe, B., Verdonck, P., Prendergast, P.J.: Principle of matrix-elasticity sensing by cells. Eur. Cells Mater. (2010) (in press)

79. Hofmann, U.G., Rotsch, C., Parak, W.J., Radmacher, M.: Investigating the cytoskeleton of chicken cardiocytes with the atomic force microscope. J. Struct. Biol. **119**(2), 84–91 (1997)
80. Domke, J., Dannohl, S., Parak, W.J., Muller, O., Aicher, W.K., Radmacher, M.: Substrate dependent differences in morphology and elasticity of living osteoblasts investigated by atomic force microscopy. Colloids Surf. B Biointerfaces **19**(4), 367–379 (2000)
81. Mathur, A.B., Collinsworth, A.M., Reichert, W.M., Kraus, W.E., Truskey, G.A.: Endothelial, cardiac muscle and skeletal muscle exhibit different viscous and elastic properties as determined by atomic force microscopy. J. Biomech. **34**(12), 1545–1553 (2001)
82. Prendergast, P.J.: Biomechanical Techniques for Pre-Clinical Testing of Prostheses and Implants, Lecture Notes. Institute for Fundamental Technological Research, Polish Academy of Sciences, Warsaw (2001)
83. Miles, A.W., Tanner, K.E.: Strain Measurement in Biomechanics. Springer (1992)
84. Lennon, A.B., Prendergast, P.J. (eds.): Finite Element Modelling in Biomechanics and Mechanobiology with papers on patient-specific analysis, high resolution analysis, and applications in orthopaedics, cardiology, and cellular bioengineering. Trinity Centre for Bioengineering, Trinity College, Dublin (2007)
85. Campbell, V.A., O'Connell, B.: Cellular & molecular biomechanics. In: Lee, T.C., Niederer, P.F. (eds.) Basic Engineering for Medics and Biologists—an ESEM primer, pp. 202–213. IOS Press, Amsterdam (2010)
86. Huiskes, R., Chao, E.Y.S.: A survey of finite element analysis in orthopaedic biomechanics: the first decade. J. Biomech. **16**, 385–409 (1983)
87. Prendergast, P.J.: Finite element models in tissue mechanics and orthopaedic implant design. Clin. Biomech. **12**, 343–368 (1997)
88. Kiousis, D.E., Gasser, T.C., Holzapfel, G.A.: A numerical model to study the interaction of vascular stents with human atherosclerotic lesions. Ann. Biomed. Eng. **35**(11), 1857–1869 (2007)
89. Perillo-Marcone, A., Alonso-Vazquez, A., Taylor, M.: Assessment of the effect of mesh density on the material property discretisation within QCT-based FE-models: a practical example using the implanted proximal tibia. Comput. Methods Biomech. Biomed. Eng. **6**(1), 17–20 (2003)
90. Capelli, C., Taylor, A.M., Migliavacca, F., Bonhoeffer, P., Schievano, S.: Patient-specific reconstructed anatomies and computer simulations are fundamental for selecting medical device treatment: application to a new percutaneous pulmonary valve. Philos. Trans. R. Soc. A Math. Phys. Eng. Sci. **368**(1921), 3027–3038 (2010)
91. Reggiani, B., Cristofolini, L., Varini, E., Viceconti, M.: Predicting the subject-specific primary stability of cementless implants during pre-operative planning: preliminary validation of subject-specific finite-element models. J. Biomech. **40**(11), 2552–2558 (2007)
92. Khayyeri, H., Checa, S., Tägil, M., Aspenberg, P., Prendergast, P.J.: Individual-specific cell process rates explains variability in tissue differentiation experiment. In: Proceedings of the 17 Congress of the European Society of Biomechanics, European Society of Biomechanics, Edinburgh, Scotland, UK (2010); CDROM

Finite Element Modeling of Cellular Mechanics Experiments

Noa Slomka and Amit Gefen

Abstract The mechanical and biological response of cells to various loading regimes is a subject of great interest in the research field of biomechanics. Extensive utilization of different cellular mechanics experimental designs has been made over the years in order to provide better insight regarding the mechanical behavior of cells, and the mechanisms underlying the transduction of the applied loads into biological reactions. These experimental protocols have limited ability in directly measuring different mechanical parameters (e.g. internal cellular strains and stresses). In addition, they are very costly and involve highly complex apparatuses and experimental designs. Thus, further understating of cellular response can be achieved by means of computational models, such as the finite element (FE) method. FE modeling of cells is an emerging direction in the research field of cellular mechanics. Its application has been rapidly growing over the last decade due to its ability to quantify deformations, strains and stresses in and around cells, thus providing basic understating of the mechanical state of cells and allowing identification of mechanical properties of cells and cellular organelles when coupled with appropriate experiments. In this chapter, we review the two-dimensional (2D) and three-dimensional (3D) reported cell models of various cell types, subjected to different applied mechanical stimuli, e.g. compression, micropipette aspiration, indentation.

N. Slomka and A. Gefen (✉)
Department of Biomedical Engineering, Faculty of Engineering, Tel Aviv University, Tel Aviv, Israel
e-mail: gefen@eng.tau.ac.il

Stud Mechanobiol Tissue Eng Biomater (2011) 4: 331–344
DOI: 10.1007/8415_2010_31

Published Online: 11 September 2010

1 Introduction

Mechanical stimulation applied to cells is known to affect their shape, structure and mechanical properties, and elicit changes in their biological responses. The mechanical and biological response of cells to various loading regimes is therefore a subject of great interest, specifically in the research field of biomechanics, where extensive utilization of different cellular mechanics experimental designs has been made over the years in order to provide insight regarding the mechanical behavior of cells and the mechanisms underlying the transduction of the applied loads into biological reactions. These experimental designs include compression, static and cyclic stretching, indentation, micropipette aspiration, magnetic bead cytometry, shear flow and hydrostatic pressure. Although these experiments provide important information regarding cellular responses, their ability to directly measure internal stresses and strains is very limited. In addition, they are very costly and involve highly complex apparatuses and experimental designs. Thus, further understating of cellular responses can be achieved by means of computational models, such as finite element (FE) models.

The FE method is a numerical computational tool which enables calculation of the mechanical state of a complex object. In this method, the geometry of the object is commonly predesigned using mechanical computer-aided design (CAD) programs, e.g. SolidWorks and CATIA, and then imported into a custom-made or commercial FE solver e.g. ABAQUS, NASTRAN and ANSYS where it is divided into a mesh composed of geometrically separate elements. The model is then assigned mechanical properties for each component, interactions and contact definitions between the different components and boundary conditions. The FE method is presently the primary computational tool for assessment of mechanical conditions in the field of biomechanics, including cellular mechanics.

FE modeling of cells is an emerging direction in the research field of cellular mechanics. Its application has been rapidly growing over the last decade due to its ability to quantify deformations, strains and stresses in and around cells, thus providing basic understating of the mechanical state of the cells and allowing identification of mechanical properties of cells and cellular organelles when coupled with appropriate experiments. Two-dimensional (2D) and three-dimensional (3D) models of different cell types, e.g. epithelial cells [5], endothelial cells [4, 7, 31], smooth muscle cells [3], myoblasts [24, 29], and chondrocytes [1, 22], are reported in literature, employing either idealized or image-based cellular geometry. Development of models with 2D geometry naturally requires idealization of the cellular geometry [1, 4, 14, 18, 22, 24, 29]. Extension of the geometry of the cell models to 3D increases their complexity. Several reported studies developed 3D models, but still employed idealized geometrical representation of the cells, e.g. spheres or ellipsoids [3, 7, 11, 19, 30], while others studies reconstructed real image-based cell geometry [5, 9, 29]. Three-dimensional models of cells, as well as 2D models, can also be divided into two clearly distinguished categories: (1) non-structural models, where the whole cell is described as one

bulk with homogenous mechanical representation, and (2) structural models, where several sub-cellular components are described—each assigned a separate mechanical representation. Naturally, the latter presents a more challenging modeling task, particularly in numerically representing mechanical interactions at the cell scale (μm-scale), coupled with interactions at scales that are orders-of-magnitude smaller, e.g. involving the plasma membrane or cytoskeletal fibers (for which characteristic dimensions are at a nm-scale). However, it provides a higher level of accuracy in terms of simulations results. Some of the above mentioned 2D and 3D studies incorporated sub-cellular components, e.g. nucleus and cytoskeletal fibers [3, 4, 6, 7, 9, 14, 19, 22, 29].

Utilization of the FE method for the purpose of simulating cellular mechanics experiments potentially enriches studies involving classic cell loading designs. It provides the mechanical state of the loaded cell specifically to each cell type and experimental setup. In this chapter we will review the relevant studies reported in literature, modeling 2D and 3D cells of different types under varying loading regimes, as related to experiments in the field of cellular mechanics.

2 Two-Dimensional Models

2.1 Non-Structural Models

Few authors have developed 2D non-structural models of individual cells, describing the entire cell as a homogenous volume [1, 24, 27] Baaijens et al. [1] created such a 2D model of a chondrocyte, described as an elastic sphere, subjected to micropipette aspiration (Fig. 1). In order to study the ability of different

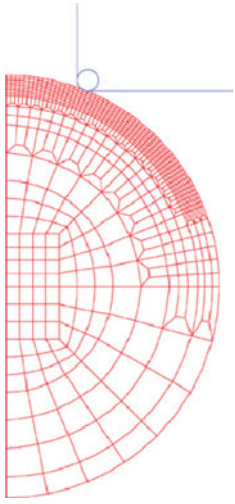

Fig. 1 Finite element geometrical model and mesh of a micropipette aspiration simulation (reproduced with permission from [1])

constitutive models to predict the aspiration response of the cells (i.e. aspiration length and creep response), the cell was modeled using finite strain incompressible and compressible elastic models, a two-mode compressible viscoelastic model, and a biphasic elastic or viscoelastic model.

Peeters et al. [24] modeled a myoblast as an axisymmetric half-sphere, in order to estimate its mechanical properties in compression using inverse engineering methods based on their experimentally obtained results of cell compression tests. Overall, 12 individual myoblasts were modeled, each assigned specific geometrical features (e.g. base radius and height) based on confocal images. The cell was modeled as an incompressible Neo-Hookean material:

$$\sigma = -pI + \tau \tag{1}$$

where σ is the Cauchy stress tensor, p is the hydrostatic pressure, and τ is an extra stress tensor.

An FE simulation of fluid flow stimulation was also reported (Salvi et al. 2009). As part of their study, aimed at determining the validity of various experimental protocols of fluid flow stimulations, the authors examined the affect of cell height on the uniformity of shear stresses when cells are subjected to unidirectional and oscillatory fluid flow. In this case, cells were modeled again as homogenous spheres, with linear elastic material properties.

2.2 Structural Models

Structural cell models typically include a combination of nucleus, cytoplasm, plasma membrane, and cytoskeletal fibers. Reported 2D structural models are idealized-shaped models, most of which include the nucleus and cytoplasm only [4, 18, 22]. Caille et al. [4] created models of round and spread individual endothelial cell and of isolated nuclei, subjected to compression (Fig. 2). Their goal was obtaining mechanical properties of the nucleus and cytoplasm in an inverse FE method based on their experimental data.

The geometrical characteristics of cells were based on digitized video images of the cells during compression tests, and the relative position of the nucleus within the cells was determined by visualization of cells stained with the fluorescent DNA marker Syto 13, with a confocal laser scanning microscope. In their study, both the nucleus and cytoplasm were assumed to be homogenous, incompressible hyperelastic materials, with a Mooney–Rivlin SED function, W:

$$W = -pC^{-1} + \mu\left(\frac{1}{2} + \beta\right)C + \mu\left(\frac{1}{2} - \beta\right)I \tag{2}$$

where p is the hydrostatic pressure, C is the right Cauchy-Green tensor, μ is the shear modulus, β is a constant, and I is the identity tensor. McGarry [18] created similar models of round and spread cells which geometries were also based on

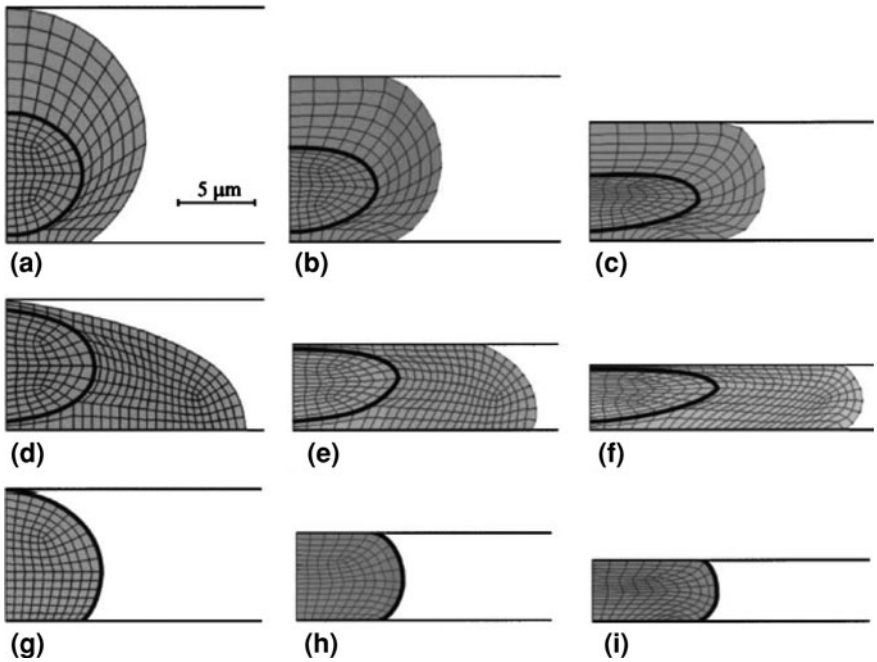

Fig. 2 Finite element geometrical models and mesh of a compression experiment simulation of **a** round endothelial cells, **d** spread endothelial cells, and **g** isolated nuclei, and their corresponding deformed shape calculated at 30% compression (**b**, **e**, **h**), and 50% compression (**c**, **f**, **i**) (reproduced with permission from [4])

experimentally observed round and spread chondrocytes [12], and endothelial cells [4]. However in order to model the viscoelastic cell behavior, different linear viscoelastic properties were assumed for both the nucleus and cytoplasm. Ofek et al. [22] also modeled an idealized-shaped individual cell (chondrocyte) composed of nucleus and cytoplasm in order to obtain the mechanical properties of the compressed nucleus and cytoplasm in an inverse FE method, based on experimental data from Leipzig and Athanasiou [15]. The cytoplasm and nucleus in this case were assumed to be linear elastic.

Our research group reported an additional 2D idealized-shaped model of a compressed myoblast [29], composed of plasma membrane enveloping the cytoplasm (Fig. 3). The geometry of the cell was represented as an idealized sphere with local curvature at the periphery of the cell base due to cell spreading (focal adhesions). The cell was assumed to be compressible Neo-Hookean material, with strain energy density (SED) function, W:

$$W = \frac{1}{2}k\left(J_3^{\frac{1}{3}} - 1\right)^2 + \frac{1}{2}G\left(J_1 - 3J_3^{\frac{1}{3}}\right) \tag{3}$$

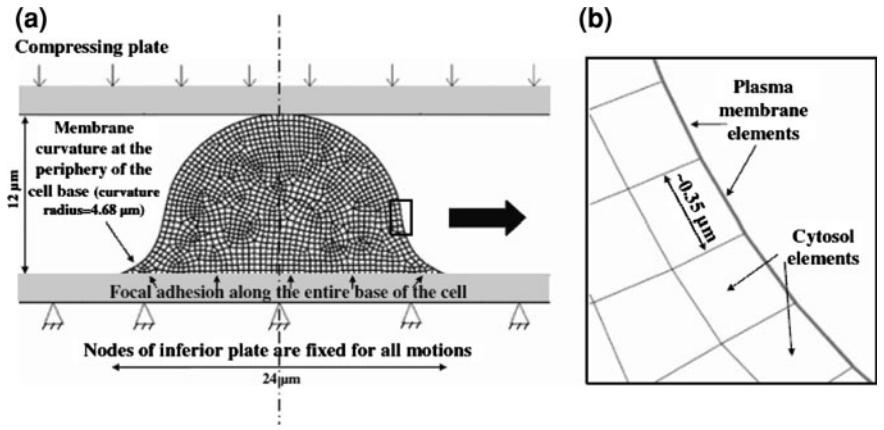

Fig. 3 The finite element model of the single adhered myoblast subjected to compression, showing **a** cell geometry, mesh, and boundary conditions, and **b** a magnification of the mesh, clearly exhibiting the plasma membrane (reproduced with permission from Slomka et al. [29])

where k is the bulk modulus, G is the instantaneous shear modulus, and J_i are the invariants of the Finger tensor B. The model was compressed and analyzed for tensional membrane strains.

A 2D model incorporating all typically modeled cellular components, i.e. nucleus, cytoplasm, membrane (in this case modeled as a cortical layer), and cytoskeletal fibers, was reported by Jean et al. [14]. The authors created a simplified geometrical model of an adhered endothelial cell based on experimental data from Jean et al. [13], and studied adhesion–cytoskeleton–nucleus mechanotransduction pathways during endothelial cell rounding. The model components were treated as incompressible Neo-Hookean materials, and the loss of tension of the fibers during cell rounding was also represented by reactive forces acting on the nucleus.

3 Three-Dimensional Models

3.1 Non-Structural Models

Extending the geometry of cells to 3D further complicates the computational simulations, both geometrically and numerically. The basic cell representation is a non-structural model, with an idealized shape, which is naturally more common in the case of 2D models. Bursa et al. [3] developed such a model of a vascular smooth muscle cell undergoing tension tests in 3D, for the purpose of evaluation of the material parameters, based on previously reported experimental results of tensile tests [21]. In this study, the cell was assumed to be a homogenous continuum with an elastic behavior described by the five-parameter Mooney–Rivlin hyperelastic strain energy density function W:

$$W = \alpha_1(i_1 - 3) + \alpha_2(i_2 - 3) + \alpha_3(i_1 - 3)^2 + \alpha_2(i_4 - 3)(i_2 - 3) + \alpha_5(i_2 - 3)^2 + \frac{k}{2}(i_3 - 1)^2 \quad (4)$$

where i_i are modifies invariants of the right Cauchy-Green deformation tensor, k is the bulk modulus and α_i are Mooney–Rivlin constants.

Zhao et al. [30] also reported a non-structural idealized-shaped 3D cell model in order to estimate the viscoelastic properties of porcine aortic valve interstitial cells by FE analyses of micropipette aspiration in an inverse FE method. Their ultimate goal was to determine the level of difference in the prediction of mechanical properties between analytical and inverse FE estimation methods. The cell was represented as a deformable sphere with homogenous material properties, which were described by a finite strain viscoelastic model (time domain generalization of a nearly incompressible hyperelastic Neo-Hookean constitutive model) with a relaxation shear modulus $G(t)$ represented by a one-term Prony series:

$$G(t) = G_0\left[1 - \alpha_1\left(1 - e^{-(t/(1-\alpha_1)\tau)}\right)\right] \quad (5)$$

where G_0 is the instantaneous shear modulus, α_1 is the dimensionless relaxation modulus, and τ is the creep time constant.

Another basic 3D non-structural model type reported in literature involves 3D geometry of a slab of the cell as opposed to whole-cell models. These models are typically developed for simulation of magnetic bead cytometry [20, 23, 31]. The shape of the cell section is either rectangular [20, 23] or cylindrical [31] as shown for example in Fig. 4a, b, respectively, and a rigid bead is embedded in the cell continuum.

The general purpose of these studies is estimation of the mechanical properties of the cells. Cells are modeled either as an homogenous linear elastic material [20, 31], or as an homogenous quasi-incompressible hyperelastic Neo-Hookean material, with a Neo-Hookean strain energy density function (Eq. 4) [23]:

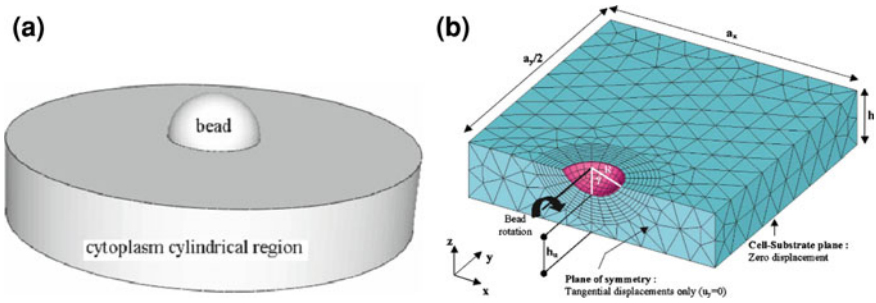

Fig. 4 Examples of **a** cylindrical (reproduced from Zeng et al. [31]), and **b** rectangular (reproduced with permission from Ohayon and Tracqui [23]) geometrical models of magnetic bead cytometry experiments, including a cell slab and bead

3.2 Structural Models

Structural 3D cell models can be divided into idealized-shaped geometrical models, usually adherent spheres or ellipsoids, and reconstructed image-based geometrical models, which provide realistic cell-specific geometries of the overall cell shape and of sub-cellular components, based on confocal or multimodal fluorescence images.

3.2.1 Idealized-Shaped Models

Few authors developed idealized-shaped 3D models of an adherent eukaryotic cell, including cellular components that are commonly considered as being structurally significant (i.e. nucleus, cytoplasm, plasma membrane, and the cytoskeletal fibers), in order to examine the ability of the model to describe the non-linear structural behavior of cells under different mechanical tests, e.g. tension with micropipettes, indentation and magnetic tweezers tests. McGarry and Prendergast [19] created six models of adherent cells at increasingly spread shapes—from immediately post attachment to 3 h after attachment (Fig. 5). The models were based on images of

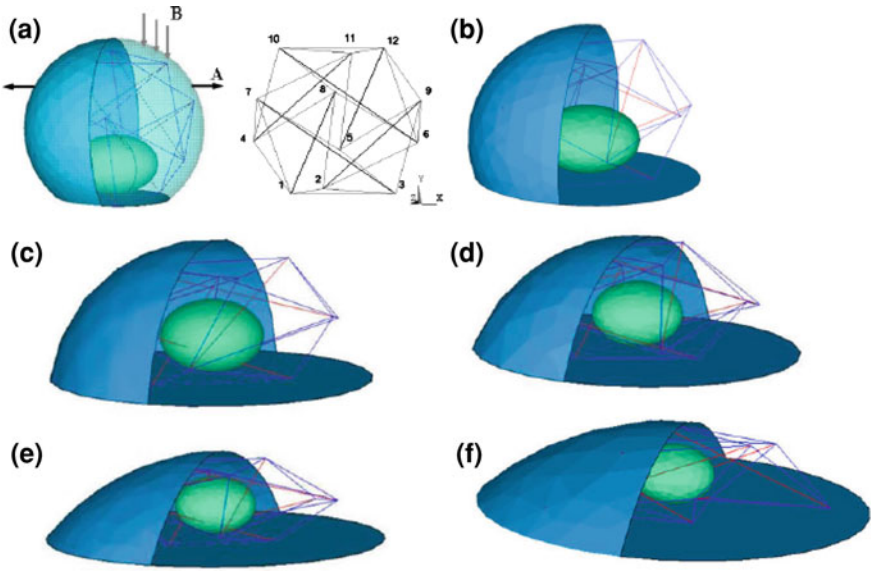

Fig. 5 Three-dimensional finite element models **a**–**f** of adherent cells at increasingly spread shapes, including nucleus, cytoplasm, plasma membrane and cytoskeletal fibers, (reproduced with permission from McGarry and Prendergast [19]). The internal cytoskeleton consisting of a three-dimensional tensegrity network of interconnected microtubule and microfilaments, and the location of horizontal force application (marked 'A') and vertical indentation force application (marked 'B') are additionally shown in **a**

spreading chick embryo fibroblasts, published in Frisch and Thoumine [10], and corresponded to the contact angle and contact radii of the imaged cells. The internal cytoskeleton consisted of a tensegrity network of 6 compression-bearing struts and 24 tensional cables, which represented the aggregate behavior of microtubules and microfilaments, respectively (Fig. 5). Sites of 'receptors', where actin filaments cluster at adhesion complexes, were represented by connection of each strut to 4 cables, thus creating 12 common nodes. Material properties were considered linear elastic, and the cytoskeleton was assigned pre-stress. External loads were transmitted to the tensegrity structure via its nodes, representing membrane receptors. Loads were applied either horizontally to 2 membrane surface nodes marked 'A' in Fig. 5a, in opposite directions, or vertical indentation forces applied to membrane surface nodes marked 'B' in Fig. 5a. Overall, the authors concluded that their model could be very useful in computing cellular structural behavior in response to various in vitro mechanical stimuli, or for the use in algorithms that attempt to stimulate mechanobiological processes.

Based on this model, Bursa and Fuis [2] developed a similar model of adherent eukaryotic cell, consisting of the same structural components and mechanical behavior. As opposed to the tensegrity network modeled in McGarry and Prendergast [19], which could not transmit the loads from the receptors to the nucleus, Bursa and Fuis [2] modeled a more complex tensegrity structure. The structure consisted of both external and internal tensegrities, which represented pre-strained cortical cell cytoskeleton (actin filaments) and the nuclear skeleton, respectively. Interconnecting members, representing deep cytoskeleton, were additionally modeled between the nodes of both external and internal tensegrities. In order to test the ability of their developed model to simulate mechanical tests of individual cells, simulations of tensional test and indentation tests were performed (see example in Fig. 6). Results showed that this improved model is also capable of simulating global load-deformation response of the cell under various types of loadings. In a previous study, Bursa et al. [3] created a similar model of a smooth muscle cell and applied it for simulation of indentation tests as well. However, it included a much simplified tensegrity structure, composing of 66 struts that represented microtubule and 24 cables that represented microfilaments.

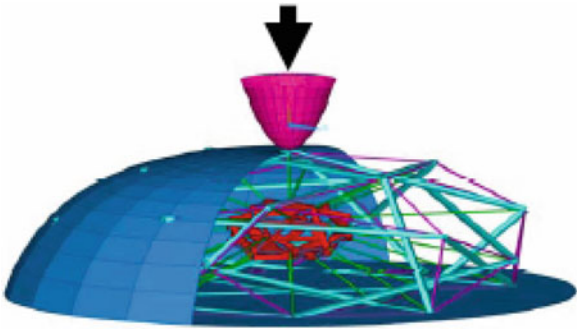

Fig. 6 Finite element model of an indentation tests (reproduced with permission from Bursa and Fuis [2])

Gladilin et al. [11] applied the inverse FE method to simulate uniaxial stretching of a rat embryonic fibroblast model consisting of nucleus and cytoplasm. In this study, the cell contour was based on series of images captured using an inverted microscope during stretching experiments. Geometrical consideration and captured images were combined for the estimation of the location of the nucleus within the cell bulk. Both the nucleus and cytoplasm were modeled as hyperelastic materials, characterized by the generalized Hooke's law:

$$\sigma(\varepsilon) = \frac{E}{1+\upsilon}\left(\frac{\upsilon}{1-2\upsilon} tr(\varepsilon) I + \varepsilon\right) \tag{6}$$

where σ is the Cauchy stress tensor, ε is the strain tensor, E is Young's modulus, and v is Poisson's ratio.

Another non-structural idealized-shaped cell model, of an adherent vascular endothelial cell, was developed by Deguchi et al. [7], in order to show how pre-stress is influential in cell structure subjected to external tensile forces. This model included an individual cell, composed of nucleus, cytoplasm and plasma membrane, adhered to an elastic substrate, stretched in the lateral direction (Fig. 7a). As in previous models, all materials were assumed to be linear elastic, and the effect of pre-stress in the sub-cellular components was assessed using a virtual thermal contraction or expansion, given by:

$$P_s = AT \tag{7}$$

where P_s is thermal strain, A is thermal expansion, and T is change in temperature. Authors investigated the induced mechanical strains in cell components for different combinations of potent mechanical parameters (e.g. pre-stress, elastic modulus and Poisson's ratio), for a substrate stretched under the existence of pre-strain (Fig. 7b). These results were combined with experiments and FE

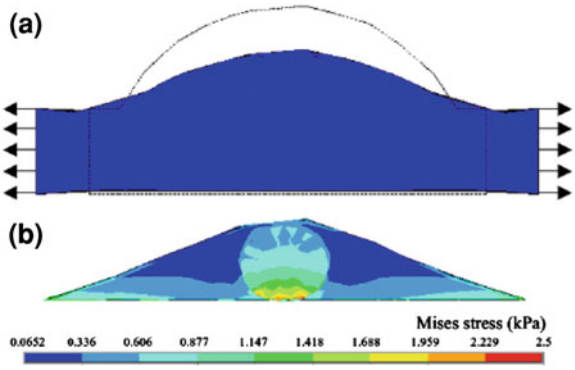

Fig. 7 Finite element simulations of substrate stretching of a cell structure subjected to external tensile forces, via substrate stretching, showing **a** the morphological change of the cell model subjected to stretch and contraction (original shape is marked in *dashed curve*), and **b** the equivalent Von-Mises stress field in the middle cross-section of the cell model, subjected to stretch and cytoplasmic contraction (reproduced with permission from Deguchi et al. [7])

simulations aimed at exploring the effect of the same mechanical parameters used in the stretching simulations on vertical cell morphology.

3.2.2 Image-Based Models

Image-based FE modeling is presently considered a leading biomechanical research methodology at the organ scale [16, 17, 25, 26]. A set of planar images of the organ, obtained by traditional imaging techniques, e.g. magnetic resonance imaging or computed tomography, are used to reconstruct a 3D geometrical model. In order to employ this methodology at a cellular scale and create realistic 3D representation of individual cells, different imaging techniques are required. Ferko et al. [8] have developed integrated methods in fluorescence imaging and image processing for the development of solid models with cell-specific topographies and sub-cellular organelles [9]. They applied these methodologies, along with total internal reflection fluorescence microscopy, to reconstruct a cell-specific endothelial cell model from a cultured confluent monolayer. The cytoplasm of the cell was stained with calcein-AM, and the nucleus was counterstained with Hoechst 33258. Their model included cytoplasm and nucleus, which was assumed to be linear elastic, and focal adhesions, which were represented as discrete attachment points located based on experimental identification. FE simulations of fluid flow and magnetic bead twisting tests were performed in order to calculate stress transmission throughout the cell.

Two additional studies involved reconstruction of 3D realistic cell-specific models; however, these studies utilized confocal microscopy images as the imaging tool of choice. In both studies, z-stack (transverse) parallel confocal images of the cell were taken from the cell base to the cell apex at constant intervals. The consequent images were then imported into a CAD package and loaded into parallel planes at the same z-coordinate intervals obtained from the confocal scans. The 3D geometries of the cell components were subsequently created on the basis of these scanned images. Dailey et al. [5] applied this method to reconstruct 3D morphologically accurate models of alveolar epithelial cells from confocal scans of subconfluent and confluent monolayers, taken at 0.2 μ intervals. The confocal microscopy images were used to obtain cross-sectional boundary curves that defined the apical surface of the cell. Boundary curves were then used to generate a 3D CAD model and surface map of the monolayer. Finally, FE models of individual cells were created. 16 cell models were created: 8 were of cells from a confluent monolayer and the other 8 of cells from subconfluent monolayers. Prior to confocal scanning, the cytoplasm of the cells was stained with calcein-AM. Cell models included cytoplasm and plasma membrane, which were assumed to be linear elastic materials. The models were analyzed for hydrodynamic stresses on the cells for the case of bubble propagation in a fluid-filled parallel-plate flow channel.

Our research group also reported image-based 3D realistic cell-specific models of undifferentiated myoblasts from subconfluent monolayers, based of confocal

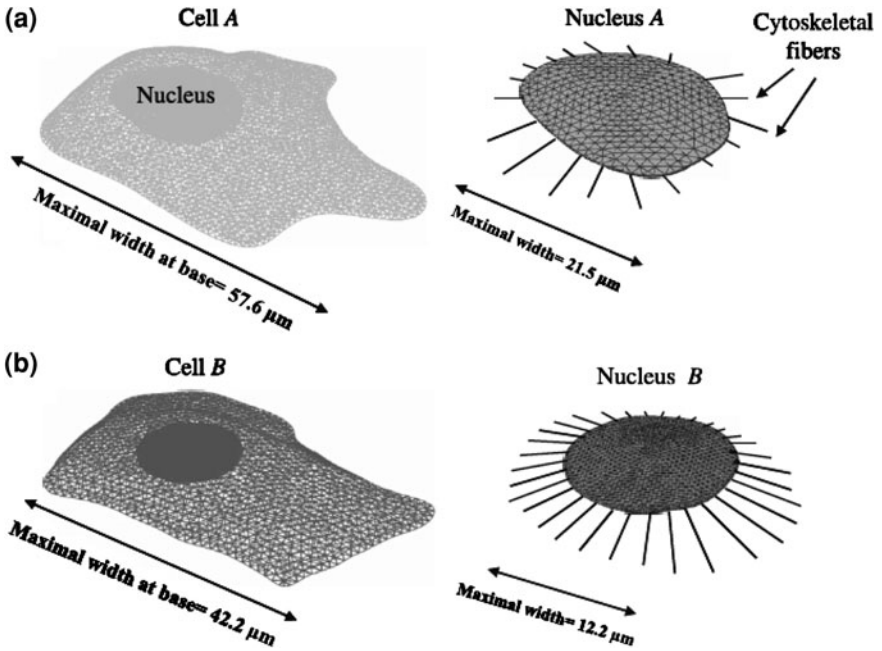

Fig. 8 The finite element meshes of the two modeled myoblasts, A (**a**) and B (**b**). The meshes of the isolated nuclei (with cytoskeletal fibers) are shown on the right frame for each cell (reproduced with permission from Slomka et al. [29])

images of FITC-labeled Phalloidin stained cells taken at 0.4 μ intervals. The contours of the boundaries of cells and their nuclei were manually drawn per each slide and lofted into 3D bodies, by connecting overlying planar slide-contours using splines. The cytoskeletal fibers were incorporated into the confocal-based cell geometries so they connected the nucleus with the plasma membrane, representing bundles of protofilaments. Two cells were modeled, composing of nucleus, cytoplasm, plasma membrane, and cytoskeletal fibers (Fig. 8). The nucleus, cytoplasm, and membrane were assumed to be compressible materials, with a Neo-Hookean SED function (Eq. 3), and the cytoskeletal fibers were assumed to be linear elastic. The cells were subjected to direct compressive and tensional loads, and were analyzed for tensional strains in the plasma membrane and nuclear surface area.

4 Summary and Conclusions

FE modeling of cells is a new direction in cellular mechanics, allowing quantification of deformations, strains and stresses in and around cells, as well as

identification of mechanical properties of cells and cellular organelles when coupled with appropriate experiments. This chapter reviewed relevant reported studies in literature, which applied the FE method to the field of cellular biomechanics and utilized it to simulate experimental designs which are typically used in cellular mechanics, e.g. cell compression, stretching, indentation, micropipette aspiration, magnetic bead cytometry, shear flow and hydrostatic pressure. Up-to-date methodology currently enables 3D image-based cell-specific modeling, including the main sub-cellular components that are considered structurally significant (i.e. nucleus, cytoplasm, plasma membrane, and the cytoskeletal fibers), and that further allows large deformation analyses of cells and subcellular structures [28]. Taken together, the results of the studies reviewed herein indicate that computational modeling of individual cells provides an excellent research tool for predicting structural behaviors and mechanical responses of cells and cell organelles, when subjected to various types of applied stimuli. We expect that such growing use of cell modeling will enrich cellular mechanics studies by providing a better insight into the mechanical and mechanobiological cell responses.

References

1. Baaijens, F.P., Trickey, W.R., Laursen, T.A., Guilak, F.: Large deformation finite element analysis of micropipette aspiration to determine the mechanical properties of the chondrocyte. Ann. Biomed. Eng. **33**, 494–501 (2005)
2. Bursa, J., Fuis, V.: Finite element simulation of mechanical tests of individual cells. In: IFMBE Proceedings WC 2009, pp. 16–19 (2009)
3. Bursa, J., Lebis, R., Janicek, P.: FE models of stress–strain states in vascular smooth muscle cells. Technol. Health Care **14**, 311–320 (2006)
4. Caille, N., Thoumine, O., Tardy, Y., Meister, J.J.: Contribution of the nucleus to the mechanical properties of endothelial cells. J. Biomech. **35**, 177–187 (2002)
5. Dailey, H.L., Ricles, L.M., Yalcin, H.C., Ghadiali, S.N.: Image-based finite element modeling of alveolar epithelial cell injury during airway reopening. J. Appl. Physiol. **106**, 221–232 (2009)
6. De Santis, G., Boschetti, F., Lennon, A. B., Prendergast, P.J., Verdonck, P., Verhegghe, B.: How an eukaryotic cell senses the substrate stiffness? An extrapolation using a finite element model with cytoskeleton modelled as tensegrity structure. In: Proceedings of the ASME 2009 Summer Bioengineering Conference, Resort at Squaw Creek, Lake Tahoe, CA, USA, 17–21 June 2009
7. Deguchi, S., Fukamachi, H., Hashimoto, K., Lio, K., Tsujioka, K.: Measurements and finite element modeling of the force balance in the vertical section of adhering vascular endothelial cells. J. Mech. Behav. Biomed. Mater. **2**, 173–185 (2009)
8. Ferko, M.C., Bhatnagar, A., Garcia, M.B., Butler, P.J.: Finite-element stress analysis of a multi-component model of sheared and focally-adhered endothelial cells. Ann. Biomed. Eng. **35**, 208–223 (2007)
9. Ferko, M.C., Pattersom, B.P., Butler, P.J.: High-resolution solid modeling of biological samples imaged with 3D fluorescence microscopy. Microsc. Res. Tech. **69**, 648–655 (2006)
10. Frisch, T., Thoumine, O.: Predicting the kinetics of cell spreading. J. Biomech. **35**, 1137–1141 (2002)
11. Gladilin, E., Micoulet, A., Hisseini, B., Rohr, K., Spatz, J., Elis, R.: 3D finite element analysis of uniaxial cell stretching: from image to insight. Phys. Biol. **4**, 104–113 (2007)

12. Huang, W., Anvari, B., Torres, J., Lebaron, R., Athanasiou, K.: Temporal effects of cell adhesion on mechanical characteristics of the single chondrocyte. J. Orthop. Res. **21**, 88–95 (2003)
13. Jean, R.P., Gray, D.S., Spector, A.A., Chen, C.S.: Characterization of the nuclear deformation caused by changes in endothelial cell shape, J. Biomech. Eng. 126(5): 552–558 (2004)
14. Jean, R.P., Chen, C.S., Spector, A.A.: Finite-element analysis of the adhesion–cytoskeleton–nucleus mechanotransduction pathway during endothelial cell rounding: axisymmetric model. J. Biomech. Eng. **127**, 594–600 (2005)
15. Leipzig, N.D., Athanasiou, K.A.: Static compression of single chondrocytes catabolically modifies single-cell gene expression. Biophys. J. **94**, 2412–2422 (2008)
16. Lenaerts, L., van Lenthe, G.H.: Multi-level patient-specific modeling of the proximal femur. A promising tool to quantify the effect of osteoporosis treatment. Philos. Trans. A Math. Phys. Eng. Sci. **367**, 2079–2093 (2009)
17. Linder-Ganz, E., Shabshin, N., Itzchak, Y., Gefen, A.: Assessment of mechanical conditions in sub-dermal tissues during sitting: a combined experimental-MRI and finite element approach. J. Biomech. **40**, 1443–1454 (2007)
18. McGarry, J.P.: Characterization of cell mechanical properties by computational modeling of parallel plate compression. Ann. Biomed. Eng. **37**, 2317–2375 (2009)
19. McGarry, J.G., Prendergast, P.J.: A three-dimensional finite element model of an adherent eukaryotic cell. Eur. Cell Mater. **16**, 27–34 (2004)
20. Mijailovich, S.M., Kojic, M., Zivkovic, M., Fabry, B., Fredberg, J.J.: A finite element model of cell deformation during magnetic bead twisting. J. Appl. Physiol. **93**, 1429–1436 (2002)
21. Miyazaki, H., Hasegawa, Y., Hayashi, K.: Tensile properties of contractile and synthetic vascular smooth muscle cells. JSME Int. J. **45**, 870–879 (2002)
22. Ofek, G., Natoli, R.M., Athanasiou, K.A.: In situ mechanical properties of the chondrocyte cytoplasm and nucleus. J. Biomech. **42**, 873–877 (2009)
23. Ohayon, J., Tracqui, P.: Computation of adherent cell elasticity for critical cell-bead geometry in magnetic bead twisting. Ann. Biomed. Eng. **33**, 131–141 (2005)
24. Peeters, E.A.G., Oomens, C.W.J., Boute, C.V.C., Bader, D.L., Baaijens, F.P.T.: Mechanical and failure properties of single attached cells under compression. J. Biomech. **38**, 1685–1693 (2005)
25. Pistoia, W., van Rietbergen, B., Lochmuller, E.M., Lill, C.A., Eckstein, F., Ruegsegger, P.: Image-based micro-finite-element modeling for improved distal radius strength diagnosis: moving from bench to bedside. J. Clin. Densitom. **7**, 153–160 (2004)
26. Portnoy, S., Yizhar, Z., Shabshin, N., Itzchak, Y., Kristal, A., Dotan-Marom, Y., Siev-Ner, I., Gefen, A.: Internal mechanical conditions in the soft tissues of a residual limb of a trans-tibial amputee. J. Biomech. **41**, 1897–1909 (2008)
27. Salvi, J.D., Lim, J.Y., Donahue, H.J.: Finite element analyses of fluid flow conditions in cell culture. Tissue Eng. Part C Methods 16(4): 661–670 (2010)
28. Slomka, N., Gefen, A.: Confocal microscopy-based three-dimensional cell-specific modeling for large deformation analyses in cellular mechanics. J. Biomech. (2010). doi:10.1016/j.jbiomech.2010.02.011
29. Slomka, N., Or-Tzadikario, S., Sassun, D., Gefen, A.: Membrane-stretch-induced-cell death in deep tissue injury: computer model studies. Cell Mol. Bioeng. **2**, 118–132 (2009)
30. Zhao, R., Wyss, K., Simmons, C.A.: Comparison of analytical and inverse finite element approaches to estimate cell viscoelastic properties by micropipette aspiration. J. Biomech. **42**, 2768–2773 (2009)
31. Zeng, D., Juzkiw, T., Read, A.T., Chan, D.W., Glucksberg, M.R., Ethier, C.R., Johnson, M.: Young's modulus of elasticity of Schlemm's canal endothelial cells. Biomech. Model. Mechanobiol. **9**, 19–33 (2010)

Multiscale Computation of Cytoskeletal Mechanics During Blebbing

Sorin Mitran and Jennifer Young

Abstract Cellular blebbing occurs when detachment of the underlying cytoskeleton from a portion of the plasma membrane leads to the formation of protrusions under the influence of cytosol pressure. Blebbing is associated with cellular apoptosis and has been linked to diseased states such as cancer. Multiple phenomena at disparate scales occur during blebbing. At the molecular scale there are biochemical reactions governing actin polymerization, cross-linkage, and formation of membrane adhesion complexes. At the cellular level, forces on the cell membrane lead to deformation of the cytoskeleton and localized mechanical stress. Fluid motion during protrusive activity modifies local concentrations of free actin monomers as well as other molecules that participate in cytoskeleton formation. A computational model of cellular blebbing has to link these disparate scales. In this work a general multiscale interaction procedure is applied to the problem of cellular blebbing. The procedure simultaneously advances in time three models of the cytoskeleton at three different length scales. At the smallest length scale the Langevin dynamics of small actin filament segments is computed by solving stochastic differential equations. At larger scales the cytoskeleton actin network is characterized by probability distribution functions for parameters such as actin filament length and orientation. A Fokker–Planck equation is formulated for the probability distribution functions and advanced in time. At an even larger scale the cytoskeleton is modeled as a continuum, and inhomogeneous elasticity equations are solved. The overall procedure is efficient enough to show cellular level effects produced by changes at the microscopic level, such as biochemical reaction rates.

S. Mitran (✉) and J. Young
Department of Mathematics, University of North Carolina, Chapel Hill, NC 27599-3250, USA
e-mail: mitran@unc.edu

J. Young
e-mail: jendjoy@email.unc.edu

Stud Mechanobiol Tissue Eng Biomater (2011) 4: 345–371
DOI: 10.1007/8415_2010_18

Published Online: 2 December 2010

1 Introduction

The cytoskeleton is the scaffold animal cells use to interact mechanically with the environment. The cytoskeleton provides protection, enables movement, and determines cell shape. It is involved in most cellular processes and abnormalities in the cytoskeleton usually result in disease [34]. The role the cytoskeleton has in combating penetration of the cell by infectious micro-organisms, both mechanical and chemical, is presented in [37]. Hyperactive cytoskeleton reconfiguration has been associated with cancer (Fig. 1), and drugs targeting disruption of the cytoskeleton in cancerous cells are used therapeutically [34].

Qualitative understanding of the physiological role of the cytoskeleton has been rapidly accumulating. A quantitative link between overall mechanical properties of a cell and detailed biochemical reactions or microscopic configuration within the cytoskeleton is still lacking. Much progress has been made in characterizing small portions of the cytoskeleton or in constructing viable coarse grained models. Some of this work is reviewed below. Yet, the ultimate goal of linking therapeutic agents acting on the biochemistry of the cytoskeleton to mechanical properties of the entire cell is not fulfilled.

In this work we propose an approach to the fundamental computational modeling difficulty of describing a system that is not at equilibrium at microscopic scales. Full computational simulation at microscopic scales is prohibitively expensive. Coarse grained simulation at larger scales is incomplete, typically requiring the specification of a time-varying constitutive law that encapsulates missing microscopic information. Here we apply a general algorithm [29] for non-equilibrium multiscale phenomena. The basic approach detailed in Sects. 3–6 is to simultaneously advance forward in time continuum, kinetic, and molecular descriptions of the cytoskeleton. At the continuum level the cytoskeleton is treated as a plastic material with properties that vary in space and time. The kinetic level of description consists of evolution equations for probability distribution functions characterizing the microscopic system. Moments of the probability distribution functions provide constitutive closures needed at the continuum level. Microscopic ensembles constructed from the probability distribution functions are used to

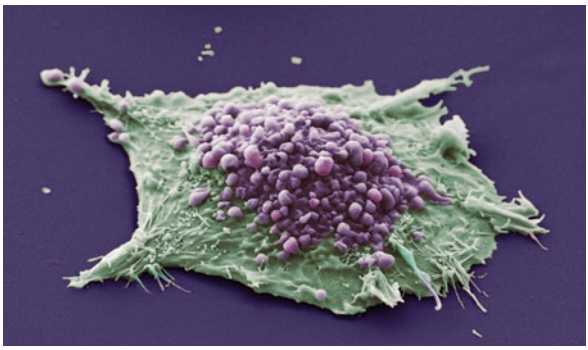

Fig. 1 Carcinoma cell with multiple small blebs. (Image by Anne Weston, London Research Institute, Cancer Research UK, copyright Wellcome Images)

furnish initial conditions for simulations at a quasi-molecular level for small actin segments that makes up the cytoskeleton. The main difficulty in such multiscale computation is information transfer between scales. Minimal entropy changes of the kinetic probability distributions and optimal transport ideas are used in this work.

The presentation is organized as follows. An overview of cytoskeleton structure and current computational models is presented in Sect. 2. Section 3 presents an overview of the overall computational procedure and introduces notation. Section 4 presents the microscopic, kinetic, and continuum models of the cytoskeleton respectively. Some results on the overall model are shown in Sect. 5 and conclusions and further work are presented in Sect. 6.

2 The Cytoskeleton

A typical animal cell is approximately 10 μm in diameter, and consists of organelles (such as the nucleus, mitochondria) suspended in a fluid cytosol surrounded by the cytoskeleton. All of these cellular components are encased by a thin plasma membrane. The cytoskeleton of the animal cell is a complex structure that gives the cell mechanical support and integrity [1, 30]. This dynamic network of intertwined filaments participates in and orchestrates many cellular activities such as cell migration, mitosis, apoptosis and mechanotransduction [30].

2.1 Actin Filaments

The protein polymers that comprise the cytoskeleton include actin filaments, microtubules and intermediate filaments [1, 4, 30], and these fibers are crosslinked to one another by proteins such as filamin and α-actinin [1]. The main types of filaments participating in protrusive activities such as blebbing and lamellipodium formation are actin polymers. Actin filaments are long polymer chains built from actin protein subunits. These subunits are approximately 5 nm in diameter [1]. Free monomers of actin carry a molecule of ATP and are known as G-actin or globular-actin. When a G-actin subunit joins a growing polymer chain the ATP molecule is hydrolyzed into ADP and the subunit is attached. The actin protein in filament form is known as F-actin (filamentous-actin). Actin filaments have different rates of growth and shrinkage at their two ends. The "plus" end has a faster rate of elongation and shortening than the "minus" end [1]. The subunits in a filament are held together by weak, noncovalent bonds that can be broken by thermal fluctuations [1]. Actin subunit chains are often bound together in parallel to form a stronger double-stranded helical structure.

Filament length can vary depending on cell type, but they generally are 1–20 μm long and about 8 nm wide [4, 21]. They can be as long as 50–100 μm

in muscle cells [20], and as short as 0.2–0.35 μm in cytoskeleton meshes [8]. In either case, they are several orders of magnitude longer than they are wide.

Actin filaments are classified as semi-flexible polymers [21]. A single actin filament can withstand an elongation force of about 110–250 pN before breaking, and it only stretches about 0.2–0.3% under these forces [21]. It has a stiffness of approximately 45–65 pN/nm for actin filaments of length 1 μm [21]. On average, the Young's modulus of an actin polymer is 0.5 to 2×10^9 N/m^2 [4, 21]. In comparison to stretching, actin filaments bend quite easily. Their flexural rigidity has been found to be on the order of 10^{-26} N/m^2, based on a persistence length of 10–20 μm [4]. This large difference in magnitude between the stretching and bending properties of actin filaments allows them to be classified as an elastic string for modeling purposes.

The total number of actin filaments within a cell varies by cell type and concentration levels of actin. In red blood cells, actin fibers form a one to two filament thick network of short filaments [39]. This amounts to approximately 120,000–300,000 short actin filaments in a red blood cell cytoskeleton. Boal estimates that cells with high actin densities of 5 mg/ml or more, have approximately 1.9×10^{20} filaments length 1 μm^3 [4]. This translates to about 200,000, 1 μm filaments in a 10 μm diameter animal cell.

2.2 Filament Networks

The cytoskeleton is a mesh-like actin structure with crosslinks formed by proteins such as spectrin and filamin. Spectrin is a long 100 nm, flexible protein found close to the intracellular side of the plasma membrane. Two spectrin molecules link together head to head to create two actin filament binding sites that are spaced approximately 75–200 nm apart depending if the spectrin polymer is in a convoluted position or stretched out straight [1, 4]. This distance is quite large compared to the other proteins which bind actin bundles in tight configurations about 14–30 nm apart, and leads to large flexibility in the cytoskeleton. For example, the ability of red blood cells to deform enough to squeeze through capillaries is associated with the low spectrin spring constant of approximately 2×10^{-6} J/m^2. Filamin is another binding protein that crosslinks two filaments together almost at right-angles to one another forming a loose grid of actin polymers [1, 30]. Filamin is also found binding the actin mesh to the plasma membrane in platelets.

Binding of the actin network to the plasma membrane is also accomplished by other proteins. In muscle cells, the dystrophin protein carries out this role. In red blood cells, a protein in the plasma membrane known as band 3 attaches to another protein called ankyrin which in turn attaches to the spectrin proteins on the cytoskeleton [1]. Other adhesive proteins include ezrin, radixin, and moesin [1] (Fig. 2).

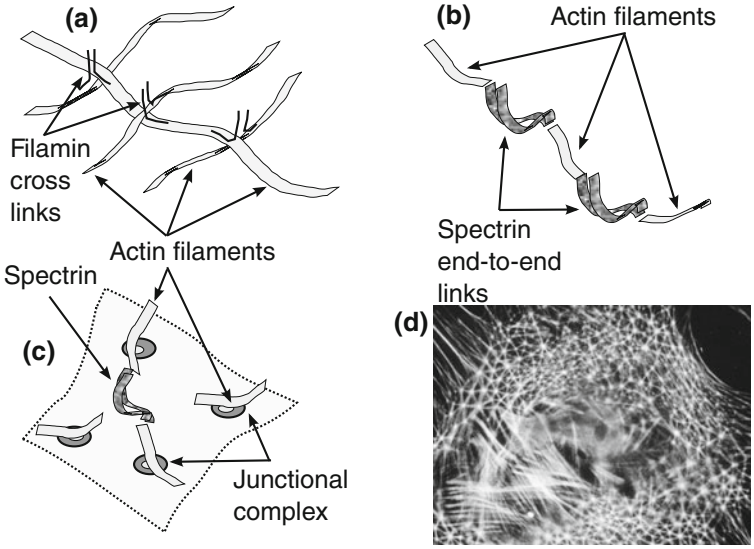

Fig. 2 Diagrams of actin network formation and attachment to plasma membrane. **a** Almost right-angle filamin crosslinks between actin filaments. **b** Spectrin end-to-end links. **c** Attachment to plasma membrane. **d** Micrograph of cytoskeleton in a fibroblast (Catherine Nobes and Alan Hall, copyright Wellcome Images)

The cytoskeleton is typically between 5 nm and 2-microns thick [11, 39]. The size of the gaps in the actin mesh range from 10 to 100 nm [12, 38, 40], depending on cell type. The aggregate elastic moduli of an actin network differ markedly from the single filament values. For instance, the estimated Young's modulus for 1 mg/ml of crosslinked F-actin is 100, 000 dyn/cm^2 which is 10 kPa and the shear modulus is approximated at 1, 000 dyn/cm^2 or 100 Pa [21]. Charras et al. [12] estimated the elastic modulus of the actin cortex in a filamin-depleted melanoma cell line to be 1–3 kPa. In general, the Young's modulus for the actin network is lower than the individual actin filaments. This is due to the fact that crosslinking proteins such as spectrin are more elastic than actin, so they make the overall mesh less stiff.

The cytoskeletal network is acted upon by myosin II motor proteins that produce forces between actin filaments [1, 24, 28, 33]. Such forces play a central role in the cell's protrusive and locomotive activities. Myosin II, like actin, is found in all eukaryotic cells [1]. Myosin II is a long protein composed of two heavy chains and two light chains. Near the end of the two heavy chains is a "head" region from which forces can be generated [1]. Myosin II subunits join to form a filament by bundling their tails together. This creates a bipolar filament with myosin heads facing in opposite directions along the fiber. Alternating myosin heads can attach to actin and exert a force ranging from 0.8 to 8 pN [4, 12, 41].

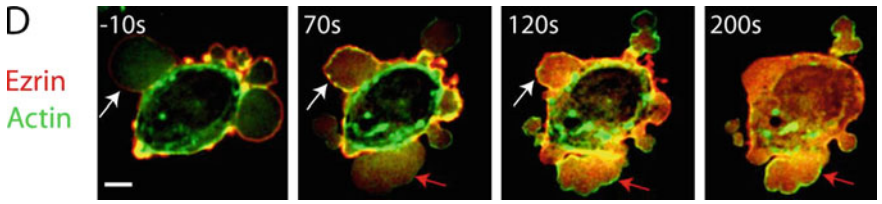

Fig. 3 An expanding and retracting bleb. Actin is labelled in *green*. After the bleb has fully inflated (frame 2), actin that arrives in the bleb builds a new cortex leading to bleb retraction [11]

2.3 Cellular Blebbing

Breakdown, rearrangement and rebuilding of the cytoskeleton produces various types of cellular protrusions which include lamellipodia, microvilli and blebs. A bleb is a balloon-like, cytosol-filled protrusion of the plasma membrane. Unlike lamellipodia and microvilli, this type of protrusion is not formed by active growth and rearrangement of the cytoskeleton [12, 14]. The onset of bleb formation is triggered by a contraction of the actin network, such that it detaches from the plasma membrane over some region. A gap size of 0.5–1 μm in the cytoskeleton/membrane connections is enough to initiate bleb formation [39]. Once a gap is formed, the typical 20–300 Pa [10, 35] overpressure in the cytosol with respect to ambient leads to bleb formation in 3–7 s. Typical bleb diameters range from 1 to 10 μm [11]. The bleb stays fully inflated for about 10–20 s. After this time interval, enough free actin monomers have begun to reorganize the cytoskeleton inside the bleb for retraction to occur [11]. The new cortex is built to a thickness of 10–20 nm (3–4 actin filaments thick) with gap sizes of approximately 200 nm [11] (see Fig. 3). Myosin II, present in this new cytoskeleton, creates contractions which pull the blebbed membrane inward to be reattached to the base cytoskeleton [11, 24].

2.4 Computational Challenges

The main difficulty in building realistic computational models of the cytoskeleton is the large number of filaments, the role of binding and motor proteins, and the dynamic nature of the network. Homogenized models of the cytoskeleton treated as a continuum are of limited utility since the elastic properties change in time as new links are formed and broken between actin filaments at a microscopic level. There are about 10^5 one-micron long filaments in a typical cell [4]. The filaments are crosslinked and the typical length of a filament segment between crosslinks is on the order of 100 nm [43]. This means there are approximately 10^6 filament segments in the cytoskeleton and roughly 5×10^5 crosslink protein complexes. The time scale of the cytoskeleton network is set by rate constants for actin polymerization, binding of various proteins to the network, myosin stepping rates,

and the elastic behavior of individual actin filaments. Time steps on the order of 10^{-6} s are required to capture all mentioned phenomena, leading to 3×10^7 time steps over the 30-s duration of a typical bleb. Evolving a system with approximately $N = 3 \times 10^6$ degrees of freedom over 3×10^7 time steps is prohibitively expensive since crosslink formation implies a computational complexity of the algorithm of $\mathcal{O}(N^2)$.

2.5 Current Work on Cytoskeleton

Given the aforementioned difficulties of direct numerical simulation at the scale of actin segments, much prior work has focused on constructing simplified models. A more complete review is available in the book by Kamm and Mofrad [23].

2.5.1 Coarse Grained Models

Coarse graining of the cytoskeleton degrees of freedom has been used by Li et al. [26] and Pivkin et al. [32] to create models of the red blood cell cytoskeleton during deformation. Simplification of the network geometry has been investigated by Boey et al. [5] using a sixfold, two-dimensional network. Palmer et al. [31] use the eight-chain symmetric network proposed by Arruda and Boyce [3] to deduce a constitutive model for the stress–strain relationship of actin networks which compares favorably with experimental work of Gardel et al. [15].

2.5.2 Detailed Microscopic Models

The coarse-grained models gloss over the details of the microscopic structure. To elucidate whether this is an acceptable hypothesis several research groups have undertaken the task of thoroughly modeling a small portion of the cytoskeleton to understand its mechanical response to various stresses. Kwon et al. [25] consider a 400^3 nm^3 block with approximately 100 crosslinked filaments of 350 nm length represented as elastic Euler–Bernoulli beams to determine the components of a general elastic tensor C_{ijkl} in the linear elasticity regime $\sigma_{ij} = C_{ijkl}\varepsilon_{kl}$ (σ, stress tensor; ε, strain tensor). The model performs well for isotropic and nearly isotropic systems, but exhibits large errors when the distribution of filament orientations is far from uniform. In a similar study, Huisman et al. [18] create an actin network model to examine its mechanical behavior under shear strain. The filaments were found to reorient themselves in the direction of applied shear, and the computed shear stiffening was compared to experimental findings. They conclude that the response of the network is highly dependent upon the topology of the filament mesh. Head et al. [16] explore the response of two-dimensional model networks to extensional and shear stresses to determine how strain is distributed in such

networks, dependent on crosslink density and filament length. They distinguish two distinct regimes, one where strains are uniformly distributed (affine deformation) and another in which strains are non-uniformly distributed (non-affine deformation). Buxton et al. [7] recently present a dynamic computational model in which an initial network comprising 100 one-micron long actin filaments undergoes polymerization and depolymerization. The filaments can also undergo capping, severing and crosslinking. The network develops until it reaches a statistical steady state and is then placed under shear stress in order to examine its mechanical response. Different networks were built based on different actin dynamics rates, and the mechanical responses of these networks were compared. The networks upon which these simulations were carried out typically consisted of approximately 10^2–10^3 filaments of lengths 2–9 μm, with about 10^3 crosslinks connecting them. Each simulation took about 100 h of CPU time.

2.5.3 Tensegrity Models

The tensegrity (tensional integrity) model of the cell was introduced in 1993 by Ingber in [19] to model the deformation of cells adhering to a substrate. This model consists of two types of prestressed elements: interconnected tension-bearing elements which represent the actin filaments of the cytoskeleton and compression-bearing elements, which represent microtubules [40]. This model assumes that the cell's shape and integrity derives from the cytoskeleton, an active mechanical structure capable of producing tension. The model is successful at capturing the strain-hardening observed in cells spreading over a substrate. However, it does not address the cytoskeleton's ability to rearrange and remodel itself during deformation. Stamenovic et al. [40] used this tensegrity model to analytically compute upper and lower bounds for the Young's modulus of cells. They compare their results against experimental data, finding that the empirical moduli in general fall within their theoretically derived bounds.

2.5.4 Continuum Models

The models discussed so far have been discrete in nature, characterizing the cytoskeleton as a network of crosslinked filaments. There is also a body of research dedicated to the treatment of the cytoskeleton as a continuum. Alt and Dembo [2] use a two-phase fluid description of the cytoplasm in ameboid cells. The cytosol (water-like substance within the cell) is represented as a Newtonian fluid, and the cytoskeleton is represented as a highly viscous, polymeric fluid. This characterization is used under the assumption that the crosslinks in the cytoskeleton are constantly rearranging, allowing the network to adapt and move easily (like a fluid). This model is used to simulate the formation of a lamellipodium during cell migration. During this phenomenon, the cytoskeleton undergoes many structural rearrangements. The model of Alt and Dembo is used for understanding

the general stages of this process. Charras et al. [9, 12], characterize the cytoskeleton as a solid porous medium. They propose that the actin network with interspersed cytoplasmic fluid should be thought of as a "sponge" with pressure diffusion occurring over time. They demonstrate experimentally that localized contractions of the actin mesh can create local pressure increases that do not instantaneously equilibrate across the cell. They develop a linear constitutive law for the cytoskeleton/cytosol complex using concepts from mixture theory. The stress–strain relationship is of the form: $\sigma = E\varepsilon - p$, with σ the stress, E the bulk elasticity modulus, ε the strain, and p the fluid pressure. Darcy's law for flow through porous media is used to update the fluid pressure term. Their theoretical model was developed to explain the cellular phenomenon of bleb formation.

2.6 Open Questions in Computational Cytoskeleton Models

The fundamental difficulty in all the above models is that experimental observations of cellular cytoskeletons highlight the dynamic nature of the network. While homeostatic behavior might reasonably be captured by coarse grained models, there is significant interest in large changes in cytoskeleton configuration since such changes are often associated with diseased states. Elucidating cytoskeleton behavior in such situations might suggest therapeutic approaches. The continuum models of Alt and Dembo [2] and Charras et al. [9, 12] represent the microstructure of the polymer network through a constitutive closure law. This constitutive law is complex and time-varying, and dependent on the microstructure of the medium. Without representing this microstructure in some way, the models in [2] and [9] do not reflect the changes and rearrangements occurring in the cytoskeleton that lead to varying mechanical properties. The detailed microscopic models that treat small portions of the cytoskeleton provide a great deal of insight into the mechanical response of small patches of actin networks, but do not apply to the entire cellular network due to the inhomogeneity and anisotropy of the cytoskeleton. Huisman et al. [18] specifically state that the stiffness response of the network is highly dependent on the concentrations of the different proteins in the cytoskeleton. These protein levels can certainly vary in different parts of the cortex as the cell undergoes locomotion and shape change. The detailed microscopic models also highlight the consequences of increasing anisotropy as the cytoskeleton is observed at smaller scales, especially the non-affine distribution of strain.

3 Overview of Computational Procedure

As seen from the previous section the main challenge in quantitative cytoskeleton modeling is efficient coupling of phenomena occurring at different length scales.

The cell is subject to forces that vary over a length scale comparable to the cell diameter $D = \mathcal{O}$ (10 μm). The response to these forces is a rearrangement of the actin filaments forming the cytoskeleton at the scale of average mesh spacing $l = \mathcal{O}$ (100 nm). The cytoskeleton rearrangement response is at time scales comparable to those arising from continuum level unsteady forces during protrusion and blebbing. There is no time scale separation and the microscopic configuration of the cytoskeleton is not at equilibrium.

In this work we apply a general multiscale interaction procedure, the time-parallel continuum–kinetic–molecular (tP-CKM) algorithm [29]. This algorithm is specially constructured to treat processes not at equilibrium at the microscale. A short overview of the algorithm is presented here, with further details available in [29]. The algorithm is constructed from three solvers for each length scale, and procedures for interscale communication. The three solvers are as follows.

1. *Continuum-level solver*. This may be any numerical approximation procedure for PDEs, e.g. discontinuous Galerkin, finite difference, finite volume. A finite volume procedure is exemplified here. The continuum variables are denoted by $\boldsymbol{Q}(\boldsymbol{x}, t)$. The evolution operator that advances the continuum variables from time t to time $t + \Delta t$ at position $\boldsymbol{x}$ is denoted by $\boldsymbol{C}$,

$$\boldsymbol{Q}(\boldsymbol{x}, t + \Delta t) = \boldsymbol{C}(t, t + \Delta t, \boldsymbol{Q}(\boldsymbol{x}, t), \psi(\boldsymbol{x}, t, \boldsymbol{q})). \tag{1}$$

   The continuum operator depends on the microscopic configuration described by the probability distribution function (p.d.f.) $\psi \boldsymbol{x}, t, \boldsymbol{q})$ for the microscopic variables $\boldsymbol{q}$. Typically only a few integrals of $\psi(\boldsymbol{x}, t, \boldsymbol{q})$ are required,

$$\int g_i(\boldsymbol{q})\psi(\boldsymbol{x}, t, \boldsymbol{q})\mathrm{d}\boldsymbol{q} = G_i(\boldsymbol{x}, t), \quad i = 1, 2, \ldots, M. \tag{2}$$

   The specific form of $g_i(\boldsymbol{q})$ is problem-dependent.
2. *Kinetic-level solver*. The p.d.f. $\psi(\boldsymbol{x}, t, \boldsymbol{q})$ can be constructed from known microscopic transition probabilities between states $(\boldsymbol{q}', t')$ and $(\boldsymbol{q}, t)$,

$$P(\boldsymbol{q}, t|\boldsymbol{q}', t'). \tag{3}$$

   Some specific physical model of the microscopic system furnishes $P(\boldsymbol{q}, t|\boldsymbol{q}', t')$. At some later time $t + \Delta t$ the p.d.f is given by

$$\psi(\boldsymbol{x}, t + \Delta t, \boldsymbol{q}) = \int P(\boldsymbol{q}, t + \Delta t|\boldsymbol{q}', t)\psi(\boldsymbol{x}, t, \boldsymbol{q}')\mathrm{d}\boldsymbol{q}'. \tag{4}$$

   The transition probabilities can be characterized in various ways. One choice is to use the moments of the random variables $\boldsymbol{q} = (q_1, \ldots, q_m)$. Assume, for simplicity of presentation, that the components of $\boldsymbol{q}$ are independent. Then the moments can be expressed as

$$\boldsymbol{\mu}_n(\boldsymbol{q}', t, \Delta t) = \int (\boldsymbol{q} - \boldsymbol{q}')^n P(\boldsymbol{q}, t + \Delta t|\boldsymbol{q}', t)\mathrm{d}\boldsymbol{q}, \tag{5}$$

and Taylor series expansion leads to

$$\boldsymbol{\mu}_n(\boldsymbol{q},t,\Delta t)/n! = \boldsymbol{D}^{(n)}(\boldsymbol{q},t)\Delta t + \mathcal{O}(\Delta t^2). \tag{6}$$

This Kramers–Moyal expansion leads to the evolution equation

$$\frac{\partial \psi(\boldsymbol{x},t,\boldsymbol{q})}{\partial t} = \sum_{n=1}^{\infty}\left(-\frac{\partial}{\partial \boldsymbol{q}}\right)^n \boldsymbol{D}^{(n)}(\boldsymbol{q},t)\psi(\boldsymbol{x},t,\boldsymbol{q}). \tag{7}$$

The Fokker–Planck equation [36] arises from probability distribution functions completely characterized by the first two expansion coefficients $\boldsymbol{D}^{(1)}(\boldsymbol{q},t), \boldsymbol{D}^{(2)}(\boldsymbol{q},t)$.

3. *Molecular-level solver*. At the molecular level the system is assumed to be described by stochastic differential equations for the microscopic variables $\boldsymbol{q}(t)$. The time evolution operator is denoted by $\boldsymbol{M}$,

$$\boldsymbol{q}(t+\delta t) = \boldsymbol{M}(t, t+\delta t, \boldsymbol{q}(t)). \tag{8}$$

The relationship between continuum and microscopic variables will depend on the specific physical problem considered.

The tP-CKM algorithm advances the above solvers as depicted in Fig. 4. The overall goal is to advance the continuum variables over the time step $[t^k, t^{k+1}]$. The spatial dependence on $\boldsymbol{x}$ is suppressed for simplicity of presentation. Initial values for the continuum variables $\boldsymbol{Q}(t^k)$ and the p.d.f. $\psi(t^k, \boldsymbol{q})$ are assumed to be known from either a previous time step or physically specified initial conditions. The following steps are taken in the algorithm:

1. A continuum closure relation is computed from $\psi(t^k, \boldsymbol{q})$ using (2).
2. The continuum variables are advanced to time t^{k+1} using (1).
3. A new p.d.f. estimate at t^{k+1} is constructed, $\bar{\psi}^{(0)}(t^{k+1}, \boldsymbol{q})$, through a minimum entropy change with respect to $\psi(t^k, \boldsymbol{q})$ that reflects new continuum values. The

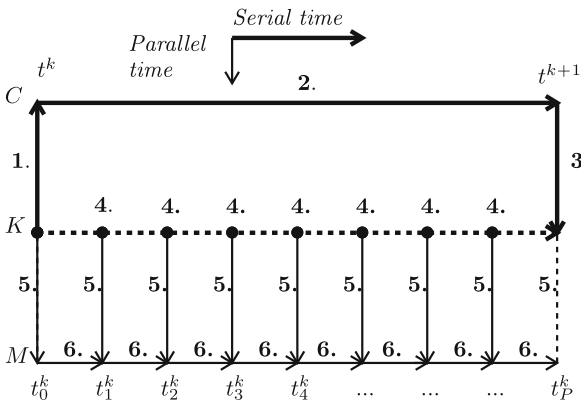

Fig. 4 Schematic of tP-CKM algorithm. *Boldface numbers* correspond to algorithm steps described in text. Portions of the algorithm executed serially in time depicted with *bold arrows*. Portions of the algorithm executed parallel in time depicted with *lighter arrows*

zero superscript indicates that this is a first approximation in an iterative refinement update.

4. The time interval $[t^k, t^{k+1}]$ is subdivided by intermediate time values $\{t^k = t_0^k, t_1^k, \ldots, t_P^k = t^{k+1}\}$. At each intermediate time value an estimate, $\bar{\psi}^{(0)}(t_j^k, \boldsymbol{q})$, of the p.d.f. is constructed using optimal transport theory.
5. From each approximate p.d.f. $\bar{\psi}^{(0)}(t_j^k, \boldsymbol{q})$ molecular-level ensembles $\mathcal{E}_j(t_j^k)$ are constructed.
6. The molecular-level ensembles are evolved forward in time to state $\mathcal{E}_j(t_{j+1}^k)$.
7. A density estimation procedure is applied to the updated molecular-level ensembles to obtain a new estimate of the p.d.f. based upon molecular level information, $\tilde{\psi}^{(0)}(t_{j+1}^k, \boldsymbol{q})$.
8. The p.d.f. estimates from minimal entropy modification and optimal transport are compared to those from the molecular level computation at the end of the continuum time step by computing an error

$$\varepsilon^{k+1} = \|\bar{\psi}^{(0)}(t^{k+1}, \boldsymbol{q}) - \tilde{\psi}^{(0)}(t^{k+1}, \boldsymbol{q})\|. \tag{9}$$

If within some tolerance, the continuum time step is accepted, and the new p.d.f. is also available for the next time advancement to t^{k+2}. If the error is too large, steps 3–7 are repeated.

The kinetic-molecular part of the algorithm can be seen as a multiphysics generalization of the parareal algorithm [27] for time-parallel solution of systems of ordinary differential equations. Whereas the parareal algorithm uses two different numerical discretizations of the same ODE system, the tP-CKM algorithm uses two different mathematical models of the same underlying physical system. One description is through p.d.f.'s describing the microscopic variables, and another description is through direct numerical simulation at the microscopic level.

Though apparently costly, the tP-CKM algorithm can be made computationally efficient by:

1. time-parallel execution at the kinetic level using P processors that work independently over each subinterval $[t_j^k, t_{j+1}^k]$;
2. further massive parallelization of the stochastic differential equations (SDEs) at the molecular level through use of modern graphics processing units (GPUs).

The iterative refinement comprising steps 3–7 of the algorithm builds ever more accurate estimates of the p.d.f.'s at times $\{t_1^k, \ldots, t_P^k\}$. The hope is that much fewer than P refinement stages will lead to an acceptable precision in (9). Indeed if P refinement stages are needed, then the physical system would have been evolved at the microscopic level over the entire continuum time step $[t^k, t^{k+1}]$ and nothing would have been gained by the multiscale interaction procedure. Numerical experiments reported below show that very few iterative refinement stages (e.g. 1–3) are needed to obtain 3–4 significant digits of precision in continuum-level variables. The time-parallelization allows large numbers of processors to be used, e.g. $P \simeq 1{,}000$ leading to significant reductions in wall-clock execution time.

One of the key aspects of such a continuum–kinetic–molecular (CKM) algorithm is the set of procedures for communicating data between different levels of description. For the continuum-to-kinetic step these procedures are:

1. A minimum entropy modification of the kinetic-level p.d.f. at time t^{k+1} to reflect information available from the continuum level;
2. Modification of the p.d.f. at times $\{t_1^k, \ldots, t_{P-1}^k\}$. by use of optimal transport theory.

A brief description of each procedure is provided here with fuller details available in [29].

3.1 Minimal Relative Entropy Modification

Consider the Kullback–Leibler [13] relative entropy functional

$$H(\psi^{k+1}, \psi^k) = \int \psi^{k+1} \log\left(\frac{\psi^{k+1}}{\psi^k}\right) \mathrm{d}\boldsymbol{q}, \tag{10}$$

which expresses the "information distance" of ψ^{k+1} with respect to ψ^k (note that it is not a distance function in the mathematical sense). After taking a continuum time step, new constraints are imposed on ψ^{k+1}. By this means boundary conditions at the continuum-scale are efficiently transferred to kinetic and hence microscopic scales. The general form of a constraint is

$$\int f_i(\boldsymbol{q}) \psi^{k+1}(\boldsymbol{q}) \mathrm{d}\boldsymbol{q} = F_i(\boldsymbol{Q}^{k+1}), \quad i = 1, 2, \ldots, L. \tag{11}$$

We seek to determine the p.d.f. that has the minimum information change with respect to the previous time step but reflects the new constraints. Instead of solving the constrained optimization problem, Lagrange multipliers $\lambda_i, 1 \leqslant i \leqslant L$ are introduced and the unconstrained problem

$$\inf_{\lambda_i} \sup_{\psi} \left[-H(\psi|\psi^k) + \sum_{i=1}^{L} \lambda_i \left(\int f_i(\boldsymbol{q}) \psi^{k+1}(\boldsymbol{q}) \mathrm{d}\boldsymbol{q} - F_i(\boldsymbol{Q}^{k+1}) \right) \right], \tag{12}$$

is solved.

3.2 Optimal Transport of Probability Density

The minimal entropy modification problem (12) is rather expensive to solve computationally because of the large-dimensional phase–space integrals of the form $\int \mathrm{d}\boldsymbol{q}$, especially in the context of rapidly providing estimates of a p.d.f. at the

intermediate times $\{t_1^k, t_2^k, \ldots, t_{P-1}^k\}$. in order to carry out time parallel computations. An immediate idea would be to carry out linear interpolation between ψ^k and $\bar{\psi}^{k+1}$. In the context of solving Fokker–Planck equations at the kinetic level, this would basically correspond to linear response theory [36].

It is however of interest to construct better intermediate estimates given the endpoint p.d.f.'s $\psi^k, \bar{\psi}^{k+1}$, especially estimates that capture the microscopic physics of the system. Optimal transport theory [42] can be used to this end.

Given $\mu : A \rightarrow \mathbb{R}$, $\nu : B \rightarrow \mathbb{R}$, two p.d.f.'s, the optimal transport problem is to find a transference plan $T : A \rightarrow B$, such that for any subset $P \subset A$, whose image under the transference plan is $T(P) \subset B$, we have

$$\int\limits_{x \in P} \mu(x) \mathrm{d}x = \int\limits_{y \in T(P)} \nu(y) \mathrm{d}y. \tag{13}$$

Assuming T is a differentiable mapping, $T \in C^1(\mathbb{R}^d)$, the integral condition (13) implies the differential equation

$$\det(\nabla T(x)) \nu(x) = \mu(x), \tag{14}$$

which is nothing more than the usual change-of-variable theorem in integral calculus.

Since there exist infinitely many differentiable mappings for which (14) holds, an optimization problem can be posed, in which a specific mapping is sought that has some desirable properties. One possibility is to introduce a distance between the two p.d.f.'s μ, ν as exemplified by the Wasserstein distance

$$d_p(\mu, \nu) = \left(\inf_T \int |T(x) - x|^p \mu(x) \mathrm{d}x \right)^{1/p}, \tag{15}$$

$d_p : A \times B \rightarrow \mathbb{R}$. The optimization (15) then seeks the transference plan closest to the identity mapping.

A number of remarkable results have shown the connection between optimal transport and several physical processes such as various types of fluid flow [6]. Here we focus on a result by Jordan, Kinderlehrer and Otto (JKO) [22] establishing a link between optimal transport and solutions of a Fokker–Planck equation. Consider a Fokker–Planck equation of the form

$$\frac{\partial \psi}{\partial t} = \frac{\partial}{\partial \boldsymbol{q}} \cdot \left(\frac{\partial \Phi}{\partial \boldsymbol{q}} \psi \right) + \frac{1}{\beta} \frac{\partial}{\partial \boldsymbol{q}} \cdot \frac{\partial \psi}{\partial \boldsymbol{q}}, \tag{16}$$

with $\Phi(\boldsymbol{q})$ a potential function in phase space. Associated with the p.d.f. $\psi(\boldsymbol{q})$ the free energy $F(\psi)$, internal energy $E(\psi)$ and entropy functionals $S(\psi)$ can be defined,

$$F(\psi) = E(\psi) + \frac{1}{\beta} S(\psi), \tag{17}$$

$$E(\psi) = \int \Phi(q)\psi(q)dq, S(\psi) = \int \psi(q)\log\psi(q)dq. \tag{18}$$

Let ψ_j^k be p.d.f.'s defined at the intermediate times t_j^k in the time interval $[t^k, t^{k+1}]$ with the constant spacing Δt. The JKO result [22] states that if the intermediate time $\psi_j^k(\boldsymbol{q})$ is chosen as the solution of the minimization problem

$$\min_{\psi}[\mathcal{F}(\psi)] = \min_{\psi}\left[\frac{1}{2}d_2\left(\psi^{(n-1)}, \psi\right) + (\Delta t)F(\psi)\right], \tag{19}$$

then in the limit $\Delta t \to 0$ we have

$$\psi\left(t_j^k, \boldsymbol{q}\right) = \psi_j^k, \tag{20}$$

meaning that the solution of the minimization problems (19) is also the solution of the Fokker–Planck equation (16). Furthermore, at each point in time in the $[t^k, t^{k+1}]$ interval, the evolution of the solution to the Fokker–Planck equation follows the steepest descent direction of the function in (19).

This result is applied in the tP-CKM algorithm to construct nonlinear interpolations of p.d.f.'s at intermediate time steps. Consider a representation of the time-varying p.d.f. as

$$\psi(\boldsymbol{q}, t) = \sum_{l=1}^{N_B} c_l(t)B_l(\boldsymbol{q}), \tag{21}$$

with $B_l(\boldsymbol{q})$ some set of basis functions in phase space. Simple linear interpolation between times would lead to intermediate expansion coefficient values

$$c_l\left(t_j^k\right) = \frac{t_j^k - t^k}{t^{k+1} - t^k}\left[c_l\left(t^{k+1}\right) - c_l(t^k)\right] + c_l(t^k). \tag{22}$$

We can however exploit the steepest descent property from the JKO theorem to specify that the tangent direction of the interpolation of $\psi(\boldsymbol{q}, t)$ in the space of coefficients c_l is given by the direction

$$\nabla_c \mathcal{F}(\psi). \tag{23}$$

With this information, a cubic interpolant can readily be constructed. A schematic of the difference between linear interpolation and the interpolation based on free-energy minimization is shown in Fig. 5. The principal benefit of this higher-order interpolation procedure is the reduction of iterative refinements between the kinetic and molecular stages.

4 A tP-CKM Model of the Cytoskeleton

We apply the computational framework described above to the problem of cytoskeleton mechanics. There is considerable scope for choosing a model at each

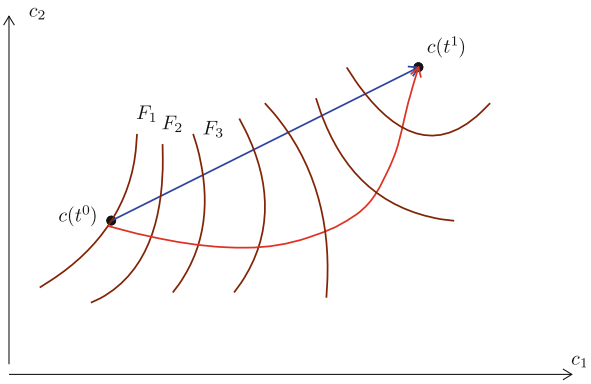

Fig. 5 Comparison between linear interpolation of p.d.f.'s in c-space and cubic interpolation based upon minimization of free energy

length scale, and the choices described are just one option, mainly made to obtain as simple a description as possible for this initial application of the tP-CKM algorithm to cytoskeleton mechanics. In particular we restrict attention to two-dimensional microscopic and one-dimensional continuum models at present.

4.1 Geometric Description of Cell Membrane, Cytoskeleton

The cell membrane is represented as a piecewise linear closed curve defined by points (X_i, Y_i), $i = 0, \ldots, N_m$. A curvilinear coordinate s is defined along the cell membrane. The cytoskeleton is assumed to be situated in a shell inside the cellular membrane and to have an average thickness $d(s)$. At the junction an outward pointing normal to the cell membrane $\mathbf{n}$ is defined along the bisector of the intersecting line segments. Displacement towards the interior of the cell by distance $d(s)/2$ defines a cytoskeleton centerline. The choice of a piecewise linear representation is motivated by the desire to capture deformations of arbitrary complexity (Fig. 6).

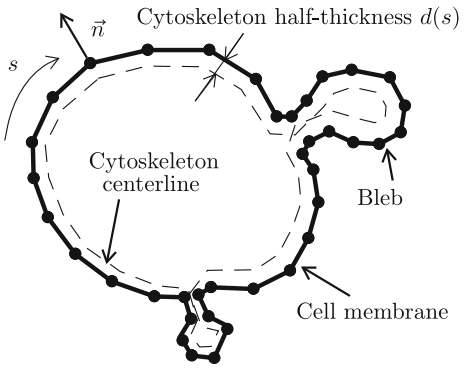

Fig. 6 Sketch of cellular membrane, cytoskeleton centerline

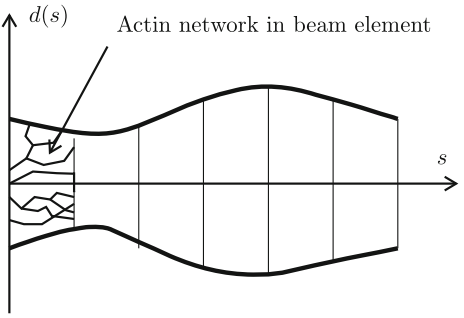

Fig. 7 Sketch of variable thickness beam composed of cross-linked filament elements model of cytoskeleton

The piecewise linear representation for the cellular membrane defines elements B_i from point (X_{i-1}, Y_{i-1}) to (X_i, Y_i), $i = 1, \ldots, N_m$. Each element has an average thickness d_i. At the continuum scale elements B_i are one-dimensional elastic bodies akin to nonlinear beams. At the microscopic scale each element B_i is formed from numerous actin filaments cross-linked in a network (Fig. 7).

4.2 Microscopic Description

A model for the formation and evolution of the actin network must be specified. This is done separately for each element B_i of the cytoskeleton that extends from s_{i-1} to s_i. Starting from s_{i-1}, N_f random walks with step-length a are generated by the following procedure.

1. Draw a direction θ from a probability distribution function ψ_θ.
2. Advance the random walk by a along direction $(\cos\theta, \sin\theta)$. Associate actin filament stretch stiffness μ with this step, and initial strain ε with this step as drawn from a probability distribution function ψ_ε.
3. With probability P_f start two new branches at angle $\varphi \simeq \pi/2$ to the current branch. This to models the nearly orthogonal cross-link formed by filamin.
4. With probability P_s generate a step of length b along the current direction θ. Associate spectrin stretch stiffness ν with this step.
5. If the random walk step crosses the cell membrane attach the end point of the random walk step to the membrane with probability P_m.
6. Stop the random walk if the edge of the beam element at s_i is reached, or if the edge of the cytoskeleton at interior thickness d_i is reached.

The above simple model involves two p.d.f.'s, one for orientation (ψ_θ) and one to characterize the strain of each filament segment (ψ_ε). The orientation and strain of the filaments is expected to respond to imposed forces at the continuum scale. The probabilities P_f, P_s, P_m encapsulate the complicated biochemical reactions that form linkages between actin filaments. In this work we are basically interested in proof-of-concept computations and P_f, P_s, P_m shall be imposed rather than obtained from detailed chemical kinetics.

At the end of the above procedure we have N_i actin and spectrin segments defining the network inside of each beam element B_i. Let $\mathbf{r}_j$ be the position vectors of the endpoints of the segments, $j = 1, \ldots, M_i$. Some of these endpoints correspond to points on the membrane or on the beam element boundaries at s_{i-1} and s_i. The motion of these points is imposed as a displacement boundary condition at each moment in time. The other endpoints change position in response to elastic forces $\mathbf{F}_j(t)$ in the filament segments ending at that particular node and at time t. Inertial effects are negligible, and the equation of motion of these nodes is given by the Langevin equation

$$\eta \frac{\mathrm{d}\mathbf{r}_\mathrm{j}}{\mathrm{d}t} = \mathbf{F}_j(\boldsymbol{r}, t) + \mathbf{w}_j(t), \tag{24}$$

with $\mathbf{w}_j(t)$ a Gaussian noise term of intensity given by the fluctuation-dissipation theorem, and $\boldsymbol{r} = (\mathbf{r}_1, \ldots, \mathbf{r}_{M_i})$. In order to more readily link the microscopic dynamics to the ψ_θ, ψ_ε p.d.f.'s it is convenient to consider the equation for the time evolution of the end-to-end vector of each filament,

$$\boldsymbol{\delta}_{jk} = \mathbf{r}_k(t) - \mathbf{r}_j(t), \tag{25}$$

that satisfies the SDE

$$\eta \frac{\mathrm{d}\boldsymbol{\delta}_\mathrm{jk}}{\mathrm{d}t} = \mathbf{F}_k(\boldsymbol{\delta}, t) - \mathbf{F}_j(\boldsymbol{\delta}, t) + \mathbf{w}_k(t) - \mathbf{w}_j(t). \tag{26}$$

The orientation and strain of the filament are immediately available as

$$\theta_{jk} = \mathrm{atan}\big[(\boldsymbol{\delta}_{jk} \cdot \mathbf{e}_y)/(\boldsymbol{\delta}_{jk} \cdot \mathbf{e}_x)\big], \varepsilon_{jk} = |\boldsymbol{\delta}_{jk}|/l_0 - 1, \tag{27}$$

with l_0 the undeformed length of the filament. Let (u_{jk}, v_{jk}) be the x, y components of the displacement $\boldsymbol{\delta}_{jk}$, such that $\theta_{jk} = \mathrm{atan}(v_{jk}/u_{jk})$

Though simple, this microscopic model is capable of capturing strain-hardening through the ψ_θ p.d.f. and also retains memory of the previous strain state through ψ_ε.

4.3 Kinetic Description

The Fokker–Planck equation associated with the Langevin dynamics specified by (26) is

$$\frac{\partial \psi}{\partial t} + \frac{\partial}{\partial u}(F_u \psi) + \frac{\partial}{\partial v}(F_v \psi) = \frac{1}{\beta}\left(\frac{\partial^2 \psi}{\partial u^2} + \frac{\partial^2 \psi}{\partial v^2}\right), \tag{28}$$

with ψ a function of time and the filament end-to-end displacements, $\psi(t, u, v)$. The principal modeling difficulty is establishing the relationship between the

forces $\mathbf{F}_j(\boldsymbol{\delta}, t)$ defined in the microscopic description and some general functions ($F_u(u, v)$, $F_v(u, v)$) needed in the kinetic-level equation (28).

The simplest approach is to assume that the elastic filament forces come from a potential

$$\mathbf{\Phi}(u, v) = \frac{\mu}{2}\Big[(u - U_i)^2 + (v - V_i)^2\Big], \tag{29}$$

with (U_i, V_i) the average displacement in block B_i, a hypothesis that corresponds to affine distribution of strain among the filaments. It has been established by a number of researchers [17], that affine strain distributions are obtained at large densities of actin filaments, but that as the number of filaments decreases the strain distribution can differ markedly from the average strain in a control volume. The drawback of using an affine distribution of strain at the kinetic level is attenuated in the context of the tP-CKM algorithm. The probability distribution function $\psi(t, u, v)$ is used only to instantiate microscopic ensembles according to the procedure outlined in 4.1. The subsequent time evolution is however carried out at the molecular level by evolving the SDEs (26) forward in time, through what is assumed to be a physically correct model. The kinetic-level computation simply acts as a predictor step to be corrected by the molecular level evolution. The availability of a predictor step is computationally convenient since it furnishes the required approximation of the initial conditions at the time substeps $\{t_1^k, \ldots, t_{P-1}^k\}$, and thereby allows time-parallel computations. Also, the branching defined by step (3) of random walk procedure randomizes initial orientations with respect to the average strain direction specified by the potential (29).

An alternative to the affine deformation hypothesis expressed by (29) is to use a Kramers–Moyal expansion. During the microscopic evolution the first two moments of the probability transition function $P\ (u, v, t + \Delta t|u', v', t)$ can be computed by accumulating statistics from the numerical solution of the SDEs (26). The moments defined by

$$M_{m,n}(u', v', \Delta t) = \int (u - u')^m (v - v')^n P(u, v, t + \Delta t|u', v', t)\mathrm{d}u'\mathrm{d}v', \tag{30}$$

are approximated by time sampling over n_t time steps, and an interpolation of the sampling can be used to determine the coefficients $\boldsymbol{D}^{(1)}(u, v, t) \in \mathbb{R}^2$, $\boldsymbol{D}^{(1)} = (D_u^{(1)}, D_v^{(2)}), \boldsymbol{D}^{(2)}(u, v, t) \in \mathbb{R}^{2\times 2}$ needed in the Fokker–Planck equation

$$\frac{\partial \psi}{\partial t} + \frac{\partial}{\partial u}\Big(D_u^{(1)}\psi\Big) + \frac{\partial}{\partial v}\Big(D_u^{(1)}\psi\Big) = \frac{1}{\beta}\nabla_{(u,v)} \cdot \Big(\boldsymbol{D}^{(2)}(u, v, t)\nabla_{(u,v)}\psi\Big). \tag{31}$$

Though capable of capturing non-affine strain distributions in the filament network, this approach is much more costly, due to the necessity of accumulating statistics. Tests in this work are done using affine instantiation of the filament network.

4.4 Continuum Description

In this simple model, the cytoskeleton is seen as a variable thickness, curved beam at the continuum level (Fig. 8).

Let $\mathbf{r}(s, t)$ be the position vector of a point along the one-dimensional beam model of the cytoskeleton, $\boldsymbol{\tau}(s,t), \boldsymbol{\nu}(s,t)$ the tangent and normal vectors, and $\kappa(s, t)$ the curvature. Assuming slow, non-inertial motion the beam equation of motion in this case is

$$\eta\frac{\mathrm{d}\mathbf{r}}{\mathrm{d}t} = \Delta p(s,t)\boldsymbol{\nu} + \frac{\mathrm{d}}{\mathrm{d}s}\left(T\boldsymbol{\tau} + EI\frac{\mathrm{d}\kappa}{\mathrm{d}s}\boldsymbol{\nu}\right), \tag{32}$$

with Δp the difference between cytosol and ambient pressure, $T(s, t)$ the tension in the beam, and EI the flexural rigidity. For small displacements during a time step the flexural rigidity can be expressed as $EI = MR = M/\kappa$, with R the radius of curvature. The beam tension T is expressed in terms of the filament forces $\mathbf{f}$ as

$$T = \frac{1}{L_i}\left(\int_{B_i}\mathbf{f}\mathrm{d}s\right)\boldsymbol{\tau}, \tag{33}$$

with L_i the length of beam element B_i. The tension can also be expressed as an average over deformation states of the beam as

$$T = \mu\int(u\tau_x + v\tau_y)\psi(u,v)\mathrm{d}u\mathrm{d}v, \tag{34}$$

using the p.d.f. of displacement state $\psi(u, v)$, μ the stretching stiffness of a filament and (τ_x, τ_y) the components of the tangent vector. The moment in the beam can also be computed either as a spatial average

$$M = \frac{1}{L_i}\int_{-L_i/2}^{L_i/2}(\mathbf{f}\cdot\boldsymbol{\nu})s\mathrm{d}s, \tag{35}$$

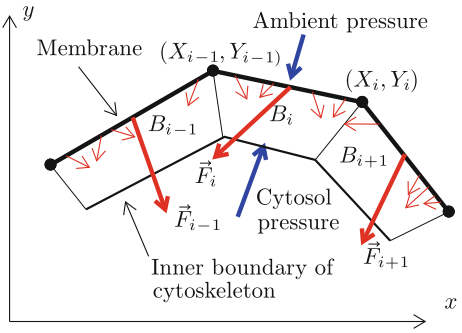

Fig. 8 Sketch of pressure and cytoskeleton forces acting on cellular membrane elements

or an average over deformation states by evaluating

$$M = a\mu \int (uv_x + vv_y) \cos\theta \psi(u, v) \mathrm{d}u\mathrm{d}v\mathrm{d}\theta. \tag{36}$$

Expression (36) evaluates the torque of the filament forces normal to the beam element, over all possible filament displacements and orientations. Relations (33–36) furnish the requisite lengths between continuum and microscopic models. When seeking continuum closure relations from a known microscopic state the integrals (33–36) are evaluated directly.

Consider some numerical method applied to (32) to advance $\mathbf{r}(s, t^k)$ to a new time level t^{k+1}. The average displacements in beam element B_i of length Δs_i can be evaluated as

$$U_i^{k+1}\mathbf{e}_x + V_i^{k+1}\mathbf{e}_y = \left(\frac{\partial \mathbf{r}}{\partial s}\right)_i^{k+1} \Delta s_i. \tag{37}$$

These average displacements are imposed as constraints on the p.d.f. for the microscopic displacements at the new time level

$$U_i^{k+1} = \int u\psi(u, v, t^{k+1})\mathrm{d}u\mathrm{d}v, \quad V_i^{k+1} = \int v\psi(u, v, t^{k+1})\mathrm{d}u\mathrm{d}v, \tag{38}$$

constraints to be satisfied by the minimal entropy modification of $\psi(u, v, t^k)$.

5 Results

We now turn to a proof-of-concept computation. The parameters chosen here are meant to qualitatively capture blebbing phenomena, but no claim is made that this initial demonstration of the method accurately captures biological phenomena.

An initial circular shape is assumed for a cell of diameter $D = 10$ μm. The overpressure of the cytosol with respect to ambient is set as $\Delta p = 100$ Pa. The boundary is discretized in $N_m = 4 \times 10^3$ elements. Initial uniform distributions for the filament orientation are chosen in each element. In each element the random walk generation procedure is repeated until there are $N_i > 10^3$ actin filaments in each element, and at least $N_{c,i} > 50$ connections of the filaments in each element with the cellular membrane. Probabilities $P_m = 0.5$, $P_s = 0$, $P_f = 0.25$ are chosen in the network generation procedure. This corresponds to a 50% chance that a filament that crosses the cellular membrane attaches to the membrane, no spectrin elements, and that, on average, at every fourth random walk step of length $a = 20$ nm we encounter a crosslink. The system is allowed to equilibrate by advancing the SDEs (26) and constraining the motion of all nodes on the membrane to be along radii until the cytosol overpressure is balanced by stretching forces within the network. The sequence of shapes obtained during this equilibration

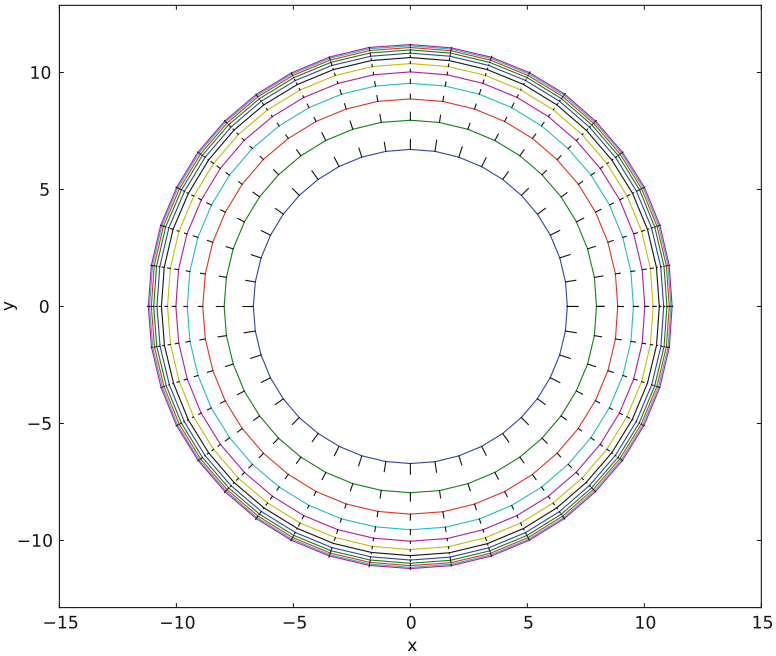

Fig. 9 Initial equilibration of a circular model of a cell. The forces on the membrane elements are shown by the line segments pointing outward from the circular cell model. Time slices at 10-s intervals from $t = 0$ to $t = 120$ s

process are shown in Fig. 9. The equilibration process is a non-trivial test showing that uniform distributions of the orientations of the filaments in each continuum block, and using sufficient filaments to have affine distributions of strain, maintains symmetry of the computation.

After the initial equilibration, the formation of blebs is simulated by modifying the probability of attachment of a filament to the membrane,

$$P_m(t) = 0.01 + 0.49\left(1 - \frac{1}{1 + e^{20-t}} + \frac{1}{1 + e^{40-t}}\right), \tag{39}$$

which models the formation of a bleb over an interval of 20 s, by changing the baseline membrane attachment probability from 0.5 to 0.01 (Fig. 10). The change is imposed on various regions of the cell, both localized to represent a small bleb and over large regions.

The main intent of these initial tests is to ascertain whether bleb formation occurs and is then retracted. Detachment of the cytoskeleton occurs as expected. A sequence of membrane shapes during the bleb formation stage is shown in Fig. 11. A detail of the formation of a small bleb is shown in Fig. 12. After some time ($t > 40$) the probability of reattachment of the cytoskeleton network to the membrane is set to the initial value $P_m = 0.5$ and the membrane reverts to a quasi-circular shape. Figure 13, shows the final stage of retraction of a small bleb.

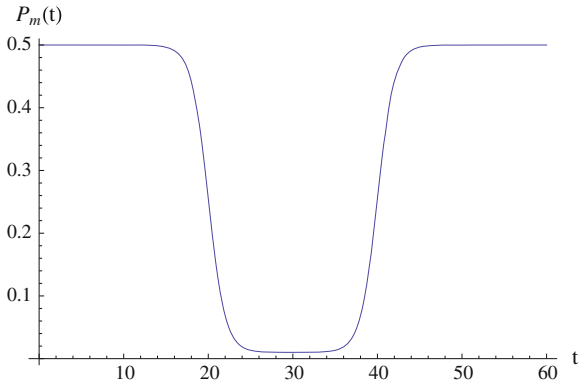

Fig. 10 Imposed time variation of actin filament to membrane attachment probability

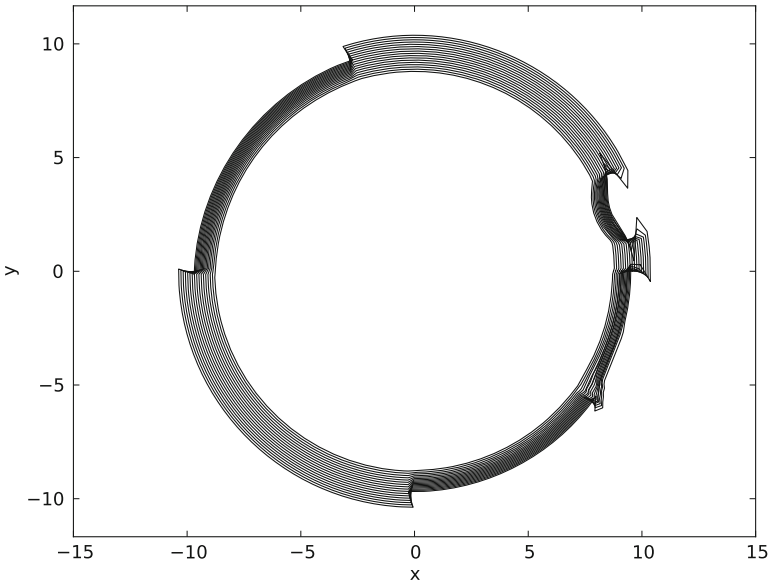

Fig. 11 Sequence of membrane shapes at $\Delta t = 0.5$ s intervals from $t = 19$ to $t = 24$ *s*

6 Conclusions

Development of quantitative models that link overall cytoskeleton mechanical behavior to microscopic phenomena exemplified by biochemical reactions is a challenging endeavour. Such quantitative models are however of great interest since many diseased states manifest themselves at large scales, but are caused by breakdowns in biochemical processes at the molecular scale. In this work we have carried out an initial application of a general multiscale interaction framework

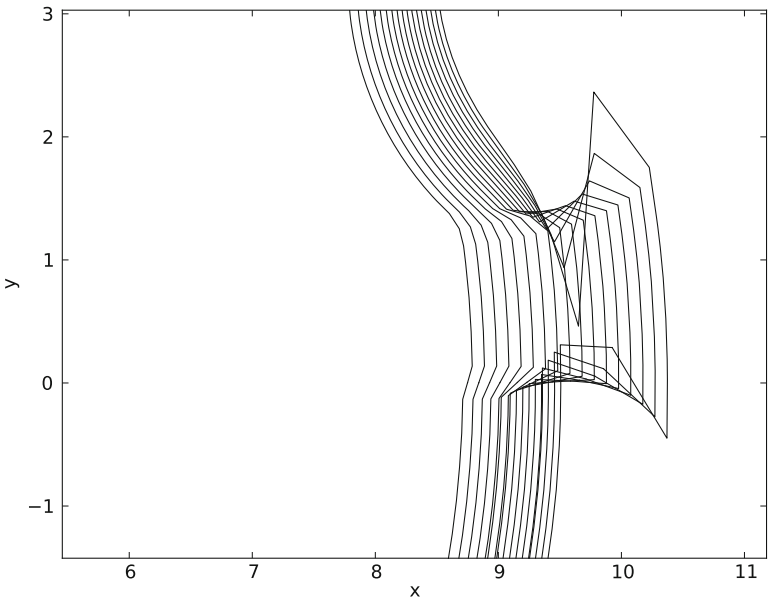

Fig. 12 Sequence of membrane shapes in bleb formation. ($\Delta t = 0.5$ s time intervals between successive membrane positions)

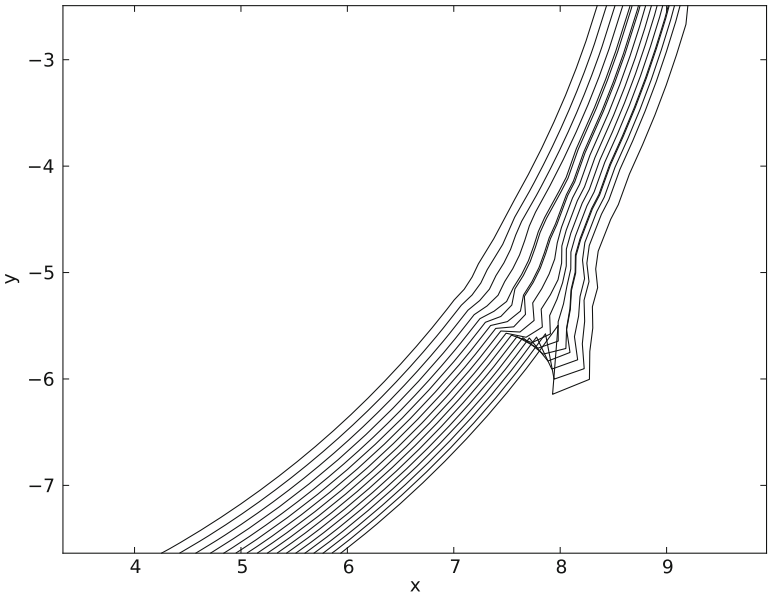

Fig. 13 Late stage retraction of a bleb ($\Delta t = 0.5$ s, from $t = 38$ to $t = 46$ s)

constructed to facilitate linkage between molecular and continuum phenomena. The main features of the tP-CKM framework that are of utility in constructing cytoskeleton models are:

1. The repeated regeneration of the cytoskeleton network through refined estimates of the p.d.f. ψ describing the network geometry mimics the continual rearrangement exhibited by real biological systems.
2. Time parallelization allows large-scale models to be simulated.
3. The interpolation between time steps of the p.d.f. using optimal transport theory allows larger continuum time steps to be taken by comparison to linear response Fokker–Planck theory.

This initial application of the tP-CKM framework to a simplified cytoskeleton model is not yet fully realistic. Biochemical kinetics must be included in the model in order to determine rates at which actin filaments form crosslinks or attach to the membrane in response to local concentrations. A model for the action of myosin on the network must be included. We have however shown that imposing smaller probabilities of filament to cellular membrane attachment does lead to the formation of a protrusion (a bleb) that is subsequently retracted when the actin network reforms. Work is underway to construct models that incorporate more of the known biology of the cytoskeleton.

Acknowledgments This work was supported in part by NIH grants 1S10RR023069-01 (UNC BASS supercomputer system equipped with GPUs), R01-HL077546-5401A2 (UNC Virtual Lung project) and DOE grant A10-0486-001.

References

1. Alberts, B., Johnson, A., Lewis, J., Raff, M., Roberts, K., Walter, P.: Molecular Biology of the Cell, 4th edn. Garland, New York (1994)
2. Alt, W., Dembo, M.: Cytoplasm dynamics and cell motion: two-phase fluid models. Math. Biosci. **156**(1–2), 207–228 (1999)
3. Arruda, E., Boyce, M.: A three-dimensional constitutive model for the large stretch behavior of rubber elastic materials. J. Mech. Phys. Solids **41**(2), 389–412 (1993)
4. Boal, D.: Mechanics of the Cell. Cambridge University Press, Cambridge (2002)
5. Boey, S., Boal, D., Discher, D.: Simulations of the erythrocyte cytoskeleton at large deformation I. Microscopic models. Biophys. J. **75**(3), 1573–1583 (1998)
6. Brenier, Y.: Optimal transport, convection, magnetic relaxation and generalized Boussinesq equations. J. Nonlinear Sci. **19**, 547–570 (2008)
7. Buxton, G., Clarke, N., Hussey, P.: Actin dynamics and the elasticity of cytoskeletal networks. Exp. Polym. Lett. **3**(9), 579–587 (2009)
8. Cano, M.L., Lauffenburger, D.A., Zigmond, S.H.: Kinetic analysis of f-actin depolymerization in polymorphonuclear leukocyte lysates indicates that chemoattractant stimulation increases actin filament number without altering the filament length distribution. J. Cell Biol. **115**, 677–687 (1991)
9. Charras, G.T.: A short history of blebbing. J. Microsc. **231**(3), 466–478 (2008)
10. Charras, G.T., Coughlin, M., Mitchison, T.J., Mahadevan, L.: Life and times of a cellular bleb. Biophys. J. **94**(5), 1836–1853 (2008)

11. Charras, G.T., Hu, C., Coughlin, M., Mitchison, T.J.: Reassembly of contractile actin cortex in cell blebs. J. Cell Biol. **175**(3), 477–490 (2006)
12. Charras, G.T., Yarrow, J.C., Horton, M.A., Mahadevan, L., Mitchison, T.J.: Non-equilibration of hydrostatic pressure in blebbing cells. Nature **435**, 365–369 (2005)
13. Cover, T.: Elements of Information Theory. Wiley, New York (1991)
14. Cunningham, C.C.: Actin polymerization and intracellular solvent flow in cell surface blebbing. J. Cell Biol. **129**(6), 1589–1599 (1995)
15. Gardel, M.L., Shin, J.H., MacKintosh, F.C., Mahadevan, L., Matsudaira, P., Weitz , D.A.: Elastic behavior of cross-linked and bundled actin networks. Science **304**, 1301–1305 (2004)
16. Head, D., Levine, A., MacKintosh, F.: Deformation of cross-linked semiflexible polymer networks. Phys. Rev. Lett. **91**(10) (2003)
17. Head, D., Levine, A., MacKintosh, F.: Distinct regimes of elastic respone and deformation modes of cross-linked cytoskeletal and semiflexible polymer networks. Phys. Rev. E **68**, 061,907 (2003)
18. Huisman, E.M., van Dillen, T., Onck, P.R., der Giessen, E.V.: Three-dimensional cross-linked f-actin networks: relation between network architecture and mechanical behavior. Phys. Rev. Lett. **99** (2007)
19. Ingber, D.: Cellular tensegrity: defining new rules of biological design that govern the cytoskeleton. J. Cell Sci. **104**, 613–627 (1993)
20. Isambert, H., Maggs, A.C.: Dynamics and rheology of actin solutions. Macromolecules **29**, 1036–1040 (1996)
21. Janmey, P.A., Tang, J.X., Schmidt, C.F.: Actin filaments (unpublished)
22. Jordan, R., Kinderlehrer, D., Otto, F.: The variational formulation of the Fokker–Planck equation. SIAM J. Math. Anal. **29**, 1–17 (1999)
23. Kamm, R.D., Mofrad, M.R.K.: Cytoskeletal Mechanics: Models and Measurements. Cambridge University Press, Cambridge (2006)
24. Keller, H., Eggli, P.: Protrusive activity, cytoplasmic compartmentalization, and restriction rings in locomoting blebbing walker carcinosarcoma cells are related to detachment of cortical actin from the plasma membrane. Cell Motil. Cytoskeleton **41**(2), 181–193 (1998)
25. Kwon, R.Y., Lew, A.J., Jacobs, C.R.: A microsturcturally informed model for the mechanical response of three-dimensional actin networks. Comp. Methods Biomech. Biomed. Eng. **11**(4), 407–418 (2008)
26. Li, J., Dao, M., Lim, C.T., Suresh, S.: Spectrin-level modeling of the cytoskeleton and optical tweezers stretching of the erythrocyte. Biophys. J. **88**, 3707–3719 (2005)
27. Lions, J.L., Maday, Y., Turinici, G.: Resolution dedp par un schema en temps parareel. C. R. Acad. Sci. Paris **332**, 661–668 (2001)
28. Mitchison, T.J., Cramer, L.P.: Actin-based cell motolity and cell locomotion. Cell **84**, 371–379 (1996)
29. Mitran, S.: A time-parallel continuum–kinetic–molecular interaction algorithm for computation of nonequilibrium phenomena. J. Comput. Phys. (submitted) (2010)
30. Mofrad, M.R.K.: Rheology of the cytoskeleton. Ann. Rev. Fluid Mech. **41**, 433–453 (2009)
31. Palmer, J., Boyce, M.: Constitutive modeling of the stress strain behavior of f-actin filament networks. Acta Biomater. **4**(3), 597–612 (2008)
32. Pivkin, I., Karniadakis, G.: Accurate coarse-grained modeling of red blood cells. Phys. Rev. Lett. **101**(1), 118,105 (2008)
33. Pullarkat, P.A.: Loss of cell–substrate adhesion leads to periodic shape oscillations in fibroblasts. eprint arXiv:physics/0612156 (2006)
34. Ramaekers, F.C., Bosman, F.T.: The cytoskeleton and disease. J. Pathol. **204**, 351–354 (2004)
35. Rand, R.P., Burton, A.C.: Mechanical properties of the red cell membrane. i. Membrane stiffness and intracellular pressure. Biophys. J. **4**(2), 115–135 (1964)
36. Riskin, H.: The Fokker–Planck Equation. Springer, Heidelberg (1989)
37. Rottner, K., Lommel, S., Wehland, J., Stradal, T.: Pathogen-induced actin filament rearrangement in infectious diseases. J. Pathol. **204**, 396–406 (2004)

38. Seifert, U.: Modeling nonlinear red cell elasticity. Biophys. J. **75**(3), 1141–1142 (1998)
39. Sheetz, M.P., Sable, J.E., Döbereiner, H.: Continuous membrane–cytoskeleton adhesion requires continuous accommodation to lipid and cytoskeleton dynamics. Annu. Rev. Biophys. Biomol. Struct. **35**, 417–434 (2006)
40. Stamenovic, D., Coughlin, M.: A quantitative model of cellular elasticity based on tensegrity. J. Biomech. Eng. **122**(1), 39–43 (2000)
41. Takagi, Y., Homsher, E., Goldman, Y., Shuman, H.: Force generation in single conventional actomyosin complexes under high dynamic load. Biophys. J. **90**, 1295–1307 (2006)
42. Villani, C.: Optimal Transport: Old and New. Springer, Heidelberg (2009)
43. Wilhelm, J., Frey, E.: Elasticity of stiff polymer networks. Phys. Rev. Lett. **91**(10) (2003)

Mechanobiology and Finite Element Analysis of Cellular Injury During Microbubble Flows

Samir N. Ghadiali and Hannah L. Dailey

Abstract Microbubble flows and their effects on the lung epithelium are a key component of the acute respiratory distress syndrome (ARDS), a condition commonly treated by mechanical ventilation. Recent clinical evidence suggests that it may be difficult to choose a ventilation protocol that completely eliminates the damaging mechanical forces experienced by the epithelium. In this chapter, we describe our research group's use of both experimental and computational techniques to investigate how strategic changes in the cells' cytotskeletal structure and mechanical properties can be used to alter the way these cells respond to the hydrodynamic forces generated during microbubble flows. First, we present experimental data which describes the relationship between hydrodynamic conditions and cell necrosis during microbubble flows. The experimental results were then used to develop validated finite element models that provided quantitative information about cellular deformation during microbubble flows. These models suggested several pharmaco-protective strategies for reducing epithelial cell (EpC) injury by altering cell mechanics and these predictions were confirmed by a new set of clinically relevant experimental studies. We also discuss the future potential for combined experimental and computational approaches to treating lung injury

S. N. Ghadiali (✉)
Department of Biomedical Engineering, The Ohio State University,
Columbus, OH 43210, USA
e-mail: ghadiali.1@osu.edu

S. N. Ghadiali
Division of Pulmonary, Allergy, Critical Care and Sleep Medicine,
Department of Internal Medicine, Davis Heart and Lung Research Institute,
The Ohio State University Medical Center, Columbus, OH 43210, USA

H. L. Dailey
Medical Engineering Design and Innovation Centre, Cork Institute of Technology,
Bishopstown, Co, Cork, Ireland

Stud Mechanobiol Tissue Eng Biomater (2011) 4: 373–429
DOI: 10.1007/8415_2010_25

Published Online: 28 August 2010

and how these techniques may help elucidate the mechanotransduction of microbubble forces into inflammatory signaling and other processes that contribute to the pathology of ARDS.

Abbreviations

ALI	Acute lung injury
ARDS	Acute respiratory distress syndrome
EpC	Epithelial cells
Mβ-CD	Methyl-β-cyclodextrin
PEEP	Positive end expiratory pressure
VILI	Ventilator-induced lung injury

1 Introduction

1.1 Overview of Microbubble Flows

Microbubble flows have emerged as an important area of research in a wide range of disciplines, with applications ranging from microfluidic devices [9, 20, 74] to biomedical uses including enhancement of ultrasound images and drug delivery [11, 48, 60, 90, 110, 119]. Unfortunately, microbubbles are also known to cause injury to several physiological systems. For example, the microbubbles generated during cardiac surgery can occlude the small blood vessels which supply nutrients to vital organs [34, 77, 97] and can damage the cerebral capillaries [30, 81] leading to significant cellular and tissue damage. In addition to causing damage in the systemic circulation, the lung is particularly vulnerable to microbubble-induced injury. The hydrodynamic forces associated with microbubble flows in small pulmonary airways [12, 54] are associated with lung injury. For example, during acute respiratory distress syndrome (ARDS), which is the most severe manifestation of acute lung injury (ALI), the small pulmonary airways become occluded with fluid due to disruption of the alveolar–capillary barrier [118]. Patients with ALI must be placed on a mechanical ventilator in order to survive. However, these ventilation protocols generate microbubble flows which exacerbate the existing lung injury [25, 54, 88].

Although the physics of microbubble flows has been extensively investigated [20, 40, 69], the effects of microbubble flows on physiological systems are not well established and these interactions are the focus of current research efforts. Previous studies [40, 43] indicate that these microbubble flows impart complex hydrodynamic forces to the epithelial cells (EpC) which line airway walls (see Fig. 1). These forces include compressive pressure and shear stress and complex spatial and temporal gradients of these stresses. These forces may cause both

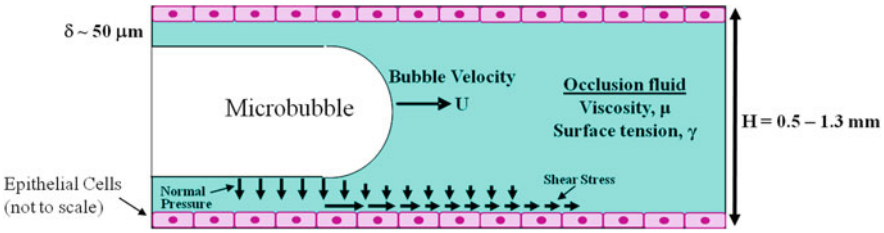

Fig. 1 Schematic diagram of an in vitro model of microbubble-induced injury and the forces applied to the epithelium

mechanical and biological injury to the lung epithelium. First, depending on the EpC microrheology (i.e. elasticity or viscoelasticity), these forces may cause cellular deformation, rupture of the plasma membrane and cell necrosis/death [12, 59, 123, 124]. The hydrodynamic forces may also alter the molecular interactions responsible for cell–substrate adhesion and lead to cell detachment and further disruption of the alveolar–capillary barrier [123, 124].

In addition to causing physical injury, the mechanical forces associated with microbubble bubble flows may be sensed by the lung epithelium and translated via *mechanotransduction* into complex biochemical signals including the up-regulation of inflammatory signals [41, 53]. This mechanically induced up-regulation of inflammation may be extremely important in the context of ALI and ventilation-induced lung injury. Specifically, the majority of patients suffering from ALI die from systemic inflammation and multiple system organ failure even though the initial bacterial/viral insult responsible for ALI has been cleared. The mechanotransduction of microbubble forces into inflammatory signals may result in the release of inflammatory cytokines into the systemic circulation and the inflammatory response to microbubble conditions in the lung may therefore be a significant source of injury and mortality in ARDS/ALI patients.

1.2 ARDS and ALI

The ARDS, and its more severe manifestation ALI, are devastating disorders in which the obstruction of distal lung regions (airways and alveoli) leads to reduced gas exchange and severe hypoxia. The most common causes of ARDS/ALI include bacterial/viral infection of the pulmonary system (i.e. pneumonia) and sepsis from a systemic source such as the gastrointestinal tract [118]. This initial insult typically results in the injury and shedding of alveolar epithelial cells which normally provide a barrier between the alveolar air space and interstitial fluid [118]. As a result, the acute phase of ARDS is characterized by the influx of a protein rich edema fluid into the alveolar air space due to an increased permeability of the alveolar capillary membrane [85]. In most cases, mechanical ventilation is necessary to stabilize patients with ARDS/ALI. However, these ventilators generate

injurious mechanical forces which exacerbate the existing lung trauma, a condition referred to as ventilator-induced lung injury (VILI). The abnormal mechanical environment during ventilation may include over-distention of lung epithelial cells, higher airway opening pressures and the complex forces associated with reopening fluid-filled or collapsed airways with a microbubble of air (see Fig. 1). These abnormal mechanical forces may in turn cause significant cell injury/death, further barrier disruption and an exacerbation of the existing inflammatory condition. Recent advances in the treatment of the predisposing factors for ARDS (e.g. sepsis) and improvements in the supportive care of these critically ill patients have resulted in a reduction in mortality [118]. Although pharmaceutical therapies including surfactant replacement therapy [68, 94] have had limited clinical success, improved mechanical ventilation techniques that minimize additional lung injury have been used to reduce the in hospital mortality to $\sim$30% [6]. However, other modifications to ventilator strategies such as positive end expiratory pressure (PEEP) have not been as successful in reducing mortality rates [15]. As a result, the mortality rates for ALI/ARDS remain high and the development of improved ventilator and/or pharmaceutical therapies is a major public health issue.

1.3 Ventilation-Induced Lung Injury

Extracorporeal and intravascular membrane systems can be used to artificially oxygenate patients with ARDS/ALI, but these devices are typically only used as an adjunct to the most common and effective treatment for ALI/ARDS, mechanical ventilation [10, 44, 117]. Historically, the primary goal of various ventilation techniques was to restore adequate blood oxygenation by opening up the lung and recruiting a majority of the unventilated regions. As a result, most patients were ventilated at a large tidal volume (i.e. V_T = 10–12 mL/kg) compared to normal (5–7 mL/kg). Although this type of mechanical ventilation temporarily restores normal gas exchange, several studies [4, 6] have demonstrated that ventilation at high lung volumes can exacerbate the existing lung injury (volutrauma). Specifically, over-distension of the basement membrane imparts large stretching deformations to the epithelial cells and results in plasma membrane disruptions, cellular injury and apoptosis, and increased permeability of the alveolar-capillary barrier [16, 106, 115]. In addition to volutrauma, the mechanical stresses associated with the repeated closure and reopening of collapsed or fluid-filled lung units during low V_T ventilation may also result in cellular injury (atelectrauma) [25, 41, 76]. Unlike volutrauma where substrate stretching directly imparts deformation to the epithelial cells, the amount of cellular deformation (and therefore injury) during atelectrauma may depend on both the magnitude of the imposed forces and the rheological properties of the epithelial cells (i.e. the cells' resistance to deformation).

Optimization of mechanical ventilation parameters can be used to minimize these components of lung injury and the effects of varying the tidal volume, V_T,

and end-expiratory pressure have been extensively investigated. Clinical trials have clearly demonstrated that ventilation at high lung volumes results in significant cellular and tissue damage and increased mortality rates [6]. Tidal volume reduction mitigates ventilation-induced lung injury by minimizing the stretching deformations applied to lung epithelial cells. However, a unilateral reduction in V_T may also result in lung injury due to atelectrauma [25, 41, 76]. At low lung volumes, the cyclic closure and reopening of fluid-filled airways will generate microbubble flows (see Fig. 1) that impart damaging mechanical forces to lung epithelial cells. Experimental studies from several laboratories including our own indicate that these mechanical forces can cause cell necrosis [12, 124], further barrier disruption [123, 124], and the up-regulation of inflammatory pathways [24, 53, 88]. Several investigators have attempted to set PEEP during ventilation in order to prevent the closure of distal lung units at low lung volumes [84]. Although PEEP may minimize atelectruma, the inappropriate setting of large PEEP may also result in a higher end-inspiratory volume and thus lung over-distension [33]. The difficulty in setting the appropriate PEEP value was demonstrated by the ARDS Network ALVEOLI trial [15] where the use of a higher PEEP value did not significantly reduce the mortality rate. These results suggest that it may be difficult to choose a ventilation protocol that prevents both volutrauma and atelectrauma, so potentially injurious mechanical loads on the epithelium may be an ever-present feature of mechanical ventilation.

1.4 In vitro Models of Lung Injury

As we have seen, the development of VILI may be due to a variety of injury mechanisms including volutrauma and atelectrauma. However, most investigators have focused on volutrauma during high V_T ventilation where distension of the basement membrane is translated into deformation of the attached epithelial cells (EpC). Several investigators have developed sophisticated in vitro cell stretching devices [95, 105] that mimic these in vivo conditions. These devices typically involve culturing cells on a deformable silicoelastic membrane which is uniformly stretched (strained) in a static or cyclic fashion. The strains applied to the EpC can be directly verified and these devices allow for greater control over the mechanical environment compared to the in vivo system. The response of alveolar EpC to stretching deformation has been extensively investigated and comprehensively reviewed by several authors [112, 120]. In addition to triggering biological responses (see Sect. 1.6), large-amplitude and high-frequency cyclic stretching produces more deformation-induced cell injury than small-amplitude and low-frequency stretching protocols [106]. Increasing the strain magnitude in these experiments induces more apoptosis and necrosis [46]. Large stretching deformations also disrupt the cell–cell junctions, which compromises the alveolar–capillary barrier [16, 17].

In addition to basement membrane stretching, the hydrodynamic loads exerted by moving air–liquid interfaces have been implicated in the pathogenesis of ARDS/VILI. Several investigators have presented experimental and theoretical models of airway reopening via bubble propagation through fluid-occluded channels. Results from rigid-walled airway reopening experiments indicate that the large pressure gradients generated near the bubble tip are responsible for epithelial cell necrosis [12, 59]. Several theoretical investigations [49, 78, 79] have also studied the combined effects of wall stretching and hydrodynamics stress generation during bubble propagation through flexible airways. These results indicate that surfactant administration may reduce the cellular strains induced by wall stretch during reopening of a collapsed airway. Unfortunately, surfactant administration may have limited clinical applicability because of surfactant deactivation in the presence of plasma proteins [14]. Our laboratory has developed and used microfluidic systems to expose epithelial cells to repeated microbubble flows and airway reopening events [123, 124]. We have used this system to investigate the effect of airway diameter, reopening velocity, cell morphology and cytoskeletal structure/mechanics on the amount of cell necrosis and barrier disruption. We have also developed a series of computational, finite element-based models of cell deformation during these in vitro microbubble flows to analyze and interpret our experimental results [28, 29].

1.5 Stress versus Strain in Cell Injury Studies

It is important to note the fundamental differences in the mechanical loads applied during biaxial stretch (volutrauma) and airway reopening (atelectrauma) experiments. Biaxial stretch protocols directly apply a defined strain magnitude, regardless of the cells' mechanical properties. In contrast, airway reopening and microbubble flow experiments alter the hydrodynamic stresses applied to the cells by changing the bubble velocity, fluid properties, and airway geometry. Strains that develop in cells during these experiments are not known a priori and will depend on several factors including the magnitude and type of hydrodynamic loads, the cells' biomechanical and/or rheological properties, and cell morphology. However, current experimental imaging techniques cannot quantify the strains that develop in cells under these conditions because of limitations in resolving small strains using fluorescence microscopy [113], especially when loads are applied and removed on very short timescales (i.e. less than 200 ms) as is the case during microbubble flows. Given the difference between applied-strain (biaxial stretch) and applied-stress (airway reopening) experiments and the intractability of measuring stress and strain experimentally, we must use caution in discussing the results reported in the literature regarding the influence of cell mechanical properties on the risk of cell necrosis and injury. For example, Vlahakis et al. [116] observed an increase in the apparent stiffness of A549 human alveolar EpC when the cells were cooled from 37 to 4°C. Conversely, they observed a decrease in

apparent cell stiffness after disrupting the cytoskeleton with cytochalasin D. Both the cooled (stiffer) cells and the cytoskeleton-disrupted (less stiff) cells exhibited increased cell necrosis after cyclic biaxial stretching. The authors attributed this finding to reduced deformation-induced lipid trafficking (DILT), which actively remodels the cell membrane after loading and is inhibited by cooling and cytoskeletal alterations. These results suggest that during biaxial stretch experiments, cell mechanical properties do not have a significant influence on the risk of cell injury. However, it is important to remember that biaxial stretch protocols apply uniform strain or cell deformation, regardless of cell mechanical properties. Thus, uniform strain experiments cannot fully ascertain the role of cell mechanics in flow-induced cell injury during ARDS because the hydrodynamic stresses experienced by cells produce intracellular strains that will depend on the cells' morphological and biomechanical properties.

1.6 Role of Mechanotransduction in Lung Injury

In addition to causing cell necrosis/death and barrier disruption, several investigators have demonstrated that the mechanical forces exerted on epithelial cells during ventilation may also be sensed and transduced into altered biochemical signaling events via a process known as mechanotransduction [103]. For example, cyclic stretching of EpC results in altered cell migration rates [31], altered surfactant secretion profiles [7], changes in protein and gene expression [22], up-regulation of inflammatory pathways [80], and secretion of inflammatory cytokines [56, 114]. EpC have also been shown to respond to hydrodynamic stimuli such as fluid shear stress. Exposure of EpC to moderate shear stress (30 dyne/cm^2) produces time-dependent disassembly of keratin intermediate filaments [89], while exposure to low levels of shear stress (0.1–1 dyne/cm^2) produces increased mucus secretion [35]. In addition, Sidhaye [92] demonstrated that 1–3 dyne/cm^2 shear stress results in reduced paracellular permeability and decreased aquaporin-5 expression. Finally, EpC can also sense and respond to compressive transmural pressure forces. For example, exposure of tracheal EpC to static transmembrane pressures increases early growth response-1 (EGR1) and transforming growth factor-β1 (TGFβ1) gene expression [87]. Ressler et al. [87] also demonstrated that the expression of these genes is time- and pressure-dependent and that EpC do not respond to hydrostatic pressures. Tschumperlin and colleagues [107, 108] demonstrated that human bronchial EpC also respond to static transmembrane pressures by up-regulating a variety of pro-fibrotic pathways. Compressive pressure stresses also activate the epidermal growth factor receptor (EGFR) [104] and chronic exposure to pressure for 14 days results in an increased number of mucus producing cells [82].

Although it is well established that EpC can sense and respond to mechanical forces, the exact mechanisms responsible for this mechanotransduction are still being investigated. The mechanisms by which cells sense and transduce

mechanical force into biochemical signals are complex and in addition to the important role of focal adhesions [18], cell–cell junctions [73], and ion-channels [96], the actin cytoskeleton likely plays a key role. Specifically, mechanical forces applied at the apical surface of cells may transmitted along the cytoskeleton to various signaling sites including focal adhesions [52] and stretch-sensitive ion-channels [3]. In addition, force-transmission along the cytoskeleton may be sensed and transduced into biochemical signals by proteins directly associated with cytoskeletal filaments [47]. Changes in cytoskeletal structure may also result in concurrent changes in cell rheology [63, 123] which may simultaneously influence the amount of intracellular strain/deformation for a given amount of mechanical force [28]. Changes in intracellular strain magnitude can directly influence mechanotransduction mechanisms such as the opening of stretch-activated ion-channels and may also lead to altered activation of different mechanosensitive enzymes. As a result, knowledge of intracellular deformation during applied load is critical to elucidating the mechanisms responsible for mechanotransduction in lung EpC.

1.7 Combined Experimental and Computational Approaches to Lung Injury

The current body of evidence from clinical trials suggests that despite recent advances in mechanical ventilation protocols, it may be difficult to prevent both alveolar over-distention (volutrauma) and cyclic airway collapse and reopening during ventilation (i.e. atelectruma). Therefore, it may be difficult to completely eliminate the damaging mechanical forces associated with microbubble flows. As we have seen in the preceding discussion, these conditions are responsible for direct cellular injury (necrosis) as well as a host of biochemical signaling events that reinforce the inflammatory response of the lung and may contribute to the high mortality rates among ARDS/VILI patients. An alternative approach to minimizing the damage caused by the mechanical forces generated during ventilation is to alter how the EpC respond to these forces. In this chapter, we will describe our laboratories experimental and computational approach to investigate the mechanisms responsible for EpC injury and how these techniques have been used to design a new class of therapies that minimize cellular injury by altering cellular mechanical properties (see Fig. 2). We focus on:

- experimental data describing the relationship between hydrodynamic conditions and EpC necrosis during microbubble flows,
- development of image-based finite element models of microbubble-induced EpC deformation,
- validation of the computational models by direct comparison to the experimental measurements,
- predictions from the models regarding altering cell mechanics to prevent microbubble-induced injury, and

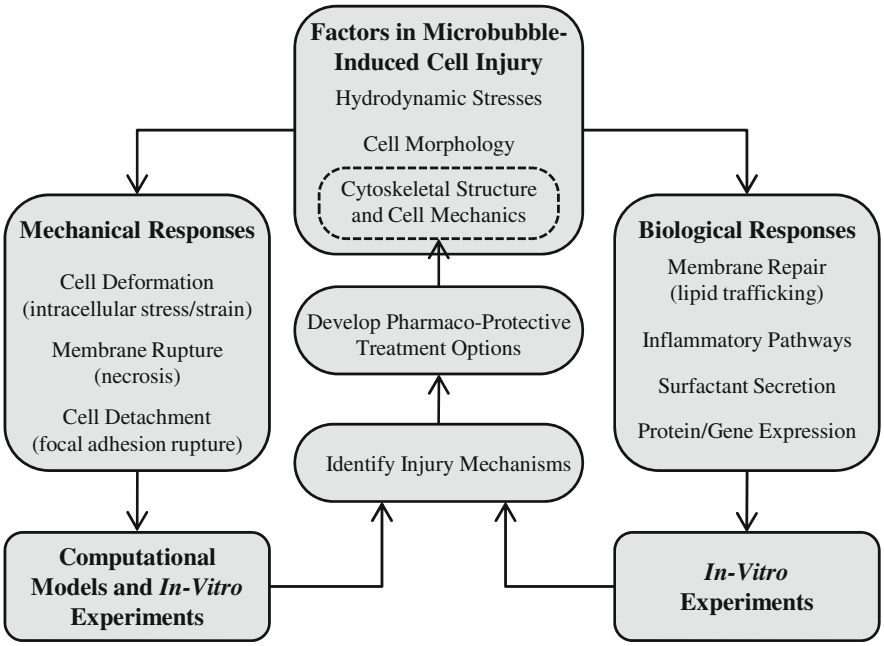

Fig. 2 Mechanical and biological injury due to microbubble flows and the overall goal of using computational and experimental methods to identify mechanisms of injury and identify new treatments

- clinical translation of these predictions into new pharmaco-mechanical treatments that prevent microbubble-induced injury of the epithelium.

2 Experimental Analysis of Cell Injury during Microbubble Flows

2.1 In Vivo and In Vitro Airway Reopening Models

A number of in vivo studies have clearly demonstrated that the air–liquid interface (i.e. microbubble) flows associated with reopening of fluid-filled and compliant airways results in additional lung injury. Briefly, Muscedere et al. [75] showed that ventilation at normal physiological volumes and zero end-expiratory pressure results in a significant increase in lung injury while D'Angelo and colleagues [24, 25, 27] have utilized an open-chest rabbit model to demonstrate that prolonged mechanical ventilation (3–4 h) at normal lung volumes and zero end-expiratory pressure can result in barrier disruption and the activation of inflammatory pathways. D'Angelo [26] also demonstrated that decreasing the surface tension

resulted in significantly less epithelial cell necrosis, less cell detachment and barrier disruption but no significant reduction in inflammation while increasing surface tension resulted in a significant increase in mechanical damage (cell death and detachment). Finally, Frank et al. [39] used an acid-induced lung injury model to investigate whether recruitment maneuvers such as PEEP could alter lung injury patterns. Interestingly, these authors report that although recruitment maneuvers decrease endothelial injury, they do not reduce alveolar epithelial cell injury.

These in vivo studies clearly indicate that additional lung injury occurs during cyclic airway closure and reopening, but it is difficult to identify the consequences of a particular mechanical stimulus in whole lung models due to the spatial and temporal diversity of ALI and the complex morphology of the lung. In contrast, in vitro cell culture models allow for a greater degree of control over the mechanical environment and therefore a more efficient means of evaluating how EpC respond to a given mechanical stimulus. In addition to the systems designed to investigate how EpC respond to stretching deformations (see Sect. 1.4–1.6), several investigators have recently utilized in vitro cell culture systems to investigate the mechanisms responsible for EpC injury during microbubble flows and airway reopening events. Gaver and colleagues [12] were the first to simulate microbubble-induced injury by propagating a long finger of air in a parallel-plate flow chamber at a constant velocity over a monolayer of cultured rat pulmonary EpC. In this study, two reopening velocities were investigated, and the results indicated that slower reopening velocities increased the level of cell necrosis. Bilek et al. [12] also developed a computational model of airway reopening and correlated each component of the hydrodynamic force generated by the microbubble with Capillary number, *Ca*, or dimensionless bubble speed.

$$\frac{(\tau_s)_{\max}}{\gamma/H} = 0.69Ca^{0.36} \tag{1}$$

$$\frac{(\mathrm{d}\tau_s/\mathrm{d}x)_{\max}}{\gamma/H^2} = 0.22 + 0.2Ca^{0.75} \tag{2}$$

$$\frac{(\mathrm{d}P/\mathrm{d}x)_{\max}}{\gamma/H^2} = 0.34Ca^{-0.29} \tag{3}$$

where $Ca = \mu U/\gamma$, μ is the fluid viscosity, U is the bubble speed, γ is the surface tension of the air–liquid interface, τ_s and $\mathrm{d}\tau_s/\mathrm{d}x$ are the shear stress and shear stress gradient, $\mathrm{d}P/\mathrm{d}x$ is the pressure gradient, H is the channel half-height, and x is the axial coordinate in the flow direction. These correlations indicated that the only force that increases in magnitude as the bubble velocity decreases is the pressure gradient, $\mathrm{d}P/\mathrm{d}x$. As a result, these authors concluded that cell necrosis and plasma membrane rupture in this system is due to the presence of a spatial gradient in pressure across the length of an EpC. Bilek et al. [12] also demonstrated that doping the occlusion fluid with a large concentration of exogenous surfactant (Infasurf, ONY Inc.) could be used to reduce the surface tension from $\sim$70 to

$\sim$25 dyne/cm^2 and prevent cell necrosis at all bubble speeds. In a follow up study from this same laboratory, Kay et al. [59] conducted similar experiments with a higher viscosity fluid to demonstrate that the increased cell necrosis at low bubble speeds was not due to the increased exposure time, and therefore the membrane damage was most likely due to the larger magnitude of spatial gradients in normal pressure.

Although the seminal studies by Gaver and colleagues have indirectly implicated spatial gradients in pressure as the mechanical force that causes cell necrosis during microbubble flows, the effect of several important biological and physiological parameters as well as the precise mechanisms of pressure-gradient induced injury were not known. Our laboratory subsequently conducted a variety of experimental studies which specifically investigated how changes in airway dimensions, cellular morphology/typology and cellular rheology influence the amount of necrosis during airway reopening. These studies are summarized below and although some of the experimental results were counter-intuitive, analysis of this data with a novel set of image-based finite element models of cell deformation during microbubbles (see Sects. 1.4 and 1.5) have been used to interpret these experimental findings.

2.2 *Effect of Bubble Velocity and Channel Height*

The motivation for this study [124] was that the bifurcating structure of the lung results in a wide range of airway diameters and that the total cross-sectional area of the lung increases as the airway generation number increases [67]. As a result, the bubble velocity responsible for reopening will be different in different lung regions. Although the effect of bubble velocity has been investigated [12], previous computational studies [40] also indicate that the magnitude of the fluid mechanical stresses exerted on the EpC is inversely proportional to airway diameter. We therefore hypothesized that changes in both airway diameter and bubble velocity will alter degree of cellular injury observed during reopening.

For this study [124], rat pulmonary EpC line (CCL-149, American Type Culture Collection, Manassas, VA) were cultured onto 30 mm diameter coverslips placed in six well plates and were grown under standard culture conditions (37°C, 5% CO_2 and 95% air) for 4 days to obtain a confluent monolayer (100%). To investigate the role of channel height, a POC mini chamber system (Hemogenix, Colorado Springs, CO), which was specifically designed for high resolution live-cell microscopy, was modified to create an adjustable-height parallel-plate flow chamber (see [124] for details). This system consisted of a variable-thickness silicone gasket that was "sandwiched" between a lower coverglass seeded with cells and a rigid upper coverglass. The silicone gasket contained a 10 $\times$ 25 mm flow channel and channel height was governed by the thickness of the silicone gasket. Channel heights of 0.5, 0.8 and 1.7 mm were used to capture the diameters of terminal and respiratory bronchioles [122]. A syringe pump was then used to fill

the flow chamber with phosphate-buffered saline (PBS) and then reversed to create a microbubble of air which removed the occlusion fluid at a constant rate. Finally, the chamber was refilled with a live/dead stain and incubated before visualization. Note that the initial filling of the chamber as well as the re-filling of the chamber with the live/dead stain involves the "backward" propagation of an air–liquid interface. Control experiments indicated that this "backward" air–liquid interface propagation did not cause significant cell necrosis. For normal breathing conditions of $V_T = 500$ mL and 12 breaths/min, the expected range of reopening velocities in terminal and respiratory bronchioles is 1–10 mm/s. A baseline bubble velocity of 3 mm/s was selected to correspond to this range. Order-of-magnitude changes in reopening velocity (i.e. 30 and 0.3 mm/s) were also investigated.

To visualize the cells and quantify cell injury, the flow chamber was mounted on an IX-71 inverted microscope with fluorescence capabilities (Olympus, Melville, NY). The live/dead stain (Invitrogen, Carlsbad CA) consisted of 1.2 μM ethidium homodimer 1 and 1.2 μM calcein AM, in PBS. Calcein AM freely diffuses into living cells where it is converted into a membrane-insoluble product. As it accumulates inside the cell, the cytoplasm of the cell can be viewed in green color. In contrast, ethidium homodimer cannot enter through intact cell membranes. If the plasma membrane is ruptured, the dye enters the cell and binds to nuclear DNA, allowing the cell to be viewed in red color. For each control and experimental condition, 5–10 fluorescent images were obtained from the centerline of the channel to eliminate any possible stress magnification effects near the side walls of the channel. The number of live cells (i.e. calcein positive) and dead cells (i.e. ethidium positive) in each image were counted using the Metamorph image analysis software (Molecular Devices Co., Downington, PA). The percentage of dead cells was calculated as the number of dead cells divided by the total number of cells in each image. For each experimental condition, the percentage of dead cells was quantified and the mean and standard error of these values were calculated. An analysis of variance (ANOVA) with $P < 0.05$ was used to document statistically significance differences.

For each of the three bubble velocities (0.3, 3, and 30 mm/s), we investigated the effect of varying channel height (Fig. 3). Results are presented as percentage of cell death (mean ± SE). For all channel heights, control experiments result almost no injury (<1%). The highest injury level was observed at a channel height of 0.5 mm and a bubble velocity of 0.3 mm/s (40.4 ± 3.6%) while the lowest injury was observed at a channel height of 1.7 mm and a bubble velocity of 30 mm/s bubble velocity (0.5 ± 0.01%). Note that the decrease in cell injury with increasing bubble velocity is consistent with previous studies [12]. The results presented in Fig. 3 also indicate that cellular injury is likely to be highest in distal regions of the lung where the airway diameter is smallest. This experimental data clearly demonstrates that the amount of cell necrosis due to plasma membrane rupture is inversely proportional to the channel height as well as the bubble velocity. In Sect. 1.5, we will show how this experimental data was also used to validate the choice of constitutive model used in our finite element simulations of cell deformation during transient microbubble flows. Specifically, we will show

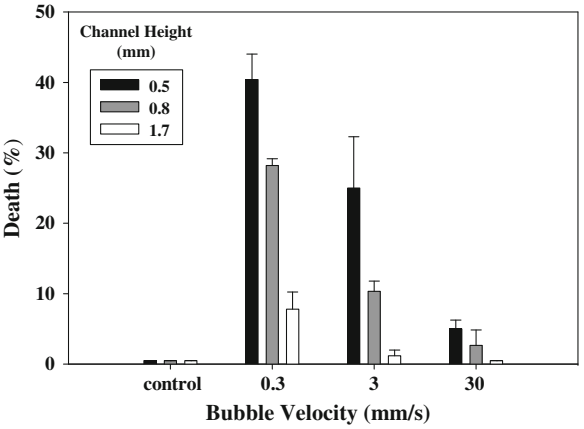

Fig. 3 Effect of channel height and bubble velocity on the percentage of dead cells (i.e. plasma membrane rupture). Data are mean ± SE and all mean values, except for the control values, are statistically different (ANOVA, $P < 0.01$) (With permission from Yalcin et al., J. Appl. Physiol., 2007, Am. Physiol. Soc.)

how modeling the cells' power-law rheology, rather than using a simpler linear viscoelastic model, is necessary to produce results that are consistent with all of the experimental data presented in Fig. 3.

2.3 Effect of Cell Morphology

During ARDS, the type I EpC, which exists as a tight monolayer, are most susceptible to bacterial/viral induced necrosis and detachment [118]. This results in a subconfluent monolayer of primarily type II cells. Previous investigators have demonstrated that the morphological, structural and typological differences between confluent type I and subconfluent type II EpC leads to differential injury responses during cyclic stretching [105]. Changes in morphology between confluent and subconfluent conditions may also alter the EpC's susceptibility to the hydrodynamic forces generated during microbubble flows. We therefore hypothesized that the level of cellular confluence will alter the degree of EpC injury observed during microbubble flows.

To investigate this hypothesis, rat pulmonary epithelial cells were cultured for just 1 day to obtain a subconfluent monolayer (25%). These cells were then exposed to microbubble flow conditions using the modified perfusion chamber described in Sect. 2.2. However, for these studies, the use of a high surface tension occlusion fluid, i.e. PBS, resulted in a large amount of cell detachment even after one microbubble passage [124]. Since this cell detachment would lead to significant errors and bias in quantifying cell necrosis/death, an alternative lower surface tension fluid, cell culture media, was used to evaluate differences in cell necrosis between confluent and subconfluent cells. Figure 4 shows the percentage of cell death (mean ± SE) for the various conditions in which cell culture media was used as the occlusion fluid. For both high-confluence and low-confluence monolayers, control experiments resulted in almost no death (<1%). A two-way

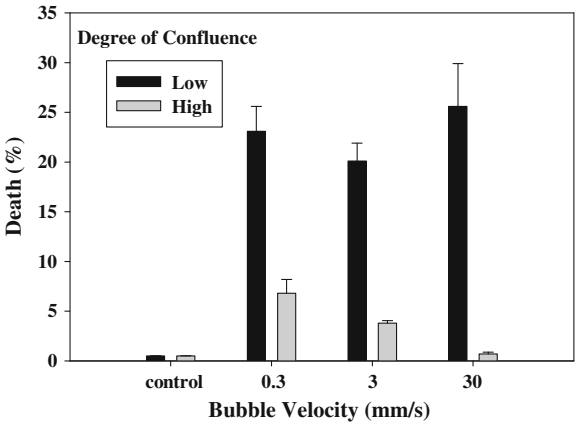

Fig. 4 Effect of monolayer confluence on the percentage of dead cells at different reopening velocities (channel height = 0.5 mm). Data are mean ± SE and differences between high and low confluent conditions at all velocities are statistically significant (ANOVA, $P < 0.01$) (With permission from Yalcin et al., J. Appl. Physiol., 2007, Am. Physiol. Soc.)

ANOVA indicated that there was significantly less death in the high-confluence monolayers than in the low-confluence monolayers at all three velocities ($F = 111$, $P < 0.01$). In addition, the two-way ANOVA indicated that the degree of cellular injury observed at different velocities in the low-confluence monolayers was not statistically different ($F = 0.91$). This data clearly demonstrates that subconfluent cells are more susceptible to microbubble-induced injury than confluent cells.

One possible explanation for the increased susceptibility of subconfluent cells to microbubble-induced damage is that changes in cell morphology lead to an amplification of the hydrodynamic stress exerted on subconfluent cells compared with the magnitude of the stress exerted on confluent cells. Jacob and Gaver [55] conducted a computational study in which they demonstrated that the amount of stress amplification in this system is primarily a function of aspect ratio. To compare the aspect ratios of our confluent (~100%) and subconfluent (~25%) cells, we used laser scanning microscopy (LSCM). Cells were fluorescently dyed using 2 μM of calcein AM, incubated in the dark for 10 min, and then viewed with a Zeiss LSM 510 Meta confocal microscope at 40× magnification. Each confocal image was created by stacking 20–40 sequential 0.2-μm thick scans, depending on the height of the cell layer. To calculate cell aspect ratio, we measured cell height, width, and length and calculated two different aspect ratios, h_c/W and h_c/L, where h_c is the cell height, W is the width and L is the length. The results showed that although the subconfluent cells were taller and wider than confluent cells (Fig. 5), the mean aspect ratios were not statistically different (ANOVA, $F = 0.118$). Specifically, the height-to-width ratios were 0.14 ± 0.04 and 0.12 ± 0.04 for subconfluent and confluent cells, respectively, while the height-to-length rations were 0.09 ± 0.03 and 0.074 ± 0.03 for subconfluent and confluent cells, respectively. Therefore, the differences in cell death between confluent and subconfluent cells (see Fig. 4) were not likely due to a change in the magnitude of the applied hydrodynamic stresses. In Sect. 1.4, we will use this data to validate the computational modeling technique and show that morphological differences between

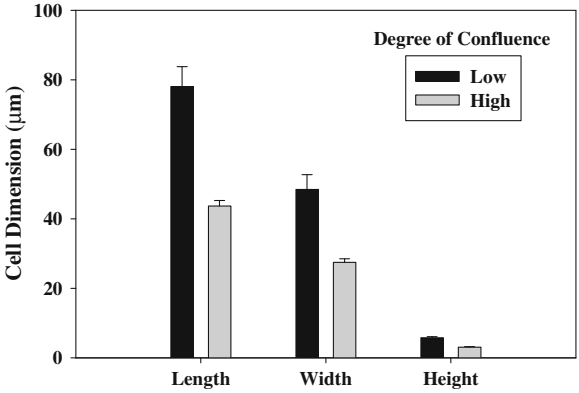

Fig. 5 Measurement of rat pulmonary EpC height, width and length from confocal images of both subconfluent and confluent monolayers (With permission from Yalcin et al., J. Appl. Physiol., 2007, Am. Physiol. Soc.)

cells can alter the way the hydrodynamic forces are distributed within the cell. This change in stress distribution leads to higher membrane strain in the subconfluent cells compared with the confluent cells and may be responsible for the higher rate of membrane rupture observed among subconfluent cells.

3 Cell Mechanics and Mechanobiology

3.1 Continuum Approach to Cell Mechanics

As we have previously discussed, pulmonary microbubbles flows are associated with both physical injury to the epithelium, plasma membrane rupture, and an upregulation of the inflammatory response in the lung (i.e. a proinflammatory cytokine cascade) [118], which contributes to the maintenance of edematous conditions in the deep lungs. Therefore a better understanding of how cells respond to their mechanical environment is critical for the development of improved therapies that seek to mitigate microbubble-induced injury by altering the mechanical and/or rheological properties of the cells. Although the cells are clearly a highly complex and heterogeneous structure, we have taken a continuum mechanics approach to model the cells. In this approach, we seek to only incorporate relevant features needed to replicate or simulate the experimental data. The advantage of this approach is that we develop tractable models that can be efficiently used to suggest new experiments and therapeutic approaches. However, it is critical that these simplified models be validated by comparison to experimental data. Below we describe the various continuum mechanics models we have utilized and in Sects. 1.4 and 1.5 we provide more detail with respect to comparisons with experimental data.

Continuum mechanics describes a set of assumptions applied to a material when we repeatedly divide it into smaller and smaller segments, with each

consecutive subdivision having the same properties as the bulk material from which it came. When we talk about continuous media, we neglect the quantum–mechanical and atomic nature of all matter, usually because the length scale of the object we are analyzing is much larger than the atoms that comprise it. We are also neglecting microstructural inhomogeneity within a material in favor of representative bulk properties. In cell mechanics, this often means that we measure the collective contribution of individual cytoskeletal components such as actin filaments or microtubules to give an estimate of whole-cell mechanical properties.

Applying continuum mechanics assumptions yields three interrelated quantities—stress, displacement, and strain—that describe how a material responds to applied forces. *Stresses* are the forces at work on or within a body, written as force per unit area. *Displacements* are the motions induced within a body by applied stresses. *Strains* are dimensionless measurements of change in shape that may be calculated by knowing displacements inside a body. Stresses, strains, and displacements are connected by three types of equations in continuum mechanics: equilibrium conditions (or equations of motion in moving systems), kinematic relations, and constitutive equations. The *equilibrium conditions* are relationships between different components of stress based on their spatial derivatives. In linear static problems, the equilibrium equations do not contain strains or displacements. In dynamic problems involving bodies in motion, the equilibrium conditions are expanded and called *equations of motion*, which contain time derivatives of the displacements (velocities). The next set of equations, the *kinematic relations*, is used to describe strains in terms of displacements within a body. The final set of relationships, known as the *constitutive equations*, depend upon the properties of the material in question and describe the relationship between stress and strain. Thus, the mechanical characterization of a material involves the development of a constitutive equation that fits the experimentally observed relationship between stress and strain for that material.

3.2 Linear Elastic Mechanics

In recent years, the mechanical characterization of living cells has undergone an evolutionary process in which experimental observations have been correlated with increasingly sophisticated constitutive models. Early experiments were matched to linear elastic and linear viscoelastic models [70]. The simplest possible constitutive equation, Hooke's law, gives a relationship between stress and strain:

$$\sigma^s = E\varepsilon, \tag{4}$$

where σ is the normal stress, ε is the normal strain, and the proportionality constant, E is the Young's modulus or stiffness of the material. Materials that can be described using Eq. 4 are called *linear elastic materials* because stress and strain are related linearly by the constant E. More complicated combinations of normal

and shear stresses and strains in three dimensions (x, y, and z) require the generalized Hooke's law [5]:

$$\sigma_{ij}^{s} = \frac{E}{1+v}\varepsilon_{ij} + \frac{vE}{(1+v)(1-2v)}\varepsilon_{kk}\delta_{ij} \tag{5a}$$

$$\varepsilon_{ij} = \frac{1}{2}\left(\frac{\partial d_i}{\partial x_j} + \frac{\partial d_j}{\partial x_i}\right). \tag{5b}$$

Here ε_{ij} is the Lagrangian strain tensor, $\varepsilon_{kk} = \varepsilon_{11} + \varepsilon_{22} + \varepsilon_{33}$ is the strain invariant, v is the Poisson ratio, and E is the Young's modulus. All equations are written in standard indicial notation. In Sect. 1.4, we describe a technique for modeling cells using linear elastic assumptions to look at peak deformations during microbubble flows.

3.3 Linear Viscoelastic Models

Linear elastic models have limitations when applied to living cells because cells are enveloped in a membrane (lipid bilayer), filled with fluid (cytosol), and supported by a polymeric scaffold (cytoskeleton). This combination of fluid and semi-solid components gives cells *viscoelasticity*, or both fluid-like (viscous) and solid-like (elastic) characteristics. Early cell mechanics measurements were characterized using linear viscoelastic models [70] in which the elastic and viscous characteristics of the material were modeled as discrete mechanical elements, such as linear springs and dashpots. A *linear spring* is a mechanical element that has a linear relationship between the applied load and the resulting deformation, or $F = kx$, where F is the applied force, x is the change in length of the spring, and k is a proportionality constant. In viscoelastic modeling, the spring represents the relationship between stress and strain in a linear elastic material, so the spring equation becomes Hooke's Law (Eq. 4). Notice that the spring equation does not depend on time, so when an elastic material experiences a stress load, it responds instantaneously and achieves a constant strain, which is determined by the Young's modulus. The other common mechanical element, the *dashpot*, represents viscous resistance in the system and has a linear relationship between the force applied and the deformation rate,

$$\sigma_d = \eta\frac{\mathrm{d}\varepsilon}{\mathrm{d}t}, \tag{6}$$

where the viscosity, η, is a constant and the $\mathrm{d}\varepsilon/\mathrm{d}t$ is the strain rate. Unlike the spring, a dashpot experiencing a stress load does not deform instantaneously, but rather stresses develop gradually with time, a behavior known as *creep*. In addition, an ideal dashpot placed under a constant-stress loading will deform continuously for all times. Springs and dashpots can be combined to produce a variety of

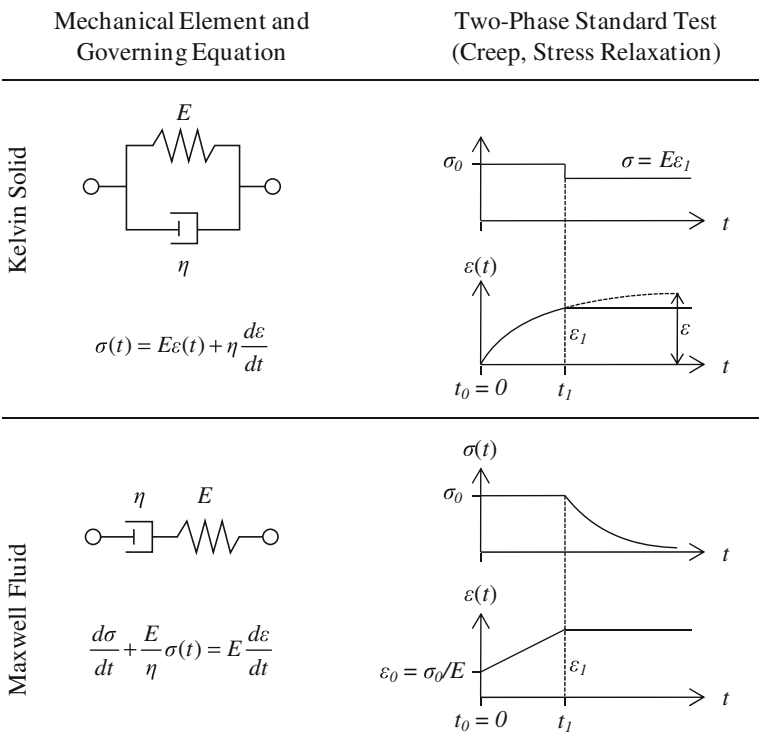

Fig. 6 The Kelvin solid and Maxwell fluid are simple viscoelastic material models consisting of one spring and one dashpot. The creep and stress relaxation phases of the standard two-phase test are shown. Adapted from Flügge [38]

material models. Two simple linear viscoelastic material models that have been correlated with cell mechanics measurements are the Maxwell fluid and Kelvin solid (see Fig. 6).

When the spring and dashpot are arranged in parallel, the strain in both elements is always equal and the total stress is the sum of the stress carried in the spring and dashpot; this material is known as a *Kelvin solid*. Using Eqs. 4 and 6 and $\sigma = \sigma_s + \sigma_d$ yields the governing equation for the Kelvin solid.

$$\sigma = E\varepsilon + \eta\frac{\mathrm{d}\varepsilon}{\mathrm{d}t}. \tag{7}$$

In contrast, when the spring and dashpot are in series, the stress in both elements is always equal and the total strain is the sum of the strain in the spring and dashpot; this material is known as a *Maxwell fluid*. Rewriting the basic spring and dashpot Eqs. 4 and 6 and using $\varepsilon = \varepsilon_s + \varepsilon_d$ produces the governing equation for the Maxwell fluid.

$$\frac{\mathrm{d}\sigma}{\mathrm{d}t} + \frac{E}{\eta}\sigma(t) = E\frac{\mathrm{d}\varepsilon}{\mathrm{d}t}. \tag{8}$$

To understand the behavior of the Kelvin solid and Maxwell fluid, we perform a two-stage standard test (see Fig. 6). Initially, there is no stress or strain in the system. In the first stage, at time $t_0 = 0$, we apply a constant stress, σ_0, and look at the time-dependent response of the strain, $\varepsilon(t)$. Stage one is the creep phase of the standard test. In the second stage, which begins at time t_1, we clamp the system at the current strain $\varepsilon_1 = \varepsilon(t_1)$ and watch how the stress evolves with time. Stage two is the stress relaxation phase of the standard test.

For the Kelvin solid in stage one, we solve Eq. 7 with the initial conditions $\sigma(0) = \sigma_0$ and $\varepsilon(0) = 0$ because the dashpot resists instantaneous deformation. This produces an exponential solution for the creep function $\varepsilon(t)$.

$$\varepsilon(t) = \frac{\sigma_0}{E}\left(1 - \mathrm{e}^{-t/\tau}\right), \tag{9}$$

where $\tau = \eta/E$ is the characteristic relaxation time of the material. If stage one were infinitely long, the Kelvin solid would approach a finite strain limit, $\varepsilon_\infty = \sigma_0/E$. In stage two, the material is clamped at the constant strain, ε_1, and the dashpot no longer bears any stress because the strain is not changing with time. The total stress is thus the stress borne in the spring.

$$\sigma(t) = E\varepsilon_1 \quad \text{for } t > t_1 \tag{10}$$

See Fig. 6 for a visualization of the two-phase standard test on a Kelvin solid.

For a Maxwell fluid in stage one, we solve Eq. 8 with initial conditions $\sigma = \sigma_0$ and $\varepsilon(0) = \sigma_0/E$ because the spring can extend instantaneously, but the dashpot resists instantaneous deformation. This leads to a linear form solution for the creep function $\varepsilon(t)$.

$$\varepsilon(t) = \sigma_0\left(\frac{t}{\eta} - \frac{1}{E}\right). \tag{11}$$

As with the Kelvin solid, the Maxwell fluid is clamped at the start of stage two at a constant strain, ε_1. The dashpot prevents the spring from immediately relaxing and the system returns to a zero-stress state via an exponential decay.

$$\sigma(t) = \sigma_0 \mathrm{e}^{-t/\tau} \quad \text{for } t > t_1, \tag{12}$$

where again $\tau = \eta/E$ is the characteristic relaxation time. See Fig. 6 for a visualization of the two-phase standard test on a Maxwell fluid.

The governing equations for these linear viscoelastic materials can also be used to derive the frequency-domain response function, or complex modulus $E^*(\omega)$. For example, for a Maxwell fluid, we define a sinusoidal stress input function,

$$\sigma(t) = A\mathrm{e}^{i\omega t}, \tag{13}$$

where A is the amplitude of the input and ω is the frequency in Hz. If we substitute the load function from Eq. 13 into Eq. 8 and integrate, we arrive at the complex strain response.

$$\varepsilon(t) = Ae^{i\omega t}\left[\frac{1}{E} + \frac{1}{i\omega t}\right]. \tag{14}$$

Noting that the complex modulus, $E^*(\omega)$, is the ratio of the stress input and strain response, we see that the $Ae^{i\omega t}$ terms cancel and we can write E^* in standard form,

$$E^*(\omega) = \frac{E\omega^2\eta^2 + iE^2\omega\eta}{E^2 + \omega^2\eta^2}, \tag{15}$$

where as before, E is the spring stiffness, η is the dashpot viscosity and ω is the frequency. The expression for the Maxwell fluid's complex modulus, along with many other linear viscoelastic material models, can also be found in tables developed by Flügge [38]. When comparing this formulation to typically reported experimental measurements, note that $E^*(\omega)$ is related to the complex shear modulus by $G^* = E^*/[2(1 + \nu)]$. Previous investigators have used $\tau_R = \eta/E = 1$ s in linear viscoelastic models of cell mechanics and deformation [50, 58, 111]. The frequency-dependent response of a Maxwell fluid with $\tau_R = 1$ s is shown in Fig. 7a.

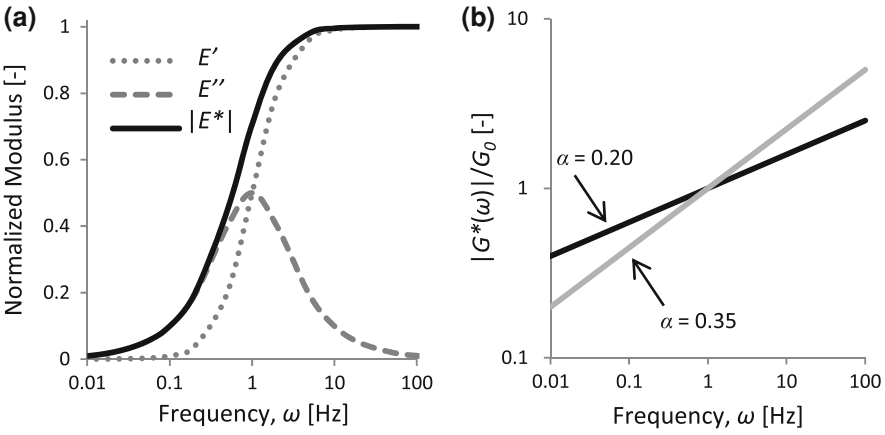

Fig. 7 Frequency responses of Maxwell fluid and power-law material models. **a** Maxwell fluid with $\tau_R = 1$ s. E' and E'' are the real and imaginary parts of Eq. 15. **b** Power-law functions defined according to Eq. 16 with $\alpha = 0.20$ and 0.35. Modulus normalized by $G_0 = G^*(\omega_0 = 1\text{ Hz})$

3.4 Soft Glassy Rheology (SGR)

Linear elastic and linear viscoelastic models can be used to elucidate some aspects of cell mechanics and mechanobiology. However, to predict the dynamic response of EpC to the transient stress wave induced by microbubble flows, we need to consider a constitutive model that captures the cells' viscoelastic mechanics as characterized by the most sophisticated experiments available. Recent microrheology measurements have consistently indicated that cultured adherent mammalian cells exhibit characteristics typically referred to as SGR [2, 36, 51, 100]. The theoretical formulation for SGR mechanics, which can be described using the modified Herschel–Bulkeley equation, was originally developed to describe the behavior of industrial materials such as pastes, slurries, and even food products such as ketchup [93]. Unlike simple linear viscoelastic material models, which can be described using a single characteristic relaxation time, τ_R, power-law materials have a wide and densely distributed array of characteristic relaxation times [8]. In biological cells, it has been hypothesized that this distribution of relaxation times may arise from the variety of length scales represented in the interconnected subunits of the actin cytoskeleton [8]. Regardless of their origin, the combined response of a broad array of relaxation times produces storage and loss moduli, $G'(\omega)$ and $G''(\omega)$, that have a weak power-law relationship with the excitation frequency, ω, over several orders of magnitude. In terms of the complex modulus, $G^*(\omega)$, this power-law can be written,

$$|G^*(\omega)| = G_0\left(\frac{\omega}{\omega_0}\right)^{\alpha}, \tag{16}$$

where $G_0 = G^*(\omega_0)$ is an arbitrarily chosen reference value. See Fig. 7b for an illustration of typical power-law response functions on a log–log scale with $\alpha = 0.2$ and 0.35. The power-law behavior of living cells has been observed over a broad frequency spectrum, using both active and passive experimental techniques, with internal and external probes, and a range of probe length scales [2, 32, 51, 101]. Although the magnitudes of G' and G'' inferred from these studies vary over several orders of magnitude, their frequency-dependence has been remarkably consistent [86]. For the cell type of interest in ARDS (i.e. alveolar EpC) the power-law exponent, α, has been measured at approximately 0.2 [2, 101, 121]. Based on this evidence, we must consider that time-dependent computational models of alveolar EpC deformation should have the capability to include a power-law rheology constitutive model with parameter values drawn from experimental microrheology studies. In Sect. 1.5, we describe a simple but highly effective way to incorporate power-law rheology into finite element models of cell deformation and demonstrate that only models that account for time-scale invariant properties are able to accurately reproduce all of the experimental data presented in Fig. 3.

4 Image-Based Modeling of Cell Deformation during Microbubble Flows

Previous investigators have used experimental techniques to elucidate some of the fluid-mechanical and biological processes involved in lung injury. However, direct experimental measurement of stress and strain within the cell is intractable and limited data is available on the mechanical response (i.e. deformation) of the epithelium during airway reopening. Computational models can help fill this gap in our understanding of the mechanisms responsible for cell injury by quantifying the strains experienced by EpC during airway reopening. In this section, we describe a finite element technique for investigating the instantaneous peak strains that occur in the cell membrane during airway reopening. These morphologically accurate 3D finite element models are based on confocal microscopy images of in vitro cell shape [29]. As a result, we are able to uses these image-based computational models to identify the potential mechanisms responsible for increased cell injury observed experimentally in subconfluent versus confluent cells (see Fig. 4).

4.1 Cell Culture, Imaging, and Modeling

Human A549 alveolar EpC (CCL-185, American Type Culture Collection, Manassas, VA) were cultured at passage number 20–30 and grown under standard culture conditions (37°C, 5% CO_2, and 95% air) for 1 day to obtain a subconfluent ($\sim$25%) monolayer or 4 days to obtain a confluent ($\sim$100%) monolayer. When the cell monolayers achieved the desired confluence, they were visualized using the confocal microscopy technique described in Sect. 2.3. The confocal scans revealed that cells in the subconfluent monolayer were tall and rounded while cells in the confluent monolayer were flat and closely packed. These two characteristic morphology groups were chosen to serve as models for the thin/spread morphology of type I EpC (confluent group) and the larger/taller morphology of type II EpC (subconfluent group). See Fig. 8 for a comparison of confluent and subconfluent monolayer scans.

After LSCM visualization, eight cells from both the confluent and subconfluent groups were chosen at random from their respective confocal images without foreknowledge of cell morphometry or proximity to neighboring cells. Quantitative morphology data showed statistically significant differences between the groups. Subconfluent cells were taller than the confluent cells ($H_{max} = 9.8 \pm 1.7$ vs. 3.1 ± 0.51 μm, $P < 0.001$ by homoscedastic t test) and had a larger height-to-length aspect ratio ($H/L = 0.21 \pm 0.08$ vs. 0.08 ± 0.02, $P < 0.001$), reflecting the difference in the characteristic shape between the two groups.

To generate the solid models, a series of parallel cross-section images were extracted from confocal image of the monolayer. Each cross-section contained a transverse slice of the cells, from the substrate to the apex. The images were then

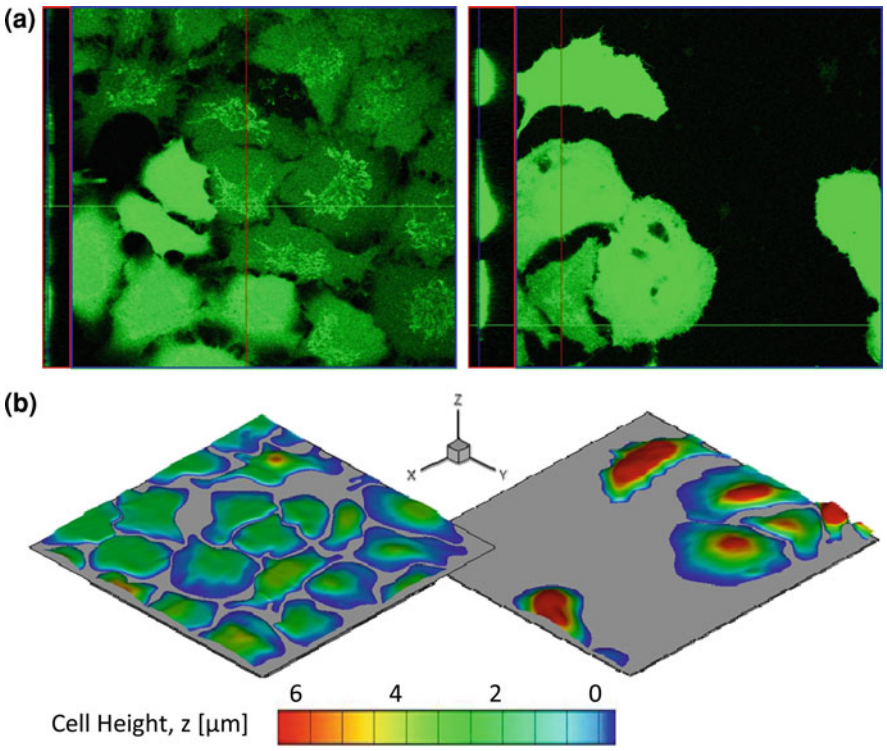

Fig. 8 Confocal microscopy scans **a** of confluent (*left*) and subconfluent (*right*) monolayers were used to build 3D morphologically accurate reconstructions of individual cell bodies **b**

imported into the Rhinoceros (Seattle, WA) CAD package. For each image, boundary curves were generated to define the cells' apical surfaces using cubic non-uniform rational B-splines (NURBS). The network of boundary curves was then used to create apical and basal surfaces and form a closed volume for each cell. Using this method, we produced 3D surface maps of the EpC in both confluent and subconfluent monolayers (see Fig. 8).

Finite element models were created by exporting individual cell geometry bodies to the ADINA 8.4 (Watertown, Mass.) finite element package. Eight cells were modeled from the confluent group and eight cells were modeled from the subconfluent group. All cells were meshed with four-node tetrahedral isotropic solid elements for the cell body and four-node triangular shell elements for the cell membrane. The maximum element edge length was chosen to be $d_{\max} = 0.1$ μm, which captured the essential features of the cell's geometry. The confluent cell models had on average 9,590 ± 3,417 solid elements and 1,963 ± 410 shell elements. The subconfluent cell models had on average 28,889 ± 8,650 solid elements and 3,572 ± 1,438 shell elements. Here we report averages as mean ± standard deviation. For detailed images showing each of the cells modeled in this study, we refer the reader to [29].

4.2 Hydrodynamic Loads and Boundary Conditions

During the propagation of an air bubble in a fluid-occluded parallel-plate flow chamber, cells experience a sharp peak in hydrodynamic stress as the bubble tip propagates through the channel (see Fig. 1). As discussed in Sect. 1.2, several previous experimental and computational studies have implicated the large pressure gradients near the bubble tip as the likely cause of cell damage during airway reopening [55, 59, 124]. In particular, Bilek et al. [12] showed that cell damage increases with decreasing bubble velocity, which also correlates with increasing the maximum pressure gradient near the bubble tip. To quantify the maximum deformation of EpC during airway reopening, these maximum instantaneous hydrodynamic loads were calculated using the correlation functions of Bilek et al. [12] (Eqs. 1–3). These peak loads were applied at the cells' apical surfaces as a superposition of normal and tangential stress tractions. Tangential shear stresses were applied in the direction of flow (x-direction). Spatial gradients in pressure and shear stress were defined with respect to the flow direction. Pressure magnitudes were controlled by an upstream reference value, $P_{\text{ref}} = 0.3\gamma/H$. System scaling variables were chosen to match typical experimental conditions: $H = 0.05$ cm, $\mu = 0.007$ g/cm s, and $\gamma = 70$ dyn/cm. Cell–cell attachments were neglected and the cells were rigidly fixed at the basal surface. The membrane/cortex and cell interior were coupled with a no-slip boundary condition.

4.3 Cell and Membrane Mechanics

Cell deformation in the ADINA finite element models is governed by a standard stress balance relationship, $\partial\sigma_{ij}/\partial x = 0$, and a linear elastic material model (Eq. 5). Estimates of cell Young's modulus (stiffness), E_{cell}, by various experimental microrheology techniques have shown significant variability, with published stiffness values ranging from tens of Pascals to a few kPa [51]. These values are tabulated and reported in Dailey et al. [29]. To account for the equivocation in reported cell stiffness values, the cell interior is modeled as an elastic isotropic medium with a range of Young's moduli, $200 < E_{\text{cell}} < 10{,}000$ dyn/cm^2.

Structural and mechanical differences between the deep cytoskeleton and the sub-membrane cortical region in alveolar EpC suggest different mechanical properties (i.e. stiffness) for these two regions [64, 65]. Modeling the membrane/cortex region of the cell as an elastic shell was carried out in two ways. One model included only the mechanical contributions of the lipid bilayer, which has a thickness, $h \approx 5$ nm [13]. The second model included the contribution of the actin cortex, which has a thickness, $h \approx 100$ nm [126]. In both cases, the membrane/cortex region can be thought of as a material that resists extension, bending, and

shear. The moduli that describe this resistance to deformation (k_e, k_b, and k_s) can be estimated from the literature and are reported in Dailey et al. [29]. These experimental values were incorporated into the computational models by noting the following relationships between k_e, k_b, and k_s and the Young's modulus, E, and shear modulus, G, of the membrane as derived from classical plate theory [98, 109].

$$k_e = \frac{Eh}{2(1-v)} \tag{17}$$

$$k_b = \frac{Eh^3}{12(1-v^2)} \tag{18}$$

$$k_s = 2hG, \tag{19}$$

where h is the thickness of the membrane and v is the Poisson ratio. The extension modulus (Eq. 17) is similar to a surface tension [dyn/cm] and it reflects the force per unit length required to induce a unit area expansion of the surface. The bending modulus (Eq. 18), which is also commonly referred to as the flexural rigidity, has units of torque [dyn-cm] and reflects the bending moment required to induce a unit change in curvature. Finally, the shear modulus (Eq. 19) also has units of tension [dyn/cm] and reflects the force per unit length required to induce a unit angular deformation. The cells are assumed to be nearly incompressible, so $v = 0.49$. For materials with isotropic mechanical properties, the shear modulus and Young's modulus are related by $G = E/2(1 + v)$. However, this isotropic formulation overestimates the shear resistance to the membrane/cortex by six orders of magnitude. As an alternative, an elastic orthotropic shell model [1] can be used to independently define E_{mem} and G_{mem}, and thus match the k_s value of the membrane/cortex more closely. Matching E_{mem} and G_{mem} to the experimentally reported values was carried out by first selecting the extension modulus, k_e, from the available data. The target moduli values k_e, k_b, and k_s, and the resulting modeling parameters, E_{mem}, G_{mem}, and h, are reported in Dailey and Ghadiali [28] for the lipid bilayer and membrane/cortex models.

Throughout this study, cell deformation was quantified in terms of effective strain in the cell membrane,

$$\varepsilon_{\text{eff}} = \sqrt{\frac{2}{3}\varepsilon_{ij} \cdot \varepsilon_{ij}} = \left\{\frac{2}{3}\left[\varepsilon_{xx}^2 + \varepsilon_{yy}^2 + \varepsilon_{zz}^2 + 2\left(\varepsilon_{xy}^2 + \varepsilon_{xz}^2 + \varepsilon_{yz}^2\right)\right]\right\}^{1/2}, \tag{20}$$

where ε_{ij} are the strain components calculated in the finite element analysis. Maximum effective strain, $\varepsilon_{\text{eff, max}}$, was reported to quantify localized peak strains within the cells. Statistical analysis was performed using SPSS 15.0 (Chicago, IL) assuming a log-normal probability distribution, which was confirmed by a Kolmogorov–Smirnov test (all $P \geq 0.483$).

4.4 Influence of Cell Morphology and Membrane Mechanics on Cell Deformation

The finite element models described above were used to investigate the influence of cell morphology and membrane mechanics on cell deformation during airway reopening and the risk of cell injury during microbubble flows. First we compared the two cell populations (subconfluent and confluent) with the two different membrane models (lipid bilayer only or bilayer plus cortex) as shown in Fig. 9. In all cases, cells were exposed to bubble-induced stresses according to Eqs. 1–3 at $Ca = 5E{-}5$, which is typical for experimental airway reopening conditions [12, 59, 124]. As expected, increasing cell stiffness decreased the amount of cell deformation. In general, the subconfluent cell models predicted higher strains than the confluent cell models. ANOVA indicated that cell type (confluent vs. subconfluent) and cell stiffness were both statistically significant factors (all $P < 0.001$ for both the lipid bilayer and cortex models). Among confluent or subconfluent cells only, differences between the lipid bilayer and cortex models were statistically significant (all $P < 0.001$ by ANOVA). For all data shown in Fig. 9, all E_{cell} treatment levels were significantly different [all $P < 0.001$ by a least significant difference (LSD) post hoc test].

The preceding results compared the two baseline membrane models: the lipid bilayer only and the bilayer with an actin cortex. In these models, the membrane thickness, Young's modulus, and shear modulus were simultaneously changed to produce the desired bending, extensional, and shear moduli. To quantify the role of each mechanical property specified in our models, systematic variations were carried out for the three independent membrane mechanics parameters: E_{mem}, G_{mem}, and h (see Fig. 10). In each case, variations were performed from the baseline cortex model using the confluent and subconfluent cell populations with $E_{\text{cell}} = 1{,}500$ dyn/cm^2.

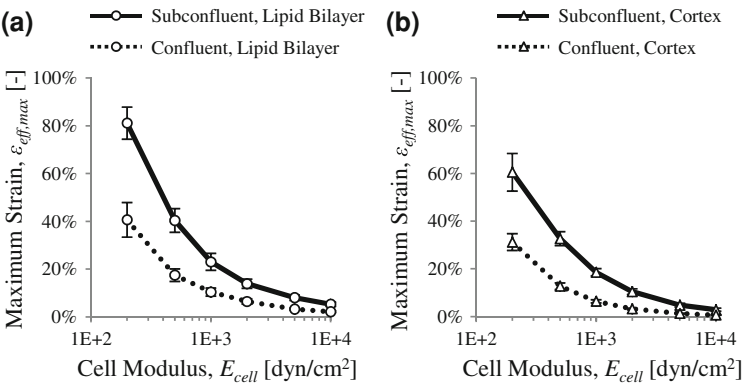

Fig. 9 Maximum effective strain for subconfluent and confluent cells with the baseline lipid bilayer model **a** and baseline cortex model **b**. Strain decreases with increasing E_{cell}. Figures report geometric mean ± 70% confidence intervals (With permission from Dailey et al., J. Appl. Physiol., 2009, Am. Physiol. Soc.)

First, variations of the Young's modulus of the membrane, E_{mem}, were performed keeping h and G_{mem} at the baseline cortex values (Fig. 10a). The cortex stiffness range included several orders of magnitude above and below the baseline value of $E_{mem} = 4.5E7$ dyn/cm^2. Increasing E_{mem} generally decreased the membrane strain magnitudes and this effect was most significant for the subconfluent cells. ANOVA indicated that E_{mem} was a statistically significant factor ($P < 0.001$). Strain localization patterns within the cells showed a strong dependence on E_{mem} (see Fig. 11). When the cortex had low stiffness ($E_{mem} = 4.5E4$ dyn/cm^2; Fig. 11a, c), the strain patterns indicated that the cell experienced relatively uniform deformation in the direction of flow. The cell flattened out and bulged over the downstream edge, creating large regions of high strain. This type of bulging deformation was previously hypothesized to lead to membrane rupture and cell death [12], and our models have confirmed that this

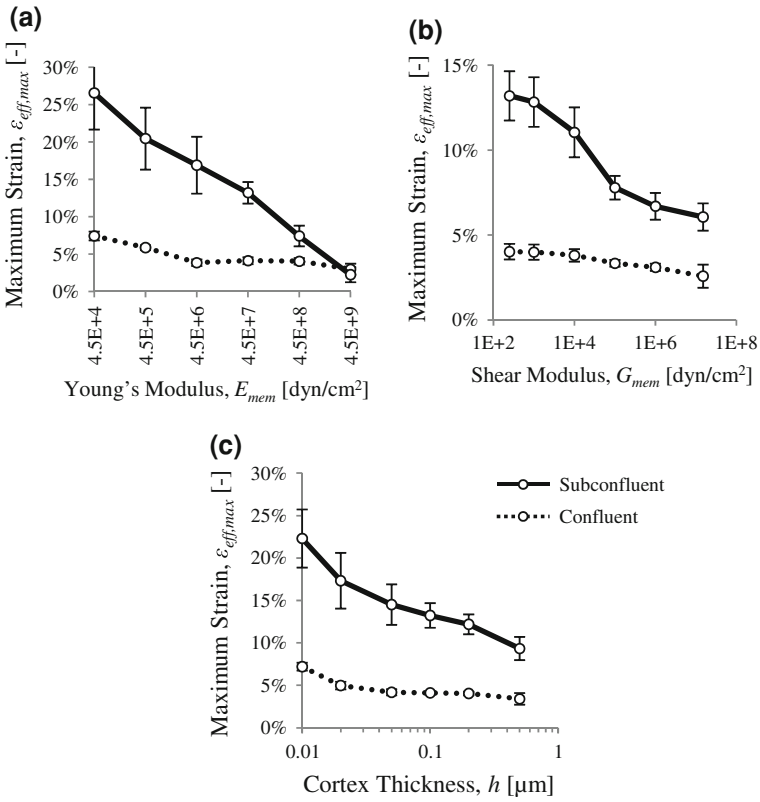

Fig. 10 Effect of membrane shell mechanics on maximum effective strain for confluent and subconfluent cells. **a** Effect of Young's modulus, E_{mem}, was statistically significant for both cell types (all $P < 0.001$). **b** Effect of shear modulus, G_{mem} was statistically significant for both cells types (all $P < 0.001$). **c** Effect of cortex thickness, h, was statistically significant for both cell types (all $P < 0.001$). Figures report geometric mean ± 70% confidence intervals (With permission from Dailey et al., J. Appl. Physiol., 2009, Am. Physiol. Soc.)

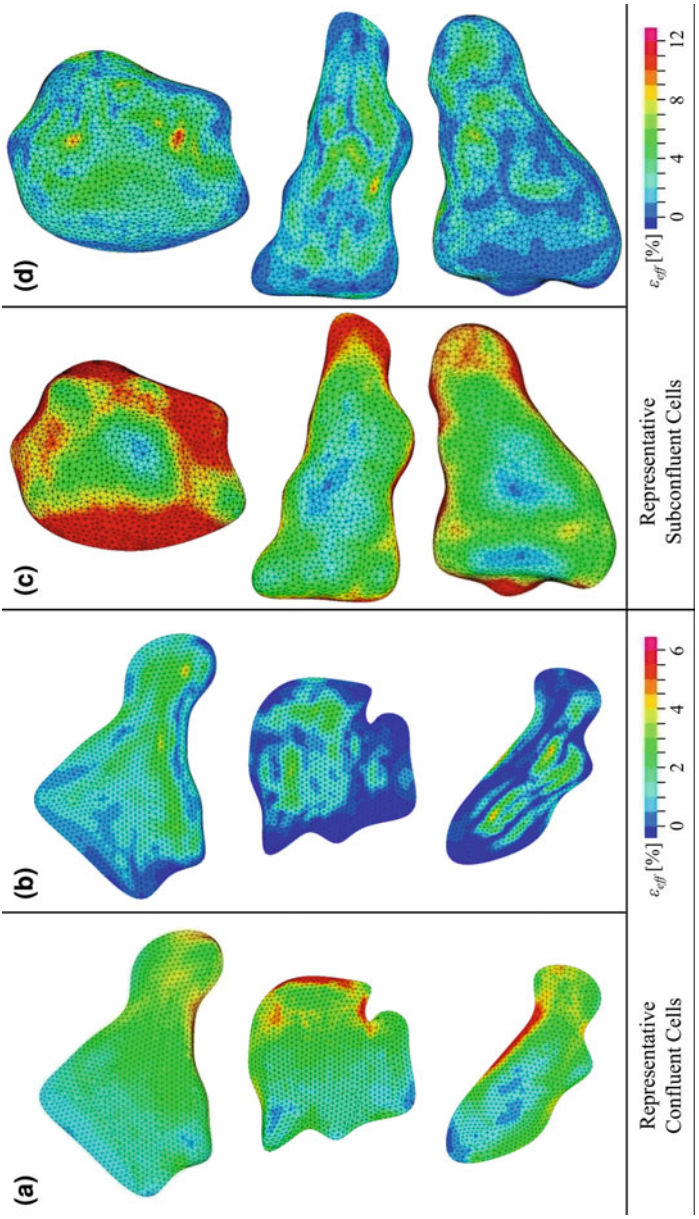

Fig. 11 Strain localization contour plots for representative confluent cells **a**, **b** and subconfluent cells (**c**, **d**). For each cell type, cells are shown with a soft cortex ($E_{mem} = 4.5E4$ dyn/cm^2, **a**, **c**) and a normal cortex ($E_{mem} = 4.5E7$ dyn/cm^2, **b**, **d**). Results shown are for $Ca = 5E{-}5$, $E_{cell} = 1{,}500$ dyn/cm^2. Cells with the soft cortex experienced uniform whole-cell deformation in the direction of flow (*left* to *right*) and a downstream "bulge". Cells with the normal cortex did not exhibit this downstream bulge. Flow direction is *left* to *right* (With permission from Dailey et al., J. Appl. Physiol., 2009, Am. Physiol. Soc.)

behavior could arise under the influence of the large pressure gradients found near the bubble tip. However, as E_{mem} increased, the strain localization patterns were significantly altered. When the cortex stiffness matched the experimental baseline ($E_{mem} = 4.5E7$ dyn/cm^2; Fig. 11b, d), the cells did not exhibit the downstream bulge and strain localization patterns did not have a distinct upstream–downstream trend. As expected from Fig. 10a, these strain localization trends were most pronounced in the subconfluent cells.

Next, variations of the shear modulus, G_{mem}, were performed keeping h and E_{mem} at the baseline cortex values (Fig. 10b). The lower limit was defined by the G_{mem} required to match the published experimental value for $k_s = 0.0025$ dyn/cm and the upper limit was prescribed by an equivalent isotropic membrane model ($k_s = 150$ dyn/cm). Increasing the shear modulus of the membrane region generally decreased membrane strain. ANOVA indicated that G_{mem} was a statistically significant factor for confluent cells ($P = 0.035$) and subconfluent cells ($P < 0.001$), but an LSD post hoc test showed that this effect was only significant when comparing very low shear moduli to very high shear moduli. No statistically significant changes in strain were found for single order-of-magnitude changes in G_{mem} among confluent cells. However, $\varepsilon_{eff,\ max}$ did show significant changes with single order-of-magnitude changes in G_{mem} among subconfluent cells only, which suggests that subconfluent cells may be more sensitive to the membrane shear modulus than confluent cells.

Finally, variations of the cortex thickness, h, were performed keeping E_{mem} and G_{mem} at the baseline cortex values (Fig. 10c). The h range was chosen to include a lower limit of double the thickness of a lipid bilayer ($h = 0.01$ μm) and an upper limit of five times the experimental baseline ($h = 0.5$ μm). Increasing cortex thickness generally decreased the maximum strain magnitudes and h was a statistically significant factor ($P < 0.001$). Again, we repeated our examination of the strain localization behavior and observed a decrease in the magnitude of the peak strains with increasing cortex thickness, but no noteworthy changes in the strain localizations patterns (images not shown). For these simulations, the chosen baseline E_{mem} value prevented whole-cell deformation patterns like those shown in Figs. 11a, c.

So far, all comparisons between subconfluent and confluent cells have assumed that the two populations have identical mechanical properties. However, previous investigators observed microstructural differences between subconfluent and confluent cells, particularly in the redistribution of actin [124]. These structural differences may be associated with differences in the mechanical properties of the cytoskeleton or cortex region. For example, Yalcin et al. [124] observed a diffuse, relatively homogeneous actin network in their confluent EpC and a redistribution of actin to the cell periphery in the subconfluent EpC. The analogous finite element data sets would be confluent cells with the lipid bilayer and subconfluent cells with the thicker cortical region (see Fig. 12). Even when the membrane/cortex mechanical contribution is chosen to maximize strain in the confluent cells and minimize strain in the subconfluent cells, the subconfluent group still exhibits higher maximum strains. Statistically significant differences between the two cell populations were observed with $P < 0.001$ by ANOVA. The correlation between

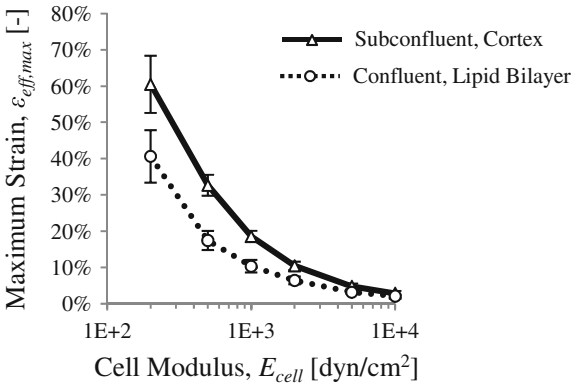

Fig. 12 Even when membrane models are chosen to maximize strains in the confluent cells (lipid bilayer model) and minimize strains in subconfluent cells (cortex model), the subconfluent group still has higher strains than the confluent group due to their morphology. Differences between subconfluent and confluent groups were statistically significant (all $P < 0.001$ by ANOVA) (With permission from Dailey et al., J. Appl. Physiol., 2009, Am. Physiol. Soc.)

the computational predictions and experimental data not only validates the computational models but also suggests that morphological differences between cell types is an important parameter in determining microbubble-induced cell injury.

The computational modeling results presented above suggest that given the same hydrodynamic loading conditions, subconfluent cells develop higher membrane strains than confluent cells. If we assume that membrane strain correlates positively with the risk of cell injury, these results are in agreement with the experimental findings of Yalcin et al. [124] who saw higher death rates for subconfluent cells than confluent cells (see Fig. 4). Based on measurements of the cell aspect ratio, they concluded that hydrodynamic stress amplification was not the source of the observed differences in cell death rate between the confluent and subconfluent groups. The finite element modeling results support the idea that cell morphology alone can have a significant effect on injury susceptibility for a given loading condition. Specifically, the more rounded morphology of the subconfluent cells makes them more prone to bending and bulging deformations that lead to large membrane strains and a greater risk for membrane rupture. In the strain localization images (Fig. 11), similar strain patterns appeared in both subconfluent and confluent cells, but the trends were significantly amplified in the subconfluent cell group.

This finding has interesting implications for the health of the epithelium and lung mechanics during ARDS. The type II A549 alveolar EpC used to generate the finite element models exhibit significant changes in characteristic morphology depending on the degree of confluency of the monolayer. In a low-confluence monolayer, A549 cells are tall and rounded, which corresponds to the typical morphology of type II cells. However, as the monolayer approaches 100% confluence, the morphology of the cells changes to a more thin and spread profile, which is consistent with the morphology of type I cells. The models suggested that subconfluent cells with type II morphology develop higher strains than confluent

cells with type I morphology. Assuming that higher strains are associated with an increased risk of injury, this data suggests that due to their morphology, type II cells may be at higher risk for injury than type I cells during airway reopening. Morphology-dependent preferential injury of type II cells could lead to a loss of surfactant secretion and additional challenges to the ARDS-stressed lung. The finite element models also suggested that cell mechanics has a strong influence of on the risk of cell injury during airway reopening. Specifically, maximum membrane strain decreased with increasing cell stiffness (Fig. 9) and showed a statistically significant dependence on the membrane model (lipid bilayer versus bilayer plus actin cortex). In addition, the models suggested that stiffening of the membrane/cortex region could by cytoprotective. As described in Sect. 6.1, our laboratory has recently tested this hypothesis by altering the amount of cortical actin in A549 cells and investigating how these changes in cortical actin influence microbubble-induced necrosis and membrane rupture. Those results suggest that altering the microstructure and mechanical properties of the membrane/cortex region may be an effective way to reduce microbubble-induced cell injury during the ventilation of patients with ARDS.

5 Transient Dynamic Cell Deformation during Microbubble Flows

One limitation of the models presented in Sect. 1.4 is in the use of instantaneous peak hydrodynamic stresses applied to cells with linear elastic mechanical properties. Although this technique facilitates the investigation of questions pertaining to cell morphology, it neglects the dynamic component of airway reopening. The in vitro model of airway reopening (Fig. 1) involves the propagation of a microbubble through a channel, which generates transient hydrodynamic stresses on the EpC lining the channel wall. The cells, which are inhomogeneous viscoelastic bodies, have a transient dynamic response to this stress wave. Most computational studies of cells with viscoelastic properties have used linear viscoelastic models such as the Maxwell fluid. However, recent experimental measurements of cell rheology, or dynamic mechanical properties, have repeatedly suggested that biological cells behave like soft glassy materials with power-law rheology [51, 121]. In a previous study, we have described a technique for investigating dynamic intracellular strains during airway reopening using an optimized Prony–Dirichlet series to model the cells' power-law rheology [28].

5.1 Prony–Dirichlet Series Model for Power-Law Cell Mechanics

Most measurements of power-law cell mechanics are carried out in the frequency domain using oscillatory techniques such as magnetic twisting cytometry (MTC).

In the time domain, whole-cell uniaxial stretching rheometry (USR) experiments have shown that the creep function, $J(t)$, of living cells also follows a power-law relationship with time [32],

$$J(t) = A_0 \left(\frac{t}{t_0}\right)^{\alpha} \tag{21}$$

where $J(t_0) = A_0$ is an arbitrarily chosen reference value. Furthermore, the exponent α agrees with the power law exponent observed in the frequency domain (Eq. 16) [32]. This is significant because many biomechanical and physiological problems of interest involve simulation of cell deformation under complicated transient load conditions. In addition to airway reopening flows, cardiovascular flows have complex time-domain characteristics and are known to contain multiple fundamental frequencies [37, 83].

To form a basis for a time-domain model of power-law rheology, we first use Laplace transforms to show the correspondence between the time-domain creep function and the frequency-domain complex modulus. In the time domain, the strain, $\varepsilon(t)$, produced by a step stress, σ_0, can be described as follows:

$$\varepsilon(t) = \sigma_0 J(t) \tag{22}$$

where $J(t)$ is the creep function. The strain due to a second step load, $\Delta\sigma_i$, applied some time, τ_i, later is:

$$\varepsilon_i(t) = \Delta\sigma_i J(t - \tau_i) \tag{23}$$

We can continue in this manner, adding $\Delta\sigma_i$ increments to represent any time-dependent stress load. We then apply the Boltzman Superposition Principle and write the Hereditary Integral, which describes the strain induced by an arbitrary time-varying stress as follows:

$$\begin{aligned} \varepsilon(t) &= \sigma_0 J(t) + \sum_{i=1}^{\infty} \mathrm{d}\sigma_i J(t - \tau_i) \\ &= \sigma_0 J(t) + \int_0^t \left(\frac{\mathrm{d}\sigma}{\mathrm{d}t}\right)_{t=\tau} J(t - \tau)\mathrm{d}\tau. \end{aligned} \tag{24}$$

Laplace Transforms can be applied to the Hereditary Integral, from which we develop the following stress strain relationship.

$$\tilde{\varepsilon}(s) = s\tilde{\sigma}(s)\tilde{J}(s) \tag{25}$$

$$\frac{\tilde{\sigma}(s)}{\tilde{\varepsilon}(s)} = \frac{1}{s\tilde{J}(s)} = \tilde{G}(s) \tag{26}$$

Noting the relationship between Fourier and Laplace Transforms, $\hat{f}(\omega) = \tilde{f}(i\omega)$, we can rewrite the stress–strain relationship.

$$\hat{\varepsilon}(\omega) = i\omega\hat{\sigma}(\omega)\hat{J}(\omega) \tag{27}$$

$$\frac{\hat{\sigma}(\omega)}{\hat{\varepsilon}(\omega)} = \frac{1}{i\omega\hat{J}(\omega)} = \hat{G}(\omega). \tag{28}$$

Thus, because $\hat{f}(\omega) = \tilde{f}(s = i\omega)$, there exists a single complex modulus, $G^*(\omega)$, such that,

$$G^*(\omega) = \frac{1}{i\omega\hat{J}(\omega)} = \frac{1}{i\omega\tilde{J}(i\omega)} = \frac{1}{J^*(\omega)} \tag{29}$$

where $J^*(\omega) = s\tilde{J}(s)\big|_{s=i\omega}$ is the complex creep function.

For a time-domain creep function with a power-law form, we can find the equivalent frequency-domain complex modulus as follows. Starting from the creep function, $J(t)$ (Eq. 21), the reference time, t_0, is often chosen to be 1 s for convenience. Taking the Laplace transform then yields the following:

$$\tilde{J}(s) = \mathcal{L}[J(t)] = \frac{A_0\Gamma(\alpha+1)}{t_0^{\alpha}s^{\alpha+1}}. \tag{30}$$

Here, $\Gamma(\alpha + 1)$ is the Gamma factorial function, given in Euler integral form as follows:

$$\Gamma(\alpha+1) = \int_0^{\infty} t^{\alpha}\mathrm{e}^{-t}\mathrm{d}t = \alpha! \tag{31}$$

Again, noting $J^*(\omega) = s\tilde{J}(s)\big|_{s=i\omega}$, we substitute Eq. 30 into Eq. 29 and write the complex modulus.

$$G^*(\omega) = \frac{1}{i\omega\tilde{J}(i\omega)} = \frac{t_0^{\alpha}(i\omega)^{\alpha}}{A_0\Gamma(\alpha+1)} \tag{32}$$

Finally, we take the principal value of this infinite-valued function, noting that $\mathrm{PV}[(i)^{\alpha}] = \mathrm{e}^{i(\pi/2)\alpha}$, which allows us to write the shear storage and loss moduli, $G'(\omega)$ and $G''(\omega)$, which are the in-phase and out-of-phase components of the complex modulus, $G^*(\omega)$.

$$G'(\omega) = \frac{t_0^{\alpha}\omega^{\alpha}}{A_0\Gamma(\alpha+1)}\cos\left(\frac{\pi}{2}\alpha\right) \tag{33a}$$

$$G''(\omega) = \frac{t_0^{\alpha}\omega^{\alpha}}{A_0\Gamma(\alpha+1)}\sin\left(\frac{\pi}{2}\alpha\right). \tag{33b}$$

Comparing Eqs. 21 and 33a, we observe that the creep function, $J(t)$, and the complex modulus, $G^*(\omega)$, have the same power-law exponent, α.

The simple power-law model for the complex modulus of cells exhibiting soft glassy properties (Eq. 16) is a good fit with the experimental data, but it is not conveniently formulated for implementation in finite element models. In a previous study, we presented a time-domain computational formulation of power-law rheology that captures the frequency-dependence of $G'(\omega)$ and $G''(\omega)$ and can also be used to simulate the time-dependent response of biological cells to transient loading conditions [28]. This model captures power-law rheological behavior using a time-dependent material model based on a Prony–Dirichlet series.

A Prony–Dirichlet series is well-suited to modeling cell mechanics because it is inherently reflective of the underlying mechanics of the cytoskeleton. Previous investigators have proposed that the cytoskeleton is a self-similar [32], interconnected network of mechanical elements ranging in size from individual actin filaments to intracellular structures such as actin bundles to the whole cell [8]. The combined mechanical response of this network can be described using a chain of spring-dashpot units, each with a different characteristic time representing a different length scale of the system. This chain of viscoelastic elements would have a shear modulus, $G(t)$, and bulk modulus, $K(t)$, defined by a Prony–Dirichlet series with N terms.

$$G(t) = G_\infty + \sum_{i=1}^{N} G_i e^{-t/\tau_i} \tag{34a}$$

$$K(t) = K_\infty + \sum_{i=1}^{N} K_i e^{-t/\tau_i}. \tag{34b}$$

Here $G(t)$ and $K(t)$ are the shear and bulk moduli of the viscoelastic material, G_∞ and K_∞ are the long-term moduli, G_i and K_i are the coefficients of the Prony series, and τ_i are the time constants. The shear and bulk moduli are related by the Poisson ratio, v.

$$K = \frac{2(1+v)G}{3(1-2v)} \tag{35}$$

where the $v = 0.49$ for the nearly incompressible materials used in this study. This material model is implemented in the finite element formulation through the following convolution integrals which relate stress and strain history.

$$s_{ij}(t) = 2G(0)e_{ij}(t) + 2\int_0^t e_{ij}(t-\tau)\frac{dG(\tau)}{d\tau}d\tau \tag{36a}$$

$$\sigma_{kk}(t) = 3K(0)e_{kk}(t) + 3\int_0^t \varepsilon_{kk}(t-\tau)\frac{dK(\tau)}{d\tau}d\tau \tag{36b}$$

where $s_{ij} = \sigma_{ij} - \frac{1}{3}\delta_{ij}\sigma_{kk}$ is the deviatoric stress, $e_{ij} = \varepsilon_{ij} - \frac{1}{3}\delta_{ij}\varepsilon_{kk}$ is the deviatoric strain, δ_{ij} is the Kronecker delta, σ_{ij} is the stress, and ε_{ij} is the strain.

To achieve a power-law response using the Prony–Dirichlet series given in Eq. 34, we note that $G^*(\omega) = s\tilde{G}(s)\big|_{s=j\omega}$, where $\tilde{G}(s)$ is the Laplace transform of $G(t)$, which yields the following expression for the complex modulus when the long-term moduli are set to zero.

$$G^*(\omega) = G'(\omega) + jG''(\omega) = \sum_{i=1}^{N} \frac{G_i\tau_i^2\omega^2 + j\omega G_i\tau_i}{1 + \tau_i^2\omega^2}. \tag{37}$$

First we assign the time constants, τ_i, according to a log-distribution in the range $\tau_{\min} \leq \tau_i \leq \tau_{\max}$. The maximum time constant, $\tau_{\max} = 300$ s, was chosen to match the result reported by Balland et al. [8] for A549 cells based on an analysis of the correlation between the power-law prefactor G_0 and the exponent α. The chosen minimum time constant, $\tau_{\min} = 3 \times 10^{-3}$ s, controls the upper frequency limit of power-law behavior in this fitted series. To assign the series prefactors, G_i, corresponding to each τ_i, we implemented a non-negative constrained least squares algorithm. The algorithm showed that increasing the number of terms in the Prony series improved the representation of power-law behavior for $\alpha = 0.20$. Ultimately, a modest number of terms, $N = 7$, was used to produce a coefficient of determination $R^2 = 0.999$ for all six power-law regressions: $\alpha = [0.15, 0.20, 0.25, 0.3, 0.35, 0.40]$. In our previous study [28], these fitted series were then implemented in a validation finite element model based on the oscillating optical tweezers microrheology technique. Over a range of oscillation frequencies, bead displacement amplitude and phase data were used to calculate the complex modulus of the surrounding medium. The simulations were repeated for a range of α values and in each case, the power-law calculated from bead displacements showed excellent agreement with the α used to fit the Prony–Dirichlet series. This range of α included the consensus baseline for cultured mammalian cells ($\alpha \sim 0.2$) and the potential for variability in response to mechanical environment and loading (e.g. pharmacological treatments [125] or stretch-induced fluidization [99]).

As previously discussed, there is some precedent for modeling viscoelastic cell mechanics using the Maxwell fluid formulation [57, 58]. To investigate the usefulness of this model for cells under airway reopening conditions, we performed simulations with both models and present the Maxwell and power-law results side-by-side. In these simulations, the magnitudes of the complex moduli in each model were matched at $\omega_0 = 1$ rad/s, or $G^*(\omega_0)|_{\text{Maxwell}} = G^*(\omega_0)|_{\text{power-law}}$.

5.2 Finite Element Model Development

The cells used in this study were developed according to the cell culture, confocal imaging, and geometry modeling techniques described in Sect. 4.1. The eight

confluent cells had the following morphometric parameters: $H_{cell} = 3.1 \pm 0.51$ μm and $L_{cell} = 43.0 \pm 7.1$ μm for a cell height-to-length aspect ratio $H_{cell}/L_{cell} = 0.09 \pm 0.02$ (reporting mean ± standard deviation). As before, cells were meshed with four-node tetrahedral isotropic solid elements for the cell body and four-node triangular shell elements for the cell membrane. The cell models had an average of 9,590 ± 1,963 solid elements and 3,417 ± 410 shell elements (reporting mean ± standard deviation). The membrane model was chosen to represent the lipid bilayer with an actin cortex, as previously described in Sect. 4.3.

Transient hydrodynamic stresses were modeled to correspond to in vitro microbubble flow experiments [12, 59, 124]. For microbubble flows, the shape of the air–liquid interface and the transient hydrodynamic stresses exerted on the apical surface of the EpC depend on the capillary number, $Ca = \mu U/\gamma$, where μ is the fluid viscosity, U is the bubble speed and γ is the surface tension of the air–liquid interface. To calculate the hydrodynamic stresses, the boundary element method was used to solve the microbubble flow field and generate dimensionless normal and shear stress profiles under steady-state, surfactant-free conditions. Gaver and colleagues previously published the details regarding boundary element solutions of bubble flow in both a smooth axisymmetric tube [42, 43] and in a Hele-Shaw cell [45]. In the present study, we chose the Hele-Shaw cell (i.e. a 2D channel with large width to height ratio) to provide a better computational analogue to the in vitro experiments [12, 59, 124]. For more information on boundary element solutions of bubble propagation in 2D channels we refer the reader to the previous work of Halpern and Gaver III [45] and Bilek et al. [12].

The hydrodynamic loads calculated from the boundary element solutions were applied to the apical surface of the EpC as a superposition of normal and tangential stress tractions. Tangential shear stresses were applied in the direction of flow. Dimensionless wall stresses, $\tau(x)$, were extracted from the boundary element solutions as functions of dimensionless wall position, x (Fig. 13).

During steady-state airway reopening, a cell on the wall experiences the entire stress profile, so the dimensionless spatial coordinate, x, was converted to a dimensional time history according to,

$$t = \frac{Hx}{U} \tag{38}$$

where t is time, H is the channel half-height and U is the bubble velocity. The dimensionless stress magnitudes, τ, were also scaled as shown below.

$$\tau_{dim} = \frac{\gamma\tau}{H} \tag{39}$$

where τ_{dim} is the dimensional stress magnitude and γ is the surface tension. Dimensional stress gradients, $d\tau_{dim}/dx_{dim}$, were defined by calculating the change in stress magnitude over the length of each cell at every point in the time history. When scaling the dimensionless stress profiles, a range of channel half-height

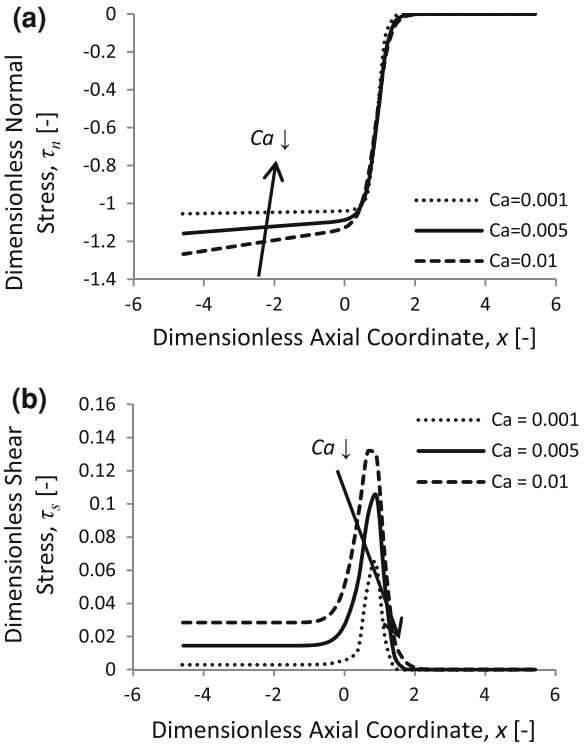

Fig. 13 Boundary element solutions yield dimensionless normal and shear stresses as functions of dimensionless wall position for several *Ca*

values, $0.25 \leq H \leq 0.85$ mm, and a range of bubble speeds, $0.15 \leq U \leq 1.5$ cm/s, were chosen to include the parameters used in previously published in vitro microbubble flow experiments [124]. Note that these U values correspond to the estimated airway reopening velocities expected in terminal and respiratory bronchioles [124]. We also scaled stresses using typical experimental values for surface tension, $\gamma = 70$ g/s^2. However, due to a fluid viscosity of $\mu_{\text{experiments}} = 0.8$ cP, the capillary numbers used in these experiments were very low, $Ca_{\text{experiments}} \approx 10^{-5}$ to 10^{-4}. Since the boundary element method is not able to simulate these low *Ca* numbers, we follow the precedent set by previous investigators [12, 55] in which boundary element solutions at higher *Ca* (i.e. $Ca = 10^{-3}$ to 10^{-2}) are used to elucidate certain aspects of microbubble flows. To achieve the physiologically relevant bubble speeds of $0.15 \leq U \leq 1.5$ cm/s and higher *Ca* values we specified a larger viscosity value of $\mu = 47$ cP in our computational models.

Previous experimental studies demonstrated that the degree of cell injury is primarily a function of the maximum pressure gradient, $(\mathrm{d}P/\mathrm{d}x)_{\max}$, generated during reopening. In addition, Kay et al. [59] demonstrated that the amount of cell injury is not a function of exposure time, Δt, where Δt is the duration that cells are exposed to the maximum normal stress gradient, $(\mathrm{d}P/\mathrm{d}x)_{\max}$. The values for Δt and $(\mathrm{d}P/\mathrm{d}x)_{\max}$, can be calculated as [59]:

$$\Delta t = 2.94\frac{HCa^{0.29}}{U} = 2.94\frac{H\mu^{0.29}}{U^{0.71}\gamma^{0.29}} \tag{40}$$

$$\left(\frac{dP}{dx}\right)_{max} = 0.34\frac{(\gamma/H^2)}{Ca^{0.29}} = 0.34\frac{\gamma^{1.29}}{(\mu U)^{0.29}H^2}. \tag{41}$$

As Ca decreases, the stress wave near the bubble tip becomes sharper and the maximum pressure gradient increases while the time a cell is exposed to that gradient decreases. For equivalent H and U values, the stresses from $Ca \geq 1E{-}3$ boundary element solutions have slightly lower maximum pressure gradients and longer exposure times than in the in vitro microbubble flow experiments. However, we note that the range of Δt and $(dP/dx)_{max}$ values simulated in our computational models are comparable to the range explored experimentally and capture the entire range explored by Gaver and colleagues [12, 59] who only used flow channels with $H = 0.85$ mm. Values for Δt and $(dP/dx)_{max}$ under typical experimental conditions and in our computations which utilize equivalent H and U values but higher Ca and μ values have been discussed in detail in our previous study [28].

As with the models presented in Sect. 1.4, we assumed that increasing strain in the cell membrane correlates with an increased risk that the membrane will rupture, leading to cell necrosis. Therefore, we quantified cell deformation in terms of effective strain in the cell membrane. Statistical analysis was performed using SPSS 15.0 (Chicago, IL) assuming a log-normal probability distribution. Log-normality of results were confirmed by a Kolmogorov–Smirnov test (all $P \geq 0.251$).

5.3 *Influence of Cell Rheology on Cell Deformation during Airway Reopening*

Previous experimental investigations of the relationship between bubble hydrodynamics and cell injury have used two key parameters to vary the stresses applied: channel half-height, H, and bubble speed, U. Equations 40 and 41 show the relationship between the physical parameters H and U and two hydrodynamic parameters of interest: the maximum pressure gradient near the bubble tip, $(dP/dx)_{max}$, and the duration that cells are exposed to that maximum stress, Δt. The experimental results have suggested that $(dP/dx)_{max}$ is the primary physical factor responsible for cell injury during airway reopening [12, 124] and that cell injury does not correlate with Δt [59]. The computational models can be used to investigate whether this observation is due to the viscoelastic mechanics of the cells and whether a simple Maxwell fluid model can capture this behavior.

First we examined the effect of channel height, H, on intracellular strain for cells with the Maxwell fluid and power-law material models and a fixed bubble

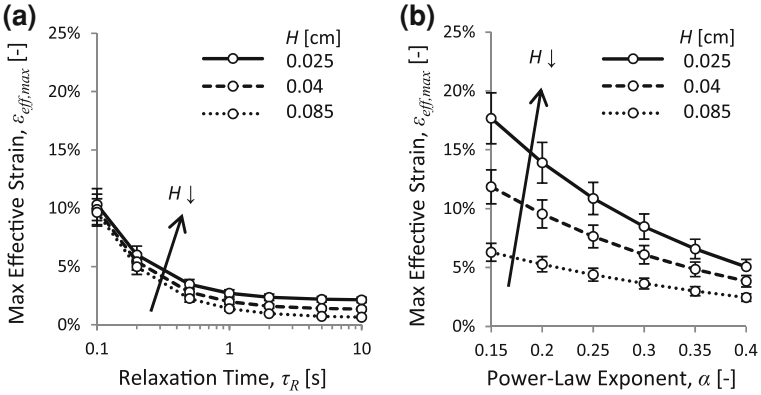

Fig. 14 Increasing channel half-height, H, decreased membrane strain (i.e. risk of cell death) for cells with the Maxwell (**a**) and power-law (**b**) models. Figures report geometric mean ± 70% confidence intervals (With permission from Dailey et al., Biomech. Model. Mechanobiol., 2010)

speed of $U = 0.3$ cm/s. As shown in Fig. 3, previous in vitro experimental studies have clearly demonstrated that EpC undergo significantly less membrane rupture (i.e. cell necrosis) as H increases [124]. The computational models also showed that decreasing channel height leads to an increase in maximum strain for both cell viscoelasticity models (see Fig. 14). For cells with the Maxwell material model, this effect was minor and its significance depended on the choice of τ_R (significant changes with H were only observed for $\tau_R > 2$ s; $P \leq 0.031$ by two-tailed homoscedastic t tests). In contrast, cells with the power-law material model exhibited a dramatic increase in membrane strains as H decreased and this effect was significant for all values of α ($P < 0.013$ by t tests).

We also examined the effect of bubble speed, U, on intracellular strain for cells with the Maxwell fluid and power-law material models and a fixed channel half-height of $H = 0.04$ cm. Previous in vitro experimental studies have clearly demonstrated that EpC exhibit significantly more necrosis (i.e. membrane rupture) as U decreases [12, 59, 124]. As shown in Fig. 15, the computational models also showed that decreasing U produces larger membrane strains for both Maxwell and power-law cells. However, in the Maxwell model, this effect of U on membrane strain was only significant for $\tau_R \leq 1$ s ($P \leq 0.026$ by t tests). In contrast, we observed statistically significant increases in strain at lower U for a large range of α values (i.e. for $\alpha \geq 0.2$; $P \leq 0.027$ by t tests) in the power-law cells (see Fig. 15).

In the results presented in Figs. 14 and 15, which independently varied H and U, both the exposure duration, Δt, and maximum pressure gradient, $(\mathrm{d}P/\mathrm{d}x)_{\max}$, changed simultaneously (refer to Eqs. 40 and 41). To study the effects of $(\mathrm{d}P/\mathrm{d}x)_{\max}$ and Δt separately, we carefully specified both H and Ca to keep either pressure gradient or exposure duration constant while varying the other parameter. For example, choosing $H = [0.025, 0.040, 0.077$ cm] and $Ca = [0.001, 0.002, 0.005]$ produced a range of maximum pressure gradients, $(\mathrm{d}P/\mathrm{d}x)_{\max} = [28.23,$

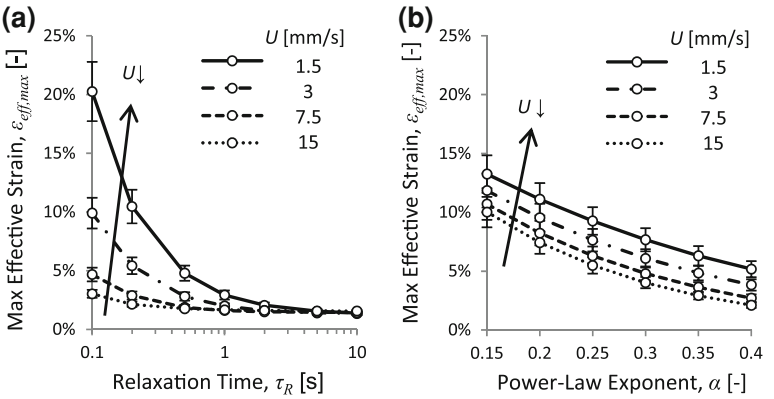

Fig. 15 Increasing bubble speed, U, decreased membrane strain (i.e. risk of cell death) for cells with the Maxwell **a** and power-law **b** models. Figures report geometric mean ± 70% confidence intervals (With permission from Dailey et al., Biomech. Model. Mechanobiol., 2010)

9.02, 1.87 dyn/cm^2 μm] and a constant $\Delta t = 0.065$ s. Note that this exposure duration is equivalent to the Δt in the most damaging case reported by Yalcin et al. [124]. Conversely, choosing $H = [0.04,\ 0.045,\ 0.050$ cm] and $Ca = [0.005,\ 0.002,\ 0.001]$ produced a range of exposure durations, $\Delta t = [0.034,\ 0.073,\ 0.133$ s] and a constant $(\mathrm{d}P/\mathrm{d}x)_{\max} = 7$ dyn/cm^2.μm. Note that this maximum pressure gradient is comparable to the $(\mathrm{d}P/\mathrm{d}x)_{\max}$ associated with the maximum cell damage reported by Kay et al. [59].

Following this procedure, we first studied the case when the hydrodynamic stresses had a constant exposure duration, $\Delta t = 0.065$ s, and variable maximum pressure gradient. As expected, increasing $(\mathrm{d}P/\mathrm{d}x)_{\max}$ increased the maximum strain in the cell membrane (see Fig. 16). For the Maxwell cells, although statistically significant differences between all three $(\mathrm{d}P/\mathrm{d}x)_{\max}$ groups were found at all τ_R ($P \leq 0.017$ by t tests), >2% differences in strain between $(\mathrm{d}P/\mathrm{d}x)_{\max}$ groups was only found for $\tau_R \leq 1$ s. For the power-law cells, significant differences between all three $(\mathrm{d}P/\mathrm{d}x)_{\max}$ groups were found at all α levels ($P \leq 0.006$ by t tests) and >5% differences in strain were found for all α levels.

Next we investigated the effect of varying Δt for a constant pressure gradient, $(\mathrm{d}P/\mathrm{d}x)_{\max} = 7$ dyn/cm^2 μm. The effects of varying Δt depend on the viscoelastic material model used for the cells (see Fig. 17). For the Maxwell cells with a low τ_R, maximum strain increased with increasing exposure duration ($\tau_R \leq 1$ s; all significant $P \leq 0.047$ by t tests). This dependence of strain on exposure duration was not observed in the cells modeled with power-law rheology. For the power-law cells, comparisons of the Δt groups at each α treatment level showed that significant differences arose only at the highest α values (for $\alpha \geq 0.35$; $P \leq 0.027$ by t tests).

A comparison of the data in Figs. 16 and 17 with previously published experimental observations highlights a significant limitation of the Maxwell material model. Specifically, experiments have clearly demonstrated that the amount of cell necrosis via membrane rupture is strongly correlated with the

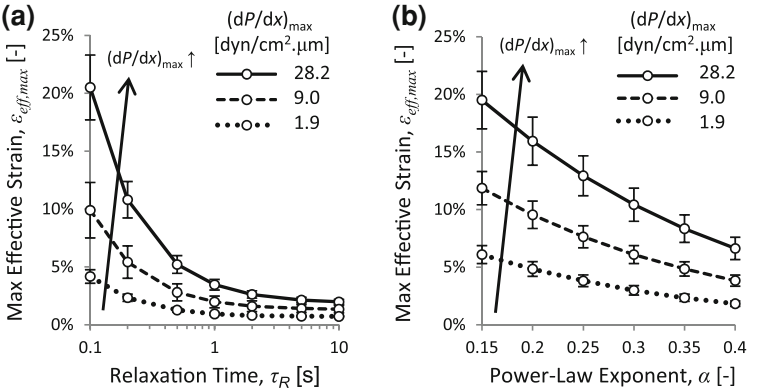

Fig. 16 Independent variation of maximum pressure gradient for a constant exposure duration, $\Delta t = 0.065$ s. For cells with both the Maxwell **a** and power-law **b** models, increasing $(dP/dx)_{max}$ increases maximum membrane strain (i.e. risk of cell death). Figures report geometric mean ± 70% confidence intervals (With permission from Dailey et al., Biomech. Model. Mechanobiol., 2010)

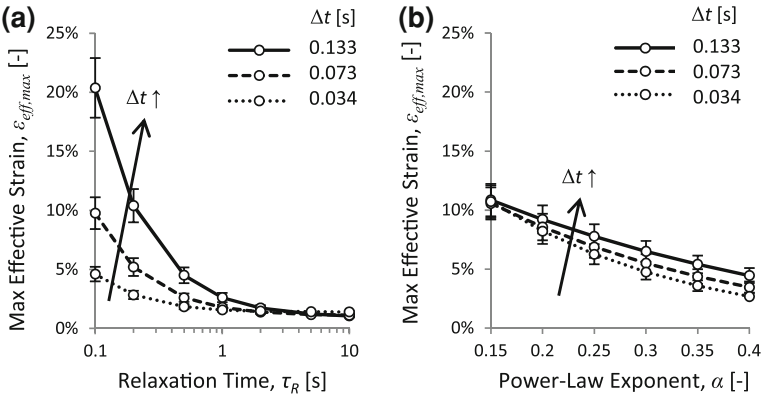

Fig. 17 Independent variation of exposure duration for a constant maximum pressure gradient, $(dP/dx)_{max} = 7$ dyn/cm^2 μm. Results for membrane strain (i.e. risk of cell death) show that cells with the Maxwell model **a** were more sensitive to Δt than cells with the power-law model **b**. Figures report geometric mean ± 70% confidence intervals (With permission from Dailey et al., Biomech. Model. Mechanobiol., 2010)

applied pressure gradient, $(dP/dx)_{max}$ [12, 124] and independent of the exposure duration, Δt [59]. However, only Maxwell models with $\tau_R \leq 1$ s exhibited a strong dependence of membrane strain on $(dP/dx)_{max}$ while only Maxwell models with $\tau_R \geq 2$ s demonstrated no correlation between membrane strain and Δt. As a result, it is not possible to select one Maxwell model (i.e. one time constant) that is consistent with all of the experimental data. In contrast, a majority of our power-law models (i.e. $\alpha \geq 0.2$) predicted both strong dependence of membrane strain on $(dP/dx)_{max}$ and no correlation between membrane strain and Δt, and were therefore

consistent with all experimental observations. This analysis strongly indicates that computational models of cell deformation must include power-law rheology in order to capture the experimentally observed behavior with respect to cell necrosis.

The computational models presented in this section relied on a time-domain Prony–Dirichlet series formulation to capture the cells' power-law rheological properties. We implemented this material model in our finite element simulations and investigated dynamic cell deformation during microbubble flows. Comparison of our computations with experimental results indicated that a power-law rheology model is required to capture the observed link between pressure gradient and cell death and the lack of correlation between exposure duration and cell necrosis. This comparison with experiments validates the computational approach and suggests that the wide distribution of time constants associated with power-law rheology may be the reason why EpC are sensitive to pressure-gradients but not exposure duration. In addition, these models highlight the importance of including time-scale invariant material properties when simulating the deformation of biological cells under complex transient loading conditions.

Furthermore, in all of the results presented in Figs. 14, 15, 16, 17, cells with a slower viscoelastic response (i.e. increased α) had decreased maximum membrane strain. The power-law exponent, α, controls whether the cell behaves more like an elastic solid or a viscous fluid. In the limit $\alpha \to 0$, the material behaves like an elastic solid that develops strain instantaneously in response to applied stress. As α increases, the material becomes more fluid-like and experiences a delayed response to applied stress. The computational models showed that cells with higher α values develop lower strains during microbubble flows (see Fig. 18). These results suggest that fluidization of the cell (i.e. an increase in α) may have a cytoprotective effect during the microbubble flows associated with ARDS.

As described in Sect. 6.2, our laboratory has recently tested this hypothesis by altering the cytoskeletal mechanics of A549 cells and investigating how these changes influence the measured power-law exponent, α, and the risk of microbubble-induced necrosis. These results suggest that altering the cells' rheological properties may be an effective way to reduce cell injury during the ventilation of patients with ARDS.

6 Pharmaco-Mechanical Therapies: Computational Predictions and Experimental Validation

Several investigators have focused on minimizing EpC damage by reducing or eliminating the injurious mechanical forces generated during ventilation. For example, low volume ventilation techniques have been used to minimize the stretching deformations that cause cell necrosis and activate inflammatory pathways [118]. However, it is difficult to eliminate all of the pathological mechanical forces generated during ventilation. In particular, the patho-physiology of ALI involves disruption of the alveolar–capillary barrier and the flooding of small

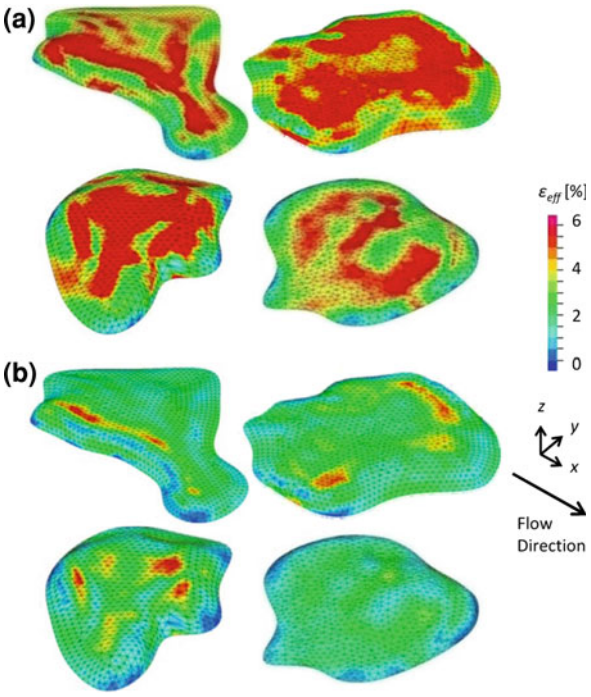

Fig. 18 Computational models predict that cell fluidization (increase in power-law exponent, α) can reduce membrane strain and the risk of cell injury during airway reopening. Results shown for **a** $\alpha = 0.2$ and **b** $\alpha = 0.35$

pulmonary airways and alveoli. In order to restore normal gas exchange, these fluid-filled regions must be re-aerated and "reopened" during ventilation. Unfortunately, the reopening of these fluid-filled regions requires the propagation of air–liquid interfaces and microbubble flows over the airway/alveolar epithelium. As demonstrated by the experimental data summarized in Sect. 1.2, these microbubble flows can cause significant damage and cellular necrosis and therefore are an important component of VILI. In addition to the fact that microbubble flows are likely unavoidable during ALI, the most effective way to reduce the magnitude of microbubble associate forces, lowering of the surface tension via surfactant replacement therapy, has had limited clinical success [68, 94] partially due to surfactant deactivation by plasma proteins that leak into the airway/alveolar space [14].

Instead of reducing the magnitude of the damaging mechanical forces, an alternative way to reduce microbubble-induced injury is to modify the way EpC respond to the damaging mechanical stimuli. In particular, the computational models developed and described in Sects. 1.4 and 1.5 indicate that specific changes in cell rheology and mechanics might be effective in reducing microbubble-induced cell deformation and necrosis (i.e. membrane rupture due to large localized strains). In support of these predictions, our laboratory has recently conducted several experimental studies to investigate how changes in cellular mechanics might influence the amount of cell necrosis and detachment during microbubble

flows [123]. In these studies, the mechanical properties of the cells were altered by treating EpC with drugs that alter the cell's main structural component, the actin cytoskeleton. In addition to altering the amount of cell deformation, changes in the cytoskeleton may be useful in modifying the way cells sense and transduce forces into inflammatory signals. This inflammatory "mechanotransduction" response may be an important source of injury/mortality and our lab has recently initiated a series of experiments to identify how changes in the actin cytoskeleton influence inflammation and mechanotransduction [53].

The actin cytoskeleton is composed of long filamentous polymers known as F-actin. The monomeric or globular form of actin polymerizes into F-actin and disruption of this process can be used to destabilize the cytoskeleton while other agents can promote localized polymerization of actin in specific sub-cellular regions. These changes in the actin cytoskeleton will have subsequent changes on the cell's global mechanical properties and rheology. One focus of our lab is to find suitable drug agents that alter the deformation response of EpC to microbubble flows by altering the cell's cytoskeletal and biomechanical properties. To this end, we have used the validated computational models developed and described in Sects. 1.4 and 1.5 to predict what types of changes in cell mechanics and actin cytoskeletal structure would prevent cell deformation and injury during microbubble flows. We then designed in vitro experiments to validate these computational predictions. Below, we describe two specific drug-screening applications in which computational predictions were tested using our in vitro experimental system. We also describe recent experimental studies that show how changes in cell mechanics may also be used to mitigate the inflammatory response of the EpC to microbubble flows.

6.1 Membrane/Cortex Mechanics

As shown graphically in Fig. 10, the computational models predict that changes in membrane/cortex mechanics will have a significant impact on cellular deformation and membrane strain/rupture. Specifically, the models predict that increases in membrane/cortical stiffness will decrease the amount of cellular deformation and membrane strain. We would therefore expect less microbubble-induced necrosis in cells with a "stiffer" membrane/cortex. To test this hypothesis, alveolar EpC (A549) were pretreated with methyl-β-cyclodextrin (Mβ-CD) for 1 h prior to being expose to either 1, 5 or 9 microbubble passages using the microfluidic system described by Yalcin et al. [124]. Mβ-CD depletes cholesterol from the plasma membrane and previous investigators have demonstrated that this depletion results in increased cellular stiffness for endothelial cells and polymerization of actin in the cortical region for leukocytes [66]. To confirm cortical actin polymerization in alveolar EpC, confocal microscopy was used to image the actin cytoskeleton before and after treatment with Mβ-CD. As shown in Fig. 19a, b, intensity matched images clearly demonstrated that Mβ-CD induces cortical actin

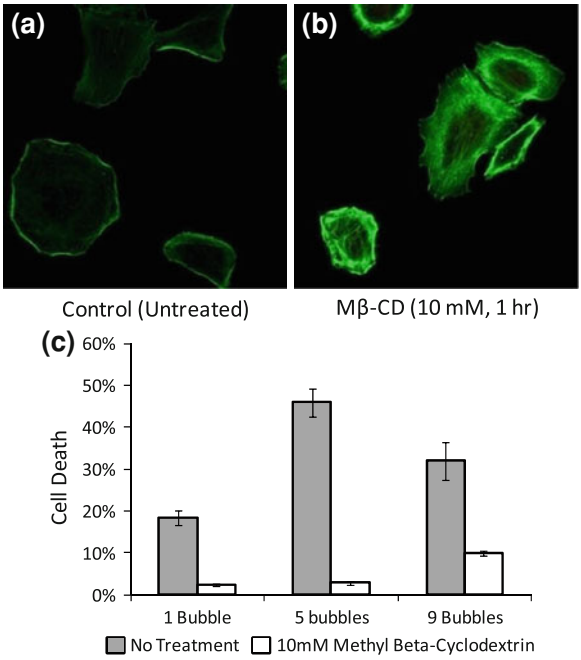

Fig. 19 Effect of cholesterol depletion on cortical actin and microbubble-induced injury. Intensity matched fluorescent images of the actin cytoskeleton in **a** untreated cells and **b** cells treated with methyl-β cyclodextran. **c** Treatment with MβCD results in reduced cell necrosis for multiple bubble passages

polymerization in the EpC. This would correspond to an increase in membrane/cortex stiffness (i.e. E_{mem} in Fig. 10) and we therefore expect the Mβ-CD cells to experience less deformation and necrosis. As shown in Fig. 19c, the Mβ-CD treated cells exhibited large and statistically significant reductions in cell necrosis compared to normal cells. We therefore conclude that altering the membrane/cortex stiffness might be an effective way to prevent microbubble-induced injury.

6.2 Cytoskeletal Fluidization

Correlations between the viscoelastic computational models of transient cell deformation during microbubble flows (Sect. 1.5) with the experimental data from Kay et al. [59] and in Fig. 3, clearly indicate that only models that account for the cell's complex power-law rheology are accurate. As shown in Fig. 14b and 15b, these power-law models predict that increasing the fluid-like nature of the cells, i.e. an increase in α, will reduce the maximum membrane strain that develops during microbubble flows. To test the prediction that "fluidization" will reduce microbubble-induced cell necrosis, A549 EpC were either pretreated with a marine toxin Latrunculin A or held at 37°C as opposed to room temperature [123]. Latrunculin A sequesters G-actin and thereby prevents the polymerization of G-actin into F-actin. Without active polymerization, F-actin rapidly degrades and undergoes "depolymerization." Previous investigators have demonstrated that

actin depolymerization results in a reduction in the power-law exponent as well as a decrease in cellular stiffness [63]. To confirm these changes in cellular biomechanics in alveolar EpC, we used an optical tweezer based microrheometer [121] to measure the frequency dependence of the cell's elastic and complex shear modulus under control conditions, after 1 h treatment with Latrunculin A and for cells held at 37°C. The frequency data was analyzed with a power-law type relationship similar to Eq. 16 and the power-law exponent is reported in Fig. 20a. Both the Latrunculin A treated cells and the cells held at 37°C exhibited statistically significant increases in the power-law exponent. Therefore, based on our computational models we would expect both the Latrunculin A treated cells and the cells held at 37°C to exhibit less microbubble-induced cell necrosis. Cells were exposed to 1 or 5 microbubble passages and as shown in Fig. 20b, both the Latrunculin A and 37°C conditions results in significantly lower amount of cell death. We therefore conclude that fluidization of the actin cytoskeleton may be a very effective way to prevent microbubble-induced injury.

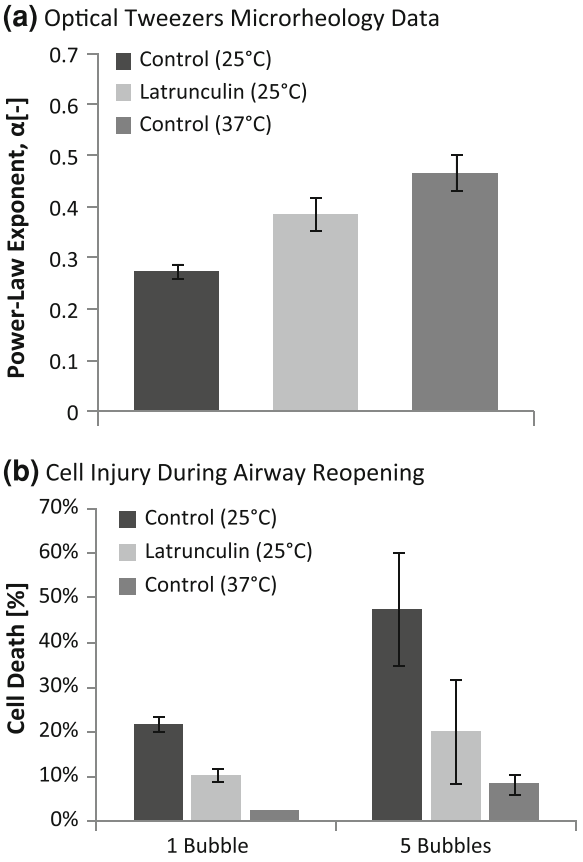

Fig. 20 Influence of fluidization on microbubble induced cell injury. Treatment of A549 cells with Latrunculin A or 37°C results in **a** increased power-law exponents and **b** reduced cell necrosis after multiple bubble passages

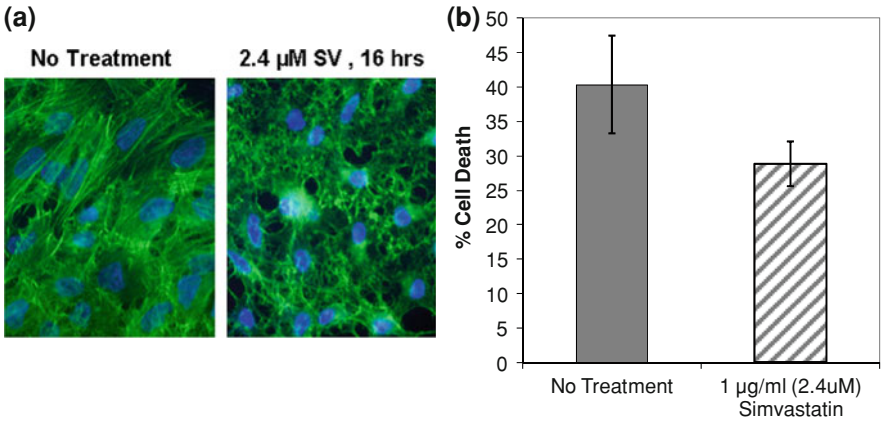

Fig. 21 Effect of 16 h treatment with 2.4 μM simvastatin on **a** actin cytoskeleton and **b** amount of cell necrosis after microbubble flows

It is important to note that although Latrunculin A is clearly not a clinically relevant compound, i.e. it is a marine toxin, several other clinically relevant compounds are known to have similar effects on the actin cytoskeleton. For example, Chen et al. [19] demonstrated that the common serum cholesterol reducing drug, simvastatin, can attenuate actin stress fiber formation and cause disruptions in the cytoskeleton of endothelial cells. These changes in actin cytoskeleton are consistent with fluidization. As shown in Fig. 21a, we have used immunofluorescent imaging of the actin cytoskeleton to confirm that treatment with simvastatin for 16 h at 2.4 μM also causes "fluidization" like changes in the cytoskeleton of EpC, i.e. it attenuates actin stress fiber formation. Furthermore, as shown in Fig. 21b, simvastatin treated cells experience less microbubble-induced cell necrosis and this result is consistent with our computational predictions of less cell deformation and membrane rupture for fluidized cells.

This preliminary data represents an exciting clinical translation of our combined computational and experimental approach to identifying pharmacological agents that prevent cellular injury by altering specific biomechanical properties. We note that there has recently been intense interest and debate in the clinical community about how to use simvastatin to treat ALI and reduce lung inflammation [62, 91]. Our studies indicate that in addition to reduced inflammation, simvastatin therapy may also prevent physical damage to the lung caused by microbubble flows. Clearly additional in vitro studies are needed to more completely investigate how simvastatin influences microbubble-induced cell injury. In addition, future studies should also utilize in vivo animal models to confirm the protective effect of simvastatin on EpC viability and barrier function.

6.3 Mechanotransduction and Inflammation

The development and maintenance of an inflammatory state plays a key role in several respiratory disorders. In particular, the inflammatory response of alveolar EpC to pathologic stretching deformations during mechanical ventilation has been recognized as a key factor in the development of ventilation-induced lung injury [71]. Cyclic stretching of alveolar EpC results in the production and secretion of pro-inflammatory cytokines IL-8 and IL-6 [56, 114] and stretching of fetal lung EpC results in the nuclear translocation of NF-κB [22], a "rapid-acting" primary transcription factor for a large number of inflammatory genes [72]. In addition to in vitro studies, the role of stretch-induced inflammation has also been demonstrated in in vivo [21]. Although cyclic stretching of alveolar EpC can activate pro-inflammatory pathways, there is limited information about how the various mechanical forces associated with microbubble flows influences the activation of NF-κB inflammatory pathways. In addition, although the cytoskeleton has been implicated in mechanotransduction, there is limited information about how changes in actin cytoskeletal structure influence mechanotransduction processes. Our laboratory has recently used in vitro modeling techniques to investigate how static and dynamic pressures might influence NF-κB activation and how changes in cytoskeletal structure may mitigate mechanotransduction [53]. In this study, A549 EpC were grown to confluence in a transwell insert and exposed to static 14 cmH_2O pressure and oscillatory pressure at both moderate and low frequencies (0.18 and 0.125 Hz). Additional studies were also conducted by pre-treating cells with Latrunculin A for 1 h prior to pressure exposure. Subsequent to pressure loading, the amount of NF-κB activation and nuclear translocation was assessed with an ELISA technique that quantifies that amount of NF-κB bound to DNA. Results indicate that both static and oscillatory pressure activate NF-κB. Interestingly, for static loading, cells treated with Latrunculin A exhibited more NF-κB activation than unloaded controls. Conversely, for oscillatory loading at 0.18 Hz, Latrunculin A treated cells exhibited significantly less NF-κB activation. This data suggests that for low frequency conditions, the lower Young's modulus in Latrunculin A treated cells leads to more cellular deformation and therefore increased activation of NF-κB. However, at higher frequencies, the more fluid-like Latrunculin A treated cells may experience less deformation than the control cells and thus exhibit less NF-κB activation. Specifically, the increased viscous properties of Latrunculin treated cells allow them to "damp-out" or dissipate the higher frequency loads. These preliminary results therefore highlight the importance of both loading conditions (i.e. frequency) and cytoskeletal structure and cell mechanics on the transduction of mechanical forces into biochemical signaling. Finally, Huang et al. [53] conducted additional studies to investigate the mechanisms of pressure-induced NF-κB activation and these studies suggest that intracellular strains and the release of intracellular calcium may be more important than the opening of stretch-induced calcium channels in the plasma membrane. Clearly, application

of the computational models to these in vitro experimental conditions is needed to test and analyze the validity of this hypothesis.

7 Conclusions and Future Model Development

The biomechanical and biological mechanisms responsible for microbubble-induced cell injury are complex. In this chapter we have described how our laboratory is using an integrated experimental–computational approach to not only identify the mechanical and biological mechanisms responsible for microbubble-induced injury but also the application of our models to develop new pharmaco-mechanical therapies for ALI. In our approach, computational models account for the minimal level of complexity required to accurately capture experimental data. Although we attempt a minimalist approach, often models that account for significantly complex dynamics and rheology (i.e. power-law) are required to capture experimental data. Once validated, the computational models are used to predict what types of structural changes would be required to protect EpC from microbubble-induced injury. Finally, these computational predictions are then tested with additional experimental studies.

Using this approach we have demonstrated that type II alveolar EpC are more susceptible to microbubble-induced injury than type I cells due differences in morphology. This finding has important clinical implications since bacterial and viral toxins preferentially damage the type I cells leaving the type II cells intact. Normally, the type II cells can differentiate into type I cells and thus provide a source for repair of the denuded epithelium. However, our results indicate that during mechanical ventilation, microbubble flows would cause significant damage to the remaining type II cells and that this may explain why repair processes are also hindered by mechanical ventilation. We have also demonstrated that the complex power-law rheology of EpC is partially responsible for the sensitivity of these cells to spatial pressure gradients and that only models that account for time-scale independent properties (i.e. power-law rheology) can capture all of the experimental data. Our computational models predicted that cytoskeletal agents that either increase membrane/cortical stiffness or increase the fluid-like properties of the cells would protect the cells from microbubble-induced damage. In vitro experiments were then used to confirm these predictions. Although initial experiments used toxic agents, preliminary work indicates that clinically relevant agents such as simvastatin may also be utilized to produce the desired change in cell rheology/structure.

Finally, we recognize the important role that mechanotransduction and inflammation play in the etiology of ALI. We have therefore conducted preliminary studies which demonstrate that alveolar EpC can transduce mechanical forces into inflammatory signaling and that changes in the actin cytoskeleton may be useful in attenuating this transduction event. However, the experimental results indicate that mitigation of inflammation may depend on loading conditions as well

as cytoskeletal structure and therefore the application of the computational models described in this chapter to mechanotransduction issues might lead to important mechanistic insight. In this regard we briefly describe some of our ongoing and future model development projects.

7.1 Inflammatory Responses and Modeling the Cell Nucleus

One key structural element in the mechanotransduction process is the cell nucleus, a relatively large membrane-enclosed organelle that contains the cell's DNA. The nucleus maintains mechanical connectivity with the rest of the cell through the cytoskeleton. In the models we have explored, the cell is modeled as a membrane-bound homogeneous medium with no nucleus. However, we have already established the tools and techniques for imaging and modeling a cell with a mechanically distinct nucleus. We could extend our cell models to investigate stress-transmission to the cell nucleus as part of a directed study of microbubble-induced mechanotransduction and biochemical signaling. Signaling activity could be monitored through immunohistochemistry (IHC), the process of tagging specified antigens within the cell using fluorescently labeled antibodies. In particular, IHC could be used to tract the nuclear translocation of NF-κB while standard DAPI stains could be used to reconstruct the nucleus. These studies would require an experimental setup that can perform in situ confocal imaging of cells for geometric reconstruction, expose cells to microbubble flows, and then reimage the same cells with the desired IHC protocol. In addition to quantifying NF-κB activation, the development of computational models based on the IHC imaging data would allow for quantification of the intracellular stresses and strains. In addition, the computational models could be used to investigate how mechanical changes in the external and nuclear membranes as well as the cytoskeleton influence stress/strain transmission. As a result, these computational models may be useful in identifying the types of structural changes that would mitigate the inflammatory response.

7.2 Traction Force Microscopy and Repair Mechanisms

Although preventing additional lung injury during ventilation is an important component for the successful treatment of ALI, abnormal repair processes can also contribute to mortality and morbidity. Specifically, the denuded epithelium must be repaired by efficient and rapid migration of the remaining EpC and this is a complex process that is regulated by many biochemical factors including growth factors, chemokines and cytokines [23]. Control of cell migration during repair is critical since long-term tissue remodeling can lead to a fibro-proliferative phase of ALI in which fibrotic processes make the lung stiff and thus hinder ventilation. Recently, Trepat et al. [102] have used traction force microscopy to investigate

the biomechanical mechanisms that regulate the collective migration of epithelial sheets. Unlike the classic models in which "leader cells" drive the migration of the monolayer, these investigators demonstrate that the traction forces driving collective cell migration arise many cell rows behind the leading edge. Recently, our laboratory demonstrated that activation of specific biochemical signaling pathways increases the migration rate of lung EpC monolayers [61]. In addition, atomic force microscopy was used to demonstrate that cells near the leading edge exhibit altered biomechanical properties compared with cells far from the leading edge [74]. However, it is unclear how important the changes in cellular biomechanics near the leading edge are for increased cell migration. In this regard, a computational model of collective cell migration that accounts for the unique traction force dynamics observed by Trepat et al. [102] and heterogeneous distributions in cell mechanical properties may be useful in identifying the structural changes that promote rapid and efficient cell migration and wound repair. For these models, traction field data could be translated to node-by-node stresses applied to the basal surfaces of image-based cell models while atomic force microscopy data could be used to specify power-law rheology on a cell-by-cell basis. As a result, these computational models may be useful in identifying the types of structural changes that would enhance the repair process critical to the resolution of ALI.

References

1. ADINA R&D: Theory and Modeling Guide, vol. i. Adina 8.4. Watertown (2006)
2. Alcaraz, J., Buscemi, L., Grabulosa, M., Trepat, X., Fabry, B., Farre, R., Navajas, D.: Microrheology of human lung epithelial cells measured by atomic force microscopy. Biophys. J. **84**(3), 2071–2079 (2003)
3. Alenghat, F.J., Nauli, S.M., Kolb, R., Zhou, J., Ingber, D.E.: Global cytoskeletal control of mechanotransduction in kidney epithelial cells. Exp. Cell Res. **301**(1), 23–30 (2004)
4. Amato, M.B., Barbas, C.S., Medeiros, D.M., Magaldi, R.B., Schettino, G.P., Lorenzi-Filho, G., Kairalla, R.A., Deheinzelin, D., Munoz, C., Oliveira, R., Takagaki, T.Y., Carvalho, C.R.: Effect of a protective-ventilation strategy on mortality in the acute respiratory distress syndrome. N. Engl. J. Med. **338**(6), 347–354 (1998)
5. Archer, R.R., Cook, N.H., Crandall, S.H., Dahl, N.C., McClintock, F.A., Rabinowicz, E., Reichenbach, G.S.: An Introduction to the Mechanics of Solids. McGraw-Hill Series in Engineering Sciences. McGraw-Hill, New York (1959)
6. ARDS Network: Ventilation with lower tidal volumes as compared with traditional tidal volumes for acute lung injury and the acute respiratory distress syndrome. The acute respiratory distress syndrome network. N. Engl. J. Med. **342**(18), 1301–1308 (2000)
7. Arold, S.P., Bartolak-Suki, E., Suki, B.: Variable stretch pattern enhances surfactant secretion in alveolar type ii cells in culture. Am. J. Physiol. Lung Cell Mol. Physiol. **296**(4), L574–L581 (2009)
8. Balland, M., Desprat, N., Icard, D., Fereol, S., Asnacios, A., Browaeys, J., Henon, S., Gallet, F.: Power laws in microrheology experiments on living cells: comparative analysis and modeling. Phys. Rev. E **74**, 021911 (2006)
9. Baroud, C.N., Willaime, H.: Multiphase flows in microfluidics. Comptes Rendus Phys. **5**(5), 547–555 (2004)

10. Bein, T., Weber, F., Philipp, A., Prasser, C., Pfeifer, M., Schmid, F.X., Butz, B., Birnbaum, D., Taeger, K., Schlitt, H.J.: A new pumpless extracorporeal interventional lung assist in critical hypoxemia/hypercapnia. Crit. Care Med. **34**(5), 1372–1377 (2006)
11. Bekeredjian, R., Grayburn, P.A., Shohet, R.V.: Use of ultrasound contrast agents for gene or drug delivery in cardiovascular medicine. J. Am. Coll. Cardiol. **45**(3), 329–335 (2005)
12. Bilek, A.M., Dee, K.C., Gaver, D.P., 3rd: Mechanisms of surface-tension-induced epithelial cell damage in a model of pulmonary airway reopening. J. Appl. Physiol. **94**(2), 770–783 (2003)
13. Boal, D: Mechanics of the Cell. Cambridge University Press, Cambridge (2002)
14. Braun, A., Stenger, P., Warringer, H., Zasadzinski, J., Lu, K., Taeusch, H.: A freeze-fracture transmission electron microscopy and small angle x-ray diffraction study of the effects of albumin, serum, and polymers on clinical lung surfactant microstructure. Biophys. J. **93**(1), 123–139 (2007)
15. Brower, R.G., Lanken, P.N., MacIntyre, N., Matthay, M.A., Morris, A., Ancukiewicz, M., Schoenfeld, D., Thompson, B.T.: Higher versus lower positive end-expiratory pressures in patients with the acute respiratory distress syndrome. N. Engl. J. Med. **351**(4), 327–336 (2004)
16. Cavanaugh, K.J., Jr., Margulies, S.S.: Measurement of stretch-induced loss of alveolar epithelial barrier integrity with a novel in vitro method. Am. J. Physiol. Cell Physiol. **283**(6), C1801–C1808 (2002)
17. Cavanaugh, K.J., Jr., Oswari, J., Margulies, S.S.: Role of stretch on tight junction structure in alveolar epithelial cells. Am. J. Respir. Cell Mol. Biol. **25**(5), 584–591 (2001)
18. Chen, C.S.: Mechanotransduction—a field pulling together? J. Cell Sci. **121**(Pt 20), 3285–3292 (2008)
19. Chen, W., Pendyala, S., Natarajan, V., Garcia, J.G., Jacobson, J.R.: Endothelial cell barrier protection by simvastatin: Gtpase regulation and nadph oxidase inhibition. Am. J. Physiol. Lung Cell Mol. Physiol. **295**(4), L575–L583 (2008)
20. Chung, P.M.Y., Kawaji, M., Kawahara, A., Shibata, Y.: Two-phase flow through square and circular microchannels—effects of channel geometry. J. Fluids Eng. Trans. ASME **126**(4), 546–552 (2004)
21. Copland, I.B., Kavanagh, B.P., Engelberts, D., McKerlie, C., Belik, J., Post, M.: Early changes in lung gene expression due to high tidal volume. Am. J. Respir. Crit. Care Med. **168**(9), 1051–1059 (2003)
22. Copland, I.B., Post, M.: Stretch-activated signaling pathways responsible for early response gene expression in fetal lung epithelial cells. J. Cell. Physiol.**210**(1), 133–143 (2007)
23. Crosby, L.M., Waters, C.M.: Epithelial repair mechanisms in the lung. Am. J. Physiol. Lung Cell. Mol. Physiol. **298**(6), L715–L731 (2010)
24. D'Angelo, E., Koutsoukou, A., Valle, P.D., Gentile, G., Pecchiari, M.: Cytokine release, small airway injury, and parenchymal damage during mechanical ventilation in normal open-chest rats. J. Appl. Physiol. **104**(1), 41–49 (2008)
25. D'Angelo, E., Pecchiari, M., Baraggia, P., Saetta, M., Balestro, E., Milic-Emili, J.: Low-volume ventilation causes peripheral airway injury and increased airway resistance in normal rabbits. J. Appl. Physiol. **92**(3), 949–956 (2002)
26. D'Angelo, E., Pecchiari, M., Gentile, G.: Dependence of lung injury on surface tension during low-volume ventilation in normal open-chest rabbits. J. Appl. Physiol. **102**(1), 174–182 (2007)
27. D'Angelo, E., Pecchiari, M., Saetta, M., Balestro, E., Milic-Emili, J.: Dependence of lung injury on inflation rate during low-volume ventilation in normal open-chest rabbits. J. Appl. Physiol. **97**(1), 260–268 (2004)
28. Dailey, H.L., Ghadiali, S.N.: Influence of power-law rheology on cell injury during microbubble flows. Biomech. Model. Mechanobiol. **9**(3), 263–279 (2010)
29. Dailey, H.L., Ricles, L.M., Yalcin, H.C., Ghadiali, S.N.: Image-based finite element modeling of alveolar epithelial cell injury during airway reopening. J. Appl. Physiol. **106**(1), 221–232 (2009)

30. Deklunder, G., Roussel, M., Lecroart, J.L., Prat, A., Gautier, C.: Microemboli in cerebral circulation and alteration of cognitive abilities in patients with mechanical prosthetic heart valves. Stroke **29**(9), 1821–1826 (1998)
31. Desai, L.P., Chapman, K.E., Waters, C.M.: Mechanical stretch decreases migration of alveolar epithelial cells through mechanisms involving rac1 and tiam1. Am. J. Physiol. Lung Cell. Mol. Physiol. **295**(5), L958–965 (2008)
32. Desprat, N., Richert, A., Simeon, J., Asnacios, A.: Creep function of a single living cell. Biophys. J. **88**, 2224–2223 (2005)
33. Dreyfuss, D., Saumon, G.: Ventilator-induced lung injury: Lessons from experimental studies. Am. J. Respir. Crit. Care Med. **157**(1), 294–323 (1998)
34. Eckmann, D.M., Lomivorotov, V.N.: Microvascular gas embolization clearance following perfluorocarbon administration. J. Appl. Physiol. **94**(3), 860–868 (2003)
35. Even-Tzur, N., Kloog, Y., Wolf, M., Elad, D.: Mucus secretion and cytoskeletal modifications in cultured nasal epithelial cells exposed to wall shear stresses. Biophys. J. **95**(6), 2998–3008 (2008)
36. Fabry, B., Maksym, G.N., Butler, J.P., Glogauer, M., Navajas, D., Fredberg, J.J.: Scaling the microrheology of living cells. Phys. Rev. Lett. **87**(14), 148102 (2001)
37. Ferreira, L.F., Harper, A.J., Barstow, T.J.: Frequency-domain characteristics and filtering of blood flow following onset of exercise: Implications for kinetics analysis. J. Appl. Physiol. **100**, 817–825 (2006)
38. Flügge, W.: Viscoelasticity. Blaisdell Publishing Company, Waltham (1967)
39. Frank, J.A., McAuley, D.F., Gutierrez, J.A., Daniel, B.M., Dobbs, L., Matthay, M.A.: Differential effects of sustained inflation recruitment maneuvers on alveolar epithelial and lung endothelial injury. Crit Care Med **33**(1), 181–188; discussion 254–185. doi:00003246-200501000-00027 [pii] (2005)
40. Ghadiali, S.N., Gaver, D.P.: The influence of non-equilibrium surfactant dynamics on the flow of a semi-infinite bubble in a rigid cylindrical capillary tube. J. Fluid Mech. **478**, 165–196 (2003)
41. Ghadiali, S.N., Gaver, D.P.: Biomechanics of liquid–epithelium interactions in pulmonary airways. Respir. Physiol. Neurobiol. **163**(1–3), 232–243 (2008)
42. Ghadiali, S.N., Gaver, D.P., III.: The influence of non-equilibrium surfactant dynamics on the flow of a semi-infinite bubble in a rigid cylindrical capillary tube. J. Fluid Mech. **478**, 165–196 (2002)
43. Ghadiali, S.N., Halpern, D., Gaver, D.P., III.: A dual-reciprocity boundary element method for evaluating bulk convective transport of surfactant in free-surface flows. J. Comput. Phys. **171**, 534–559 (2001)
44. Golob, J.F., Federspiel, W.J., Merrill, T.L., Frankowski, B.J., Litwak, K., Russian, H., Hattler, B.G.: Acute in vivo testing of an intravascular respiratory support catheter. ASAIO J. **47**(5), 432–437 (2001)
45. Halpern, D., Gaver, D.P., III.: Boundary element analysis of the time-dependent motion of a semi-infinite bubble in a channel. J. Comput. Phys. **115**, 366–375 (1994)
46. Hammerschmidt, S., Kuhn, H., Grasenack, T., Gessner, C., Wirtz, H.: Apoptosis and necrosis induced by cyclic mechanical stretching in alveolar type ii cells. Am. J. Respir. Cell Mol. Biol. **30**(3), 396–402 (2004)
47. Han, B., Bai, X.H., Lodyga, M., Xu, J., Yang, B.B., Keshavjee, S., Post, M., Liu, M.: Conversion of mechanical force into biochemical signaling. J. Biol. Chem. **279**(52), 54793–54801 (2004)
48. Harvey, C.J., Pilcher, J.M., Eckersley, R.J., Blomley, M.J.K., Cosgrove, D.O.: Advances in ultrasound. Clin. Radiol. **57**(3), 157–177 (2002)
49. Hazel, A.L., Heil, M.: Three-dimensional airway reopening: The steady propagation of a semi-infinite bubble into a buckled elastic tube. J. Fluid Mech. **478**, 47–70 (2003)
50. Hénon, S., Lenormand, G., Richert, A., Gallet, F.: A new determination of the shear modulus of the human erythrocyte membrane using optical tweezers. Biophys. J. **76**, 1145–1151 (1999)

51. Hoffman, B.D., Massiera, G., Van Citters, K.M., Crocker, J.C.: The consensus mechanics of cultured mammalian cells. Proc. Natl. Acad. Sci. USA **103**(27), 10259–10264 (2006)
52. Hu, S., Chen, J., Fabry, B., Numaguchi, Y., Gouldstone, A., Ingber, D.E., Fredberg, J.J., Butler, J.P., Wang, N.: Intracellular stress tomography reveals stress focusing and structural anisotropy in cytoskeleton of living cells. Am. J. Physiol. Cell Physiol. **285**(5), C1082–C1090 (2003)
53. Huang, Y., Haas, C., Ghadiali, S.N.: Influence of transmural pressure and cytoskeletal structure on nf-κb activation in respiratory epithelial cells. Cell. Mol. Bioeng. Rev. (2010)
54. Hubmayr, R.D.: Perspective on lung injury and recruitment: a skeptical look at the opening and collapse story. Am. J. Respir. Crit. Care Med. **165**(12), 1647–1653 (2002)
55. Jacob, A.M., Gaver, D.P.: An investigation of the influence of cell topography on epithelial mechanical stresses during pulmonary airway reopening. Phys. Fluids **17**(3) (2005)
56. Jafari, B., Ouyang, B., Li, L.F., Hales, C.A., Quinn, D.A.: Intracellular glutathione in stretch-induced cytokine release from alveolar type-2 like cells. Respirology **9**(1), 43–53 (2004)
57. Kaazempur Mofrad, M.R., Bathe, M., Karcher, H., Younis, H.F., Seong, H.C., Shim, E.B., Chan, R.C., Hinton, D.P., Isasi, A.G., Upadhyaya, A., Powers, M.J., Griffith, L.G., Kamm, R.D.: Role of simulation in understanding biological systems. Comput. Struct. **81**, 715–726 (2003)
58. Karcher, H., Lammerding, J., Huang, H., Lee, R.T., Kamm, R.D., Kaazempur-Mofrad, M.R.: A three-dimensional viscoelastic model for cell deformation with experimental validation. Biophys. J. **85**, 3336–3349 (2003)
59. Kay, S.S., Bilek, A.M., Dee, K.C., Gaver, D.P., III.: Pressure gradient, not exposure duration determines the extent of epithelial cell damange in a model of pulmonary airway reopening. J. Appl. Physiol. **97**, 269–276 (2004)
60. Kim, J.H., Eun, H.W., Lee, H.J., Goo, D.E., Choi, D.L.: Clinical use of renal perfusion imaging by means of harmonic sonography with a microbubble contrast agent in patients after renal transplantation—preliminary study. J. Ultrasound Med. **24**(6), 755–762 (2005)
61. Knoell, D.L., Lai, J.P., Bao, S., Mihai, C., Ghadiali, S.N.: Inhibition of phosphatase and tensin homolog deleted on chromosome 10 (pten) enhances lung epithelial migratory capacity. In: American Thoracic Society Annual Meeting, New Orleans (2010)
62. Kor, D.J., Iscimen, R., Yilmaz, M., Brown, M.J., Brown, D.R., Gajic, O.: Statin administration did not influence the progression of lung injury or associated organ failures in a cohort of patients with acute lung injury. Intensive Care Med. **35**(6), 1039–1046 (2009)
63. Laudadio, R.E., Millet, E.J., Fabry, B., An, S.S., Butler, J.P., Fredberg, J.J.: Rat airway smooth muscle cell during actin modulation: rheology and glassy dynamics. Am. J. Physiol. Cell Physiol. **289**(6), C1388–C1395 (2005)
64. Laurent, V.M., Cañadas, P., Fodil, R., Planus, E., Asnacios, A., Wendling, S., Isabey, D.: Tensegrity behavior of cortical and cytosolic cytoskeletal components in twisted living adherent cells. Acta Biotheor. **50**, 331–356 (2002)
65. Laurent, V.M., Fodil, R., Cañadas, P., Féréol, S., Louis, B., Planus, E., Isabey, D.: Partitioning of cortical and deep cytoskeleton responses from transient magnetic bead twisting. Ann. Biomed. Eng. **31**, 1263–1278 (2003)
66. Levitan, I., Gooch, K.J.: Lipid rafts in membrane-cytoskeleton interactions and control of cellular biomechanics: actions of oxldl. Antioxid. Redox Signal. **9**(9), 1519–1534 (2007)
67. Levitzky, M.G.: Pulmonary Physiology, 7th edn. McGraw-Hill, New York (2007)
68. Lewis, J.F., Veldhuizen, R.: The role of exogenous surfactant in the treatment of acute lung injury. Annu. Rev. Physiol. **65**, 613–642 (2003)
69. Li, H.Y., Tseng, F.G., Pan, C.: Bubble dynamics in microchannels. Part ii: Two parallel microchannels. Int. J. Heat Mass Transf. **47**(25), 5591–5601 (2004)
70. Lim, C.T., Zhou, E.H., Quek, S.T.: Mechanical models for living cells—a review. J. Biomech. **39**, 195–216 (2006)

71. Lionetti, V., Recchia, F.A., Ranieri, V.M.: Overview of ventilator-induced lung injury mechanisms. Curr. Opin. Crit. Care **11**(1), 82–86 (2005)
72. Liu, S.F., Malik, A.B.: Nf-kappa b activation as a pathological mechanism of septic shock and inflammation. Am. J. Physiol. Lung Cell Mol. Physiol. **290**(4), L622–L645 (2006)
73. Liu, W.F., Nelson, C.M., Tan, J.L., Chen, C.S.: Cadherins, rhoa, and rac1 are differentially required for stretch-mediated proliferation in endothelial versus smooth muscle cells. Circ. Res. **101**(5), e44–e52 (2007)
74. Marmottant, P., Hilgenfeldt, S.: A bubble-driven microfluidic transport element for bioengineering. Proc. Natl. Acad. Sci. USA **101**(26), 9523–9527 (2004)
75. Mihai, C., Huang, Y., Bao, S., Knoell, D.L., Ghadiali, S.N.: Influence of pten inhibition on the biomechanical mechanisms responsible for rapid cell migration and wound repair. In: American Thoracic Society Annual Meeting, New Orleans, (2010)
76. Muscedere, J.G., Mullen, J.B.M., Gan, K., Slutsky, A.S.: Tidal ventilation at low airway pressures can augment lung injury. Am. J. Respir. Crit. Care Med. **149**, 1327–1334 (1994)
77. Muth, C.M., Shank, E.S.: Gas embolism. N. Engl. J. Med. **342**(7), 476–482 (2000)
78. Naire, S., Jensen, O.E.: An asymptotic model of unsteady airway reopening. J. Biomech. Eng. **125**(6), 823–831 (2003)
79. Naire, S., Jensen, O.E.: Epithelial cell deformation during surfactant-mediated airway reopening: a theoretical model. J. Appl. Physiol. **99**(2), 458–471 (2005)
80. Ning, Q.M., Wang, X.R.: Response of alveolar type ii epithelial cells to mechanical stretch and lipopolysaccharide. Respiration **74**(5), 579–585 (2007)
81. Obrien, J.J., Butterworth, J., Hammon, J.W., Morris, K.J., Phipps, J.M., Stump, D.A.: Cerebral emboli during cardiac surgery in children. Anesthesiology **87**(5), 1063–1069 (1997)
82. Park, J.A., Tschumperlin, D.J.: Chronic intermittent mechanical stress increases muc5ac protein expression. Am. J. Respir. Cell Mol. Biol. **41**(4), 459–466 (2009)
83. Persson, P.B.: Spectrum analysis of cardiovascular time series. Am. J. Physiol. Regul. Integrative Comp. Physiol. **273**, 1201–1210 (1997)
84. Pinhu, L., Whitehead, T., Evans, T., Griffiths, M.: Ventilator-associated lung injury. Lancet **361**(9354), 332–340 (2003)
85. Pugin, J., Verghese, G., Widmer, M.C., Matthay, M.A.: The alveolar space is the site of intense inflammatory and profibrotic reactions in the early phase of acute respiratory distress syndrome. Crit. Care Med. **27**(2), 304–312 (1999)
86. Pullarkat, P.A., Fernández, P.A., Ott, A.: Rheological properties of the eukaryotic cell cytoskeleton. Phys. Rep. **449**, 29–53 (2007)
87. Ressler, B., Lee, R.T., Randell, S.H., Drazen, J.M., Kamm, R.D.: Molecular responses of rat tracheal epithelial cells to transmembrane pressure. Am. J. Physiol. Lung Cell. Mol. Physiol. **278**(6), L1264–L1272 (2000)
88. Ricard, J.D., Dreyfuss, D., Saumon, G.: Ventilator-induced lung injury. Eur. Respir. J. Suppl. **42**, 2s–9s (2003)
89. Ridge, K.M., Linz, L., Flitney, F.W., Kuczmarski, E.R., Chou, Y.H., Omary, M.B., Sznajder, J.I., Goldman, R.D.: Keratin 8 phosphorylation by protein kinase c delta regulates shear stress-mediated disassembly of keratin intermediate filaments in alveolar epithelial cells. J. Biol. Chem. **280**(34), 30400–30405 (2005)
90. Sheikov, N., McDannold, N., Vykhodtseva, N., Jolesz, F., Hynynen, K.: Cellular mechanisms of the blood-brain barrier opening induced by ultrasound in presence of microbubbles. Ultrasound Med. Biol. **30**(7), 979–989 (2004)
91. Shyamsundar, M., McKeown, S.T., O'Kane, C.M., Craig, T.R., Brown, V., Thickett, D.R., Matthay, M.A., Taggart, C.C., Backman, J.T., Elborn, J.S., McAuley, D.F.: Simvastatin decreases lipopolysaccharide-induced pulmonary inflammation in healthy volunteers. Am. J. Respir. Crit. Care Med. **179**(12), 1107–1114 (2009)
92. Sidhaye, V.K., Schweitzer, K.S., Caterina, M.J., Shimoda, L., King, L.S.: Shear stress regulates aquaporin-5 and airway epithelial barrier function. Proc. Natl. Acad. Sci. USA **105**(9), 3345–3350 (2008)

93. Sollich, P.: Rheological constitutive equtaion for a model of soft glassy materials. Phys. Rev. E **58**(1), 738–759 (1998)
94. Spragg, R.G., Lewis, J.F., Walmrath, H.D., Johannigman, J., Bellingan, G., Laterre, P.F., Witte, M.C., Richards, G.A., Rippin, G., Rathgeb, F., Hafner, D., Taut, F.J., Seeger, W.: Effect of recombinant surfactant protein c-based surfactant on the acute respiratory distress syndrome. N. Engl. J. Med. **351**(9), 884–892 (2004)
95. Stroetz, R.W., Vlahakis, N.E., Walters, B.J., Schroeder, M.A., Hubmayr, R.D.: Validation of a new live cell strain system: characterization of plasma membrane stress failure. J. Appl. Physiol. **90**(6), 2361–2370 (2001)
96. Sukharev, S., Corey, D.P.: Mechanosensitive channels: multiplicity of families and gating paradigms. Sci STKE 2004 (219):re4 (2004)
97. Suzuki, A., Eckmann, D.M.: Embolism bubble adhesion force in excised perfused microvessels. Anesthesiology **99**(2), 400–408 (2003)
98. Timoshenko, S., Woinowsky-Krieger, S.: Theory of Plates and Shells, 2nd edn. McGraw-Hill, New York (1959)
99. Trepat, X., Deng, L., An, S.S., Navajas, D., Tschumperlin, D.J., Gerthoffer, W.T., Butler, J.P., Fredberg, J.J.: Universal physical responses to stretch in the living cell. Nature **447**, 592–596 (2007a)
100. Trepat, X., Deng, L., An, S.S., Navajas, D., Tschumperlin, D.J., Gerthoffer, W.T., Butler, J.P., Fredberg, J.J.: Universal physical responses to stretch in the living cell. Nature **447**(7144), 592–595 (2007b)
101. Trepat, X., Grabulosa, M., Buscemi, L., Rico, F., Farré, R., Navajas, D.: Thrombin and histamine induce stiffening of alveolar epithelial cells. J. Appl. Physiol. **98**, 1567–1574 (2005)
102. Trepat, X., Wasserman, M.R., Angelini, T.E., Millet, E., Weitz, D.A., Butler, J.P., Fredberg, J.J.: Physical forces during collective cell migration. Nat. Phys. **5**(6):426–430 (2009)
103. Tschumperlin, D.J., Boudreault, F., Liu, F.: Recent advances and new opportunities in lung mechanobiology. J. Biomech. **43**(1), 99–107 (2010)
104. Tschumperlin, D.J., Dai, G., Maly, I.V., Kikuchi, T., Laiho, L.H., McVittie, A.K., Haley, K.J., Lilly, C.M., So, P.T., Lauffenburger, D.A., Kamm, R.D., Drazen, J.M.: Mechanotransduction through growth-factor shedding into the extracellular space. Nature **429**(6987), 83–86 (2004)
105. Tschumperlin, D.J., Margulies, S.S.: Equibiaxial deformation-induced injury of alveolar epithelial cells in vitro. Am. J. Physiol. **275**(6 Pt 1), L1173–1183 (1998)
106. Tschumperlin, D.J., Oswari, J., Margulies, A.S.: Deformation-induced injury of alveolar epithelial cells. Effect of frequency, duration, and amplitude. Am. J. Respir. Crit. Care Med. **162**(2 Pt 1), 357–362 (2000)
107. Tschumperlin, D.J., Shively, J.D., Kikuchi, T., Drazen, J.M.: Mechanical stress triggers selective release of fibrotic mediators from bronchial epithelium. Am. J. Respir. Cell Mol. Biol. **28**(2), 142–149 (2003)
108. Tschumperlin, D.J., Shively, J.D., Swartz, M.A., Silverman, E.S., Haley, K.J., Raab, G., Drazen, J.M.: Bronchial epithelial compression regulates map kinase signaling and hb-egf-like growth factor expression. Am. J. Physiol. Lung Cell. Mol. Physiol. **282**(5), L904–L911 (2002)
109. Ugural, A.C.: Stresses in Plates and Shells, 2nd edn. McGraw-Hill, New York (1999)
110. Unger, E.C., Porter, T., Culp, W., Labell, R., Matsunaga, T., Zutshi, R.: Therapeutic applications of lipid-coated microbubbles. Adv. Drug Deliv. Rev. **56**(9), 1291–1314 (2004)
111. Vaziri, A., Kaazempur Mofrad, M.R.: Mechanics and deformation of the nucleus in micropipette aspiration experiment. J. Biomech. **40**, 2053–2062 (2007)
112. Vlahakis, N.E., Hubmayr, R.D.: Response of alveolar cells to mechanical stress. Curr. Opin. Crit. Care **9**(1), 2–8 (2003)
113. Vlahakis, N.E., Hubmayr, R.D.: Cellular stress failure in ventilator-injured lungs. Am. J. Respir. Crit. Care Med. **171**(12), 1328–1342 (2005)

114. Vlahakis, N.E., Schroeder, M.A., Limper, A.H., Hubmayr, R.D.: Stretch induces cytokine release by alveolar epithelial cells in vitro. Am. J. Physiol. **277**(1 Pt 1), L167–L173 (1999)
115. Vlahakis, N.E., Schroeder, M.A., Pagano, R.E., Hubmayr, R.D.: Deformation-induced lipid trafficking in alveolar epithelial cells. Am. J. Physiol. Lung Cell. Mol. Physiol. **280**(5), L938–L946 (2001)
116. Vlahakis, N.E., Schroeder, M.A., Pagano, R.E., Hubmayr, R.D.: Role of deformation-induced lipid trafficking in the prevention of plasma membrane stress failure. Am. J. Respir. Crit. Care Med. **166**(9), 1282–1289 (2002)
117. von Mach, M.A., Kaes, J., Omogbehin, B., Sagoschen, I., Wiechelt, J., Kaiser, K., Sauer, O., Weilemann, L.S.: An update on interventional lung assist devices and their role in acute respiratory distress syndrome. Lung **184**(3), 169–175 (2006)
118. Ware, L.B., Matthay, M.A.: The acute respiratory distress syndrome. N. Engl. J. Med. **342**(18), 1334–1349 (2000)
119. Watanabe, R., Matsumura, M., Chen, C.J., Kaneda, Y., Fujimaki, M.: Characterization of tumor imaging with microbubble-based ultrasound contrast agent, sonazoid, in rabbit liver. Biol. Pharm. Bull. **28**(6), 972–977 (2005)
120. Waters, C.M., Sporn, P.H., Liu, M., Fredberg, J.J.: Cellular biomechanics in the lung. Am. J. Physiol. Lung Cell. Mol. Physiol. **283**(3), L503–L509 (2002)
121. Wei, M.T., Zaorski, A., Yalcin, H.C., Wang, J., Hallow, M., Ghadiali, S.N., Chiou, A., Ou-Yang, H.D.: A comparative study of living cell micromechanical properties by oscillatory optical tweezers. Opt. Express **16**(12), 8594–8603 (2008)
122. Weibel, E.R.: Morphometry of the Human Lung. Academic Press, New York (1963)
123. Yalcin, H.C., Hallow, K.M., Wang, J., Wei, M.T., Ou-Yang, H.D., Ghadiali, S.N.: Influence of cytoskeletal structure and mechanics on epithelial cell injury during cyclic airway reopening. Am. J. Physiol. Lung Cell Mol. Physiol. **297**(5), L881–L891 (2009)
124. Yalcin, H.C., Perry, S.F., Ghadiali, S.N.: Influence of airway diameter and cell confluence on epithelial cell injury during airway reopening. J. Appl. Physiol. **103**, 1796–1807 (2007)
125. Yamada, S., Wirtz, D., Kuo, S.C.: Mechanics of living cells measured by laser tracking microrheology. Biophys. J. **78**, 1736–1747 (2000)
126. Zhelev, D.V., Needham, D., Hochmuth, R.M.: Role of the membrane cortex in neutrophil deformation in small pipets. Biophys. J. **67**, 696–705 (1994)

Mathematical Modelling of Cell Adhesion in Tissue Engineering using Continuum Models

Liesbet Geris and Alf Gerisch

Abstract Key factors in the formation of cell aggregates in tissue engineering and other fields are the cell–cell and cell–matrix interactions. Other important factors are culture conditions such as nutrient and oxygen supply and the characteristics of the environment (medium versus hydrogel). As mathematical models are increasingly used to investigate biological phenomena, it is important that processes such as cell adhesion are adequately described in the models. Recently a technique was developed to incorporate cell–cell and cell–matrix adhesion in continuum models through the use of non-local terms. In this study we apply this technique to model adhesion in a cell-in-gel culture set-up often found in tissue engineering applications. We briefly describe the biological issues underlying this study and the various modelling techniques used to capture adhesive behaviour. We furthermore elaborate on the numerical techniques that were developed in the course of this study. Finally, we consider a tissue engineering model that describes the spatiotemporal evolution of the concentration of cells, matrix, hydrogel, matrix degrading enzymes and oxygen/nutrients in a cell-in-gel culture system. Sensitivity analyses indicate a clear

L. Geris (✉)
Division of Biomechanics and Engineering Design, K.U.Leuven,
Celestijnenlaan 300C (2419), 3001 Leuven, Belgium
e-mail: liesbet.geris@ulg.ac.be; liesbet.geris@mech.kuleuven.be

L. Geris
Prometheus division of Skeletal Tissue Engineering, K.U.Leuven,
Herestraat 49, 3000 Leuven, Belgium

L. Geris
Biomechanics Research Unit, Université de Liège,
Chemin des Chevreuils 1 B52/3, 4000 Liège, Belgium

A. Gerisch
Fachbereich Mathematik, Technische Universität Darmstadt,
Dolivostrasse 15, 64293 Darmstadt, Germany
e-mail: gerisch@mathematik.tu-darmstadt.de

Stud Mechanobiol Tissue Eng Biomater (2011) 4: 431–450
DOI: 10.1007/8415_2010_33

Published Online: 2 November 2010

influence of the different adhesive processes on the final cell and collagen density and distribution, demonstrating the significance of cell adhesion in tissue engineering and the potential of the proposed mathematical technique.

1 Introduction

How cells organize into structured tissues has been a long-standing question in the field of developmental biology. Recently a new paradigm was proposed in the tissue engineering field that states that in order to obtain successful tissue engineering products, these developmental processes should be recapitulated in vitro, using cell aggregates as building blocks [19]. Crucial factors in the formation of these aggregates are cell–cell and cell–matrix interactions. When mathematical modelling aims to actively contribute to the unraveling and control of tissue engineering processes, it needs to be able to describe these adhesion processes.

In this study we apply a recently developed technique to model cell adhesion on a continuum level. This chapter starts by a brief presentation of the importance of cell adhesion in tissue engineering. It continues by describing the modelling techniques that have been proposed in the literature, both on a discrete and continuum level, to model cellular adhesion, followed by a detailed description of the use of non-local terms to model cell adhesion on a continuum level. A mathematical model describing a number of biological processes in a generic cell-in-gel culture system is presented and the necessary numerical tools for its implementation are elaborated on. Simulations of the mathematical model demonstrate the potential of the applied non-local technique in capturing cell adhesive behaviour.

1.1 Cell Adhesion in Tissue Engineering

Stem cell characteristics are determined by the cell's microenvironment as schematically represented in Fig. 1 [26]. Current research is focussing intensely on controlling stem cell differentiation by influencing the microenvironment through the use of growth factors, cytokines, hormones, mechanical stimuli, culture conditions (e.g. O_2 and nutrients) and various types of (3D) biomaterials with their specific chemical and physical characteristics. A plethora of studies is available in the literature describing the construction of cell-biomaterial constructs that are able to deliver desired behaviour in vitro or in vivo (such as the production of mineralised collagen in the case of bone tissue engineering) by manipulating one or more of these microenvironmental factors.

However, a functional cell-biomaterial construct does not automatically equal a piece of functional tissue. A major challenge will be to establish the appropriate topological interactions and spatial organization of cells leading to specific

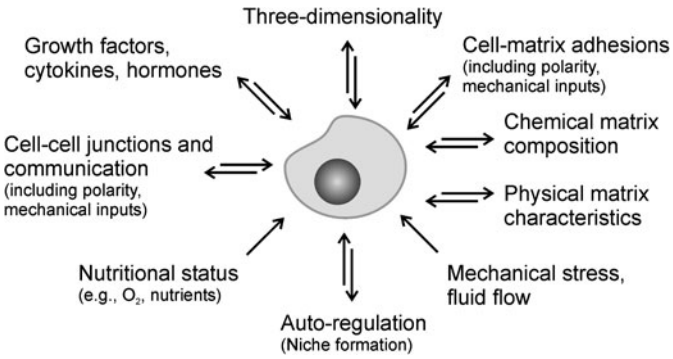

Fig. 1 Microenvironmental factors affecting cell behaviour (adapted from [26])

morphological patterns [17, 18]. The concept of developmental engineering states that in order to arrive at high quality cell-derived tissue products, developmental processes (including morphogenetic patterning) need to be recapitulated in vitro [19]. As described in [14] and references cited therein, cell adhesive processes (including cell–cell and cell–matrix adhesion) are a major driving force behind the spatial organization in the developing embryo [3]. As cell adhesion is a critical factor in determining tissue integrity and function, elucidation of the cellular and molecular mechanisms that regulate cell adhesion as well as the influence from the previously mentioned microenvironmental factors on these mechanisms, is fundamentally important for the tissue engineering field.

1.2 Discrete and Continuum Models for Adhesion

The approaches most often followed for the modelling of the behaviour of a cluster of cells are the use of cellular automata and agent-based modelling in which individual cells are simulated and followed based upon a set of biophysical rules (for comprehensive reviews we refer the reader to [1, 2, 7] and [21]. These methods are particularly useful for studying the interactions of individual cells with each other and with their microenvironment. Since these methods are based on a series of rules for each cell, it is straightforward to translate biological processes into model rules. However, these models can be difficult to study analytically and the computational cost increases rapidly with the number of cells modelled. With the number of cells needed for bone tissue engineering applications (10^6 cells or more), these methods can quickly become unwieldy [20].

For such larger-scale applications, continuum methods provide a good modelling alternative. Much research into the use of ordinary and partial differential equations (PDEs) for the modelling of cell aggregates has been carried out over the past decade, especially in the field of tumour growth, as reviewed by [20].

Various mechanisms have been implemented in these models to account for cell migration. Most models describe cell movement based on chemotactic and/or haptotactic cues (as in the authors' previous work on bone fracture healing [8]). However, other cues from the microenvironment such as the presence of other cells and extracellular matrix will also direct cell motion. A number of models incorporate cell–cell adhesion in the form of a surface tension force on the tumour surface which then controls the evolution of the tumour shape during growth [20, 5, 6]. Other groups use mesoscopic models to study cell invasion in the extracellular matrix [15, 22]. Recently a continuum description of cell motility due to cell–cell and cell–matrix adhesion has been introduced [4, 13] which is achieved by the inclusion of a non-local interaction term to account for adhesion in the PDE model.

1.3 Non-local Model for Cell Adhesion

In this section we will review and extend the derivation for an integro-partial differential equation model for cell–cell and cell–matrix adhesion first developed in [4]. The principle of conservation of mass for an adhesive cell population, with time- and space-dependent density $c(t, \mathbf{x})$, leads to the conservation equation

$$\frac{\partial c(t,\mathbf{x})}{\partial t} = -\nabla \cdot \mathbf{J}(t,\mathbf{x}) + P(t,\mathbf{x}) \quad \text{for} \quad \mathbf{x} \in \Omega, t > 0.$$

Here, P describes the production or loss of cells and $\mathbf{J}$ is the cell flux within Ω. We assume that the cell flux $\mathbf{J}$ is the cumulative effect of cell random motility governed by

$$\mathbf{J}_{\text{random}}(t,\mathbf{x}) = -D_c \nabla c(t,\mathbf{x})$$

with cell random motility coefficient $D_c > 0$ and a flux $\mathbf{J}_{\text{adhesion}}(t, \mathbf{x})$ due to adhesion, to be specified below, i.e.

$$\mathbf{J}(t,\mathbf{x}) = \mathbf{J}_{\text{random}}(t,\mathbf{x}) + \mathbf{J}_{\text{adhesion}}(t,\mathbf{x}).$$

We do not include a cell flux due to chemotactic or haptotactic cell migration.

The generic expression for the adhesive flux is $\mathbf{J}_{\text{adhesion}}(t, \mathbf{x}) = \mathbf{v}(t, \mathbf{x})\, c(t, \mathbf{x})$ where $\mathbf{v}$ denotes the velocity field generated through cell adhesion. Consider a spherical particle of radius $\hat{R}$ moving through a fluid having (dynamic) viscosity η and let $\mathbf{v}$ denote the relative velocity between particle and fluid (far away from the particle). Then Stokes' formula states that the force $\mathbf{F}$ exerted by the fluid on the particle is given by $\mathbf{F} = 6\pi\eta\hat{R}\mathbf{v}$. Under the *assumption* that cells can be regarded as spherical particles in such a flow, we can thus express the adhesive flux as

$$\mathbf{J}_{\text{adhesion}}(t,\mathbf{x}) = \frac{c(t,\mathbf{x})}{6\pi\eta\hat{R}}\mathbf{F}(t,\mathbf{x}),$$

where $\mathbf{F}(t, \mathbf{x})$ denotes the force exerted on cells at $\mathbf{x}$ at time t which is generated by cell adhesion. Defining $\Phi := \frac{1}{6\pi\eta}$ results in the expression for the adhesive flux

$$\mathbf{J}_{\text{adhesion}}(t, \mathbf{x}) = \frac{\Phi c(t, \mathbf{x})}{\hat{R}} \mathbf{F}(t, \mathbf{x}),$$

as defined first in [4] and later used in, for instance [13] and [14].

The force $\mathbf{F}(t, \mathbf{x})$ is assumed to be the result of non-local adhesive interactions of the cells at $\mathbf{x}$ with cells or the extracellular matrix in its vicinity, i.e. at $\mathbf{x} + \mathbf{r}$. Here $\mathbf{r}$ ranges over a finite region $V \subset \mathbb{R}^n$, the so-called *sensing region*, which is for our purposes assumed independent of $\mathbf{x}$. Let $m(t, \mathbf{x})$ denote the density of the extracellular matrix. We first express the force exerted on cells at $\mathbf{x}$ through cells or matrix at $\mathbf{x} + \mathbf{r}$ by

$$f(t, \mathbf{x}, \mathbf{r}) := \frac{\mathbf{r}}{|\mathbf{r}|} g(c(t, \mathbf{x} + \mathbf{r}), m(t, \mathbf{x} + \mathbf{r})) \Omega(|\mathbf{r}|).$$

Here, the first factor defines the force direction from $\mathbf{x}$ towards $\mathbf{x} + \mathbf{r}$, the second factor describes through the function g how cells and matrix present at $\mathbf{x} + \mathbf{r}$ contribute to the force, and the final factor accounts through the function Ω for the potential effect that the distance $|\mathbf{r}|$ between the two locations under consideration has on the force[1]. We require $\Omega(|\mathbf{r}|) \geq 0$. Specific functional forms for g and Ω will be given below and in the model specification in Sect. 2. The force $\mathbf{F}(t, \mathbf{x})$ is now the accumulated effect of all forces $f(t, \mathbf{x}, \mathbf{r})$, i.e.

$$\mathbf{F}(t, \mathbf{x}) = \int_V f(t, \mathbf{x}, \mathbf{r}) \mathrm{d}\mathbf{r}.$$

We would like to emphasise that the size of the sensing region V is at least the size of an individual cell but typically considerable larger due to cell protrusions (lamellipodia, filopodia). This creates the non-local character of cellular adhesion.

The basic assumption that the more cells or matrix are at a place $\mathbf{x} + \mathbf{r}$ the more adhesive interaction can take place between cells at $\mathbf{x}$ and cells or matrix at $\mathbf{x} + \mathbf{r}$ is reflected in the dependence of g on c and m at $\mathbf{x} + \mathbf{r}$ and by requiring that $g \geq 0$. The most simple, linear form of g is given by

$$g(c(t, \mathbf{x}), m(t, \mathbf{x})) = S_{cc} c(t, \mathbf{x}) + S_{cm} m(t, \mathbf{x}).$$

Here $S_{cc} \geq 0$ is the self-adhesion coefficient quantifying the strength of adhesive interaction of the cells with other cells and $S_{cm} \geq 0$ is the cross-adhesion coefficient quantifying the strength of adhesive interaction of the cells with the matrix. Whereas this form is able to account for adhesive aggregation of cells it may at the same time lead to a too strong aggregation, an unrealistic overcrowding in space, see [4] and [14]. In order to avoid, or at least mitigate, this effect, the adhesive interaction should be reduced in crowded regions. Let us assume that c and m are scaled such that they correspond to the volume fractions occupied by cells and

[1] The function Ω is of course distinct from the spatial domain Ω but no confusion should arise.

matrix, respectively. Then the desired effect can be achieved with the following functional form

$$g(c(t,\mathbf{x}),m(t,\mathbf{x})) = (S_{cc}c(t,\mathbf{x}) + S_{cm}m(t,\mathbf{x}))(1 - c(t,\mathbf{x}) - m(t,\mathbf{x}))^{+},$$

where $(\cdot)^{+} = \max\{0,\cdot\}$. The boundedness of solutions of particular models of cell aggregation and cancer invasion using this functional form is analysed in [23]. We will also make use of this form of g in our model.

The nonnegative function $\Omega(\cdot)$ is defined for nonnegative arguments and may be utilised to describe that the adhesive interaction over longer distances is weaker than over shorter distances. In this case $\Omega(|\mathbf{r}|)$ should decrease with increasing $|\mathbf{r}|$. If such an effect is not present or is not intended to be modelled, then $\Omega(|\mathbf{r}|)$ may be chosen constant. We follow this line in our model, see below Gerisch & Chaplain [13] give a sensible normalisation condition for the function Ω.

We now turn to the spatially one-dimensional situation which is of interest for the work presented here. In this case consider the sensing region $V := (-R, R)$ with the sensing radius $R > 0$. Clearly, we should have $R > \hat{R}$, i.e. the sensing radius is larger than the radius of a single cell, but we also assume that $2R$ is less than the diameter of the spatial domain Ω. We extend the function $\Omega(\cdot)$ as an odd function to the real line. Then we can rewrite the adhesive flux as (dropping the bold face in the notation since all quantities are scalar now)

$$\mathbf{J}_{\text{adhesion}}(t,x) = c(t,x)v(t,x), \tag{1}$$

$$v(t,x) = \frac{\Phi}{\hat{R}} \int_{-R}^{R} g(c(t,x+r),m(t,x+r))\Omega(r)\mathrm{d}r. \tag{2}$$

In order to emphasize the non-local character, we denote the velocity also in the form

$$v(t,x) = A\{\mathbf{u}(t,\cdot)\}(x) = \frac{\phi}{\hat{R}} \int_{-R}^{R} g(\mathbf{u}(t,x+r))\Omega(r)dr, \tag{3}$$

where we have assumed that c and m are components of a vector-valued function $\mathbf{u}(t, x)$. In this work we consider the case that

$$\Omega(r) := \begin{cases} \text{sign}(r)\frac{1}{2R} & r \in [-R,R] \\ 0 & \text{otherwise,} \end{cases} \tag{4}$$

i.e., it is a (piecewise) constant function.

Systems of partial differential equations must be supplemented with boundary conditions in order to guarantee a unique solution. The choice of boundary condition has a significant effect on the definition of the non-local force $F(t, x)$ for points x near the boundary of the spatial domain Ω. We discuss some options in the spatially one-dimensional setting below.

1.3.1 Periodic Boundary Conditions

Here one assumes that $c(t, \cdot)$ and $m(t, \cdot)$ as well as all terms depending on x are extended periodically outside of the domain Ω to the whole of $\mathbb{R}$. In this case we can simply exploit that periodicity and $v(t, x)$ is well defined for all $x \in \Omega$. Considering $g(c(t, x), m(t, x))$ as a function of t and x, also denoted $g(t, x)$, this means that we extend $g(t, x)$ periodically outside of Ω.

1.3.2 Zero-flux Boundary Conditions

These typically model the case of an isolated domain Ω, e.g. representing a Petri dish, and neither cells nor matrix can cross the boundary. For the cells this means that the normal component of the cell flux must vanish on $\partial\Omega$. In the one-dimensional setting this implies that the flux $J(t, x) = 0$ for all $x \in \partial\Omega$. A difficulty arises here for the evaluation of $v(t, x)$ when $x \in \Omega$ is closer than R to $\partial\Omega$. In this case, $g(c(t, x + r), m(t, x + r))$ is not defined for some $r \in V$ since c and m are not defined outside of Ω. However, the case of an isolated domain also means that cells cannot reach outside of Ω for adhesive interaction and consequently it is appropriate to define $g(c(t, x), m(t, x)) := 0$ for all $x \notin \Omega$, i.e. we extend function $g(t, x)$ by zero outside of Ω. It is important to note that this extension of $g(t, x)$ is a modelling issue and part of the model specification. In particular, we here assume for simplicity that the cells have no adhesive interaction with the boundary of Ω itself. If this would however be the case, for example because the Petri dish is coated with a substance which cells like to adhere to, then zero-flux boundary conditions for the cells are still appropriate but $g(t, x)$ must be extended to reflect this additional adhesive interaction.

1.3.3 Symmetry Boundary Conditions

Symmetries in the PDE problem often allow to reduce the size of the spatial domain Ω and are therefore of computational interest. In one-dimensional space, if the solution is symmetric around $x_s = 0$ then $\Omega = (-L, L)$ can be reduced to $\Omega := (0, L)$ and at $x_s = 0$ symmetry boundary conditions apply. Let $x_s \in \partial\Omega$ be a boundary point where symmetry boundary conditions apply. Then it follows that there can be no cell flux through that boundary point as this would violate the symmetry. Therefore, a zero-flux boundary condition applies for the cell density c at $x = x_s$, i.e. $J(t, x_s) = 0$ and, as in the zero-flux boundary condition case above, for $x \in \Omega$ with $|x - x_s| < R$ the velocity $v(t, x)$ is not defined. Again, as above, we have to extend function $g(t, x)$ across $x_s \in \partial\Omega$ for $x \notin \Omega$. However, in this case and in contrast to the zero-flux boundary condition case, we do not extend g by zero but must do so by symmetry around x_s. This is because here cells can reach outside of Ω across the symmetry boundary for adhesive interaction because this boundary is not physical but only a theoretical construct to reduce the problem to a smaller

domain. Also in contrast to the zero-flux boundary condition case, this extension of $g(t, x)$ is not a modelling issue but follows strictly from the assumed symmetry.

1.3.4 Dirichlet Boundary Conditions

If at some point $x_D \in \partial\Omega$ Dirichlet boundary conditions are prescribed for c or m then again information is missing to evaluate the non-local term at $x \in \Omega$ with $|x - x_D| < R$ and again function $g(x, t)$ must be extended appropriately. A sensible extension is again part of the modelling process in this case. Since in the sequel we do not consider problems with Dirichlet boundary conditions for any of the variables involved in the non-local term we do not discuss this case any further.

Of course, symmetry and zero-flux boundary conditions for the cell density $c(t, x)$ can also be combined. Below in our model we consider the case of a symmetry boundary condition at $x = 0$ and a zero-flux boundary condition for $c(t, x)$ at $x = L$. We emphasise that both conditions look the same at the level of the PDE but they differ in the way how the non-local term is evaluated near the boundaries.

2 Modelling Adhesion in Cell Aggregate Behavior

To illustrate the potential of modelling cell–cell and cell–matrix adhesion on a continuum level, we use a model that represents a generic cell-in-gel 3D culture situation. The model encompasses five variables: cell density *(c)*, hydrogel density *(w)*, matrix degrading enzyme density *(e)*, collagen (extracellular matrix) density *(m)* and oxygen/nutrient density *(n)*. Let $\mathbf{u} := (c, w, e, m, n)$ be the vector of the five variables. The spatiotemporal evolution of these five variables is described by a system of partial differential equations (PDEs) in which the various terms describe the migration of cells (random migration and cell–cell and cell–matrix adhesion), enzymes (diffusion) and nutrients (diffusion), cell proliferation and death (influenced by spatial and nutrient constraints), hydrogel degradation (by matrix-degrading enzymes), enzyme production (by cells) and degradation (half-life), collagen production (influenced by spatial constraints) and oxygen/nutrient consumption (by cells). Each of the five PDE equations will be briefly described below.

The motion of the cells is assumed to be governed by random motility and by adhesion to other cells and the matrix (both the hydrogel and the collagen). Furthermore, the cells are assumed to proliferate, modelled by a logistic growth law, which takes into account the space occupied not only by cells (which would lead to a simple logistic growth law $\mu_1 c(1 - c)$) but also by the hydrogel as well as the produced matrix to avoid overcrowding as explained above. The proliferation of cells is only possible when sufficient oxygen/nutrients are present, which is modelled by introducing a mask function $M_1 = n^6(K_p^6 + n^6)^{-1}$. Finally cell death

occurs under very poor oxygen/nutrient conditions ($M_2 = 1 - n^6(K_d^6 + n^6)^{-1}$). This leads to the following equation:

$$\frac{\partial c}{\partial t} = \nabla \cdot [D_c \nabla c - cA\{\mathbf{u}(t, \cdot)\}] + \mu_1 c(1 - c - w - m)M_1 - \mu_2 M_2 c. \quad (5)$$

The non-local term $A\{\mathbf{u}(t, \cdot)\}$, also referred to as the adhesion velocity, is a function of x and for a one-dimensional spatial domain takes the form see Eq. (3):

$$A\{\mathbf{u}(t, \cdot)\}(x) = \frac{\phi}{\hat{R}} \int_{-R}^{R} g(\mathbf{u}(t, x + r))\Omega(r)dr, \quad (6)$$

as described in detail in Sect.1.3. In this study the weight of all the points in the sensing region is assumed to be equal and so $\Omega(r)$ is given by Eq. (4). The following form for g is used: $g(c, w, m) = (S_{cc}c + S_{cw}w + S_{cm}m)(1 - c - w - m)^+$. S_{cc} is the cell–cell adhesion coefficient, S_{cw} is the cell–hydrogel adhesion coefficient and S_{cm} is the cell–extracellular matrix adhesion coefficient. Similarly to the logistic growth term, the factor $(1 - c - w - m)^+$ ensures that a space point which is already densely filled (or even overcrowded) with cells and/or matrix does not attract more cells via adhesive interaction. In this way unbounded aggregation is avoided.

The hydrogel is considered to be non-motile matter and changes in its distribution are due solely to its local degradation by matrix degrading enzymes at a rate γ.

$$\frac{\partial w}{\partial t} = -\gamma we \quad (7)$$

Matrix-degrading enzymes are produced by active cells (when sufficient oxygen/nutrients are present, M_1) at a constant rate α, are removed from the system at rate λ and are assumed to diffuse freely in the spatial domain.

$$\frac{\partial e}{\partial t} = \nabla \cdot [D_e \nabla e] + \alpha M_1 c - \lambda e \quad (8)$$

The extracellular matrix is produced by the cells at rate β under favourable nutrient/oxygen conditions (M_1) within the physical limitations of space (factor $(1 - c - w - m)$)

$$\frac{\partial m}{\partial t} = \beta c(1 - c - w - m)M_1. \quad (9)$$

Oxygen and nutrients, which are modelled as a single variable for simplicity reasons, are assumed to diffuse freely in the spatial domain and are consumed by the cells at a constant rate α_s.

$$\frac{\partial n}{\partial t} = \nabla \cdot [D_n \nabla n] - \alpha_s cn \quad (10)$$

Equations (5–10) have been obtained after the original variables $\mathbf{u}$ have been scaled with respect to time and space using a characteristic time of 1,000 s and a characteristic length of 0.1 cm. They have furthermore been scaled with respect to

$\mathbf{u_0}$ containing characteristic densities/concentrations and are hence in non-dimensionalised form. The following set of non-dimensionalised parameters is used in this study.

$$\begin{aligned} &D_c = 0.1, \quad S_{cc} = 0.1, \quad S_{cw} = 0.5, \quad S_{cm} = 0.25, \quad \mu_1 = 0.1, \quad \mu_2 = 1, \\ &K_p = 0.5, \quad K_d = 0.1, \quad \gamma = 1, \quad D_e = 10^{-2}, \quad \alpha = 0.1, \\ &\lambda = 0.5, \quad \beta = 0.1, \quad D_n = 10^{-4}, \quad \alpha_s = 0.1, \quad \Phi = 1. \end{aligned} \tag{11}$$

The (dimensional) cell radius was set at 5 μm, giving a non-dimensional $\hat{R} = 5 \times 10^{-3}$, the sensing radius was fixed at five cell diameters, i.e. $R = 50 \times 10^{-3}$. As the main purpose of this study is to illustrate the potential of modelling cell–cell and cell–matrix adhesion at a continuum level, no further attempts were made to experimentally determine the value of the parameters for a specific cell-in-gel culture set-up.

As mentioned in the previous section, the 1D domain used in this study is derived from a cell-in-gel set-up as represented in Fig. 2. The hydrogel is surrounded by medium in a Petri dish. For symmetry reasons only one half of the domain is used in the calculations. This leads to symmetry boundary conditions on the left boundary, $x = 0$, for all variables. Apart from the oxygen/nutrients, which can diffuse from the medium into the hydrogel, all other variables are assumed to be restricted to the hydrogel. Therefore, we apply zero-flux boundary conditions on the right edge of the domain, $x = L = 4$, for the cell density and the matrix degrading enzyme concentration. The hydrogel and collagen density is zero for $x > L = 4$ (no boundry condition is prescribed since the equations for w and m involve no transport, but the zero-values are used in the non-local term evalution). For the oxygen/nutrient variable, a Dirichlet boundary conditions is applied as we assume the medium surrounding the hydrogel gets sufficiently often refreshed to maintain a constant level of oxygen and nutrients. At the onset of the simulations, we assume a low concentration of cells, homogeneously distributed throughout the (low-density) hydrogel. Collagen and matrix-degrading enzymes are not present at

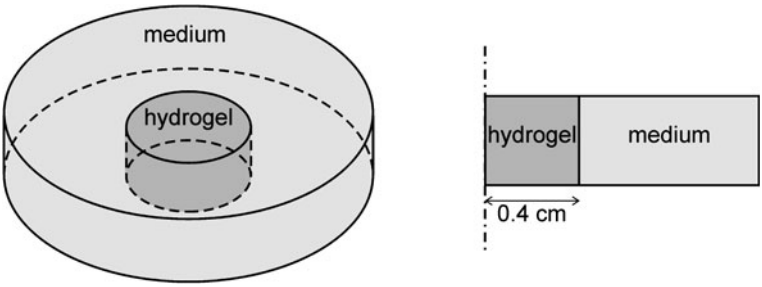

Fig. 2 Derivation of modelling domain. *Left* cells are homogeneously encapsulated in a hydrogel that is placed in a Petri dish and surrounded by medium. *Right* the 1D domain used in this study is a horizontal cross-section of the hydrogel. We assume there is no variation in the *vertical direction*

the onset of the simulations. An initial oxygen/nutrient profile is assumed, representing the diffusional limitations of oxygen into the hydrogel and the resulting hypoxic condition in the centre of the gel [9].

3 Numerical Technique

The Method of Lines (MOL) is applied for the numerical solution of the model equations in this chapter. In the MOL the discretisation of spatial and temporal derivatives is separated. We apply the so-called vertical MOL here, in which the spatial derivatives are discretised first, followed by temporal discretisation.

For the model considered in this work, we discretise the spatial derivatives on a uniform spatial grid with N grid cells covering the one-dimensional spatial domain $\Omega = (0, L)$. Each grid cell, or finite volume, is an interval of length $h := L/N$.[2] We employ a Finite Volume Method (FVM) of order two on this grid, see, e.g. [12], or more general the book by Hundsdorfer & Verwer [16]. The result of this discretisation in space is a large and in general stiff initial value problem (IVP) for a system of ordinary differential equations (ODEs), the MOL-ODE system,

$$\frac{\mathrm{d}\mathbf{U}(\mathrm{t})}{\mathrm{d}t} = \mathscr{F}(t, \mathbf{U}(t)), \quad \mathbf{U}(0) = \mathbf{U_0}. \tag{12}$$

The MOL-ODE together with the initial data $\mathbf{U_0}$ represents the PDE model on the spatial grid. As is customary when using the FVM, the components of the MOL-ODE system are approximations to the averages of the PDE solution in each grid cell. Since the model (5–10) has five equations, the MOL-ODE has dimension $5N$.

The numerical solution of the IVP (12) constitutes the second step of the MOL and an appropriate time integration scheme must be selected. Implicit time integration schemes can deal efficiently with the inherent stiffness of the MOL-ODE. We favour the fourth order linearly-implicit Runge-Kutta method ROWMAP [25]. The multiple Arnoldi process used within this method for the solution of the linear equation systems in each time step makes this scheme particularly suited for the large ODE system at hand. Furthermore, the method does not require any computation of the Jacobian of the MOL-ODE by the user; the required Jacobian-times-vector products are computed automatically by a suitable finite difference approximation using the right-hand side $\mathscr{F}$ of the MOL-ODE.

The FVM described in [12] has been applied to taxis-diffusion-reaction systems. There difficulties arise in regions of strong variation of the solution of the PDE, e.g. near moving fronts. These are due to the taxis term of the model and special attention was given to ensure that the discretisation of that term does not introduce oscillations or negative solution values in the solution of the MOL-ODE.

[2] For our model, see Sect. 2, we have $L = 4$ and in the corresponding model simulations presented in Sect. 4 we employ $N = 1{,}600$, leading to $h = 2.5 \times 10^{-3}$

This goal can be achieved, while maintaining the order two of the FVM as much as possible, using a second-order upwind discretisation together with a nonlinear limiter function. The model of this chapter has a non-local adhesion term which is similar to the taxis terms in [12]. So we apply the same discretisation to that term, with the added difficulty of the approximation of the integral defining the adhesive velocity. This is explained in more detail in the following with particular emphasis on the incorporation of boundary conditions.

Recall that the adhesive velocity takes, in the one-dimensional setting, the form, cf. Eq. (2),

$$v(t,x) = \frac{\Phi}{\hat{R}} \int_{-R}^{R} g(c(t,x+r), m(t,x+r))\Omega(r)\mathrm{d}r,$$

where function g and Ω and the parameters R, $\hat{R}$, and Φ are user-specified. The adhesive velocity $v(t, x)$, and consequently the integral must be approximated on each grid cell interface $x = jh$, $j = 0, 1, ..., N$, of the spatial grid for each evaluation of the right-hand side $\mathscr{F}$ of the MOL-ODE. This task constitutes the computational bottleneck of the whole numerical solution process. In [10] an approximation procedure for the adhesion velocity is described which yields

$$v(t,\ jh) \approx v_j(t) := \frac{\Phi R}{\hat{R}} \sum_{l=-l^-}^{l^+} w_l G_{j+l}(t) \quad \text{with} \quad G_j(t) := g(C_j(t), M_j(t)), \tag{13}$$

where $C_j(t)$ and $M_j(t)$ are components of vector $\mathbf{U}(t)$ of the MOL-ODE system and approximate the averages of cell density and matrix density in the jth grid cell, that is in $[(j-1)h, jh]$, respectively. The weights w_l, $l = -l^-, ..., l^+$, define the integration formula and l^- and l^+ are related to the sensing region and are roughly equal to R/h, for details see [10]. The factor $\Phi R/\hat{R}$ compensates for the fact that [10] considers the special case $\hat{R} = R$ and $\Phi = 1$. It is important to stress that the weights w_l depend on the function $\Omega(r)$, on the spatial grid width h, and on the sensing radius R but on nothing else. In particular, they are independent of the function g and of the cell and matrix densities. This implies that the weights can be computed once $\Omega(r)$, R, and h are fixed, i.e. before a simulation run is started.

We first briefly outline how periodic boundary conditions are employed in the evaluation of the adhesion velocity. This is the case considered in [10] and it sets the stage for the zero-flux and symmetry boundary conditions which are of interest for the model considered in this work. As discussed in Sect. 1.3, in the case of periodic boundary conditions function g, as a function of x, is extended periodically. This implies that $G_j(t)$ is defined for all integers j and that it is N-periodic in j. With this, $v_j(t)$ is well-defined for all $j = 1, ..., N$ according to (13) and $v_j(t)$ also becomes N-periodic in j, in particular $v_0(t) = v_N(t)$. Furthermore, (13) can be written as the matrix–vector product

$$\mathbf{v}(t) = \frac{\Phi R}{\hat{R}} A^{(\mathrm{p})} \mathbf{G}(t), \tag{14}$$

where

$$\mathbf{v}(t) := [v_1(t), v_2(t), \ldots, v_N(t)]^{\mathsf{T}} \quad \text{and} \quad \mathbf{G}(t) := [G_1(t), G_2(t), \ldots, G_N(t)]^{\mathsf{T}}. \quad (15)$$

Here, $A^{(\mathrm{p})} \in \mathbb{R}^{N,N}$ is a circulant matrix defined by the weights w_l of the integration formula, consequently $A^{(p)}$ is known before a simulation run starts. The superscript (p) is used to refer to the case of periodic boundary conditions. Circulant matrices enjoy favourable properties [24]: any circulant matrix A is (i) defined by its first column $\mathbf{a}$ and (ii) diagonalised by the discrete Fourier transform matrix with eigenvalues given by the discrete Fourier transform of $\mathbf{a}$. Property (1) allows for a memory-efficient storage of A and (2) facilitates the efficient computation of matrix–vector products using the fast Fourier transform (FFT) and its inverse (iFFT) through

$$A\mathbf{G} = \mathrm{iFFT}(\mathrm{FFT}(\mathbf{a}) \otimes \mathrm{FFT}(\mathbf{G})),$$

where $\otimes$ denotes the element-wise product of two vectors.

The first column of matrix $A^{(\mathrm{p})}$ is given by

$$\mathbf{a}^{(\mathrm{p})} := [w_0, w_{-1}, \ldots, w_{-l^-}, 0, \ldots, 0, w_{l^+}, w_{l^+-1}, \ldots, w_1]^{\mathsf{T}} \in \mathbb{R}^N. \quad (16)$$

Even though matrix $A^{(\mathrm{p})}$ has many zero entries due to its banded structure of width characterised by l^- and l^+, it pays off computationally, in matrix–vector products, not to exploit this fact but rather the circulant structure of the matrix by using the FFT. This is because refining the spatial grid leads to an increase in the dimension of matrix $A^{(\mathrm{p})}$ but also to an increase of its bandwidth. As a result, the fraction of non-zero elements in $A^{(\mathrm{p})}$ remains constant for $h \to 0$ and exploiting the zeros would, in consequence, lead to a matrix–vector product of complexity $\mathcal{O}(N^2)$. The FFT approach, in contrast, requires only $\mathcal{O}(N \log N)$ complexity and is thus overall more efficient. We note that the growth of the bandwidth of $A^{(\mathrm{p})}$ with decreasing h and the associated constant fraction of non-zero entries is a characterising feature of the non-local term in the PDE model and distinguishes it from, for instance, a diffusion term. A matrix representation of the latter involves a matrix where the fraction of non-zero entries tends to zero for $h \to 0$.

If we depart from periodic boundary conditions then the circulant structure is lost, at least on first sight but can be recovered. We will consider two cases: (A) zero flux boundary conditions on both ends of the domain Ω and (B) a symmetry boundary condition at the left end and a zero-flux boundary condition on the right end of Ω. The second scenario applies in the simulations for this chapter. In both cases we compute $N + 1$ adhesion velocities

$$\mathbf{v}(t) := [v_0(t), v_1(t), \ldots, v_N(t)]^{\mathsf{T}} \in \mathbb{R}^{N+1}.$$

In case (A), recall from Sect. 1.3 that function g is extended by zero outside of the domain Ω. Hence, $\mathbf{v}(t)$ can be computed from a matrix–vector product

$$\mathbf{v}(t) = \frac{\Phi R}{\hat{R}} A^{(\mathrm{zz})} \mathbf{G}(t),$$

where $\mathbf{G}(t) \in \mathbb{R}^N$ is given as in the case of periodic boundary conditions. The matrix $A^{(\mathrm{zz})} \in \mathbb{R}^{N+1,N}$ is now rectangular and has a Toeplitz structure. The superscript (zz) refers to the case that function g has been extended by zeros to the left and right of the domain Ω. A Toeplitz matrix is defined by specifying its first row and column. For $A^{(\mathrm{zz})}$ these are given by

$$[w_1, w_2, \ldots, w_{l^+}, 0, \ldots] \in \mathbb{R}^N \quad \text{and} \quad [w_1, w_0, \ldots, w_{-l^-}, 0, \ldots]^\mathsf{T} \in \mathbb{R}^{N+1},$$

respectively, in particular, $A^{(\mathrm{zz})} \in \mathbb{R}^{N+1,N}$ is a banded Toeplitz matrix with upper bandwidth $l^+ - 1$ and lower bandwidth $l^- + 1$.

In case (B), recall from Sect. 1.3 that function g is extended by symmetry to the left of Ω and by zeros to the right of Ω. Again, $\mathbf{v}(t)$ can be computed from a matrix–vector product

$$\mathbf{v}(t) = \frac{\Phi R}{\hat{R}} A^{(\mathrm{vz})} \mathbf{G}(t),$$

where now $\mathbf{G}(t)$ is given by

$$\mathbf{G}(t) := [G_{l^-+1}, G_{l^-}, \ldots, G_1, G_1, G_2, \ldots, G_N]^\mathsf{T} \in \mathbb{R}^{N+l^-+1},$$

where the first $l^- + 1$ entries represent the extension by symmetry on the left. Matrix $A^{(\mathrm{vz})} \in \mathbb{R}^{N+1,N+l^-+1}$ is a rectangular Toeplitz matrix with first row and column given by

$$[w_{-l^-}, w_{-l^-+1}, \ldots, w_{l^+}, 0, \ldots] \in \mathbb{R}^{N+l^-+1} \quad \text{and} \quad [w_{-l^-}, 0, \ldots]^\mathsf{T} \in \mathbb{R}^{N+1},$$

respectively. In particular, the lower bandwidth of $A^{(\mathrm{vz})}$ is zero and the upper bandwidth is $l^- + l^+$. The superscript (vz) refers to the case that function g has been extended by some "values" to the left of Ω and zeros to the right of Ω. The "values" are in our case defined by symmetry but they could be any other values, e.g. representing some sort of Dirichlet boundary.

Matrix–vector products with Toeplitz matrices cannot be handled directly by FFT techniques. However, rectangular Toeplitz matrices can be embedded in square circulant matrices of often just slightly larger size and then the matrix vector product can again be computed as in the case of periodic boundary conditions [11]. To this end let $T \in \mathbb{R}^{N_1,N_2}$ be a banded Toeplitz matrix with lower bandwidth $0 \leq l^- < N_1$ and upper bandwidth $0 \leq l^+ < N_2$ and first row and column given by

$$[t_0, t_1, \ldots, t_{l^+}, 0, \ldots] \in \mathbb{R}^{N_2} \quad \text{and} \quad [t_0, t_{-1}, \ldots, t_{-l^-}, 0 \ldots]^\mathsf{T} \in \mathbb{R}^{N_1},$$

respectively. Assume that $t_{-l^-} \neq 0$ and $t_{l^+} \neq 0$. Then the following holds.

(a) The matrix T can be embedded in the circulant matrix $C \in \mathbb{R}^{\ell,\ell}$, defined by its first column $\mathbf{c}$ given by

$$\mathbf{c} = (t_0, t_{-1}, \ldots, t_{-l^-}, 0 \ldots, 0, t_{l^+}, t_{l^+-1} \ldots, t_1)^{\mathsf{T}} \in \mathbb{R}^{\ell},$$

where C is 2×2 block-structured with (1,1) block equal to T, i.e.

$$C = \begin{pmatrix} T & M_{12} \\ M_{21} & M_{22} \end{pmatrix},$$

and ℓ is minimal and given by $\ell = \max\{N_1 + l^+, N_2 + l^-\}$.

(b) It holds $\ell < N_1 + N_2$.

(c) Let $\mathbf{G} \in \mathbb{R}^{N_2}$. The Toeplitz matrix–vector product $T\mathbf{G}$ can be computed using a circulant matrix–vector product by

$$T\mathbf{G} = \left[C\tilde{\mathbf{G}}\right]_{1,\ldots,N_2},$$

where $\tilde{\mathbf{G}} := (\mathbf{G}\,\mathbf{0})^{\mathsf{T}} \in \mathbb{R}^{\ell}$ and C is the circulant matrix from (a).

The application of this embedding result to the two Toeplitz matrices $A^{(\mathrm{zz})} \in \mathbb{R}^{N+1,N}$ and $A^{(\mathrm{vz})} \in \mathbb{R}^{N+1,N+l^-+1}$ corresponding to the boundary condition cases (A) and (B), respectively, yields that a matrix–vector product with these matrices can be accomplished by computing an FFT-based matrix–vector product with a circulant matrix C of dimension $\ell = N + \max\{l^+, l^- + 1\}$ in case (A) and of dimension $\ell = N + l^- + l^+ + 1$ in case (B).

4 Results and Discussion

Simulations performed with the model given by Eqs. (5–10) using the parameter set (11) for an initially homogeneously distributed cell population show an increased cell density in the periphery of the gel (right hand side of the domain) and a stagnation of cell density in the centre of the gel (left hand side of the domain) under the influence of the local oxygen/nutrient conditions (Fig. 3). As already at the start of the simulations the oxygen/nutrient concentration is low in the centre of the gel, cells are not able to degrade the hydrogel or produce collagen. Towards the periphery of the gel where oxygen/nutrient conditions are more favourable, cells are able to degrade the surrounding hydrogel, proliferate and produce collagen. The peak in collagen density at the right edge is due to the locally high concentration of nutrients/oxygen. The initial increase in cell density increases the consumption of oxygen limiting the increase in cellular density beyond what is shown in Fig. 3. With the values of the adhesion parameters used in this simulation, the influence of any of the adhesive processes on the simulation result is minimal with the exception of the drop in cell density at the outer edge of the gel (right boundary of the domain). This drop is a modelling effect

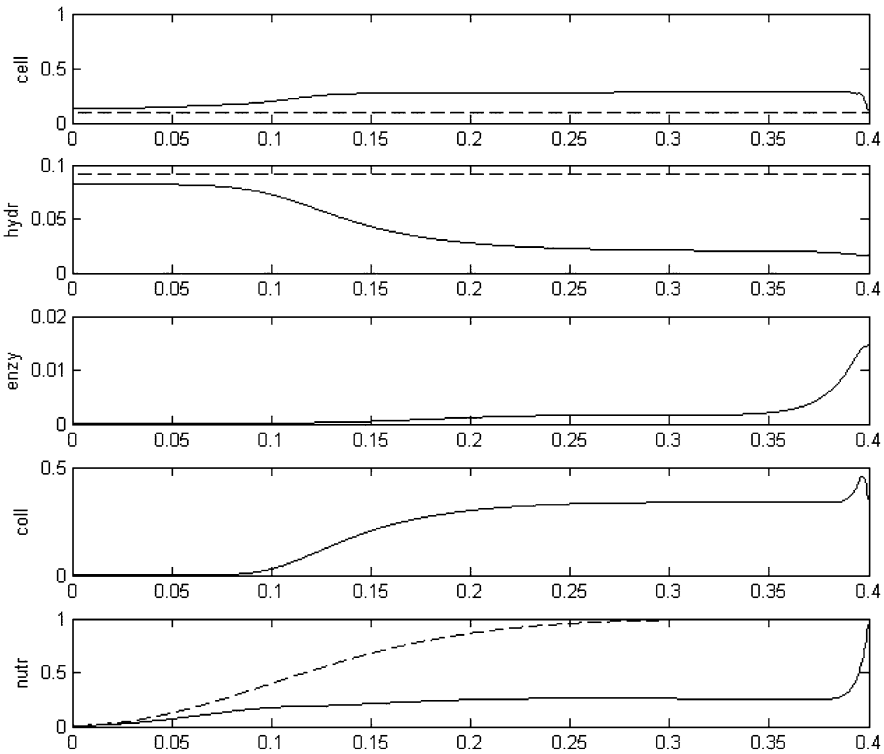

Fig. 3 Simulation results for the model given by Eqs. (5–10). Shown are the (non-dimensional) cell density (*cell*), the hydrogel density (*hydr*), the matrix degrading enzyme concentration (*enzy*), the collagen density (*coll*) and the oxygen/nutrient concentration (*nutr*) over the simulated domain (*x*-axis in cm). *Dashed lines* indicate the initial conditions (the matrix degrading enzyme concentration and the collagen density are initially zero in the entire domain), *full lines* correspond to the time point $t = 50$ (1 week of culture)

(zero-flux boundary condition) since cells are only pulled from the left at/near the right boundary (no cells are present outside the gel).

Increasing the parameter values related to each of the cell adhesive processes encapsulated in the model (cell–cell, cell–hydrogel and cell–collagen adhesion) clearly shows the effect of these processes on the density and distribution of cells and the produced collagen (Fig. 4).

A tenfold increase of the cell–cell adhesion parameter (S_{cc}) causes clustering of the cells in small aggregates throughout the gel. As oxygen/nutrient consumption causes hypoxic conditions in the centre of each aggregate, the collagen production is highest at the edges of each aggregate.

A tenfold increase of the cell–hydrogel adhesion parameter (S_{cw}) leads to the accumulation of cells in the centre of the gel. This accumulation is due to a continuous migration of cells from the periphery of the gel towards the centre. Once they arrive at the centre of the gel they will become inactive (no proliferation,

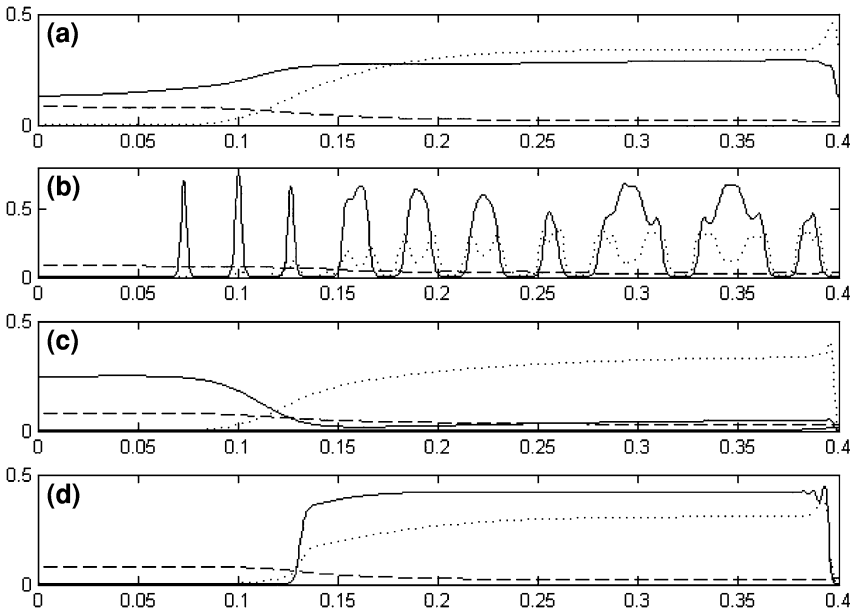

Fig. 4 Simulation results for the model given by Eqs. (5–10) for increased values of the adhesion parameters. Shown in each subfigure are the (non-dimensional) cell density (*full line*), the hydrogel density (*dashed line*) and the collagen density (*dotted line*) at time point $t = 50$ over the simulated domain (x-axis in cm). **a** Results using the basic parameter value set (11). **b** Cell–cell adhesion increased by factor 10. **c** Cell–hydrogel adhesion increased by factor 10. **d** Cell–collagen adhesion increased by factor 10

hydrogel degradation or collagen production) due to the low concentration of oxygen/nutrients present there. In the periphery of the gel, cells do proliferate, produce collagen and degrade the hydrogel. This maintains the adhesive velocity being directed towards the centre of the gel.

Finally, a tenfold increase of the cell–collagen adhesion parameter (S_{cm}) leads to an almost complete depletion of cells in the centre of the gel. As collagen can only be produced in the periphery of the gel where the nutritional conditions allow so, the adhesive velocity will be directed away from the centre towards the periphery of the gel. Due to the accumulation of the cells, nutritional conditions will deteriorate in the periphery of the gel as well causing a halt in the increase in cell density and collagen density.

For the simulation results shown above, the cell sensing radius was chosen to be five cell diameters. Increasing the sensing radius by a factor 10 initially leads to the formation of less aggregates but bigger ones (Fig. 5). These bigger aggregates provide less favourable conditions to the cells inside the aggregate which results in overall less cell proliferation and collagen production at the end of the simulation period when compared to the simulations with a smaller sensing radius.

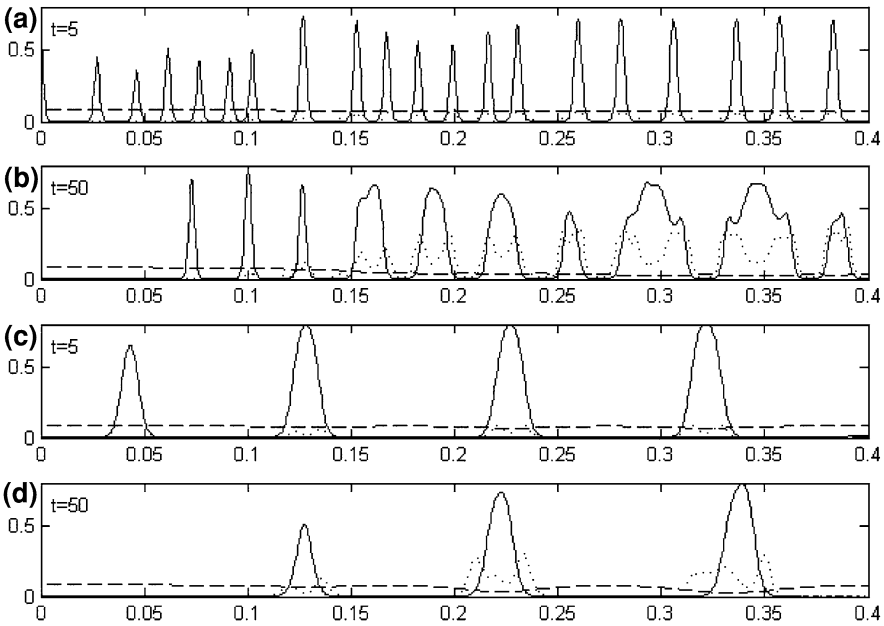

Fig. 5 Simulation results for the model given by Eqs. (5–10) for different cell sensing radii. Shown in each subfigure are the (non-dimensional) cell density (*full line*), the hydrogel density (*dashed line*) and the collagen density (*dotted line*) over the simulated domain (x-axis in cm). Parameter set (11) was used with the cell–cell adhesion (S_{cc}) increased by a factor 10. Simulation results are shown for simulation times $t = 5$ (**a**,**c**) and $t = 50$ (**b**,**d**), using a cell sensing radius of five cell diameters (**a**,**b**) or 50 cell diameters (**c**,**d**)

We remark that the total density (cell + hydrogel + collagen) always remains below the maximal available space due to the use of the physical space restriction factor that was used in the terms describing cellular proliferation, cellular adhesion and collagen production. As stated above, this prevents the occurrence of non-physical unlimited growth and aggregation in the model.

The way in which the zero-flux boundary conditions are currently implemented assumes that cells have no particular adhesive interaction with the boundary of the domain itself. When studying situations where this is the case, such as a cell culture in a Petri dish which has been coated with an adhesive substance, the function describing how cells and matrix at a particular location contribute to the adhesive force needs to be elaborated compared to its formulation used in the current study.

Apart from the determination of the parameter values for a specific cell-in-gel culture set-up, other model extension can be considered in the future. One example is the right edge boundary condition on the matrix degrading enzymes which now considers the enzymes to be trapped inside the gel, while more likely they can freely leave the gel and enter the medium similar to the oxygen/nutrient variable. Furthermore in this study adhesion is assumed to generate forces resulting in cell

migration whereas the signalling that is initiated through cell–cell and cell–matrix binding also has an influence on many other facets of cell behaviour, including proliferation and apoptosis. Including these phenomena in the model will further enhance its relevance to understanding the role of adhesion in the biological processes under scrutiny.

5 Conclusions

In this chapter we discussed the critical role played by cellular adhesion in tissue engineering processes. A brief review of existing models, discrete and continuous, has demonstrated that for larger-scale applications, continuum models using the recently introduced non-local technique are very well suited to model these adhesive processes. Here we expanded the derivation of this model with respect to previous works [4] and [14] to allow for its application in finite non-periodic spatial domains with various boundary conditions. A generic cell-in-gel culture model was presented to illustrate the technique, showing a clear influence of the different adhesive processes on the final cell and collagen density and distribution. Both the theoretical discussion and the modelling example provided in this chapter show the feasibility of using the non-local technique to capture cell adhesive behaviour in continuum models.

Acknowledgments L.G. is a postdoctoral research fellow of the Research Foundation Flanders (FWO). This work is part of Prometheus, the Leuven Research & Development Division of Skeletal Tissue Engineering of the Katholieke Universiteit Leuven: http://www.kuleuven.be/prometheus. A.G. gratefully acknowledges financial support by the Division of Mathematics, University of Dundee during a long-term visit in 2007 introducing him to the topic.

References

1. Alber, M.S., Kiskowski, M.A., Glazier, J.A., Jiang, Y.: On cellular automaton approaches to modelling biological cells. In: Rosenthal, J., Gilliam, D.S. (eds) Mathematical Systems Theory in Biology, Communication, and Finance, IMA. Springer, New York, pp. 1–40 (2002)
2. Anderson, A., Chaplain, M.A.J., Rejniak, K.: Single-cell Based Models in Biology and Medicine. Birkhäuser, Basel (2003)
3. Armstrong, N., Painter, K., Sherratt, J.: Adding adhesion to a chemical signaling model for somite formation. Bull. Math. Biol. **71**(1), 1–24. doi:10.1007/s11538-008-9350-1
4. Armstrong, N.J., Painter, K.J., Sherratt, J.A.: A continuum approach to modelling cell–cell adhesion. J. Theor. Biol. **243**(1), 98–113 (2006). doi:10.1016/j.jtbi.2006.05.030
5. Byrne, H.M., Chaplain, M.A.J.: Modelling the role of cell-cell adhesion in the growth and development of carcinomas. Math. Comput. Model. **24**(12), 1–17 (1996). doi:10.1016/S0895-7177(96)00174-4
6. Cristini, V., Lowengrub, J., Nie, Q.: Nonlinear simulation of tumor growth. J. Math. Biol. **46**, 191–224 (2003)

7. Drasdo, D.: On selected individual-based approaches to the dynamics of multicellular systems. In: Alt,W., Chaplain, M., Griebel, M. (eds) Multiscale modelling. Birkhäuser, Basel (2003)
8. Geris, L., Gerisch, A., Sloten, J.V., Weiner, R., Oosterwyck, H.V.: Angiogenesis in bone fracture healing: a bioregulatory model. J. Theor. Biol. **251**(1), 137–158 (2008). ISSN 0022-5193. doi:10.1016/j.jtbi.2007.11.008
9. Geris, L., Peiffer, V., Demol, J., Van Oosterwyck, H.: Modelling of in vitro mesenchymal stem cell cultivation, chondrogenesis and osteogenesis. J. Biomech. **41**, 466 (2008)
10. Gerisch, A.: On the approximation and efficient evaluation of integral terms in PDE models of cell adhesion. IMA J Numer Anal **30**(1), 173–194 (2010). doi:10.1093/imanum/drp027
11. Gerisch, A.: Numerical treatment of nonperiodic boundary conditions in a nonlocal continuous model of cell adhesion. In preparation (2010)
12. Gerisch, A., Chaplain, M.A.J.: Robust numerical methods for taxis–diffusion–reaction systems: applications to biomedical problems. Math. Comput. Model. **43**, 49–75 (2006). doi:10.1016/j.mcm.2004.05.016
13. Gerisch, A., Chaplain, M.A.J.: Mathematical modelling of cancer cell invasion of tissue: Local and non-local models and the effect of adhesion. J. Theor. Biol. **250**, 684–704 (2008). doi:10.1016/j.jtbi.2007.10.026
14. Gerisch, A., Painter, K.: Mathematical modelling of cell adhesion and its applications to developmental biology and cancer invasion. In Arnaud, C., Luigi, P., Verdier C. (eds) Cell Mechanics: From Single Scale-Based Models to Multiscale modelling, chapter 12. CRC Press, pp. 313–341 (2010). http://www.crcpress.com/product/isbn/9781420094541
15. Hillen, T.: M^5 mesoscopic and macroscopic models for mesenchymal motion. J. Math. Biol. **53**(4), 585–616 (2006). doi:10.1007/s00285-006-0017-y
16. Hundsdorfer, W., Verwer, J.G.: Numerical Solution of Time-Dependent Advection-Diffusion-Reaction Equations, volume 33 of Springer Series in Computational Mathematics. Springer, New York (2003)
17. Khademhosseini, A., Langer, R., Borenstein, J., Vacanti, J.P.: Microscale technologies for tissue engineering and biology. Proc. Natl. Acad. Sci. USA **103**, 2480–2487 (2006)
18. Langer, R., Tirrell, D.A.: Designing materials for biology and medicine. Nature **428**, 487–492 (2004)
19. Lenas, P., Moos, M., Luyten, F.P.: Developmental engineering: A new paradigm for the design and manufacturing of cell-based products. Part I. From three-dimensional cell growth to biomimetics of in vivo development. Tiss. Eng. B **15**, 381–394 (2009)
20. Macklin, P., Lowengrub, J.: Nonlinear simulation of the effect of microenvironment on tumor growth. J. Theor. Biol. **245**, 677–704 (2007)
21. Moreira, J., Deutsch, A.: Cellular automata models of tumour developmenta critical review. Adv. Complex Syst. **5**, 247–267 (2002)
22. Painter, K.: Modelling cell migration strategies in the extracellular matrix. J. Math. Biol. **58**, 511–543 (2009). doi:10.1007/s00285-008-0217-8
23. Sherratt, J.A., Gourley, S.A., Armstrong, N.J., Painter, K.J.: Boundedness of solutions of a non-local reaction-diffusion model for adhesion in cell aggregation and cancer invasion. Eur. J. Appl. Math. **20**(01), 123–144 (2009). ISSN 0956-7925. doi:10.1017/S0956792508007742
24. Strang, G.: The discrete cosine transform. SIAM Rev. **41**(1), 135–147 (1999). doi:10.1137/S0036144598336745
25. Weiner, R., Schmitt, B.A., Podhaisky, H.: ROWMAP—a ROW-code with Krylov techniques for large stiff ODEs. Appl. Numer. Math. **25**, 303–319 (1997). doi:10.1016/S0168-9274(97)00067-6
26. Yamada, K.M., Cukierman, E.: modelling tissue morphogenesis and cancer in 3d. Cell **130**, 601–610 (2007)

Cell–Material Communication: Mechanosensing Modelling for Design in Tissue Engineering

J. M. García-Aznar, J. A. Sanz-Herrera and P. Moreo

Abstract We present an active mechanosensing theory based on an extension of the classical Hill′s model for skeletal muscle behavior where cells actively generate contractile forces and use this information to sense mechanical environment through interaction with material. In this sense, we consider that the cytoskeleton (CSK) of cells is mechanically prestressed. This prestress is generated by molecular motors that generate forces transmitted by the actin network and through adhesion plaques to the material that counterbalances these forces. This model has been numerically implemented to investigate possible mechanosensing mechanisms of how cells interact with materials, such as, durotaxis, tensotaxis and contact guidance. All these effects should be considered for controlling the behaviour of multiple cells working together and interacting with the material in an orchestrated way with a structural mission as the regeneration of a tissue, fundamental aspect in the design of scaffolds for tissue engineering.

J. M. García-Aznar (✉) and J. A. Sanz-Herrera
Group of Structural Mechanics and Materials Modelling,
The Aragón Institute of Engineering Research (I3A),
University of Zaragoza, Zaragoza, Spain
e-mail: jmgaraz@unizar.es

J. M. García-Aznar and J. A. Sanz-Herrera
Centro de Investigación Biomédica en Red en Bioingeniería, Biomateriales y Nanomedicina (CIBER-BBN), Zaragoza, Spain

J. A. Sanz-Herrera
School of Engineering, University of Seville, Seville, Spain
e-mail: jsanz@us.es

P. Moreo
EBERS Medical Technology S.L. Zaragoza, Zaragoza, Spain
e-mail: pmoreo@ebersmedical.com

Stud Mechanobiol Tissue Eng Biomater (2011) 4: 451–462
DOI: 10.1007/8415_2010_13

Published Online: 12 June 2010

1 Introduction

Our body is a complex structure, designed by the blind force of natural selection, and organized in a hierarchical way: cells together with extracellular matrix (ECM) form tissues, and tissues form organs. One key aspect to unravel this complex organization is to understand how cells communicate with their environment to fabricate organized structures [1]. This factor is specially relevant when tissues are injured and regenerative treatments have to be used, specially in the case of tissue engineering. Indeed, tissue engineering requires the combination of cells, growth factors, materials, mechanics and engineering methods to effectively improve or replace functional tissues [2]. To achieve a controlled and reproducible regeneration of tissues under multiple different conditions it is fundamental to understand the cell–material interaction. It is currently accepted that cells integrate information through many different channels. In fact, Fig. 1 shows an overview of known factors influencing cell and tissue organization [3], which may be classified into mechanical, topographical and chemical cues. In this work, we have mainly focused on the mechanical-based mechanisms that regulate cell–material interaction. In the last few years, it has become clear that cells exert contractile forces on the extracellular matrix in which they are anchored in order to explore the mechanical properties of their environment. Several different structures have been proposed as mechanosensors: extracellular matrix molecules, the cytoskeleton, transmembrane proteins, proteins at the membrane–phospholipid interface, elements of the nuclear matrix, chromatin and the lipid bilayer [4]. Currently, there is a strong research activity in this topic with different perspectives: experimental, theoretical and computational.

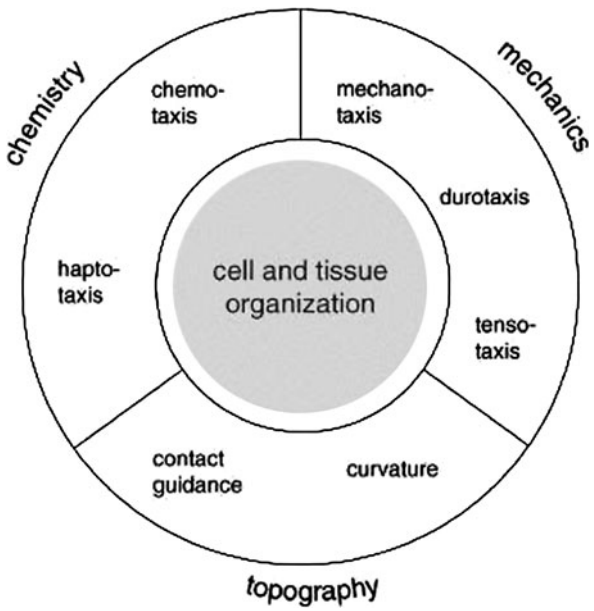

Fig. 1 The organization of cells and tissues results from cell behaviour that integrates different kinds of input signals from the environment [3]

In particular, some experiments have demonstrated that the speed and direction of cell crawling, as well as their rate of proliferation vary with the substrate stiffness and strain: durotaxis (preferential migration towards stiffer areas) [5, 6], tensotaxis (preferential migration towards strained areas) [7]; decrease of cell crawling speed on high stiffness areas [6, 8]; increase of cell proliferation rate on stiffer areas [8], cell migration responds to the substrate curvature they are anchored to, when curvature is comparable to cell size [9, 10].

From a theoretical point of view, significant efforts have been recently addressed to the study of cell mechanosensing mechanism: based on mechanics [11], thermodynamics [12] or the dynamics of focal adhesions [13].

In this work we present a simplified mechanosensing model valid for adherent cells based on the behavior of the mechanically most relevant constituents of the cell in order to predict the preferential cell migration regulated by durotaxis, tensotaxis or topography.

2 Mechanosensing Model

In previous works [14, 15], a constitutive model that describes the mechanical behavior of adherent cells interacting with the material has been proposed. This model, although presenting some limitations, for example, it does not consider the dynamics of focal adhesions nor the cytoskeleton remodeling (CSK), incorporates the main mechanical components of the cell when it is interacting with the material sensing the environment. In fact, this model assumes that the main mechanical contributions of the cell is due to its CSK and the membrane. In particular, this contribution is simplified assuming that the CSK body is composed of a network of fibers where each fiber bundle can be divided into three main components (see Fig. 2).

- The active part of the cell: the actomyosin contractile system (AM). Actin bundles can bind to myosin, a motor protein able to move the bundles relative to each other by hydrolyzing ATP, creating what is known as a stress fibre that is the structure able to generate forces in the cell.
- The actin filaments (E_{act}), is the main component that bears tension and works in conjunction with the actomyosin system.
- The passive component of the rest of the cell (E_{pas}) is due to the contribution of the microtubules and the cell membrane linked to the external ECM through focal adhesions and transmembrane integrins.

This mechanical scheme agrees with the tensegrity hypothesis pioneered introduced by Ingber [16], since tensile forces generated in the actin CSK are balanced by the compression of the microtubules and the external substrate.

In this model it is assumed that focal adhesions are predefined and describe a rigid union between cell and material. Hence, the cell–material communication is mainly controlled by the mechanical equilibrium between the cell and the material,

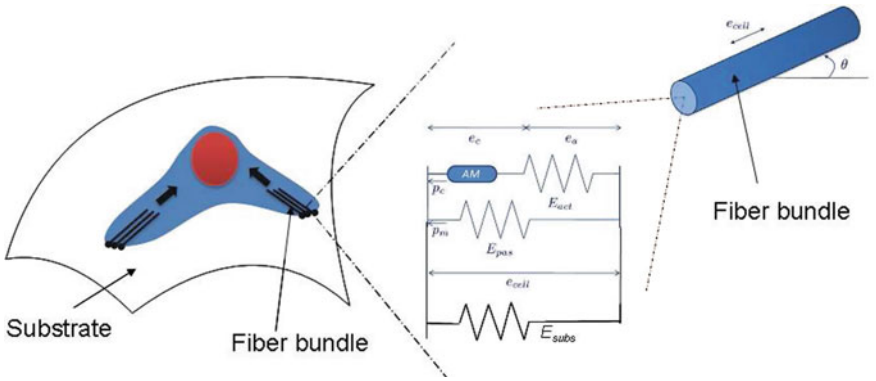

Fig. 2 Mechanical scheme of a cell interacting with the material [15], where filament bundles oriented in the space define the mechanical behaviour of the cell. Each filament bundle is simplified to consider two main components: the passive part E_{pas} and the active part that is also formed by two main elements (the molecular motors and the actin filaments E_{act}). The interaction between the cell and the material is assumed to be predefined and not changes with the time, therefore, the interaction with the material is developed through its mechanical properties E_{subs}

which is defined through its mechanical properties (E_{subs}). Therefore, the mechanical equilibrium of the substrate working together with the cell body can be expressed as the typical equilibrium equation in continuum mechanics:

$$\nabla \cdot (\boldsymbol{\sigma}_{\text{cell}} + \boldsymbol{\sigma}_{\text{ecm}}) + \rho \mathbf{f}_{\text{ext}} = \mathbf{0} \tag{1}$$

where $\boldsymbol{\sigma}_{\text{cell}}$ is the stress tensor that describes the active contractile forces exerted by the adherent cells to the substrate where they are anchored, whereas $\boldsymbol{\sigma}_{\text{ecm}}$ defines the passive mechanical behaviour of the substrate. If, additionally, the substrate is bearing external forces $\mathbf{f}_{\text{ext}}$, these must be in equilibrium with the corresponding tensional state of the substrate and the cell. As a first approach [14], the model assumes a general linear viscoelastic behavior that allows to evaluate $\boldsymbol{\sigma}_{\text{ecm}}$ as a function of the ECM displacements $\mathbf{u}$ and $\dot{\mathbf{u}}$.

The averaged continuum stress tensor $\boldsymbol{\sigma}_{\text{cell}}$ developed by the adherent cells on the material is due to the active contractile forces exerted by each fiber bundle that define the cell CSK (see Fig. 2). In fact, this tensor defines the average forces exerted by the cell through its fiber network using a simple homogenization procedure around all the spatial directions [15]:

$$\boldsymbol{\sigma}^{\text{cell}} = \frac{1}{\pi} \int_{-\frac{\pi}{2}}^{\frac{\pi}{2}} \begin{pmatrix} p_{\text{cell}}(\theta) \cos^2 \theta & \frac{p_{\text{cell}}(\theta)}{2} \sin 2\theta \\ \frac{p_{\text{cell}}(\theta)}{2} \sin 2\theta & p_{\text{cell}}(\theta) \sin^2 \theta \end{pmatrix} d\theta \tag{2}$$

where $p_{\text{cell}}(e_{\text{cell}}, \theta)$ is the the force that each fiber bundle oriented θ in the space, effectively transmits to the substrate, depending on the level of deformation of the cell e_{cell}. Indeed, the definition of $p_{\text{cell}}(e_{\text{cell}}, \theta)$ depends on the mechanical behaviour of the cell and, therefore, depends on its constitutive law. Following the mechanical scheme of the cell proposed in Fig. 2 this force can be defined by the

contribution of the active force generated by the AM contractile machinery p_c and the passive force supported by the passive elements of the cell p_m:

$$p_{\text{cell}}(\theta) = p_c(\theta) + p_m(\theta) \tag{3}$$

Therefore, the passive force supported by the cell can be easily evaluated following:

$$p_m(\theta) = E_{\text{pas}} \cdot e_{\text{cell}}(\theta) \tag{4}$$

However, the active force exerted by the actomyosin molecular motor is defined as function of the relative slide between actin filaments and myosin tail. Here, this relative slide is qualitatively quantified through the macroscopic deformation e_c in the fibre direction θ (see Fig. 2). Additionally, the force that the system is developing depends on how the actin filaments and myosin tail are aligned. In fact, we assume that when both elements are completely aligned the force exerted is maximum and is decreasing when the alignment is different. In this way, we can consider the effect of substrate curvature [15], because this fact regulates how the alignment between actin filaments and myosin tail. Therefore, with this assumption in mind, we propose to evaluate the active force p_c following the curve shown in Fig. 3 as:

$$p_c(\theta) = \begin{cases} \frac{E_{\text{act}}\, p_{\max}(\theta)}{E_{\text{act}} 1 - p_{\max}(\theta)}(e_1 - e_{\text{cell}}(\theta)) & e_1 \le e(\theta) \le e^{\star} \\ \frac{E_{\text{act}}\, p_{\max}(\theta)}{E_{\text{act}} \cdot e_2 - p_{\max}(\theta)}(e_2 - e_{\text{cell}}(\theta)) & e^{\star} < e_{\text{cell}}(\theta) \le e_2 \\ 0 & \text{otherwise} \end{cases} \tag{5}$$

where e_1, e_2 and $e^{\star}$ are parameters model that define the range of validity of the constitutive law for the cell behaviour. In fact, two first are parameters, whereas the last one is defined by other parameters $e^{\star} = p_{\max}(\theta)/E_{\text{act}}$ where $p_{\max}$ is the

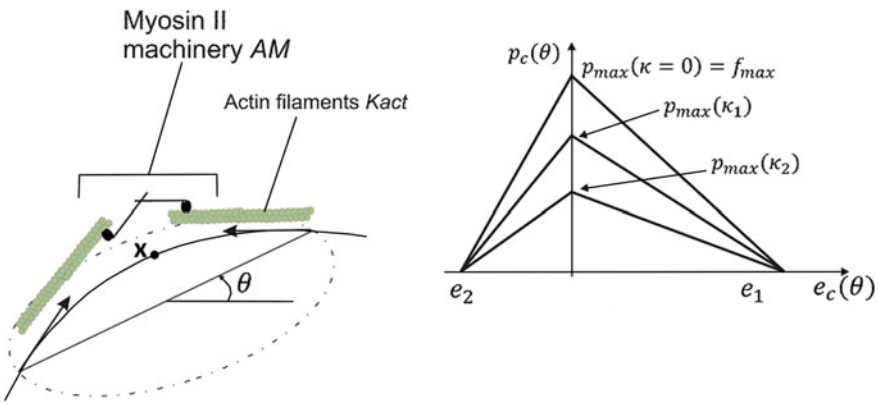

Fig. 3 The contractile force exerted by the actomyosin system depends on the relative alignment $k(\theta)$ and sliding between actin filaments and myosin tail $e_c(\theta)$ [15], where filament bundles oriented in the space through θ

maximal contractile force that the actomyosin system is able to exert depending on the alignment of the actin fibres and the myosin tail with this expression that follows the curve shown in Fig. 3:

$$p_{\max}(\kappa(\theta)) = \begin{cases} f_{\max} \cdot (1 - |\kappa(\theta)|/\alpha) & |\kappa(\theta)| < \alpha \\ 0 & |\kappa(\theta)| \geq \alpha \end{cases} \tag{6}$$

where $f_{\max}$ is determined along the direction of the filament θ, at each material point of the CSK contained at the substrate surface, as shown in Fig. 3, and α is the maximum curvature for which the cell is able to activate the contractile system. κ denotes the directional curvature.

The microscopic deformation e_{cell} in the direction of the fiber bundle θ can be evaluated through the macroscopic CSK deformation tensor $\boldsymbol{\varepsilon}^{\text{cell}}$ as,

$$e_{\text{cell}}(\theta) = \varepsilon_{11}^{\text{cell}} \cos^2\theta + \varepsilon_{22}^{\text{cell}} \sin^2\theta + \varepsilon_{12}^{\text{cell}} \sin 2\theta. \tag{7}$$

Therefore, with this simple model and keeping in mind their main limitations, we are able to estimate or qualitatively evaluate the mechanical interaction between cell and material, sensing the mechanical environment.

3 Some Numerical Examples

This constitutive model for the mechanosensing mechanism proposed previously has been implemented numerically using the Finite Element Method (FEM) to model the mechanical behaviour of the cell body interacting with a substrate. This implementation has been developed in the FE commercial code ABAQUS through a user subroutine [17]. Two different geometrical configurations of the substrate have been analyzed: planar and curved. In the first case, two different mechanical conditions have been simulated when the substrate presents an anisotropic behaviour and when the substrate is loaded with different forces on each direction. Model parameters were obtained from the literature for fibroblasts such that $E_{\text{pas}}/E_{\text{act}} = 0.015, -f_{\max}/(E_{\text{act}} e_1) = 0.01, -e_1/e_2 = 0.4$ [15].

3.1 Anisotropic and Planar Substrate

Substrate is considered to be a flat fibered orthotropic material showing different elasticity ratios E_2/E_1 along the two perpendicular axis. Figure 4 shows the principal stresses of $\boldsymbol{\sigma}_{\text{cell}}$ in a Lame's ellipsoid fashion. Interestingly, $\boldsymbol{\sigma}_{\text{cell}}$ aligns with the stiffer axis which is a key experimentally observed issue termed durotaxis as previously discussed. On the other hand, we can observe the force exerted by the cell machinery, $\boldsymbol{\sigma}_c$, along the different axis versus their rigidity in Fig. 5. We can observe that the cell generates a higher stress along the axis of

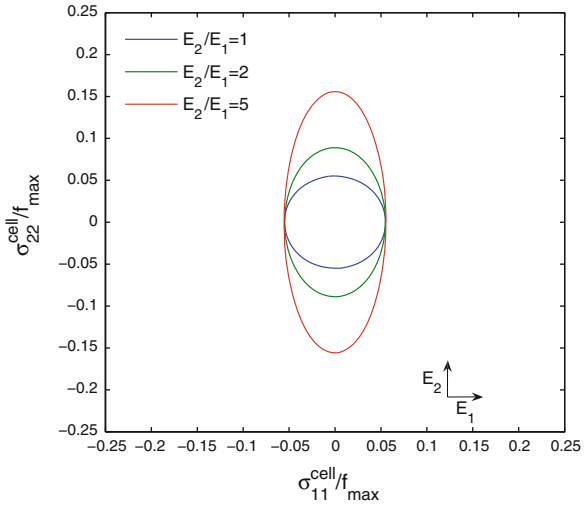

Fig. 4 Principal net stresses of the cell $\boldsymbol{\sigma}_{\text{cell}}$ in a Lame's ellipsoid, for different elasticity ratios E_2/E_1 in equilibrium with a flat fibered orthotropic material

maximum stiffness, i.e., direction 2. A fraction of the force exerted by the myosin machinery of the cell is applied to deform the microtubulus network of the cell cytoskeleton. Therefore, since the system must be balanced by the substrate (see additionally Fig. 2) $\boldsymbol{\sigma}_c$ are typically larger than $\boldsymbol{\sigma}_{\text{cell}}$ in the absence of external forces. Figure 5 suggests that the cell may preferentially move along the axis of maximum rigidity where the cell locomotory system exerts a higher force. This has been a consequence of our simple proposed model which is in connection with lab results. Moreover, note that since the orthotropy axis are oriented along the perpendicular axis, these are the principal directions for both $\boldsymbol{\sigma}_{\text{cell}}$ and $\boldsymbol{\sigma}_c$ tensors.

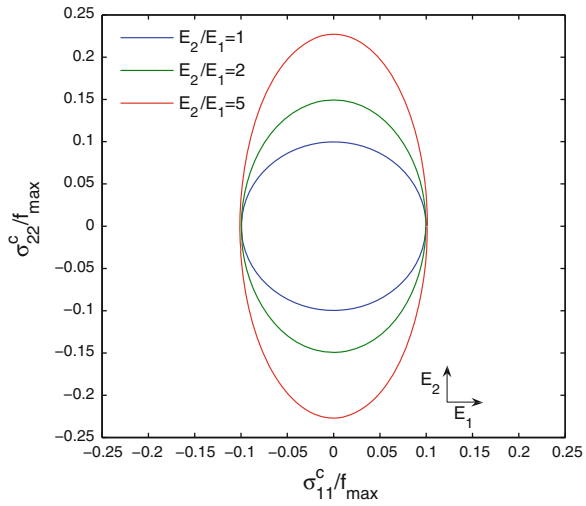

Fig. 5 Principal stresses exerted by the cell active machinery $\boldsymbol{\sigma}_c$ in a Lame's ellipsoid, for different elasticity ratios E_2/E_1 in equilibrium with a flat fibered orthotropic material

3.2 Planar Substrate Under Directional Forces

In this section, we consider an external applied force to the cell–substrate system considering an isotropic substrate (see Fig. 2). The nature of this force may represent an imposed substrate stress (deformation) to experimentally validate the phenomenon of tensotaxis, previously introduced. This effect is simulated with our proposed model. Figure 6 shows the principal stresses of $\boldsymbol{\sigma}_{\text{cell}}$ tensor for different values of an external force along the direction 1. We can observe a clear alignment of $\boldsymbol{\sigma}_{\text{cell}}$ along the direction of the applied force even for low values of the force. Additionally, the stress $\boldsymbol{\sigma}_c$ exerted by the cell aligns as well along the axis of the external force according to Fig. 7, although less abruptly than $\boldsymbol{\sigma}_{\text{cell}}$. Therefore, we may predict a movement of the cell along the axis of the applied force, or equivalently, along the axis where the cell senses the stress and generates higher contractile forces accordingly through the active machinery, i.e., tensotaxis, in agreement with the experience.

3.3 Curved Substrate

The details of this simulation are shown in a previous work [15]. Here, we focus on showing the most relevant results in relation with the main aim of this paper. In this example, a cell anchored to the surface of a hyperbolic paraboloid substrate is computationally simulated.

Cell is centered on the horse-chair point of the surface, where maximal curvatures are found. We simulate a case where the curvature in the direction 1 is higher than in the direction 2. In fact, we consider $a/b = 0.5$ and $a^2/r_0 = 0.0288$

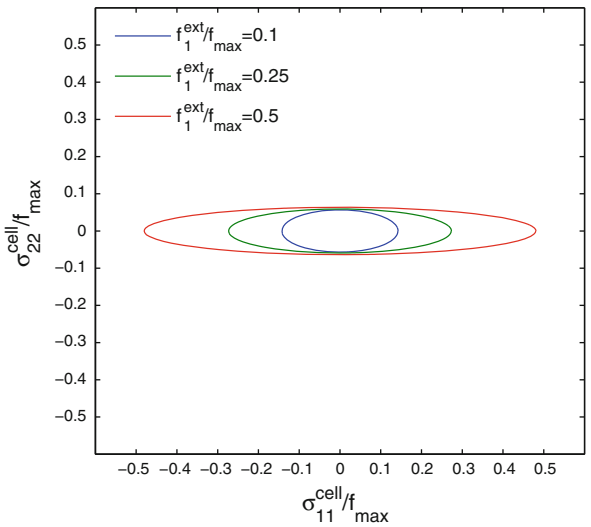

Fig. 6 Principal net stresses of the cell $\boldsymbol{\sigma}_{\text{cell}}$ in a Lame's ellipsoid, under the effect of different applied external forces considering an isotropic substrate

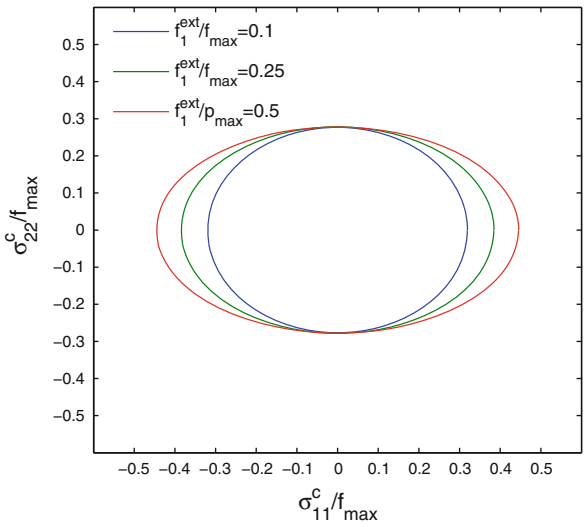

Fig. 7 Principal stresses exerted by the cell active machinery $\boldsymbol{\sigma}_c$ in a Lame's ellipsoid, under the effect of different applied external forces considering an isotropic substrate

being a and b the parameters that define the specific shape of the hyperbolic paraboloid of the substrate, and r_0 is the radius of the cell. In order to simplify the model a dimensionless approach has been considered, where $E_{\text{subs}}/E_{\text{act}} = 1$ and $v = 0.2$. Moreover, cells are linked with the material through focal adhesions and transmembrane integrins that, as a first approach, are assumed as rigid.

Given the shape of the hyperbolic paraboloid, we have to keep in mind the directional curvature decreases as getting farther from the cell centre, which causes a non-homogeneous stress distribution on the cell body as can be seen in Fig. 8. These figures show the net force exerted by the cell along its cytoskeleton at directions 1 and 2. In fact, cell forces are higher in the direction 2 in comparison with 1, meaning that the cell would adapt its CSK towards this direction regulating its movement in this direction of minimal curvature. Moreover, it can be seen that stresses become larger at peripheral locations of the cell, because as was previously explained curvature decreases as getting farther from the cell centre.

In this work, the main assumption is that we considered a nonlinear membrane with null bending rigidity. However, recently Bitton and Safran [18] have developed a theoretical model to understand how cells respond to curvature, where the bending stiffness was not underestimated.

4 Some Conclusions

The mechanism of how cells sense the environment is fundamental in many processes of tissue growth, development, maintenance and regeneration. This mechanism is regulated by a high number of factors and interactions that require a robust control for an effective functionality. One of the key aspects in these

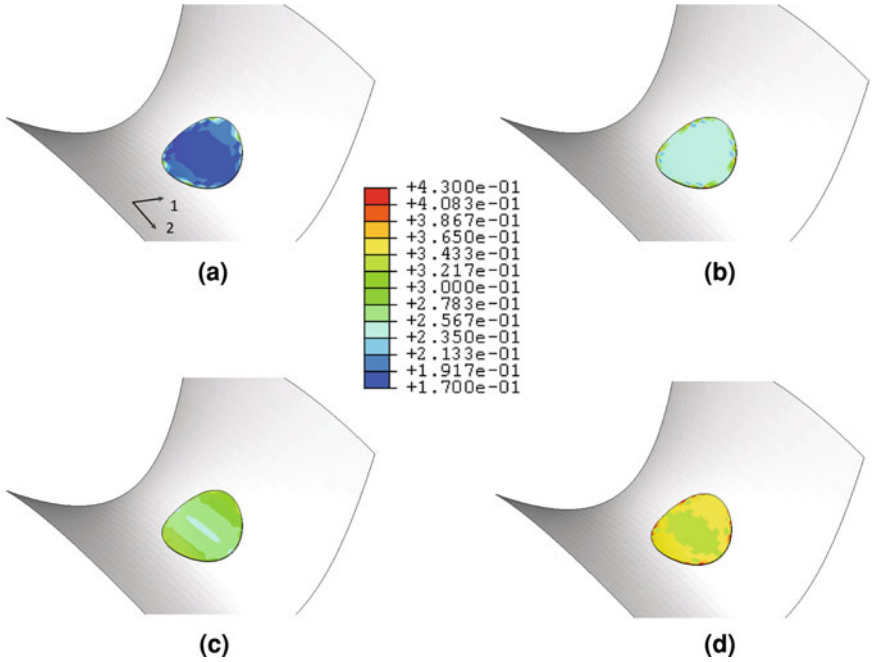

Fig. 8 Net and contractile stresses, at principal directions of curvature, exerted by a cell anchored to the surface of a hyperbolic paraboloid: **a** σ_1^{cell}/f_{max}, **b** σ_2^{cell}/f_{max}, **c** σ_1^{c}/f_{max}, **d** σ_2^{c}/f_{max} [15]

sensing mechanisms is the cell–material communication, where in particular the mechanical interaction between the cell and the material are fundamental. The cell adheres to the material through focal adhesions that are located along their external surface. The focal adhesions are as well connected to the cytoskeleton through the actin fibers that in coordination with the actomyosin contractile system develop contractile forces in the internal body of the cell. Hence, in this way, the cells are able to sense the mechanical environment and respond to it by remodeling their focal adhesions and their cytoskeleton. This fact implies, therefore, changes in the forces developed by the cells on the substrate in value and orientation, closing an interactive feedback loop between cell and material (see Fig. 9). In this work, we have presented a model only focused on the modelling of the mechanosensing

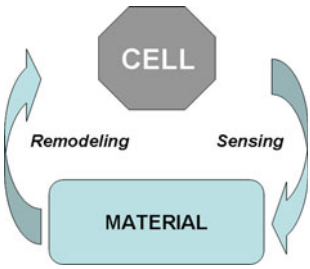

Fig. 9 Simplified scheme that shows the cell–material feedback loop through which both communicate via mechanical interactions: cell contraction (mechanosensing mechanism) and consequently cell response (cytoskeletal and focal adhesions remodeling)

mechanism of the cell, based on previous works by the same authors [14, 15]. To evaluate the predictive potential of this model we have modified the mechanical conditions of the material with which the cell is interacting. Therefore, we have considered the effect of three different phenomena known in the literature: durotaxis, tensotaxis and topography effect. In the three cases, the constitutive model proposed predicts an orientation of the mechanical forces that cells exert on the material, showing clear tendencies.

- Forces that cells develop increase with highest `stiffness` of the substrate, orienting the actin stress fibers in this direction.
- External mechanical `forces` also increases the forces that cells develop.
- Substrate `curvature` determines the stress distribution in the cell and may regulate the cell polarization for cell migration in the direction of minimal curvature.

Therefore, the coordinated mechanical interaction between cell and material (with adequate biochemical conditions) may help to define a local favorable environment for tissue regeneration, allowing to control the preferential movement of cells, its regulated proliferation and the controlled differentiation. One of the most relevant challenges in tissue engineering is the mechanical design of tissue replacements (scaffolds) with sufficient mechanical integrity to bear loads during tissue regeneration and that as well allows the creation of this favorable mechanical environment.

Acknowledgements This work has been supported by the Ministerio de Ciencia e Innovación of Spain (DPI2009-14115-C03-01) and the Instituto de Salud Carlos III (CIBER initiative).

References

1. Buxboim, A., Ivanovska, I.L., Discher. D.E.: Matrix elasticity, cytoskeletal forces and physics of the nucleus: how deeply do cells 'feel' outside and in? J. Cell Sci. **123**(Pt 3), 297–308 (2010)
2. Discher, D.E., Mooney, D.J., Zandstra, P.W.: Growth factors, matrices, and forces combine and control stem cells. Science **324** (5935), 1673–1677 (2009)
3. Schwarz. U.S., Bischofs. I.B.: Physical determinants of cell organization in soft media. Med. Eng. Phys. **27**, 763–772 (2005)
4. Janmey, P.A., McCulloch, C.A.: Cell mechanics: integrating cell responses to mechanical stimuli. Annu. Rev. Biomed. Eng. **9**, 1–34 (2007)
5. Wong, J.Y., Velasco, A., Rajagopalan, P., Pham, Q.: Directed movement of vascular smooth muscle cells on gradient-compliant hydrogels. Langmuir **19**, 1908–1913 (2003)
6. Lo, C., Wang, H., Dembo, M., Wang, Y.: Cell movement is guided by the rigidity of the substrate. Biophys. J. **79**, 144–152 (2000)
7. Beloussov, L.V., Louchinskaia, N.N., Stein, A.A.: Tension-dependent collective cell movements in the early gastrula ectoderm of xenopus laevis embryos. Dev. Genes Evol. **210**, 92–104 (2000)
8. Ghosh, K., Pan, Z., Guan, E, et al.: Cell adaptation to a physiologically relevant ecm mimic with different viscoelastic properties. Biomaterials **28**, 671–679 (2007)

9. Smeal, R.M., Rabbitt, R., Biran, R., Tresco, P.A.: Substrate curvature influences the direction of nerve outgrowth. Ann. Biomed. Eng. **33**, 376–382 (2005)
10. James, J., Goluch, E.D., Hu, H., Liu, C., Mrksich, M.: Subcellular curvature at the perimeter of micropatterned cells influences lamellipodial distribution and cell polarity. Cell. Mot. Cytos. **65**, 841–852 (2008)
11. Bischofs, I.B., Schwarz, U.S.: Cell organization in soft media due to active mechanosensing. Proc. Natl. Acad. Sci. U.S.A. **100**, 9274–9279 (2003)
12. Nicolas, A., Geiger, B., Safran, S.A.: Cell mechanosensitivity controls the anisotropy of focal adhesions. Proc. Natl. Acad. Sci. U.S.A. **101**, 12520–12525 (2004)
13. Schwarz, U.S., Erdmann, T., Bischofs, I.B.: Focal adhesions as mechanosensors: the two-spring model. Biosystems **83**, 225–232 (2006)
14. Moreo, P., Garcia-Aznar, J.M., Doblare, M. Modeling mechanosensing and its effect on the migration and proliferation of adherent cells. Acta Biomater. **4**, 613–621 (2008)
15. Sanz-Herrera, J.A., Moreo, P., Garcia-Aznar, J.M., Doblare, M.: On the effect of substrate curvature on cell mechanics. Biomaterials **30**(34), 6674–6686 (2009)
16. Ingber, D.E.: Tensegrity I. Cell structure and hierarchical systems biology. J. Cell Sci. **116**, 1157–1173 (2003)
17. Hibbit, D., Karlsson, B., Sorensen, P.: Abaqus User's Manual v.6.2. HKS Inc., Pawtucket, RI (2001)
18. Biton, Y.Y., Safran, S.A.: The cellular response to curvature-induced stress. Phys. Biol. **6**(4) 046010 (2009)

Part IV
Mechanobiology in Cancer

Structure–Mechanical Property Changes in Nucleus arising from Breast Cancer

Qingsen Li and Chwee Teck Lim

Abstract Nuclear mechanics has attracted much attention in recent years, not only because of its functional role in cell biology, but also its structural role in cell mechanics and mechanotransduction. However, little has been done so far to investigate the nuclear mechanics in the context of cancer cells. Here, nanoindentation using an atomic force microscope was used to characterize the elasticity of isolated nuclei of benign (MCF-10A) and malignant (MCF-7) human breast epithelial cells. Isolated nuclei of malignant cells (MCF-7) were found to have an apparent Young's modulus that is half of the non-malignant cells (MCF-10A). The underlying lamina (lamin A/C) structure of both cell types was also investigated by confocal microscopy to understand its possible contribution to the mechanical property change of nucleus. This study can potentially provide better insights into metastasis, where a possible contributing factor is the softening of cancer cells arising from a more deformable nucleus.

1 Introduction

Nucleus is known to be one of the most important organelles inside the cell as it contains the 'secret of life' (DNA) and is a site of major metabolic activities, including DNA replication, gene transcription, RNA processing and ribosome

Q. Li and C. T. Lim (✉)
MechanoBiology Institute, National University of Singapore,
Singapore, Singapore
e-mail: ctlim@nus.edu.sg

C. T. Lim
Division of Bioengineering and Department of Mechanical Engineering,
National University of Singapore, Singapore, Singapore

Stud Mechanobiol Tissue Eng Biomater (2011) 4: 465–475
DOI: 10.1007/8415_2010_19

Published Online: 2 December 2010

subunit maturation and assembly. More than its functional role, nucleus has also gradually been found to be important as a structural component inside the cell. Consequently, nuclear mechanics has attracted more and more interest in recent years [10, 20] as nucleus has been found to play an important role in contributing to whole cell mechanical behavior [5]. Moreover, experimental findings suggest that nucleus is directly involved in mechanotransduction [10] as evidences have already showed that there are physical connections from the surface adhesion molecule (integrin receptor) to the cytoskeleton (actin filament) and finally the nucleus [26]. This physical connection may serve as a channel to transmit the mechanical signals received by the adhesion molecule, from outside of the cell directly to the nucleus and regulate gene expression. Therefore, any change in the nuclear structure can cause impaired nuclear mechanics and hence, alter the mechanotransduction pathway leading to certain diseases. One typical example is laminpathesis, which is a group of diseases caused by the mutation of the nuclear lamin A/C gene leading to impaired mechanical integrity of nucleus. Thus, understanding nuclear mechanics and its link to overall cell mechanics, will be a first step in revealing the role of nucleus in mechanotransduction and the pathology of certain diseases related to the malfunction of nucleus.

Nucleus is separated from cytoplasm by a nuclear envelope. As shown in Fig. 1 [37], the nuclear envelope consists of an inner nuclear membrane (INM), an outer nuclear membrane (ONM, an extension of rough endoplasmic reticulum (ER)) and nuclear lamina [34]. INM and ONM are joined at the nuclear pore complexes (NPC), which allow nuclear–cytoplasmic transport. The nuclear lamina, which is the major

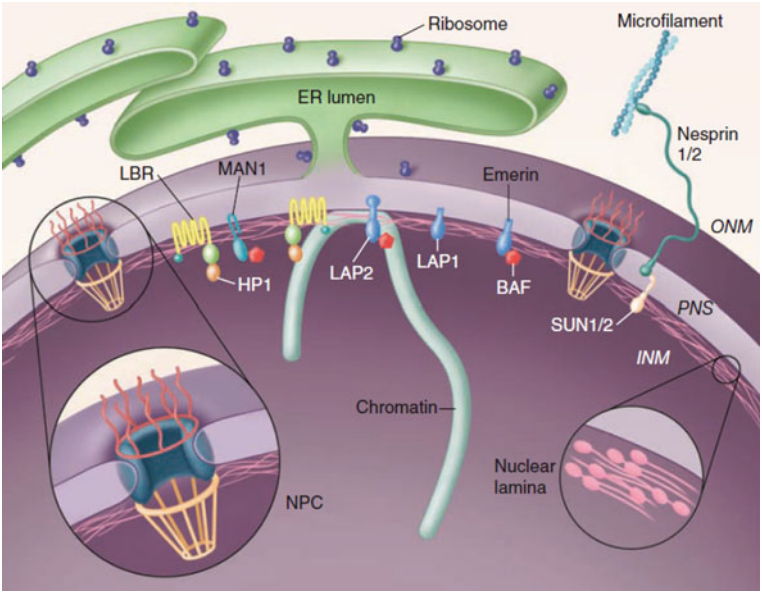

Fig. 1 Schematic diagram of nuclear envelope organization [37]

structural component of nuclear envelope, is a dense network of lamins plus lamin-associated proteins lying beneath the INM. Lamins are also found to exist inside the nucleus in the form of stable nucleoplasmic structures [14, 17, 18, 29].

Lamins are part of the intermediate filament (IF) gene family and are thought to be the evolutionary progenitors of IF proteins. The IF gene super family comprises five groups with about 60 members. Group I–IV are cytoplasmic IF, and lamins belong to the group V IF family. Lamins are classified into types A and B according to their difference in biochemical properties, expression pattern and behavior during mitosis [38]. A-type lamins, which include lamin A and C, are products of alternative splicing from the *LMNA* gene, and B-type lamins are encoded by two separate genes, *LMNB1* and *LMNB2*. Type B lamins are present in all mammalian cells as they are essential for cell viability, but type A lamins are developmentally regulated. Type A lamins are absent in human embryonic stem cells, but are expressed only after cells differentiate and generally increased during terminal differentiation and grow arrest [34].

Lamins are very important in their contribution to nuclear structure. They not only determine nuclear integrity, but are also involved in numerous nuclear functions. Especially, A-type lamins play a major role in maintenance of nuclear shape [11, 21, 36], stability [2, 9, 22] and structural integrity [2, 21, 37]. Moreover, lamins regulate and support protein complexes involved in gene expression, nuclear positioning [27], DNA replication, transcription and repair [33], and aging [36].

In the context of cancer, the nuclear lamina is involved in many nuclear activities which are implicated in tumor formation including transcriptional activation, heterochromatin organization, senescence and apoptosis [30]. It has been found that there are dramatic changes in nuclear architecture including nuclear size and shape, numbers and sizes of nucleoli, and chromatin texture, during malignant transformation [47]. In fact, the physical irregularity of the nucleus has been observed for a long time as a common feature for many types of cancer cells. Nuclear morphology analysis has been used to detect certain types of cancer since the nineteenth century [47]. Deviation of the nuclear lamins and their associated proteins are thought to be an additional event involved in malignant transformation and tumor progression, which can be a potential novel target for anti-cancer drug development [34].

The absence or low levels of type A lamins are often observed in many types of human hematological malignancies. For non-hematological malignancies, the main changes are aberrant localization and reduction in expression of lamins A/C, which are frequently correlated with aggressiveness of cancer, proliferation rate and differentiation state. Lamin A/C has been found to be reduced in some skin cancers (basal cell and squamous cell) [31, 44], gastrointestinal tract neoplasms including adenocarcinoma of stomach and colon, lung cancer [3, 19], testicular germ cell tumors [25] and cancerous prostate tissues [6]. It is also reduced in breast cancer [30]. However, they are not sufficiently specific to be used in histopathological diagnosis [1]. Based on these observations, we hypothesize that there is a corresponding change in mechanical properties of nuclei of cancer cells when compared to normal cells.

Another common feature in cancer cell nuclei is their enlarged size compared to those of normal cell [28]. Studies have shown that the nucleus plays an import role in the mechanical properties of the whole cell [5, 12, 47]. While in the context of cancer metastasis, cancer cells migrate and traverse in blood vessels and small capillaries, the whole cell and its nucleus undergoes extremely large deformation, as shown in an in vivo study [46] and also in our microfluidic study which mimics the process of cancer cells traversing small capillaries [16]. Therefore for cancer cells, their enlarged and structurally modified nuclei could play a more significant role in contribution to their mechanical behavior and subsequently the outcome of metastasis.

Therefore it is important to characterize the mechanical properties of cancer cell nucleus, as it will contribute not only towards understanding of the structural changes of nuclei in malignant transformation and subsequent cancer detection, but also shed light on their contribution to cell mechanics and its role in cancer metastasis.

Mechanical properties of nuclei of different cell types have been characterized using different techniques (for review please refer [45]), including micropipette aspiration [8, 12, 15, 32, 35], atomic force microscopy (AFM) indentation [8, 42], particle nanotracking [23, 41], cell stretcher [21, 22], custom-made microplate [5, 40], as well as cellular compression device [4]. Computational modeling such as finite element modeling was also utilized to investigate the nuclear mechanical behavior [42, 43]. Using micropipette aspiration, Guilak et al. [15] showed that isolated nuclei of articular chondrocytes behave as viscoelastic solid materials with an equilibrium Young's modulus in the order of 1 kPa, which is 3–4 times stiffer than the cytoplasm. Deguchi et al. [12] found the elastic modulus of endothelial nuclei to be 0.42 ± 0.12 kPa and it increases to 0.62 ± 0.15 kPa after exposure to shear flow. Using microplate compression combined with finite element model analysis, Caille et al. [5] found the elastic modulus of endothelial nucleus to be on the order of 5, and 8 kPa for isolated nuclei, which is about ten times stiffer than the cytoplasm. Using micropipette aspiration and AFM, Dahl et al. characterized the apparent elastic modulus of isolated nuclei to be 2–8 kPa.

However, little has been done to study nuclear mechanics in the context of cancer. Here, we characterized the mechanical properties of breast cancer cell nuclei, investigated their underlying lamina structure and compared with that of normal breast epithelial cells. The possible contribution of nucleus to cell mechanics was also discussed.

2 Materials and Methods

MCF-7 (human breast adenocarcinoma cell line) and MCF-10A (non-tumorigenic epithelial cell line) cells were maintained at 37°C in a 5% CO_2 incubator (Sanyo, Japan). Cells harvested from the subculture were seeded and kept in a six-well microplate which was placed in the incubator for 2–3 days until confluent before

nuclear isolation. The medium was changed 1 day after seeding to clear any dead cells.

Nuclear isolation (adapted from [5, 40]):

1. Confluent MCF-10A (or MCF-7) cells grown in six-well chamber were rinsed once with PBS.
2. Cells were treated for 5 min with 1 ml of a 0.01% Igepal CA-630 (a non-ionic detergent, Sigma), 1% citric acid solution in water. Nuclei were expelled while the cytomatrix remained adherent.
3. The medium was collected, mixed with 5 ml PBS, and centrifuged at 300*g* for 5 min.
4. The nuclei-rich pellet was resuspended in PBS, 60–100 µl suspended nuclei solution was dropped onto a 12-mm coverslip for 1 h and the nuclei would stick to the coverslip.

For fluorescence staining, 12-mm coverslips with isolated nucleus seeded on them were fixed by cold methanol for 10 min at −20°C. After washing the sample with PBS, the samples were incubated with Image-iT FX signal enhancer (Invitrogen) for 30 min at room temperature, and followed by incubation with 10% goat serum for 1 h at room temperature. Then samples were incubated with primary antibody rabbit polyclonal lamin A/C (H-110) (Santa Cruz, USA) for 1 h at room temperature, and followed by incubation with secondary antibody Alexa Fluor 488 goat anti-rabbit IgG for 1 h at room temperature. Finally, samples were labeled with 5 µg/ml DAPI (Sigma-Aldrich, USA) for 5 min. Fluorescence images were taken using a confocal microscope (Nikon TE2000, Japan).

For indentation studies, isolated nuclei were seeded onto the 12-mm coverslip and incubated at room temperature for 1 h for the nuclei to stick to the substrate. For AFM indentation, the same protocol as for indentation on cells was used. For details, please refer to [24]. In brief, a Nanoscope IV multimode AFM with a picoforce scanner (Digital Instruments Inc., USA) was used to carry out the experiments. A modified silicon nitride AFM cantilever (NovaScan, USA) having a spring constant of 0.01 N/m with a 4.5 µm diameter polystyrene bead adhered to the tip was used to indent the nucleus. During the experiment, the glass coverslip was mounted on the AFM stage and the nuclei were kept in PBS using a standard fluid cell (Digital Instruments Inc., USA). Indentation was carried out at the nuclei centre using different loading rates from 0.03 to 1 Hz. The ramp size used in this study was 3 µm [7] and an indentation force of 200 pN was applied during the tests in order to ensure that a small deformation was exerted on the nuclei and minimize any substrate contributions. The Young's modulus was subsequently determined using Hertz's contact model [7] (for details, please refer to [24]):

$$F = \frac{4}{3}\frac{E}{(1-\nu^2)}\sqrt{R\delta^3} \tag{1}$$

where F is the indentation force, E the Young's modulus to be determined, v the Poisson's ratio, R the radius of the spherical bead, and δ indentation depth. The cell was assumed incompressible and a Poisson's ratio of 0.5 was used [7].

3 Results and Discussion

3.1 Consistency of AFM Indentation on Isolated Nucleus

To test the consistency of our AFM indentation on nucleus, we repeatedly indented the same location of the nucleus and see whether there was any change in the force–indentation depth curve. Figure 2 shows that the force–indentation depth curves for both MCF-10A and MCF-7 highly overlap with each other after repeatedly indentation at 0.3 Hz for more than 15 times. These results suggest that our experiment is highly reproducible and that there is no permanent damage or plastic deformations induced by the AFM probe. Also these results suggest that the nucleus behaves as an elastic material within the condition of our test, which is consistent with other studies [15]. Interestingly, the reproducibility was still maintained even when we used very large force (0.8 nN indetation force with about 1 μm indentation depth, data not shown). However, the current Hertz's model that we had used will not apply to large deformation (the large deformation region deviated from Hertz's model prediction). So we chose to extract the apparent elastic modulus based on the region below 200 pN.

As shown in Fig. 3 repeated indentation using increasing force again confirmed the reproducibility of AFM indentation as there is no hysteresis in force–depth curves. We can also see that isolated nuclei of MCF-7 appear softer than that of MCF-10A, as less deformation of the formers compared with the laters using the same indentation force.

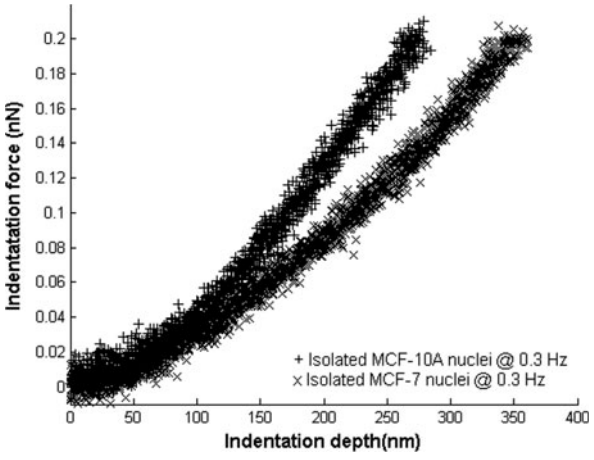

Fig. 2 Indentation force versus depth curves of repeated indentation ($n = 20$) at the same location of isolated nuclei of both MCF10A and MCF-7 cells using the same force (0.2 nN)

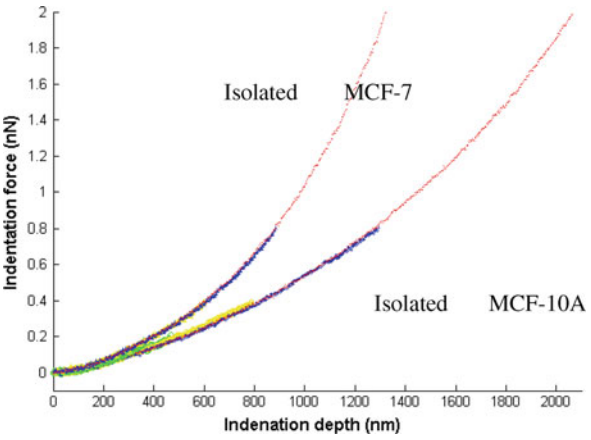

Fig. 3 Indentation force versus depth curves of repeated indentation ($n = 20$) at the same location of an isolated MCF-7 nucleus using increasing force (0.2, 0.4, 0.8, 2 nN)

3.2 Apparent Young's Modulus of Isolated Nuclei of MCF-7 and MCF-10A

Based on the above analysis, we extracted the apparent Young's modulus and compare between MCF-10A and MCF-7 nuclei. As shown in Fig. 4, we can see that at different loading rates, nuclei of MCF-10A appear twice stiffer than that of MCF-7. Also, apparent Young's modulus increased with loading rate due to the viscoelastic nature of nucleus, which is also reported in other studies [8, 15]. The distinct difference in deformability of isolated nucleus of MCF-10A and MCF-7 can potentially serve as a biomarker to detect cancer cells from normal cells.

3.3 Lamin A/C Structure of Nucleus

To understand the possible reason underlying the difference in the deformability of nuclei of MCF-10A and MCF-7 cells, we stained and investigated the lamin A/C

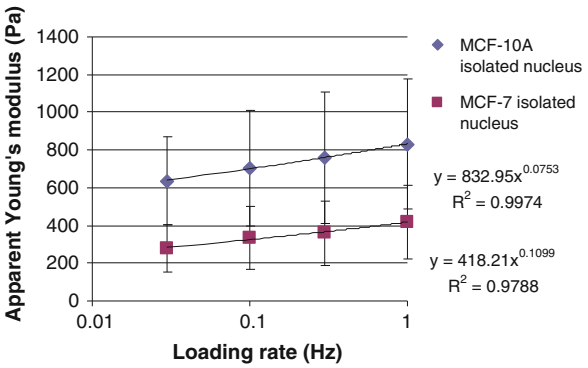

Fig. 4 Comparison between apparent Young's modulus of isolated nucleus of MCF-10A and MCF-7

structure of isolated nucleus of both types of cells. Lamin A/C was chosen as studies have shown that they play an important role in determining nuclear mechanics [21]. Aberrant localization and reduction in expression of lamins A/C were observed in many malignancies [34]. Many studies have reported that there is reduction in lamin A/C expression during malignant transformation of different types of cells [3, 6, 19, 25, 31, 44], including breast cancer [30]. All these reasons make lamin A/C a most promising target structure which might contribute to the difference that we have observed between the stiffness of isolated nuclei of MCF-10A and MCF-7 cells. As shown in Fig. 5, lamin A/C is uniformly distributed at the peripheral region of isolated nucleus of a MCF-10A cell, while this is not the case for the MCF-7 cell. We have also analyzed the intensity profile of one typical section of the fluorescence image of the nucleus. In the isolated nucleus of MCF-10A, there is high concentration of lamin A/C at the peripheral region than that of the interior. While in the isolated nucleus of MCF-7, the level of intensity is lower compared with that of MCF-10A and it is not highly concentrated at the peripheral of the nucleus. Generally, lamin A/C of isolated nucleus of MCF-10A has higher intensity and higher concentration at the peripheral region than that of MCF-7, which might contribute to their difference in stiffness.

However, another possible reason is the chromatin inside the nucleus as studies have shown that it is a force-bearing element inside the nucleus [8]. As nucleus of MCF-7 cell is generally larger than that of MCF-10A cell, the concentration of chromatin is less in MCF-7 compared to MCF-10A if we assume the same amount of chromatin material, and this might make MCF-7 nucleus more compliant. Moreover, the internal structural change including chromatin and associated

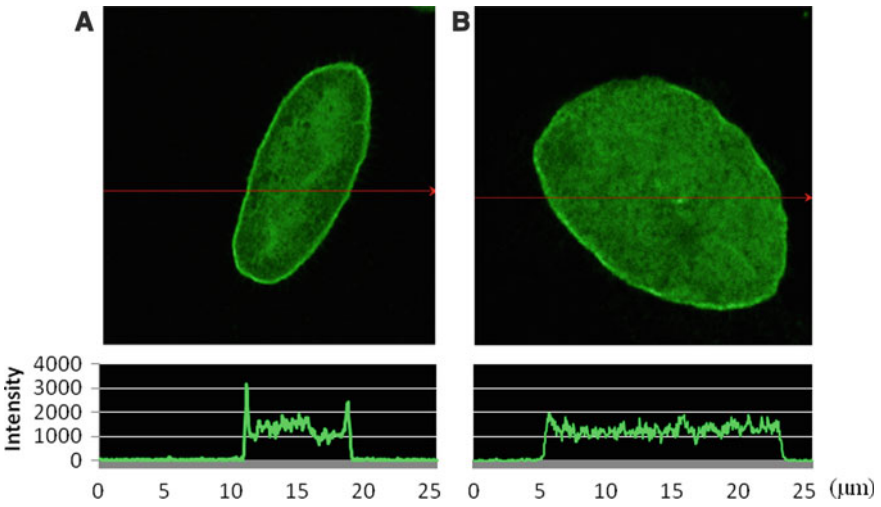

Fig. 5 Lamin A/C structures of isolated nuclei of (**a**) MCF-10A and (**b**) MCF-7 cells (intensity profile corresponds to the red sectioning line of fluorescence image)

proteins during malignant transformation might also contribute to the observed difference in deformability, which needs further studies.

4 Concluding Remarks

In this study, the Young's moduli of isolated nuclei of cancer cells were characterized using AFM indentation based on previous established protocol. We reported that there is a decrease in elasticity of isolated nuclei of malignant breast cells compared with that of non-malignant ones. Considering the fact that absence or low levels of type A lamins are often observed in many types of human hematological malignancies, the related decrease of nuclear stiffness can be quite promising as a distinct feature of malignancy. Our study showed that characterizing the mechanical properties of cancer nucleus using AFM is a one potential method to distinguish malignant breast cells from nonmalignant ones. A method established by Beale in 1860 and used as a "gold standard" for detecting cancer is to examine unstained cell structure and to observe any variations in nuclear size and shape [47]. In our study, any change in mechanical properties of the nucleus can now be quantitatively and more accurately determined. This may possibly aid in the detection of cancer and thus, forms the basis for the development of new diagnostic tools.

Finally, more detailed information on the mechanical properties of the nucleus is needed to understand its role in mechanotransduction and in the overall mechanical behavior of cancer cells, which may in turn provide further insights in the process of malignant transformation and metastasis.

References

1. Bosman, F.T.: The nuclear matrix in pathology. Virchows Arch. **435**(4), 391–399 (1999)
2. Broers, J.L., Kuijpers, H.J. et al.: Both lamin A and lamin C mutations cause lamina instability as well as loss of internal nuclear lamin organization. Exp. Cell Res. **304**(2), 582–592 (2005)
3. Broers, J.L., Raymond, Y. et al.: Nuclear A-type lamins are differentially expressed in human lung cancer subtypes. Am. J. Pathol. **143**(1), 211–220 (1993)
4. Broers, J.L.V., Peeters, E.A.G. et al.: Decreased mechanical stiffness in LMNA−/− cells is caused by defective nucleo-cytoskeletal integrity: implications for the development of laminopathies. Hum. Mol. Genet. **13**(21), 2567–2580 (2004)
5. Caille, N., Thoumine, O. et al.: Contribution of the nucleus to the mechanical properties of endothelial cells. J. Biomech. **35**(2), 177–187 (2002)
6. Coradeghini, R., Barboro, P. et al.: Differential expression of nuclear lamins in normal and cancerous prostate tissues. Oncol. Rep. **15**(3), 609–613 (2006)
7. Costa, K.D.: Single-cell elastography: probing for disease with the atomic force microscope. Dis. Markers **19**(2–3), 139–154 (2003)
8. Dahl, K.N., Engler, A.J. et al.: Power–law rheology of isolated nuclei with deformation mapping of nuclear substructures. Biophys. J. **89**(4), 2855–2864 (2005)

9. Dahl, K.N., Kahn, S.M. et al.: The nuclear envelope lamina network has elasticity and a compressibility limit suggestive of a molecular shock absorber. J. Cell Sci. **117**(Pt 20), 4779–4786 (2004)
10. Dahl, K.N., Ribeiro, A.J. et al.: Nuclear shape, mechanics, and mechanotransduction. Circ. Res. **102**(11), 1307–1318 (2008)
11. Dahl, K.N., Scaffidi, P., et al.: Distinct structural and mechanical properties of the nuclear lamina in Hutchinson–Gilford progeria syndrome. Proc. Natl. Acad. Sci. USA **103**(27), 10271–10276 (2006)
12. Deguchi, S., Maeda, K., et al.: Flow-induced hardening of endothelial nucleus as an intracellular stress-bearing organelle. J. Biomech. **38**(9), 1751–1759 (2005)
13. Dong, C., Skalak, R., et al.: Cytoplasmic rheology of passive neutrophils. Biorheology **28**(6), 557–567 (1991)
14. Goldman, R.D., Gruenbaum, Y., et al.: (2002) Nuclear lamins: building blocks of nuclear architecture. Genes Dev. **16**(5), 533–547.
15. Guilak, F., Tedrow, J.R., et al. Viscoelastic properties of the cell nucleus. Biochem. Biophys. Res. Commun. **269**(3), 781–786 (2000)
16. Hou, H.W., Li, Q.S., et al.: Deformability study of breast cancer cells using microfluidics. Biomed. Microdev. **11**(3), 557–564 (2009)
17. Hozak, P., Sasseville, A., et al.: Lamin proteins form an internal nucleoskeleton as well as a peripheral lamina in human cells. J. Cell Sci. **108**(2), 635–644 (1995)
18. Hutchison, C.J.: Lamins: building blocks or regulators of gene expression? Nat. Rev. Mol. Cell Biol. **3**(11), 848–858 (2002)
19. Kaufmann, S.H., Mabry, M., et al.: Differential expression of nuclear envelope lamins A and C in human lung cancer cell lines. Cancer Res. **51**(2), 581–586 (1991)
20. Lammerding, J., Dahn, K.N., Discher, D.E., Kamm, R.D.: Nuclear mechanics and methods. Methods Cell Biol **83**, 269–294 (2007)
21. Lammerding, J., Fong, L.G., et al.: Lamins A and C but not lamin B1 regulate nuclear mechanics. J. Biol. Chem. **281**(35), 25768–25780 (2006)
22. Lammerding, J., Schulze, P.C., et al.: Lamin A/C deficiency causes defective nuclear mechanics and mechanotransduction. J. Clin. Invest. **113**(3), 370–378 (2004)
23. Lee, J.S.H., Hale, C.M., et al.: Nuclear lamin A/C deficiency induces defects in cell mechanics, polarization, and migration. Biophys. J. **93**(7), 2542–2552 (2007)
24. Li, Q.S., Lee, G.Y., et al.: AFM indentation study of breast cancer cells. Biochem. Biophys. Res. Commun. **374**(4), 609–613 (2008)
25. Machiels, B.M., Ramaekers, F.C., et al.: Nuclear lamin expression in normal testis and testicular germ cell tumours of adolescents and adults. J. Pathol. **182**(2), 197–204 (1997)
26. Maniotis, A.J., Chen, C.S., et al.: Demonstration of mechanical connections between integrins cytoskeletal filaments, and nucleoplasm that stabilize nuclear structure. Proc. Natl. Acad. Sci. USA **94**(3), 849–854 (1997)
27. Meaburn, K.J., Misteli, T.: Cell biology: Chromosome territories. Nature **445**(7126), 379–381 (2007)
28. Mihailovic, D., Dordevic, B., et al.: Nuclear volume in type I gastric intestinal metaplasia. Anal. Quant. Cytol. Histol. **21**(2), 143–144 (1999)
29. Moir, R.D., Yoon, M., et al.: Nuclear lamins A and B1: different pathways of assembly during nuclear envelope formation in living cells. J. Cell Biol. **151**(6), 1155–1168 (2000)
30. Moss, S.F., Krivosheyev, V., et al.: Decreased and aberrant nuclear lamin expression in gastrointestinal tract neoplasms. Gut **45**(5), 723–729 (1999)
31. Oguchi, M., Sagara, J., et al.: Expression of lamins depends on epidermal differentiation and transformation. Br. J. Dermatol. **147**(5), 853–858 (2002)
32. Pajerowski, J.D., Dahl, K.N., et al.: Physical plasticity of the nucleus in stem cell differentiation. Proc. Natl. Acad. Sci. USA **104**(40), 15619–15624 (2007)
33. Parnaik, V.K., Manju, K.: Laminopathies: multiple disorders arising from defects in nuclear architecture. J. Biosci. **31**(3), 405–421 (2006)

34. Prokocimer, M., Margalit, A., et al.: The nuclear lamina and its proposed roles in tumorigenesis: projection on the hematologic malignancies and future targeted therapy. J. Struct. Biol. **155**(2), 351–360 (2006)
35. Rowat, A.C., Foster, L.J., et al.: Characterization of the elastic properties of the nuclear envelope. J. R. Soc. Interface **2**(2), 63–69 (2005)
36. Scaffidi, P., Misteli, T.: Lamin A-dependent nuclear defects in human aging. Science **312**(5776), 1059–1063 (2006)
37. Stewart, C.L., Roux, K.J., et al.: Blurring the boundary: the nuclear envelope extends its reach. Science **318**(5855), 1408–1412 (2007)
38. Stuurman, N., Heins, S., et al.: Nuclear lamins: their structure, assembly, and interactions. J. Struct. Biol. **122**(1–2), 42–66 (1998)
39. Sugitate, T., Kihara, T., et al.: Mechanical role of the nucleus in a cell in terms of elastic modulus. Curr. Appl. Phys. **9**(4), e291–e293 (2009)
40. Thoumine, O., Ott, A., et al.: Microplates: a new tool for manipulation and mechanical perturbation of individual cells. J. Biochem. Biophys. Methods **39**(1–2), 47–62 (1999)
41. Tseng, Y., Lee, J.S.H., et al.: Micro-organization and visco-elasticity of the interphase nucleus revealed by particle nanotracking. J. Cell Sci. **117**(10), 2159–2167 (2004)
42. Vaziri, A., Lee, H. et al.: Deformation of the cell nucleus under indentation: mechanics and mechanisms. J. Mater. Res. **21**(8), 2126–2135 (2006)
43. Vaziri, A., Mofrad, M.R.: Mechanics and deformation of the nucleus in micropipette aspiration experiment. J. Biomech. **40**(9), 2053–2062 (2007)
44. Venables, R.S., McLean, S., et al.: Expression of individual lamins in basal cell carcinomas of the skin. Br. J. Cancer **84**(4), 512–519 (2001)
45. Verstraeten, V., Lammerding, J.: Experimental techniques for study of chromatin mechanics in intact nuclei and living cells. Chromosome Res. **16**(3), 499–510 (2008)
46. Yamauchi, K., Yang, M., et al.: Real-time in vivo dual-color imaging of intracapillary cancer cell and nucleus deformation and migration. Cancer Res. **65**(10), 4246–4252 (2005)
47. Zink, D., Fischer, A.H., et al.: Nuclear structure in cancer cells. Nat. Rev. Cancer **4**(9), 677–687 (2004)

Adhesion and Signaling of Tumor Cells to Leukocytes and Endothelium in Cancer Metastasis

Cheng Dong

Abstract Heterotypic cell–cell adhesion in the near wall region under dynamic shear forces has been studied. In particular, we focus on neutrophil (PMN)–melanoma cell emboli formation in a non-linear shear flow and subsequent tethering to the vascular endothelium (EC) as a result of cell–cell aggregation. The extent of tumor cell adhesion to a vessel wall is governed by the kinetic formation/disruption of receptor–ligand bonds, soluble signaling proteins within the tumor microenvironment, and the hydrodynamic shear within the circulation. Upon tumor cell arrest on the endothelium, retraction of EC during tumor cell extravasation occurs due to the disruption of intercellular channels or disassembly of the vascular endothelial (VE)-cadherin homodimers that allow the passage of soluble proteins and cells. Preliminary studies have found tumor-elicited PMNs increase melanoma cell extravasation, which involves PMNs tethering on the EC and subsequently capturing/maintaining melanoma cells in close proximity to the EC. Results have indicated a novel finding that PMN-facilitated melanoma cell arrest on the EC is mediated by binding between the intercellular adhesion molecule (ICAM)-1 (expressing on both melanoma cells and ECs) and β_2 integrins on PMNs, influenced by tumor-induced inflammatory cytokines, e.g., interleukin (IL)-8, and hydrodynamic shear rates. Furthermore, the adherens junctions in terms of VE-cadherin are regulated by endothelial mitogen activated protein kinases (MAPK) in response to tumor cell adhesion to the EC, as well as to IL-8 and several other soluble signaling proteins within the tumor microenvironment. These studies will yield new evidence for the complex role of hemodynamics, protein signaling, and heterotypic cell adhesion in the recruitment of metastatic cancer

C. Dong (✉)
Department of Bioengineering, The Pennsylvania State University,
University Park, PA 16802, USA
e-mail: cxd23@psu.edu

Stud Mechanobiol Tissue Eng Biomater (2011) 4: 477–521
DOI: 10.1007/8415_2010_21

Published Online: 2 November 2010

cells to the EC in the microcirculation during metastasis, which will be significant in fostering new cross-disciplinary approaches to cancer treatment.

1 Introduction

Cancer is a complicated disease that requires the coordination of many different cellular processes. Metastasis is the spread of tumor cells (TC) from a primary tumor site to a secondary site and is the cause of most cancer related deaths. There are several pathways for a tumor to spread—through the vasculature or the lymph system to an adjacent organ. The studies presented here examine several possible mechanisms by which melanoma extravasation to secondary tumor sites occurs through the vasculature and how the inflammatory microenvironment may affect TC adhesion to and migration through the EC barrier under dynamic flow conditions from the circulation.

1.1 Tumor Cell Adhesion and Extravasation

Human leukocytes, including PMNs, actively participate in the inflammatory response via adhesion to the EC [89]. It has become evident from in vivo studies that the mechanisms utilized by leukocytes and metastatic tumor cells to adhere to a vessel wall prior to extravasation are very different [56]. One observation from in vivo video microscopy has indicated that tumor cells are trapped in capillaries and only arrest on the EC on the basis of vessel-size restriction in the microcirculation [8]. It has also been suggested that initial microvascular arrest of metastasizing tumor cells (from cell lines of six different histological origins) does not exhibit "leukocyte-like rolling" adhesive interaction with the EC [92]. In contrast, another in vivo study has discovered that the B16 melanoma cells could adhere to the walls of pre-sinusoidal vessels in mice pretreated with IL-1α [79]. They suggested that the release of inflammatory cytokines into the bloodstream could cause the arrest of melanoma cells in portal venules, by a chemoattraction and adhesion-mediated mechanism, rather than by a size restriction-only mechanism. Clearly these studies are somewhat contradictory and additional work is needed to characterize the event in TC adhesion to the EC, subsequent TC extravasation and metastasis.

Several ligands for inducible endothelial adhesion molecules have been identified on various types of tumor cells [103]. For example, Miele et al. [60] reported that a dose- and time-dependent increase in surface expression of ICAM-1 was found in human malignant melanoma cells. They also found that inhibiting ICAM-1 reduced melanoma lung metastasis in vivo. All these studies have supported an adhesive mechanism between TC and EC, rather than a simple mechanical entrapment, such as vessel-size restriction. Although melanoma cells express high

levels of ICAM-1, they do not express β_2 integrins (CD11a/CD18 or LFA-1; CD11b/CD18 or Mac-1), sLe^x or other sialylated molecules at levels to effectively adhere to the EC within the circulation [108]. An interesting study showed that PMNs and activated macrophages increased the ability of rat hepatocarcinoma cells to adhere to an EC monolayer [90]. In addition, tumor-elicited PMNs, in contrast to normal PMNs, were found to enhance metastatic potential and invasiveness of rat mammary adenocarcinoma cells in an in vivo tumor-bearing rat model [102]. Using light and electron microscopy, circulating PMNs were discovered in close association with metastatic TCs, including at the time of TC arrest [10]. These studies have clearly suggested that the immune system, and PMNs in particular, could affect tumor cell metastasis. However there is little understanding of tumor immunoediting and the adhesion mechanisms involved [4, 17, 41, 52].

1.2 Inflammatory Cytokines and Signaling

Chemokines represent a large family of polypeptide signaling molecules that are notable for their role in chemotaxis, leukocyte homing, and directional migration. Melanomas, and the cells derived from them, have been found to express a number of chemokines, including IL-8, growth-related oncogene (GRO)α-γ, and monocyte chemotactic protein (MCP)-1, which are implicated in melanoma cells themselves and the tumor infiltrating leukocytes [71]. Although several chemokines have been implicated in influencing adhesive properties of transformed cells, IL-8 is of particular interest. IL-8 has a wide range of pro-inflammatory effects, which mediate PMN migration from the circulation to sites of infection via activation of CXC chemokine receptors 1 and 2 (CXCR1/2) on PMNs [32, 65, 100]. IL-8 secretion is also a marker for increasing metastatic potentials, e.g., as an important promoter for melanoma growth [78, 83, 84]. Melanoma cells secrete IL-8 which alters adhesion molecule expression on PMNs [86]. IL-8 could potentially enhance PMN binding to melanoma cells and EC. In addition to IL-8, other factors such as IL-1β, IL-6, MCP-1, tumor necrosis factor (TNF)-α or GRO-α have also been shown to regulate immune responses and modulate tumor behavior [6, 63]. Chemokines or cytokines secreted by TCs and/or PMNs may play an important role in communication between melanomas and PMN and affect the interactions between them as well [25]. However, mechanisms regulating chemokine expression in a tumor microenvironment and roles played by endogenous chemokines in mediating TC extravasation from the circulation are unknown.

From in vitro models, interactions between ICAM-1 expressing cells and β_2 integrins on PMNs could potentially enhance melanoma cell adhesion to the EC mediated by PMN tethering, which further promote extravasation under dynamic flow conditions [53, 57, 87]. While IL-8 has been shown to promote melanoma angiogenesis and metastasis [2], involvement of PMNs in this process and mechanistic basis by which these cells could promote this process in vivo remains unclear. To dissect involvement of IL-8 secreted by melanoma cells and PMNs in

development of lung metastases, most recent mice studies by Huh et al. [36] showed that transient metastatic melanoma cells attached to PMNs in the lungs were significantly affected by high levels of IL-8. Secreted IL-8 increased β_2 integrin expressions (specifically Mac-1 molecules) on PMNs promoting tethering of ICAM-1 expressing melanoma cells to the EC via binding to the PMNs [52]. Therefore, Huh's in vivo work found that enhanced melanoma cells co-localization with PMNs increased the retention of TCs in the lungs resulting in enhanced trans-endothelial migration and subsequent metastasis development. Reducing expression of IL-8 using small interfering (si)RNA, decreased extracellular levels of IL-8 and Mac-1 expressions on PMNs, which reduced interactions between melanomas and PMNs. This resulted in fewer melanoma cells being tethered to the lung endothelium and retained in the lung thereby decreasing extravasation and metastasis development in vivo.

1.3 Cell Adhesion Kinetics

Cellular adhesion is mediated by the formation of receptor–ligand bonds. The combination of a receptor and a ligand that results in cellular adhesion can be considered as a chemical reaction. Kinetics is the study of the rates of chemical reactions and has been used to study cellular adhesion. The kinetics of leukocyte adhesion to the EC has been widely studied and various kinetic parameters of the molecules involved have been reported [1, 67, 88]. However, the kinetic mechanisms involved in melanoma cell adhesion, especially involving heterotypic cell–cell adhesion, have not been studied extensively and the steps leading to melanoma extravasation from the circulation are still poorly understood. As discussed earlier, melanoma cells have not been observed to roll along the EC similar to PMNs [92]. Previous investigations have determined that melanoma cells do not express selectin ligands or β_2 integrins at sufficient levels to mediate rolling or direct adhesive interactions with EC. Melanoma cells, however, do express ICAM-1, which can possibly bind to the integrins expressed by PMNs.

Resting PMNs express very few β_2 integrins in their high affinity states. Approximately 1,000 of the 15,000 expressed Mac-1 molecules and 9,000 of the 50,000 LFA-1 molecules expressed per cell are in a high affinity state before activation [82]. Many adhesion studies have shown that LFA-1 is more important for the initial tethering step of PMN adhesion to ICAM-1, whereas Mac-1 serves to stabilize already formed adhesions [29, 68]. For the interactions of LFA-1 with ICAM-1, a range of values have been determined for the dissociation rate under zero pulling force using different methods. Zhang et al. [109] calculated a dissociation rate of 0.17 s^{-1} using an LFA-1 expressing T-cell hybridoma line and immobilized ICAM-1 to perform atomic force microscopy and applying Bell's model [3]. A dissociation rate of 0.3 s^{-1} was estimated by Vitte et al. [97] using a parallel-plate flow chamber experiment utilizing Jurkat cells and immobilized ICAM-1, and Tominaga et al. [94] estimated a rate of 0.1 s^{-1} using a surface

plasmon resonance assay using soluble forms of both ICAM-1 and LFA-1. There is a higher variability in the association rates estimated using the different assays and cell types. Association rate estimates were calculated from the SPR assay as 200,000 M^{-1} s^{-1} [94] and from the parallel-plate flow chamber assay as 82 M^{-1} s^{-1} [97]. We therefore closely followed the method by Vitte et al. [97] in determining melanoma–PMN adhesion kinetic parameters.

1.4 Role of Fluid Dynamics Parameters

Under static in vitro conditions, melanoma cells do migrate through the EC. However, when they were exposed to a shear flow under stress 4 dyn/cm^2, the TC extravasation was found to be significantly decreased [86]. When PMNs were introduced to the TC suspension under the same shear conditions, 85% of the melanoma cell extravasation was recovered. This evidence has led to the hypothesis that PMNs may facilitate melanoma cell adhesion to and migration through the EC under flow conditions. Parallel-plate flow chamber experiments of TC–PMN aggregation under varying flow conditions showed fewer TCs adhered to the EC at higher shear rates [53]. As shear flow is always present in the body and these studies suggest that the properties of the fluid flow itself may influence the mechanism of melanoma cell adhesion and extravasation, especially when interacting with PMNs.

Fluid transport might govern flow-enhanced cell tethering [16, 110]. Results from a novel extravasation or a parallel-plate flow chamber have suggested that intercellular contact time, which is proportional to the inverse of wall shear rate, has a greater influence in the TC adhesion efficiency than the wall shear stress [50, 51, 58]. Wall shear stress (τ_w) and shear rate ($\dot{\gamma}$) are related by the definition $\tau_w = \mu\dot{\gamma}$ where μ is the viscosity of the fluid. If the magnitude of the fluid viscosity is increased and that of the shear rate is decreased proportionally, the shear stress remains constant. Several published experiments have been designed around this principle to distinguish the effect of the shear rate from that of shear stress [27, 76]. Under the same shear rate with varying fluid viscosity (or shear stress), no significant difference in the number of extravasated melanoma cells was observed; however, under a constant shear stress and decreasing shear rate, there was a significant increase in melanoma extravasation [87]. The same trends were observed for the aggregation of melanoma cells with PMNs in parallel-plate flow chamber experiments using the same variations in flow parameters [53]. These studies have suggested that TC arrest on the EC is a necessary step in PMN-mediated TC extravasation under flow conditions. This mechanism is regulated by hydrodynamic shear rates, which potentially affects TC–PMN contact time, revealing it is possibly convection driven. However, such fluid dynamics problems are not well studied, especially involving heterotypic cell adhesion in cancer.

Cell deformability has been shown to play an important role in affecting cell adhesion in a shear flow [5, 15, 35, 46]. Usually, an increase in shear force would

have a stronger tendency to detach a cell from its substrate or separate a cell from cell–cell aggregations; however, at the same time increasing shear stress also increases cell–cell contact areas due to the cell deformation that provides stronger adhesion. Therefore, hydrodynamics plays a complex role in the cell adhesion process.

1.5 Computational Fluid Dynamics and Cell Models

Computational fluid dynamics, or CFD, has been used to investigate the mechanisms involved in PMN adhesion to the EC. Numerical models of cellular in vitro systems have been created in order to determine effects of adhesion properties, fluid properties, and deformability on the efficiency of adhesion [37, 40, 66]. The majority of these models did not include a second (or heterotypic) cell type interacting with PMNs and ECs within the circulation; with the exception of Migliorini et al. [61], who modeled a red blood cell (RBC) colliding with a PMN. This is significantly different from modeling adhesion-specific TC–PMN interactions, due to the lack of specific RBC–PMN adhesion. A recent study developed by Hoskins et al. [34] extended these models by modeling TC interactions with a PMN adherent to the EC.

Currently the most sophisticated numerical models of PMN adhesion to the EC represent PMNs as 3-D deformable bodies with spring-type microvilli and adhesion molecules scattered on the membrane [37, 40, 66]. These models all employ membrane-tracking algorithms that do not discretize the outer membrane of the cells explicitly. These methods are less computationally intensive than an explicit method, but do not precisely resolve the location of the cell membrane or the fluid dynamics in the immediate vicinity of the cell membrane. Hoskins et al. [34] explicitly tracked the location of the deformable membrane and modeled the internal and external fluids separately. This will yield a more accurate representation of the cell deformation and fluid behavior.

The deformation of passive PMNs using the micropipette aspiration technique has been widely studied to determine material parameters of PMNs [19, 20, 104]. As PMNs traverse the circulation, they often encounter blood vessels with a smaller radius than the cell radius. Several in vitro experiments were used to recreate that situation [22]. Many numerical models have been developed which attempt to recreate the behavior of PMNs as they undergo the large deformations induced in the micropipette experiments [18, 23]. Although the deformation that will be modeled in the current work is less significant, the insight that has been gained by completing those studies can guide the modeling process.

Kunz et al. [44] have developed a CFD code, NPHASE, which has been developed, applied and validated for numerous single-phase and multi-phase flows. NPHASE incorporates several elements of modern CFD analysis including overset and unstructured meshes, parallel processing, fluid–structure interaction and moving/deforming meshes, each of which will be applied in the proposed cell

system modeling. In the current study, NPHASE will be applied in a DNS framework, where each cell in the system is explicitly resolved. The code has been specifically validated [34, 47] for the very low Reynolds number cellular system flows of interest here.

1.6 Endothelial Junction Adherence

Interendothelial adherens junctions account for the majority of barrier function of normal endothelium, and are responsible for regulating the passage of proteins and circulating cells [11]. Adherens junctions are characterized by the localization of VE-cadherin, a transmembrane protein, its cytoplasmic tail interacts directly with important cytoskeletal and signaling proteins, including α-actinin, α/β-catenin, plakoglobin, and actin [45]. VE-cadherin participates in most of the stages of transmigration of inflammatory cells. The loss of homophilic binding of VE-cadherins weakens the adhesive interaction between neighboring ECs, permitting transvascular cell penetration [12]. Homophilic binding activity of VE-cadherin is, in part, regulated by tyrosine-phosphorylation of its cytoplasmic tail [98], suggesting a direct role for protein tyrosine kinases in regulating interendothelial junctions, and subsequent transvascular cell migration.

Tumor cell-initiated signaling events that lead to changes in EC integrity have not been extensively characterized. High expression levels of $\alpha_4\beta_1$ integrin associated with highly metastatic melanoma cells is correlated with a marked increase in melanoma extravasation through endothelial layers [43, 81]. While several studies have focused on the effects of $\alpha_4\beta_1$ and vascular adhesion molecule-1 (VCAM-1) interactions on metastasis and adhesion of melanoma cells to the endothelium [26, 48, 75, 77, 99], recent studies have found that these adhesion events lead to the disassembly of VE-cadherin which facilitates melanoma transendothelial migration [39, 72, 73]. However, melanoma cells themselves secrete large amounts of soluble proteins including IL-8, IL-6, IL-1β, and GRO-α. Melanoma cells with high metastatic potential have been shown to secrete higher amounts of IL-8 [70, 74]. These results were further supported by in vivo studies showing an overall decrease in tumorigenicity and metastasis when mice lacking CXCR2 (the receptor for IL-8) were injected with melanoma cells [85].

Peng et al. [73] monitored the $[Ca^{2+}]_i$ in human umbilical vein endothelial cells (HUVEC) following contact with human melanoma cells. They showed that transient rise in endothelial $[Ca^{2+}]_i$ was elicited specifically by melanoma cells, and this response recruited the classical $[Ca^{2+}]_i$ release mechanism via pertussis toxin (PT)-sensitive G proteins in the EC. In addition, they demonstrated that the loss of VE-cadherin integrity in EC appeared at the interendothelial border in response to melanoma cell contacts. The regulation of melanoma cell-mediated junctions was independent of tyrosine phosphorylation of VE-cadherin. Most importantly, melanoma cells induced junction disassembly in the manner strongly

related to phospholipase C (PLC) activation, since inhibition of PLC significantly reduced the disruptions of VE-cadherin by melanoma cells. Phosphatidylinositol-3-kinase (PI3K), however, was not responsible for the melanoma cell-associated VE-cadherin redistribution. In addition, melanoma cell transendothelial migration was diminished in the absence of PLC or PI3K activity. These findings suggest an involvement of PLC in endothelial signaling pathways recruited by melanoma cells in breaching the vasculature.

It is well established that p38 MAPK activation plays a key role in the initial break down of VE-cadherin junctions to facilitate cell migration through the EC [69, 95]. Some recent studies have shown that the VCAM-1 receptor on the endothelium induces intercellular gap formation through the Rho-like GTPase Rac1 signaling that results in activation of p38 MAP kinase proteins further downstream of the Rac pathway [39, 96]. The question remains as to whether melanoma cells trigger VE-cadherin disassembly primarily through cell–cell contact mediated events or through soluble protein events. Furthermore, could these tumor-induced events modulate specific intracellular pathways in the endothelium leading to disassembly of VE-cadherin homodimers?

2 Experimental Materials and Methods

2.1 Cell Preparation

Human melanoma cell lines WM35 and WM9 were provided by Dr. Meenhard Herlyn (Wistar Institute, Philadelphia, PA, USA) and maintained in Roswell Park Memorial Institute 1640 medium (RPMI 1640; Biosource, Inc., Camarillo, CA, USA) supplemented with 10% fetal bovine serum (FBS; Biosource, Inc.) and 100 units/ml penicillin–streptomycin (Biosource, Inc.) at 37°C under 5% CO_2. 1205Lu cells (from Dr. Gavin P. Robertson, Penn State Hershey Medical Center, Hershey, PA, USA) and C8161 cells (from Dr. Danny Welch, University of Alabama, Birmingham, AL, USA) were cultured respectively in Dulbecco's Modified Eagle's Medium (DMEM) and DMEM-F12 (Biosource, Inc.) supplemented with 10% FBS in a standard cell culture condition (5% CO_2/37°C). Correlation of tumor metastatic potentials with melanoma cell invasiveness, chemotactic migration and adhesiveness is shown in Table 1.

Fibroblast L-cells that had been transfected to express human E-selectin and ICAM-1 (EI cells) were provided by Dr. Scott Simon (University of California, Davis, CA, USA), which were maintained in culture as described elsewhere [27]. The EI cells were used in our initial experiments as a model of an endothelial monolayer for studying TC–EC, PMN–EC, and TC–PMN–EC adhesion.

Human umbilical vein endothelial cells were obtained from American Type Culture Collection (ATCC) (Manassas, VA, USA) and maintained in F12-K medium with 10% FBS, 30 μg/ml of EC growth supplement, 50 μg/ml heparin

Table 1 "Metastatic" potential was qualitatively determined from the cell line origin; "Chemotactic" potential was measured by cell static migration toward soluble type IV collagen (CIV; 100 μg/ml) using Boyden chamber; and "Adhesion" potential was quantified by comparing relative mean fluorescence levels of ICAM-1 expression obtained by flow cytometry

Cell line	Potentials			References
	Metastatic	Chemotactic (CIV)	Adhesion (ICAM-1)	
1205Lu	++++	+++	+++	[80]
C8161	+++	++	++	[101, 106]
WM 9	++	++	+++	http://www.wistar.upenn.edu/herlyn/melcell.htm
A2058	+	++	++	[14]
WM35	−	+	+	http://www.wistar.upenn.edu/herlyn/melcell.htm

(Mallinckrodt Baker, Inc.), 100 units/ml of penicillin–streptomycin (Biofluids, Inc.) [39, 73].

Fresh human blood was drawn from healthy donors under informed consent as approved by the Pennsylvania State University Institutional Review Board. PMNs were separated from blood using Ficoll-Hypaque (Histopaque; Sigma Chemical Co.). After centrifugation at 620*g* for 30 min, PMNs were carefully isolated and suspended in Dulbecco's phosphate-buffered saline (DPBS) with 0.1% human serum albumin (HSA; Sigma Chemical Co.). Erythrocytes were lysed using ACK lysis buffer (0.15 M NH_4Cl, 10 mM $KHCO_3$, 0.1 mM Na_2EDTA; [pH 7.4]) and removed. The cells were washed and resuspended in 0.1% HSA/DPBS, and gently rocked until they were used in experiments. The cell preparations were 99.5% pure PMNs, as analyzed by a Diff-Quick stain (Dade Behring Inc., Newark, DE, USA). PMNs were resuspended in RPMI 1640 medium supplemented with 5% FBS and cultured with or without melanoma cells.

For PMN and melanoma cell co-culture, PMNs were added to the confluent melanoma cells, either directly or separated by a Transwell insert with 0.4 μm pore size. In some experiments, PMNs or ECs were stimulated with recombinant human IL-8 (12.5, 25 or 125 ng/ml), IL-1β (5, 10 or 25 ng/ml), IL-6 (50 or 100 ng/ml), GRO-α (100 or 200 ng/ml) (Biosource, Inc.) or a combination of IL-8, IL-1β, IL-6 and GRO-α cytokines with chosen concentrations, respectively.

2.2 Tumor Conditioned Medium

Selected melanoma cells were cultured in 75 cm^2 flasks under growth conditions described above to 90–95% confluency, after which medium was aspirated and replaced with fresh 5 ml of RPMI (for WM35 cells) or DMEM (for A2058 and 1205Lu cells) with 2% FBS. The medium was then removed after a 24-h period of chosen tumor cell culture and centrifuged in 50 ml conical tubes at 1,500 rpm at 4°C for 5 min to remove any remaining cells.

2.3 Small Interfering RNA (siRNA) Targeting IL-8

SiRNA (100 pmol) was introduced into 1.0×10^6 1205Lu, C8161.Cl9 via nucleofection using an Amaxa Nucleofector using Solution R/program K-17 [52, 80]. Transfection efficiency was >95% with 80–90% cell viability [80]. Following siRNA introduction, cells were allowed to recover for 2 days and then replated in 96-well plates. Five days later, cell viability was measured using the MTS assay (CellTiter 96 AQueous Cell Proliferation Assay, Promega, Madison, WI, USA).

Duplexed Stealth siRNA (Invitrogen, Carlsbad, CA) were used for the IL-8 studies. The following siRNA sequences were used for targeting IL-8 [36]. *IL-8#1*: GCA GCU CUG UGU GAA GGU GCA GUU U, *IL-8#2:* CCA AGG AGU GCU AAA GAA CUU AGA U.

2.4 Western Blots

Cells were collected and washed with cold PBS, then whole cell extracts were prepared by resuspending cells in lysis buffer (10 mM Tris–HCl [pH 7.4], 150 mM NaCl, 1 mM EDTA [pH 8.0], 2 mM Na_3VO_3, 10 mM NaF, 10 mM $Na_4P_2O_7$, 1% NP-40, 1 mM PMSF, 2 ng/ml pepstatin A). Lysates were incubated on ice for 30 min followed by a centrifugation at 16,000*g* for 1 min at 4°C. The pellet was discarded and the supernatant was mixed with 2× SDS running buffer (0.2% bromophenol blue, 4% SDS, 100 mM Tris [pH 6.8], 200 mM DTT, 20% glycerol) in 1:1 ratio. Samples were boiled for 3 min and 15 μl were loaded onto a 12 or 15% SDS-PAGE gel and proteins were transferred to a 0.2 μm PVDF membrane (Millipore Co., Billerica, MA, USA) by electroblotting. Primary antibodies included rabbit anti-human IL-8 (Biosource, Inc.) and anti-β-actin IgG1 (Sigma Chemical Co.). Secondary antibodies were peroxidase-conjugated goat anti-rabbit IgG or goat anti-mouse IgG. Proteins were detected using the Enhanced Chemiluminescence Detection System (Amersham Pharmacia Biotech, Arlington Heights, IL, USA).

2.5 Enzyme-linked Immunosorbent Assays

At the end of assays, cell-free supernatants were collected by a centrifugation at 430*g* for five minutes and stored at −80°C until Enzyme-linked immunosorbent assays (ELISA) was performed. ELISA detection of protein secretion was performed at the Pennsylvania State University NIH Cytokine Core Lab. Mouse anti-human capture antibody to specific target chemokine or cytokine was diluted to 2 μg/ml in coating buffer (0.1 M $NaHCO_3$ [pH 8.2]) and 50 μl was added to each well of the 96-well ELISA plate for overnight incubation at 4°C. The plate was

then washed four times with 20% Tween 20 in phosphate-buffered saline (PBST) [pH 7.0] and blocked with 1% BSA in PBS for 2 h at room temperature. 100 µl target chemokine or cytokine standards and samples were added to each well for overnight incubation at 4°C. The plate was washed four times next day and 100 µl of 0.2 µg/ml biotinylated affinity purified goat anti-human polyclonal detection antibody was added to each well, followed by 2 h incubation at room temperature. The plate was then washed six times and incubated with 10 µl streptavidin peroxidase (1 µg/ml, Sigma Chemical Co.) for 30 min at room temperature. 100 µl of 2,2′-Azino-bis (3-ethylbenzothiazoline-6-sulfonic acid) diammonium salt (Sigma Chemical Co.)/peroxide substrate solution was then added for 1 h in the dark. The plate was read using a microtiter plate reader (Packard, Downers Grove, IL, USA) at a wavelength of 405 nm.

2.6 Flow Cytometry

The cells of interest were treated with murine anti-human CD marker primary antibodies (e.g., anti-CD11a, anti-CD11b, or anti-ICAM-1; 1 µg Ab/10^6 cells) (CalTag Laboratories) for 30 min at 4°C. The cells were then treated with secondary antibody, FITC-conjugated goat anti-mouse IgG $F(ab)_2$ fragment (1 µg/10^6 cells) (Jackson ImmunoResearch, West Grove, PA, USA) for 25 min at 4°C. In the case of blocking CXCR1 and CXCR2 receptors on PMNs, PE-conjugated anti-CD11b (1 µl/10^6 cells; CalTag Laboratories) was used to avoid binding secondary antibody to the existing CXCR1 and CXCR2 antibodies. The samples were fixed with 2% formaldehyde (Sigma) and analyzed using a Coulter EPICS XL (Coulter Corp., Fullerton, CA, USA) flow cytometer. Control cases used to determine background fluorescence were samples treated with secondary antibody only or PE-conjugated isotype control (CalTag Laboratories).

2.7 In vitro Flow Extravasation Assays

A flow extravasation assay was performed in a modified 48-well chemotactic Boyden chamber consisting of a top and bottom plate separated by a gasket. In brief, a 7 cm × 2 cm opening cut from the center of a 0.02 inch-thick gasket between top and bottom plates forms the flow field (Fig. 1; top right). The wall shear stress (τ_w) is related to the volumetric flow rate (Q) by $\tau_w = 6\mu Q/wh^2$, where μ is the fluid viscosity, h is height and w is width of the flow field. EI cells, which had been transfected from fibroblasts to express human E-selectin and ICAM-1, were used as a substrate for cell adhesion and as a model of an endothelial monolayer. E-Selectin and ICAM-1 levels were periodically checked by flow cytometry to verify expression level. ICAM-1 levels on EI cells were shown to be comparable with IL-1β stimulated HUVECs [27]. Hence, a monolayer was formed

by growing EI cells to confluence on sterilized PVP-free polycarbonate filters (8-μm pore) coated with fibronectin (30 μg/ml) [86]. The bottom side of the filter was scraped prior to use to remove any potential cell growth. Soluble type IV collagen (CIV; 100 μg/ml), which has been shown to induce melanoma cell chemotaxis [30, 31], was chosen as the chemoattractant in the center 12 wells. Typical experiments involved cases such as: PMNs; melanoma cells (respective cell lines with varied metastatic phenotypes from Table 1); PMNs + selected-type melanoma cells (5×10^5 cells of each cell type). The entire flow-migration assay was conducted in a 37°C, 5% CO_2 incubator for 4 h. To quantify migration, the filter was removed from the chamber and immediately stained with HEMA-3 (Fisher Scientific). The cells on the bottom side of each filter were imaged. No cells were found in the attractant wells after 4-h of migration. Three pictures were taken of each filter in different locations. The number of cells migrated was quantified/averaged for each filter. A minimum of three filters were analyzed for each data point. Background migration was subtracted from each sample as appropriate. Control experiments showed no PMNs migrated toward CIV.

2.8 Parallel-plate Flow Assays

Cell collision and adhesion experiments were performed in a parallel-plate flow chamber (Glycotech, Rockville, MD, USA) mounted on the stage of a phase-contrast optical microscope (Diaphot 330, Nikon, Japan). A syringe pump (Harvard Apparatus, South Natick, MA, USA) was used to generate a steady flow field in the flow chamber. A petri dish (35 mm) with a confluent EI cell monolayer was attached to the flow chamber [53]. All experiments were performed at 37°C. The field of view was 800 μm long (direction of the flow) by 600 μm. The focal plane was set on the EI monolayer. The flow chamber was perfused with appropriate media over the EI monolayer for 2–3 min at a shear rate of 40 s^{-1} for equilibration before the introduction of a predetermined concentration (1×10^6 cells/ml) of PMNs and WM9. PMNs were stimulated with 1 μM fMLP for 1 min or 1 ng/ml IL-8 for 1 h before the perfusion into parallel-plate flow chamber. After allowing PMNs and WM9 cells to contact the EI monolayer at a shear stress of 0.1–0.3 dyn/cm^2 for 2 min, we adjusted the shear stresses to the experimental range of 0.6–2 dyn/cm^2 and kept constant for 6–7 min. Experiments were performed in triplicate and analyzed off-line.

2.9 Animal Studies

Animal experimentations were performed according to protocols approved by the Institutional Animal Care and Use Committee at the Pennsylvania State University College of Medicine [36, 52, 80].

Tumor formation was measured in athymic-Foxn1^{nu} nude mice purchased from Herlan Sprague–Dawley (Indianapolis, IN, USA). 500 pmol of siRNA was nucleofected into 5.0×10^6 cells and after 48 h of recovery, 1.0×10^6 cells were collected in 0.2 ml of 10% FBS-DMEM to inject subcutaneously above both the left and right rib cages of 4–6 week old female mice. Dimensions of developing tumors were measured on alternate days using calipers.

To characterize in vivo interactions of melanoma cells with human PMNs, 100 pmol of siRNA were nucleofected into 1.0×10^6 GFP-tagged 1205Lu. After 36 h 0.5×10^6 cells in 0.2 ml of HBSS were collected. PMNs were isolated and were stained with CellTracker Orange CMTMR (C2927, Invitrogen, Carlsbad, CA, USA) according to manufactures protocol. Melanoma cells were injected i.v. into the left lateral tail vein of athymic-Foxn1^{nu} nude mice and human PMNs were injected i.v into the right lateral tail vein of nude mice. After 24 h, mice were sacrificed, lungs removed and analyzed for melanoma cells interacting with PMNs using Nikon SMZ 1500 dissecting microscope with fluorescence detection capabilities (for GFP; ex470/em500, for CellTracker Orange CMTMR; ex550/em600). Percentages of melanoma cells co-localized with PMNs were counted in fields where melanoma cells and PMNs coexisted [36].

To study mouse experimental metastasis, 100 pmol of siRNA were nucleofected into 1.0×10^6 GFP-tagged 1205Lu and C8161.Cl9 cells. After 36 h 0.5×10^6 cells in 0.2 ml of HBSS were injected i.v. into the lateral tail vein of nude mice. Mice were sacrificed 18 days later, necropsied, and lungs analyzed for presence of fluorescent metastases using a Nikon SMZ 1500 dissecting microscope with a Plan Apo 1.6× objective. Images were photographed at 48× magnifications from the ventral surface of each lung and number of fluorescent metastases as well as area occupied by metastases scored in pixels using IP lab imaging software (Scanalytics, Fairfax, VA, USA).

2.10 Statistical Analysis

All results are shown using mean ± standard error of the mean (SEM) unless otherwise stated. One-way ANOVA analysis was used for multiple comparisons and *t* tests were used for comparisons between two groups. $P < 0.05$ was considered to be significant.

3 Computational Models

3.1 Diffusion and Convection of Solutes in a Shear Flow

A two-dimensional Couette flow model was used to simulate the transport of IL-8 released by tumor cells in the circulation. The inputs used in the model are tabulated in Table 2.

Table 2 Description and source of variables as inputs for Comsol simulation

Variable	Description	Value	Source
Q	Volumetric flow rate	0.025 ml/min, 0.04 ml/min and 0.08 ml/min	Experimental setting
D_{AB}	IL-8 diffusion coefficient	2.59×10^{-10} m^2/s	[62, 107]
C_0	IL-8 secreted by a melanoma cell	Liang et al. [51]	Detected using ELISA from medium collected after flow assay
a	Distance from the center of channel to the wall	63.5 μm	Parallel plate chamber geometry
ρ	Density of fluid	1.0×10^3 kg/m^3	Known constant
u	Melanoma cell velocity	9.046×10^{-5}, 1.447×10^{-4}, 2.894×10^{-4} m/s	Calculated from Eqs. 3 and 4
μ	Viscosity	1.0, 2.0, 3.2 cP	Experimental setting

IL-8 distribution under flow conditions was modeled computationally using the commercial software package Comsol Multiphysics 3.2 (Comsol, Stockholm, Sweden), which employs a finite element method to solve the governing partial differential equations. To simulate the IL-8 transport, the convection and diffusion application mode was selected and the Navier–Stokes application mode was used to calculate the velocity pattern. The convection–diffusion equation solved is shown in Eq. 1:

$$\frac{\partial c_i}{\partial t} + \nabla(c_i u) = D_i \nabla^2 c_i, \tag{1}$$

where c_i is the IL-8 concentration, u is the velocity, and D_i is the solute diffusion coefficient. The diffusion coefficient for IL-8 was obtained from literature [62]. It has been shown that for small proteins, the diffusion coefficient is proportional to molecular weight [105, 107]. A constant flux was assigned at the cell surface and complete dilution was assumed very far from the cell; mathematically stated as:

$$c = C_0 \text{ at } r = R \quad \text{and} \quad c \to 0 \text{ as } r \to \infty$$

where C_0 is the IL-8 concentration and R is the tumor cell radius. It was assumed that the secreted IL-8 would not be re-consumed by the secreting tumor cell and C_0 be uniform over the surface of the cell.

The velocity profile was calculated using the Navier–Stokes application mode, which solves the incompressible momentum and mass conservation:

$$\begin{aligned} &\rho \frac{\partial u}{\partial t} + \rho(u \cdot \nabla)u + \nabla p - \mu \nabla^2 u = 0 \\ &\nabla \cdot u = 0 \end{aligned} \tag{2}$$

where u is the velocity, ρ is the density of fluid, μ is the viscosity and p is the pressure. The fluid was assumed to be Newtonian, incompressible, steady and laminar. A no-slip boundary condition was implemented at the channel walls. Uniform velocity and constant pressure were prescribed at the inlet and outlet, respectively. In the fully developed region, the classical parabolic velocity profile (Poiseuille flow) was obtained. The velocity at a given location in the chamber can be calculated from the equation below:

$$u = \left(\frac{\Delta P a^2}{4\mu L}\right)\left[1 - \left(\frac{r}{a}\right)^2\right] \tag{3}$$

where the $\Delta P/L$ is the driving force, r is the distance from the center of the channel to the location, μ is the viscosity, and a is the distance from the center of the channel to the channel wall. The driving force, $\Delta P/L$, can be derived from the equation:

$$\frac{\Delta P}{L} = \frac{8\mu Q}{\pi a^4} \tag{4}$$

where Q is the volumetric flow rate.

The relation between diffusion coefficient and solvent viscosity can be calculated using the Stokes–Einstein equation as follows.

$$D_{AB}\mu_B = \frac{k_b}{6\pi R_A} \tag{5}$$

where D_{AB} is the diffusion coefficient of solute A in solvent B, R_A is the hydrodynamic radius of solute A, k_b is Boltzmann's constant, T is the Kelvin temperature, and μ_B is the solvent viscosity. Note that the Stokes–Einstein equation usually gives poor accuracy when solute A is a large molecule. Recently, a modification of the Stokes–Einstein equation for small molecules was proposed by Kooijman [42]. However, both equations have shown that the diffusion coefficient is inversely proportional to the solution viscosity.

3.2 Receptor–ligand Binding Association Rate

A molecular model of receptor–ligand binding has been developed and used in simulations of cell–cell adhesion [13]. In this model, the association rate, k_{on}, governs the likelihood of a receptor to form a bond with a ligand on another cell, whose equation is shown in Eq. 6:

$$k_{on} = A_L(n_L - n_B)k_{on}^0 \exp\left(\frac{-\sigma_{ts}(\varepsilon - \lambda)^2}{2k_bT}\right) \tag{6}$$

where A_L is the surface area on a ligand-bearing cell that is available to a receptor, n_L is the number of ligands on a cell, n_B is the number of bonds already formed. These values and the separation distance between two cells, ε, are determined by the geometry and properties of a chosen cell. The association rate for the receptor–ligand binding under zero-force conditions, k_{on}^{0}, was determined for LFA-1 and Mac-1 binding with ICAM-1 in a companion effort [33]. The bond spring constant, σ_{ts}, and equilibrium length, λ, as well as the Boltzmann's constant, k_b, were assigned values found in the literature [13].

3.3 Melanoma–PMN Adhesion to the EC in a Shear Flow

A 3D model of a PMN and a tumor cell in flow has been developed in a companion effort to simulate the adhesion of a melanoma cell to a tethered PMN under flow conditions [34]. The model is used here to compare the force exerted on a melanoma cell, bound to a stationary PMN via a single bond, under varying flow conditions. Since bond formation is a random occurrence, which is based on the proximity of cells, receptor and ligand surface densities and locations, and molecular properties, bonds may form in any position between a melanoma cell and a PMN. Here, a direct comparison of bond force time history in various flow conditions is desired; thus the same initial location was assumed for the melanoma cell and the single bond in all simulations.

One stationary, adherent PMN was modeled on the bottom plate of the parallel plate flow chamber geometry and a free stream tumor cell was modeled above and slightly upstream of the PMN in the flow [51]. A single bond, treated as a linear bond spring, was seeded between the two cells. The forces on the tumor cell due to the fluid and the bond were used to calculate the cell motion.

Two commercial codes were used to simulate the two cell system. Harpoon (Sharc, Manchester, UK) automatically generates the computational grids, and AcuSolve (ACUSIM Software, Mountain View, CA, USA) calculates the flow profile and force distributions. The cell motion calculation was completed by Kunz-developed Python script[44], which also controls the overall simulation. The order of operations controlled by the script was described in details from Hoskins et al. [34].

Harpoon is a grid generator that creates hexahedra-dominant meshes in a very short time. In the simulations used in this study, a new grid was generated at each time step with the new tumor cell location.

AcuSolve is an incompressible flow solver based on the Galerkin/Least Squares finite element method (GLS). The steady, incompressible Navier–Stokes and continuity equations were solved, as shown in Eq. 2. Variables are also as defined for Eq. 2.

The solution of Newton's Second Law, shown in Eq. 7, governed the spherical tumor cell motion.

$$\frac{d^2\vec{x}}{dt^2} = \frac{\vec{F}}{m}$$
$$\frac{d^2\vec{\theta}}{dt^2} = \frac{\vec{\tau}}{I} \tag{7}$$

where $\vec{x}$ and $\vec{\theta}$ are the tumor cell translations and rotations, $\vec{F}$ and $\vec{\tau}$ are the force and torque vectors on the tumor cell and m and I are the cell's mass and mass moment of inertia. These equations were solved assuming the tumor cell is a rigid body.

To represent the interactions between the microvilli on the cells' surfaces, a repulsion force with the form of a non-linear spring force, as shown in Eq. 8, was applied to the tumor cell.

$$F_{rep} = -kd + bd^3 \tag{8}$$

where k and b are constants and d is the distance between the cells. This force was applied along the normal to the PMN surface at the point of minimum separation distance between the cells. The line of the normal does not generally go through the center of the tumor cell, thus a torque is also applied.

4 Results

4.1 PMN-facilitated Tumor Cell Extravasation under Flow Conditions

An in vitro extravasation model (Fig. 1) was developed using a modified 48-well chemotactic "flow-migration" Boyden chamber [86].

The "PMN tethering frequency" was determined experimentally as the number of PMNs that adhered to the EC per unit time and area using a parallel-plate flow chamber (Fig. 1, bottom), including both rolling and firmly-arrested cells [53]. This frequency was normalized by cell flux to the surface to compensate for the different concentration of cells passing the same area of substrate at different shear rates. This normalization followed the procedure of Rinker et al. [76] based on equations derived by Munn et al. [64]. Melanoma–PMN aggregation on the EC was subsequently analyzed. Quantification started at the onset of experimental shear rate ($t = 0$ min) and lasted for 5 min. Aggregates could be characterized by differences in cell sizes and velocities (Fig. 1, bottom). Aggregation variables to be quantified included: the total number of tethered PMNs; number of collisions of melanoma cells (from the free stream near the EC) to tethered PMNs; aggregation of melanomas with tethered PMNs as a result of the collision; and final attachment of melanoma–PMN aggregates on the EC. For some cases in which more than one melanoma cell adhered to a PMN, we count such a case as two aggregates if two melanoma cells adhered to a PMN.

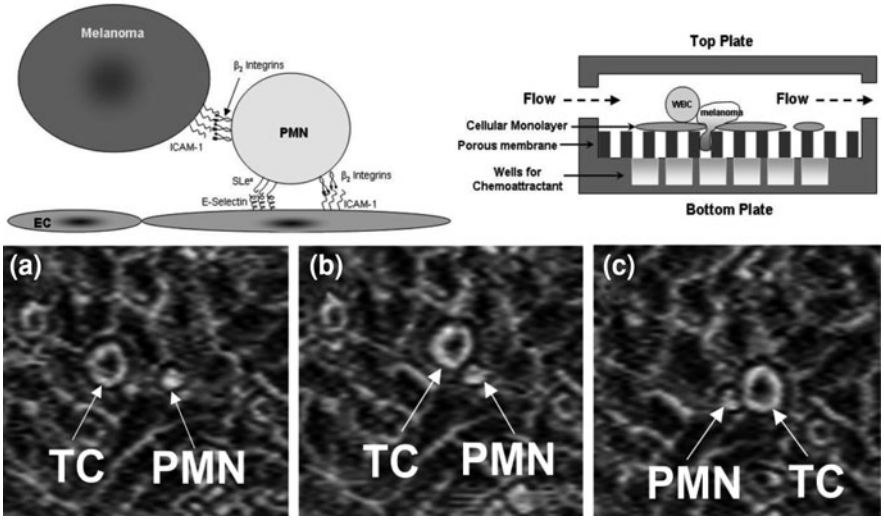

Fig. 1 Schematic of PMN-facilitated melanoma adhesion to the EC in a shear flow. *Top left* a melanoma cell in close proximity to the EC (using the EI cell model) via a tethered PMN. Melanoma cells are captured/retained by tethered PMN on the EI via β_2 integrins/ICAM-1 interactions. *Top right* cross-section view of the flow-migration chamber. *Bottom* representative aggregation of melanoma tumor cells (*TC*) to tethered PMN on an endothelial monolayer. Flow direction is from *left* to *right*: **a** a melanoma cell and a PMN on the monolayer at 0 s, **b** collision between a PMN and a melanoma cell after 20 s, and **c** arrest of a melanoma cell to the monolayer due to the formation of PMN–melanoma aggregates after 30 s

"Melanoma adhesion efficiency" was expressed by the following ratio [53]:

$$\text{Melanoma adhesion efficiency} = \frac{\text{Number of melanoma cells arrested on the monolayer}}{\text{Number of melanoma collisions to PMNs}}$$

where, the numerator is the number of melanoma cells arrested on the EI at the end of the entire flow assay as a result of collision between entering melanoma cells and tethered PMNs. The denominator is the total number of melanoma–PMN collisions near the EI surface counted as a transient accumulative parameter throughout the entire flow assay.

As a negative control, non-metastatic melanocyte migration was first tested under the static condition and found to be at a background level (Fig. 2a, bottom). In comparison, highly-metastatic C8161 and WM9 cells were more actively migratory under the no-flow condition than low-metastatic WM35 cells (Fig. 2a, "Static"). When exposed to a shear flow ($\sim$0.4 dyn/cm^2), extravasations of C8161, WM9 and WM35 cells toward CIV were all significantly less than those under static conditions (Fig. 2a), at a level similar to the melanocyte case. Addition of PMN to the melanoma cell suspension significantly enhanced tumor

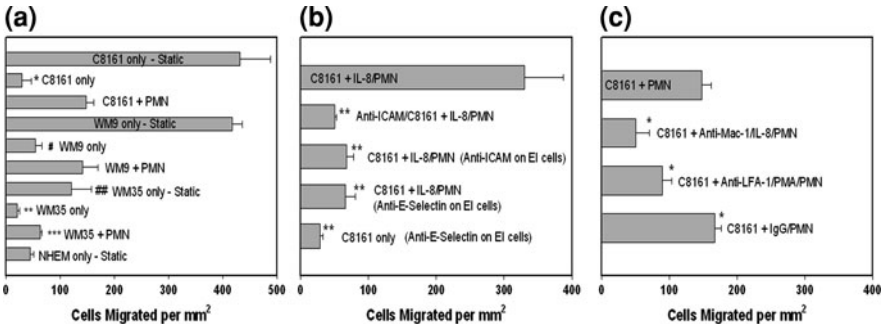

Fig. 2 **a** PMN affects C8161, WM9 and WM35 cell migration under shear conditions. NHEM are non-cancerous melanocyte used as a negative control. All cases were under a flow shear stress at 0.4 dyn/cm^2, unless labeled "Static" ($^*P < 0.01$ with respect to C8161 static case, $^{\#}P < 0.05$ with respect to WM9 static case, $^{**}P < 0.01$ with respect to WM35 static case, $^{\#\#}P < 0.05$ with respect to both C8161 and WM9 static cases, and $^{***}P < 0.02$ with respect to both C8161 + PMN and WM9 + PMN cases). **b** ICAM plays an important role in PMN-facilitated melanoma cell migration. The *second bar* shows disrupting C8161–PMN aggregation by blocking ICAM-1 on melanomas significantly reduces melanoma cell migration (PMNs were activated by IL-8). The *third* and *fourthbars* show inhibiting IL-8-stimulated PMN adhesion to the endothelium by blocking E-selectin or ICAM-1 on the EI also decreases C8161 cell migration ($^{**}P < 0.01$ with respect to C8161 + IL-8/PMN case at 0.4 dyn/cm^2). **c** Differential role of LFA-1 and Mac-1. Both Mac-1 and LFA-1 (to lesser degree) contribute to PMN-mediated melanoma extravasation. The *last bar* shows migration with isotype antibody-treated PMNs, as a control ($^*P < 0.05$ with respect to C8161 + PMN case at 0.4 dyn/cm^2). All the values are mean ± SEM for $N \geq 3$

cell extravasation under shear conditions compared with melanoma cells only (all P values < 0.05). Obviously, tumor metastatic potential correlates with melanoma cell extravasation behavior.

Figures 2b, c indicate that each binding step between EC, PMNs and melanoma cells affects tumor cell extravasation under flow conditions. ICAM-1 was functionally blocked on the C8161 cells and EI cells, respectively. Functionally blocking of ICAM-1 on C8161 cells or EI cells significantly reduced melanoma extravasations. Blocking E-selectin on the EI cells reduced C8161 melanoma cell migration by 80% compared with the C8161 + IL-8-activated PMN case (Fig. 2b). However, blocking E-selectin on the EI cells without PMN did not really change melanoma extravasation (Fig. 2b, bottom). To investigate whether PMN–melanoma interactions are mediated by receptor–ligand binding via β_2 integrins (on PMN) and ICAM-1 (on melanoma cells), melanoma cell extravasations were assayed in the presence of PMNs, in which CD11a (for LFA-1) and CD11b (for Mac-1) on PMNs were inhibited respectively with blocking antibodies. Blocking CD11b resulted in the greatest reduction in C8161 migration (66% reduction as compared to C8161 + PMN under 0.4 dyn/cm^2 shear stress; Fig. 2c). Similar results are shown that migration of melanomas was decreased by 40% in the presence of CD11a-blocked PMN.

4.2 Shear Rate Mediated Fluid Convection Affects PMN-Facilitated Melanoma Arrest on the EC

Using dextran to vary the medium viscosity (μ) of the cell suspension, either shear rate ($\dot{\gamma}$) or shear stress ($\tau = \mu\dot{\gamma}$) was held constant while the other was varied in order to determine how fluid shear impacts melanoma cell extravasation. We used ultra-high molecular weight dextran (2×10^6 MW) to avoid potential shielding effects [76] and to achieve a range of media viscosities from 0.7 cP (0% dextran) to 7.0 cP (4% dextran). Control experiments showed 0–4% dextran did not affect cellular adhesion molecule expression or media osmolarity [87]. Cases in which shear stress was held constant and shear rate varied from 55.5 to 555 s^{-1} yielded dramatic variation in C8161 cell extravasation (183 ± 24 cells per mm^2 at 555 s^{-1} to 290 ± 37 cells per mm^2 at 55.5 s^{-1}) that was inversely proportional to the shear rate ($P = 0.041$; Fig. 3a). In contrast, cases in which shear rate was held constant and shear stress ranged from 0.4 to 18 dyn/cm^2 resulted in C8161 migration levels that were not statistically different (Fig. 3b, c). These results suggest that PMN-facilitated migration of melanoma cells is affected by local hydrodynamic convection (which is inversely proportional to cell–cell adhesion contact time), not by the shear stress (which is proportional to fluid force).

To examine how PMN–C8161 cell aggregates adhere to the EI cell monolayer, the PMN tethering frequency was quantified using a parallel-plate flow chamber [53] at 3 shear rates (62.5, 100 and 200 s^{-1}) and 3 media viscosities (1.0, 2.0 and 3.2 cP). As seen in Fig. 4a, the PMN tethering frequency was significantly affected by both shear rate and shear stress. All frequencies were corrected for the decrease in cell flux with increasing shear rate and viscosity, and normalized against the lowest shear stress case. These results are different from the PMN-mediated C8161 migration and tumor adhesion efficiency results shown in Fig. 4b, c. As we see, melanoma *extravasation* and *adhesion efficiency* mediated by PMNs were both affected only by the shear rate, not the shear stress.

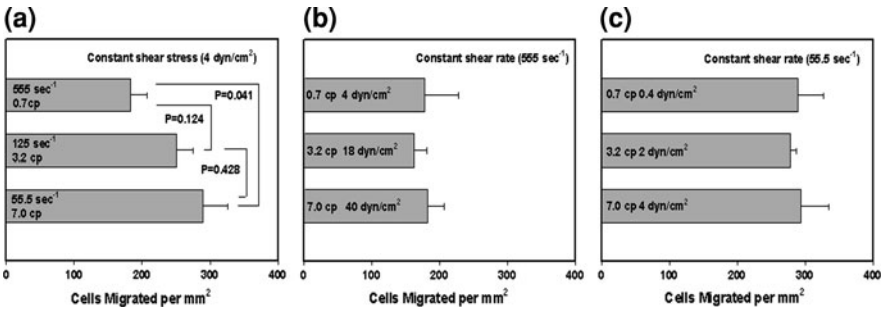

Fig. 3 Shear rate and shear stress were isolated by varying viscosity with dextran-supplemented medium (0–4%). **a** Melanoma migration varies under constant shear stress but increasing shear rate. **b**, **c** Constant shear rate data; migration is unchanged over an order of magnitude of shear stress. All *error bars* are mean ± SEM for $N \geq 3$

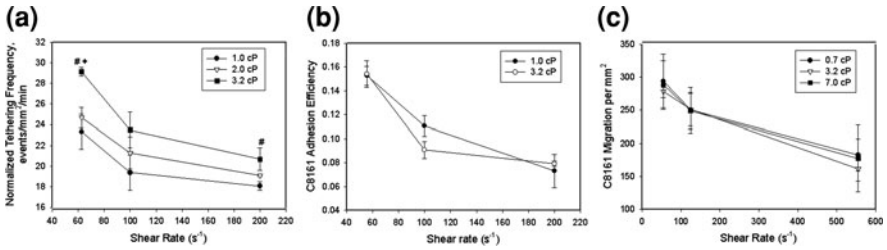

Fig. 4 Effects of shear stress on PMN tethering frequency, melanoma adhesion efficiency and extravasation at fixed shear rates. **a**, **b** fMLP-stimulated PMNs (1×10^6 cells/ml) were perfused into a parallel-plate chamber together with tumor cells (1×10^6 cells/ml). **c** Extravasation of C8161 melanoma cells with PMNs at 3 shear rates with 3 different viscosity media. All *error bars* are mean ± SEM for $N \geq 3$ and tethering data were corrected for cell flux as described by Liang et al. [53]. "**#**" indicates $P > 0.05$ as compared to 1.0 cP case and "**+**" indicates $P > 0.05$ as compared to 2.0 cP case

4.3 Relative Role of LFA-1/Mac-1 and ICAM-1 in PMN-mediated Melanoma Adhesion Efficiency

Function-blocking mAbs against CD11a and CD11b were used to elucidate how melanoma–PMN aggregates were arrested on the EC under shear conditions [53]. Blocking CD11a or CD11b, respectively, inhibited PMN-facilitated melanoma adhesion efficiency partially under all shear conditions tested (Fig. 5a). Results indicate that both LFA-1 and Mac-1 are required for melanoma cells to be maintained on the EI via aggregation to PMNs, but may have different roles. For example, blocking CD11b did not significantly alter the rate of aggregation between entering WM9 cells and tethered PMNs, and LFA-1 alone supported WM9 aggregation with tethered PMNs on the EI initially (Fig. 5b). However, after a period of 3 min, disaggregation of WM9–PMN aggregates on the EI surface proceeded more rapidly in the presence of anti-CD11b mAb than in the control. In comparison, Mac-1-dependent contact with the EI (in the presence of anti-CD11a) proceeded more slowly and reached a maximum which was approximately 25% of the control case. These aggregates remained stably adhered to the EI surface over 5 min (Fig. 5b). These results suggest that LFA-1 alone is necessary and sufficient for the initial formation of melanoma–PMN aggregates, and plays a primary role in the recruitment of melanoma cells to the EC. Mac-1 maintains the stability of melanoma arrest on the EI via the melanoma–PMN aggregation after the initial capture by PMNs.

Blocking ICAM-1 on WM9 (disrupting melanoma adhesion to PMNs) significantly reduced melanoma adhesion efficiency to the monolayer similarly to the cases of blocking E-seletin or ICAM-1 on the EI cells, suggesting that EC activation for PMN tethering is necessary in mediating melanoma cell arrest within the microcirculation.

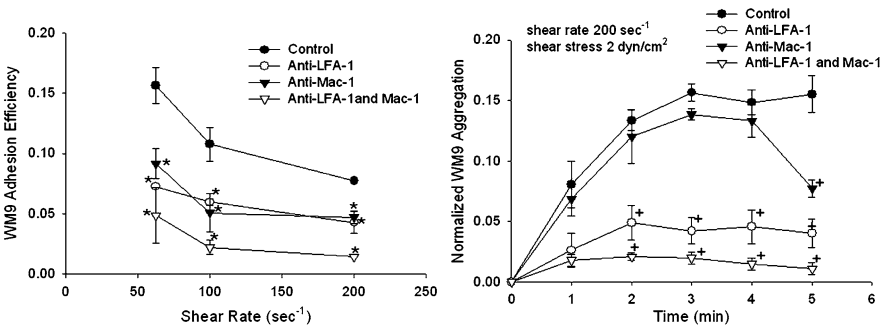

Fig. 5 Contributions of LFA-1 and Mac-1 to WM9 arrest to the EI substrate as a result of WM9-PMN collisions. **a** WM9 adhesion efficiency at different shear rates over a period of 5 min. Shear stress was 2 dyn/cm^2 for the data shown. **b** Normalized WM9 aggregation during each time course in the entire parallel-plate flow assay. $^*P < 0.05$ compared with control at the same shear rate. $^+P < 0.05$ compared with control at the same time point. Values are mean ± SEM for $N \geq 3$

4.4 Melanomas Increase Endogenous Production of IL-8 in PMNs

We first used a commercial cytokine blot (Raybiotech) to screen cytokines/chemokines in PMN–melanoma cell co-culture media. Melanoma cells and PMNs (cell # ratio was 1:1) were co-cultured in contact with each other for 6 h as described [86]. The blot detects for 42 separate cytokines in the layout shown in Fig. 6. Our first set of experiments examined those soluble factors that were secreted from C8161–PMN or WM9–PMN co-culture. In particular, we found: IL-1β, IL-6, IL-8, MCP-1 and GRO.

ELISA was subsequently used to determine the relationship between tumor metastatic potential and cytokine expressions in melanoma–PMN co-culture. Four human melanoma cell lines 1205Lu, WM9, C8161 and WM35 (ranged from high to low in metastatic potential; [74], were examined for cytokine and chemokine induction in melanoma–PMN co-cultures. PMNs co-cultured either in a Transwell (non-contact) or in contact with C8161, WM9, 1205Lu increased IL-8 expression above summed background levels from individual cell-type culture, but there was no change in IL-8 following co-culture with WM35 (Fig. 7a). In addition, co-culture of 1205Lu or WM9 with PMNs induced IL-8 production in a time-dependent manner (Fig. 7b). In contrast, the IL-8 production from WM35–PMN co-culture did not change over time. The induction of IL-8 was comparable whether cells were cultured in direct-contact or separated in a Transwell culture system indicating that *soluble signaling factorsare actively involved*. In further experiments to identify which cell type contributed to the increased amount of IL-8 in PMN–melanoma co-cultures, cell lysates were prepared from PMNs and melanoma cells following Transwell co-culture, and levels of IL-8 were detected

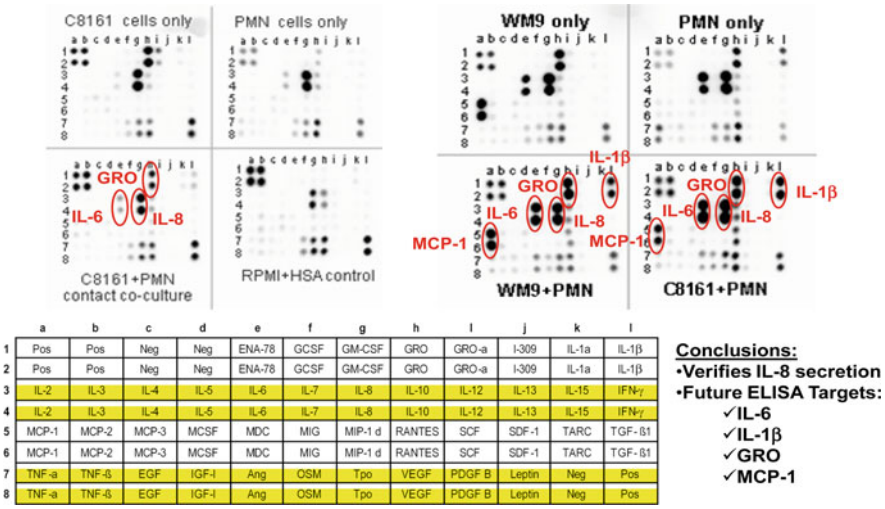

	a	b	c	d	e	f	g	h	i	j	k	l
1	Pos	Pos	Neg	Neg	ENA-78	GCSF	GM-CSF	GRO	GRO-a	I-309	IL-1a	IL-1β
2	Pos	Pos	Neg	Neg	ENA-78	GCSF	GM-CSF	GRO	GRO-a	I-309	IL-1a	IL-1β
3	IL-2	IL-3	IL-4	IL-5	IL-6	IL-7	IL-8	IL-10	IL-12	IL-13	IL-15	IFN-γ
4	IL-2	IL-3	IL-4	IL-5	IL-6	IL-7	IL-8	IL-10	IL-12	IL-13	IL-15	IFN-γ
5	MCP-1	MCP-2	MCP-3	MCSF	MDC	MIG	MIP-1 d	RANTES	SCF	SDF-1	TARC	TGF-ß1
6	MCP-1	MCP-2	MCP-3	MCSF	MDC	MIG	MIP-1 d	RANTES	SCF	SDF-1	TARC	TGF-ß1
7	TNF-a	TNF-ß	EGF	IGF-I	Ang	OSM	Tpo	VEGF	PDGF B	Leptin	Neg	Pos
8	TNF-a	TNF-ß	EGF	IGF-I	Ang	OSM	Tpo	VEGF	PDGF B	Leptin	Neg	Pos

Fig. 6 Raybiotech cytokine blot from respective C8161 and WM9 co-culture with the PMNs found IL-1β, IL-6, GRO, and MCP-1. The sensitivity for Raybiotech was at 1 pg/ml

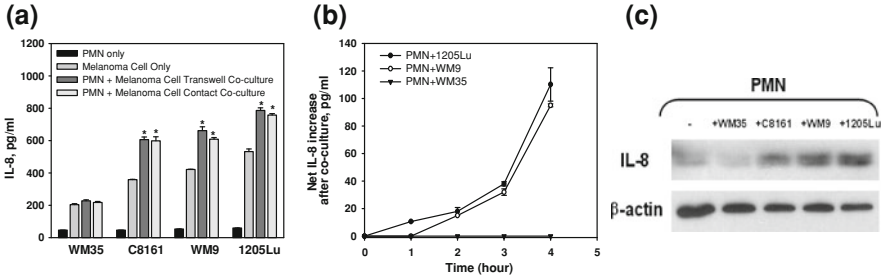

Fig. 7 Co-culturing PMNs with melanoma cells induces IL-8 increase. **a** Induction of IL-8 in PMN–melanoma cell (1205Lu, WM9 and C8161) co-cultures (contact or Transwell). $*P < 0.05$ compared with the sum of IL-8 expression from the PMN and melanoma only. **b** IL-8 increased after PMN co-culturing with 1205Lu and WM9 in a time-dependent manner. Co-culturing PMNs with WM35 did not increase IL-8 secretion over time. Values are mean ± SEM for $N \geq 6$. **c** Melanoma cells induce IL-8 production in PMNs. PMN lysates were analyzed by Western blotting with mAb against IL-8. The same blot was stripped and re-probed with mAb to β-actin. C8161, WM9 and 1205Lu induced IL-8 production in PMNs, whereas WM35 did not. Results are representative of three experiments

by Western blotting [74]. As shown in Fig. 7c, melanoma cells with higher metastatic potentials (1205Lu, WM9 and C8161) induced higher IL-8 production in PMNs, while WM35 did not induce IL-8 protein in PMNs. In contrast, IL-8 expression in melanoma cells *did not* significantly change when co-cultured in the presence or absence of PMNs [21].

4.5 Endogenous IL-8 Influence PMN Recruitment in Melanoma Cells

To characterize immunoediting of PMN activation, especially via the endogenous IL-8 chemokine within the PMN–melanoma microenvironment, Mac-1 expression on PMNs co-cultured with C8161 cells was examined using flow cytometry. Untreated PMNs and PMNs treated with blocking antibodies for IL-8 receptors CXCR1/2 were co-cultured with C8161 cells either in contact or separated by a Transwell insert [87]. Figure 8a indicates that non-CXCR1/2-blocked PMNs co-cultured with C8161 cells experienced a nearly four-fold increase in Mac-1 expression levels over those cultured alone for 4 h. The increase in Mac-1 was apparent after only 30 min of co-culture and became significant after 2 h of co-culture (data not shown). PMNs with antibody blocked CXCR1/2 showed no change in Mac-1 levels after co-cultured with C8161 cells compared with PMNs cultured alone (Fig. 8a). To understand the possibility that secreted soluble factors could be an immuno-stimulus responsible for melanoma–PMN communication, receptors CXCR1/2 on PMNs were functionally blocked. C8161 cell extravasation (assayed by the flow-migration chamber) dramatically decreased at a shear rate of 55.5 s^{-1} in the presence of CXCR1/2-blocked PMNs compared with unblocked PMNs (39% decrease), or additional IL-8-activated PMNs (73% decrease) as shown in Fig. 8b. Such effects on C8161 cell extravasation will be amplified under higher shear-rate conditions. Neutralizing anti-IL-8 mAb (1 μg/ml) was also used to bind soluble IL-8, induced or liberated by the melanoma cells, which showed similar inhibitory effects on melanoma migration as those CXCR1/2-receptor blocked PMN cases (Fig. 8b).

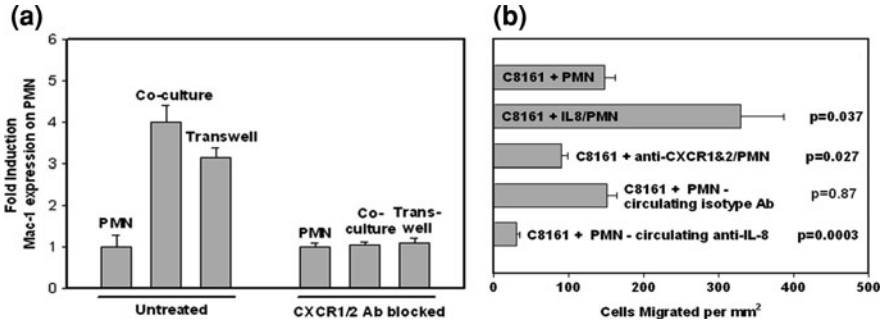

Fig. 8 Melanoma cell extravasation under flow conditions is modulated by endogenous IL-8. **a** Fold induction of Mac-1 on PMNs after co-culture with C8161. Blocking the IL-8 receptors on PMNs resulted in no increase in Mac-1. **b** Effects of IL-8 on melanoma migration mediated by PMNs. Isotype control found statistically the same as the case of "C8161 + PMN". All co-cultures were in 4 h, and all flow shear stresses were 0.4 dyn/cm^2

4.6 IL-1β and IL-6 Synergistically, but not Individually, Stimulate IL-8 Production in PMNs

After 4-6 h of co-culture, ELISAs were preformed to measure GRO-α, IL-1β, IL-6 and MCP-1 from supernatants obtained from cultures of individual cell types (e.g., PMNs only or melanomas only) or PMN–melanoma co-cultures. For all 4 melanoma cell lines tested, co-culture of PMNs with highly metastatic 1205Lu cells significantly induced IL-6 above the summed IL-6 from separate cultures (data not shown). IL-1β was produced by PMNs or melanoma cells cultured alone. It was increased after C8161, WM9 and 1205Lu were co-cultured with PMNs, albeit at a small amount (<10 pg/ml). In addition, GRO-α and MCP-1 were constitutively expressed by melanomas and co-culturing with PMNs did not change their production levels.

To investigate potential effects of different soluble factors induced or liberated by melanoma cells on IL-8 production in PMNs, human recombinant proteins including GRO-α, IL-6, and IL-1β were used to stimulate PMNs [74]. ELISA results indicated that none of these cytokines or chemokines alone was sufficient to induce IL-8 production compared with untreated PMNs (Fig. 9); however, stimulating cells with the combination of IL-1β and IL-6 increased IL-8 production in PMNs. We further confirmed the combinatorial role of IL-1β and IL-6 in melanoma-induced IL-8 induction by showing that IL-8 was significantly reduced from 781 ± 6.3 pg/ml to 680 ± 10.1 pg/ml ($P < 0.05$) in 1205Lu melanoma–PMN co-culture in the presence of neutralizing antibody against IL-1β and IL-6 (only together; not individually), indicating that IL-1β and IL-6 provide a *synergistic activation* of IL-8 in PMNs in response to melanomas.

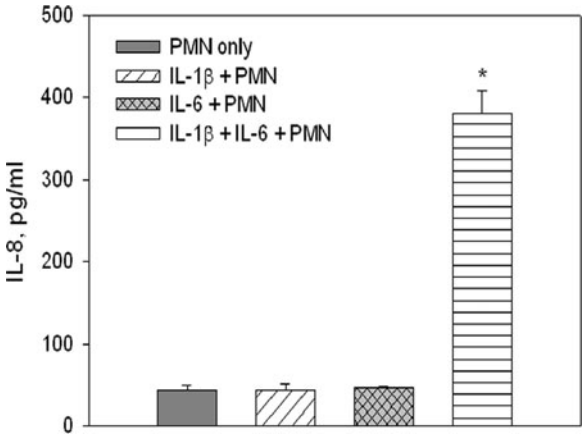

Fig. 9 IL-1β and IL-6 synergistically increased IL-8 production in PMNs compared with untreated PMNs. *$P < 0.05$ compared with other three cases. Values are mean ± SEM for $N > 3$

4.7 Fluid Convection Affects IL-8-mediated PMN Activation Within the Tumor Microenvironment

To investigate how the fluid convection affects IL-8 signaling by melanoma cells, which in turn affects the expression of LFA-1 and Mac-1 on PMNs and modifies tumor cell adhesion to the EC, Comsol Multiphysics was used to simulate the convection and diffusion of IL-8 from a moving cell under flow conditions (Fig. 10). To simulate the system, a tumor cell was assumed to be in the free stream in the near-wall region and its velocity was derived based on the shear flow condition, using Eq. 3. A PMN was assumed to roll on the EC at the experimentally derived average rolling velocity for the shear condition. The local IL-8 concentration near a rolling PMN and the time at which the PMN is activated by the transported IL-8 were derived to determine the extent of LFA-1 and Mac-1 activation.

Results indicate that altering the shear rate affects the IL-8 concentration near a rolling PMN at different time points (Fig. 11). When the shear rate was constant at 62.5 s^{-1}, the IL-8 concentration near a rolling PMN and the stimulation time remained constant under various shear stresses (Fig. 11a). In contrast, when the shear stress was constant at 2 dyn/cm^2 and shear rate increased from 62.5 to 200 s^{-1}, it took less time to activate the PMNs under a higher shear rate (Fig. 11b). These data suggest that the fluid convection affects the local concentration of IL-8 near a downstream PMN as well as the time needed to activate the PMN, which is important in up-regulating the expression of LFA-1 and Mac-1.

The changes of LFA-1 and Mac-1 site densities on a rolling PMN upon stimulation from IL-8 secreted by a tumor cell in a shear flow were then calculated based on the flow cytometry measurements on LFA-1/Mac-1 expressions on

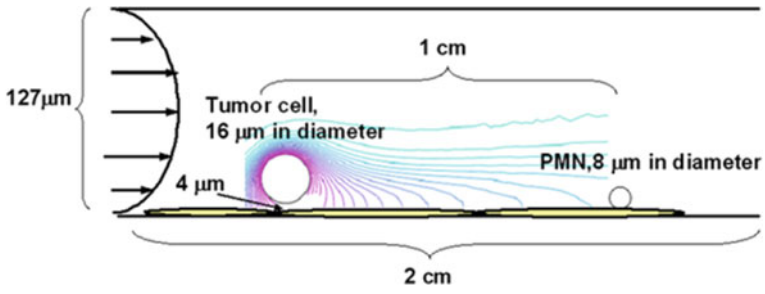

Fig. 10 A parallel plate is 2 cm in length and 127 μm in height. IL-8 was assumed to be constitutively secreted from a moving tumor cell and evenly distributed on cell surface. The concentration of IL-8 secreted by one tumor cell was determined by ELISA as described in Sect. 2. The tumor cell was assumed to travel in a shear flow near the EC substrate; while a PMN was assumed to be rolling on the EC in the downstream. Simulation started when a tumor cell and a PMN were 1 cm apart. The concentration of IL-8 secreted by the moving tumor cell near the rolling PMN was derived by using Comsol Multiphysics simulation under various shear flow conditions

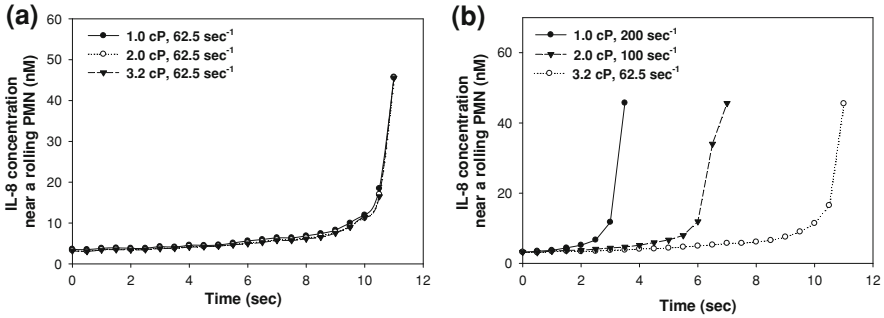

Fig. 11 The concentration of IL-8 near PMN and the time it activates PMN under different shear flow conditions. Comsol Multiphysics was used to simulate the diffusion of IL-8 as described in Sect. 2, and then the concentration of IL-8 near the PMN was derived. The activation time of IL-8 on the PMN was determined by the duration melanoma cell used to reach the PMN. **a** IL-8 concentration near a rolling PMN and the time it activated the PMN was about the same under same shear rate but different shear stresses, **b** the higher shear rate let tumor cell travel faster towards PMN, resulting in shorter period of stimulation on PMN under same shear stress but different shear rates

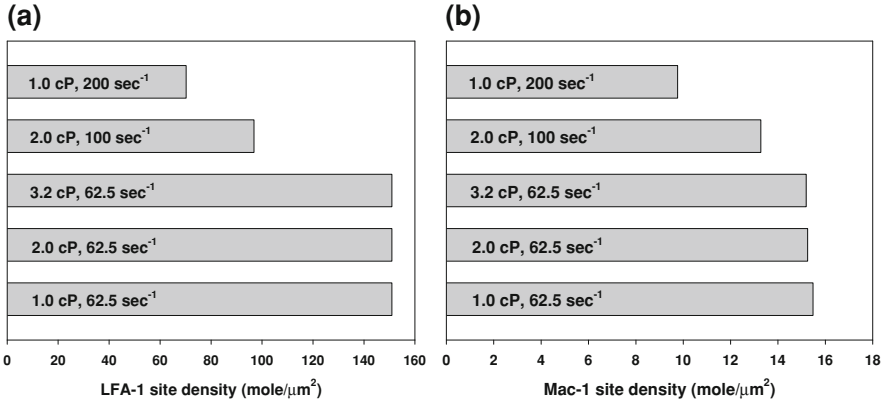

Fig. 12 LFA-1 and Mac-1 expressions upon activation of IL-8 from tumor cell under different shear flow conditions. LFA-1 and Mac-1 site densities on the PMN under various shear conditions were derived using the site density expression data [51] and the simulation data shown in Fig. 11. **a** Mac-1 expression, **b** LFA-1 expression. At the same shear rate, LFA-1 and Mac-1 expressions on PMN did not have much difference although the shear stresses were different. In contrast, when the shear stress is the same, the increase of shear rates reduced LFA-1 and Mac-1 expressions

PMNs stimulated by dose-dependent IL-8 (Fig. 12). Results indicate that at a constant shear rate, 62.5 s^{-1}, varying the shear stress does not alter the expressions of LFA-1 and Mac-1 on PMNs. However, at a constant shear stress, 2 dyn/cm^2, LFA-1 and Mac-1 expressions on PMNs were reduced when shear rate is increased.

4.8 Melanoma–PMN Binding Association Rate is Affected by the Shear Rate

To quantify the increase in binding potential when a PMN is stimulated by IL-8 secreted from a melanoma cell, the association rate governing the binding of the cells was calculated. The likelihood of binding between the two cells is determined by the number and availability of adhesion molecules on both cells, as well as the intrinsic binding properties of the molecules. Equation 6 was used to calculate the association rate for an LFA-1 and a Mac-1 molecule binding with an ICAM-1 molecule when a melanoma cell is 1 μm from a rolling PMN under various shear conditions. The surface densities of LFA-1 and Mac-1 molecules on a PMN stimulated by melanoma cell-derived IL-8 (Fig. 12) were used for n_L (Eq. 6). A constant separation distance and contact area were assumed for the six shear flow conditions.

The association rates indicate that the likelihood of an LFA-1/ICAM-1 bond forming between a melanoma cell and PMN is almost doubled when the shear rate is decreased from 200 to 62.5 s^{-1} and the shear stress is considered constant (Fig. 13). For Mac-1/ICAM-1 binding, the likelihood increases by more than twice when the shear rate is decreased. When the shear rate remains constant, however, and the shear stress is increased, the binding potential for both molecules remains constant [51].

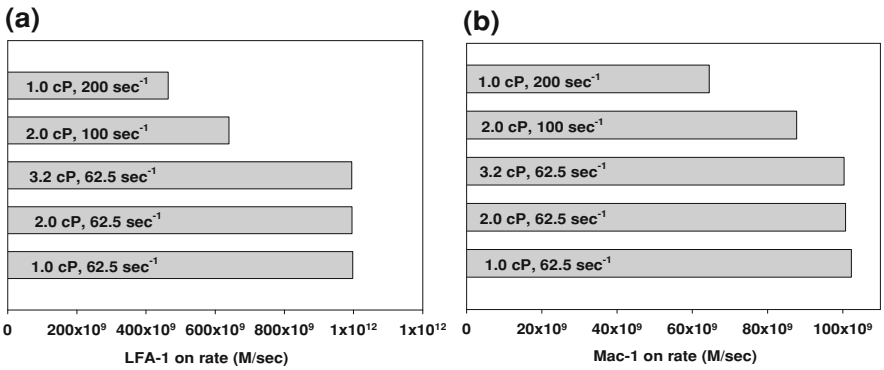

Fig. 13 Association-rate for LFA-1 and Mac-1 binding to ICAM-1 upon stimulation from IL-8 under different shear flow conditions. Association-rates for LFA-1 and Mac-1 binding to ICAM-1 when the molecules are up-regulated due to IL-8 stimulation from an upstream melanoma cell. **a** LFA-1/ICAM-1 binding association-rate, **b** Mac-1/ICAM-1 binding association-rate. Both the LFA-1/ICAM-1 and Mac-1/ICAM-1 association-rates are dependent on the shear rate and not the shear stress of the flow

4.9 Bond Force Between Melanoma Cell and PMN Under Different Shear Conditions

The dissociation of β_2 integrin bonds with ICAM-1 is governed by the force applied to them. In order to compare the effect the shear rate and shear stress have on the bond dissociation, a single bond was examined under various flow conditions. A numerical model was used to simulate a melanoma cell and a stationary PMN to determine the peak force applied to the melanoma cell due to a single bond between the cells under various shear conditions [34, 51]. In all simulations, the melanoma cell was initially located above and slightly downstream of the stationary PMN (Fig. 14) and then was allowed to move freely at its steady state velocity for each flow condition. The melanoma cell was acted upon by the fluid, bond, and repulsion forces until a maximum bond force was reached. Although adhesion between a melanoma cell and a PMN may be mediated by more than a single bond, the trend in bond dissociation over various flow conditions is expected to be similar for all bonds.

Results indicate that increasing the shear rate from 62.5 to 200 s^{-1}, while maintaining a constant shear stress, increased the maximum bond force by approximately 11%, but increased the rate at which it was reached by almost four times (Fig. 15). Increasing the shear stress from 0.625 to 2 dyn/cm^2, while keeping a constant shear rate, increased the maximum bond force by almost twice, and decreased the rate which it was reached by almost five times. Together, these results suggest that the dissociation of bonds between the melanoma cell and PMN is governed by both the shear stress and the shear rate.

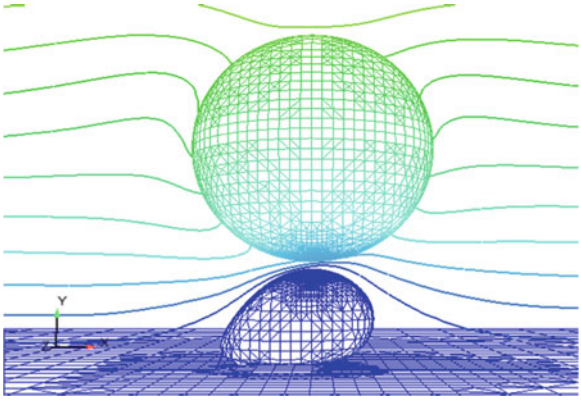

Fig. 14 Melanoma cell bound to a stationary PMN via a single bond. Initial configuration of the cells, with a line between them to represent the location of the bond

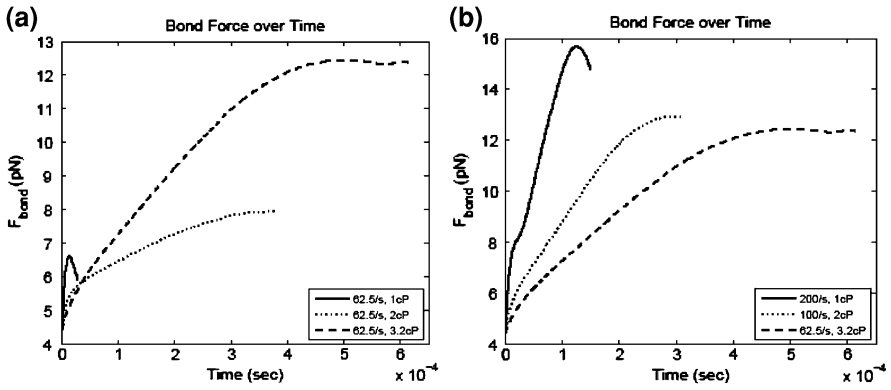

Fig. 15 Force on a melanoma cell due to a single bond with a stationary PMN under various shear conditions. Melanoma cell motion was simulated numerically due to the action of a single bond with a PMN. **a** Under the same shear rate, at higher shear stress (due to higher viscosity), the bond force peaks slower, but at a greater force than at lower shear stress, **b** Under the same shear stress, at a higher shear rate, the bond force reaches a maximum faster and at a greater force than at lower shear rates. These results indicate the maximum force applied to the melanoma cell due to the bond and the time it takes to reach it is dependent on both shear rate and shear stress

4.10 Melanoma Interactions with the Endothelial Cells

Melanoma cells induce VE-cadherin junction disassembly through tumor-secreted soluble proteins and endothelial VCAM-1 receptor-mediated events. Fluorescence imaging of HUVECs stained for VE-cadherin showed disruption of VE-cadherin junctions when co-cultured with A2058 melanoma cells over time (Fig. 16). Compared to intact VE-cadherin junctions in the case of HUVECs cultured in control medium (Fig. 16a), the breakdown of VE-cadherin was evident through the discontinuity of the green fluorescent line labeling the VE-cadherin junctions (gaps at 45 min are shown in Fig. 16b). The corresponding bright field images (Fig. 16c) show that the A2058 melanoma cells were located within the sites of gap formation. These results show that highly metastatic melanoma cells induce breakdown of VE-cadherin junctions.

Disruption of VE-cadherin was identified from analysis of discontinuity of green fluorescence at VE-cadherin junctions between HUVECs. Gap area within disrupted VE-cadherin junctions was determined from six images (see asterisks in Fig. 16b as an example). Gap area was quantified as the ratio of pixels within all the gaps and the total number of pixels in one image [39]. The average% endothelial gaps was calculated from six images and plotted as a function of time (Fig. 16d).

To determine if VE-cadherin disassembly was primarily mediated by soluble factor or receptor/ligand binding signals, HUVECs were brought in contact with tumor conditioned medium (TCM) or melanoma cells with increasing metastatic potential for 45 min. Melanoma cells with increased metastatic potential, or TCM

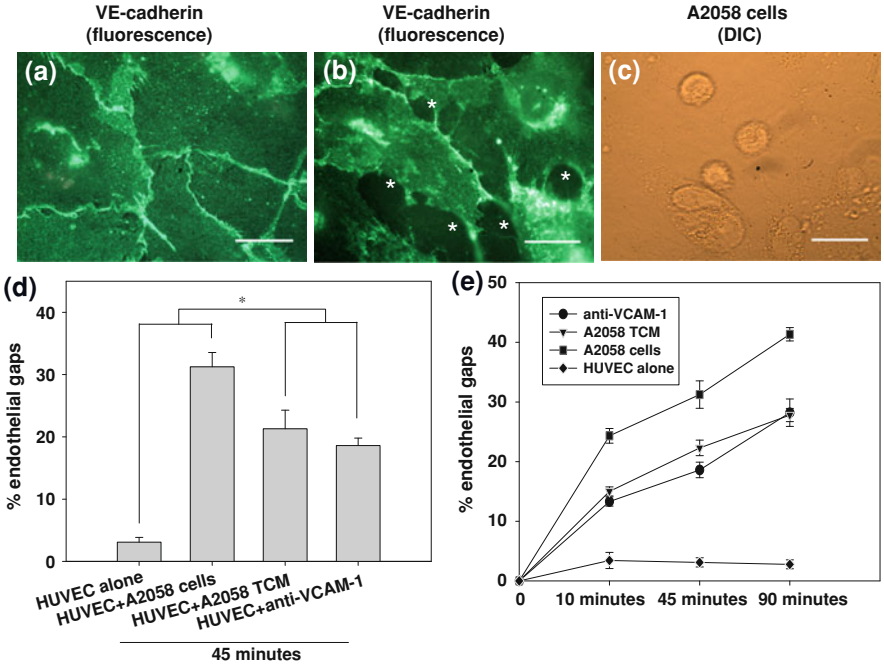

Fig. 16 Melanoma cells induce VE-cadherin disassembly. *Bars* 5 μm (**a**–**h**). **a** VE-cadherin junctions in HUVECs without A2058 melanoma cells. HUVECs were fixed, permeabilized, and stained with anti-VE-cadherin mAb followed by Alexa 488. Representative fields were examined and show intact VE-cadherin junctions indicated by intact *green fluorescent borders*. **b** Disruption of VE-cadherin junctions after HUVECs were in direct contact with A2058 tumor cells for either 10, 45, or 90 min (45 min is shown) using FITC. **c** The same field of view captured under bright field, shows tumor cells in regions coinciding with gap formation. *Asterisks* show disruption of VE-cadherin homodimers. **d** HUVECs co-cultured with TCM or anti-VCAM-1 significantly increase % gap formation compared to HUVECs alone, but less gap formation than A2058 cells co-cultured with HUVECs. *P* values are comparing % endothelial gap of HUVEC + TCM and HUVEC + anti-VCAM-1 with % endothelial gap of HUVEC alone and HUVEC + A2058 cells ($^*P < 0.05$). For all experiments, values are mean ± SD. **e** The % endothelial gaps as a function of time are plotted. Experiments show the % endothelial gaps over time when A2058 TCM, anti-VCAM-1, or A2058 cells are co-cultured with HUVECs over 10, 45, or 90 min

from those cells showed a significant increase in ability to induce gap formation, indicating an increase in VE-cadherin disassembly (Fig. 16d). Also, HUVECs stimulated with anti-VCAM-1 showed a significant increase in gap formation (Fig. 16d) similar to that seen in the presence of TCM. However neither anti-VCAM-1 nor TCM induced the same degree of endothelial gaps as A2058 cells in co-culture with HUVECs (Fig. 16d).

Since both anti-VCAM-1 and TCM induced a gradual increase in the percentage endothelial gap formation over time (Fig. 16e), Khanna et al. [39] further found that VCAM-1 induces a transient VE-cadherin disassembly, while soluble

proteins show a prolonged effect thus enlarging existing gaps to allow the passage of melanoma cells, where the number of gaps after 90 min.

4.11 Secretion of IL-8 and IL-1β by Melanoma Regulates VE-cadherin Junction Disassembly

Cytokines present within TCM secreted by melanoma cells over 24 h were analyzed using a Raybiotech cytokine blot. We found that several cytokines were secreted by melanoma cell types at high concentrations including IL-8, IL-6, IL-1β, and GRO-α [39]. These cytokines were further quantified using ELISA. Clearly, highly metastatic melanoma cells (e.g., 1205Lu) produce higher concentrations of these soluble cytokines compared with those of lesser metastatic potential (e.g., WM35). Stimulating HUVECs with recombinant forms of individual cytokines (at the same concentrations as that in A2058 TCM) showed little increase in the percentage of gap area (Fig. 17a). Combining cytokines in TCM, specifically IL-8 and IL-1β only had additive effects on VE-cadherin disassembly rather than being synergistic (Fig. 17b, c).

Since concentrations of cytokines in TCM are simply the bulk concentrations, HUVECs in direct contact with melanoma cells may sense much higher local concentrations of cytokines within the cell–cell contact region than that found in TCM. We therefore specifically addressed whether IL-8 or IL-1β is involved in this response by neutralizing these cytokines secreted from melanoma cells that are in contact with HUVECs. Neutralization of either IL-8 or IL-1β decreased VE-cadherin disassembly; however, the endothelial gaps were still comparable to that induced by anti-VCAM-1 and there are still more gaps compared to HUVECs alone (Fig. 17d). However, simultaneous neutralization of IL-8 and IL-1β reduced the breakdown of VE-cadherin junctions (Fig. 17e). These results show the importance of these cytokines in melanoma induced VE-cadherin disassembly in the presence of VCAM-1 interactions. Furthermore, using neutralization antibodies we confirmed that IL-8 and IL-1β both play significant roles in the breakdown of VE-cadherin junctions.

Recent studies by Khanna et al. [39] has further found that melanoma signals via TCM soluble proteins and VCAM-1-mediated receptor induce phosphorylation of p38 MAP kinase that regulates VE-cadherin disassembly. The functional role of p38 in endothelial cells during melanoma extravasation has also been examined using small interfering RNA (siRNA) approaches. siRNA mediated knockdown of p38 (and thus p-p38) in HUVECs was confirmed using western blotting. When p38 expression was knocked down, melanoma extravasation through the endothelial barrier (after 4 h) decreased to nearly 40% compared to the control [39]. These results show that p38 is not only important in the regulation of VE-cadherin junctions, but also in overall tumor extravasation.

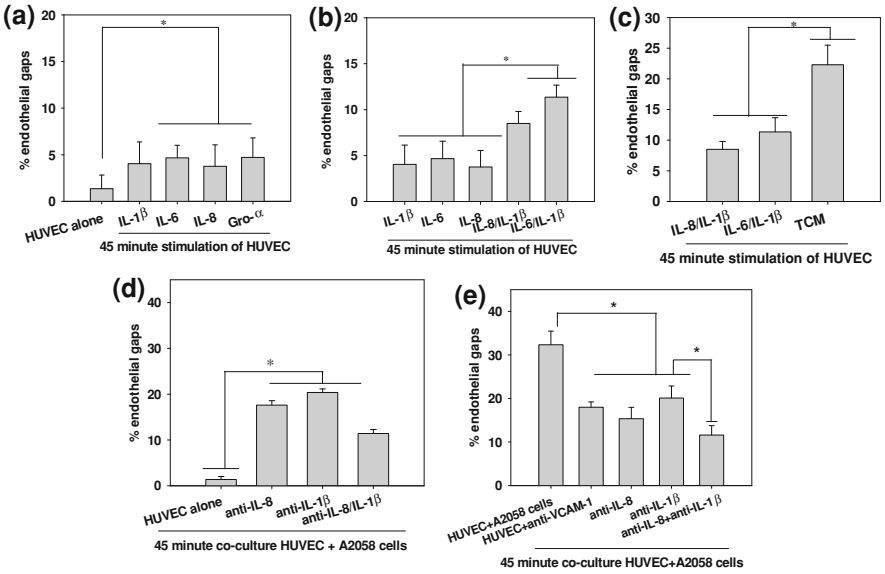

Fig. 17 **a–c** IL-8 and IL-1β have additive rather than synergistic effects on VE-cadherin disassembly: **a** the indicated cytokines induced VE-cadherin disassembly. *P* values are comparing % gap induced by cytokines with % gap of HUVEC alone ($^*P < 0.05$). **b** Stimulation of HUVECs with recombinant combined forms of IL-8/IL-1β or IL-6/IL-1β induced additive effects on endothelial gap formation compared with individual forms. Concentrations of cytokines were based on TCM concentrations measured using ELISA [39]. *P* values ($^*P < 0.05$) compare % gap area of combinations of cytokines with % gap of HUVEC + IL-8, HUVEC + IL-6, HUVEC + IL-1β. **c** Combinations of cytokines induced significantly less gap formation than TCM alone. *P* values are comparing % gap area of TCM with % gap of HUVEC + IL-8/IL-1β, HUVEC + IL-6/IL-1β. **d–e** Anti-VCAM-1 and neutralization of both IL-8 and IL-1β dramatically reduces the breakdown of VE-cadherin: **d** HUVECs were contacted with A2058 cells + anti-IL-8, A2058 cells + anti-IL-1β, or A2058 cells + anti-IL-8 + anti-IL-1β. *P* values are comparing each experimental condition with % endothelial gap areas during HUVEC alone ($^*P < 0.05$). **e** Using the same controls as in panel **d**, data was graphed to make comparisons between the effects of neutralizing individual and pairs of cytokines. HUVECs were contacted with either A2058 cells, A2058 cells + anti-VCAM-1, A2058 cells + anti-IL-8, A2058 cells + anti-IL-1β, or A2058 cells + anti-IL-8 + anti-IL-1β. Neutralization of both IL-8 and IL-1β dramatically decreased % endothelial gaps compared to HUVECs stimulated with anti-VCAM-1 or anti-IL-8 and anti-IL-1β alone. *P* values are comparing each experimental condition with % endothelial gap areas for HUVEC + anti-VCAM-1, HUVEC + A2058 cells + anti-IL-8, and HUVEC + A2058 cells + anti-IL-1β ($^*P < 0.05$). Values for graphs are mean ± SD

4.12 Transient Melanoma Cells in Lungs Secrete IL-8 to Attract PMNs Thereby Promoting Retention in vivo

To demonstrate that transient metastatic melanoma cells in lungs secrete IL-8, which recruited PMNs resulting in cellular interactions promoting melanoma cell retention, GFP-tagged 1205Lu human melanoma cells nucleofected with siRNA targeting IL-8 were injected into the lateral tail vein of nude mice. One hour later

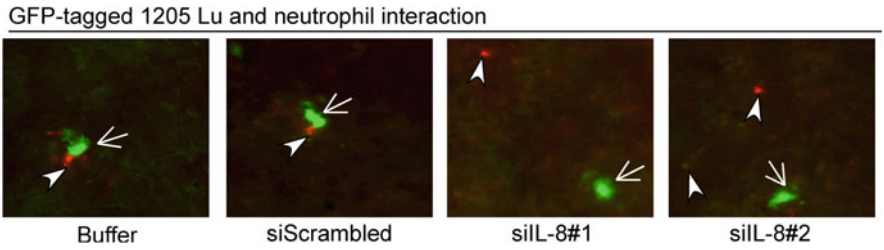

Fig. 18 Decreasing IL-8 secretion from melanoma cells reduced interaction with exogenously added human PMNs in lungs. Co-localized PMNs (*red; arrow heads*) and melanoma cells (*green; arrows*) were more abundant in controls compared to melanoma cells having reduced IL-8 secretion (siIL-8#1&2; 100×)

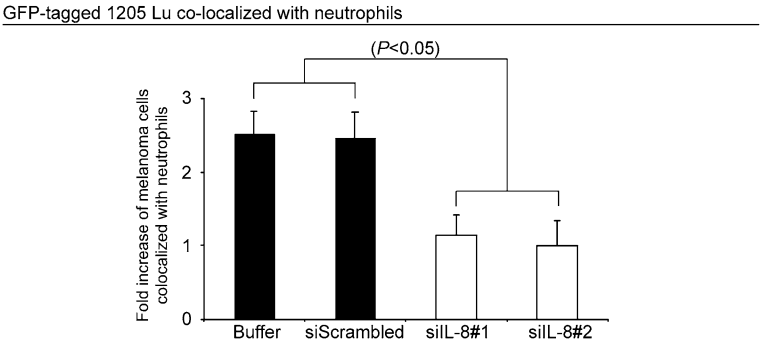

Fig. 19 Decreased IL-8 secretion from melanoma cells, reduced human PMN co-localization with melanoma cells in the lungs of nude mice. All data are mean ± SEM, representing at least 2 independent experiments

human CellTracker Orange CMTMR stained human PMNs were injected in the opposite tail vein. Twenty-four hours later, co-localized green melanoma cells and red PMNs were photographed and quantified (Fig. 18).

Decreasing IL-8 expression in melanoma cells (cases in siIL-8#1 and siIL-8#2) reduced co-localization with PMNs by ~60% compared to buffer and scrambled siRNA controls (Fig. 19). Thus, transient melanoma cells secrete IL-8 to attract PMNs, which then interact with the melanoma cells promoting shear-resistant tethering retention within the lung circulation to enhance the possibility of extravasation under flow conditions and subsequent metastasis development.

4.13 Decreasing Secreted IL-8 from Metastatic Melanoma Cells Reduced in vivo Lung Metastasis Development

While decreasing IL-8 secreted from melanoma cells led to less interaction with PMNs and retention of fewer cells in lungs, it was uncertain whether retained cells

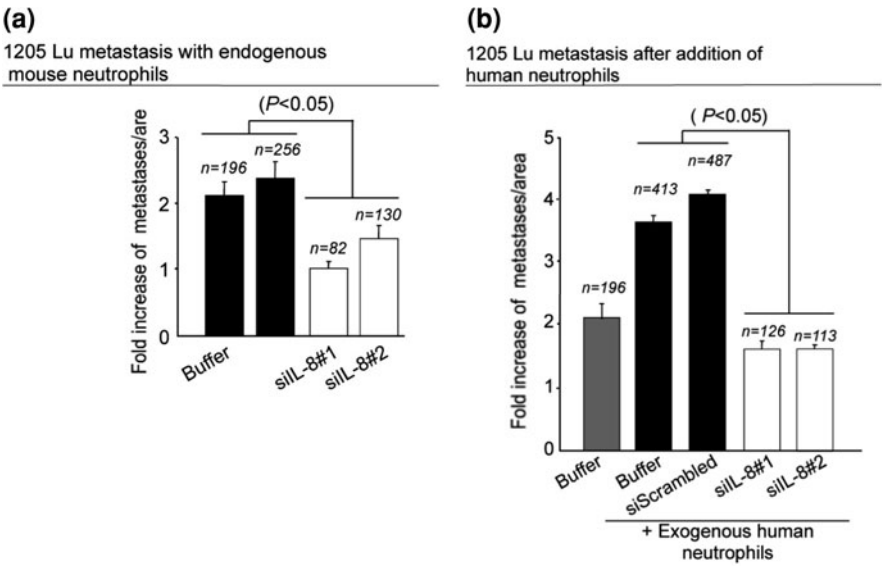

Fig. 20 Decreasing IL-8 expression in melanoma cells reduced lung metastases formation. SiRNA-mediated targeting of IL-8 in melanoma cells, decreased development of GFP-tagged 1205Lu lung metastasis development in the presence of **a** endogenous mouse PMNs; and **b** exogenous human PMNs. Human PMNs doubled rate at which melanoma lung metastases developed. Decreasing IL-8 secretion from melanoma cells reduced lung metastasis formation to control levels. All data are mean ± SEM, representing at least 2 independent experiments

would develop into more lung metastases. Therefore, siRNA was used to decrease IL-8 protein levels in GFP-tagged 1205Lu cells that were injected into the tail vein of nude mice with only the endogenous mouse PMNs present. Total number of metastatic nodules in the lungs was quantified by fluorescence microscopy 18 days later. Reducing IL-8 expression in and secretion from melanoma cells, decreased number of metastases by 50–60% for 1205Lu (Fig. 20a). Similar results were observed for C8161.Cl9 cells (data not shown).

To show that PMNs in the mouse bloodstream directly interact with transient IL-8 secreting melanoma cells, GFP-tagged 1205Lu cells having endogenous or reduced IL-8 expression were injected into the lateral tail vein of a nude mouse. One hour later, human CellTracker Orange CMTMR stained human PMNs were injected in the opposite tail vein. Total number of metastatic nodules in the lungs was quantified by fluorescence microscopy 18 days later. Addition of human PMNs doubled the number of metastases developing in the lungs of mice compared to that observed with just endogenous mouse PMNs and siRNA-mediated targeting of IL-8 reduced interaction to that observed in control cells (Fig. 20b; scale set to that in Fig. 20a). Thus, decreasing IL-8 levels secreted by melanoma cells reduced interaction with PMNs, which led to the development of fewer lung metastases.

5 Discussions

It is well reported in the literature that tumor cells do not use the same processes that have been described for leukocyte adhesion and migration through an endothelial barrier. While not true of all tumor cells, melanoma cells characterized as highly metastatic, express neither ligands for endothelial selectin molecules nor β_2 integrins at a level necessary to maintain shear-resistant adhesion to endothelial ICAM-1. It has been suggested that initial microvascular arrest of metastasizing tumor cells (from cell lines of six different histological origins) does not occur "leukocyte-like rolling" adhesive interaction with the EC [92].

Recent study showed under dynamic flow conditions, PMNs could influence melanoma cell adhesion to the EC by binding to ICAM-1 on both melanoma and ECs with their β_2 integrins thereby enhancing subsequent melanoma cell migration through the EC (Figs. 2, 5). The difference between the melanoma cell migration and the PMN tethering results under hydrodynamic forces supports the theory that PMNs facilitate TC migration. If melanoma cells used the traditional extravasation mechanism of binding to the EC itself, the response to shear would have been expected to be similar to that seen in single cell tethering (Fig. 4a). However, this is not the case. The results indicate two separate bonds are necessary for melanoma cell migration (Figs. 1a, 2) and the interesting shear-rate dependence becomes apparent (Figs. 3, 4c). The migration experiments examine adhesion of TCs to PMNs after PMNs have already adhered to the EC, whereas the tethering results more specifically focus on PMN to EC adhesion. The migration data shows TC to PMN adhesion is shear-rate dependant and parallel-plate flow chamber data of PMN to TC aggregation shows a similar trend (Fig. 4b). PMN tethering interactions, mediated by selectins, are a prerequisite for subsequent adherence, mediated by β_2 integrins on PMNs binding to ICAM-1 on the EC. Shear rate is inversely proportional to intercellular contact time. By decreasing shear rates, PMNs are in contact with the EC longer, which allows firm binding to occur. The same mechanism may be at play between PMNs and melanoma cells; a lower shear rate may increase the time the cells are in contact, therefore allowing more heterotypic binding and consequently more extravasation.

Jadhav and Konstantopoulos [38] have shown that ICAM-1-expressing colon carcinoma cells (HCT-8) bind to PMN under shear as a function of both contact duration and shear stress whereas sLe^x-expressing carcinoma cells (LS174T) bind to PMN as a function of only contact duration. Their experimental setup was a cone-plate viscometer where two cell types (PMN and TC) were allowed to collide and aggregate under a shear in a free suspension. Similar recent work by Liang et al. [49, 54] had shown shear-rate dependent PMN–melanoma binding under the flow using the cone-plate shear assay. In contrast, the data presented here is from a three-cell system (Fig. 1; PMN, TC and EC) where two separate binding events must occur near a planar surface. Cone-plate shear results on heterotypic cell–cell binding provided excellent insight into the kinetics of PMN–TC aggregation, but might not be expected to explain the results of PMN–TC aggregation mediated

melanoma cell adhesion to and migration through the EC presented here, due to the binding of PMN on the EC in addition to PMN–melanoma aggregation.

IL-8 plays a crucial role in regulating cell function for host defense and natural immunity [91]. IL-8 is released by various cell types, including PMNs, monocytes, T lymphocytes and ECs, upon exposure to inflammatory stimuli, such as TNF-α, IL-1 and LPS [7, 59]. IL-8, in particular, is a major mediator of PMN activation and migration. IL-8 has been previously shown to activate Mac-1 up-regulation in PMNs which facilitates melanoma cell migration under flow conditions [86]. Consistent with this observation, we have also found that IL-8 neutralization leads to a reduction in melanoma transmigration (Fig. 8).

Melanoma cells have been reported to express IL-8 and this influences their oncogenic properties [71], including their metastatic abilities. In the current study [74], we have shown that IL-8 is constitutively produced by melanoma cells regardless of their metastatic potentials (Fig. 7). Furthermore, PMNs do not influence IL-8 expression in melanoma cells. However, tumor metastatic potentials were directly related to the ability of the melanoma cells to induce IL-8 production in PMNs (Fig. 7). IL-8 has been shown to induce Mac-1 expression in PMNs; therefore, melanoma cells with high metastatic potentials (1205Lu, WM9 and C8161) directly alter the microenvironment by modifying PMN function and expression of chemokines and integrins to promote extravasation through β_2 integrin-ICAM-1 bindings under flow conditions, while there is no significant effect under static conditions.

PMN-generated CXC chemokines can act through autocrine or paracrine mechanisms to amplify PMN inflammatory activities via suppression of apoptosis [28]. In the study, paracrine mechanisms are operative since melanoma-derived IL-8 is required for induction of IL-8 in PMNs (Fig. 8). IL-8 binds with high affinity to two distinct receptors, CXCR1 and CXCR2. Blocking these two receptors on PMNs significantly reduced IL-8 induction after PMN and melanoma cells are co-cultured, but did not reduce the production of IL-8 to the summed background level of the PMN and melanoma cells indicating that there are cytokines other than IL-8, such as IL-1β and IL-6, which are responsible for the increase of IL-8 secretion after co-culture (Fig. 9).

One important mode of intercellular communication in cancer hematogenous metastasis occurs through the soluble chemokines released by involved cells, which may be affected by hydrodynamic shear flow. Melanoma cells constitutively secrete the inflammatory chemokine IL-8. When in a shear flow, this IL-8 is transported and stimulates other cells in the flow. A numerical model was employed to investigate the effects of the transported IL-8 on PMNs in a shear flow [51]. Results show that shear rate, rather than shear stress, affects the IL-8 concentration near a rolling PMN at different time points (Fig. 11). Thus, the surface density of LFA-1 and Mac-1 on the stimulated PMN is also shear rate dependent (Fig. 12). The binding potential of IL-8 stimulated PMNs (mediated by both LFA-1/ICAM-1 and Mac-1/ICAM-1 binding) followed the same shear rate dependent trend, which implies the transport of IL-8 to a rolling PMN contributes

to the shear rate dependence of melanoma cell adhesion to the EC in the presence of PMNs in a hydrodynamic shear flow.

The dissociation of melanoma cells from PMNs is determined by the force applied to the intercellular bonds. In the numerical simulations presented, the force applied to a single bond between the cells was modeled in order to directly compare the results under various flow conditions. Though cell adhesion is expected to be mediated by more than one bond, the trend of bond dissociation is expected to be similar to the trend seen in the single bond situation. Thus, we can make a general conclusion on the trend in bond dissociation between the cells based on the numerical simulations. Changing either the shear rate or the shear stress altered the trend of the force applied to the melanoma cell by a single bond. This suggests that the dissociation of the bonds between a melanoma cell and a PMN is dependent on both the shear rate and shear stress. Since the melanoma cell–PMN aggregation through β_2 integrins and ICAM-1 is affected by shear rate, but the dissociation of bonds between the cells is dependent on both the shear rate and shear stress, it is probable that the formation of bonds between the two cells plays a more important role in determining the aggregation potential than the bond dissociation (Fig. 15).

The interaction of TCs with ECs is a key step in facilitating melanoma metastasis. However, research on drug therapies to treat such cancers has focused on single cell studies without considering the effects of tumor interactions with normal cell physiology. In several studies A2058 melanoma cells were used to study VE-cadherin disassembly since they are characterized by highly invasive capabilities and secrete high levels of soluble proteins, including growth factors and moderate levels of IL-8, IL-6, IL-1β, and GRO-α, and serve as an ideal system in studying metastasis [55, 74, 93]. Melanoma cells induce an increase in endothelial gap formation with increasing tumor cell concentration. In addition, melanoma cells with higher metastatic capabilities induce larger sized gap areas that increase over time corresponding to a higher degree of VE-cadherin disassembly. Khanna et al. [39] showed that anti-VCAM-1 initially induces the breakdown of VE-cadherin gap formation, with an increase in the number of gaps with a size of 100,000 pixels or greater after 10 min (Fig. 16). However, after 45 and 90 min, there is a decrease in the number of larger gaps (>100,000 pixels), which shows that the gaps formed by anti-VCAM-1 are closing after 10 min. On the other hand, the release of soluble cytokines including IL-8 and IL-1β prolong the time over which gaps remain open, which correlates with greater VE-cadherin disassembly (Fig. 16). This phenomenon is shown by the gradual increase in the number of large gaps (size of 100,000 pixels or greater) over 90 min. The changes in the number of gaps correlate with phosphorylation of p38 MAP kinase where greater phosphorylation levels of p38 correlate with an increase in the number of gaps [39].

In vivo studies have illustrated that VE-cadherin junction breakdown is an important event during melanoma metastasis [24]. These results show that the injection of nude mice with BV13 (anti-VE-cadherin antibody, which induces VE-cadherin disassembly) results in a four-fold increase in tumor metastasis and

an increase in overall permeability of the endothelial layer. While these studies have focused on the in vivo aspects of VE-cadherin roles, our present in vitro studies provide the evidence that shows the importance of soluble cytokines released from melanoma in regulating VE-cadherin junctions. In particular, we found IL-8 and IL-1β play a prominent role in soluble factor mediated breakdown of VE-cadherin junctions (Fig. 17). These results are consistent with previous in vivo studies that show that $CXCR2^{-/-}$ nude mice injected with melanoma cells result in a decrease in melanoma metastasis [85]. In addition, soluble proteins alone are capable of facilitating the breakdown of these junctions showing that melanoma metastasis is not primarily mediated by adhesion events, but rather that both VCAM-1 and soluble proteins control the temporal disassembly of VE-cadherin.

IL-8, involved in which was originally identified as a PMN chemoattractant [71], is one of the potent inflammatory cytokines influencing melanoma development [2, 9, 83, 84]. However, the role that IL-8 plays mediating PMNs–melanoma interactions within the circulation and thereby promoting in vivo extravasation and subsequent metastasis development has remained uncertain until now.

Recent studies by Huh et al. [36] reported that targeting intracellular IL-8 in melanoma cells using siRNA reduces concentrations of secreted IL-8 in the extracellular microenvironment involving PMNs, which further decreases PMN–melanoma cell aggregations in vivo (Figs. 18, 19) as well as melanoma adhesion to the EC under the dynamic conditions of blood flow. PMN-mediated extravasation of melanoma cells was significantly reduced under flow conditions following inhibition of intracellular IL-8 from melanomas, which is an agreement with prior reports in using neutralizing soluble IL-8 directly within the circulation [21]. Mechanistically, decreasing secreted IL-8 from melanomas disrupted interactions between ICAM-1 expressed on melanoma cells and β_2 integrins, especially Mac-1 on PMNs, which reduced tethering of cells to the lung endothelium under flow conditions. Previous studies have shown that IL-8 secretion from melanoma cells induced endogenous IL-8 production from PMNs after co-culture of PMNs and melanoma cells [74], which was also observed in this study. Thus, tumor-recruited PMNs can play an important role modulating metastasis by holding transient melanoma cell in place within the circulation in the lungs for a sufficient period of time to facilitate extravasation across the endothelial lining to promote development of in vivo metastases (Fig. 20). While the importance of PMN-mediated melanoma extravasation in lung tissue is demonstrated in this report, it is speculated that this process also promotes metastasis in other organs. It is also possible that PMNs hold melanoma cells in place in the capillaries until the cells grow into a secondary tumor, which is a possibility that has not been explored in this study.

In summary, secreted IL-8 from metastatic melanoma cells do not seem to affect cellular growth or tumor development but attracted PMNs to melanoma cells. Up-regulated β_2 integrin expression on PMNs facilitates interaction with melanoma cells, which promoted shear-resistant binding between ICAM-1

expressing melanoma cells and PMNs to the EC, thereby promoting melanoma extravasation and subsequent lung metastasis development. Thus, IL-8 plays an important role in PMN-mediated melanoma cell retention in the lungs and if targeted, could have significant therapeutic potential to reduce metastasis development.

Acknowledgment The author thanks his former and current graduate students for their outstanding contributions to the work presented in this chapter, especially Dr. Margret Slattery, Dr. Shile Liang, Dr. Hsin H. Peng, Dr. Meghan Hoskins, Ms. Payal Khanna and Ms. Tara Yunkunis. He greatly acknowledges Dr. Gavin Robertson, Dr. Arati Sharma, Dr. Avery August, and Dr. Robert Kunz (all from Penn State University), who have contributed significant collaboration to the work. Gratitude also extends to Dr. Meenhard Herlyn (Wistar Institute, Philadelphia, PA, USA), Dr. Danny Welch (University of Alabama, Birmingham), and Dr. Scott Simon (UC Davis, CA, USA) for kindly providing cell lines and reagents. This work was supported in part by the National Institutes of Health grants CA97306 and CA-125707, the National Science Foundation grant CBET-0729091, the Johnson & Johnson Innovative Technology, and the PA Dept. of Health Research Fund SAP #41000-26343.

References

1. Alon, R., Chen, S.Q., Puri, K.D., Finger, E.B., Springer, T.A.: The kinetics of L-selectin tethers and the mechanics of selectin-mediated Rolling. J. Cell Biol. **138**, 1169–1180 (1997)
2. Bar-Eli, M.: Role of interleukin-8 in tumor growth and metastasis of human melanoma. Pathobiology **67**, 12–18 (1999)
3. Bell, G.I.: Models for the specific adhesion of cells to cells. Science **200**, 618–627 (1978)
4. Burdick, M.M., McCarty, O.J.T., Jadhav, S., Konstantopoulos, K.: Cell–cell interactions in inflammation and cancer metastasis. IEEE Eng. Med. Biol. Mag. **20**, 86–89 (2001)
5. Cao, J., Donell, B., Deaver, D.R., Lawrence, M.B., Dong, C.: In vitro side-view imaging technique and analysis of human T-leukemic cell adhesion to ICAM-1 in shear flow. Microvasc. Res. **55**, 124–137 (1998)
6. Cassatella, M.A.: The production of cytokines by polymorphonuclear neutrophils. Immunol. Today **16**, 21–6 (1995)
7. Cassatella, M.A.: Neutrophil-derived proteins: selling cytokines by the pound, Adv. Immunol. **73**, 369–509 (1999)
8. Chambers, A.F., MacDonald, I.C., Schmidt, E.E., Morris, V.L., Groom, A.C.: Clinical targets for anti-metastasis therapy. Adv. Cancer Res. **79**, 91–121 (2000)
9. Crawford, S., Belajic, D., Wei, J., Riley, J.P., Dunford, P.J., Bembenek, S., Fourie, A., Edwards, J.P., Karlsson, L., Brunmark, A.: A novel B-RAF inhibitor blocks interleukin-8 (IL-8) synthesis in human melanoma xenografts, revealing IL-8 as a potential pharmacodynamic biomarker. Mol. Cancer. Ther. **7**, 492–499 (2008)
10. Crissman, J.D., Hatfield, J., Schaldenbrand, M., Sloane, B.F., Honn, K.V.: Arrest and extravasation of B16 amelanotic melanoma in murine lungs: a light and EM study. Lab Invest **53**, 470–478 (1985)
11. Dejana, E., Corada, M., Lampugnani, M.G.: Endothelial cell-to-cell junctions, FASEB J **9**, 910–918 (1995)
12. Del Maschio, A., Zanetti, A., Corada, M., Rival, Y., Ruco, L., Lampugnani, M.G., Dejana, E.: Polymorphonuclear leukocyte adhesion triggers the disorganization of endothelial cell-to-cell adherens junctions. J. Cell. Biol. **135**, 497–510 (1996)
13. Dembo, M., Torney, D.C., Saxaman, K., Hammer, D.: The reaction-limited kinetics of membrane-to surface adhesion and detachment. Proc. R. Soc. Lond. **234**, 55–83 (1988)

14. Dong, C., Aznavoorian, S., Liotta, L.A.: Two phases of pseudopod protrusion in tumor cells revealed by a micropipette. Microvasc. Res.**47**, 55–67 (1994)
15. Dong, C., Cao, J., Struble, E., Lipowsky, H.H.: Mechanics of leukocyte deformation and adhesion to endothelium in shear flow. Ann. Biomed. Eng.**27**, 298–312 (1999)
16. Dong, C., Lei, X.: Biomechanics of cell rolling: Shear flow, cell-surface adhesion, and cell deformability. J. Biomechanics **33**, 35–43 (2000)
17. Dong, C., Robertson, G.P.: Immunoediting of leukocyte functions within the tumor microenvironment and cancer metastasis development. Biorheology **46**, 265–279 (2009)
18. Dong, C., Skalak, R.: Leukocyte deformability: finite element modeling of large viscoelastic deformation. J. Theor. Biol. **158**, 173–193 (1992)
19. Dong, C., Skalak, R., Sung, K.L.P., Schmid-Schonbein, G.W., Chien, S.: Passive deformation analysis of human leukocytes. J. Biol. Eng. **110**, 27–36 (1988)
20. Dong, C., Skalak, R., Sung, K.L.P.: Cytoplasmic rheology of passive neutrophils. Biorheology **28**, 557–567 (1991)
21. Dong, C., Slattery, M.J., Liang, S., Peng, H.H.: Melanoma cell extravasation under flow conditions is modulated by leukocytes and endogenously produced interleukin 8. Mol. Cell. Biomech. **2**, 145–159 (2005)
22. Dong, C., Slattery, M.J., Rank, B.M., You, J.: In vitro characterization and micromechanics of tumor cell chemotactic protrusion, locomotion, and extravasation. Ann Biomed Eng **30**, 344–355 (2002)
23. Drury, J.L., Dembo, M.: Aspiration of human neutrophils: effects of shear thinning and cortical dissipation. Biophys. J. **81**, 3166–3177 (2001)
24. Esser, S., Lampugnani, M.G., Corada, M., Dejana, E., Risau, W.: Vascular endothelial growth factor induces VE-cadherin tyrosine phosphorylation in endothelial cells. J. Cell Sci. **111**, 1853–1865 (1998)
25. Frederick, M.J., Clayman, G.L.: Chemokines in cancer. Expert Rev Mol Med. **200**, 1–18 (2001)
26. Giavazzi, R., Foppolo, M., Dossi, R., Remuzzi, A.: Rolling and adhesion of human tumor cells on vascular endothelium under physiological flow conditions. J. Clin. Invest. **92**, 3038–3044 (1993)
27. Gopalan, P.K., Smith, C.W., Lu, H., Berg, E.L., McIntire, L.V., Simon, S.I.: Neutrophil CD18-dependent arrest on intercellular adhesion molecule 1 (ICAM-1) in shear flow can be activated through L-selectin. J. Immunol. **158**, 367–375 (1997)
28. Grutkoski, P.S., Graeber, C.T., Ayala, A., Simms, H.H.: Paracrine suppression of apoptosis by cytokine-stimulated neutrophils involves divergent regulation of NF-kappaB, Bcl-X(L), and Bak, Shock **17**, 47–54 (2002)
29. Hentzen, E.R., Neelamegham, S., Kansas, G.S., Benanti, J.A., McIntire, L.V., Smith, C.W., Simon, S.I.: Sequential binding of CD11a/CD18 and CD11b/CD18 defines newtuophil capture and stable adhesion to intercellular adhesion molecule-1. Blood **95**, 911–920 (2000)
30. Hodgson, L., Dong, C.: [Ca^{2+}] as a potential down regulator of $\alpha_2\beta_1$ integrin-mediated A2058 tumor cell migration to type IV collagen. Am. J. Physiol. Cell Physiol. **281**, C106–C113 (2001)
31. Hodgson, L., Henderson, A.J., Dong, C.: Melanoma cell migration to type IV collagen requires activation of NF-kappaB. Oncogene **22**, 98–108 (2003)
32. Holmes, W.E., Lee, J., Kuang, W.J., Rice, G.C., Wood, W.I.: Structure and functional expression of human interleukin-8 receptor. Science **253**, 1278–1280 (1991)
33. Hoskins, M.H., Dong, C.: Kinetics analysis of binding between melanoma cells and neutrophils. Mol. Cell Biomech. **3**, 79–87 (2006)
34. Hoskins, M.H., Kunz, R.F., Bistline, J., Dong, C.: Coupled flow-structure-biochemistry simulations of dynamic systems of blood cells using an adaptive surface tracking method. J. Fluids Struct. **25**, 936–953 (2009)
35. House, S., Lipowsky, H.: In vivo determination of the force of leukocyte-endothelium adhesion in the mesenteric microvasculature of the cat. Circ. Res. **63**, 658–668 (1988)

36. Huh, S.J., Liang, S., Sharma, A., Dong, C., Robertson, G.P.: Transiently entrapped circulating tumor cells interact with neutrophils to facilitate lung metastasis development. Cancer Res. **70**, 6071–6082 (2010)
37. Jadhav, S., Eggleton, C.D., Konstantopoulos, K.: A 3-D computational model predicts that cell deformation affects selectin-mediated leukocyte rolling. Biophys. J. **88**, 96–104 (2005)
38. Jadhav, S., Konstantopoulos, K.: Fluid shear- and time-dependent modulation of molecular interactions between PMNs and colon carcinomas. Am. J. Physiol. Cell Physiol. **283**, C1133–C1143 (2002)
39. Khanna, P., Yunkunis, T., Muddana, H.S., Peng, H.H., August, A., Dong, C.: p38 MAP kinase is necessary for melanoma-mediated regulation of VE-cadherin disassembly. Am. J. Physiol. Cell Physiol. **298,** C1140–C1150 (2010)
40. Khismatullin, D., Truskey, G.: Three-dimensional numerical simulation of receptor-mediated leukocyte adhesion to surfaces: Effects of cell deformability and viscoelasticity. Phys. Fluids. **17**, 031505-1–21 (2005)
41. Konstantopoulos, K., Thomas, S.N.: Cancer cells in transit: the vascular interactions of tumor cells. Annu. Rev. Biomed. Eng. **11**, 177–202 (2009)
42. Kooijman, H.A.: A modification of the Stokes–Einstein equation for diffusivities in dilute binary mixtures. Ind. Eng. Chem. Res. **41**, 3326–3328 (2002)
43. Kramer, R.H., Nicolson, G.L.: Interactions of tumor cells with vascular endothelial cell monolayers: a model for metastatic invasion. Proc. Natl. Acad. Sci. USA **76**, 5704–5708 (1979)
44. Kunz, R.F., Yu, W.S., Antal, S.P., Ettorre, S.M.: An unstructured two-fluid method based on the coupled phasic exchange algorithm. AIAA Paper # AIAA-2001-2672. In: AIAA Computational Fluid Dynamics Conference, 15th, Anaheim, June 11–14, (2001)
45. Lampugnani, M.G., Corada, M., Caveda, L., Breviario, F., Ayalon, O., Geiger, B., Dejana, E.: The molecular organization of endothelial cell to cell junctions: differential association of plakoglobin, beta-catenin, and alpha-catenin with vascular endothelial cadherin (VE-cadherin). J. Cell Biol. **129**, 203–217 (1995)
46. Lei, X., Lawrence, M.B., Dong, C.: Influence of cell deformation on leukocyte rolling adhesion in shear flow. J. Biomech. Eng. **121**, 636–643 (1999)
47. Leyton-Mange, J., Sung, Y., Henty, M., Kunz, R.F., Zahn, J., Dong, C.: Design of a side-view particle imaging velocimetry flow system for cell-substrate adhesion studies. J. Biomech. Eng **128**, 271–278 (2006)
48. Liang, S., Dong, C.: Integrin VLA-4 enhances sialyl-Lewisx/a-negative melanoma adhesion to and extravasation through the endothelium under low flow conditions. Am. J. Physiol. Cell. Physiol. **295**, C701–707 (2008)
49. Liang, S., Fu, C., Wagner, D., Guo, H., Zhan, D., Dong, C., Long, M.: 2D kinetics of β_2 integrin-ICAM-1 bindings between neutrophils and melanoma cells. Am. J. Physiol. **294**, C743–C753 (2008a)
50. Liang, S., Hoskins, M.H., Dong, C.: Tumor cell extravasation mediated by leukocyte adhesion is shear rate-dependent on IL-8 signaling. Mol. Cell. Biomech. **7**(2), 77–91 (2009)
51. Liang, S., Hoskins, M.H., Khanna, P., Kunz, R.F., Dong, C.: The tumor-leukocyte microenvironment in a shear flow and how it affects melanoma–neutrophil adhesion to the endothelium. Cell. Mol. Bioeng. **1**, 189–200 (2008b)
52. Liang, S., Sharma, A., Peng, H.H., Robertson, G., Dong, C.: Targeting mutant (V600E) B-Raf in melanoma interrupts immunoediting of leukocyte functions and melanoma extravasation. Cancer Res **67**, 5814–5820 (2007)
53. Liang, S., Slattery, M., Dong, C.: Shear stress and shear rate differentially affect the multi-step process of leukocyte-facilitated melanoma adhesion. Exp. Cell Res. **310**, 282–292 (2005)
54. Liang, S., Slattery, M.J., Wagner, D., Simon, S.I., Dong, C.: Hydrodynamic shear rate regulates melanoma–leukocyte aggregation, melanoma adhesion to the endothelium, and subsequent extravasation. Ann. Biomed. Eng. **36**, 661–671 (2008c)
55. Liao, F., Doody, J.F., Overholser, J., Finnerty, B., Bassi, R., Wu, Y., Dejana, E., Kussie, P., Bohlen, P., Hicklin, D.J.: Selective targeting of angiogenic tumor vasculature by vascular

endothelial-cadherin antibody inhibits tumor growth without affecting vascular permeability. Cancer Res. **62**, 2567–2575 (2002)
56. Liotta, L.A.: Cancer cell invasion and metastasis. Sci. Am. **266**, 54–63 (1992)
57. Lynam, E., Sklar, L.A., Taylor, A.D., Neelamegham, S., Edwards, B.S., Smith, C.W., Simon, S.I.: Beta2-integrins mediate stable adhesion in collisional interactions between neutrophils and ICAM-1-expressing cells. J. Leukoc. Biol. **64**, 622–630 (1998)
58. Ma, Y.P., Wang, J., Liang, S., Dong, C., Du, Q.: Application of population dynamics to study heterotypic cell aggregations in the near-wall region of a shear flow. Cell. Mol. Bioeng. **3**(1), 3–19 (2010)
59. Marie, C., Roman-Roman, S., Rawadi, G.: Involvement of mitogen-activated protein kinase pathways in interleukin-8 production by human monocytes and polymorphonuclear cells stimulated with lipopolysaccharide or mycoplasma fermentans membrane lipoproteins. Infect. Immun. **67**, 688–693 (1999)
60. Miele, M.E., Bennett, C.F., Miller, B.E., Welch, D.R.: Enhanced metastatic ability of TNF-treated maliganant melanoma cells is reduced by intercellular adhesion molecule-1 (ICAM-1) antisense oligonucleotides. Exp. Cell Res. **214**, 231–241 (1994)
61. Migliorini, C., Qian, Y.H., Chen, H.D., Brown, E.B., Jain, R.K., Munn, L.L.: Red blood cells augment leukocyte rolling in a virtual blood vessel. Biophys. J. **83**, 1834–1841 (2002)
62. Moghe, P.V., Nelson, R.D., Tranquillo, R.T.: Cytokine-stimulated chemotaxis of human neutrophils in a 3-D conjoined fibrin gel assay. J. Immunol. Meth. **180**, 193–211 (1995)
63. Muller, A., Homey, B., Soto, H., Ge, N., Catron, D., Buchanan, M.E., McClanahan, T., Murphy, E., Yuan, W., Wagner, S.N., Barrera, J.L., Mohar, A., Verastegui, E., Zlotnik, A.: Involvement of chemokine receptors in breast cancer metastasis. Nature **410**, 50–6 (2001)
64. Munn, L.L., Melder, R.J., Jain, R.K.: Analysis of cell flux in the parallel plate flow chamber: implications for cell capture studies. Biophys. J. **67**, 889–895 (1994)
65. Murphy, P.M., Tiffany, H.L.: Cloning of complementary DNA encoding a functional human interleukin-8 receptor. Science **253**, 1280–1283 (1991)
66. N'Dri, N.A., Shyy, W., Tran-Son-Tay, R.: Computational modeling of cell adhesion and movement using a continuum-kinetics approach. Biophys. J. **85**, 2273–2286 (2003)
67. 'Neelamegham, S.: Transport features, reaction kinetics and receptor biomechanics controlling selectin and integrin mediated cell adhesion. Cell Commun. Adhes. **1**, 35–50 (2004)
68. Neelamegham, S., Taylor, A.D., Burns, A.R., Smith, C.W., Simon, S.I.: Hydrodynamic shear shows distinct roles for LFA-1 and MAC-1 in neutrophil adhesion to intercellular adhesion molecule-1. Blood **72**, 1626–1638 (1998)
69. Nwariaku, F.E., Chang, J., Zhu, X., Liu, Z., Duffy, S.L., Halaihel, N.H., Terada, L.: Turnage RH The role of p38 map kinase in tumor necrosis factor-induced redistribution of vascular endothelial cadherin and increased endothelial permeability. Shock **1**, 82–5 (2002)
70. Okamoto, M., Liu, W., Luo, Y., Tanaka, A., Cai, X., Norris, D.A., Dinarello, C.A., Fujita, M.: Constitutively active inflammasome in human melanoma cells mediating autoinflammation via caspase-1 processing and secretion of interleukin-1β. J. Biol. Chem. **285,** 6477–6488 (2010)
71. Payne, A.S., Cornelius, L.A.: The role of chemokines in melanoma tumor growth and metastasis. J. Invest. Dermatol. **118**, 915–922 (2002)
72. Peng, H.H., Dong, C.: Systemic analysis of tumor cell-induced endothelial calcium signaling and junction disassembly. Cell. Mol. Bioeng. **2**(3), 375–385 (2009)
73. Peng, H.H., Hodgson, L., Henderson, A.J., Dong, C.: Involvement of phospholipase C signaling in melanoma cell-induced endothelial junction disassembly. Frontiers Biosci. **10**, 1597–1606 (2005)
74. Peng, H.H., Liang, S., Henderson, A.J., Dong, C.:Regulation of interleukin-8 expression in melanoma-stimulated neutrophil inflammatory response. Exp. Cell Res. **313**, 551–559 (2007)
75. Qi, J., Chen, N., Wang, J., Siu, C.H.: Transendothelial migration of melanoma cells involves N-cadherin-mediated adhesion and activation of the beta-catenin signaling pathway. Mol. Biol. Cell. **16**, 4386–4397 (2005)

76. Rinker, K.D., Prabhakar, V., Truskey, G.A.: Effect of contact time and force on monocyte adhesion to vascular endothelium. Biophys. J. **80**, 1722–1732 (2001)
77. Sandig, M., Voura, E.B., Kalnins, V.I., Siu, C.H.: Role of cadherins in the transendothelial migration of melanoma cells in culture. Cell Motil Cytoskelet. **38**, 351–64 (1997)
78. Schadendorf, D., Mohler, T., Haefele, J., Hunstein, W., Kelholz, U.: Serum interleuckin-8 is elevated in patients with metastatic melanoma and correlates with tumor load. Melanoma Res. **5**, 179–181 (1995)
79. Scherbarth, S., Orr, F.W.: Intravital video microscopic evidence for regulation of metastasis by the hepatic microvasculature: Effects of interleukin-1 on metastasis and the location of B16F1 melanoma cell arrest. Cancer Res. **57**, 4105–4110 (1997)
80. Sharma, A., Tran, M., Liang, S., Sharma, A.K., Amin, S., Smith, C.D., Dong, C., Robertson, G.P.: Targeting mitogen-activated protein kinase/extracellular signal-regulated kinase kinase in the mutant (V600E) B-Raf signaling cascade effectively inhibits melanoma lung metastases. Cancer Res. **66**, 8200–8209 (2006)
81. Shay-Salit, A., Shushy, M., Wolfovitz, E., Yahav, H., Breviario, F., Dejana, E., Resnick, N.: VEGF receptor 2 and the adherens junction as a mechanical transducer in vascular endothelial cells. Proc. Natl. Acad. Sci. USA **99**, 9462–9427 (2002)
82. Simon, S.I., Green, C.E.: Molecular mechanics and dynamics of leukocyte recruitment during inflammation. Annu. Rev. Biomed. Eng. **7**, 151–185 (2005)
83. Singh, R.K., Gutman, M., Radinsky, R., Bucana, C.D., Fidler, I.J.: Expression of interleukin 8 correlates with the metastatic potential of human melanoma cells in nude mice. Cancer Res. **54**, 3242–3247 (1994)
84. Singh, R.K., Varney, M.L.: Regulation of interleukin-8 expression in human malignant melanoma cells. Cancer Res.**58**, 1532–1537 (1998)
85. Singh, S., Varney, M., Singh, R.K.: Host CXCR2-dependent regulation of melanoma growth, angiogenesis, and experimental lung metastasis. Cancer Res. **69**, 411–5 (2009)
86. Slattery, M.J., Dong, C.: Neutrophils influence melanoma adhesion and migration under flow conditions. Int. J. Cancer **106**, 713–722 (2003)
87. Slattery, M.J., Liang, S., Dong, C.: Distinct role of hydrodynamic shear in leukocyte-facilitated tumor cell extravasation. Am. J. Physiol. Cell Physiol. **288**(4), C831–839 (2005)
88. Smith, M.J., Berg, E.L., Lawrence, M.B.: A direct comparison of selectin-mediated transient, adhesive events using high temporal resolution. Biophys. J. **77**, 3371–3383 (1999)
89. Springer, T.A.: Traffic signals for lymphocyte recirculation and leukocyte emigration: the multistep paradigm. Cell **76**, 301–314 (1994)
90. Starkey, J.R., Liggitt, H.D., Jones, W., Hosick, H.L.: Influence of migratory blood cells on the attachment of tumor cells to vascular endothelium. Int. J. Cancer **34**, 535–543 (1984)
91. Strieter, R.M., Kasahara, K., Allen, R.M., Standiford, T.J., Rolfe, M.W., Becker, F.S., Chensue, S.W., Kunkel, S.L.: Cytokine-induced neutrophil-derived interleukin-8. Am. J. Pathol. **141**, 397–407 (1992)
92. Thorlacius, H., Pricto, J., Raud, J., Gautam, N., Patarroyuo, M., Hedqvist, P., Lindbom, L.: Tumor cell arrest in the microcirculation: lack of evidence for a leukocyte-like rolling adhesive interaction with vascular endothelium in vivo. Clin. Immunol. Immunopathol. **83**, 68–76 (1997)
93. Todaro, G.J., Fryling, C., De Larco, J.E.: Transforming growth factors produced by certain human tumor cells: polypeptides that interact with epidermal growth factor receptors. Proc. Natl. Acad. Sci. USA **77**, 5258–62 (1980)
94. Tominaga, Y., Kita, Y., Satoh, A., Asai, S., Kato, K., Ishikawa, K., Horiuchi, T., Takashi, T.: Affinity and kinetic analysis of the molecular interaction of ICAM-1 and leukocyte function-associated antigen-1. J. Immunol. **161**, 4016–4022 (1998)
95. Tremblay, P.L., Auger, F.A., Huot, J.: Regulation of transendothelial migration of colon cancer cells by E-selectin-mediated activation of p38 and ERK MAP kinases. Oncogene **25**, 6563–73 (2006)
96. Van Wetering, S., van den Berk, N., van Buul, J.D., Mul, F.P., Lommerse, I., Mous, R., ten Klooster, J.P., Zwaginga, J.J., Hordijk, P.L.: VCAM-1-mediated Rac signaling controls

endothelial cell–cell contacts and leukocyte transmigration. Am. J. Physiol. Cell Physiol. **285**, 343–352 (2003)
97. Vitte, J., Pierres, A., Benoliel, A.M., Bongrand, P.: Direct quantification of the modulation of interaction between cell- or surface-bound LFA -1 and ICAM-1. J. Leukoc. Biol. **76**, 1–9 (2004)
98. Volberg, T., Zick, Y., Dror, R., Sabanay, I., Gilon, C., Levitzki, A., Geiger, B.: The effect of tyrosine-specific protein phosphorylation on the assembly of adherens-type junction. EMBO J. **11**, 1733–1742 (1992)
99. Voura, E.B., Sandig, M., Siu, C.H.: Cell–cell interactions during transendothelial migration of tumor cells. Microsc Res Tech. **43**, 265–275 (Review) (1998)
100. Walz, A., Peveri, P., Aschauer, A.O., Baggiolini, M.: Purification and amino acid sequencing of NAF, a novel neutrophil activating factor produced by monocytes. Biochem. Biophys. Res. Commun **149**, 755–761 (1987)
101. Welch, D.R., Bisi, J.E., Miller, B.E., Conaway, D., Seftor, E.A., Yohem, K.H., Gilmore, L.B., Seftor, R.E.B., Nakajima, M., Hendrix, M.J.C.: Characterization of a highly invasive and spontaneously metastatic human malignant melanoma cell line. Int. J. Cancer **47**, 227–237 (1991)
102. Welch, D.R., Schissel, D.J., Howrey, R.P., Aeed, P.A.: Tumor-elicited polymorphonuclear cells, in contrast to "normal" circulating polymorphonuclear cells, stimulate invasive and metastatic potentials of rat mammary adnocardinoma cells. Proc. Natl. Acad. Sci. USA **86**, 5859–5863 (1989)
103. Yamada, K.M.: Introduction: Adhesion molecules in cancer. Part I. Semin. Cancer Biol. **4**, 215–218 (1993)
104. Yeung, A., Evans, E.: Cortical shell-liquid core model for passive flow of liquid-like spherical cells into micropipets. Biophys. J. **56**, 139–149 (1989)
105. You, J., Mastro, A.M., Dong, C.: Application of the dual micropipette technique to the measurement of tumor cell locomotion. Exp. Cell Res. **248**, 160–171 (1999)
106. You, J., Miele, M.E., Dong, C., Welch, D.R.: Suppression of human melanoma metastasis by introduction of chromosome 6 may be partially due to inhibition of motility but not invasion. Biochem. Biophys. Res. Commun. **208**, 476–484 (1995)
107. Young, M.E., Carroad, P.A., Bell, R.L.: Estimation of diffusion coefficients of proteins. Biotechnol. Bioeng. **22**, 947–955 (1980)
108. Zetter, B.R.: Adhesion molecules in tumor metastasis. Semin. Cancer Biol. **4**, 219–229 (1993)
109. Zhang, X.H., Wojcikiewicz, E., Moy, V.: Force spectroscopy of the leukocyte function-associated antigen-1/intercellular adhesion molecule-1 interaction. Biophys. J. **83**, 2270–2279 (2002)
110. Zhu, C., Yago, T., Lou, J., Zarnitsyna, V.I., McEver, R.P.: Mechanisms for flow-enhanced cell adhesion. Ann. Biomed. Eng. **36**, 604–621 (2008)

Cellular Mechanics of Acute Leukemia and Chemotherapy

Wilbur A. Lam and Daniel A. Fletcher

Abstract Cellular mechanics plays a major role in the pathophysiology of hematologic diseases, in which the alterations of biophysical properties of circulating blood cells influence vascular flow and contribute to vascular complications. In particular, the cellular mechanical alterations that occur in acute leukemia or, cancer of blood cell precursors, may lead to life-threatening complications that result in microvascular compromise of vital organs such as the brain and lung. As such, pharmacological agents that modulate the cellular mechanics of leukemia cells have the potential to both improve and worsen the symptoms and outcome of this complication. Recent technological advances have provided the necessary tools to study leukemia and cellular mechanics and have vastly improved our understanding of the biophysical aspects of leukemia pathophysiology. In this chapter, we review studies from our laboratory and other researchers that focus on the interactions between cellular mechanics, pharmacological agents, and leukemia biology, and we also highlight the novel tools and techniques developed to conduct those experiments. These studies clearly stress the important role the nascent field of cellular mechanics will have in clinical medicine in the near future.

W. A. Lam (✉) and D. A. Fletcher
Department of Bioengineering, University of California, Berkeley, CA 94720, USA
e-mail: wilbur.lam@emory.edu; fletch@berkeley.edu

W. A. Lam
Division of Pediatric Hematology/Oncology, Department of Pediatrics,
University of California, San Francisco, CA 94143, USA

D. A. Fletcher
Graduate Group in Biophysics, University of California, Berkeley, CA 94720, USA

Stud Mechanobiol Tissue Eng Biomater (2011) 4: 523–558
DOI: 10.1007/8415_2010_27

Published Online: 27 November 2010

1 Introduction

1.1 Overview

Over the last several decades, the underlying genetic and biochemical mechanisms of numerous diseases have been characterized at the cellular and molecular levels. More recently, researchers have begun to investigate how the mechanical and physical properties of cells and subcellular structures influence normal biological processes as well as disease [25]. With the development of new tools that enable mechanical measurements at the single-cell and nanoscale levels, this nascent field of cellular mechanics has already made remarkable strides in increasing our understanding of human biology and disease. In fact, mechanical cues have recently been shown to influence cell signaling pathways and play significant roles in processes as diverse as cancer metastasis, osteoarthritis, and stem cell differentiation [30, 71, 102]. In this chapter, we focus on the cell mechanics of blood and its link to acute leukemias and their therapies by reviewing a series of studies from our laboratory and other researchers.

Cellular mechanics is particularly important in the study of hematologic disorders, as blood is a suspension of trillions of cells dynamically interacting with each other and the blood vessel wall while constantly subjected to varying degrees of shear stress due to blood flow [33]. Leukocyte rolling and transmigration, platelet activation, clot formation, and atherosclerosis are all examples of biological processes that are dependent upon biofluidic dynamics and blood cellular mechanical properties, such as cell deformability and adhesion. In addition, in hematologic diseases, alterations in blood cell mechanical properties can profoundly affect the cells' ability to normally flow in the microvasculature [62]. Here, blood cells are in intimate contact with the vessel wall of the microvasculature and must deform to pass through the vascular network [62, 98]. Any alterations in cell deformability, adhesiveness, or transmigration may lead to microvascular occlusion, tissue ischemia, hemorrhage, and ultimately failure of vital organs like the brain and lung. In recent years, it has become clear that altered blood cell mechanical properties contribute to the pathophysiology of several other important hematologic diseases such as sickle cell disease, malaria, sepsis, and diabetes [1, 7, 8, 17, 19, 27, 29, 32, 61, 95, 96, 102]. Therefore, a comprehensive understanding of blood pathology requires the ability to analyze biophysical properties of blood and its component elements: blood cells and plasma with its constituent proteins.

Although bulk measurements of blood rheology have been in use for the last half-century [9], the sensitivity of single-cell measurements have proven to be more clinically useful as pathological processes originate in small cellular subpopulations not detectable with bulk techniques [21, 73]. For hematologic diseases, flow cytometry has been an effective tool for single-cell analysis and has been widely used to quantify cell surface protein expression and signaling activity, among others [47]. Flow cytometry, however, cannot measure cellular mechanical

properties. Since single mechanically altered blood cells are theoretically sufficient to induce microvascular pathology [3, 5], a clinical need exists in hematology and hematopathology for improved single blood cell mechanical analysis.

1.2 Acute Leukemia

The leukemias are a group of cancers characterized by the accumulation of malignant precursor blood cells in the bone marrow and the blood. These abnormal cells cause symptoms because of bone marrow failure (i.e. anemia, low leukocytes, or low platelets) and infiltration of organs (e.g. liver, spleen, lymph nodes, meninges, brain, skin, or testes), which are due in part to their pathologically altered cellular mechanical properties.

1.2.1 Classification of Acute Leukemia

The main classification of leukemia is into four types—acute and chronic leukemias which are further subdivided into lymphoid and myeloid. "Acute" leukemias are usually aggressive diseases in which the malignant transformation causes accumulation of early bone marrow hematopoietic progenitors, called blast cells, in the bone marrow and subsequently the blood vessels. The dominant clinical feature of these diseases is usually bone marrow failure caused by accumulation of leukemia, or blast cells, although tissue infiltration also occurs. If untreated these diseases are usually rapidly fatal but, paradoxically, they are also easier to cure than chronic leukemias [68]. Acute leukemia is defined as the presence of over 30% of blast cells in the bone marrow at clinical presentation. It is further subdivided into acute myeloid leukemia (AML) and acute lymphoblastic leukemia (ALL) on the basis of whether the blasts are shown to be myeloblasts or lymphoblasts.

1.2.2 Acute Lymphoblastic Leukemia

ALL is caused by an accumulation of lymphoblasts, or immature lymphocytes, and is the most common malignancy of childhood [80]. ALL can be subclassified on the basis of morphology of immunological markers. Immunologically, ALL can be divided into precursor B-cell ALL, T-cell ALL, or mature B-cell ALL. ALL is the most common form of leukemia in children; its incidence is highest at 3–7 years [26]. The common (CD10+) precursor B-cell type which is the most usual in children has an equal sex incidence; there is a male predominance for T-cell ALL. There is a lower frequency of ALL after 10 years of age with a secondary rise after the age of 40.

Combinations of at least three chemotherapeutic agents are now usually used to increase the cytotoxic effect, improve remission rates and reduce the frequency of

emergence of drug resistance [80]. The aim of cytotoxic therapy is first to induce a remission (absence of any clinical or conventional laboratory evidence of the disease) and then to eliminate the hidden leukemia cell population by courses of consolidation therapy [46].

The aim of remission induction is to kill rapidly most of the tumor cells and get the patient into a state of remission (defined as less than 5% blasts in the bone marrow, normal peripheral blood counts, and no other symptoms or signs of the disease). Dexamethasone, vincristine, and asparaginase are the drugs usually used and effectively achieve remission [46]. However, in remission a patient may still be harboring large numbers of tumor cell and without further chemotherapy virtually all patients will relapse.

Consolidation and/or intensification courses use high doses of multidrug chemotherapy in order to reduce the tumor burden to very low levels [31]. The doses of chemotherapy are near the limit of patient tolerability and during intensification blocks patients may need a great deal of supportive care. Typical protocols involve the use of vincristine, cyclophosphamide, cytosine arabinoside, daunorubicin, etoposide, thioguanine, or mercaptopurine.

There is a great variation in the chance of individual patients achieving a long-term cure based on a number of biological variables. Age is important—around 70–90% of children can expect to be cured whereas in adults this drops significantly to less than 5% over the age of 65 years [26]. Cytogenetics are also important, particular the presence of the Philadelphia chromosome, the incidence of which rises which age. Hyperploidy (multiple sets of chromosomes) and rearrangements of the *TEL* gene are associated with good outcome.

1.2.3 Acute Myeloid Leukemia

AML is classified according to morphology and divided into eight variants, which indicate the general lineage and degree of differentiation (non-differentiated or red cell, monocytic, granulocytic, or platelet precursors) [106]. Although the distinct AML subtypes are in fact different genetic diseases their grouping together is valid as generally their treatment and prognosis is similar. However, differences in treatment according to subtype have been introduced.

AML occurs in all age groups and is the most common form of acute leukemia in adults with increasing incidence with age. Several genetic aberrations detected within the leukemia cells correlate with prognosis. Whereas t(15;17), t(8;21), and inv(16) correlate with a favorable prognosis, deletions of chromosome 5 or 7, Flt-3 or 11q23 mutations, and t(6;9) connate a poor prognosis [78].

Specific therapy for AML primarily involves intensive chemotherapy. The most commonly used drugs include cytosine arabinoside, daunorubicin, idarubicin, 6-thioguanine, mitoxantrone, or etoposide [84]. These drugs are extremely toxic with limited selectivity between leukemic and normal marrow cells and therefore marrow failure is severe, necessitating prolonged and intensive supportive therapy [48]. All the AML subtypes are treated similarly except for the acute

promyelocytic leukemia (APML) subtype associated with the t(15;17) translocation in which all-trans retinoic acid (ATRA) and arsenic is added to the initial chemotherapy [81]. In addition, monoclonal antibodies targeted against specific cell surface molecules or aberrant proteins specific to AML cells are now being assessed as possible additions to AML therapy.

AML prognosis has improved steadily over the years, particularly for younger patients [26]. Perhaps 50% of children and young adults may expect a long-term 'cure'. Cytogenetic abnormalities and initial response to treatment are major predictors of prognosis. For the elderly the situation is poor and only 5% of those over 65 years of age can expect long-term remission.

1.3 Leukostasis in Acute Leukemia

Approximately 10–13% of ALL cases and 15–20% of AML cases present with hyperleukocytosis, which is defined as a peripheral leukocyte concentration exceeding 100,000 cells per microliter [85]. Hyperleukocytosis may in turn lead to leukostasis, in which leukemic cells accumulate and aggregate in the vasculature (Fig. 1). Although this often fatal phenomenon can occur in almost any organ, it most commonly occurs in the brain and lungs, leading to intracranial hemorrhage and respiratory failure, and it has an estimated mortality rate of approximately 20–40% [77]. Autopsy results in patients who died from leukostasis reveal infiltrates of leukemia cells and hemorrhage in the vasculature, interstitium, and parenchyma of the lungs and brain.

Several potential mechanisms leading to leukostasis have been proposed over the years. Originally, symptoms of leukostasis were thought to be simply due to the high number of leukemic blast cells in the circulation leading to increased blood viscosity. However, this does not explain the entire pathophysiological process, as myeloid leukemias like AML were noted to cause symptoms of leukostasis at lower white blood cell, or leukocyte, counts than lymphoid leukemias (ALL) [79].

Lichtman developed an alternate model of leukostasis in the 1970s contending that the fractional volume of white blood cells, called leukocrit, needed to increase the blood viscosity to the point of leukostasis was approximately (12–15%) and this volume is a function of the mean cell volume (MCV) [57]. Therefore, because the leukemic cells of AML, or myeloblasts, have larger MCVs than the leukemic cells of ALL, or lymphoblasts, fewer myeloblasts than lymphoblasts are necessary to cause symptoms of leukostasis. However, leukemic blast counts are rarely sufficiently high to cause leukocrits of 12–15% and in addition, as the leukocrit rises, the number of red blood cells usually decreases, yielding a protective effect against hyperviscosity [99]. These observations suggested that leukostasis is not simply due to the size, concentration and mechanical properties of the blast cell. Indeed, rare cases of leukostasis have been reported in leukemic patients without markedly elevated white blood cell counts [58, 97]. In addition, the fact that most

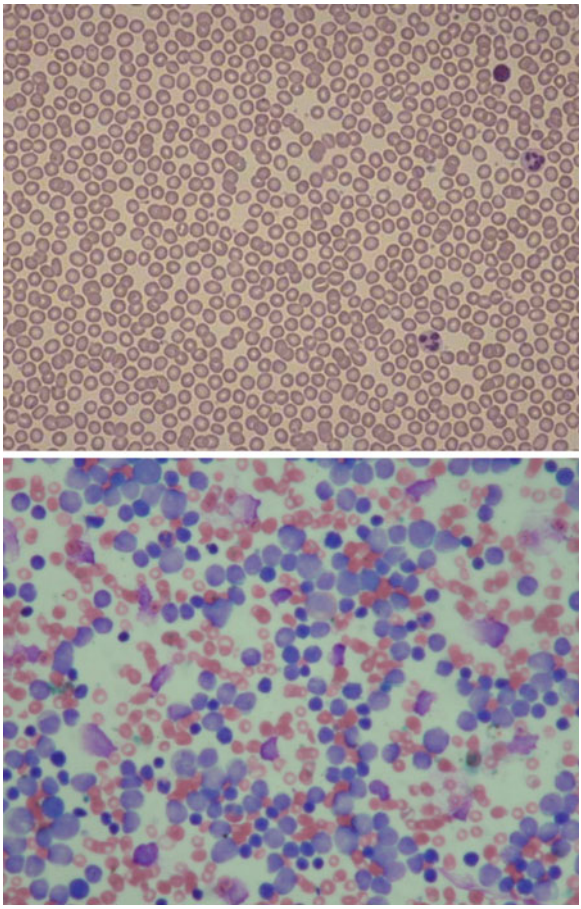

Fig. 1 Hyperleukocytosis in acute leukemia. *Top panel* a blood smear from a healthy adult with a leukocyte count of 7,000 cells/μL. *Bottom panel* a blood smear from a 2-year-old child with newly diagnosed ALL and hyperleukocytosis with a leukocyte count of 1,132,000 cells/μL (>90% of leukocytes were leukemic cells). This patient subsequently died of leukostasis after initiation of chemotherapy

cases of leukostasis occur in the brain and lungs suggests that there is some organ specificity and that local factors may play a role as well.

Recent research has show that leukostasis may result from the adhesive interactions between leukemic cells and the endothelium of the vasculature. Myeloblasts, which are thought to be "stickier" than lymphoblasts, may have a higher propensity to aggregate, possibly accounting for some of the disparities seen between AML and ALL leukostasis cases [16]. Interactions between normal leukocytes and endothelial cells via expression of adhesion molecules have been well characterized and expression of adhesion molecules of leukemic cells has also been investigated [67]. Stucki et al. [100] have shown that due to secretion of certain cytokines by myeloblasts, expression of several adhesion molecules on the surface of endothelial cells is upregulated resulting in an increased number of myeloblasts attached to the endothelium. Once adhered, leukemic cells may then cause endothelial damage by migrating into perivascular space [69] (Fig. 2). Recent studies have shown that at least for AML, upregulation of the adhesion

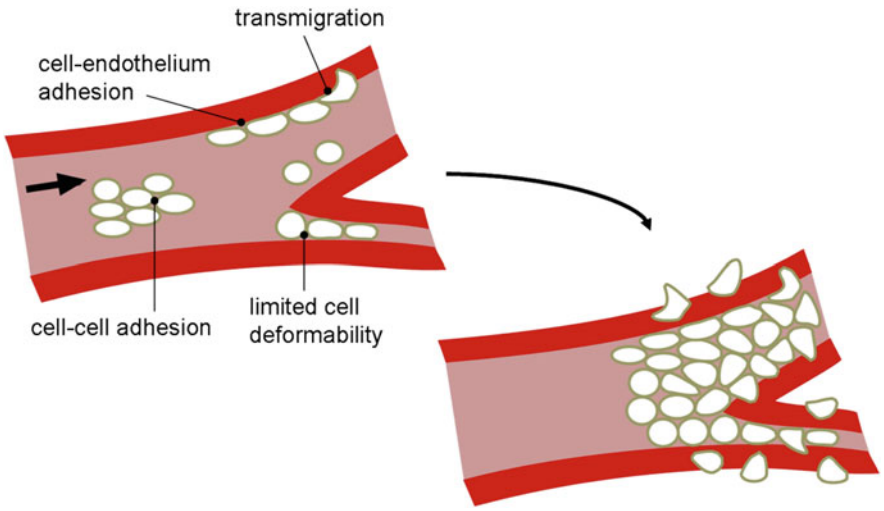

Fig. 2 Possible mechanisms of leukostasis in acute leukemia. Leukostasis is most likely caused by a combination of cell mechanical alterations including decreased cell deformability of leukemia cells compared to their more mature counterparts, aberrant and dysregulated leukemia cell-leukemia cell and leukemia-endothelial cell adhesion, and leukemia cell extravasation leading to vascular damage and hemorrhage

molecule NCAM on the surface of leukemia cells correlated with leukostasis and therefore may have a role in pathophysiology [74, 75].

Numerous questions remain regarding the pathophysiology of leukostasis. Although several studies have investigated whether the stiffness of leukemic cells plays a role in leukostasis, these studies either did not assess whole-cell deformability [56] or used an indirect measurement such as cellular transit time through capillary pores via microfiltration [43, 94]. As recent research has shown, leukemic blast cells and endothelial cells may indeed interact dynamically leading to adhesion and transmigration [22, 69, 100]. However, these studies utilized qualitative assays and the relative contributions each interaction may have to the overall pathophysiology remains unknown. In addition, few definitive studies have been reported that compare the biomechanical and adhesive properties of myeloid blast cells versus lymphoid blast cells, and no studies have been reported that assess the propensity for leukemic cells to adhere each other, which may be a vital component of leukostasis. Most importantly, no published study to date has investigated whether biophysical differences exist between leukemic cells taken from patients with leukostasis versus leukemic cells taken from asymptomatic patients. These data are necessary to determine if cell mechanical measurements can be used for the diagnosis and/or prevention of leukostasis in acute leukemia.

Currently, the mainstay of treatment for leukostasis is prompt leukocytoreduction, or removal of leukemic cells from the circulation, via exchange transfusion or leukapheresis, in addition to aggressive intravenous hydration, which

prevents renal failure from leukemic breakdown products. Although extremely effective and rapid in reducing the number of leukemic cells, these techniques are only temporizing and delay the initiation of chemotherapy, the definitive therapy for leukemia. In addition, other disadvantages include: invasive placement of deep intravenous lines (which may be difficult in small children), the need for anticoagulation, and limited availability in some hospitals. The most appropriate and optimal use of these techniques remains unclear, and the few trials reported show no significant decrease in mortality when leukocytoreduction is compared to hydration alone [79]. Leukapheresis and exchange transfusion do not address the issue of leukemic cell adhesion leading to endothelial damage, which may be the reason why these techniques have not been shown to improve survival in leukostasis. Therefore, a more complete and clarified view of the pathophysiology of leukostasis is needed in order to guide the most effective therapy when presented with this life-threatening emergency.

1.4 Acute promyelocytic leukemia and ATRA syndrome

In APML, a specific subtype of AML, there is an abnormal accumulation of immature leukocytes called promyelocytes, which are precursors to granulocytic cells such as neutrophils. The disease is characterized by the t(15;17) chromosomal translocation involving the retinoic acid receptor alpha (*RARα* or *RARA*) gene and is unique from other forms of AML in its responsiveness to ATRA, a derivative of vitamin A [74]. Use of this new class of chemotherapeutic that directly targets the biological aberration of APML has led to a significant decrease in mortality for this subtype of AML. Indeed, the majority of APML patients can now be completely cured as the 5-year disease-free survival rate in patients receiving ATRA has climbed to 70–80% in the last decade [101].

However, 2–27% of APML patients receiving ATRA develop a life-threatening complication called retinoic acid syndrome, which is characterized by fever, pulmonary infiltrates seen on X-rays, respiratory failure often requiring mechanical ventilation, significantly decreased blood pressure, and kidney failure [76]. Without appropriate therapy, a 30% mortality rate is associated with this syndrome [101].

Retinoic acid syndrome is often, but not always, associated with the development of hyperleukocytosis. Retinoic acid is known to cause differentiation of promyelocytic leukemia cells into more mature granulocytes and acute differentiation of these cells may lead to dramatic activation and subsequent sequestration and infiltration within vital organs. Autopsies revealed an interstitial infiltrate of maturing myeloid cells in the lungs of patients with relative patency of the lung alveoli themselves differentiating this process from leukostasis in acute leukemia [101].

The pathophysiology of retinoic acid syndrome in APML is poorly understood, but several mechanisms have been proposed. There is evidence that cathepsin, a

protease which is known to increase capillary permeability, is stimulated in APML patients receiving ATRA [92]. ATRA also increases the expression of LFA-1 and other cellular adhesion molecules on the surface of APML cells resulting in increased binding to epithelial cells [14]. Soluble factors such as interleukin-1-β, TNF-α, and interleukin-6, which all promote leukocyte activation, may play significant roles as well [28]. Recently, administration of anti-inflammatory steroids has decreased the mortality and incidence of retinoic acid syndrome in APML significantly and the incidence of this complication in patients receiving both ATRA and prophylactic steroids has decreased to 5% overall [101].

However, as our understanding of the underlying mechanisms of retinoic acid syndrome remains unclear, many clinically relevant questions remain. For example, there are not any reliable factors or methods that can effectively predict and identify which patients fall into the 5% who will develop retinoic acid syndrome and which patients should receive prophylactic steroids. In addition, although retinoic acid syndrome primarily occurs at the initiation of therapy immediately after diagnosis, some patients spontaneously develop this complication later in their course of therapy for reasons that are completely unknown at this time. To address these issues, further research into the physiological effects of retinoic acid on promyelocytic leukemia cells is required.

2 Leukemia Cell Mechanical Alterations in Leukostasis

2.1 Leukemia Cell Deformability via Atomic Force Microscopy

Decreased deformability of leukemia cells is thought to be linked to contribute leukostasis [57]. Better knowledge of biophysical changes in leukemia cells such as deformability is necessary for improved understanding of the disease, but no widely accepted method or model exists for quantifying the mechanical properties of leukemia cells relevant to leukostasis.

Atomic force microscopy (AFM), first developed as a surface imaging tool [12], can also be used to measure the stiffness of cells firmly adhered to a substrate [83]. The primary method of measuring stiffness is indenting the cell with a flexible cantilever driven at a constant extension rate (piezo extension rate) with respect to the sample. The deflection of the cantilever as it indents the cell, which is linearly related to loading force for small deflections, is recorded by reflecting a laser off the cantilever into a split photodiode. A linear elastic model of the cell based on Hertzian mechanics [44] is commonly used with AFM deflection data to determine cell elasticity [82].

Non-adhesive cells, such as normal and malignant leukocytes prior to activation of the inflammatory response, pose a challenge for AFM because they tend to slip from under the cantilever tip under an applied load. To address this problem, we used microfabricated wells (Fig. 3) to mechanically immobilize and study the

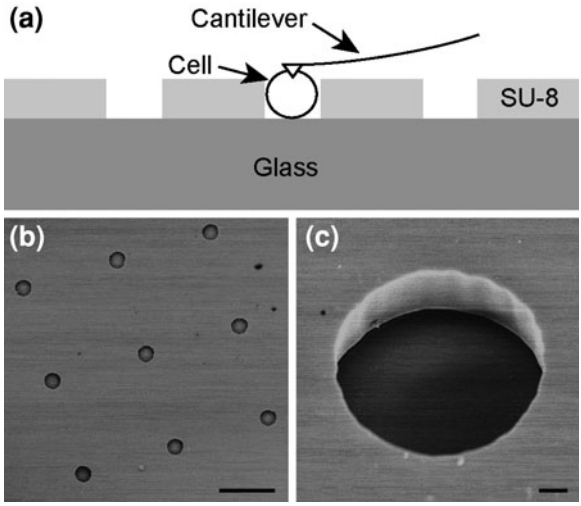

Fig. 3 Microfabricated wells for force microscopy of non-adherent cells. **a** Schematic diagram of the microwells showing SU-8 photoresist structures on a glass wafer in which non-adherent cells sit. Cells resting inside the microwells are mechanically immobilized for force microscopy with an AFM cantilever. **b** Scanning electron micrograph (SEM) of microwells fabricated in 8 × 8 arrays. Scalebar is 50 μm. **c** SEM of a single microwell showing the vertical sidewalls of the SU-8. Scalebar is 2 μm (from Rosenbluth et al.,*Biophysical Journal*, 2006)

deformability of acute leukemia cells. We characterized and determined that a Hertzian mechanics model appropriately described leukemia cell deformability and applied that model for analysis of our experimental data [87].

2.1.1 Increased Leukemia Cell Stiffness is Associated with Symptoms of Leukostasis in ALL

To determine if cell stiffness is associated with leukostasis, we used our AFM technique to measure the stiffness of individual leukemia cells taken from patients with and without symptoms consistent with leukostasis focusing initially on ALL. Blood was obtained, with informed consent, from 15 pediatric ALL patients with >10% leukemia cells in their peripheral blood. Leukemic cells were then immediately isolated via density-gradient centrifugation and measured with AFM. Measurements were performed with the methodology previously described using a Hertzian mechanics model [87]. Cells were immobilized in microfabricated wells to prevent movement during AFM measurements. Media was constantly perfused into and out of the sample chamber, and measurements were taken at 37°C using a heated stage.

As the central nervous system (CNS) and lungs are the major leukostasis target organs [79], symptoms and signs of neurological and pulmonary dysfunction were considered evidence of leukostasis only when the onset occurred at presentation and no other etiology could be identified, similar to previous studies on leukostasis [74, 75]. Out of the 15 patients with pediatric ALL and peripheral blasts, four had symptoms and/or abnormalities on physical examination or diagnostic imaging consistent with CNS or pulmonary leukostasis. All patients were newly diagnosed, with the exception of patient 1, who had multiply relapsed refractory disease and was receiving only end-of-life palliative care at the time of this study. This patient ultimately died of respiratory failure, and leukemia cell stiffness was measured daily during his last 3 days of life. Leukostasis symptoms resolved for the other three patients during induction chemotherapy.

Leukemia cell stiffness was then measured for each patient sample (Fig. 4c) [49]. The median leukemia cell stiffness was higher in the four patients with symptoms consistent with neurologic and respiratory leukostasis than in the 11 patients without symptoms ($p < 0.001$) via Mann–Whitney analysis and the 10, 25, 75, and 90 percentile cell stiffness values were also higher in the symptomatic than asymptomatic patients (p range: 0.005–0.01). Finally, the cell stiffness variance was more prominent in symptomatic patients, suggesting that perhaps a small proportion of stiff cells within the population may be sufficient to trigger leukostasis.

In general, leukostasis is associated with an elevated white blood cell count, or hyperleukocytosis [64], although the exact relationship remains unclear. Our results showed no significant difference in WBC count between symptomatic and asymptomatic patients ($p < 0.40$), suggesting that increased cell stiffness may be an additional independent leukostasis risk factor. However, our sample size is small and more data is required before a more definitive conclusion can be made.

In addition, the median leukemia cell stiffness during Patient 1's last 3 days of life showed a significant increase from 0.07 to 0.41 kPa ($p < 0.0001$) to 0.69 kPa ($p < 0.01$). The patient subsequently died of leukostasis-related respiratory failure but the increase in leukemia cell stiffness preceded the development of any symptoms, thus indicating that cell stiffness trends may possibly be used to predict the onset of leukostasis (Fig. 4d).

Although the observations in this study are intriguing and clinically relevant, the exact underlying cause for the leukemia cell stiffness increase in leukostasis is unclear. Previous work in our laboratory has shown that chemotherapy-induced cell death increases leukemia cell stiffness (see below) [49]. No patient in this study received chemotherapy prior to leukemia cell collection, however. Inflammatory mediators and cytokines (e.g. tumor necrosis factor-α), which are known to increase neutrophil stiffness in sepsis leading to microvascular occlusion [95, 96], may also alter cell stiffness in acute leukemia. However, further research is required to elucidate the cause of leukemia cell stiffness and the exact role it has in the development of leukostasis.

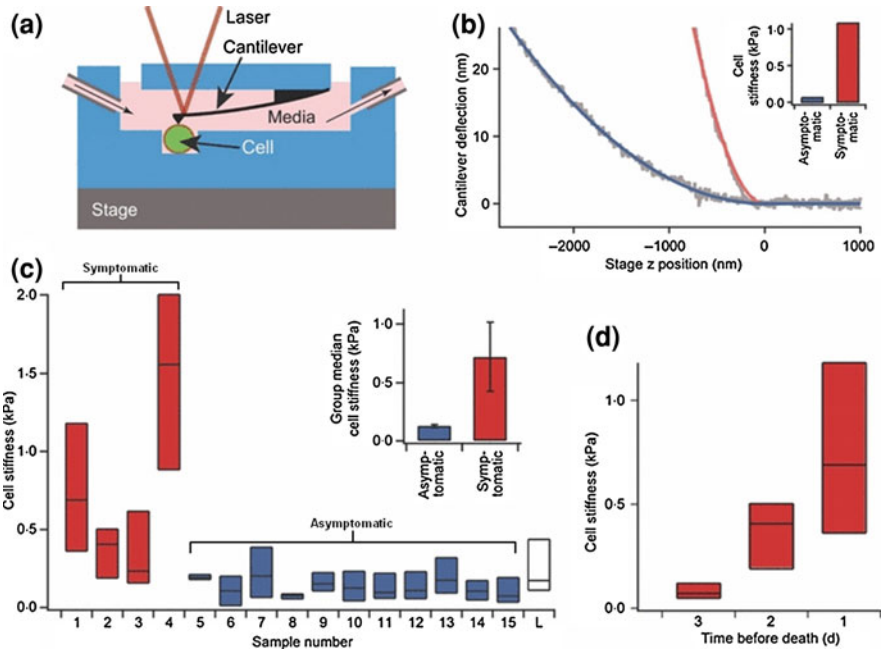

Fig. 4 Leukaemia cell stiffness, as measured with atomic force microscopy (AFM), is higher in pediatric acute lymphoblastic leukaemia (ALL) patients with leukostasis symptoms than in asymptomatic patients. **a** Suspensions of ALL cells were pipetted into a flow chamber for AFM measurements. All stiffness measurements were taken on a heated stage held at 37°C. Cells were immobilized in microfabricated wells to prevent movement during experiments, and media was perfused into and out of the chamber. Illustration not to scale. $n \geq 15$ cells for all populations. **b** Typical AFM cantilever deflection versus distance curves (raw data in *grey*). The cell stiffness can be determined using a Hertzian (*fit lines*). Shown here are the curves of an ALL cell with a stiffness of 1.1 kPa taken from a patient with leukostasis symptoms (samples 1–4) and an ALL cell with a stiffness of 0.06 kPa taken from an asymptomatic patient (samples 5–15). **c** Stiffness of leukaemia cell populations taken from the peripheral blood of patients with symptoms of leukostasis and asymptomatic patients. For each sample, 75 percentile, median, and 25 percentile stiffness values are represented by the *top*, *middle*, and *bottom lines*, respectively, of each bar. A population of normal lymphocytes (*white* labelled 'L') taken from a healthy individual via the same isolation protocol were used as controls for comparison. All reported stiffness values represent the average of five consecutive AFM measurements. *Inset* Group median stiffness of the symptomatic and asymptomatic patients were 0.72 ± 0.29 and 0.13 ± 0.01 kPa, respectively ($p < 0.001$, errors represent standard error of the mean). **d** Serial cell stiffness measurements, represented by 75 percentile, median, and 25 percentile values, taken daily from a 15-year-old boy with relapsed, refractory ALL (patient 1) receiving only palliative care during his last 3 days of life. Median leukaemia cell stiffness significantly increased during that time from 0.07 to 0.41 kPa ($p < 0.0001$) to 0.69 kPa ($p < 0.01$). Cell stiffness values taken at 1 d prior to patient 1's death are used in (**c**) for this patient (from Lam et al., *The British Journal of Haematology*, 2008)

2.1.2 Increased Leukemia Cell Stiffness is Associated with Symptoms of Leukostasis in AML

Although cell stiffness measurements have only been conducted on four AML patients, one of whom developed and ultimately died of neurologic leukostasis at presentation, we observe a trend similar to our ALL data (Fig. 5).

However, with AML patients, the differences in cell stiffness between the leukostasis positive patient and the asymptomatic patients are less prominent than in ALL. Although more clinical data is required before any definitive conclusion can be drawn it is likely that cell stiffness has less of a role in leukostasis in AML than ALL. It is apparent that the leukostasis pathophysiology is likely different for these two different leukemia types as leukostasis incidence is higher in AML than for ALL, and symptoms of leukostasis occur at lower leukocyte concentrations in AML than in ALL [79]. As AML cells are noted to be more adhesion and adhesive molecules are more dynamic in AML cells, cell adhesion may be the dominant factor in leukostasis in AML.

2.2 Leukemia Cell Deformability via Biophysical Flow Cytometry

Although cell mechanical information at the single cell level can be obtained with AFM, throughput in these systems are relatively low. However, microfluidic systems have the potential to achieve high-throughput single-cell analysis of cell deformability for clinical applications. Coupled with techniques such as shear

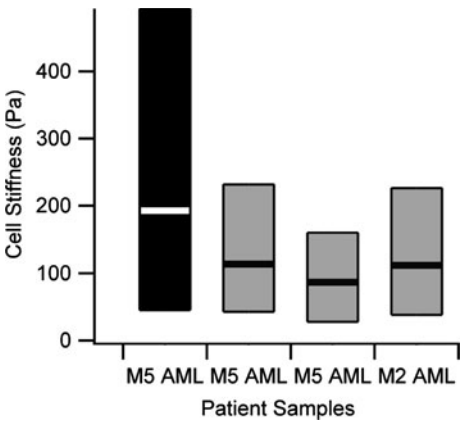

Fig. 5 Leukemia cell stiffness of AML patients with and without leukostasis. Stiffness of leukemia cell populations taken from the peripheral blood of a patient who died of CNS leukostasis (*black*) and asymptomatic patients (*grey*). For each sample, 75 percentile, median, and 25 percentile stiffness values are represented by the top, middle, and bottom lines, respectively, of each bar. $p < 0.05$ for all pair-wise comparisons between the leukostasis positive and asymptomatic patients

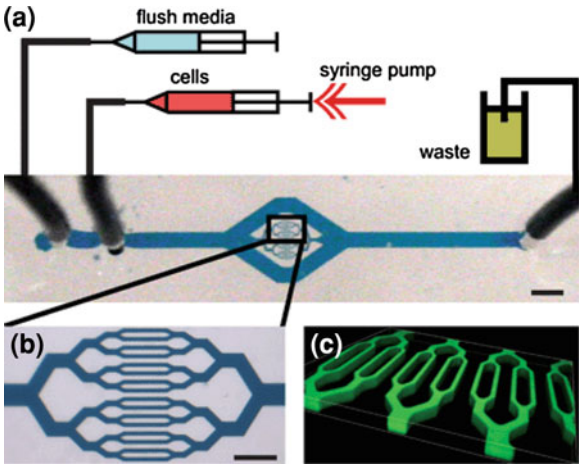

Fig. 6 Biophysical flow cytometer device. **a** Blood cells were loaded into a syringe and flowed into the device at a constant flow rate. The cytometry device trifurcates into two wide bypass channels and a network of bifurcating channels which split into 64 parallel capillary-like microchannels. *Scale bar* 1 mm. **b** 16 of these microchannels are shown here. Scale bar 100 μm. **c** A confocal image of fluorescein solution inside several of the microchannels (from Rosenbluth et al., *Lab on a Chip*, 2008)

flow [13], capillary-like microchannels [2, 34, 35, 104, 108], or optical stretching [54, 60], microfluidic-based systems have enabled cellular biological analysis with resolution at single cell level. We generally and collectively refer to these devices as biophysical flow cytometry (BFC), and like flow cytometry, these systems are capable of high-throughput single-cell analysis.

We have previously shown that our BFC system, a simple PDMS microfluidic device developed with standard microfabrication techniques, can be used to rapidly generate clinically useful single cell mechanical data that provides new insight into hematologic diseases states [87] (Fig. 6). Using automated image analysis to track large numbers of individual cells, our device quantifies the effect of blood cell deformability on cellular transit times as the cells flow through a microfluidic capillary network under in vivo microvascular hemodynamic conditions. We utilized this system to investigate leukemia cell mechanical properties as they relate to leukostasis.

2.2.1 Leukostasis Symptoms in Acute Leukemia Correlates with the Distribution of Transit Times Using Biophysical Flow Cytometry

As mentioned in previous sections, leukostasis is a poorly understood and often fatal complication of acute leukemia in which leukemia cells aggregate in the microvasculature of vital organs [77]. In addition, no reliable diagnostic test currently exists to predict leukostasis. However, work in our lab has previously

shown that leukostasis symptoms correlated with increased leukemia cell stiffness [49]. Furthermore, chemotherapy has been shown to drastically increase leukemia cell stiffness by up to nearly 100-fold [50], establishing the clinical importance of monitoring blood cell stiffness in disease states. Use of biophysical flow cytometry enables high-throughput measurements and quantitative comparisons of transit time of the leukemia cells from patients with and without leukostasis. As the mechanical properties of thousands of leukemia cells can be measured, cellular subpopulations with distinct biophysical properties can be detected. Whether these differences are due to a shift in the entire population or due to an increase in the number of outliers can also be examined. Increased knowledge of the biophysical differences among leukemia cells in patients with leukostasis would then provide the basis for developing future assays to identify patients at risk for leukostasis.

Using our BFC system, we analyzed leukemia cells isolated from an AML patient with leukostasis (AML2), an AML patient without leukostasis (AML1), and two ALL patients without leukostasis, in addition to normal neutrophils and red blood cells (RBC) from healthy control volunteers. Transit times of leukemia cells from the leukostasis-positive AML patient sample cells were significantly longer than those from the leukostasis-negative AML patient and the ALL patients, as well as normal neutrophils and RBCs ($p < 0.001$). Histogram data of leukemia cell transit times reveal bell-shaped distributions of all samples and that the majority of all leukemia cell populations traversed the microchannels in less than 1 s (Fig. 7ai–iv). Although the median leukemia cell transit times of samples were similar, ranging between 0.13 and 0.50 s (Fig. 7b), the transit times of the leukostasis-positive leukemia cells, however, had a much more prominent subpopulation of slow outliers (Fig. 7aiv, b).

The proportion of leukemia cells isolated from the leukostasis-positive AML patient that were able to traverse and not obstruct the microchannels was also significantly lower than both the leukostasis-asymptomatic AML patient and the ALL patients, as well as the normal neutrophils and RBCs (Fig. 8a) (Chi-square, $p < 0.001$ for all comparisons with the leukostasis AML patient sample). This observation is consistent with clinical data showing leukostasis occurs at a much higher propensity in patients with AML versus ALL [79].

As cells flow into the microchannels of the BFC, any occlusion that occurs prevents upstream cells from flowing through. Using automated image processing software, we tracked the change in the number of unobstructed microchannels versus the order of cells that entered into the device (Fig. 8b). Although all leukemia cells from all patient samples tested caused some degree of microchannel obstruction over time, leukostasis-positive AML cells obstructed the microchannels at a significantly higher rate (moderated linear regression, $p < 0.001$ for all comparisons of other leukemia patient samples with the leukostasis AML patient sample), resulting in only 10% of the original channels still open (Fig. 8b). These data collectively establish that the BFC enables the detection of leukostasis in acute leukemia, even among patients with the same leukemia subtype, and could potentially serve as a system to predict and diagnose leukostasis in acute leukemia.

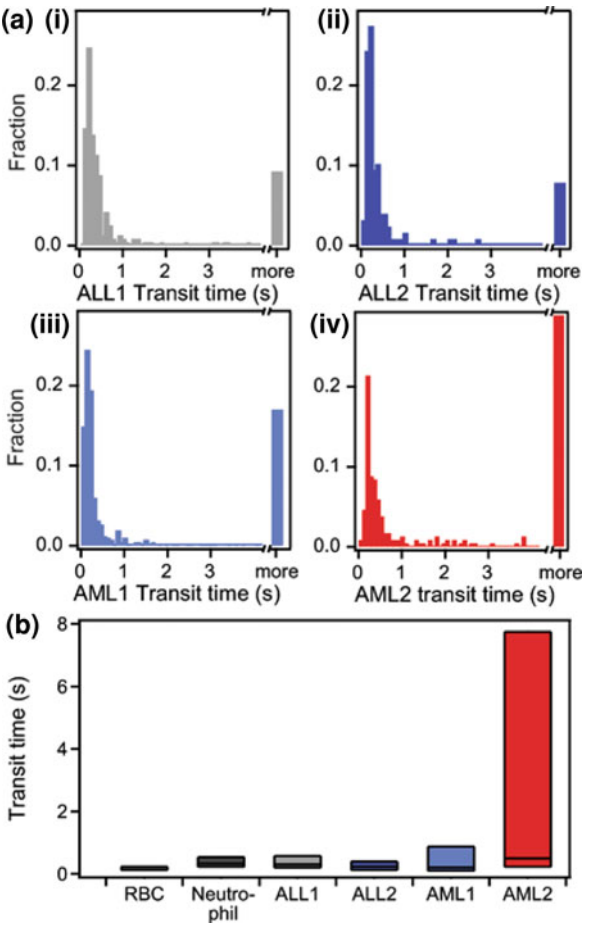

Fig. 7 The distribution of transit time of cells from a leukostasis-symptomatic patient is distinct from cells of leukostasis-asymptomatic patient cells. **a** Four patient leukemia samples were flowed through the device to determine transit time differences—two leukostasis-asymptomatic ALL samples (ALL1 and ALL2, *i–ii*, $n = 239$, 128, respectively), one leukostasis-asymptomatic AML sample (AML1, *iii*, $n = 418$), and one leukostasis-symptomatic AML sample (AML2, *iv*, $n = 239$). Distributions of the lower 50th percentile of the data are largely similar, but the upper 50th percentile substantially deviate. The leukostasis-symptomatic AML2 sample (*iv*) has a secondary subpopulation of cells with transit times ranging from 1 to 3 s. In addition, the fraction of cells that transit in greater than 4 s is substantially larger in the leukostasis-symptomatic AML2 (29%) than in the ALL and leukostasis-asymptomatic AML1 samples (9, 8, and 17%, respectively). **b** When looking at boxplots of the 25th, 50th, and 75th percentiles of the distributions, the differences in the population appear markedly different. While median transit times are substantially similar, the 75th percentile of the leukostasis-symptomatic AML2 sample is significantly higher than that of the leukostasis-asymptomatic samples and the RBCs and neutrophils (from Rosenbluth et al., *Lab on a Chip*, 2008)

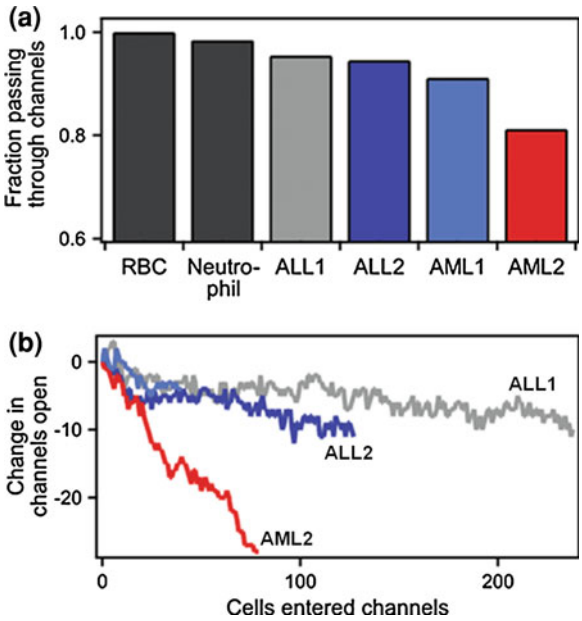

Fig. 8 Leukostasis-symptomatic patient cells have distinctively aberrant behavior when compared to leukostasis-asymptomatic patient cells and normal blood samples. **a** The fraction of cells that did not obstruct the channels is significantly lower in the leukostasis symptomatic AML2 sample versus the other samples. **b** The change in number of open channels is plotted versus the cells that entered the channels (a normalization of time for the density of cells entering the channels). Change in open channels was normalized to account for channels that were already occluded at the beginning of the experiment. A substantially reduced number of channels stayed open over time in the leukostasis-symptomatic AML2 sample than the leukostasis-asymptomatic AML1 sample or leukostasis-asymptomatic ALL samples (from Rosenbluth et al., *Lab on a Chip*, 2008)

2.2.2 Biophysical Flow Cytometry Reveals the Shifts in the Cell Mechanical Distribution of Leukemia Cells Due to Pharmacological Agents

To measure the biophysical effect of certain drugs, HL60 cells, an AML cell line, were flowed into the BFC. The transit times of the HL60 cells show a pattern similar to that of leukemia cells from the leukostasis AML sample, with a large number of long transit time outliers (Fig. 9a, b) and a significant proportion of obstructing the microchannels (Fig. 9c).

For these experiments, we used cytochalasin D, a common cell biology tool for decreasing cell stiffness and disrupting the actin cytoskeleton [38], and pentoxifylline, a phosphodiesterase inhibitor that reduces stiffness of neutrophils exposed to inflammatory cytokines while also reducing lung injury associated with hemorrhagic shock (see below) [10]. Both drugs dramatically reduced the transit time of HL60s through the microchannels ($p < 0.001$ for both drugs) and also created significant shifts in the transit time distributions. HL60 cells not exposed to either

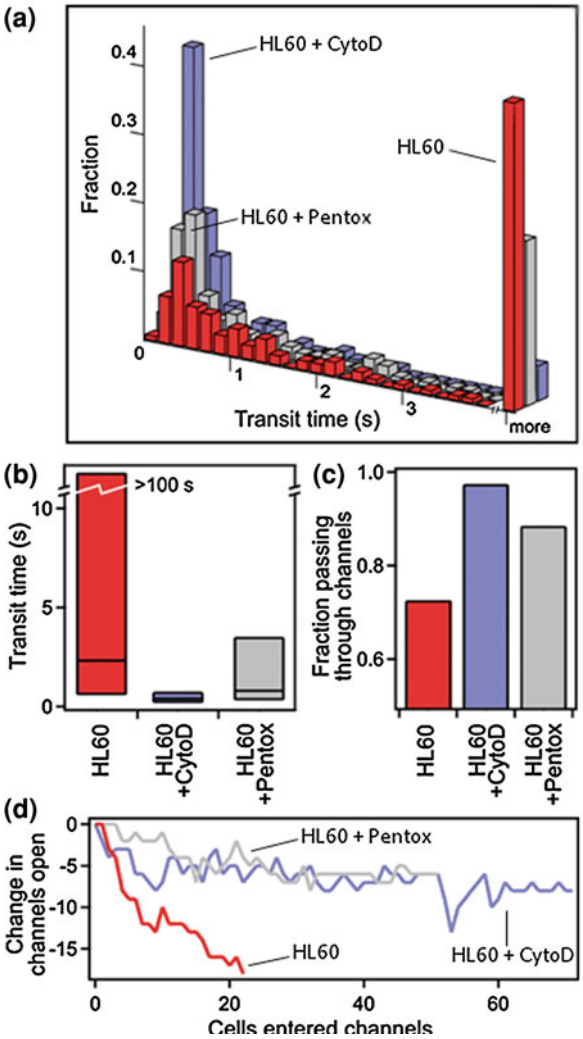

Fig. 9 Drug treatment improved flow through microchannels. **a** HL60 cells, a model AML leukemia line with a histogram profile similar to the leukostasis-symptomatic AML2 sample, were flowed through the device without exposure to any drug ($n = 146$), after exposure to pentoxifylline ($n = 157$), and after exposure to cytochalasin D ($n = 117$). Substantial shifts in the histograms can be seen after exposure to drugs, with a large fraction shifting from >4 s towards the median transit time. **b** The 25th, 50th, and 75th percentiles of the population all shifted downward after exposure to drugs, with cytochalasin D exposed cells experiencing more reduced transit time than pentoxifylline exposed cells. **c** The fraction of cells passing through the microchannels also significantly improved after exposure to cytochalasin D and pentoxifylline. **d** This resulted in a higher number of microchannels remaining open over time when drug-treated cells versus non-treated cells were flowed into the device (from Rosenbluth et al., *Lab on a Chip*, 2008)

drug showed a distribution that was spread with a low peak and a large number of slow cell outliers (>4 s) (Fig. 9a). The addition of either cytochalasin D or pentoxifylline shifted the distributions towards shorter transit times and reduced the number of slow cell outliers (Fig. 9a). Cytochalasin D and pentoxifylline reduced the median transit time from 0.63 s to 0.23 s and 0.37 s, respectively. In addition, both drugs substantially reduced the fraction of cells that obstructed the microchannels compared to HL60s that were not exposed to either drug (Chi-square $p < 0.001$ for both drugs). Finally, improved flow through the BFC was also observed with both drugs due to a reduction of the number of obstructed microchannels (Fig. 9d), indicating that decreasing the number of outlying occluding cells, which may be a relatively small subpopulation, can significantly

increase flow ($p < 0.001$). Taken together, these results suggest that the BFC and related devices can be useful for identifying new therapies and therapeutic targets for leukostasis in acute leukemia.

3 Modulation of Leukemia Cell Mechanics via Pharmacological Agents: Chemotherapy

While chemotherapy-induced cell death has been a mainstay of cancer treatment for decades and is well studied biochemically, little is known about the mechanical effects chemotherapy may have on leukemia cells. Furthermore, since hyperleukocytosis accompanies some cases of acute leukemia, mechanical changes in leukemia cells due to chemotherapy could significantly alter the overall blood rheology.

In previous work, we quantified the effect of standard induction chemotherapy on the stiffness of ALL and AML cells using an AFM coupled with an epifluorescence microscope and a Hertzian mechanics model for data analysis [50, 87]. The high force sensitivity of AFM and its ability to measure properties of individual cells over long times makes the technique particularly appropriate for measuring dynamic changes in cell stiffness. We found that when exposed to chemotherapy, leukemia cell stiffness increased by nearly two orders of magnitude at a rate dependent on the type of chemotherapy employed.

3.1 Chemotherapy-Induced Cell Death Increases Leukemia Cell Stiffness

Using a combined AFM/epifluorescence microscope, the stiffnesses of acute leukemia cells freshly isolated from the blood of newly diagnosed patients were measured in the presence of chemotherapeutic agents and were observed to increase 14 to 91-fold as cells underwent cell death (Fig. 10a–c). ALL and AML cells were exposed to typical treatment doses of dexamethasone or daunorubin, the mainstay induction chemotherapeutic agents for ALL and AML, respectively. During these measurements, positive staining with either propidium iodide (PI) or Sytox Green, markers for loss of cell membrane integrity, indicated cell death or late apoptosis. To identify early apoptosis, cresyl violet conjugated to DEVD, an indicator for early apoptotic caspase 3 and 7 activity, was used.

The mean leukemia cell stiffness of both ALL and AML cells held at 37°C and exposed to chemotherapy (mean: 4.7 kPa) was significantly higher than the mean stiffness of untreated control populations (mean: 0.2 kPa, $p < 0.05$, Fig. 10d, e). However, this increase in leukemia cell stiffness also occurred with other modes of cell death, as Fas-induced apoptotic cells and the rare dead cells in control populations were also noted to be significantly stiffer than live, untreated cells (data not shown). Although a decrease in cell volume is associated with cell death [45, 51],

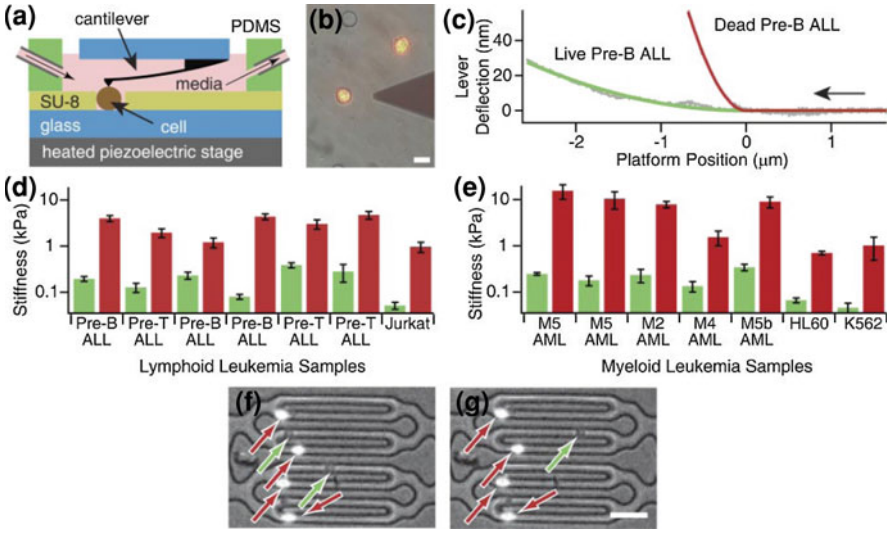

Fig. 10 *Chemotherapy*-induced cell death increases the stiffness of leukemia cell populations measured by AFM. **a** An illustration of the AFM setup (not to scale). A single cell sitting within a microwell is immobilized for force microscopy with an AFM cantilever. A polydimethylsiloxane (PDMS) collar is pressed upon the glass to create an open-air chamber. Tubes entering and exiting the chamber continually pass media through, keeping the media fresh over the long time scale of the experiments. The piezoelectric stage moves vertically, causing the cantilever to deflect against the cell. The stage is maintained at 37°C throughout the experiment. **b** An epifluorescence/brightfield overlay of a typical experiment. Seen here are an AFM cantilever tip and two dead K562 cells (PI positive, fluorescent), with the left cell immobilized in a microwell. An empty microwell is at the top. Scalebar is 20 μm. **c** Two typical cell indentation acquisitions. As the piezoelectric platform moves the cells up against the cantilever (in the direction of the arrow), the cantilever deflects. When the curves are fit to an elastic Hertzian model, the stiffness of the cells can be determined. The stiffness of a Pre-B ALL cell exposed to 1 μM dexamethasone was 4.3 kPa whereas the stiffness of a control (not exposed to chemotherapy) Pre-B ALL cell from the same patient was 0.2 kPa. **d** Dead lymphoid leukemic cells *(right dark grey bars*) exposed to 1 μM dexamethasone are significantly stiffer than untreated cells (*left light grey bars*). **e** Dead myeloid leukemic cells (*right dark grey bars*) exposed to 1 μM daunorubicin are significantly stiffer than untreated cells (*left light grey bars*). Error bars represent standard error. ($n > 15$, $p < 0.05$ for all comparisons of dead/untreated populations). **f** Dual bright field/epifluorescence microscopy of dexamethasone-exposed Pre-B ALL cells that were passed, from left to right, through PDMS microfluidic channels modeling a branching microvasculature network. Dead (PI+ and fluorescent) cells (*dark grey arrows*) were more likely than live (unstained) cells (*light grey arrows*) to initiate obstruction and cause cell aggregation in the 5 μm wide by 12 μm tall capillary-sized channels. Frame from (**g**) was taken 15 s after (**f**), illustrating the relative mobility of two live cells, one of which has left the field of view, compared to dead cells that remain fixed in place. Scalebar is 10 μm (from Lam et al., *Blood*, 2007)

we found that cell shrinkage occurs after chemotherapy-induced cell stiffening (Fig. 11). This suggests that the cell stiffness increase associated with chemotherapy exposure is not simply due to decreased volume and increased cell density.

Our results reveal that dead leukemia cells are more likely to obstruct microchannels and cause cell aggregation than live cells (Fig. 10f, g). In addition, the

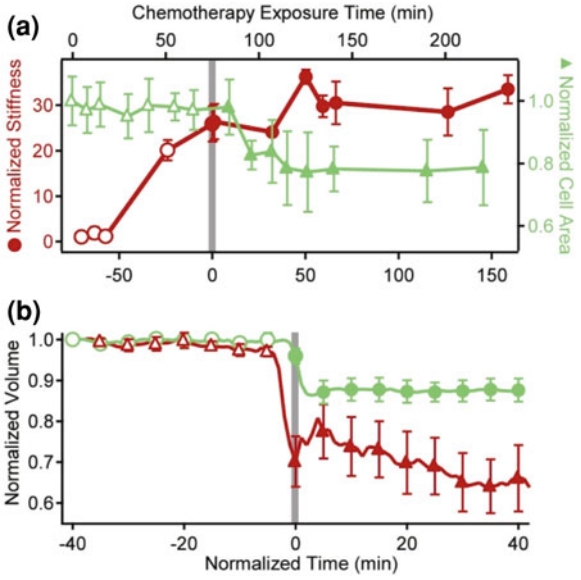

Fig. 11 Cell size changes with cell death. **a** As the stiffness of a single HL60 cell (*dark grey circles*) increases with exposure to 1 μM daunorubicin, the average cell area of the cell population (*light grey triangles*, $n = 8$–38 cells/field of view) remains constant until cell death (transition from *open* to *solid* shapes). Time is also normalized to the point of cell death (*vertical line*). **b** At the point of cell death, both HL60 (*dark grey triangles*) and Jurkat (*light circles*) cell lines show a rapid decrease in cell volume. Jurkat cells lose on average 12% of their volume and HL60 cells lose 26% of their volume within 10 min ($n = 10$ and $n = 7$, respectively). Error bars represent standard error of the mean (from Lam et al., *Blood*, 2007)

proportion of cells initiating microchannel obstruction relative to those able to traverse the entire microchannel system was approximately seven times higher for dead cells than live cells.

3.2 Kinetics of Cell Stiffness and Cell Death are Dependent on Chemotherapy Type

Serial single-cell AFM stiffness measurements were taken over several hours after chemotherapy exposure to determine the temporal relationship between increasing cell stiffness and chemotherapy exposure time. During those measurements, cells were tracked with fluorescent indicators for both early apoptosis and late apoptosis/cell death. Figure 12a shows the increase in stiffness for a single AML cell isolated from a newly diagnosed patient after daunorubicin exposure. Within an hour of exposure, cell stiffness began to increase and the rate of increase maximized after apoptosis was detected, peaking near the point of cell death. Consistent with this observation, the mean leukemia cell stiffness for populations of control

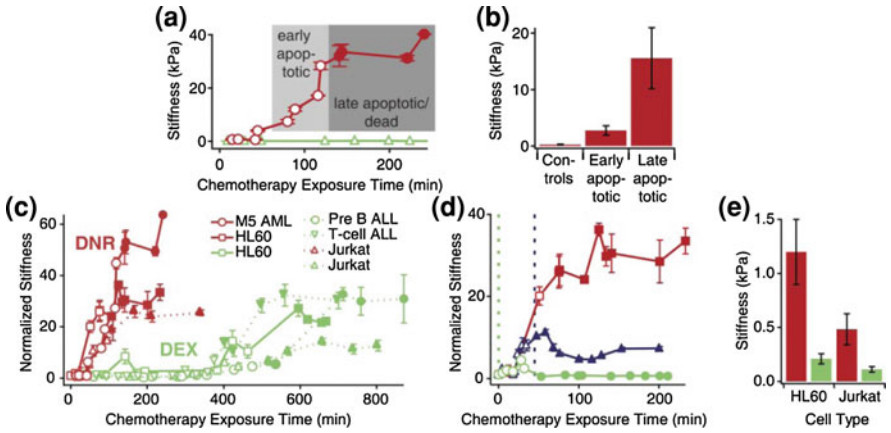

Fig. 12 Stiffness of leukemic cells increases with progression of cell death and is attenuated by disruption of the actin cytoskeleton. **a** A typical stiffness trace of a single M5 AML cell exposed to 1 μM daunorubicin (*dark grey circles*). The apparent stiffness of a typical control cell remains relatively constant (*triangles*) and does not undergo apoptosis or cell death during the course of the experiment. *Error bars* represent standard error. **b** From the same patient sample, the average apparent stiffness of a population of late apoptotic/dead AML cells was significantly stiffer than early apoptotic cells and controls ($n = 15$, $p < 0.05$). **c** Cell stiffness increases faster with 1 μM daunorubicin (DNR, *dark grey*) than 1 μM dexamethasone (DEX, *light grey*). *Solid* and *dotted lines* represent myeloid and lymphoid leukemia cells, respectively. Transition from *open* to *filled shapes* represent onset of cell death (PI positive staining). **d** Exposure to 2 μM cytochalasin D, an actin polymerization inhibitor, reduces stiffening behavior in HL60 cells exposed to 1 μM daunorubicin. The cells represented by these *three lines* were exposed to daunorubicin at time 0. The cell represented by the *light grey line* was also exposed to cytochalasin D at time 0 (*vertical light grey dashed line*) and exhibited little stiffening behavior. The cell represented by the *black line* was exposed to cytochalasin D after 45 min (*vertical black dashed line*) and exhibited little stiffening behavior after exposure. As a positive control, the cell represented by the *dark grey line* was not exposed to cytochalasin D. **e** HL60 and Jurkat cells were incubated with 1 μM daunorubicin and 2 μM cytochalasin D. The average stiffness of dead HL60 cells ($n = 15$) exposed to daunorubicin and cytochalasin D (*light grey*) was 0.2 ± 0.05 kPa, whereas the average stiffness of dead HL60 cells exposed to daunorubicin alone (*dark grey*) was 1.2 ± 0.3 kPa ($p < 0.05$). Likewise, the average stiffness of dead Jurkat cells ($n = 15$) exposed to daunorubicin and cytochalasin D (*light grey*) was 0.1 ± 0.03 kPa, whereas the average stiffness of dead Jurkat cells exposed to daunorubicin alone (*dark grey*) was 0.5 ± 0.14 kPa ($p < 0.05$) (from Lam et al., *Blood*, 2007)

cells, early apoptotic cells, and late apoptotic/dead cells showed significant increases with progression through the stages of chemotherapy-induced cell death (Fig. 12b, $p < 0.05$). Of note, cell stiffness began to increase before peak caspase activation in apoptosis, suggesting that cell stiffness changes associated with chemotherapy may occur before biological signs of apoptosis.

Experiments involving serial single-cell stiffness measurements on several different patient samples and cell lines showed that different chemotherapeutic agents were found to change cell stiffness at different rates (Fig. 12c). Drugs that lead to faster cell death rates, such as daunorubicin, led to faster rates of increase in

cell stiffness for all leukemia cell types, and drugs that lead to slower cell death rates, such as dexamethasone, led to slower rates of increase in cell stiffness.

3.3 Increase in Leukemia Cell Stiffness Due to Chemotherapy is Associated with Remodeling of the Actin Cytoskeleton

Chemotherapy-induced cell death is known to be associated with reorganization of actin in leukemic cells [38, 39, 41, 45]. To determine whether the actin cytoskeleton was involved in the observed chemotherapy-induced stiffness increase, the stiffness of single AML cells exposed to daunorubicin were tracked as cytochalasin D, an inhibitor of actin polymerization, was added (Fig. 12d). As cell death progressed, cells exposed simultaneously to both cytochalasin D and daunorubicin exhibited almost no increase in cell stiffness. When cytochalasin D was added to stiffening leukemia cells already exposed to chemotherapy, cell stiffness ceased to increase within 15 min and then decreased. The mean stiffness of dead AML cells (from the HL60 cell line) and ALL cell populations (from the Jurkat cell line) exposed simultaneously to daunorubicin and cytochalasin D was found to be significantly less than the stiffness of cells exposed to only daunorubicin ($p < 0.05$, Fig. 12e). These experiments suggest that the stiffness increase with chemotherapy-induced cell death is at least partly due to dynamic changes in the actin cytoskeleton.

3.4 Clinical Implications of Leukemia Cell Stiffening Associated with Chemotherapy Exposure

The observed associated between cell death and increasing cell stiffness may have implications for acute leukemia patients with hyperleukocytosis. Our results show that chemotherapy-induced cell death increases the stiffness of leukemia cells, which may influence microvascular flow in patients. Indeed, leukostasis that paradoxically does not occur until after chemotherapy has been initiated has been reported numerous times [63, 70, 79, 108], and alteration of leukemic cells' biophysical properties by chemotherapeutic agents has been hypothesized as a possible etiology [59, 63, 70]. Further work is required to test these hypotheses and to clarify the role, if any, of chemotherapy-induced cell stiffening on the pathophysiology of leukostasis in acute leukemia.

4 Modulation of Leukemia Cell Mechanics via Pharmacological Agents: Pentoxifylline

The tools and techniques described above have the potential to serve as drug discovery platforms for potential therapies in leukostasis. One such candidate

therapeutic agent is the phosphodiesterase inhibitor pentoxifylline, which is known to decrease red cell deformability and has been used for several decades to improve microvascular blood flow in peripheral arterial disease. More recently, pentoxifylline has been shown to modulate inflammatory processes including the attenuation of leukocyte stiffening and adhesion that occur upon activation. Therefore, recent clinical studies have concluded that this drug may be an effective adjunctive therapy for acute lung injury and other disease states in which the inflammatory response is exaggerated and detrimental for the patient. However, no reported studies have investigated the biophysical effects of leukemia cells in the context of leukostasis. Here we describe preliminary results in which we measured the effect pentoxifylline has on leukemia cell stiffness and adhesion.

4.1 Pharmacology of Pentoxifylline

Pentoxifylline, or 1-(5-oxohexyl)-3,7-dimethylxanthine, is a xanthine derivative and has been clinically approved for the treatment of symptoms due to peripheral arterial disease resulting from obstructed arteries in the limbs, and vascular dementia, in which arterial insufficiency in the brain microvasculature affects neurologic and cognitive function [89]. Pentoxifylline improves blood flow through blood vessels and therefore helps with blood circulation in the arms and legs (e.g. intermittent claudication). This drug has also been used for stroke and sickle cell disease, although clinical studies have had mixed results and there has not been definitively proven benefits in morbidity or mortality in those diseases [107].

Pentoxifylline's exact mechanism of action remains unclear and is likely complex. However, it is known that pentoxifylline functions as a phosphodiesterase inhibitor, thereby increasing intracellular cAMP, which is a common intracellular second messenger in multiple cell signaling pathways. More recently, the drug has been shown to exert anti-inflammatory and anti-thrombotic effects on leukocytes, platelets, and endothelial cells [52, 89, 107].

4.2 Effect of Pentoxifylline on Leukemia Cell Stiffness and Adhesion

Previous research has shown that pentoxifylline, for reasons that remain unclear, increases neutrophil deformability and attenuates neutrophil stiffening upon activation [4, 18, 88, 91]. In addition, there is also clinical evidence suggesting that pentoxifylline decreases mortality in disease states involving leukocyte activation leading to microvascular occlusion [20, 24, 66, 86, 90, 103].

To determine if pentoxifylline alters leukemia cell mechanical properties, we exposed HL60 promyelocytic leukemia cells to pentoxifylline and found that leukemia cell transit time through microchannels decreased significantly, as

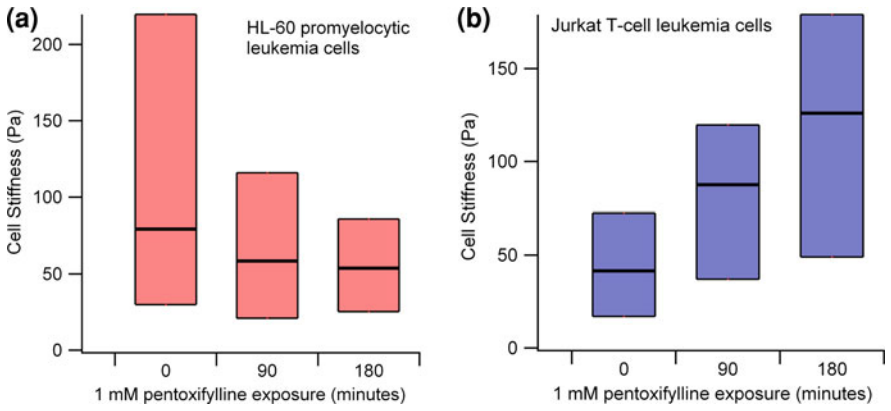

Fig. 13 Pentoxifylline alters leukemia cell stiffness in a time-dependent manner as shown by AFM. **a** The stiffness of myeloid HL-60 cells decreases over time with exposure to pentoxifylline. Cells exposed to pentoxifylline for 90 min ($n = 15$) showed a marginally significant decrease in stiffness compared to control cells ($n = 22$, $p < 0.06$), whereas a statistically significant decrease in stiffness was noted between cells exposed to pentoxifylline for 180 min ($n = 13$, $p < 0.02$) and controls. **b** In contrast, the stiffness of lymphoid Jurkat cells increases over time with pentoxifylline exposure. Cells exposed to pentoxifylline for 90 min ($n = 14$) showed a significant increase in stiffness compared to control cells ($n = 15$, $p < 0.03$). Although stiffness continued to increase with further exposure to pentoxifylline, cell exposed to pentoxifylline for 180 min ($n = 11$) only showed a marginal statistical difference when compared to the cells incubated for 90 min ($p < 0.075$)

described in Sect. 2 in The Nanofiber Matrix as an Artificial Stem Cell Niche (Fig. 9). In addition, we also used our previously published AFM protocols using microwells for cell immobilization and a flow chamber with heated stage to perform AFM measurements in an environment conducive for cell culture [50, 87]. The myeloid leukemia HL-60 cell line and lymphoid leukemia Jurkat cell line were used as models for AML and ALL cells, respectively. For each experiment, three cell subpopulations were compared: controls (no exposure to pentoxifylline), cells exposed to 1 mM pentoxifylline for 90 min, and cells exposed to 1 mM pentoxifylline for 180 min. Our data indeed showed a time-dependent change in stiffness for both cell lines when cells are exposed to pentoxifylline. Interestingly, the drug appeared to have opposite mechanical effects on the two cell lines. Stiffness for the AML cells decreased with pentoxifylline exposure over 3 h, whereas it increased for ALL cells over the same time interval (Fig. 13). These results indicate the pentoxifylline does in fact alter the mechanical properties of leukemia cells.

Pentoxifylline has also been reported to decrease the adhesive properties of blood cells, including neutrophils and lymphocytes, by decreasing leukocyte activation, downregulating expression of adhesion molecules and decreasing secretion of cytokines [23, 37, 93]. Specifically, ICAM-1, E-selectin, LFA-1, and VLA-4 expression on leukocytes decreases in the presence of pentoxifylline [15, 71].

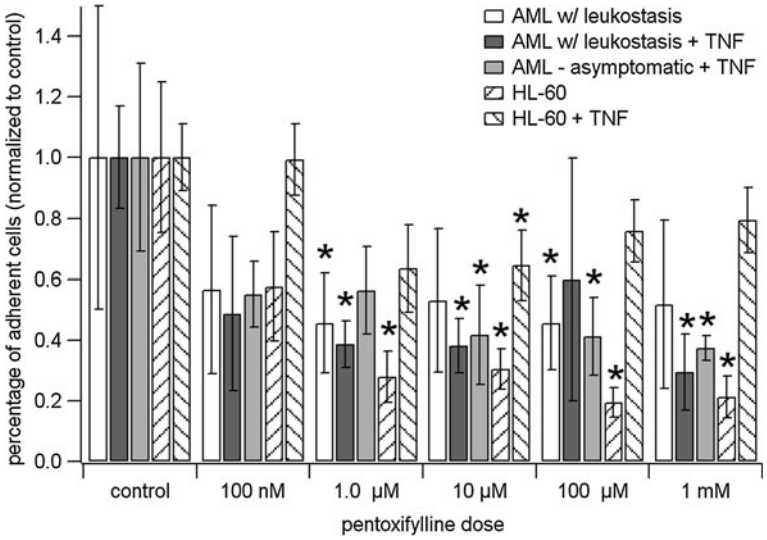

Fig. 14 Pentoxifylline decreases myeloid leukemia cell adhesion to human umbilical vein endothelial cells (HUVECs). HL-60 leukemia cells and primary AML cells taken from a patient who subsequently died of leukostasis and an asymptomatic were incubated with varying doses of pentoxifylline (with or without TNF-α) for 45 min, then co-incubated with HUVEC monolayers (with or without TNF-α) for another 45 min, and non-adherent cells were then washed away. Adherent cells were visualized and quantified with brightfield optical microscopy. Results are displayed as a percentage of remaining adherent cells relative to the corresponding control condition. *Asterisks* indicate statistically significant differences ($p < 0.05$) between the designated and the corresponding control populations

In addition, this drug also affects endothelial inflammatory responses, by attenuating cytokine-mediated adhesion molecule expression and endothelial permeability to leukocyte transmigration [6, 89].

To investigate how pentoxifylline modulates the adhesive interactions between leukemia cells and human umbilical vein endothelial cells (HUVECs), a static adhesion assay was used in which pentoxifylline-exposed leukemia and endothelial cells were co-incubated, washed, and remaining adherent cells were quantified using brightfield microscopy.

Myeloid leukemia cells showed a statistically significant decrease in adhesion to endothelial cells (Fig. 14). However, in the presence of the inflammatory cytokine TNF-α, pentoxifylline had no significant effect on altering the adherence of both HL-60 and primary AML cells to HUVECs. This suggests that pentoxifylline's effects on cell adhesion may only occur in myeloid leukemia cells that have not been activated or have dysfunctional or non-functional inflammatory signaling pathways. In addition, pentoxifylline exhibited no differential effect on leukemia cells taken from the leukostasis-positive patient versus the asymptomatic patient.

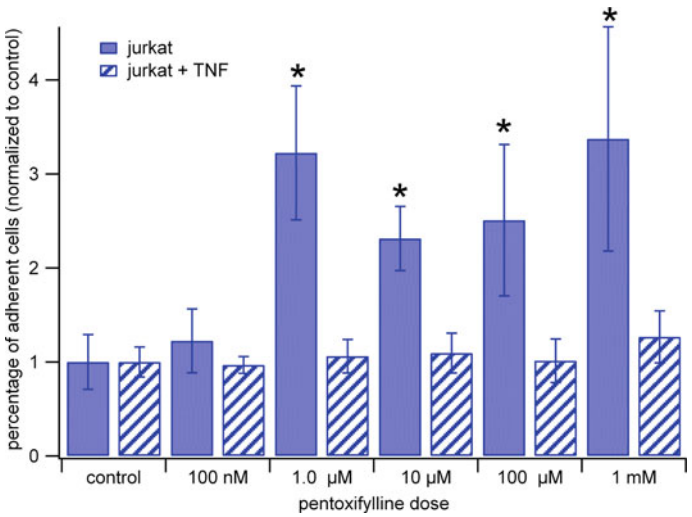

Fig. 15 Pentoxifylline increases lymphoid leukemia cell adhesion to human umbilical vein endothelial cells (HUVECs). Jurkat leukemia cells were incubated with varying doses of pentoxifylline (with and without TNF-α) for 45 min, then co-incubated with HUVEC monolayers (with and without TNF-α) for another 45 min, and non-adherent cells were then washed away. Adherent cells were visualized and quantified with brightfield optical microscopy. Results are displayed as a percentage of remaining adherent cells relative to the corresponding control condition

In contrast to the myeloid leukemia cells, lymphoid Jurkat leukemia cells increased adherence to HUVECs when exposed to pentoxifylline in the same experimental conditions (Fig. 15). There was no increased adhesion, however, when cells were exposed to TNF-α in addition to pentoxifylline, implying that in lymphoblasts, pentoxifylline may trigger similar pathways as inflammatory cytokines.

As described in the previous sections, leukostasis in acute leukemia is likely due to the biophysical alterations of leukemic cells leading to microvascular obstruction in vital organs. As pentoxifylline has been shown to soften neutrophils in both inactivated and activated states and decrease the adhesive leukocyte-endothelial interactions, this drug is a logical target for leukostasis treatment or prevention. Our data suggest that pentoxifylline does in fact affect leukemia cell mechanical properties, but interestingly, seems to have a differential effect between myeloid and lymphoid leukemia cells. Whereas pentoxifylline decreases the stiffness and endothelial cell adhesiveness of primary AML and HL-60 cells, the stiffness and adhesiveness is increased with lymphoid Jurkat T lymphoblasts. The underlying mechanisms for these effects are unclear and will require further study. In addition, more data with primary cells and other leukemia cell lines need to be collected before any definitive conclusions can be drawn regarding the potential for using pentoxifylline to prevent or treat leukostasis. However, the mechanical changes we have documented do suggest that pentoxifylline may

decrease microvascular occlusion due to AML cells and improve microcirculatory flow and justify more in vivo patient-based research to determine if this drug has the potential to ameliorate leukostasis in AML. We will continue our current studies to further clarify the biophysical effects this drug may have on leukemia cells in the context of leukostasis.

Currently, there is no medication that successfully treats and prevents the life-threatening complication of leukostasis in acute leukemia. As pentoxifylline has been in use for several decades for the treatment of other diseases and is known to be a well-tolerated drug with minimal side effects, the risk–benefit ratio is significantly low and warrants a prospective clinical trial exploring the use of this drug for newly diagnosed patients with AML.

5 Modulation of Leukemia Cell Mechanics via Pharmacological Agents: ATRA in APML

In the last decade, use of the vitamin A derivative ATRA in APML has been shown to markedly decrease mortality and increase patient survival. This novel chemotherapeutic agent selectively differentiates APML cells into more mature granulocytes. However, a potential adverse effect of this medication is retinoic acid syndrome, a life threatening complication associated with massive infiltration of vital organs by maturing myeloid cells [101]. Alterations in the cellular mechanics of APML cells induced by ATRA are thought to play a role retinoic acid syndrome [11], but little experimental data exist to support or disprove these theories.

Recently, Lautenschläger et al. applied a microfluidic optical stretcher, which traps and deforms suspended cells by optically induced surface forces from two opposing non-focused laser beams, to directly address this issue [42, 53]. This system provides the capability to investigate the mechanical properties of cells without direct contact of the cells themselves, eliminating potentially confounding effects of cell-probe contact.

To assess alterations of cell deformability associated with ATRA-induced differentiation, APML cells treated for 3 days were analyzed with their optical stretcher and compared to untreated APML cells. APML cells differentiated with ATRA were found to be 45% more compliant than control APML cells [53]. Interestingly, this cellular compliance is consistent with that of normal neutrophils taken from healthy subjects, suggesting the biophysical properties of myeloid cell differentiation coincide with biological differentiation.

Moreover, electron microscopy revealed that the mesh size of the actin cytoskeleton is increased in ATRA-differentiated APML cells versus untreated APML cells [53]. As actin mesh size is inversely related to the elastic shear modulus of polymer networks [65], this suggests that actin remodeling is involved with the ATRA-induced alterations in the biophysical properties of APML cells. In addition, depolymerization of F-actin with latrunculin A further increased the

deformability of ATRA-differentiated APML cells, further implicating the biophysical role of actin in this process.

Taken together, the data collected by Lautenschläger et al. again draw attention to the biophysical effects medications may have the cellular mechanical properties of leukemia cells, but from a different perspective than studies related to leukostasis in acute leukemia. In the case of ATRA-induced biophysical alterations of APML cells, the increase in compliance of differentiated APML cells may enhance their capabilities to infiltrate from the microcirculation into the surrounding tissues, possibly leading to organ damage. As autopsies clearly demonstrate pulmonary infiltration of mature myeloid cells in APML patients who died of retinoic acid syndrome, these experiments suggest that drug-induced cell mechanical alterations may have a role in the pathophysiology of this life-threatening complication. Further studies in this area of research are vital to fully elucidate the exact underlying biophysical mechanisms of ATRA in retinoic acid syndrome.

6 Clinical Implications and Future Work

This chapter describes the clinical relevance of the nascent field of cell mechanics and discusses how the techniques of this discipline can further our knowledge of hematologic diseases in which cell mechanical properties are altered. Specifically, this body of work uses the tools of cell mechanics to further our understanding of leukostasis, a complication of acute leukemia that is thought to be caused by alterations in leukemia cell mechanical properties, such as adhesion and cell stiffness. Interestingly, this biophysical theory of leukostasis has existed for decades, but it has never been thoroughly investigated, likely due to the lack of necessary tools. It is only because of recent technological advances, namely with the advent of atomic force microscopy and microfabrication techniques in biological research, were we able to conduct our experiments to learn more about this life-threatening complication of leukemia. In addition, novel technologies such as the optical stretcher have provided important data linking the cell mechanical alterations of the drug ATRA on APML cells. These experiments prove that biophysical alterations coincide with the differentiation of promyelocytic cells into mature neutrophils and also suggest that ATRA-induced cell deformability may play an important role in retinoic acid syndrome in APML patients.

Although these studies represent valuable contributions to the field of clinical hematology and cellular mechanics, leukostasis and retinoic acid syndrome remain to be poorly understood complications of acute leukemia and a multitude of questions remain. What is the role of adhesion molecules between leukemic and endothelial cells and how do pharmacologic agents modulate these interactions? How do cytokines and other soluble inflammatory molecules factor into these interactions? Out of the several biophysical parameters in question, which dominate and are the most significant causes of leukostasis? What role do platelets and coagulation have in leukostasis and retinoic acid syndrome?

To begin addressing some of these questions, we have recently developed a technique to modify our BFC systems so that, endothelial cell monolayers are cultured in 3D along the inner surfaces of our microdevices (Fig. 16a). This "endothelialized" microfluidic BFC system integrates cell deformability and cell adhesion under physiologic microvascular flow conditions, functioning as an in vitro microvasculature-on-a-chip. As a proof of concept, we applied the device to study the cellular mechanics of leukemia cells isolated from newly diagnosed AML patients as both cell deformability and cell adhesion are likely to have significant roles in the pathophysiology of leukostasis. Leukemia cells isolated from both an AML patient with leukostasis and another patient with the identical subtype of AML but without leukostasis were flowed into the modified BFC system (Fig. 16b). In preliminary studies, we found that leukostasis-positive AML cells were much more adherent and caused much more microchannel obstruction than leukostasis-negative AML cells. Further complementary AFM cell stiffness

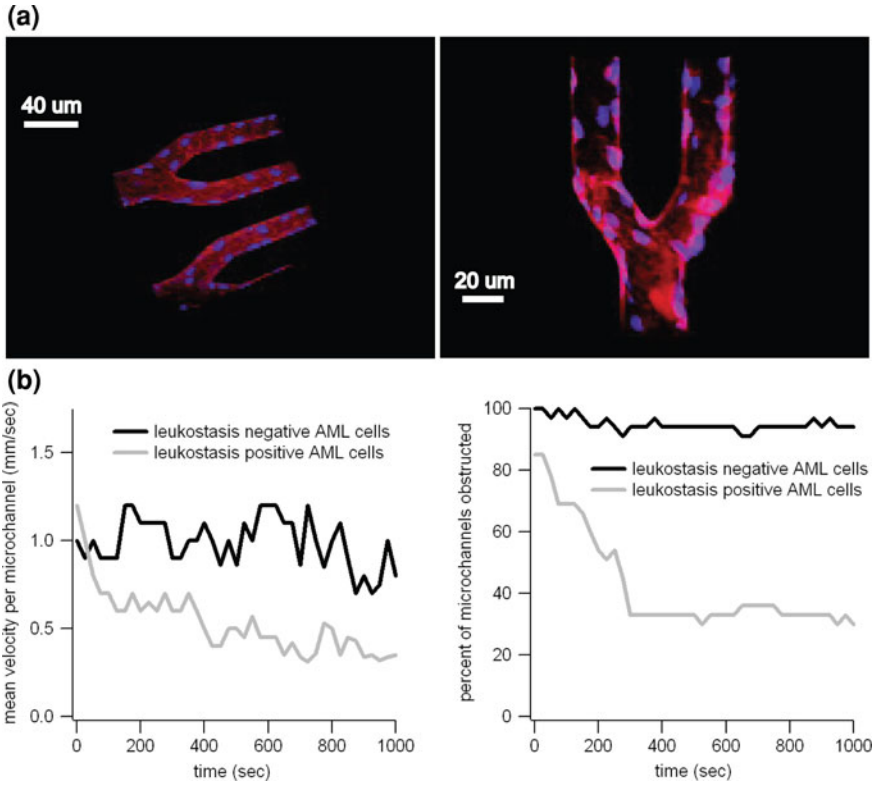

Fig. 16 Applying the microvasculature-*on-a*-chip to study leukostasis in AML. **a** 3-D culture of human endothelial cells in microfluidic channels of the BFC system (stained with cell membrane and nucleus dyes). **b** AML cells from a leukostasis-positive patient cause more microchannel obstruction and a larger decrease in microchannel velocity than AML cells from a leukostasis negative patient

measurements and parallel plate adhesion assays, when used in conjunction with the microvasculature-on-a-chip, will then determine the relative role cell deformability versus cell adhesion have in microvascular obstruction. This capability fulfills an important need in the study of cellular mechanics and hematologic diseases.

Although we have only scratched the surface in our comprehension of the interactions between cell mechanics, pharmacological agents and leukemia pathophysiology, novel tools and techniques such as those described above will enable future research to be conducted in a more efficient and informative manner. In addition, these systems have the potential to function as new classes of drug discovery platforms and diagnostic devices. In the near future, the interdisciplinary field of cellular mechanics will not only further our understanding of leukemia, but it will provide valuable insights into a myriad of other disease states where cell biology is known to interact with biophysics such as, sickle cell disease, clotting disorders, inflammatory disorders, sepsis, cardiovascular disease, and even other forms of cancer.

References

1. Abiko, T., Abiko, A., Clermont, A.C., Shoelson, B., Horio, N., Takahashi, J., Adamis, A.P., King, G.L., Bursell, S.E.: Characterization of retinal leukostasis and hemodynamics in insulin resistance and diabetes: role of oxidants and protein kinase-C activation. Diabetes **52**, 829–837 (2003)
2. Abkarian, M., Faivre, M., Stone, H.A.: High-speed microfluidic differential manometer for cellular-scale hydrodynamics. Proc. Natl. Acad. Sci. USA **103**, 538–542 (2006)
3. Aprelev, A., Weng, W., Zakharov, M., Rotter, M., Yosmanovich, D., Kwong, S., Briehl, R.W., Ferrone, F.A.: Metastable polymerization of sickle hemoglobin in droplets. J. Mol. Biol. **369**, 1170–1174 (2007)
4. Armstrong, M., Jr., Needham, D., Hatchell, D.L., Nunn, R.S.: Effect of pentoxifylline on the flow of polymorphonuclear leukocytes through a model capillary. Angiology **41**, 253–262 (1990)
5. Bagge, U., Amundson, B., Lauritzen, C.: White blood cell deformability and plugging of skeletal muscle capillaries in hemorrhagic shock. Acta Physiol. Scand. **108**, 159–163 (1980)
6. Bahra, P.S., Rainger, G.E., Wautier, J.L., Nash, G.B.: Effects of pentoxifylline on the different steps during adhesion and transendothelial migration of flowing neutrophils. Cell Biochem. Funct. **19**, 249–257 (2001)
7. Barabino, G.A., McIntire, L.V., Eskin, S.G., Sears, D.A., Udden, M.: Endothelial cell interactions with sickle cell, sickle trait, mechanically injured, and normal erythrocytes under controlled flow. Blood **70**, 152–157 (1987a)
8. Barabino, G.A., McIntire, L.V., Eskin, S.G., Sears, D.A., Udden, M.: Rheological studies of erythrocyte–endothelial cell interactions in sickle cell disease. Prog. Clin. Biol. Res. **240**, 113–127 (1987b)
9. Baskurt, O.K., Meiselman, H.J.: Hemodynamic effects of red blood cell aggregation. Indian J. Exp. Biol. **45**, 25–31 (2007)
10. Betticher, D.C., Keller, H., Maly, F.E., Reinhart, W.H.: The effect of endotoxin and tumour necrosis factor on erythrocyte and leucocyte deformability in vitro. Br. J. Haematol. **83**, 130–137 (1993)
11. Bi, K.H., Jiang, G.S.: Relationship between cytokines and leukocytosis in patients with APL induced by all-trans retinoic acid or arsenic trioxide. Cell Mol. Immunol. **3**, 421–427 (2006)

12. Binnig, G., Quate, C.F., Gerber, C.: Atomic force microscope. Phys. Rev. Lett. **56**, 930–933 (1986)
13. Bransky, A., Korin, N., Nemirovski, Y., Dinnar, U.: An automated cell analysis sensing system based on a microfabricated rheoscope for the study of red blood cells physiology. Biosens. Bioelectron. **22**, 165–169 (2006)
14. Brown, D.C., Tsuji, H., Larson, R.S.: All-trans retinoic acid regulates adhesion mechanism and transmigration of the acute promyelocytic leukaemia cell line NB-4 under physiologic flow. Br. J. Haematol. **107**, 86–98 (1999)
15. Bruynzeel, I., van der Raaij, L.M., Willemze, R., Stoof, T.J.: Pentoxifylline inhibits human T-cell adhesion to dermal endothelial cells. Arch. Dermatol. Res. **289**, 189–193 (1997)
16. Bunin, N.J., Pui, C.H.: Differing complications of hyperleukocytosis in children with acute lymphoblastic or acute nonlymphoblastic leukemia. J. Clin. Oncol. **3**, 1590–1595 (1985)
17. Chibber, R., Ben-Mahmud, B.M., Chibber, S., Kohner, E.M.: Leukocytes in diabetic retinopathy. Curr. Diabetes Rev. **3**, 3–14 (2007)
18. Chien, S., Sung, K.L., Schmid-Schonbein, G.W., Skalak, R., Schmalzer, E.A., Usami, S.: Rheology of leukocytes. Ann. NY Acad. Sci. **516**, 333–347 (1987)
19. Clermont, A.C., Bursell, S.E.: Retinal blood flow in diabetes. Microcirculation **14**, 49–61 (2007)
20. Coimbra, R., Melbostad, H., Loomis, W., Porcides, R.D., Wolf, P., Tobar, M., Hoyt, D.B.: LPS-induced acute lung injury is attenuated by phosphodiesterase inhibition: effects on proinflammatory mediators, metalloproteinases, NF-kappaB, and ICAM-1 expression. J. Trauma **60**, 115–125 (2006)
21. Davey, H.M., Kell, D.B.: Flow cytometry and cell sorting of heterogeneous microbial populations: the importance of single-cell analyses. Microbiol. Rev. **60**, 641–696 (1996)
22. De Rossi, G., Tenca, C., Cerruti, G., Favre, A., Zarcone, D., Tabilio, A., Mauro, F.R., Annino, L., Grossi, C.E.: Adhesion molecule expression on B-cells from acute and chronic lymphoid leukemias. Leuk. Lymphoma **16**, 31–36 (1994)
23. Deree, J., Lall, R., Melbostad, H., Loomis, W., Hoyt, D.B., Coimbra, R.: Pentoxifylline attenuates stored blood-induced inflammation: a new perspective on an old problem. Surgery **140**, 186–191 (2006)
24. Deree, J., Martins, J., de Campos, T., Putnam, J.G., Loomis, W.H., Wolf, P., Coimbra, R.: Pentoxifylline attenuates lung injury and modulates transcription factor activity in hemorrhagic shock. J. Surg. Res. **143**, 99–108 (2007)
25. Discher, D.E., Janmey, P., Wang, Y.L.: Tissue cells feel and respond to the stiffness of their substrate. Science **310**, 1139–1143 (2005)
26. Downing, J.R., Shannon, K.M.: Acute leukemia: a pediatric perspective. Cancer Cell **2**, 437–445 (2002)
27. Drost, E.M., Kassabian, G., Meiselman, H.J., Gelmont, D., Fisher, T.C.: Increased rigidity and priming of polymorphonuclear leukocytes in sepsis. Am. J. Respir. Crit. Care Med. **159**, 1696–1702 (1999)
28. Dubois, C., Schlageter, M.H., de Gentile, A., Balitrand, N., Toubert, M.E., Krawice, I., Fenaux, P., Castaigne, S., Najean, Y., Degos, L., et al.: Modulation of IL-8, IL-1 beta, and G-CSF secretion by all-trans retinoic acid in acute promyelocytic leukemia. Leukemia **8**, 1750–1757 (1994)
29. Eaton, W.A., Hofrichter, J.: The biophysics of sickle cell hydroxyurea therapy. Science **268**, 1142–1143 (1995)
30. Engler, A.J., Sen, S., Sweeney, H.L., Discher, D.E.: Matrix elasticity directs stem cell lineage specification. Cell **126**, 677–689 (2006)
31. Estlin, E.J., Yule, S.M., Lowis, S.P.: Consolidation therapy for childhood acute lymphoblastic leukaemia: clinical and cellular pharmacology of cytosine arabinoside, epipodophyllotoxins and cyclophosphamide. Cancer Treat. Rev. **27**, 339–350 (2001)
32. Frenette, P.S.: Sickle cell vaso-occlusion: multistep and multicellular paradigm. Curr. Opin. Hematol. **9**, 101–106 (2002)
33. Fung, Y.C.: Biomechanics: Circulation. Springer, New York (1997)

34. Gifford, S.C., Derganc, J., Shevkoplyas, S.S., Yoshida, T., Bitensky, M.W.: A detailed study of time-dependent changes in human red blood cells: from reticulocyte maturation to erythrocyte senescence. Br. J. Haematol. **135**, 395–404 (2006)
35. Gifford, S.C., Frank, M.G., Derganc, J., Gabel, C., Austin, R.H., Yoshida, T., Bitensky, M.W.: Parallel microchannel-based measurements of individual erythrocyte areas and volumes. Biophys. J. **84**, 623–633 (2003)
36. Goddette, D.W., Frieden, C.: Actin polymerization. The mechanism of action of cytochalasin D. J. Biol. Chem. **261**, 15974–15980 (1986)
37. Gonzalez-Amaro, R., Portales-Perez, D., Baranda, L., Redondo, J.M., Martinez-Martinez, S., Yanez-Mo, M., Garcia-Vicuna, R., Cabanas, C, Sanchez-Madrid, F.: Pentoxifylline inhibits adhesion and activation of human T lymphocytes. J. Immunol. **161**, 65–72 (1998)
38. Grzanka, A.: Actin distribution patterns in HL-60 leukemia cells treated with etoposide. Acta Histochem. **103**, 453–464 (2001)
39. Grzanka, A., Grzanka, D., Orlikowska, M.: Cytoskeletal reorganization during process of apoptosis induced by cytostatic drugs in K-562 and HL-60 leukemia cell lines. Biochem. Pharmacol. **66**, 1611–1617 (2003)
40. Grzanka, A., Grzanka, D., Orlikowska, M.: Fluorescence and ultrastructural localization of actin distribution patterns in the nucleus of HL-60 and K-562 cell lines treated with cytostatic drugs. Oncol. Rep. **11**, 765–770 (2004)
41. Grzanka, A., Grzanka, D., Zuryn, A., Grzanka, A.A., Safiejko-Mroczka, B.: Reorganization of actin in K-562 and HL-60 cells treated with taxol. Neoplasma **53**, 56–61 (2006)
42. Guck, J., Ananthakrishnan, R., Mahmood, H., Moon, T.J., Cunningham, C.C., Käs, J.: The optical stretcher: a novel laser tool to micromanipulate cells. Biophys. J. **81**, 767–84 (2001)
43. Hallows, K.R., Frank, R.S.: Changes in mechanical properties with DMSO-induced differentiation of HL-60 cells. Biorheology **29**, 295–309 (1992)
44. Hertz, H.: Über die Berühung fester elastischer Körper. J. Reine Angew. Math. **92**, 156–171 (1882)
45. Hessler, J.A., Budor, A., Putchakayala, K., Mecke, A., Rieger, D., Banaszak Holl, M.M., Orr, B.G., Bielinska, A., Beals, J., Baker, J., Jr.: Atomic force microscopy study of early morphological changes during apoptosis. Langmuir **21**, 9280–9286 (2005)
46. Hutchinson, R.J., Gaynon, P.S., Sather, H., Bertolone, S.J., Cooper, H.A., Tannous, R., Wells, L.M., Heerema, N.A., Sailer, S., Trigg, M.E.: Intensification of therapy for children with lower-risk acute lymphoblastic leukemia: long-term follow-up of patients treated on Children's Cancer Group Trial 1881. J. Clin. Oncol. **21**, 1790–1797 (2003)
47. Irish, J.M., Kotecha, N., Nolan, G.P.: Mapping normal and cancer cell signalling networks: towards single-cell proteomics. Nat. Rev. Cancer **6**, 146–155 (2006)
48. Kimby, E., Nygren, P., Glimelius, B.: A systematic overview of chemotherapy effects in acute myeloid leukaemia. Acta Oncol. **40**, 231–252 (2001)
49. Lam, W.A., Rosenbluth, M.J., Fletcher, D.A.: Increased leukaemia cell stiffness is associated with symptoms of leucostasis in paediatric acute lymphoblastic leukaemia. Br. J. Haematol. **142**, 497–501 (2008)
50. Lam, W.A., Rosenbluth, M.J., Fletcher, D.A.: Chemotherapy exposure increases leukemia cell stiffness. Blood **109**, 3505–3508 (2007)
51. Lang, F., Ritter, M., Gamper, N., Huber, S., Fillon, S., Tanneur, V., Lepple-Wienhues, A., Szabo, I., Gulbins, E.: Cell volume in the regulation of cell proliferation and apoptotic cell death. Cell Physiol. Biochem. **10**, 417–428 (2000)
52. Lassiter, T.F.: Medications used to prevent adhesion and clotting. Lippincotts Prim Care Pract. **4**, 619–632 (quiz 633–615) (2000)
53. Lautenschläger, F., Paschke, S., Schinkinger, S., Bruel, A., Beil, M., Guck, J.: The regulatory role of cell mechanics for migration of differentiating myeloid cells. Proc. Natl. Acad. Sci. USA **106**, 15696–701 (2009)
54. Lee, W.G., Bang, H., Yun, H., Lee, J., Park, J., Kim, J.K., Chung, S., Cho, K., Chung, C., Han, D.C., Chang, J.K.: On-chip erythrocyte deformability test under optical pressure. Lab Chip **7**, 516–519 (2007)

55. Levee, M.G., Dabrowska, M.I., Lelli, J.L., Jr, Hinshaw, D.B.: Actin polymerization and depolymerization during apoptosis in HL-60 cells. Am. J. Physiol. **271**, C1981–1992 (1996)
56. Lichtman, M.A.: Cellular deformability during maturation of the myeloblast. Possible role in marrow egress. N. Engl. J. Med. **283**, 943–948 (1970)
57. Lichtman, M.A.: Rheology of leukocytes, leukocyte suspensions, and blood in leukemia. J. Clin. Invest. **52**, 350–358 (1973a)
58. Lichtman, M.A., Heal, J., Rowe, J.M.: Hyperleukocytic leukaemia: rheological and clinical features and management. Bailliere's Clin. Haematol. **1**, 725–746 (1987)
59. Lichtman, M.A., Rowe, J.M.: Hyperleukocytic leukemias: rheological, clinical, and therapeutic considerations. Blood **60**, 279–283 (1982)
60. Lincoln, B., Wottawah, F., Schinkinger, S., Ebert, S., Guck, J.: High-throughput rheological measurements with an optical stretcher. Methods Cell Biol. **83**, 397–423 (2007)
61. Linderkamp, O., Pöschl, J., Ruef, P.: Blood cell deformation in neonates who have sepsis. Neoreviews **7**, e517–e523 (2006)
62. Lipowsky, H.H.: Microvascular rheology and hemodynamics. Microcirculation **12**, 5–15 (2005)
63. Lokich, J.J., Moloney, W.C.: Fatal pulmonary leukostasis following treatment in acute myelogenous leukemia. Arch. Intern. Med. **130**, 759–762 (1972)
64. Lowe, E.J., Pui, C.H., Hancock, M.L., Geiger, T.L., Khan, R.B., Sandlund, J.T.: Earlycomplications in children with acute lymphoblastic leukemia presenting with hyperleukocytosis. Pediatr Blood Cancer, **45**, 10-15 (2005)
65. MacKintosh, F.C., Käs, J., Janmey, P.A.: Elasticity of semiflexible biopolymer networks. Phys. Rev. Lett. **75**, 4425–4428 (1995)
66. Michetti, C., Coimbra, R., Hoyt, D.B., Loomis, W., Junger, W., Wolf, P.: Pentoxifylline reduces acute lung injury in chronic endotoxemia. J. Surg. Res. **115**, 92–99 (2003)
67. Mielcarek, M., Sperling, C., Schrappe, M., Meyer, U., Riehm, H, Ludwig, W.D.: Expression of intercellular adhesion molecule 1 (ICAM-1) in childhood acute lymphoblastic leukaemia: correlation with clinical features and outcome. Br. J. Haematol. **96**, 301–307 (1997)
68. Moricke, A., Reiter, A., Zimmermann, M., Gadner, H., Stanulla, M., Dordelmann, M., Loning, L., Beier, R., Ludwig, W.D., Ratei, R., Harbott, J., Boos, J., Mann, G., Niggli, F., Feldges, A., Henze, G., Welte, K., Beck, J.D., Klingebiel, T., Niemeyer, C., Zintl, F., Bode, U., Urban, C., Wehinger, H., Niethammer, D., Riehm, H., Schrappe, M.: Risk-adjusted therapy of acute lymphoblastic leukemia can decrease treatment burden and improve survival: treatment results of 2169 unselected pediatric and adolescent patients enrolled in the trial ALL-BFM 95. Blood (2008)
69. Mustjoki, S., Alitalo, R., Elonen, E., Carpen, O., Gahmberg, C.G., Vaheri, A.: Intercellular adhesion molecule-1 in extravasation of normal mononuclear and leukaemia cells. Br. J. Haematol. **113**, 989–1000 (2001)
70. Myers, T.J., Cole, S.R., Klatsky, A.U., Hild, D.H.: Respiratory failure due to pulmonary leukostasis following chemotherapy of acute nonlymphocytic leukemia. Cancer **51**, 1808–1813 (1983)
71. Neuner, P., Klosner, G., Pourmojib, M., Knobler, R., Schwarz, T.: Pentoxifylline in vivo and in vitro down-regulates the expression of the intercellular adhesion molecule-1 in monocytes. Immunology **90**, 435–439 (1997)
72. Ng, L., Hung, H.H., Sprunt, A., Chubinskaya, S., Ortiz, C., Grodzinsky, A.: Nanomechanical properties of individual chondrocytes and their developing growth factor-stimulated pericellular matrix. J. Biomech. **40**, 1011–1023 (2007)
73. Nolan, G.P.: Deeper insights into hematological oncology disorders via single-cell phospho-signaling analysis. Hematology Am. Soc. Hematol. Educ. Program. **509**, 123–127 (2006)
74. Novotny, J.R., Muller-Beissenhirtz, H., Herget-Rosenthal, S., Kribben, A., Duhrsen, U.: Grading of symptoms in hyperleukocytic leukaemia: a clinical model for the role of different blast types and promyelocytes in the development of leukostasis syndrome. Eur. J. Haematol. **74**, 501–510 (2005)

75. Novotny, J.R., Nuckel, H., Duhrsen, U.: Correlation between expression of CD56/NCAM and severe leukostasis in hyperleukocytic acute myelomonocytic leukaemia. Eur. J. Haematol. **76**, 299–308 (2006)
76. Patatanian, E., Thompson, D.F.: Retinoic acid syndrome: a review. J. Clin. Pharm. Ther. **33**, 331–338 (2008)
77. Porcu, P., Cripe, L.D., Ng, E.W., Bhatia, S., Danielson, C.M., Orazi, A., McCarthy, L.J.: Hyperleukocytic leukemias and leukostasis: a review of pathophysiology, clinical presentation and management. Leuk. Lymphoma **39**, 1–18 (2000)
78. Porcu, P., Danielson, C.F., Orazi, A., Heerema, N.A., Gabig, T.G., McCarthy, L.J.: Therapeutic leukapheresis in hyperleucocytic leukaemias: lack of correlation between degree of cytoreduction and early mortality rate. Br. J. Haematol. **98**, 433–436 (1997)
79. Porcu, P., Farag, S., Marcucci, G., Cataland, S.R., Kennedy, M.S., Bissell, M.: Leukocytoreduction for acute leukemia. Ther. Apher. **6**, 15–23 (2002)
80. Pui, C.H., Robison, L.L., Look, A.T.: Acute lymphoblastic leukaemia. Lancet **371**, 1030–1043 (2008)
81. Pui, C.H., Sandlund, J.T., Pei, D., Campana, D., Rivera, G.K., Ribeiro, R.C., Rubnitz, J.E., Razzouk, B.I., Howard, S.C., Hudson, M.M., Cheng, C., Kun, L.E., Raimondi, S.C., Behm, F.G., Downing, J.R., Relling, M.V., Evans, W.E.: Improved outcome for children with acute lymphoblastic leukemia: results of Total Therapy Study XIIIB at St Jude Children's Research Hospital. Blood **104**, 2690–2696 (2004)
82. Radmacher, M.: Measuring the elastic properties of living cells by the atomic force microscope. Methods Cell Biol. **68**, 67–90 (2002)
83. Radmacher, M., Fritz, M., Kacher, C.M., Cleveland, J.P., Hansma, P.K.: Measuring the viscoelastic properties of human platelets with the atomic force microscope. Biophys. J. **70**, 556–567 (1996)
84. Ravindranath, Y., Chang, M., Steuber, C.P., Becton, D., Dahl, G., Civin, C., Camitta, B., Carroll, A., Raimondi, S.C., Weinstein, H.J.: Pediatric Oncology Group (POG) studies of acute myeloid leukemia (AML): a review of four consecutive childhood AML trials conducted between 1981 and 2000. Leukemia **19**, 2101–2116 (2005)
85. Rheinhold, S.R., Lange, B.V.: Oncologic emergencies. In: Pizzo, P.A., Poplack, D.G. (eds.) Principles and Practice of Pediatric Oncology, pp. 1177–1203. Lippincott Williams & Wilkins, Philadelphia (2002)
86. Ritter, L.S., Wilson, D.S., Williams, S.K., Copeland, J.G., McDonagh, P.F.: Pentoxifylline reduces leukocyte retention in the coronary microcirculation early in reperfusion following ischemia. Int. J. Microcirc. Clin. Exp. **16**, 170–179 (1996)
87. Rosenbluth, M.J., Lam, W.A., Fletcher, D.A.: Force microscopy of nonadherent cells: a comparison of leukemia cell deformability. Biophys. J. **90**, 2994–3003 (2006)
88. Ruef, P., Poeschl, J.M., Simon, C., Altfelder, F., Craciun, E., Linderkamp, O.: Effect of activators and the phosphodiesterase inhibitors pentoxifylline and enoximone on the deformability of neutrophils in neonates and adults. Acta Paediatr. **93**, 1288–1293 (2004)
89. Samlaska, C.P., Winfield, E.A.: Pentoxifylline. J. Am. Acad. Dermatol. **30**, 603–621 (1994)
90. Schade, U.F.: Pentoxifylline increases survival in murine endotoxin shock and decreases formation of tumor necrosis factor. Circ. Shock **31**, 171–181 (1990)
91. Schmalzer, E.A., Chien, S.: Filterability of subpopulations of leukocytes: effect of pentoxifylline. Blood **64**, 542–546 (1984)
92. Seale, J., Delva, L., Renesto, P., Balitrand, N., Dombret, H., Scrobohaci, M.L., Degos, L., Paul, P., Chomienne, C.: All-trans retinoic acid rapidly decreases cathepsin G synthesis and mRNA expression in acute promyelocytic leukemia. Leukemia **10**, 95–101 (1996)
93. Seiffge, D.: Pentoxifylline: its influence on the interaction of blood cells with the vessel wall. Atherosclerosis **131** Suppl, S27–S28 (1997)
94. Sharma, K.: Cellular deformability studies in leukemia. Physiol. Chem. Phys. Med. NMR **25**, 293–297 (1993)

95. Skoutelis, A.T., Kaleridis, V., Athanassiou, G.M., Kokkinis, K.I., Missirlis, Y.F., Bassaris, H.P.: Neutrophil deformability in patients with sepsis, septic shock, and adult respiratory distress syndrome. Crit. Care Med. **28**, 2355–2359 (2000a)
96. Skoutelis, A.T., Kaleridis, V.E., Goumenos, D.S., Athanassiou, G.M., Missirlis, Y.F., Vlachojannis, J.G., Bassaris, H.P.: Polymorphonuclear leukocyte rigidity is defective in patients with chronic renal failure. Nephrol. Dial. Transplant **15**, 1788–1793 (2000b)
97. Soares, F.A., Landell, G.A., Cardoso, M.C.: Pulmonary leukostasis without hyperleukocytosis: a clinicopathologic study of 16 cases. Am. J. Hematol. **40**, 28–32 (1992)
98. Somer, T., Meiselman, H.J.: Disorders of blood viscosity. Ann. Med. **25**, 31–39 (1993)
99. Steinberg, M.H., Charm, S.E.: Effect of high concentrations of leukocytes on whole blood viscosity. Blood **38**, 299–301 (1971)
100. Stucki, A., Rivier, A.S., Gikic, M., Monai, N., Schapira, M., Spertini, O.: Endothelial cell activation by myeloblasts: molecular mechanisms of leukostasis and leukemic cell dissemination. Blood **97**, 2121–2129 (2001)
101. Tallman, M.S., Andersen, J.W., Schiffer, C.A., Appelbaum, F.R., Feusner, J.H., Woods, W.G., Ogden, A., Weinstein, H., Shepherd, L., Willman, C., Bloomfield, C.D., Rowe, J.M., Wiernik, P.H.: All-trans retinoic acid in acute promyelocytic leukemia: long-term outcome and prognostic factor analysis from the North American Intergroup protocol. Blood **13**, 4298–4302 (2002)
102. Suresh, S.: Biomechanics and biophysics of cancer cells. Acta Biomater. **3**, 413–438 (2007)
103. Tighe, D., Moss, R., Heath, M.F., Hynd, J., Bennett, E.D.: Pentoxifylline reduces pulmonary leucostasis and improves capillary patency in a rabbit peritonitis model. Circ. Shock **28**, 159–164 (1989)
104. Tsukada, K., Sekizuka, E., Oshio, C., Minamitani, H.: Direct measurement of erythrocyte deformability in diabetes mellitus with a transparent microchannel capillary model and high-speed video camera system. Microvasc. Res. **61**, 231–239 (2001)
105. Vanapalli, S.A., Duits, M.H., Mugele, F.: Microfluidics as a functional tool for cell mechanics. Biomicrofluidics, **3** 12006 (2009)
106. Ventura, G.J., Hester, J.P., Smith, T.L., Keating, M.J.: Acute myeloblastic leukemia with hyperleukocytosis: risk factors for early mortality in induction. Am. J. Hematol. **27** 34–37 (1988)
107. Ward, A., Clissold, S.P.: Pentoxifylline. A review of its pharmacodynamic and pharmacokinetic properties, and its therapeutic efficacy. Drugs **34**, 50–97 (1987)
108. Wurthner, J.U., Kohler, G., Behringer, D., Lindemann, A., Mertelsmann, R., Lubbert, M.: Leukostasis followed by hemorrhage complicating the initiation of chemotherapy in patients with acute myeloid leukemia and hyperleukocytosis: a clinicopathologic report of four cases. Cancer **85**, 368–374 (1999)

Author Index